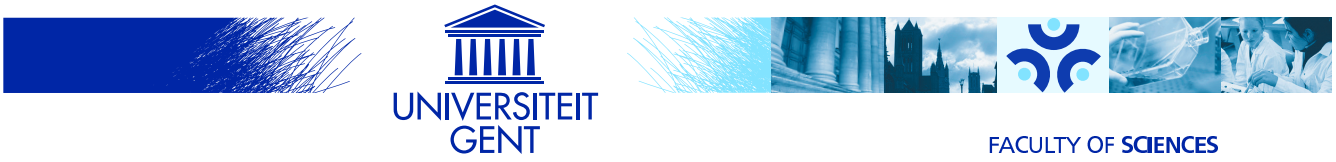

Data-driven determination of $Z(\nu\nu)$ background to new-physics searches with jets and missing transverse momentum at CMS

Piet Verwilligen

Promotoren: Prof. dr. Dirk Ryckbosch en dr. Michael Tytgat

Proefschrift ingediend tot het behalen van de academische graad van
Doctor in de Wetenschappen: Fysica

Universiteit Gent
Faculteit Wetenschappen
Vakgroep Fysica en Sterrenkunde
Academiejaar 2011-2012

Acknowledgments

Its been a long road getting here. I wish to extend a very warm thanks to everybody who supported me over the last few years. Firstly, I would like to thank my promoter, Dirk Ryckbosch, for giving me the opportunity of pursing a Ph.D. in the experimental particle physics group in Gent. Dirk, I will truly miss all non-verbal communication and the roll-playing tutor/student situations when crossing in the corridor. Thanks for your encouragement, for the nice atmosphere you created at the lab and the patience you had with me when I jumped into your office for yet another question. My friends know how much I can ask – fools would be jealous – but you answered all of them. Martin, the same holds for you, thanks for your detailed answers on all CMS, trigger and physics related questions. Thanks Michael, for introducing me to CMS, for all useful discussions we had, and – last but not least – for introducing me to the right people.

Steven, Maria, Sue Ann, Riccardo and Roberto, you guided me around the maze that is jets plus missing transverse momentum analysis. I am indebted to you for the trust you placed in me whilst working on the $Z(\nu\nu)$ background. You explained every little detail of how to do physics analysis in these exciting times. I was blown away by the deep physics, detector and accelerator knowledge you all possess. I learned so much in such a short time, it really made my head spin. I am very grateful to you for kindly adopting me as a seventh member in your office, where we spent many nights together working towards the final results. Although the pressure was huge, the atmosphere was really friendly and there was always time for a good laugh (isn't that right Sue Ann?).

I owe many thanks to everybody in the RPC community. It was a pleasure to work on such a magnificent piece of jewelry as the Resistive Plate Chambers. My gratitude goes especially to Pino, Marcello, Anna, Marcin, Tomasz and Karol for all help and useful discussions and the confidence you had in the upgrade simulations I performed. It was only afterwards that I realized how important this study was for CMS, thanks for your trust in me. Flavio, Marcello and Marcello: the discussions I had with you concerning the RPC working principles and the details of the signal creation and processing were really enlightening. I am indebted to Tim Cox, Mika Huhtinen and Ivan Mikulec for the useful discussions about the expected background in the muon system. Thanks also to Ingo Bloch for the valuable help with simulating the RPC trigger rate and Vadim Khotilovich and Rick Wilkinson for the introduction to the CSC neutron simulation code and for all help with the RPC neutron simulation. You are all very busy people, thanks for finding (making) some time to discuss all these things with me.

Ik zou ook graag Philippe Van Auwegem en Patrick Sennesael willen bedanken voor hun hulp tijdens het opbouwen van het RPC lab in Gent. Jullie bleven me verbazen met supergoede technologische oplossingen voor alle problemen die we tegen kwamen, jullie hebben echt gouden handen! Rudi, bedankt voor je hulp bij het maken van alle mooie figuren en praktische raad. Daniella en Linda, bedankt me bij te staan bij de – wijlen heroische – gevechten met SAP. Bart,

Christophe en Roland, bedankt voor alle hulp bij electronische, computationele en andere kleine probleempjes. Olivier, Shkelzen, Stephane and Joris, thanks for being with me when my jobs were at most danger. I really appreciated having a hotline in times of crisis.

Filip and Lukas: you were the best office mates I could dream of. I really appreciated your presence in the office, I hope you tolerated mine. Thanks for your understanding when bothering you with yet another question. It was great to have our own blackboard. Tom, what would the three musketeers be without d'Artagnan? Although you were not allowed in our office, since you did not (and still don't) have a driving licence, we had a lot of fun at the at the summer schools and all the official (and unofficial) occasions. Thanks guys, it was really nice to have you around! Thanks Michael, Freija, Arne, Simon, Alberto and all the other colleagues in the experimental particle physics research group. I think I can safely say that the atmosphere we have in our research group is truly unique! I had a lot of fun during the road trips to Geneva in the party bus, the nightly kubb and Frisbee games and the table tennis competition. Thanks Michael, I could always come to you for any question I had, for carefully proofreading English texts, for helping me in my never-ending quest to translate the Dutch expressions I adore using and for keeping me with both feet on the ground.

I would like to thank all my other colleagues at the Institute for Nuclear Sciences (INW) at Gent University for the really nice atmosphere: Pieter, Lesley, Brecht and many more. Unfortunately some of you had to move to more technologically orientated settlements of the university in Zwijnaarde, but you will stay forever part of us! We had glorious movie nights, late Ph.D. defense parties, fun Christmas parties, and really nice unofficial barbeques. Jutho, Matthieu, Stephane, Wouter and Eva I really enjoyed our pub-crawls in Gent and thanks for understanding. It was not always easy for me to fit these into my overly full agenda.

Mr White, thanks for coming and catching me at my desk at CERN and initiating me in the CMS Center. You were a beacon to me, introducing me into the RPC offline shifts. We spent a lot of time together in the CMS Control Room, filled with debugging code, running jobs, debugging code, debugging code and debugging code. Dazed and confused, we set the controls for the heart of the sun. I'll never forget. Thanks Raffaello and Salvatore for helping me with the CMS software, the patience you had with me while I was learning, for the solution to every little problem I had, for the help with the RPC upgrade simulations and so much more.

A special thank you goes out to all the friends I made at CERN. Thanks Gianni, Anna, Camilo, Salvatore, Claudio, and so many more, for the long hours we spent together in P5, checking cables and gas leaks, for the long hours we spent analyzing data and for the good food and nice company. Thanks Alberto for introducing me to the Colombian gang: Camilo, Andres, Juan Carlos, Luis, German, Serkan (the Meister), Guillermo and so many more, it was pleasure for me. I really enjoyed inviting you for dinners at the Belgian apartment, the nice barbecues we had, the nightly chats, playing football in the rain or just having a beer in the canteen. You made a warm home for me at CERN and helped me keep a balance between work and leisure and, not forgetting, provided a listening ear.

Een dikke dank-je-wel voor mijn vrienden uit de chiro, van de Stekense oudleiding, de Reinaertse gewesters, het verbond tot de chiro enthousiastelingen van Nationaal. Jullie zijn écht met teveel om op te noemen. Bedankt voor de zware weekendjes, leuke fietstochtjes en omdat er altijd wel iemand in de Cramme zit om een praatje met te slaan. Vossige Reinaerders, het was een geweldig leuke tijd om samen met jullie, en de vrienden van De Regio, zoveel projecten uit de

grond te stampen: SB, Aspitrant, KIC, de Krinkel. Het was plezant om met julle cursussen te begeleiden, sotte themas uit te denken en tot in de puntjes af te werken, op de PL door te bomen over de inhoudelijke lijn van de Chiro. SOM'ers, we hebben dit jaar een geweldige stap vooruit gezet in het ondersteunen van Chirogroepen in nood. Een goed begin waar véél meer uit kan groeien. Bedankt om met jullie allemaal aan de Chiro te bouwen, keep up the good work!

Mama, papa, bedankt voor wat jullie opgebouwd hebben. Hoedje af, écht waar! Het is altijd plezant terug thuis te komen, met mijn blote voeten door het gras te lopen of bij te praten met een warme tas thee, mijn rug zachtjes tegen de warme kachel gevleid. Bedankt voor het lekkere eten dat altijd in no-time op tafel wordt getoverd, 't is best leuk zo verwend te worden. Jan, 't is geweldig je jongere broer te zien veranderen in je beste vriend! Tine, bedankt voor dat stukje Koornaarstraat in Gent. Meter, pepe, mijn kleine maar gezellige familie, het blijft een plezier bij jullie binnen te springen, de gezellige zondagavonden ga ik ongelooflijk hard missen.

Bedankt Fre, Cindy, Raf, Timo, Katrien en Cedric. Het is leuk met jullie wandelingen te maken in de Polder, koffie te drinken bij een stukje taart, na al die jaren nog eens te moshen in de pitt, of gewoon mijn voeten eens onder tafel te mogen steken voor een goede maaltijd en hartige babbel en een lekkere tas thee.

Zomerstraat boys and girls! Drie jaar heb ik bij jullie mogen vertoeven, van geen enkele dag heb ik spijt, dit waren drie héél aangename jaren. Beginnend met een schuchter "Ik ben wel geinteresseerd in die kamer" tot het platlopen van elkaars deur als we nood aan gezelschap hadden, een spelletje wouden spelen of om even je hart te luchten. Ik heb een geweldige tijd gehad bij jullie, dit was een echte thuis. Stijn, Stefanie, Jesse, ik ga jullie missen!

I would like to thank everybody who painted a smile on my face. You made my day time and again! The good life is hidden in the small things, enjoy!

Contents

Introduction

During the twentieth century, enormous advances have been made in understanding the nature of the matter around us. These insights have been accomplished by equal progress in experimental physics and advances in theoretical physics. Ernest Rutherford proved the existence of the nucleus by shooting α-particles at a foil of gold. Niels Bohr established a theoretical model describing atoms as a cloud of electrons at different energy levels, circling around a positively charged nucleus. During the first part of the twentieth century quantum mechanics was established both theoretically and proved experimentally. During the second part of the twentieth century many new particles were discovered by experimentalists. This lead to the development of the Standard Model of particle physics, which describes the electromagnetic, strong and weak force.

The Standard Model describes all fundamental particles, i.e. six quarks and six leptons, and the interactions between those particles mediated by gauge bosons. The predictions of the Standard Model were verified experimentally at particle accelerators, with a precision of 1 ppm. This is an unprecedented success for a theory spanning several orders of magnitude in energy. However, there is still a part of the puzzle missing. The Standard Model is essentially a massless theory and explains only partially the mass of the particles. In 1964, the Belgian physicists Robert Brout and François Englert, and the Scotsman Peter Higgs proposed a mechanism in which the particles of the Standard Model gain mass by interaction with the so-called Higgs-field. The Higgs-particle, quantum of the Higgs-field, is not yet discovered and its observation is one of the main goals of the Large Hadron Collider (LHC), built by the European Centre for Nuclear Research (CERN), in Geneva.

The discovery of the Higgs-particle would by no means be the end of the story. If the Higgs-particle exists (there are alternative, but less straightforward theories for the generation of the masses of the particles), it would give us no clue as to why its mass will have the value required by the current experimental constraints of the precision measurements of the Standard Model. This lead to the development of a wealth of new theories, in which the Standard Model would only be the low-energy version. One of those theories is Supersymmetry and this theory predicts the existence of a mirror-particle for each existing particle in the Standard Model. This means that there should be a whole spectrum of new particles, the lightest predicted to be not much heavier than ten times the Higgs-particle. This thesis describes the search for these new supersymmetric particles in proton-proton collisions recorded in 2010 at the LHC.

The LHC started operation at centre-of-mass energy of 7 TeV on March 30$^{\text{th}}$, 2010. At the points where protons are brought into collision, experiments are constructed, aimed at reconstructing the collisions and measuring their properties. Two general-purpose experiments were built: ATLAS and CMS. Furthermore, a b-physics experiment was built: LHCb. The LHC can also accelerate and collide heavy ions, for which a dedicated heavy-ion physics experiment, ALICE,

was constructed.

The CMS experiment was built to record and reconstruct proton-proton collisions with very high precision. These events can contain muons, which produce very important signatures at hadron colliders, since they are rare and are of particular interest in studying very-high-energy phenomena. Since the muons are not well measured by traditional tracker and calorimeter detectors, special muon detectors have been built. At full intensity, the LHC will collide protons every 25 nanoseconds. This results in an average of 40 million collisions per second. At the current level of data-acquisition (DAQ) technology, it is impossible to record the data from all of these collisions. Therefore, selection procedures are in place, called "triggers". The trigger of the detector consists of two levels: the Level-1 Trigger (L1) made of custom electronics and the High-Level Trigger (HLT) which uses a farm of computers to implement advanced selection algorithms.

The muon trigger relies on dedicated muon timing detectors: Resistive Plate Chambers (RPCs), which not fully in place for the first run of LHC in 2010. The original design foresaw four layers of RPCs, but only three layers have been installed. These three layers performed very well during first collisions, but their performance will not satisfy for the LHC running at full intensity and at least four layers are thought to be necessary. Furthermore, a study performed in 2002 showed that a trigger relying on five layers of RPCs would improve the performance of the RPC trigger. Unfortunately it is not feasible to install a fully independent fifth layer, but it was suggested that incorporating the fifth plane in a double second layer of RPCs would result as well in an improved trigger performance. In this thesis the performance of the proposed double second station was studied. This part constitutes the more technical part of the work I performed for the CMS collaboration.

The thesis is outlined as follows: In the first chapter the physics motivation for the LHC and for supersymmetric particles is stated. The second and third chapter discuss the LHC accelerator and the CMS experiment. The fourth chapter is devoted to the reconstruction of the physics event, starting from the basic information recorded by the various subdetectors of CMS. In the fifth chapter the RPC trigger study is discussed. The sixth, seventh and eight chapters discuss the search for supersymmetric particles in the data recorded during the first year of physics operation of the LHC. At the end a glossary of all terms and abbreviations often used in CMS is given.

Part I

Motivation and Experimental Setup

Bliss was it in that dawn to be alive, But to be young was very Heaven!
William Wordsworth, 1770-1850

French revolution as it appeared to enthusiasts at its commencement.
Extract from “The Friend” [1].

Chapter 1

Physics Motivation

Four centuries before the common era (BCE) the Greek philosopher Democritus and his master Leucippus wondered about the origins of matter. They opposed the widespread view of all matter built up from "Earth", "Wind", "Water" and "Fire". They wondered if one could break a piece of wood an infinite amount of times. They argued that after a finite amount of breaking the wood, the wood would not be divisible anymore, consisting of just one particle carrying all characteristics of the wood, which they named "atomos", meaning indivisible.

Although these ideas are rather close to modern atom theory, one can consider this as a "lucky hypothesis", as stated by Bertrand Russell [2], since it is obvious that the Greek philosophers had no solid empirical basis for their atom theory. However, "De Rerum Natura", describing the Epicurean philosophy and written by the Roman poet Lucretius (1st century BCE) gives some insight how observations of Nature lead to the original atom theory.

Francis Bacon (1561–1621) can be considered as the father of empiricism. Bacon established the so-called "Scientific Method", where inquiry must be based on gathering empirical and measurable evidence for hypothesis. The Oxford English Dictionary states:

> **scientific method** *n.* a method of procedure that has characterized natural science since the 17th century, consisting in systematic observation, measurement, and experiment, and the formulation, testing, and modification of hypotheses.

By the beginning of the twentieth century the Scientific Method was well established. In 1911 Rutherford collided α-particles on a foil of gold and investigated particles with very high deflection angle (almost 180°), which was not expected by the current theories. Interpreting his results he discovered the existence of the nucleus inside atoms. Atoms are made of a positively charged nucleus, carrying almost all of the atoms' mass, surrounded by a cloud of electrons. Rutherfords work established the nuclear structure of matter and he is considered the father of nuclear physics. A century after the discovery of the nucleus, particle collisions are still used to shed light on the fundamentals of matter, and is still the main method to study the properties and behaviour of these particles.

Colliding particles to investigate nature can be seen as the equivalent, at very high energies, of how we observe things in our daily life. When we "see" something, that is because there is a light source, often the sun, sometimes a light, shining on an object. The object reflects (scatters) the light, and this light is focused on the retina by lens in our eye. Light sensitive nerves (detectors) transcode this information and send it to the brains, where the global image

is assembled. In high-energy physics, we study protons by colliding another proton against it, and detect the scattering products with detectors that encode the information in electrical signals, sent to computers for reconstruction of the collision.

This chapter provides a short description of the Standard Model in section 1.1. It aims in no way to give a correct historic or a fully detailed overview. It does in no way justice to all people who worked on these theories and made extremely important discoveries, finally elucidating the underlying structures and symmetries of Nature. Thereafter an overview of the successes and challenges to the Standard Model are presented in section 1.2 and 1.3. One of the most promising frameworks for the extension of the Standard Model is Supersymmetry, of which a corner of the veil is lifted in section 1.4. Finally in section 1.5 the use of protons as experimental probes to investigate Nature at the TeV scale is discussed.

1.1 Quick overview of the Standard Model

1.1.1 The particles of the Standard Model

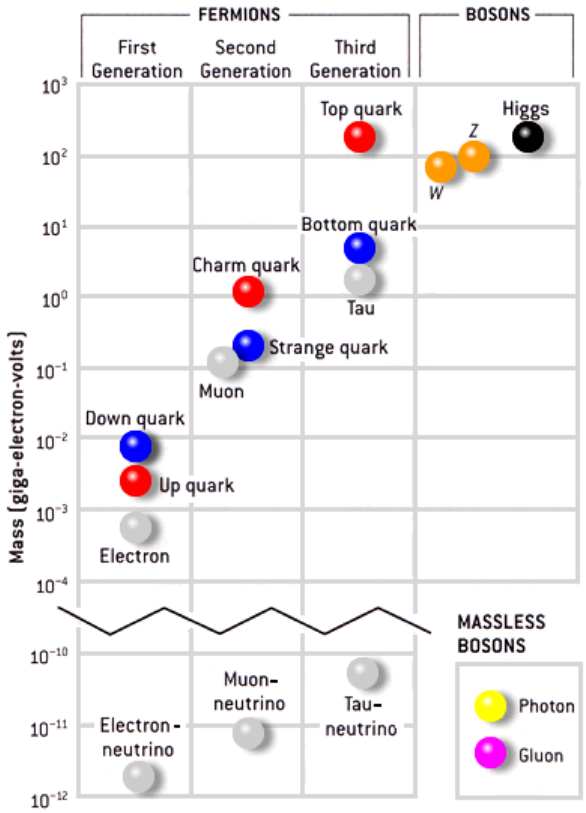

Figure 1.1: Masses of the different particles of the Standard Model. Figure taken from Reference [3].

The particles constituting all terrestrial matter are up- (u) and down- (d) quarks, combined to form protons (uud) and neutrons (udd) in the atomic nucleus, and surrounded by a cloud of electrons (e). Additionally there is a neutrino, which is created in nuclear β-decay. The quarks, electron and neutrino are fundamental particles, i.e. they do not constitute of other particles, and they are fermions, i.e. particles with half-integer spin. These fermions are the fundamental building blocks of matter in the Standard Model. The up quark has an electric charge of $+\frac{2}{3}\,e$, while the down quark has $-\frac{1}{3}\,e$. The electron has a negative unity charge: $-e$ and the neutrino is a neutral particle. All matter found on earth constitutes of these four particles, but apparently there exists three generations or families, each consisting of four particles. This means that all particles come in three variants, with exactly the same properties, except for their mass. Although all matter on earth is built from particles from the first generation, the Universe could also have been built from particles from the second or third generation, if they were stable.

The fermions of the Standard Model can be divided into quarks and leptons. The quarks are the up- (u) and down- (d) quark, the charm (c) and the strange (s) quark and the bottom (b) and

the top (t) quark. The leptons can be either charged: the electron (e), muon (μ) and tau (τ) or neutral: the neutrinos. Figure 1.1 shows a diagram of the particles, sorted by generation and ordered according to their mass. Note that the mass scale is logarithmic. Each generation is drastically more massive than the previous one. In the Standard Model, neutrinos are described as massless particles, although recent experiments demonstrated that these particles have non-vanishing but very small masses.

The Standard Model describes three of the four known forces: electromagnetism, and the weak and the strong force. These forces are mediated by the exchange of new particles, the vector bosons. Two of them are massless: the photon, responsible for the electromagnetic force and the gluon, mediating the strong force. Two others have a mass $\sim 80\,\text{GeV}$ and $\sim 90\,\text{GeV}$: the $W^{\pm}$ and the Z^0 particles, responsible for the weak force. These force-carriers are also listed in Figure 1.1, together with the postulated Higgs boson, which is responsible for the mass of all particles. This particle is not yet found and is one of the missing pieces of the Standard Model.

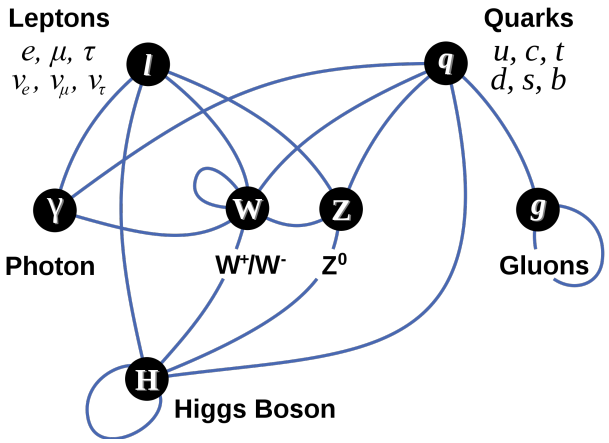

Figure 1.2: Diagram of interactions between the constituents of the Standard Model © Wikipedia.

Photons are exchanged between particles having an electric charge. Similarly gluons are exchanged between particles with a colour charge. Only quarks and gluons have colour charge and these are the only particles subject to the strong force. This colour charge comes in three flavours, named after three colours: red r, green g and blue b. Contrary to the photons, which are electrically neutral, the gluon itself has a colour charge and hence can interact with itself. The force-carriers of the weak interaction, the $W^{\pm}$ and Z^0 bosons only interact with particles with the "weak charge" (g), except for the $W^{\pm}$ which can interact with the photon as well due to its charge. All particles, apart from the gluon and the photon, carry weak charge. The postulated Higgs boson interacts with all massive particles. Figure 1.2 shows a graph of allowed interactions between the particles of the Standard Model. The Standard Model has solid mathematical foundation in the theory of gauge symmetries. This will not be detailed here, for more rigorous treatments, see textbooks, such as [4].

1.1.2 The interactions in the Standard Model

The electromagnetic interaction is described by the $U(1)$ symmetry, which has one single generator[1], leading to one single particle mediating the electromagnetic force: the photon. The weak interaction is described by the $SU(2)_L$ symmetry, with three generators[2], leading to three gauge bosons: W^+, W^-, Z^0 mediating the weak force. The subscript L indicates that the weak interaction only couples to left-handed particles. The strong force is governed by the $SU(3)$ symmetry, leading to eight different gluons. The weak and electromagnetic forces were found to be invariant under the very same symmetries and could therefore be unified by a single – electroweak – interaction, described by the $U(1)_Y \otimes SU(2)_L$ symmetry. The theoretical properties of all Standard Model fermions are provided in Table 1.1.

The electroweak interaction can be elegantly described by introducing a new quantum number: the weak isospin T. Each family of left-handed quarks and leptons forms a doublet of fermions which can transform into each other by emitting or absorbing a W boson. These left-handed fermions have weak isospin $T = 1/2$ and the third component $T_3 = \pm 1/2$. Right-handed fermions do not couple to W bosons and are described as singlet states ($T = T_3 = 0$). Conservation of T_3 requires the assignment of $T = 1$ and $T_3(W^\pm) = \pm 1$. These two states cannot be grouped in a doublet, but have to be grouped in a triplet. Hence a third state should exist with $T = 1$ and $T_3 = 0$. This cannot be the Z^0 boson, since it should couple with the same strength as the $W^\pm$ bosons to fermions. This state is denoted W^0. One now postulates the existence of an additional state B^0, which is the corresponding weak isospin singlet ($T = 0$ and $T_3 = 0$). The electroweak unification is obtained by describing the photon and the Z^0 as mutually orthogonal, linear combinations of the B^0 and W^0 states:

$$|\gamma\rangle = \cos\theta_W \left|B^0\right\rangle + \sin\theta_W \left|W^0\right\rangle, \tag{1.1}$$

$$\left|Z^0\right\rangle = -\sin\theta_W \left|B^0\right\rangle + \cos\theta_W \left|W^0\right\rangle. \tag{1.2}$$

This mixing is expressed as a rotation trough the weak mixing angle θ_W, also known as the Weinberg angle. This Weinberg angle determines the strength of the weak interaction by relating its coupling constant g to the electromagnetic interaction coupling constant e:

$$e = g \cdot \sin\theta_W. \tag{1.3}$$

The Weinberg angle can be determined from ν–e scattering, out of the width of the Z^0 boson or from the ratio of the masses of the $W^\pm$ and Z^0 bosons [5]:

$$\rho = \frac{M_W^2}{M_Z^2 \cos^2\theta_W} \equiv 1, \tag{1.4}$$

leading to:

$$\frac{M_W}{M_Z} = \cos\theta_W = 0.8819 \pm 0.0012,$$

$$\sin^2\theta_W = 0.23124 \pm 0.00024.$$

[1] The unitary group $U(N)$ has N generators.

[2] The special unitary group $SU(N)$ has $N^2 - 1$ generators.

Table 1.1: The fermionic particles of the Standard Model. Quarks can have three different colour charges: red, green or blue.

Fermions	Generations 1	2	3	Electric Charge	Colour Charge	Spin	Isospin T_3 (3^{rd} comp.)
units				$[e]$	$[r,g,b]$	$[\hbar]$	[-]
Leptons	$\begin{pmatrix}\nu_e\\ e\end{pmatrix}_L$	$\begin{pmatrix}\nu_\mu\\ \mu\end{pmatrix}_L$	$\begin{pmatrix}\nu_\tau\\ \tau\end{pmatrix}_L$	0 -1	- -	1/2 1/2	1/2 -1/2
	e_R	μ_R	τ_R	-1	-	1/2	0
Quarks	$\begin{pmatrix}u\\ d\end{pmatrix}_L$	$\begin{pmatrix}c\\ s\end{pmatrix}_L$	$\begin{pmatrix}t\\ b\end{pmatrix}_L$	+2/3 -1/3	r,g,b r,g,b	1/2 1/2	1/2 -1/2
	u_R	c_R	b_R	+2/3	r,g,b	1/2	0
	d_R	s_R	t_R	-1/3	r,g,b	1/2	0

Unfortunately, all these gauge fields are massless fields. This is not a problem for the electromagnetic and the strong interaction, mediated by massless photons and gluons, but is problematic for the weak interaction, which is mediated by massive gauge bosons. Adding mass terms to the Lagrangian leads to unrenormalizable divergences. Generation of the masses of the electroweak gauge bosons is called the electroweak symmetry breaking (EWSB) and understanding this EWSB mechanism is one of the primary goals of the LHC.

In the Standard Model, the electroweak symmetry breaking is achieved via the Higgs mechanism [6–9], based on the idea of spontaneous symmetry breaking [10–14] and comprehensibly explained in review articles [15, 16]. The Higgs mechanism uses the idea of spontaneous symmetry breaking to achieve massive $W^\pm$ and Z^0 vector bosons and, as a bonus, a scalar Higgs particle, that is not yet observed. At the same time this mechanism is also able to provide masses to all the quarks and charged leptons in the Standard Model. The Standard Model cannot be considered to be complete as long as the Higgs boson is not observed experimentally and its fundamental properties such as its mass, spin and other quantum numbers are measured [15].

1.2 Success of the Standard Model

1.2.1 Establishment of the electroweak theory

The biggest success of the Standard Model was the prediction and discovery of the $W^\pm$ and Z^0 particles. In 1932 Fermi constructed a four-point effective theory to explain the nuclear β-decay on the electromagnetic interaction, but this theory suffered divergences at high energy. In the light of the success of QED, which is the gauge theory explaining the electromagnetic interaction, physicists tried to build a gauge theory for the weak interaction. At the end of the 1960's, Glashow, Salam and Weinberg succeeded in making a gauge theory, and they predicted that, apart from the charged current interaction responsible for the nuclear β-decay, there should also be a neutral current interaction to achieve the cancellation of divergences. Shortly thereafter Veltman and 't Hooft proved that this theory was renormalizable [17], firmly estab-

lishing the mathematical foundations of the weak interaction to be a gauge theory. At CERN, the Gargamelle bubble chamber recorded neutrino – proton interactions and established the discovery of the weak neutral currents in 1973 [18–20].

Ten years later, the Super Proton Antiproton Synchrotron (Sp$\bar{\text{p}}$S) delivered $p\bar{p}$ collisions to the UA1 and UA2 experiments at centre-of-mass energies 540 GeV, leading to the discovery of the W boson in January 1983 [21, 22], followed by the discovery of the Z boson a few months later in May 1983 [23, 24]. This major success lead to the nearly instantaneous award of the Nobel prize to Carlo Rubbia and Simon van der Meer in 1984.

1.2.2 Electroweak precision measurements of W and Z bosons

A second step was the determination, with high precision, of the properties of the $W^{\pm}$ and Z^0 bosons that are responsible for the weak interaction. This was done at the Large Electron Positron (LEP) collider and at the Stanford Linear Collider (SLC). Both accelerators collided positrons on electrons and were operational from 1989 to 1995. About 17 million Z^0 bosons were created in LEP and about 600 000 Z^0 boson events were recorded at SLC. Figure 1.3(a) shows the hadronic cross section: $e^+e^- \rightarrow q\bar{q}$ as a function of the centre-of-mass energy. Both LEP and SLC scanned the Z^0-lineshape in steps of $\sim$ 1 GeV around the Z-mass peak and obtained a remarkable agreement with the Standard Model prediction.

Figure 1.3(b) shows the lineshape of the Z^0-boson as well as the Standard Model prediction given the existence of two, three or four light neutrino species. The number of light neutrino species is measured to be 2.9840 ± 0.0082, well in agreement with the known three neutrino species. At that time there was a firm belief that neutrinos were exactly massless (as the photon is) and this measurement was interpreted as the proof of the existence of exactly three generations in the Standard Model. Ten years ago measurements of the atmospheric [25] and solar [26] neutrino flux indicate that neutrinos are not massless. Therefore it is still possible that there exists a fourth, even more heavy, generation, if the mass of the fourth neutrino is higher than half of the Z^0-boson mass.

The very precise measurement of the Z^0-mass and -width at LEP and SLC, as given in Table 1.2, allowed for high precision tests of the Standard Model. Although the top quark was not yet discovered, through radiative corrections on the Z-pole data, the existence of the top could not only be established, but its mass could be predicted[3] with an incredible precision: $m_t = 173^{+13}_{-10}\,\text{GeV}/c^2$.

From 1996 to 2000 LEP ran with an increased centre-of-mass energy from 160 GeV to 210 GeV, probing the W^+W^- production. About 40 000 W-pairs were recorded and this allowed for the determination of the $W^{\pm}$ mass and width, detailed in Table 1.2. Remarkable results for the $W^{\pm}$

[3] In November 1994, before the discovery of the top quark at the Tevatron, a global analysis of the LEP-I data by the LEP Electroweak Working Group (LEP EWWG) [27] led to the indirect determination of [28]:

$$m_t = 178 \pm 11^{+18}_{-19}\,\text{GeV},$$

where the central value corresponds to an assumption of the Higgs boson mass of $M_H = 300\,\text{GeV}$, with the first uncertainty (± 11) being experimental while the second uncertainty reflects the shift in the predicted central value of the top mass (m_t) due to the assumption of $M_H = 65\,\text{GeV}$ ($-19\,\text{GeV}$) or $M_H = 1\,\text{TeV}$ ($+18\,\text{GeV}$) [28]. Later on more precise determinations of M_W, measured both at Tevatron and LEP-II, were used to improve the central value and uncertainty of the m_t prediction.

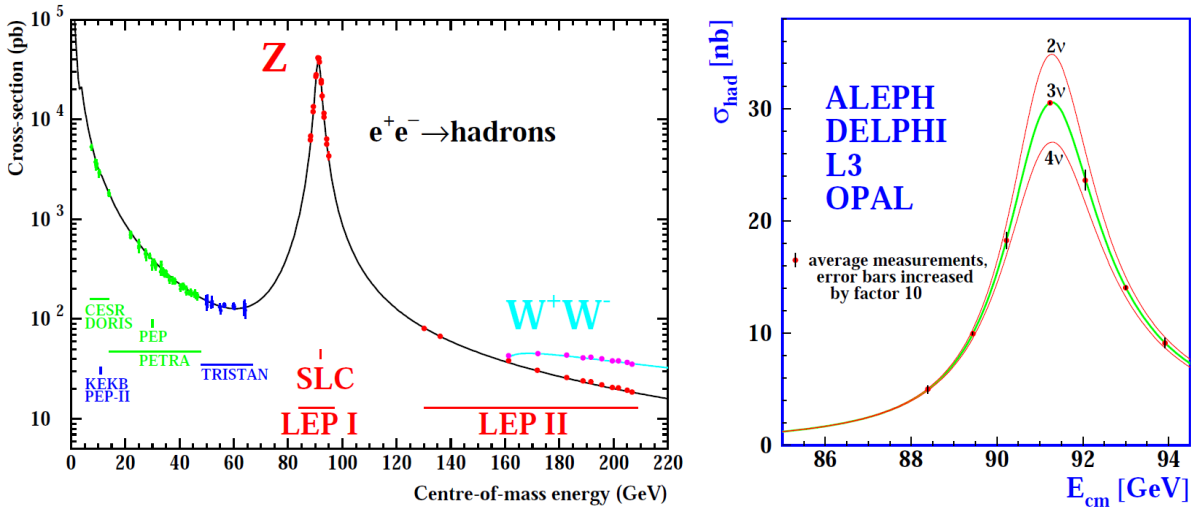

(a) Hadronic cross section (b) Z^0 lineshape

Figure 1.3: The hadronic cross section as a function of centre-of-mass energy of e^+e^- collisions (a). The solid line is the prediction of the Standard Model, the points are the experimental measurements. Also indicated are the energy ranges of the different accelerators providing the e^+e^- collisions to the experimental facilities. Detail of the measurement of the hadronic cross section around the Z resonance (b). The curves indicate the predicted cross section for two, three and four neutrino species with Standard Model couplings and negligible mass. Figures taken from Reference [29].

mass are obtained for a fit of global electroweak data (see section 1.2.3), when the experimental data on M_W is not included in the fit: $M_W = 80.363 \pm 0.032\,\text{GeV}/c^2$ [29], this precision was higher than the experimental precision at that time. Only with the advent of W physics at Tevatron, a hadron collider nota bene, an improved mass resolution was obtained, as could be seen in Table 1.2.

1.2.3 Global fits to the electroweak precision measurements

Precision measurements can be used to probe physics at higher energy scales than the masses of the particles directly involved (produced) in the experimental reactions. Therefore precision measurements are combined with accurate theoretical predictions. These theoretical predictions contain small radiative corrections, which are sensitive to physics at higher energy scale. Theory and experimental data are confronted and unknown (as well as experimentally known) model parameters are constrained by means of multi-parameter fits. For cases where the parameter space is overconstrained, it is possible to derive p-values for the compatibility between data and theoretical model and hence to directly assess the validity of the model.

Such multiparameter fits has been done by the Zfitter group [33] and the Zfitter routines [34, 35] has been used extensively by the LEP EWWG. Another group, Gfitter [36], provides regular updates on the analysis of the Standard Model in the light of the electroweak precision data [37]. Here we present the August 2011 update of these fits [32], which was the latest[4] at the time of writing. These include the newest experimental results on the top quark mass, the W mass

[4]The latest plots can be found on the Gfitter website: `http://gfitter.desy.de/` [36]. The update of May 2012 includes the direct searches for the Higgs boson performed on the LHC data collected in 2011.

Table 1.2: Precision measurement of Z^0 and $W^{\pm}$ properties. The measurements at the Z^0-pole are based on the data of LEP-I and SLC, while for the measurement of $W^{\pm}$ mass, data of LEP-II and Tevatron were used.

LEP-I: 1989-1995	$\sqrt{s} \approx 90\,\text{GeV}$		Source: [29]
Z Mass	M_Z	91.1875±0.0021	[GeV/c^2]
Z Width	Γ_Z	2.4952±0.0023	[GeV/c^2]
	ρ^{ℓ}	1.0050±0.0010	[-]
Weak Mixing Angle	$\sin^2\theta^{\ell}_{\text{eff}}$	0.23147±0.00016	[-]
LEP-II: 1996-2000	$160 \lesssim \sqrt{s} \lesssim 210\,\text{GeV}$		Source: [30]
W Mass	M_W	80.375±0.033	[GeV/c^2]
W Width	Γ_W	2.196±0.084	[GeV/c^2]
LEP-Tevatron Combination: 2007			Source: [31]
W Mass	M_W	80.398±0.025	[GeV/c^2]
W Width	Γ_W	2.140±0.060	[GeV/c^2]

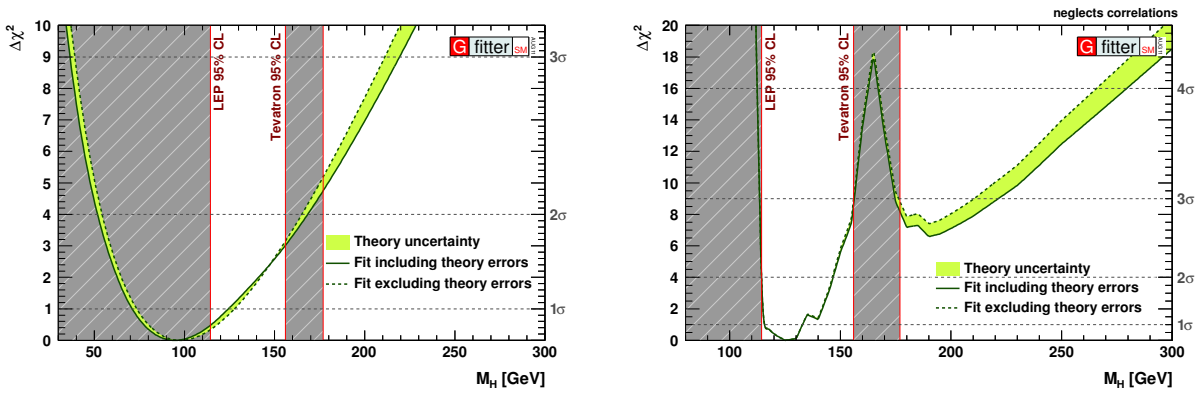

(a) (b)

Figure 1.4: $\Delta\chi^2$ as a function of the Higgs boson mass (M_H) for a global fit of the electroweak data. The gray shaded vertical bands show the exclusion of the direct Higgs searches, as of August 2011: using up to 8.6 fb^{-1} of analyzed Tevatron data and 40 pb^{-1} of analyzed ATLAS and CMS data. The left figure (a) shows the "standard fit", the right figure (b) the "complete fit", including the results of the direct Higgs boson searches. Figures taken from the Gfitter group [32].

and width and exclusion regions of the Higgs boson mass as of August 2011. Figure 1.4(a) shows the deviation ($\Delta\chi^2 = \chi^2 - \chi^2_{\text{min}}$) of the global fit of the electroweak data as a function of the hypothetical mass of the Higgs boson, resulting in a best fit for the Higgs boson mass of 94^{+31}_{-24} GeV [32]. Both at LEP and the Tevatron experiments, direct searches for the Higgs boson have been performed, which are indicated as grey shaded exclusion areas in the figure. Including these direct searches, as of August 2011, where ATLAS and CMS did not challenge the exclusion limits of the Tevatron experiments yet, a new global fit is performed as shown in Figure 1.4(b). The best fit value for the Higgs boson mass is now 120^{+12}_{-5} GeV [32]. Also the

mass of the W boson could be determined from a fit [32]:

$$M_W = (80.362 \pm 0.013)\,\text{GeV},$$

which is 1.6σ below, and exceeds in precision, the CDF and DØ combination ($\sim 1.2\,\text{fb}^{-1}$) [38]:

$$M_W = (80.420 \pm 0.031)\,\text{GeV}.$$

The world average, including also the LEP results obtained with less statistics, is [5]:

$$M_W = (80.399 \pm 0.023)\,\text{GeV}.$$

A new CDF and DØ combination ($\sim 5.3\,\text{fb}^{-1}$) was presented during the Moriond 2012 conference:

$$M_W = (80.375 \pm 0.023)\,\text{GeV},$$

with still not all Tevatron data analyzed.

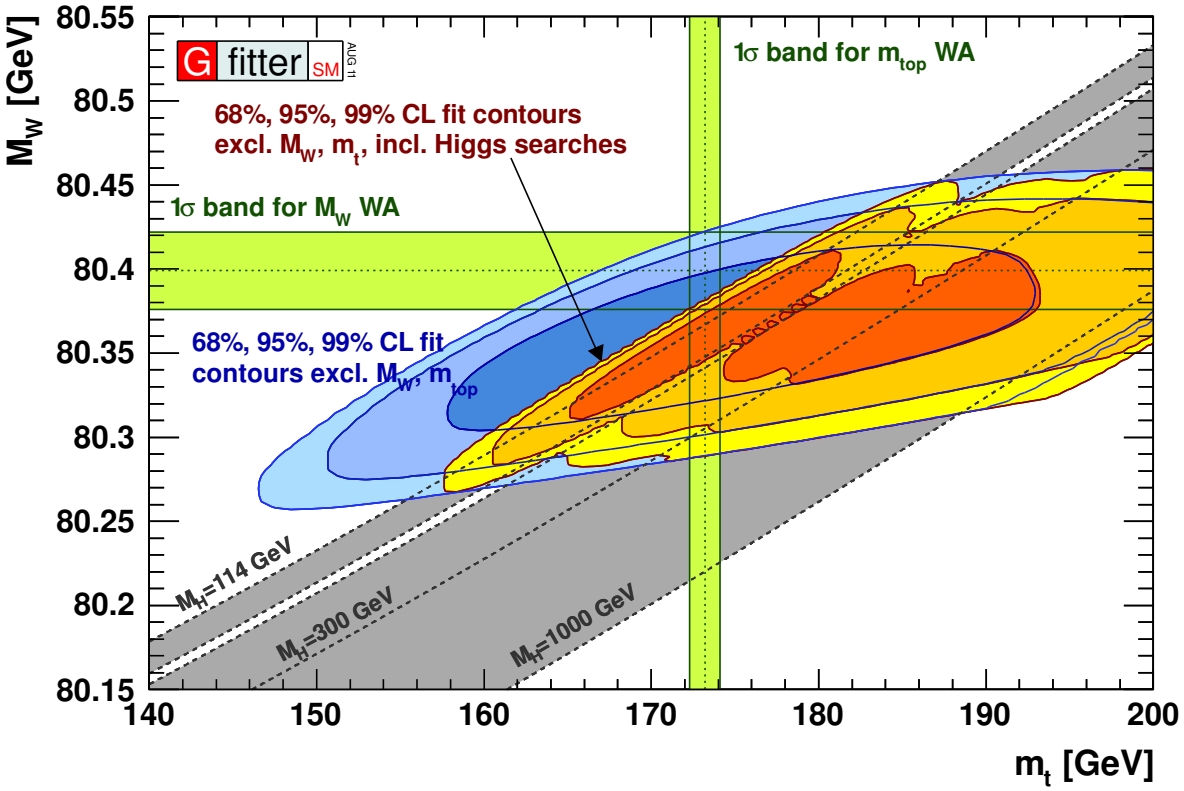

Figure 1.5: Contours of 68%, 95% and 99% CL for the global fit of the electroweak data, excluding the mass of the W-boson and the top-quark, in the m_t, M_W plane. The largest/blue (narrower/yellow) allowed regions are the results of the standard fit excluding (including) the direct Higgs boson searches at LEP and Tevatron. The grey shaded array shows the prediction of the masses as a function of the Higgs boson mass. The horizontal and vertical bands indicate the 1σ regions of the current world average (WA) of m_t and M_W measurements. Figure taken from the Gfitter group [32].

A fit of the hypothesized Higgs boson mass is also performed, discarding the experimental input of the W boson mass and top quark mass. The gray shaded vertical bands in Figure 1.5 indicate

the mass of the W boson, given the mass of the top quark for several values of the Standard Model Higgs boson mass. The small white band indicate the Higgs boson mass range excluded by the Tevatron experiments: $156 < m_H < 177\,\text{GeV}$ [39]. Further on only predictions for the W mass are made starting with a Higgs boson mass of $m_H = 114\,\text{GeV}$, since $m_H < 114\,\text{GeV}$ is excluded by the direct LEP searches for the Standard Model Higgs boson, and up to a Higgs boson mass of 1 TeV. A horizontal green shaded band indicates the experimental measurements for the W boson mass with the 1σ experimental uncertainty. Likewise the top quark mass and 1σ experimental uncertainty are shown by a vertical green shaded band. The experimental measurements tend to favor a Higgs boson mass lower than the LEP exclusion. A fit for the Higgs boson mass, given the electroweak precision data excluding the W boson and top quark mass is shown in Figure 1.5, indicating the 68%, 95% and 99% CL contours. These contours were fitted either excluding (largest/blue) or including (narrow/yellow) the direct Higgs boson searches. The indirect determination (largest/blue) without the Higgs boson searches shows agreement with the direct M_W and m_t measurements (horizontal and vertical green bands). The inclusion of the results of the direct Higgs boson searches reduces significantly the allowed region (narrow/yellow), which is still in agreement with the direct results [32]. Figure 1.4 also shows that the global fit for the Higgs boson mass is still in agreement with Standard Model measurements.

This section demonstrates the excellent precision at which the Standard Model of particle physics is known. Although the status of the Standard Model is presented at the time of writing of this thesis, this was of no influence on the search for possible extensions of the Standard Model in the data collected at the LHC in 2010.

1.3 Challenges and possible extensions to the Standard Model

In the Standard Model, the Higgs mechanism has been introduced to break the electroweak symmetry and give masses to the W and Z bosons, while the photon remained massless. Although the mechanism predicted the ratio of the W and Z mass ($\cos\theta_W$) very precisely, there is no experimental proof that this is the actual mechanism breaking the electroweak symmetry. Further on the Higgs boson mass is very sensitive to mass corrections due to all (undetected) particles living between the TeV scale and the Planck scale. The Higgs boson can easily acquire large corrections, leading to a high Higgs boson mass not allowed by the precision electroweak data. There are no known symmetries that will protect the Higgs boson from acquiring huge mass corrections, shifting the Higgs boson to higher masses, where it can not play its role in the electroweak symmetry breaking.

Physics beyond the Standard Model (BSM) is required to stabilize the Higgs boson mass, if it exists. If experiments will prove that there is no Higgs boson, there needs to be another mechanism to explain the masses of the W and Z. The clue for the mechanism of the electroweak symmetry breaking must be at the TeV scale, since without a Higgs boson the probability of WW scattering will become greater than 1, breaking unitary, at $O(1\,\text{TeV})$ [40–42].

1.3.1 Electroweak symmetry breaking

The Higgs mechanism, introduced *ad hoc* in the Standard Model, describes the breaking of the electroweak symmetry by means of a spin zero field. In quantum field theories, technical problems arise with elementary scalar particles [43, 44]. Figure 1.6 shows the one-loop quantum corrections to the Higgs boson mass. The correction (Δm_H) to the scalar boson mass diverges quadratically as the internal momentum in the loop becomes very large [44]. These corrections can be regularized introducing a cut-off scale Λ. This cut-off scale ensures that (not yet discovered) effects that are not included in the SM are only important above this scale, and that everything below this scale is well described by the Standard Model. In the lowest order in perturbation theory, we would write the Higgs boson mass as:

$$m_H^2 = m_0^2 + \Delta m_H^2 \sim m_0^2 - g^2\Lambda^2, \tag{1.5}$$

where m_0 is the bare Higgs boson mass and g is a dimensionless coupling constant. From perturbative unitary arguments [44] we believe that m_H is not larger than a few hundred GeV, so that if Λ is as large as M_{GUT}, in case the SM is embedded in a Grand Unified Theory (GUT), the two terms on the right hand side of the equation are of $O(10^{30}\,\mathrm{GeV}^2)$, and have to combine to yield an answer $\leq 10^6\,\mathrm{GeV}^2$. While this possibility cannot be logically excluded, the incredible sensitivity of the theory to the input parameters is generally regarded as "unnatural"[5] and as a shortcoming of field theories with elementary scalars [44]. If this reasoning is turned around and the theory is required not to have this incredible "fine tuning", we would end up with $\Lambda \lesssim 1$ TeV. New physics effects should manifest themselves in collisions of elementary particles at about the TeV energy scale.

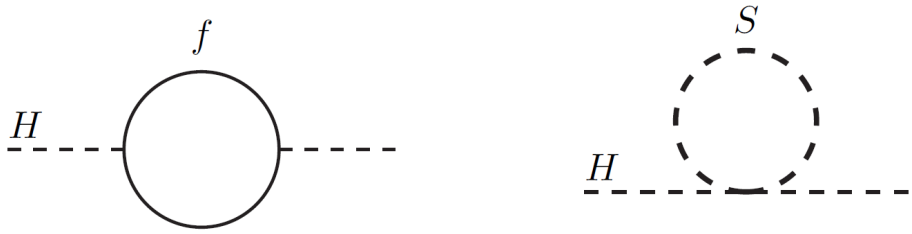

Figure 1.6: One-loop quantum corrections to the Higgs boson squared mass parameter m_H^2, due to a Dirac fermion f (left) or a scalar S (right). An example of the latter is the Higgs self interaction. Not shown are the quantum corrections due to the W and Z bosons of the electroweak interaction. Figure taken from Reference [47].

1.3.2 Possible extensions to the Standard Model

One of the most promising extensions to the Standard Model is Supersymmetry, where for each boson a fermion is introduced and vice versa, allowing for a unification of the bosons and fermions at the Planck scale. Several other frameworks were proposed to extend physics beyond the Standard Model, including Little Higgs, Composite Higgs and Higgsless scenarios,

[5] Discussions are often fed by the "naturalness" criterion. Naturalness is an aesthetic criterion. It comes from the realization that large cancellation among unrelated quantities required to achieve a small physical quantity is an unnatural situation and reflects a weakness of the model. A theory is less natural if it is more finetuned. A quantitative measure of finetuning was introduced in Reference [45] to derive upper limits on the masses of supersymmetric particles [46].

reviewed in Reference [48]. These theories borrow a lot of ideas from each other and from older ideas such as flat or warped extra dimensions and Technicolour [48].

Supersymmetry

Supersymmetry is a new space-time symmetry interchanging bosons and fermions. Supersymmetry is a well-motivated and well-studied extension of the Standard Model and is the subject of this thesis. Therefore it will be discussed in detail in section 1.4. Some attractive features of supersymmetry are [46]:

- Supersymmetry solves the gauge hierarchy problem [49–52]: the quantum corrections to the Higgs boson mass from a bosonic loop and a fermionic loop cancel exactly, if the couplings are identical and, for each boson there is a fermion with the same mass and vice versa. This symmetry has to be broken, since these supersymmetric partners have not been found yet. If the breaking occurs only in the masses and not in the couplings, the quadratic divergences still cancel [46], leaving a residual divergence which is only logarithmically sensitive to the supersymmetry breaking scale.
- Supersymmetry leads to gauge coupling unification, which is a bonus, since it was not really required from a theory that solved the hierarchy problem. When the Standard Model gauge couplings are extrapolated to a high scale $M_{\mathrm{GUT}} \sim 2 \times 10^{16}\,\mathrm{GeV}$, they meet at a single point.
- Supersymmetry triggers EWSB. Unlike the Standard Model, where artificially a negative sign in front of the scalar mass-square in the potential has to be added manually, the sign flip occurs in a dynamical way in supersymmetry.
- To conserve baryon number (and hence prohibit proton decay), R-parity has to be introduced. This parity will be discussed later, but has the consequence that the lightest supersymmetric particle (LSP) has to be stable, and this particle is a good dark matter candidate.

Supersymmetry is a very natural theory, with finetunings ranging from $\sim 1\%$ for the Minimal Supersymmetric Standard Model (MSSM) up to a few tens of % in other realizations [46], depending on the values the mass parameters take.

Little Higgs

Little Higgs theories are a new type of theories which can stabilize the electroweak scale [53–55]. The Higgs boson could be seen, for instance, as a pseudo-Nambu-Goldstone boson (PNGB) of some global symmetry that is both spontaneous and explicitly broken by some new physics at $O(10\,\mathrm{TeV})$. The explicit breaking requires extra assumptions to avoid quadratic divergences from W and Z loops. The generic solution is to introduce heavy partners for Standard Model particles canceling the divergences in the loops. The Little Higgs theory solves the hierarchy problem only temporary, it actually postpones it to the scale of $\sim 10\,\mathrm{TeV}$. Other new physics should exist at higher energies.

These partners of the Standard Model particles only provide a cancellation of the divergent term in the Higgs boson mass up to only one loop, thus not solving but rather delaying the hierarchy problem to a higher scale. If these new particles would mix up with the SM particles, this would

have been observed by the electroweak precision data. Therefore T-parity was introduced to avoid mixing of the SM particles with the new particles. As a consequence there will be a lightest partner particle, which is stable due to T-parity and makes a good dark matter candidate. This T-parity is similar to the R-parity in supersymmetry. This leads to a model very similar to Supersymmetry, with partners for all existing fermions and most of the gauge bosons, except that these partners all have the same spin. Therefore if one wants to distinguish these theories from Supersymmetric theories, one needs to measure the spin of the newly detected particles.

Composite Higgs

The Composite Higgs models emerged as an improved realization of the Little Higgs scenarios, where the Higgs boson is composite field produced by some new strong dynamics. This is a force, similar to QCD, but with a much larger characteristic energy scale. There is no symmetry to protect the Higgs boson mass, therefore the Higgs boson mass is expected to be heavy, close to the scale of the new strong dynamics. Recent developments in extra-dimensional theories and Anti de Sitter/Conformal Field Theory (AdS/CFT) correspondence provide a new tool to study these kind of models, by providing a dual description of such scenarios in a theory with extra dimensions [48].

Higgsless scenarios

If electroweak symmetry is broken by strong dynamics, it is also possible that there is no Higgs particle and the WW-scattering is unitarized by some other states. Technicolour are the original models without Higgs boson [43, 56]. The WW-scattering is then unitarized by some resonances such as techni-rho's. Similar to the composite Higgs theories, warped extra dimensions and AdS/CFT correspondence allows for alternative descriptions [48].

1.4 Supersymmetry

Supersymmetry is a symmetry that relates fermions and bosons to each other. A supersymmetric transformation turns a bosonic state into a fermionic state and vice versa [47]:

$$Q\,|\text{Boson}\rangle = |\text{Fermion}\rangle \qquad \text{and} \qquad Q\,|\text{Fermion}\rangle = |\text{Boson}\rangle\,. \tag{1.6}$$

The fermions and bosons are known as each others superpartners and are grouped in a supermultiplet, which is the irreducible representation of the supersymmetric algebra. Each supermultiplet contains a boson and a fermion with exactly the same quantum numbers for the strong and electroweak interaction, but with a different supersymmetric quantum number.

From a theoretical point of view, this is the first step on building a Supersymmetric theory. Next steps involve the construction of supersymmetric Lagrangians to allow for interactions between the supersymmetric particles and the addition of mass terms. In this section the particle content of the supermultiplets will be detailed, along with some interesting discussion on the mass spectrum of the particles and their possible production and decay, which is of interest to an experimentalist, willing to discover or exclude supersymmetric particles. More theoretical aspects of Supersymmetry, such as the construction of supersymmetric Lagrangians and the mechanisms of supersymmetry breaking will not be elaborated on. Excellent reviews of Supersymmetry can be found in References [57, 58], while the discussion of Supersymmetry is based on the excellent Reference [47].

Supersymmetry should be a broken symmetry, since, otherwise, the superpartners would have the same mass. This means that for every Standard Model particle there should be a supersymmetric partner with exactly the same mass, which is excluded by measurements. Therefore supersymmetry should be broken, with the superpartners having a mass larger than the Standard Model particles. In this thesis the Minimal Supersymmetric Standard Model (MSSM), i.e. the minimal supersymmetric extension of the Standard Model, is discussed, although non-minimal versions do exist as well. Nevertheless this "minimal" extension contains at least 124 free parameters, further on the mechanism of supersymmetry breaking is unknown and several possibilities lead to different implementations of Supersymmetry. This could not be withheld in an experimental environment. Comparing experimental results against a theory wandering around in a 124 dimensional parameter space is computationally impossible. Therefore several simplified and constrained versions of the MSSM exist, of which the most simple that has been used to compare to data will be discussed.

As a historical note, it is remarkable that supersymmetry was not developed to stabilize the Higgs boson mass (i.e. the hierarchy problem). According to References [59, 60], supersymmetry was first introduced in the middle of the sixties in the context of hadronic physics, relating mesons and baryons [61, 62], and rediscovered in the early seventies [63]. Its only in 1981 that a realistic version of the Supersymmetric Standard Model (MSSM) was developed [64, 65], proposing a solution to the hierarchy problem.

1.4.1 Supermultiplets: the particle content of the MSSM

In supersymmetry, the boson and fermion states are arranged in so-called "supermultiplets". Particles inside the same supermultiplet must have equal masses, same electric charges, same weak isospin and same colour charge. Further on, in each supermultiplet the number of fermion degrees of freedom must be equal to the number of boson degrees of freedom: $n_F = n_B$.

The simplest possibility to create a supermultiplet with a single (spin-1/2) fermion, which has two spin helicity states ($n_F = 2$) is to add two real scalars (each with $n_B = 1$), which can be assembled into a single complex scalar field. This combination of a two-component Weyl spinor and a complex scalar field is called a "chiral" or "matter" or "scalar" multiplet. The simplest possibility to create a supermultiplet to with a spin-1 vector boson, describing a massless gauge boson, is to include a massless spin-1/2 fermion. The spin-1 gauge boson has two helicity states, so $n_B = 2$, the spin-1/2 Weyl spinor has $n_F = 2$. Gauge bosons transform differently under gauge transformations, and so must their fermionic partners, which are called the "gauginos". Therefore we cannot add the known fermions of the Standard Model in a supermultiplet with the gauge bosons of the Standard Model, but we need new supersymmetric fermions, the "gauginos". A combination of spin-1 gauge bosons and spin-1/2 gauginos is called as "gauge" or "vector"supermultiplet.

The first step is to decide how the known particles of the Standard Model fit into the different supermultiplets and to give them an appropriate name. All Standard Model fermions must be members of chiral supermultiplets, since only chiral supermultiplets can contain fermions whose left-handed parts transform differently under the gauge group than the right-handed parts. The names for the superpartners of the quarks and leptons are the "squarks" and the "sleptons", with the prefix s- denoting that those particles are scalars, and not fermions. The left and right-handed parts of the quarks and leptons are described by separate Weyl spinors, so each one has

its own scalar partner. The symbols used for squarks and sleptons are the same as for the quarks and leptons, but with a tilde ($\tilde{}$) on top. For instance the superpartners of the Dirac electron, e, are the left- and right-handed selectrons, denoted $\tilde{e}_L$ and $\tilde{e}_R$. Note that the "handedness" here does not refer to the helicity of the selectrons (which are spin-0 particles), but to that of their superpartners. Similar notation and naming is valid for the smuon, the stau and the sneutrinos. The squarks are denoted $\tilde{q}_L$ and $\tilde{q}_R$, with $q = u, d, s, c, b, t$. The gauge interactions of each of these squarks and sleptons is exactly the same as for the known Standard Model quarks and leptons: a left-handed sfermion (for example $\tilde{u}_L$ or $\tilde{d}_L$) couples to the W boson, while a right-handed fermion (for example $\tilde{u}_R$ or $\tilde{d}_R$) does not.

The Higgs boson is a scalar particle and must reside in a chiral supermultiplet. However, it turns out that just one supermultiplet is not enough. Only a $Y = +1/2$ Higgs chiral supermultiplet can give mass to the up-type quarks and only a $Y = -1/2$ Higgs chiral supermultiplet can give masses to down-type quarks. Another reason comes from so-called "gauge anomalies", which are miraculously canceled in the Standard Model, but also requires the existence of two Higgs doublets. The generic nomenclature for a spin 1/2 superpartner is the appendix "-ino". The fermionic partners of the Higgs scalars are therefore called the higgsinos. There is one higgsino for every particle of the two Higgs doublets, leading to four higgsinos in total, of which two are charged and two are neutral. Both the particles and the supersymmetric particles of the Higgs supermultiplets have not been discovered.

All chiral multiplets of the MSSM are summarized in Table 1.3, together with their quantum numbers for the Standard Model gauge group: $\mathrm{SU}(3)_C \otimes \mathrm{SU}(2)_L \otimes \mathrm{U}(1)_Y$. We followed the convention, that all chiral supermultiplets are defined in terms of left-handed Weyl spinors, such that all the Hermitian conjugates of the right-handed fermion fields appear in Table 1.3.

The vector bosons of the Standard Model must be included in gauge supermultiplets. Their fermionic superpartners are referred to as gauginos. The superpartner of the $\mathrm{SU}(3)_C$ gauge interaction, the gluon, is the gluino, which is also a spin-1/2 colour octet particle. The electroweak gauge symmetry $\mathrm{SU}(2)_L \otimes \mathrm{U}(1)_Y$ is associated with the massless spin-1 gauge bosons W^+, W^-, W^0 and B^0, with spin-1/2 superpartners $\tilde{W}^+$, $\tilde{W}^-$, $\tilde{W}^0$ and $\tilde{B}^0$. After electroweak symmetry breaking the W^0 and B^0 gauge eigenstates mix to give mass eigenstates of the Z^0 and γ. In analogy, the mixing of $\tilde{W}^0$ and $\tilde{B}^0$ gives mass to the zino ($\tilde{Z}^0$) and the photino ($\tilde{\gamma}$), and these masses would be M_Z and 0, respectively, if supersymmetry were unbroken.

1.4.2 R-parity, the lightest SUSY particle and running couplings

The theoretical formulation of supersymmetry consists of a Lagrangian describing the particle content and the interactions between the particles and sparticles. There could be terms added to this Lagrangian that violate Lepton number (L) and Baryon number (B). Such processes would allow e.g. the proton to decay to a lepton and a meson, violating both Lepton and Baryon number, which has not been seen experimentally. A lower limit has been set by dedicated proton-decay experiments of about 10^{32} years, which is extremely long compared to the currently known lifetime of the universe: $(13.72 \pm 0.12) \times 10^9$ years.

In the MSSM a new symmetry is added, "R-parity", which disallows B or L violating terms in the supersymmetric Lagrangian. R-parity is defined as:

$$P_R = (-1)^{3(B-L)+2s}, \tag{1.7}$$

Table 1.3: The chiral and gauge supermultiplets in the Minimal Supersymmetric Standard Model. In the chiral supermultiplets, the spin-0 fields are complex scalars and the spin-1/2 fields are left-handed two-component Weyl fermions. For this reason the right-handed fermions are Hermitian conjugated (†) and the right-handed scalars are complex conjugated (*). The supermultiplets are formed with one spin-0 particle and one spin-1/2 particle with the same quantum numbers for the $\mathrm{SU}(3)_C \otimes \mathrm{SU}(2)_L \otimes \mathrm{U}(1)_Y$ symmetries. Table taken from Reference [47].

Chiral Supermultiplets of the MSSM			
	spin 0	spin 1/2	$\mathrm{SU}(3)_C \otimes \mathrm{SU}(2)_L \otimes \mathrm{U}(1)_Y$
squarks, quarks (×3)	$\begin{pmatrix}\tilde{u}_L & \tilde{d}_L\end{pmatrix}$	$\begin{pmatrix}u_L & d_L\end{pmatrix}$	$\begin{pmatrix}\mathbf{3} & \mathbf{2} & +\frac{1}{6}\end{pmatrix}$
	$\tilde{u}_R^*$	$u_R^\dagger$	$\begin{pmatrix}\overline{\mathbf{3}} & \mathbf{1} & -\frac{2}{3}\end{pmatrix}$
	$\tilde{d}_R^*$	$d_R^\dagger$	$\begin{pmatrix}\overline{\mathbf{3}} & \mathbf{1} & +\frac{1}{3}\end{pmatrix}$
sleptons, leptons (×3)	$\begin{pmatrix}\tilde{\nu}_L & \tilde{\ell}_L\end{pmatrix}$	$\begin{pmatrix}\nu_L & \ell_L\end{pmatrix}$	$\begin{pmatrix}\mathbf{1} & \mathbf{2} & -\frac{1}{2}\end{pmatrix}$
	$\tilde{\ell}_R^*$	$\ell_R^\dagger$	$\begin{pmatrix}\overline{\mathbf{1}} & \mathbf{1} & +1\end{pmatrix}$
Higgs, higgsinos	$\begin{pmatrix}H_u^+ & H_u^0\end{pmatrix}$	$\begin{pmatrix}\tilde{H}_u^+ & \tilde{H}_u^0\end{pmatrix}$	$\begin{pmatrix}\mathbf{1} & \mathbf{2} & +\frac{1}{2}\end{pmatrix}$
	$\begin{pmatrix}H_d^0 & H_d^-\end{pmatrix}$	$\begin{pmatrix}\tilde{H}_d^0 & \tilde{H}_d^-\end{pmatrix}$	$\begin{pmatrix}\mathbf{1} & \mathbf{2} & -\frac{1}{2}\end{pmatrix}$
Gauge Supermultiplets of the MSSM			
	spin 1/2	spin 0	$\mathrm{SU}(3)_C \otimes \mathrm{SU}(2)_L \otimes \mathrm{U}(1)_Y$
gluino, gluon	$\tilde{g}$	g	$(\mathbf{8} \quad \mathbf{1} \quad 0)$
winos, W boson	$\tilde{W}^\pm \ \tilde{W}^0$	$W^\pm \ W^0$	$(\mathbf{1} \quad \mathbf{3} \quad 0)$
binos, B boson	$\tilde{B}^0$	B^0	$(\mathbf{1} \quad \mathbf{1} \quad 0)$

where s is the spin of the particle. Now all Standard Model particles have even R-parity ($P_R = +1$), while all sparticles (squarks, sleptons, gauginos and higgsinos) have odd R-parity ($P_R = -1$). If R-parity is exactly conserved, then there will be no mixing between the particles and sparticles. Furthermore, there are three extremely important phenomenological consequences:

- The lightest sparticle with $P_R = -1$ is called the "lightest supersymmetric particle", or LSP and must be absolutely stable, else R-parity would be violated by its decay.
- Each other sparticle, not being the LSP, should eventually decay to a state containing an LSP.
- In collider experiments, where two particles collide head-on, sparticles should be produced in pairs.

One of the big achievements of supersymmetry is the apparent unification of gauge couplings in the MSSM. Figure 1.10 compares the renormalization group (RG) evolution of the α^{-1} in the Standard Model (dashed lines) and the MSSM (solid lines). In the MSSM case the sparticle mass were treated as common thresholds and were varied between 500 GeV and 1.5 TeV, while the strong coupling constant $\alpha_S(m_Z)$ is varied between 0.117 and 0.121. Although the Standard Model does not manage to unify the three couplings, the MSSM seems to contain the right particle content to have the three gauge couplings at the same strength at the unification scale

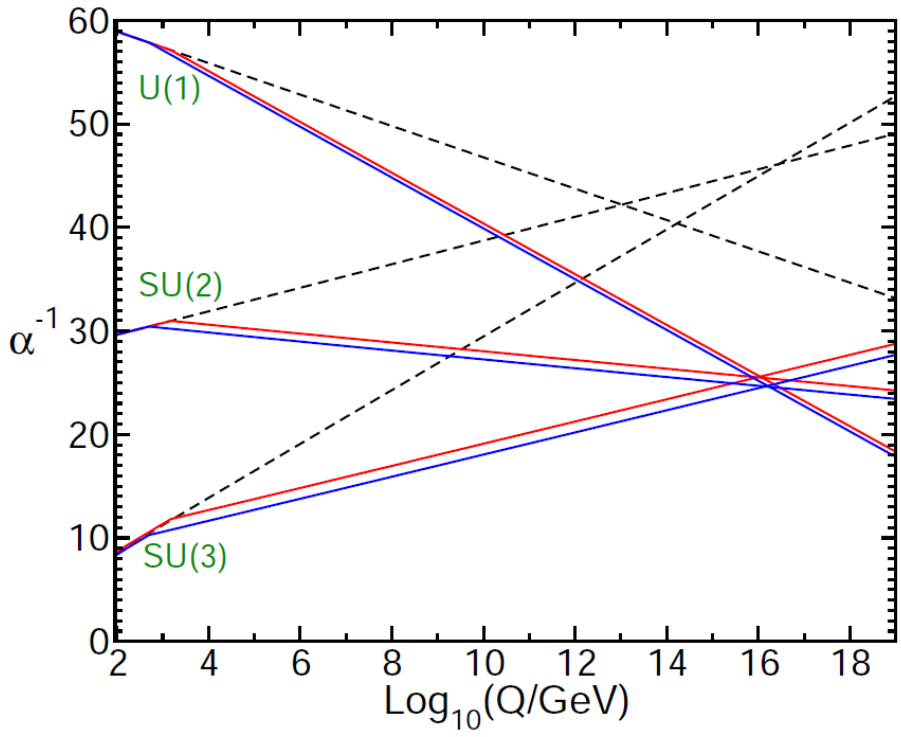

Figure 1.7: The Renormalization Group (RG) evolution of the inverse gauge couplings $\alpha^{-1}(Q)$ in the Standard Model (dashed lines) and in the MSSM (solid lines) as a function of the mass scale Q. In the MSSM, the sparticle thresholds are varied between 500 GeV and 1.5 TeV and $\alpha_S(m_Z)$ is varied between 0.117 and 0.121. Figure taken from Reference [47].

$M_U \sim 2 \times 10^{16}$ GeV. While the apparent unification of the gauge couplings might be just an accident, it may also be taken as a hint in favour of a grand unified theory (GUT) [47].

1.4.3 Supersymmetry breaking

Now that we introduced the new particles of the Minimal Supersymmetric Standard Model, the most pertinent question one can ask is: "Where are these particles?" Clearly, none of these particles are discovered yet.

An important clue on how supersymmetry should be broken can be obtained by looking back to the original motivation to introduce this theory: the hierarchy problem. We introduced two complex scalar fields for each Dirac fermion (one for each Weyl fermion), which was what we needed to cancel exactly the quadratically divergent terms to the Higgs boson mass. However, if one introduces supersymmetry breaking, the masses of the fermions and the bosons in a supermultiplet will differ and the contributions to the Higgs boson mass will not cancel exactly anymore. Therefore the first versions of supersymmetry, using dynamical breaking mechanisms [64], do not cancel the quadratic divergences to the Higgs boson mass. In 1981 soft supersymmetry breaking was introduced [65], in which the breaking terms are added separately to the Lagrangian describing supersymmetry. This separation between the supersymmetry breaking from the rest of the supersymmetric standard model requires some mediating mechanism "communicating" the supersymmetry breaking to the supersymmetric part of the Lagrangian.

For several reasons [47] the MSSM soft terms (supersymmetry breaking terms) are expected

to arise indirectly. Therefore supersymmetry breaking has to occur in a so called "hidden sector" where particles do not have direct couplings to the particles of the "visible sector", which are the particles in the chiral supermultiplets of the MSSM. However, these two sectors share interactions responsible for mediating of the supersymmetry breaking from the hidden sector to the visible sector, resulting in the soft terms. There are two main competing proposals for these mediating interactions: the gravitational interaction and the well-known electroweak and QCD gauge interactions. The first model is called the gravitational mediated supersymmetry breaking or Planck-scale mediated supersymmetry breaking (PMSB), while the latter is named the gauge-mediated supersymmetry breaking (GMSB). Considering PMSB, gravity has to be included in the supersymmetric theory, which therefore has to be a local supersymmetry theory. Examples are minimal supergravity (mSUGRA) and the constrained MSSM (CMSSM), which is a mSUGRA variant[6]. Both mSUGRA and CMSSM assume universality of the gaugino and scalar masses at high energies. This means that at the GUT scale, all fermions have the same mass $mm_{1/2}$, and that all bosons do have the same mass m_0. GMSB and AMSB (anomaly mediated supersymmetry breaking, yet another alternative mediating mechanism) will not be discussed here.

1.4.4 The experimentally observable sparticle spectrum

The description of the electroweak symmetry breaking in the MSSM is slightly complicated by the need for two complex Higgs doublets $H_u = (H_u^+, H_u^0)$ and $H_d = (H_d^0, H_d^-)$, instead of just one as is required for the Standard Model. After breaking of the electroweak symmetry, these two doublets have in total eight degrees of freedom, of which three are the Goldstone bosons, giving mass to $W^\pm$ and Z^0 bosons, leaving five degrees of freedom, which results in five Higgs bosons: two neutral (CP-even) scalars, one neutral (CP-odd and hence pseudo-) scalar and two charged scalar particles:

$$h^0, H^0, A^0, \text{ and } H^\pm.$$

At leading order, the mass of the lightest Higgs particle, M_h is bounded by $M_Z|\cos 2\beta|$, where $\tan\beta \equiv v_u/v_d$ is the ratio of the Higgs field vacuum expectation values. In the MSSM, one finds that $m_h \lesssim 135\,\text{GeV}$ and that over most of the parameter space, the lightest Higgs boson h^0 is nearly SM-like such that the SM Higgs boson searches can be directly applied to h^0 [66]. It is a fairly robust prediction of supersymmetry at the weak scale (the MSSM) that at least one of the Higgs scalar bosons must be light [47].

The electroweak symmetry breaking introduces mixing between the higgsinos and the gauginos, with mixing parameter μ. The neutral higgsinos ($\tilde{H}_u^0$ and $\tilde{H}_d^0$) and the neutral gauginos ($\tilde{B}$ and $\tilde{W}^0$) combine to form four mass eigenstates called the neutralinos, which are denoted as χ_i^0 or N_i ($i = 1, 2, 3, 4$). The charged higgsinos ($\tilde{H}_u^+$ and $\tilde{H}_d^-$) and winos ($\tilde{W}^\pm$) mix to form two mass eigenstates with charge ± 1 called charginos, which are denoted as $\chi_i^\pm$ or $C_i^\pm$ ($i = 1, 2$). The lightest neutralino χ_1^0 is usually assumed to be the LSP, unless R-parity is broken or there is a lighter gravitino.

The gluino is a colour octet fermion, so it cannot mix with any other particle in the MSSM. In this regard, it is unique among all of the MSSM sparticles. Squarks and sleptons, on the other hand can easily mix up, since particles with the same electric charge, colour charge and

[6] In mSUGRA the Higgsino mixing mass parameter μ is fixed, while in the CMSSM it is not and left as free parameter.

Table 1.4: The undiscovered particles and sparticles of the Minimal Supersymmetric Standard Model, with non-negligible sfermion mixing for the third generation [47]. Note that the Higgs bosons are R-even and are particles and not supersymmetric particles.

	spin	P_R	Gauge Eigenstates	Mass Eigenstates
Higgs bosons	0	+1	$H_u^+,\ H_u^0,\ H_d^0,\ H_d^-$	$h^0,\ H^0,\ A^0,\ H^\pm$
squarks	0	−1	$\tilde{u}_L,\ \tilde{u}_R,\ \tilde{d}_L,\ \tilde{d}_R$	(same)
			$\tilde{s}_L,\ \tilde{s}_R,\ \tilde{c}_L,\ \tilde{c}_R$	(same)
			$\tilde{t}_L,\ \tilde{t}_R,\ \tilde{b}_L,\ \tilde{b}_R$	$\tilde{t}_1,\ \tilde{t}_2,\ \tilde{b}_1,\ \tilde{b}_2$
sleptons	0	−1	$\tilde{\nu}_e,\ \tilde{e}_L,\ \tilde{e}_R$	(same)
			$\tilde{\nu}_\mu,\ \tilde{\mu}_L,\ \tilde{\mu}_R$	(same)
			$\tilde{\nu}_\tau,\ \tilde{\tau}_L,\ \tilde{\tau}_R$	$\tilde{\nu}_\tau,\ \tilde{\tau}_1,\ \tilde{\tau}_2$
neutralinos	1/2	−1	$\tilde{W}^0,\ \tilde{B}^0,\ \tilde{H}_u^0,\ \tilde{H}_d^0$	$\tilde{\chi}_i^0\ (i = 1,2,3,4)$
charginos	1/2	−1	$\tilde{W}^\pm,\ \tilde{H}_u^+,\ \tilde{H}_d^+$	$\tilde{\chi}_i^\pm\ (i = 1,2)$
gluino	1/2	−1	$\tilde{g}$	(same)

R-parity are allowed to mix. The third-family squarks and sleptons are expected to have very different masses with respect to their first- and second-family counterparts. Therefore the first- and second-family squarks are often treated together and named "squarks", while the third generation squarks are treated differently, keeping their stop and sbottom names. While the former are nearly unmixed, the latter will be substantially mixed up in pairs.

For example, the stop quarks $\tilde{t}_L$ and $\tilde{t}_R$ will particularly mix to mass eigenstates $\tilde{t}_1$ and $\tilde{t}_2$. Many models predict the lightest top squark ($\tilde{t}_1$) is the lightest squark and is predominantly $\tilde{t}_R$. The magnitude of the mixing in the sbottom and stau sectors depends on $\tan\beta$, with small mixing for $\tan\beta < 10$. In that case the mass eigenstates will not differ too much from the gauge eigenstates. For larger values of $\tan\beta$ the mixing can be quite substantial. Just as in the case of the top squarks, the lighter sbottom and stau mass eigenstates ($\tilde{b}_1$ and $\tilde{\tau}_1$) can be significantly lighter than their first- and second-generation counterparts.

The undiscovered particles of the MSSM are summarized in Table 1.4 indicating both their gauge and their mass eigenstates, in the assumption that the mixing in the first- and second-generation squarks and leptons is negligible, while mixing in the third generation is substantial. Specific models for the soft terms of supersymmetry breaking predict the masses and the mixing angles for the MSSM in a few parameters. In minimal supergravity models, all gaugino masses are unified to a single gaugino mass $m_{1/2}$, all scalar masses are unified to m_0 and all trilinear couplings (triple boson couplings) to A_0. This reduces the amount of free parameters from 124 in the unconstrained MSSM to four parameters and a sign in mSUGRA models. The entire mass spectrum in minimal supergravity models is entirely determined by:

$$m_0,\ m_{1/2},\ A_0,\ \tan\beta,\ \text{and sign}(\mu).$$

In order to translate a set of predictions at the GUT scale into physically meaningful quantities that describe physics near the electroweak scale, it is necessary to evolve the gauge couplings using their renormalization group (RG) equations. Figure 1.8 shows the RG running of scalar

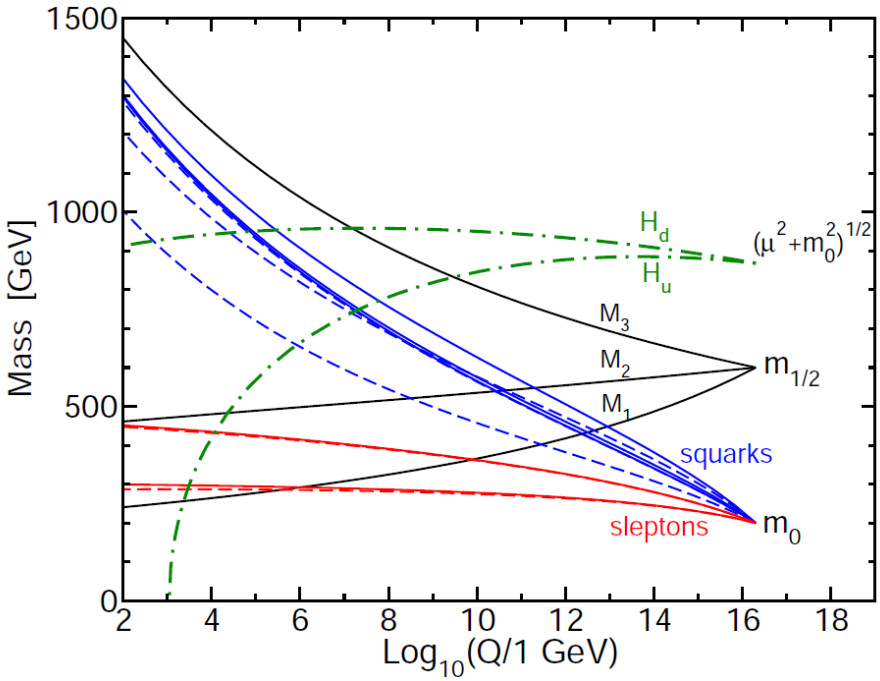

Figure 1.8: Renormalization Group evolution of scalar and gaugino mass parameters in the MSSM with typical minimal supergravity-inspired boundary conditions at $Q_0 = 2.5 \times 10^{16}$ GeV. Figure taken from Reference [47].

and gaugino masses in a typical model based on minimal supergravity boundary conditions imposed at $Q_0 = 2.5 \times 10^{16}$ GeV [47]. The parameter values used for this illustration were $m_0 = 80$ GeV, $m_{1/2} = 250$ GeV, $A_0 = -500$ GeV, $\tan\beta = 10$ and $\mu > 0$. The running gaugino masses are solid lines labeled by M_1, M_2, and M_3. The dot-dashed lines labeled H_u and H_d are the running values which appear in the Higgs potential. The value denoted by H_u runs negative, provoking electroweak symmetry breaking. The other lines are the running squark and slepton masses, with dashed lines for sfermions of the third-generation.

Figure 1.9 shows two sketches of example MSSM spectra obtained for two different types of model assumptions within minimal supergravity models. The left sketch is the mass spectrum of a mSUGRA model with $m_0^2 \ll m_{1/2}^2$ (the same parameters as used for Figure 1.8). The model is near the decoupling limit in the Higgs sector, with the lightest Higgs particle h^0 being much lighter than the other Higgs particles, which have nearly the same mass. Noteworthy is that in models with $m_0 \ll m_{1/2}$ the gluino is the heaviest superpartner and the squarks are all more heavier than the sleptons. The stop is the lightest squark, while the other squarks have nearly similar masses. There is a bino-like χ_1^0 LSP. Taking a larger m_0^2 will tend to squeeze the spectra of the squarks and the sleptons and move them to masses higher than the neutralinos, charginos and the gluino. This is illustrated in the right sketch of Figure 1.9, where $m_{1/2}^2 \ll m_0^2$. The parameters used to generate this spectrum are $m_0 = 3200$ GeV, $m_{1/2} = 320$ GeV, $A_0 = -320$ GeV, $\tan\beta = 10$ and $\mu > 0$. In this model the stop is still the lightest squark, but it is heavier that the gluino and the squark spectrum is highly compressed.

Nevertheless it would be a mistake to rely too heavily on a few specific scenarios for the MSSM mass and mixing spectrum, since the sketches above are only a tiny fraction of the available possibilities. However, they illustrate two interesting specific scenarios, the former where squark

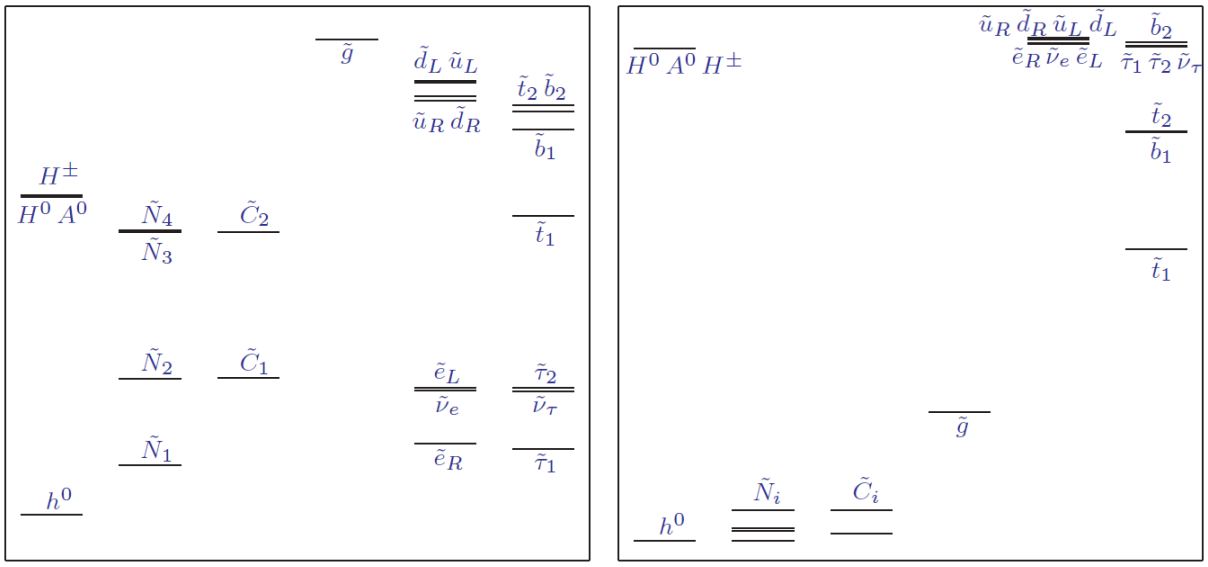

Figure 1.9: Two example mass spectra for the undiscovered particles in the MSSM, for mSUGRA with $m_0^2 \ll m_{1/2}^2$ (left) and for mSUGRA with $m_{1/2}^2 \ll m_0^2$ (right). Figure taken from Reference [47].

production by the strong interaction would be expected to dominate at hadron colliders, while for the latter strong production of the gluino would dominate, which will lead to different experimental signatures, to which the next section is devoted. The most important point is that by measuring the masses and the mixing angles of the MSSM particles, we will be able to gain a great deal of information that differentiates between competing proposals for the origin and mediation of supersymmetry breaking [47].

1.4.5 Production and decay of supersymmetric particles

Assuming R-parity, sparticles will be produced in pairs at hadron colliders, and dominantly by the strong interaction:

$$gg \rightarrow \tilde{g}\tilde{g},\ \tilde{q}\bar{\tilde{q}}, \tag{1.8}$$
$$gq \rightarrow \tilde{g}\tilde{q}, \tag{1.9}$$
$$q\bar{q} \rightarrow \tilde{g}\tilde{g},\ \tilde{q}\bar{\tilde{q}}, \tag{1.10}$$
$$qq \rightarrow \tilde{q}\tilde{q}. \tag{1.11}$$

The strong interaction will produce squarks and gluinos, while charginos, neutralinos and sleptons can also be produced by the electroweak interaction which have much smaller cross sections. In a crude first approximation, for the hard[7] parton collisions needed to make heavy particles, one may think of the Tevatron as a quark-antiquark collider, and the LHC as a gluon-gluon and gluon-quark collider (discussed in section 1.5.6). Signals extracted from data will be an inclusive combination of all kinematically allowed production channels ($\tilde{g}\tilde{g}$, $\tilde{g}\tilde{q}$, $\tilde{q}\bar{\tilde{q}}$, $\tilde{q}\tilde{q}$). The squarks and gluinos can be produced by more than one channel, which disallows for the neatly separation of the different parton collisions.

[7] A "hard" interaction is an interaction with a very high momentum exchange between the colliding partons.

At the Tevatron collider, the chargino and neutralino production process tend to have the larger cross sections, unless the squarks and gluinos are rather light, $O(300\,\text{GeV})$. At the LHC the situation is typically reversed, with production of gluinos and squarks by gluon-gluon and gluon-quark fusion usually dominant, unless the gluino and squarks are heavier than $O(1\,\text{TeV})$ [47]. Therefore we will here concentrate on the decay modes of squarks and gluinos. For the following paragraphs it is assumed that the lightest neutralino $\tilde{\chi}_1^0$ is the LSP, as all sparticles will decay producing a χ_1^0 in the final state.

If the decay $\tilde{q} \rightarrow q\tilde{g}$ is kinematically allowed, it will always dominate, because the quark-squark-gluino vertex has QCD strength. If the decay is kinematically not allowed or disfavoured, the squarks can decay to a quark and a neutralino or a chargino. While the decay to the LSP, $\tilde{q} \rightarrow q\tilde{\chi}_i^0$ or $q\tilde{\chi}_i^{\pm}$, is always kinematically favoured, several complicated decay chains are also allowed, where neutralino and chargino decay might produce leptons in the final state.

The gluino decay can only proceed through a squark, either on-shell or virtual. If the two-body decay $\tilde{g} \rightarrow q\tilde{\bar{q}}$ is kinematically allowed, it will always dominate, since the gluino-squark-quark coupling has QCD strength. This vertex is actually the very same as the one discussed above, only different assumptions are made for the gluino and the squark mass. If, instead, the squarks are heavier than the gluino, and hence are not available for the gluino decay, the gluino will undergo a three-body decay mediated by an off-shell squark: $\tilde{g} \rightarrow q\bar{q}\tilde{\chi}_i^0$ or $q\bar{q}\tilde{\chi}_i^{\pm}$. The neutralino can already be the LSP, or it will decay to the LSP by various possible decay chains, as is the case for the decay of the chargino.

The decays of the produced sparticles will thus result in final states with at least two neutralino LSPs, which will not be detected by the detector, since they interact only weakly. The LSPs carry away at least the energy equal to two times the mass of the LSP, $2m_{LSP}$, which is energy that goes missing. At hadron colliders, only the transverse component of missing energy can be measured, which is denoted $E_{\text{T}}^{\text{miss}}$. In general, the signatures we will observe at the LHC will consist of leptons, jets and $E_{\text{T}}^{\text{miss}}$. Important Standard Model backgrounds are the associated production of W and Z bosons with jets, where one of the bosons decay weakly to neutrinos, which provide the $E_{\text{T}}^{\text{miss}}$. In CMS the early SUSY searches are divided according to the number of leptons in the final state: 0, 1, 2, or more. Requiring zero leptons deselects the leptonic decay of the W boson. Therefore the jets + $E_{\text{T}}^{\text{miss}}$ signature is one of the favorite signatures for finding first evidence of supersymmetry at the LHC. It can get contributions from all types of sparticle pair production, except leptons. Investigating this promising signature will be the subject of this thesis.

Aiming at a broad coverage of the different experimental signatures, a set of mSUGRA test points has been defined in Reference [67]. The low mass test points (LM1 to LM9) were chosen to evaluate the sensitivity to SUSY signals in the early period of the LHC, but chosen to be above the Tevatron reach. Some high mass points were introduced (HM1 to HM4) near the ultimate reach of the LHC in the first years of physics ($\sqrt{s} = 14\,\text{TeV}$ with an integrated luminosity of $30\,\text{fb}^{-1}$) as scheduled in the Physics Performance TDR [67]. Their parameters as a function of m_0, $m_{1/2}$, A_0, $\tan\beta$ and $\text{sign}(\mu)$ are defined in Reference [67] and their position in the m_0, $m_{1/2}$ plane is shown in Figure 1.10. Points LM1, LM2 and LM6 are compatible with WMAP cold dark matter limits in a strict mSUGRA scenario. The other points are not, but they can made compatible [67] with CDM if universality of the Higgs boson mass parameters is abandoned, such as in Non-Universal Higgs Mass (NUHM) [68, 69] models.

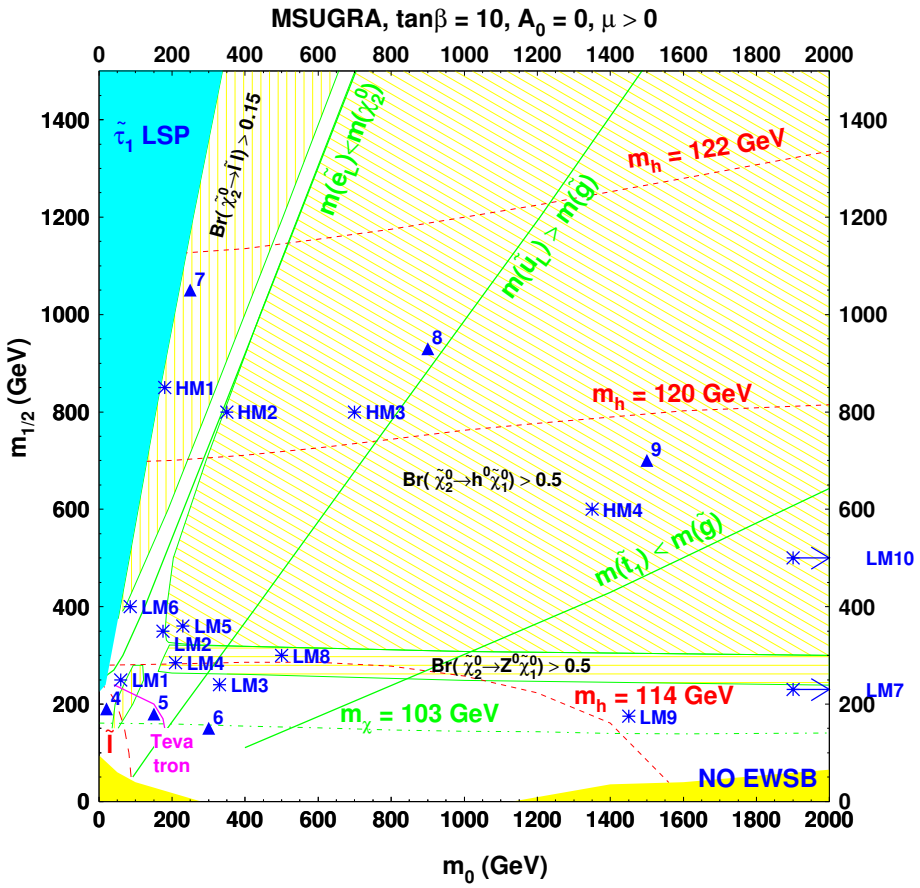

Figure 1.10: Position of the test points in the m_0 versus $m_{1/2}$ plane for $\tan\beta = 10$, $A_0 = 0$ and $\mu > 0$. The shaded regions are excluded because either the $\tilde{\tau}$ would be the LSP or because there is no radiative electroweak symmetry breaking. The regions excluded by the LEP limit on the h^0 and $\tilde{\chi}_1^{\pm}$ masses are delineated by dashed lines. The test CMS points are indicated by stars (LM7 and LM10 are outside the boundaries) and the points used in the CMS DAQ TDR by triangles. Also shown are the regions of interest for the decay of the $\tilde{\chi}_2^0$ by fine yellow shaded areas. Figure taken from the CMS Physics TDR volume II [67].

Figure 1.10 shows the intersection of the mSUGRA space with $\tan\beta = 10$, $A_0 = 0$ and $\mu > 0$, resulting in a plane in m_0 versus $m_{1/2}$. The cyan shaded area at low m_0 and increasing for higher $m_{1/2}$ leads to a (charged!) stau being the LSP, which is excluded by cosmological constraints on long-lived charged relic particles. The yellow shaded region at low $m_{1/2}$ is excluded because of lack of appropriate electroweak symmetry breaking. The regions excluded by the LEP limit on the h^0 and $\tilde{\chi}_1^{\pm}$ masses are delineated by red ($\tilde{l}$, bottom right) and green ($m_{\chi} = 103\,\text{GeV}$, bottom) dashed contours. The region excluded by the Tevatron three-lepton search is shown in a magenta solid line bottom right. Three separate regions for the decay of $\tilde{\chi}_2^0$ are indicated by yellow hatched regions with green contours. Further on Higgs boson mass isolines for the lightest Higgs boson h^0 are indicated by red dashed lines. An h^0 with low mass (114 GeV) tends to prefer a low value of $m_{1/2}$, while slightly higher masses necessitate already a huge value of $m_{1/2}$ within the mSUGRA models.

The electroweak precision data, as shown in Figure 1.4, favour a Higgs boson with mass 125-130 GeV. This is well within the expectations for a supersymmetric Higgs boson h^0, although taking into account large mass corrections. The implications of a 125 GeV Higgs scalar in

mSUGRA are stops, the lightest squarks, which have a mass of a few TeV. For $A_0 = 0$, $\tan\beta = 30$ and $\mu > 0$, one needs exceedingly high values of $m_{1/2} \sim m_0 \sim 10\,\text{TeV}$, resulting in gluino and squark masses in the 20 TeV range, way beyond the reach of the LHC. For higher values of $|A_0|$, M_h becomes nearly independent of $m_{1/2}$ and will manifest itself at lower masses of $m_0 \sim$ 3-4 TeV. In the case large m_0 values are required, scalar masses are predicted to be in the multi- TeV range, well beyond the LHC reach. However, gauginos can still be quite light and may be accessible to LHC SUSY searches [66]. One has to keep in mind that this analysis of the implications of a 125 GeV Higgs scalar is performed within the context of mSUGRA models, which is one of the most simple ideas to model. Bear in mind that, if supersymmetry exists, it might come in a totally different form than the mSUGRA model predicts.

1.4.6 Indirect and pre-LHC experimental constraints on the MSSM

Although supersymmetric particles have not yet been observed experimentally, there have been direct searches for supersymmetry since 1987 [70, 71]. Further on other experiments are sensitive (through loop contributions) to physics beyond the Standard Model, and hence also to supersymmetry. A short summary is provided below.

Indirect Constraints on the MSSM

The muon anomalous magnetic moment is one of the most precisely measured quantities in particle physics [72]. The magnetic moment of the muon is:

$$\vec{\mu} = g_\mu \frac{e\hbar}{2m_\mu c}\vec{S}, \tag{1.12}$$

with $\vec{S}$ the spin vector. The Dirac theory predict $g_\mu = 2$. Recent high precision measurements of the anomalous magnetic moment of the muon, shortly denoted $(g-2)_\mu$, has resulted in a 3.2σ deviation between theory and experiment [73], hinting at new physics beyond the Standard Model.

Within the Standard Model, the exclusive decay of the B_s^0 meson to two muons is rare, as it occurs only via loop diagrams and is helicity suppressed [74]. The branching ratio predicted by the Standard Model is [74]:

$$\text{BR}\left(B_s^0 \to \mu^+\mu^-\right)_{\text{SM}} = (3.2 \pm 0.2) \cdot 10^{-9}.$$

New Physics models, especially those with an extended Higgs sector (such as the MSSM) can significantly enhance the branching ratio, since new particles can contribute to the loops. At CDF a moderate excess was observed [75], hinting towards new physics beyond the Standard Model at the TeV scale. More recently, LHCb and CMS merged their forces by combining their results [74], using $0.34\,\text{pb}^{-1}$ and $1.14\,\text{pb}^{-1}$ of data, resulting in

$$\text{BR}\left(B_s^0 \to \mu^+\mu^-\right) < 1.08 \cdot 10^{-8} \text{ at } 95\% \text{ CL},$$

which are the best existing limits on this decay today. An enhancement of the branching ratio by more than 3.4 times the Standard Model prediction is excluded at 95% CL, still allowing for a contribution from physics beyond the Standard Model [74]. In an analysis of the impact of those limits [76], those obtained constraints can be superior to those derived from direct searches in

some SUSY scenarios. Just before this thesis went to press CMS submitted the update of the analysis, using the whole 2011 dataset [77]:

$$\mathrm{BR}\left(B_s^0 \to \mu^+\mu^-\right) < 7.7 \cdot 10^{-9} \text{ at } 95\% \text{ CL}.$$

A combination of the run 2011 ATLAS, CMS and LHCb results will follow soon [78].

Electroweak Precision Data

Although the electroweak precision data are one of the successes of the Standard Model and are well compatible with the measurements, a little stretch can be observed and interpreted as a hint for beyond the Standard Model physics. In an analysis [79] of the experimental data (excluding the m_t and M_W measurements) within the MSSM, a prediction for m_t, and M_W, were derived. The SUSY predictions for both m_t and M_W, are highly compatible with the measured values of m_t and M_W, with small remaining uncertainties. This yields an improved fit [80] when compared to the Standard Model fit.

In the Standard Model, the comparison between experimental data and theory is often made in the m_t, M_W plane, as already showed in Figure 1.5. The experimental values of m_t and m_W are essentially uncorrelated (hence the vertical ellipse of the SM fit) and m_t is an independent parameter, whereas the relation between M_W and M_Z can be predicted with high precision using m_t and M_H^{SM} [80].The correlation between m_t and the prediction for M_W is displayed in Figure 1.11 as lines of constant Higgs boson mass. A fit of the Standard Model parameters yields indirect predictions for m_t and M_H^{SM} and hence M_W. The regions of the m_t, M_W plane favoured at 68% CL by direct experimental measurements (black contour) and the SM fit (blue contour) have significant overlap, representing a non-trivial success for the SM. However, this overlap happens in a region of Higgs boson mass values excluded by the LEP Higgs boson searches: $M_H^{\mathrm{SM}} < 114.4\,\mathrm{GeV}$, indicating a certain tension between the precision observables and the Higgs limit. The direct Higgs boson searches at the Tevatron, as of December 2009, before LHC turn on in March 2010, excluded a range of $163 < M_H^{\mathrm{SM}} < 166\,\mathrm{GeV}$, which is indicated by the white diagonal line.

The SUSY prediction of the M_W (shaded green band) as a function of m_t in the unconstrained MSSM turns out to be lighter than the Standard Model prediction (shaded red band), that starts with the predictions of the SM Higgs boson with mass higher than the LEP exclusion $M_H^{\mathrm{SM}} < 114.4\,\mathrm{GeV}$. A small overlap region ($114.4 < M_H^{\mathrm{SM}} \lesssim 135\,\mathrm{GeV}$) is indicated as a shaded blue band. Fits were performed in the CMSSM and NUHM1 models, using all electroweak precision observables used in the SM fit, as well as constraints from $(g-2)_\mu$, flavour physics, cold dark matter (CDM) relic density and direct searches for the Higgs and SUSY particles, but excluding the experimental measurements of m_t and M_W. The results of the fits are also expressed as 68% CL contours in Figure 1.11 and show remarkably good agreement with the experimental measurements of m_t and M_W [80]. Although it is only a $\sim 1\sigma$ effect, the measurements of m_t and M_W from the Tevatron and LEP experiments tend to favour SUSY over the Standard Model.

Direct searches for supersymmetry prior to LHC running

Direct searches for supersymmetry have been performed with every hadron or lepton collider built since 1987. For instance, after discovering the W and Z bosons at the S$\bar{\mathrm{p}}$pS, the UA1 and UA2 collaborations did a search for supersymmetric particles [70, 71]. Direct searches for

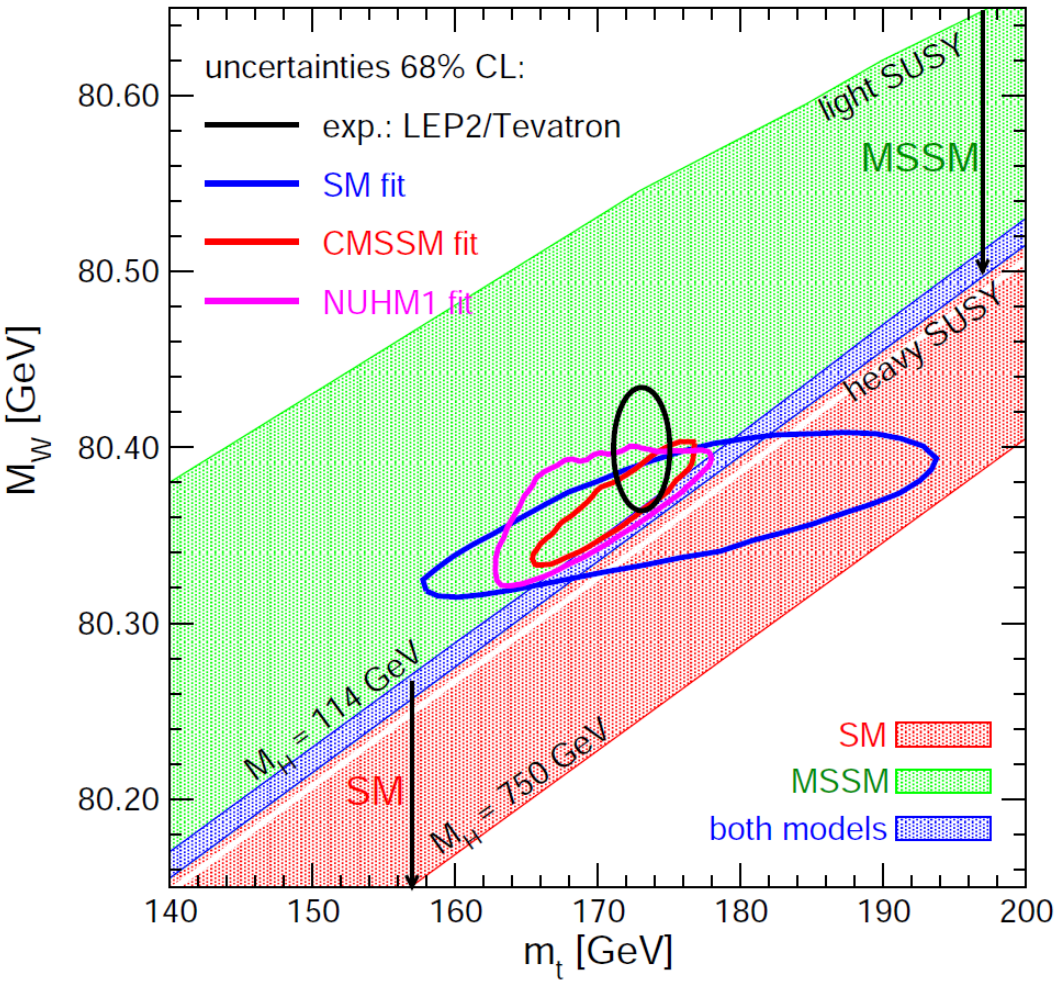

Figure 1.11: The measurement of m_t and M_W at Tevatron and LEP tend to favour SUSY over the Standard Model. The 68% CL regions in the m_t, M_W plane, predicted by a SM fit excluding the LEP Higgs boson constraint, and the CMSSM and NUHM1 fits including the LEP Higgs boson mass constraint, compared with experimental measurements from LEP2 and the Tevatron shown as the black ellipse. The medium gray (red) and the dark (blue) shaded regions show the SM prediction, existing of lines of constant M_H^{SM} values. The light gray (green) and dark (blue) regions show the prediction of the unconstrained MSSM ranging from light to heavy SUSY particles. The arrows indicate the increase of the Standard Model Higgs boson mass (M_H^{SM}) (bottom left) and the increase of the mass of the supersymmetric particles (top right) and the Higgs boson (bottom left). Figure taken from Reference [80].

supersymmetry have been performed at the LEP [81], HERA [82, 83], and Tevatron experiments [84–87], so far without any succes. The lack of succes could be interpreted as excluding a certain region in supersymmetric parameter space, and as far as the mSUGRA m_0, $m_{1/2}$ planes where the limits were set, were identical or projectable to the m_0, $m_{1/2}$ planes used for limit setting at the LHC, these limits were included and shown as shaded areas, such as in Figure 1.10, which was made before the large integrated luminosity Tevatron analyses were published.

1.5 Studying physics by the means of *pp* collisions

1.5.1 Protons

The interactions between quarks and gluons is described by a renormalizable gauge theory: Quantum Chromo Dynamics (QCD). QCD describes the strong interaction between particles carrying colour charge by modelling the exchange of a gluon. The gluon itself also carries colour charge, which is in strong contrast with the photon in Quantum Electro Dynamics (QED). The photon mediates the electromagnetic interaction between electrically charged particles, but is electrically neutral itself. Therefore the gluon can interact with other gluons, since it carries colour charge itself. This has interesting consequences for the binding of particles by the strong force.

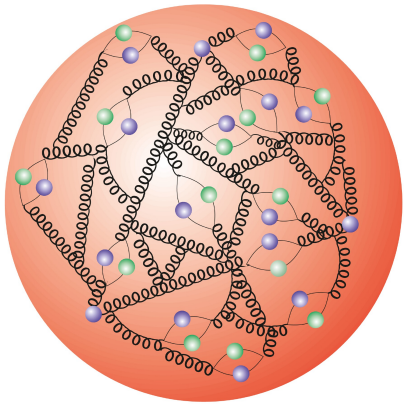

Figure 1.12: Schematic picture of the inner structure of the proton. Copyright: © DESY.

Inside hadrons, such as a proton shown in Figure 1.12, the quarks are bound together by gluons. Overlap between the quark and gluon soup of different nucleons leads to the binding of protons and neutrons inside atomic nuclei. The strength of the interaction is described by the coupling constant of the strong interaction α_S. While the coupling constant of the electromagnetic interaction α_{EM} is more or less constant[8], the coupling constant of the strong interaction decreases drastically as is shown in Figure 1.13. Asymptotically, at very high energies, or equivalently, very small distances, the strong interaction becomes very weak, leading to quarks being free. This property of QCD is called "asymptotic freedom".

Another consequence of the interaction between gluons emerges in QCD: "confinement", i.e. only colourless particles can exist. This explains why (coloured) quarks are not observed as free particles, but only in bound states: mesons being quark-antiquark states in which the quark and antiquark have opposite colour or baryons that consist of three quarks (or anti-quarks) with three different colours, summing up to zero net colour ("white").

If in a collision a quark-antiquark pair is produced, the quarks will have opposite momentum in the transverse plane and separate. When the separation is of the order of 1 fm = 5.07 GeV $^{-1}$, α_S becomes large and the colour interaction between the quarks becomes really strong. This force will decelerate the quarks, that will radiate partons, just as decelerated electromagnetic charges radiate photons by Bremsstrahlung. The original quark is never seen in its "free" state, only the colourless hadrons can experimentally be observed [4]. The strong colour interaction leads to a spray of hadrons, called "jets" and these are experimentally observable.

The reference scale in QCD for the defintion of the coupling constant is taken at the energy scale of the Z^0 mass. At this scale the coupling constant is small, hence the strong force is relatively "weak", to allow perturbation theory. The scale at which the renormalization constant diverges, $\Lambda_{QCD} \approx 200\,\text{MeV}$, is the non-perturbative scale of QCD, where the quarks interact strongly.

[8]The electromagnetic coupling constant varies from $\alpha_{EM}^{-1}(0) = 137.035\,999\,074 \pm 0.000\,000\,044$ [88] at low energy to $\alpha_{EM}^{-1}(M_Z) = 128.952 \pm 0.014$ [89] at the energy scale of the Z mass.

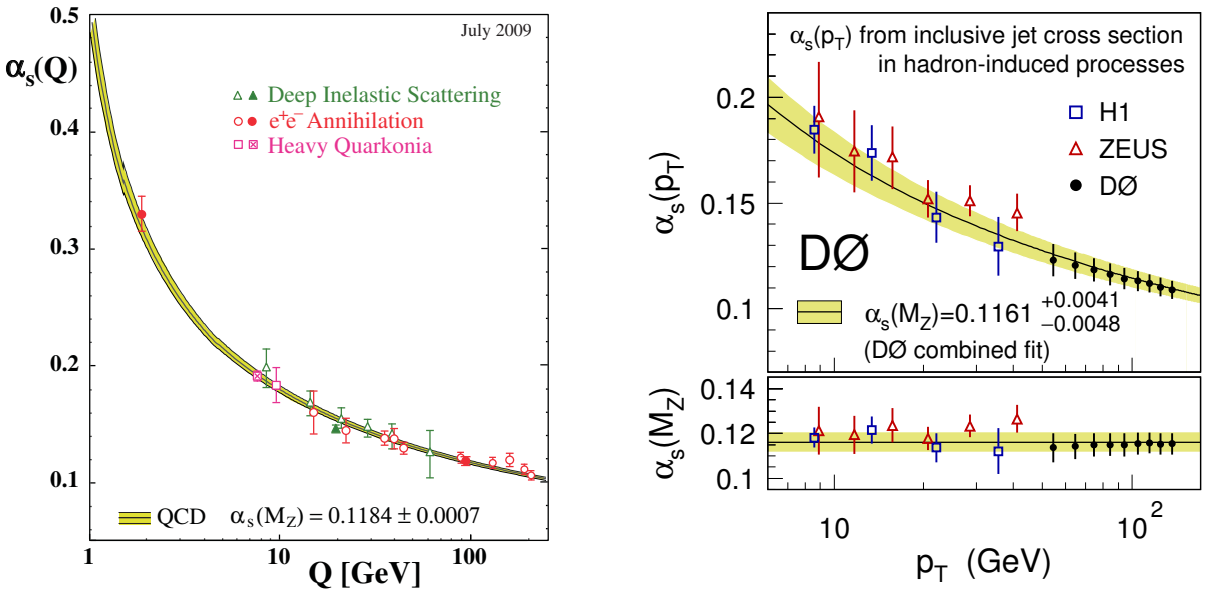

Figure 1.13: Measurement of α_S as a function of the momentum scale Q. Left: the world average as of July 2009. Right: the DØ measurement published December 2009. The curves on the left plot are the QCD predictions for the world average of α_S. Left: the measurements were performed at PETRA, HERA and LEP. Right: measurements at HERA and DØ as a function of p_T. Figures taken from References [90, 91].

1.5.2 Using protons to study Nature

A very efficient way to study a broad range of physics at the scale of particle physics is by giving particles more energy by accelerating them and subsequently collide them head on. Colliding protons on protons allows for high energy interactions between their constituents. If the energy transfer between the two interacting partons is high enough new particles could be produced following Einsteins mass-energy equivanlence. Any type of particles available in Nature could be produced, and thereafter studied, if the energy is above the mass threshold for the particle being created. By counting events, either all of them passing certain criteria, or by sorting them in different bins, according to their p_T, η, ϕ, purity, quality or more advanced physics observables that are based on these basic variables, cross sections could be estimated. These cross sections are in fact normalized event counts and they can be used as input for more advanced measurements, such as coupling constants, mass measurements, etcetera.

One could chose for colliding pointlike particles, such as electrons, rather than composite objects such as protons. Protons can be accelerated to much higher energies than electrons, but have a major drawback. They are composite particles. Each of their components, called "partons", carries a fraction x of the total proton momentum. The advantage of proton proton collisions is that they scan a broad range of collision energies, the disadvantage is that the probability to have a collision between two partons with high momentum fraction x is very small. Further on, the remnants of the proton cause a background to the signature of the two partons interacting with each other, whereas in an e^+e^- collider there is no background to the signature.

1.5.3 Proton-proton collisions

Proton-proton collisions can be subdivided in three broad categories: elastic, diffractive or inelastic:

- **Elastic collisions** preserve the total kinetic energy of both protons, only changing their direction of flight. These collisions are typically at very low momentum transfer, and the signature consists of two slightly-deflected protons at very small angles with respect to the beamline. At very low momentum, Coulomb scattering is dominant, while at higher energy the exchange of a colourless pomeron dominates.

  In addition to these real elastic collisions, there is another process giving almost the same final state with two slightly deflected protons, but where the total kinetic energy of the protons is not conserved. Each proton can also emit a photon (or pomeron) that interact with each other through a fermion line, whereby, for instance, two final state muons are produced. The signatures of these collisions are very clean, e.g. two muons, and without coloured proton remnants polluting the event.
- **Diffractive collisions**, or diffractive scattering, happens at slightly larger momentum transfer, where one (single-diffractive) or both (double-diffractive) of the protons fragment due to the exchange of a colourless pomeron. These collisions are characterized by hadronic activity at very small angles with the beamline on one or both sides of the detector (in the so-called "forward" detectors of CMS), while no activity is observed at large angles with the beamline (in the so-called "central" detector of CMS).
- **Inelastic collisions** These interactions are all non-diffractive hadronic interactions, in which two partons of each proton interact with each other. Most of the interactions happen at low four-momentum transfer, but a small fraction occurs at high four momentum transfer, and these are the interactions of interest to most of the LHC physicists (and for this thesis). These low for-momentum interactions are referred to as "Minimum Bias" interactions, since there impact on the performance of the detector is to introduce a "minimum bias" in terms of detector occupancy and p_{T} estimations, since the interesting events at high four momentum transfer are snowed under by the orders of magnitude higher soft interactions.

The LHC is designed to collide protons head on with a beam energy of $E_{\mathrm{b}} = 7\,\mathrm{TeV}$, leading to a centre-of-mass energy $\sqrt{s} = 2E_{\mathrm{b}} = 14\,\mathrm{TeV}$. The total proton-proton cross section σ_T, extrapolated from previous experiments at lower energies, is expected to be $\sim 110\,\mathrm{mb}$ at centre-of-mass energies of $\sqrt{s} = 14\,\mathrm{TeV}$, of which $\sim 30\,\mathrm{mb}$ comes from elastic scattering, $\sim 24\,\mathrm{mb}$ is due to diffractive collisions, while $\sim 55\,\mathrm{mb}$ originates from (non-diffractive) inelastic collisions. These predictions have systematic uncertainties of the order of 20%.

TOTEM [92] has measured the differential cross-section for elastic proton-proton scattering at the LHC energy of $\sqrt{s} = 7\,\mathrm{TeV}$ analysing data from a short run with dedicated optics. The total elastic cross section was measured to be $\sigma_{\mathrm{el}} = 24.8\,\mathrm{mb}$, applying the optical theorem[9] and using the CMS Luminosity measurement the total pp collision cross section at $\sqrt{s} = 7\,\mathrm{TeV}$ was measured to be $\sigma_{\mathrm{tot}} = 98.3 \pm 3\,\mathrm{mb}$ [93].

[9]The optical theorem is a general law of wave scattering theory, which relates the forward scattering amplitude to the total cross section of the scatterer.

Inelastic proton-roton collisons happen between two partons of the proton, carrying a momentum fraction x_1 and x_2 of the total proton momentum. In general x_1 and x_2 are not equal, leading to a rest frame that is boosted along the beamline. If the z-axis is placed along the beamline, with the xy-plane transverse to the beamline, the movement of the rest frame with respect to the lab frame is expressed as the rapidity y:

$$y := \frac{1}{2} \ln \frac{E + p_z}{E - p_z}, \tag{1.13}$$

with p_z the momentum along the beamline and E the energy in the rest frame. The rapidity of a particle is Lorentzinvariant under a boost, and therefore also the rapidity difference between two particles. Proton-proton collisions are better studied in a dedicated coordinate frame incorporating the rapidity. Therefore first sperhical coordinates (r, ϕ, θ) are introduced by defining the radius $r = \sqrt{x^2 + y^2 + z^2}$, polar angle θ as the angle with respect to the z-axis in the xz-plane, and azimuthal angle ϕ defined as the angle with respect to the x-axis in the xy-plane. These spherical coordinates are then replaced by modified spherical coordinates (r, ϕ, η), where the polar angle θ is replaced by an approximation of the rapidity y, the pseudorapidity η:

$$\eta := -\ln\left(\tan\frac{\theta}{2}\right). \tag{1.14}$$

In this coordinate frame, transverse quantities and differences are invariant in η under Lorentz-boosts along the beamline. As a consequence, the solid angle in η, ϕ is also invariant under longitudinal boosts.

The boost of the proton-proton collision cannot be reconstructed. Therefore, the initial centre-of-mass energy of the collision $(x_1 + x_2) \times E_\mathrm{b}$, is unknown. Only observables transverse to the collision are conserved. Two very important observables are the transverse momentum of a particle, p_T, and the missing transverse momentum , $\vec{\not{E}}_\mathrm{T}$, of an interaction. The transverse momentum, p_T, is the projection of the momentum of a particle on the transverse plane. The transverse and longitudinal momentum are defined as:

$$p_\perp \equiv p_\mathrm{T} := \sqrt{p_x^2 + p_y^2}, \tag{1.15}$$

$$p_\parallel \equiv p_\mathrm{L} := p_z. \tag{1.16}$$

The (x, y, z) components of the momentum can be obtained from the transverse momentum, the azimuthal angle ϕ and pseudorapidity η by the following formulae:

$$p_x = p_\mathrm{T} \cdot \cos\phi, \tag{1.17}$$

$$p_y = p_\mathrm{T} \cdot \sin\phi, \tag{1.18}$$

$$p_z = p_\mathrm{T} \cdot \sinh\eta. \tag{1.19}$$

The missing transverse momentum is obtained by summing all transverse momenta of the particles in a collision:

$$\vec{\not{E}}_\mathrm{T} := -\sum_i \vec{p_\mathrm{T}}(i). \tag{1.20}$$

The protons entering the pp collision have initially no transverse momentum[10], hence the sum of the transverse momenta all particles emerging from a collision should be zero. Experimentally,

[10]Neglecting the small transverse momenta of the partons inside a proton.

particles could leave the detector undetected, such as neutrinos or particles emitted close to the beamline, or transverse momenta could be mismeasured. This will result in a transverse momentum imbalance:

$$|\vec{\not{E}}_{\mathrm{T}}| \neq 0.$$

The magnitude of the transverse momentum vector, $|\vec{\not{E}}_{\mathrm{T}}|$, is called the missing transverse energy, denoted $\not{E}_{\mathrm{T}}$, $E_{\mathrm{T}}^{\mathrm{miss}}$ or MET.

1.5.4 The factorization of the hard and the soft interactions

To study the physics of the electroweak symmetry breaking, or to discover new particles that could possibly fit within the supersymmetry framework, one needs to study particle collisions with very high momentum transfer. These so-called hard interactions are interactions between the partons inside the colliding protons. The momentum fraction x carried by a parton is described by a so-called "parton distribution fuction" (pdf). There is one pdf for each quark flavour in the proton and one pdf for the gluon. The parton distribution function is defined as the probability density to find a parton with momentum fraction x at squared four-momentum transfer Q^2: $f(x, Q^2)$. This squared four-momentum transfer is a measure for the resolution at which the structure of the proton is probed[11]. Experiments at higher Q^2 probe the proton at smaller scales and at these smaller scales quarks are found to be surrounded by much softer quarks and gluons. This is called "scaling violation", and leads to an increased number of resolved partons and hence an increased probability of finding a quark at small x. This lowers the probability to find a quark with high momentum fraction x, because the high-momentum quarks lose momentum by radiating gluons. This scaling violation is shown in Figure 1.15: the pdfs of the quarks and the gluon become steeper at higher Q^2. The valence quarks are responsible for most of the protons momentum, which is reflected in the particular shapes of the u and d quark pdfs.

The partons in the proton are bound by QCD at energy scales where the coloured interaction is very strong. Therefore the parton distribution functions cannot be calculated and are obtained using experimental data. Parton distribution functions are made available by several collaborations. The best known examples come from the CTEQ [96, 97] (now CT10 [98]) and MSTW [99] groups. Figure 1.15 shows the parton distribution functions fitted by the MSTW group at $Q^2 = 10\,\mathrm{GeV}^2$ and $Q^2 = 10^4\,\mathrm{GeV}^2$. The gluon contribution is dominant at low x and is divided by ten.

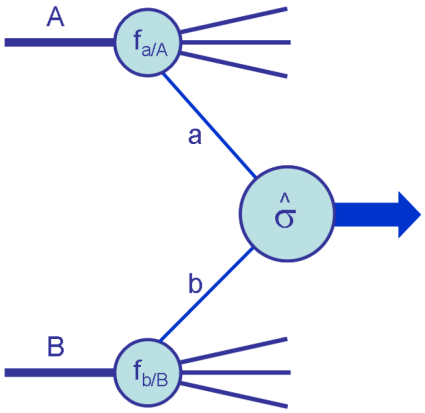

Figure 1.14: A hard scattering process. Figure taken from Reference [95].

The parton distribution functions are measured at one scale Q^2 and can be used to predict the

[11] In the Breit frame, where the energy transfer between the two colliding partons is zero, Q^2 fixes the reduced wavelength, $\lambda\!\!\!^{-}$, of the parton-parton interaction, which is the spatial resolution at which structures can be studied [94]:

$$\lambda\!\!\!^{-} = \frac{\hbar}{\sqrt{Q^2}} \tag{1.21}$$

Q^2 is often denoted as the "virtuality" and it sets the scale for the resolution at which the proton is probed.

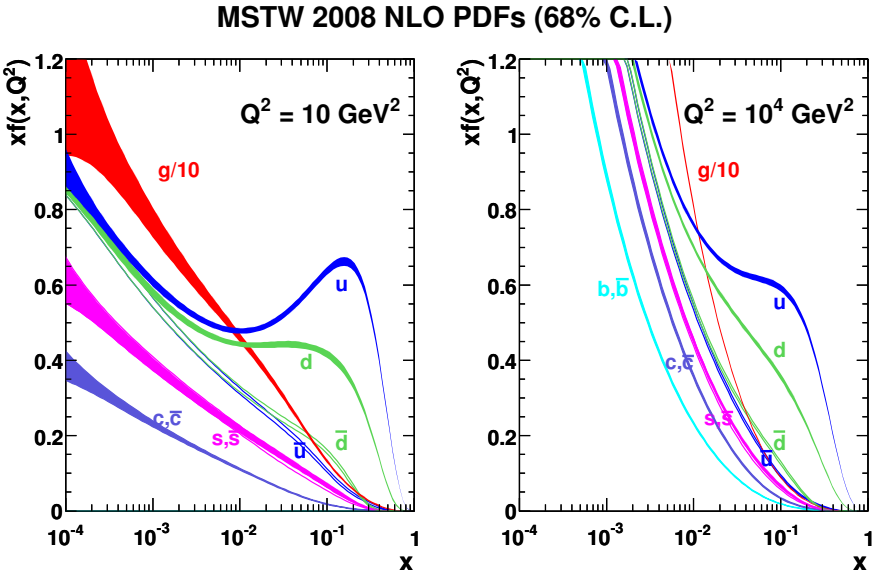

Figure 1.15: MSTW 2008 NLO pdfs at $Q^2 = 10\,\mathrm{GeV}^2$ and $Q^2 = 10^4\,\mathrm{GeV}^2$. Figure taken from Reference [99].

distribution of partons at another scale Q'^2, if both $\alpha_S(Q^2)$ and $\alpha_S(Q'^2)$ are sufficiently small, such that perturbation theory is still applicable. This feature is used to extrapolate the pdfs from DIS experiments at lower energies to the energy range of importance for the LHC.

Using these parton distribution functions, the hard part of a hadronic interaction $A + B \rightarrow X$ can be factorized. The total hadronic cross section of a hard scattering is calculated by convoluting the probability functions for finding a parton a inside a proton A, $f_{a/A}$, and for finding a parton b inside a proton B, $f_{b/B}$, with the cross section of the partonic interaction, as shown in Figure 1.14:

$$\sigma_{A+B\rightarrow X} = \int \mathrm{d}x_a \mathrm{d}x_b \cdot f_{a/A}(x_a, Q_F^2) \cdot f_{b/B}(x_b, Q_F^2) \cdot \hat{\sigma}_{a+b\rightarrow X}, \tag{1.22}$$

where Q_F^2 is called the factorization scale. This scale Q_F^2, sometimes also denoted μ_F^2, separates the hard partonic interaction, that can be calculated using perturbative QCD, and the soft, non-perturbative, interaction, which is parametrized by the parton distribution functions.

The partonic cross section $\hat{\sigma}_{a+b\rightarrow X}$ can be calculated in perturbation theory. This results in an expansion in orders of $\alpha_S(Q_R^2)$:

$$\hat{\sigma}_{a+b\rightarrow X} = \left[\hat{\sigma}_0 + \alpha_S(Q_R^2) \cdot \hat{\sigma}_1 + \ldots\right]_{a+b\rightarrow X}, \tag{1.23}$$

where Q_R^2, sometimes written as μ_R^2, is the renormalization scale of the running coupling constant of the strong interaction. In calculation the renormalization scale and the factorization scale are often chosen to be the same:

$$Q^2 \equiv Q_F^2 \equiv Q_R^2. \tag{1.24}$$

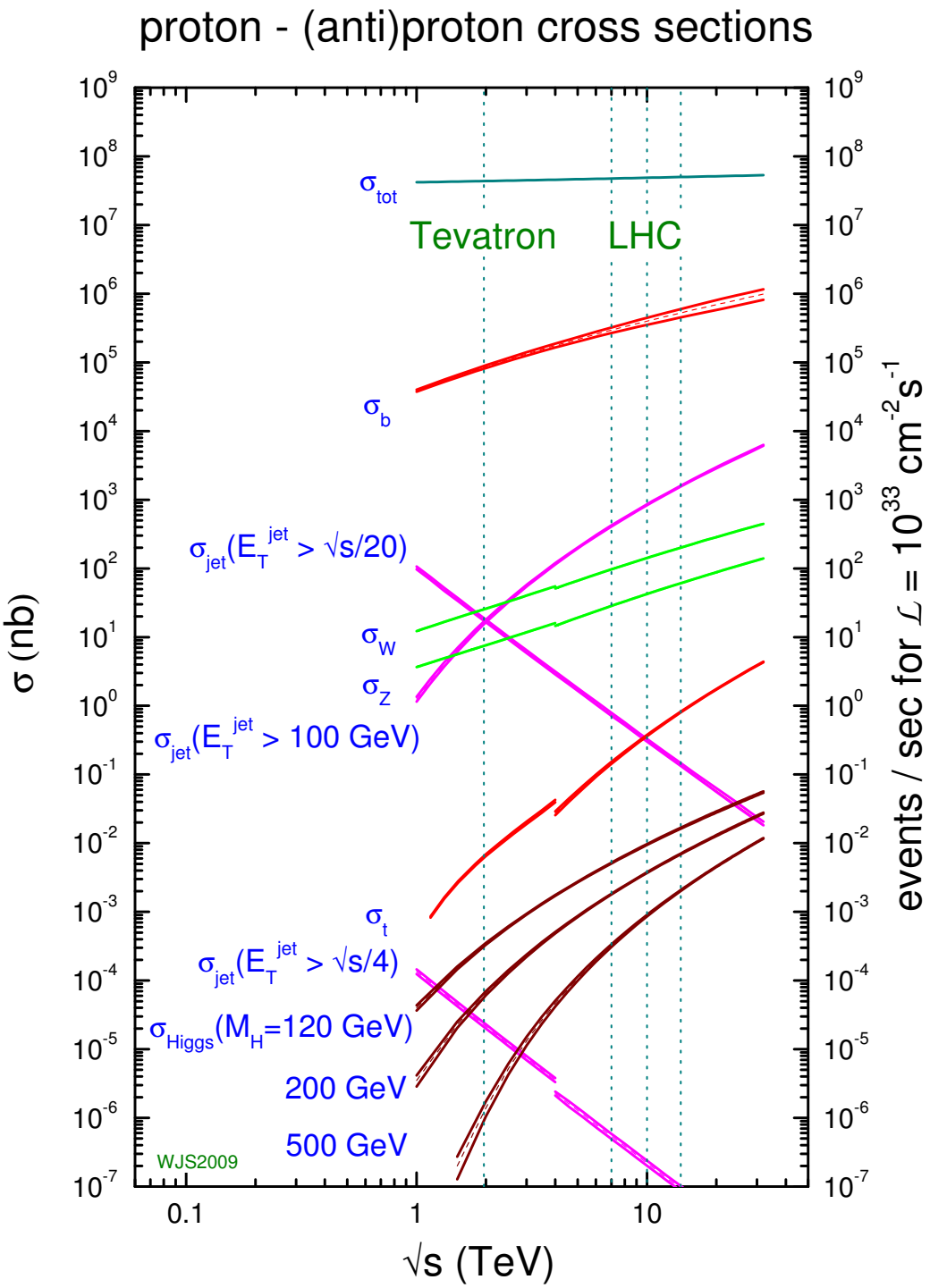

Figure 1.16: Standard Model cross sections at the Tevatron and LHC colliders as a function of centre-of-mass energy $\sqrt{s}$. The dashed lines indicate the centre-of-mass energies at which the Tevatron is run: $\sqrt{s} = 1.96$ TeV, and $\sqrt{s} = 7$, 10, and 14 TeV for LHC. On the left side the cross section of the different physics processes is indicated in nanobarn, while on the right side the event rate [Hz] is shown for an instantaneous luminosity of $\mathcal{L} = 10^{33}\,\mathrm{cm}^{-2}\mathrm{s}^{-1}$, which is typical for the first years of LHC operation. Figure taken from Reference [100].

Figure 1.16 shows the predictions for some important Standard Model cross sections at $p\bar{p}$ and pp colliders, calculated at next-to-leading order in perturbation theory, including the $\hat{\sigma}_1$ term of equation 1.23. The total cross section is orders of magnitude higher than the cross section for W and Z production. The cross section for high energetic jets follows a s^{-1} behaviour, while the cross sections for producing Higgs bosons are very small and decrease with increasing mass.

1.5.5 Inelastic proton proton collisions

The major processes that can be distinguished in inelastic proton proton collisions are shown in Figure 1.17 and listed below:

- **The hard scattering** (red blob) happens between two high energetic partons of the protons.
- **The underlying event (UE)** (magenta) is caused by the coloured remnants of the two protons, not directly involved in the hard interaction.
- **Initial state radiation (ISR)**: before the two partons interact, they have a non-negligible probability to radiate quarks and gluons.
- **Final state radiation (FSR)**: the outgoing particles of the hard scatter can, in their turn, also radiate quarks and gluons.
- **Hadronization**: all coloured particles, either coming from breaking up the proton, or produced in the hard part of the interaction will form jets of colourless hadrons.
- **Decay**: short-living hadrons and mesons produced in the hadronization process decay finally to stable particles.

When two partons with high momentum fractions x_1 and x_2 interact, the other low-x partons, not involved in the hard interaction hadronize in the underlying event. Sometimes these low(er)-x partons can undergo separate scatterings, called "multiple interactions", and depending on the "hardness" of this scattering this reaction can spoil the picture of the real hard interaction. Imagine having two separate (semi-) hard interactions, both of them are simple $2 \to 2$ scattering processes, as shown in Figure 1.18. At sufficiently high energy, each scattering process results in a QCD dijets signature, which will contaminate the measurement of the physics process where one hard scattering process results in four jets ($2 \to 4$ scattering process). Fortunately, the probability for two equally hard interactions when colliding two protons is very small. This process is described by the underlying event, which is analyzed in depth, for instance in References [101, 102].

For the simulation of high-energy physics events in this thesis, a dedicated event generator, Pythia [104] was used. Physics processes are simulated by drawing numbers from probability distributions, which are simulated using random generators based on Monte-Carlo techniques. Therefore these event simulations are called Monte-Carlo simulations, or sometimes short "Monte-Carlo". Event generators often simulate the hard scatter process only, but Pythia takes all aspects of proton proton collisions (listed above) into account, starting with the hard interaction and ending with the decay of mesons formed during hadronization.

The simulation starts with two protons, brought into collision. The proton is characterized by a set of parton distribution functions, describing the probability to find a parton with a certain fraction of the proton longitudinal momentum. A shower is initiated by one of the partons of

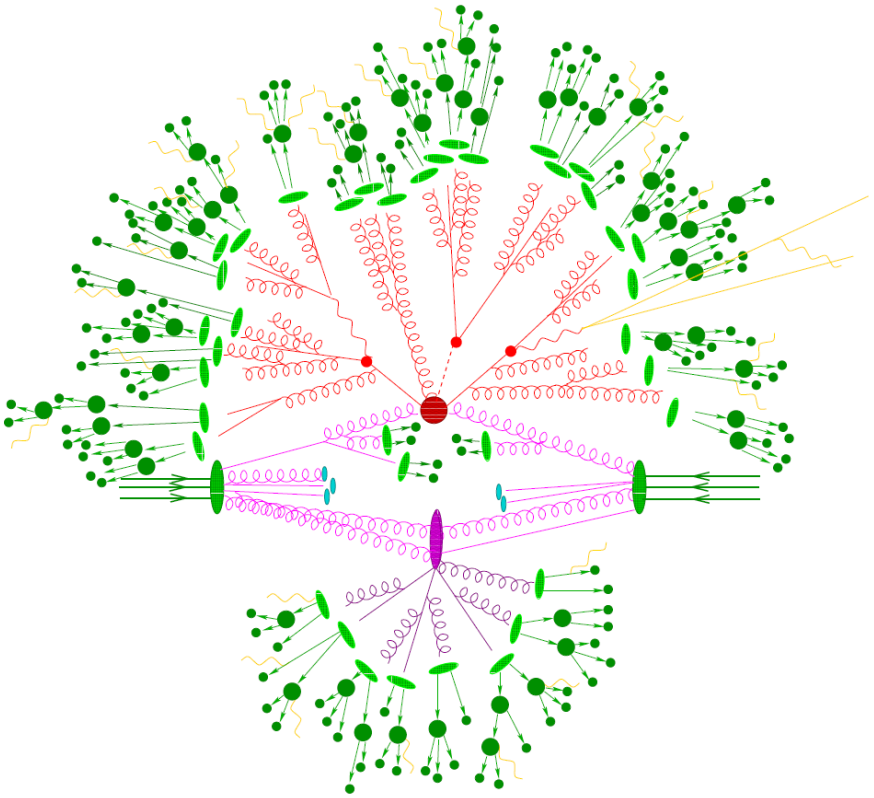

Figure 1.17: Scheme of a proton proton collision. Two partons of the incoming proton interact in the hard interaction (red), while the proton remnants (magenta) provide the underlying event. The partons created in the hard interaction hadronize (light green) and unstable hadrons decay further to stable particles (dark green). Figure taken from Reference [103].

the proton, this is an initial state radiation shower. One incoming parton from each of the two showers enters the hard process, where a number of outgoing partons is produced. It is this process that is of interest to us and that characterizes the generated event. The hard process may produce a set of short-lived resonances, for instance the Z-boson, whose decay to normal partons ($Z \rightarrow q\bar{q}$) has to be considered with the hard interaction as a whole. The outgoing partons branch, just as the incoming partons, causing final state radiated showers. In addition to the so-called hard process above, further semi-hard interactions may occur between other partons of the two protons. When a shower initiator is taken out of a beam particle, the beam remnant is left behind, with a net colour charge that is related to the rest of the final state. The QCD confinement mechanism ensures that outgoing quarks and gluons are not observable, but instead fragment to colour-neutral hadrons. Unstable hadrons, formed during the hadronization decay further to stable particles.

Apart from multi-purpose event generators such as Pythia, Sherpa [103] and Herwig [105, 106], also more specific generators exist. For the calculation of the hard scattering process, dedicated Matrix Element calculators such as MadGraph [107] and AlpGen [108] were developed. These event generators calculate the matrix element of the hard interaction with more precision (at higher orders in perturbation theory or equivalently for more outgoing partons, such as $2 \rightarrow 4$ scattering, where 4 jets are produced in the final state), where Pythia only calculates the $2 \rightarrow 2$ scattering at leading order. Higher-order processes in Pythia are then taken into account in the fragmentation of the outgoing partons. In this thesis MadGraph was used for the calcula-

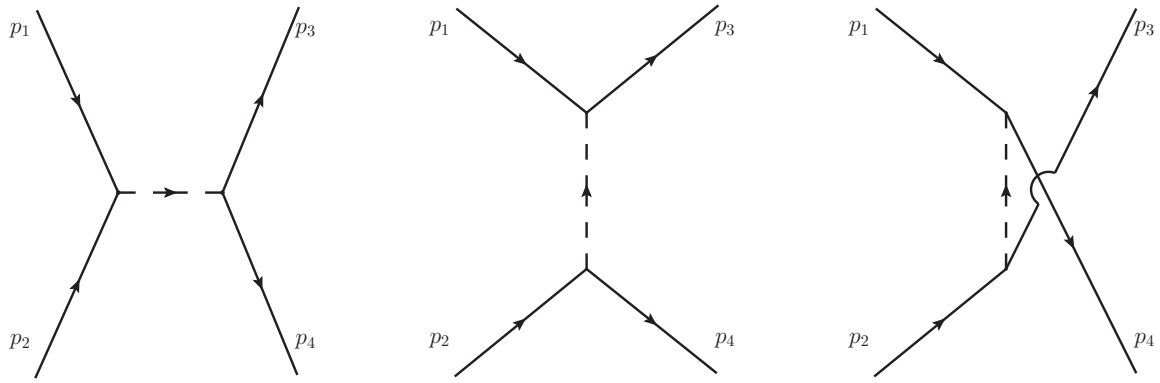

(a) s-channel (b) t-channel (c) u-channel

Figure 1.18: $2 \to 2$ scattering of partons in three different channels: the s-, t- and u-channel. In these Feynman diagrams time goes from left to right.

tion of the hard scattering process, and is then interfaced with Pythia. MadGraph receives the type and momentum of the incoming partons and delivers the outgoing partons to the Pythia framework, which then takes care of the hadronization, decay and underlying event. Since the distinction between the hard-scattering process and the parton shower process is far from trivial, care should be taken to match both generators properly, avoiding double counting as well as avoiding non-covered regions in phase-space. Basically, there are two different solutions to this problem: the MLM scheme [109, 110] and the CKKW [111, 112] scheme. Both schemes have been implemented in the various event generators and both provide good predictions. After implementing matching the hard matrix element calculations with the parton shower calculations, the soft minimum bias interactions are added to simulate the effect of the pile-up. All pp collisions happening during the same bunch crossing, i.e. when two beams cross each other, are collected in one set, which is called an **event**.

Figure 1.18 shows the three possibilities for $2 \to 2$ scattering of partons (with mass m_1, m_2, m_3, and m_4) at leading order: resonance formation in Figure 1.18(a) and scattering by the exchange of a virtual particle in Figures 1.18(b) and 1.18(c). These three possibilities are called the s, t, and u channels, since the four-momentum exchange of each of them equals the Mandelstam variables $\hat{s}$, $\hat{t}$, and $\hat{u}$ respectively:

$$\hat{s} := (p_1 + p_2)^2 = (p_3 + p_4)^2, \tag{1.25}$$

$$\hat{t} := (p_1 - p_3)^2 = (p_2 - p_4)^2, \tag{1.26}$$

$$\hat{u} := (p_1 - p_4)^2 = (p_2 - p_3)^2. \tag{1.27}$$

Energy conservation requires $\hat{s} + \hat{t} + \hat{u} = m_1^2 + m_2^2 + m_3^2 + m_4^2$, leaving only two independent variables. Often the centre-of-mass energy is expressed as the square root of the Mandelstam-$\hat{s}$ variable:

$$E_{\text{com}} = 2E_{\text{b}} = \sqrt{s}. \tag{1.28}$$

The $2 \to 2$ scattering can be extended at next to leading order by adding one more particle, leading to $2 \to 2$ scattering in which there is a loop, or $2 \to 3$ scattering in which there is an additional parton radiated. Both processes are necessary to obtain finite cross section calculations. The cross section, however, will diverge if a (massless) parton is radiated collinearly (the angle

between the two partons is zero) or a soft (massless) parton (with zero energy) is radiated. These singularities are not physical, but rather a demonstration of the breakdown of the perturbative approach. When the angle between, for instance, a radiated gluon and a quark becomes small, both particles will be contained in the same jet, which is a $2 \to 2$ scattering from an experimental point of view. On the other hand the exclusive $2 \to 3$ process is suppressed by a factor α_S with respect to the exclusive $2 \to 2$ scattering. The former process can therefore be seen as a (higher-order) correction to the latter. Singularities in the $2 \to 3$ process turn out to be canceled exactly by the (virtual) corrections to the $2 \to 2$ scattering with one loop. This renormalization procedure necessarily introduces an unphysical renormalization scale Q_R^2 or μ_R.

The parton branching in QCD will cause the coloured quarks to end up in colourless hadrons. Three types of QCD branching are allowed: a quark can radiate a gluon ($q \to qg$), a gluon can split into a quark-quark pair ($g \to q\bar{q}$) or a gluon can split into two gluons: ($g \to gg$). Singularities in the cross section of these processes arise when the gluon radiation becomes soft or when gluons are emitted at small angles. As said, these so called "infrared" and "collinear" divergences expresses rather the breakdown of perturbativity at decreasing energies due to the rising of the strong coupling constant α_S.

Due to the increase of the strong coupling constant at small energies, the parton shower can not be calculated in perturbation theory until low energy hadrons are formed. The calculation has to be followed by a non-perturbative hadronization of the partons into colour neutral hadrons. This hadronization process is not yet fully understood and cannot be calculated. However, several models were proposed that describe experimental results rather well. The Lund string model is the model implemented in Pythia.

1.5.6 Parton-parton luminosities as benchmark for the LHC

The parton distribution functions are very important to see what reactions will dominate in $p\bar{p}$ and pp interactions. This is illustrated using parton luminosities, which are a very convenient tool for estimating the physics potential of hadron colliders. The definition of the parton luminosities [95, 113] takes into account the $1/\hat{s}$ behaviour of the hard scattering interaction:

$$\frac{\tau}{\hat{s}} \frac{\mathrm{d}\mathcal{L}_{a+b\to X}}{\mathrm{d}\tau} := \frac{\tau/\hat{s}}{1+\delta_{ab}} \int_\tau^1 \frac{\mathrm{d}x}{x} \left[f_a(x) f_b(\tau/x) + f_a(\tau/x) f_b(x) \right] \tag{1.29}$$

where the mass scale of the process $M_X^2 = \hat{s}$, with the Mandelstam-$\hat{s}$ variable describing the squared momentum transfer of the parton-parton interaction of the $2 \to 2$ processes. The parton luminosity has the dimension of a cross section and for collisions with a centre-of-mass energy $\sqrt{s}$ the scaling variable τ is given by:

$$\tau = \frac{\hat{s}}{s} = \frac{M_X^2}{s}. \tag{1.30}$$

The ratio of the parton luminosities at the LHC (for the $\sqrt{s} = 7\,\mathrm{TeV}$ runs of 2010-2011 and the runs at design energy $\sqrt{s} = 14\,\mathrm{TeV}$) with respect to the parton luminosities at the Tevatron (operated at $\sqrt{s} = 1.96\,\mathrm{TeV}$) is shown in Figure 1.19(a). For this plot, the MSTW 2008 pdfs were used, with $ab = gg, \sum q\bar{q}$, where the sum runs over all light quarks. These parton luminosities describe the gain in cross section of the processes under study for higher collision energies at the LHC.

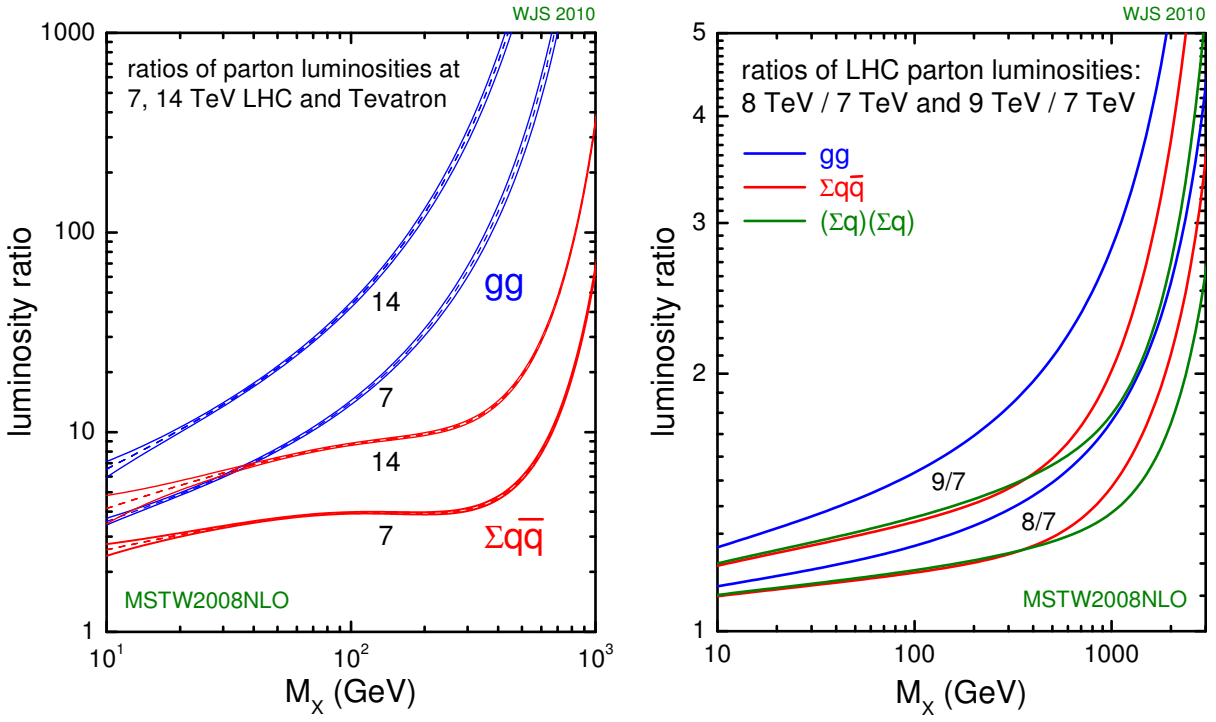

Figure 1.19: Ratio of parton luminosities using the MSTW 2008 NLO pdfs. Left: ratio of parton luminosities at $\sqrt{s} = 7$ and 14 TeV at the LHC compared to $\sqrt{s} = 1.96$ TeV at Tevatron. Right: ratio of parton luminosities at $\sqrt{s} = 8, 9$ TeV compared to $\sqrt{s} = 7$ TeV at the LHC. In the left figure, the 1σ uncertainty band is shown. Figures taken from Reference [100].

The LHC is predominantly a gluon-gluon machine, with the gluon-gluon luminosities being more than a factor 2 higher than the integrated quark-antiquark luminosity. The increase of the cross sections at the LHC with respect to the Tevatron is tremendous: at $M_X = 100$ GeV, the cross sections for quark-antiquark processes become almost a factor 10 higher, while the cross sections for gluon gluon processes will be a factor 40 higher at the LHC design center of mass energy $\sqrt{s} = 14$ TeV. This does not only mean that the cross section for interesting physics will be higher, but also that the cross section for all background processes will be of similar scale.

As an outlook to the LHC running period in 2012 a comparison between $\sqrt{s} = 8$ TeV (and also 9 TeV), planned for the 2012 run and the $\sqrt{s} = 7$ TeV of the 2010 and 2011 run is shown in Figure 1.19(b). The gain in physics potential, especially the processes at high momentum transfer, is clearly demonstrated.

Chapter 2

The Large Hadron Collider

This chapter will discuss the Large Hadron Collider (LHC) and is mainly based on the accelerator article [114] and an article that appeared in a special review of Nature on the Large Hadron Collider [115]. In section 2.1 the LHC will be presented, followed by a brief discussion of the LHC magnets in section 2.2, the collision energy and beam parameters in section 2.3, an overview of the CERN accelerator complex in section 2.4 and the future upgrades in section 2.5.

2.1 The Large Hadron Collider

The Large Hadron Collider [116–118] is a proton-proton collider, installed in the previously existing 27 km long circular Large Electron Positron (LEP) tunnel at CERN, Geneva. The LHC is designed to produce 600 million pp-collisions per second at centre-of-mass energies of $\sqrt{s} = 14\,\text{TeV}$, which means 7 times larger energies and 100 times larger collision rates than the previous most powerful accelerator: Tevatron in Fermilab, Chicago.

While LEP collided leptons in the form of electrons and positrons, which are both fundamental particles, the LHC collides composite particles such as protons and ions. This has both advantages and disadvantages. Because leptons are fundamental particles, the centre-of-mass energy of each collision was precisely determined and therefore well suited for high-precision experiments. On the other hand, when hadrons are smashed together by Tevatron or LHC, the collision actually occurs between constituent quarks and gluons, each carrying only a portion of the total proton energy. The centre-of-mass energy of these collisions is unknown and can vary significantly, so they are not well suited for high-precision experiments. The hadron colliders, however, offer a tremendous potential for the discovery of as-yet unknown particles, because they admit the possibility of collisions over a wide range of much higher energies than is otherwise possible. Protons are relatively heavy and so lose less energy than leptons (e, μ) do when being bended into a curved trajectory due to a strong magnetic field [115].

Figure 2.1 shows the layout of the LHC. The LHC is not a perfectly circular collider, but consists of eight straight sections, of 5 km in total, and 22 km of curved section divided in 8 sectors. The straight sections are used to bring beams into collision at four of the interaction regions (IRs): ATLAS and LHCf in IR1, ALICE in IR2, CMS and TOTEM in IR5 and LHCb in IR8. IR4 contains the radio-frequency (RF) accelerating cavities and IR3 and IR7 contain equipment for collimation and for protecting the machine from stray beam particles. IR6 houses the beam abort system, where the LHC beams can be extracted from the machine and their energy is absorbed safely.

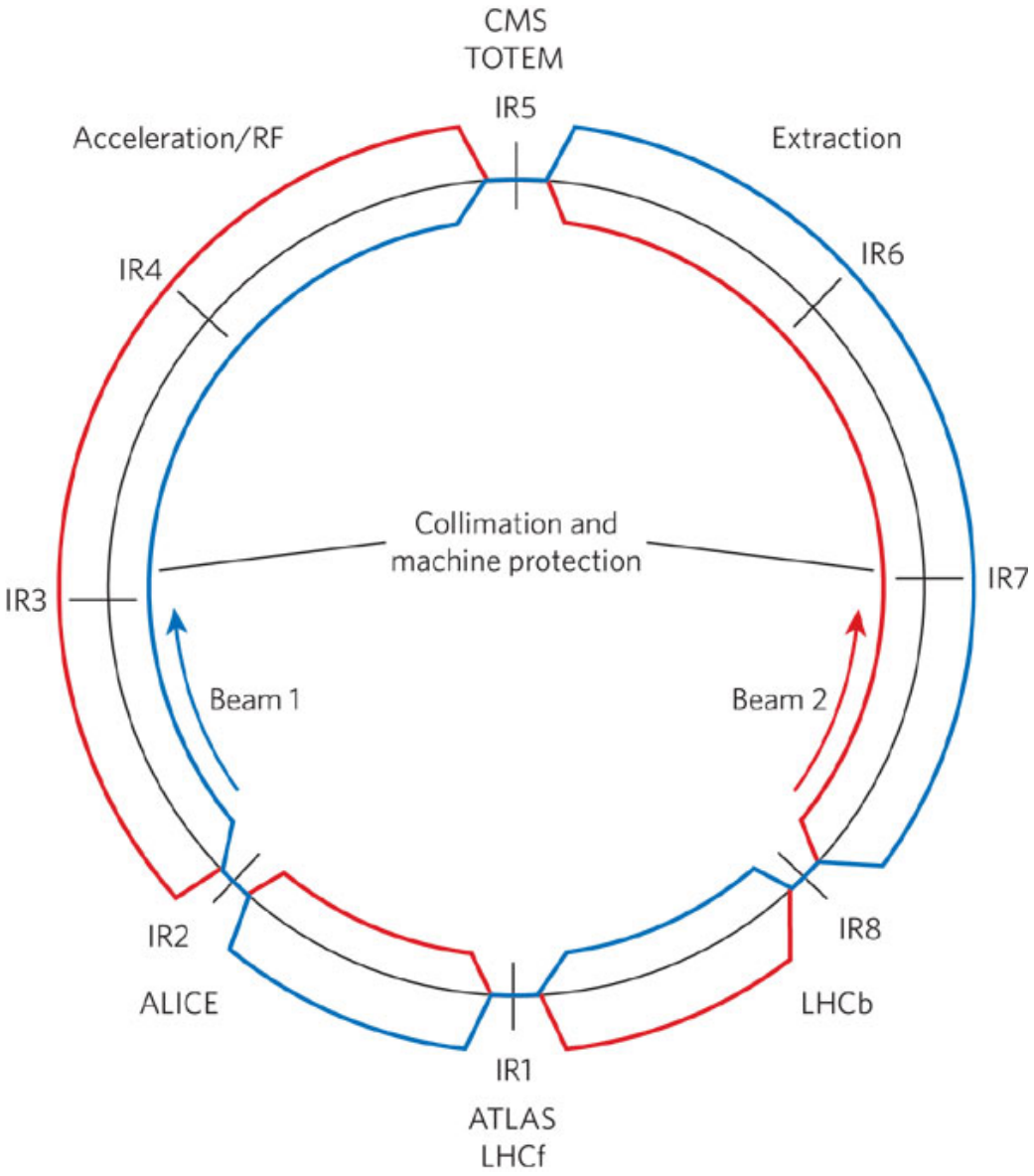

Figure 2.1: Layout of the Large Hadron Collider. Two proton beams rotate in opposite directions around the ring, crossing at four of the designated interaction regions (IRs) that contain the various experiments. Figure taken from Reference [115].

To obtain the large collision rates, high intensity beams are required. The present production rates for anti-protons are too low, therefore two counter-rotating protons beams are brought to collision. As a consequence, unlike the Tevatron and LEP, the LHC needs two separate vacuum chambers with magnetic fields of opposite polarity to deflect the counter-rotating beams in the same direction along the ring [115]. The protons inside a beam are grouped together in so-called "bunches" that are separated by 25 ns (or a multiple of 25 ns). This corresponds to a maximum bunch crossing frequency of 40 MHz. Beams consisting of series of bunches, so called "bunch-trains", do not collide head-on, but at a small angle of the order of 150-200 μrad, to avoid unwanted collisions near the interaction point. The plane containing the two beams can be rotated and is different in the four interaction points.

2.2 LHC magnets

The length of the existing LEP tunnel and the required beam energy sets the scale for the strength of the 1 232 bending dipole magnets that keep the beams in their circular trajectory. Keeping the 7 TeV beams in their closed orbits requires bending fields of 8.4 T, ~ 30 000 times stronger than the earth magnetic field. Such fields are at the limit of the existing superconducting magnet technology. To confine two counter-rotating beams in the space-limited LEP tunnel, the LHC adopted a novel two-in-one magnet design, in which the two magnetic coils have a common infrastructure and cryostat.

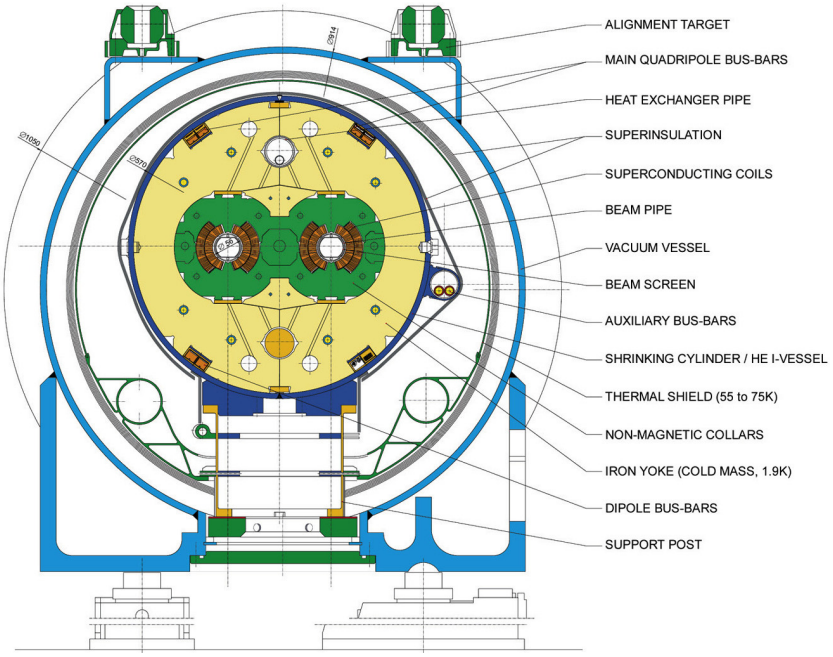

Figure 2.2: Cross-section of the two-in-one magnet design for the main LHC dipole magnets. Figure taken from Reference [119].

Figure 2.2 shows the cross section of the design for the main LHC magnets. In the centre are the two beam pipes, each with a diameter of 54 mm and separated by 194 mm. The superconducting coils, wound around the beam pipe, are constructed from superconducting NbTi cables that have to be cooled to temperatures of 1.9 K. These coils are held in place by steel collars and are surrounded by the magnet yoke. Together, these components form the cold mass of the magnet, which is insulated in a vacuum vessel immersed in superfluid Helium of 1.9 K. This resulted in 15 m long, 30 tons dipole magnets with a cryostat diameter of 0.914 m [115].

In addition to the bending fields of the dipole magnets, a circular accelerator also requires a focusing mechanism that keeps the particles centered on the design orbit. Most modern storage rings use the concept of strong focusing in which dedicated quadrupole magnets provide field components that are proportional to the deviation of the particles from the design orbit. The Lorentz force prevents divergent trajectories: the particles instead oscillate around the design orbit as they circulate in the storage ring. Each of the 8 sectors of the LHC consists of 46 series of 1 quadrupole magnet and 3 dipole magnets [115].

The operating temperature of 1.9 K and the field strength of 8.4 T constrain the LHC to a very small thermal margin before the superconducting state is lost. Even small particle losses can

cause local heating of the material. After loosing the superconducting state, the temperature in the NbTi cables will increase even further due to ohmic losses, which is known as a magnet quench. The small margins for temperature fluctuations and energy deposits in the magnet coils are combined with the extremely high energy densities inside the magnet system. The energy stored in a single beam at nominal operation is 362 MJ, where just 1 MJ of energy is enough to melt 2 kg of Copper. The stored energy in the dipoles alone is 8.5 GJ, corresponding to a 400 tonne TGV traveling at 150 km/h. The damage potential to the accelerator hardware is enormous, as was demonstrated by the 2008 September 19$^{\text{th}}$ accident in the LHC.

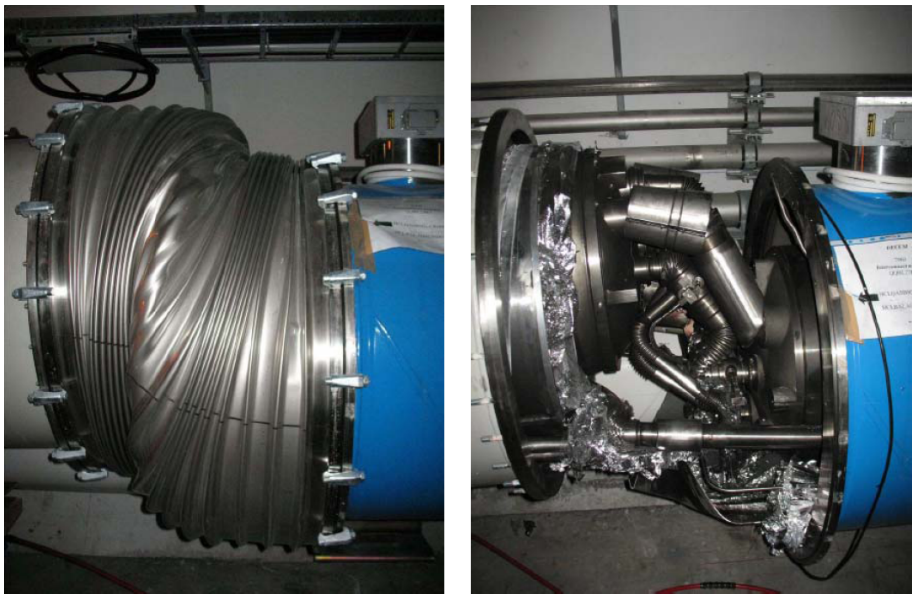

Figure 2.3: Displacement of two LHC dipoles after the September, 19$^{\text{th}}$ incident [120].

During a powering test of the main dipole circuit in Sector 3-4 of the LHC on September 19$^{\text{th}}$ 2008, a fault occurred in the electrical bus connection in the region between a dipole and a quadrupole, resulting in the melting of the copper interconnection. After evaporation of the massive copper connection, an electrical arc developed, puncturing the helium enclosure, which lead to a release of superfluid 1.9 K Helium. Approximately 2 tons of liquid helium evaporated on a very short time scale, resulting in large pressure forces that displaced dipole magnets and broke their anchors in the concrete floor. 14 quadrupole and 39 dipole magnets had to be replaced. To prevent similar accidents in the future, nearly 900 new helium pressure release valves were installed around the whole LHC machine and the magnet protection system was expanded with 6500 new detectors monitoring closely the resistance of the electrical bus connections between magnets. In November 2009, the machine was fully repaired and tested, such that beam commissioning could continue.

Before establishing collisions, the beams were carefully sent through the LHC sectors and collided on the collimators in front of the experiments. This gave rise to an enormous flux of muons created in the collimators and sent to the detectors, as could be seen in Figure 2.4(a). On November 23$^{\text{rd}}$ 2009, the first collisions were recorded in CMS at $\sqrt{s} = 900$ GeV, which is just at the injection energy $E_{\text{b}} = 450$ GeV of the beams from SPS into LHC. The beam energies were subsequently risen to $E_{\text{b}} = 1.18$ TeV on December 8$^{\text{th}}$ to test the accelerator. In the meanwhile the experiments collected data for commissioning. A dijet candidate event at $\sqrt{s} = 900$ GeV is shown in Figure 2.4(b).

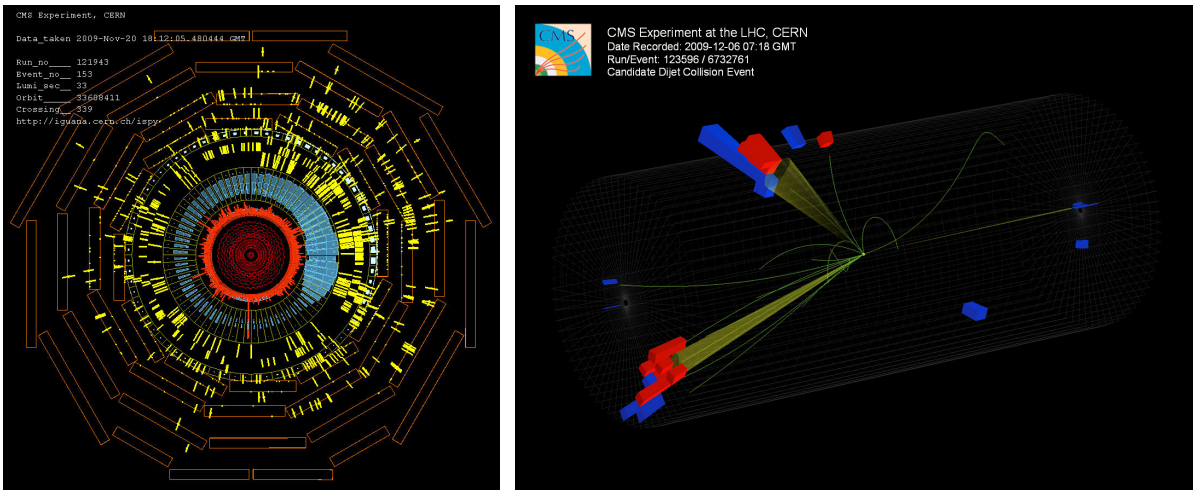

(a) Beam splash event

(b) $\sqrt{s} = 900\,\text{GeV}$ collision event

Figure 2.4: Left: Beam splash event 153 recorded in run 121 943, on November 20$^{\text{st}}$ 2009, showing the reconstructed hits in the various subsystems of the CMS detectors [121]. Right: A dijet candidate event 632 763 recorded in run 123 596, on December 6$^{\text{th}}$ 2009, at a centre-of-mass energy of $\sqrt{s} = 900\,\text{GeV}$. The event shows two jets originating from a proton-proton collision [122].

In March 2010 the beams were accelerated to an energy of $E_{\text{b}} = 3.5\,\text{TeV}$ and brought to collision for the first time March 30$^{\text{st}}$ 2010. The initial beams were of low intensity, with 10^9 protons per bunch, and both beams consist of only a single bunch, allowing for an instantaneous luminosity of $\approx 10^{25}\,\text{cm}^{-2}\text{s}^{-1}$. The LHC operators progressed very fast to increase the number of protons in the bunch to $1.15 \cdot 10^{11}$ and to collide up to 45 bunches with a bunch spacing of 150 ns, in September 2010. A technical stop was required to commission the bunch train operation (explained later) of the LHC. After the technical stop, bunches were spaced at 75 ns and 50 ns, and up to 348 bunches were colliding on each other, delivering an instantaneous luminosity of $2 \cdot 10^{32}\,\text{cm}^{-2}\text{s}^{-1}$. Details for the LHC running in 2010 can be found in Table 2.1.

2.3 The collision energy and beam luminosity

The number of collisions that can be delivered to the LHC experiments is given by the product of the cross section σ of the event (which reflects the probability for that event to be produced by a collision) and the machine luminosity $\mathcal{L}$:

$$N = \sigma \times \mathcal{L}. \tag{2.1}$$

The luminosity is determined by the proton beam parameters:

$$\mathcal{L} = \frac{f_{\text{rev}} n_b N_b^2}{4\pi\sigma_x\sigma_y} F(\phi). \tag{2.2}$$

Here, σ_x and σ_y are the horizontal and vertical transverse root mean squared (r.m.s.) beam sizes at the interaction point, f_{rev} is the revolution frequency, n_b the number of bunches in the beam, N_b the number of particles within a bunch and $F(\phi)$ a geometric luminosity reduction factor

dependent on the Piwinski angle ϕ due to the crossing angle at the interaction point:

$$F(\phi) = \frac{1}{\sqrt{1+\phi^2}}. \tag{2.3}$$

(a) (b)

Figure 2.5: Illustration of the focusing of the two beams at an interaction point: showing the beam envelope (a) and the bunch structure (b). Figure taken from [123].

The beam in LHC is accelerated by 400 MHz accelerating cavities. These provide 35640 "buckets" that contain the proton bunches. These buckets have a length of 2.5 ns and each proton bunch is separated by 9 empty buckets, such that there is a bunch spacing of 25 ns. In total there are 3564 buckets spaced at 25 ns, but not all of them can be filled, since there is need for gaps up to 3 μs to inject and extract the beams. Therefore the LHC can contain up to 2808 bunches per proton beam (n_b), each containing 1.15×10^{11} protons (N_b), with a r.m.s. beam size (σ) of 16.7 μm and a r.m.s. bunch length (σ_s) of 7.5 cm at a total crossing angle of 320 μrad at the interaction points. For beams crossing in the vertical plane, as shown in Figure 2.5, the Piwinski angle is defined as:

$$\phi_y = \frac{\theta\sigma_s}{\sigma_y}, \tag{2.4}$$

where θ is the half crossing angle, σ_s is the r.m.s. bunch length and σ_y is the vertical r.m.s. beam size. In the horizontal plane the Piwinski angle is defined similarly as $\phi_x = \theta\sigma_s/\sigma_x$. At nominal LHC operation, the parameter choice of $\theta = 160\,\mu$rad, $\sigma_y = 16.7\,\mu$m and $\sigma_s = 7.5$ cm leads to a Piwinski angle of $\phi = 0.72$ and geometric luminosity reduction factor of $F(0.72) = 0.81$. The increased angle is necessary for beams consisting of so called "bunch-trains" to avoid long-range interactions (parasitic collisions) at ± 7.5 m from the interaction point (IP). At each side of the interaction point, 15 "near-misses" (see Figure 2.5(b)) occur. Although the bunches are separated on average $9.5\,\sigma$, so called "long-range" beam-beam interactions can still happen, leading to a reduced beam intensity.

A further increase in luminosity will be obtained later by so-called "Crab cavities". These electromagnetic cavities can rotate the bunches of a proton beam, such that no geometric luminosity reduction happens. The principle of beams crossing at a so-called "Crab angle" is demonstrated in Figure 2.6. The installation of these Crab cavities is foreseen for future LHC upgrades.

An "ideal" particle inside a particle accelerator will follow the "ideal" trajectory through all magnets, closing after exactly one revolution around the ring. This is called the "closed orbit". Real particles are oscillating around this closed orbit and the number of oscillations for a complete revolution is called the tune Q (Q_x in the horizontal and Q_y in the vertical plane). Q is a machine parameter and has to be a non-integer number for the stability of the beam.

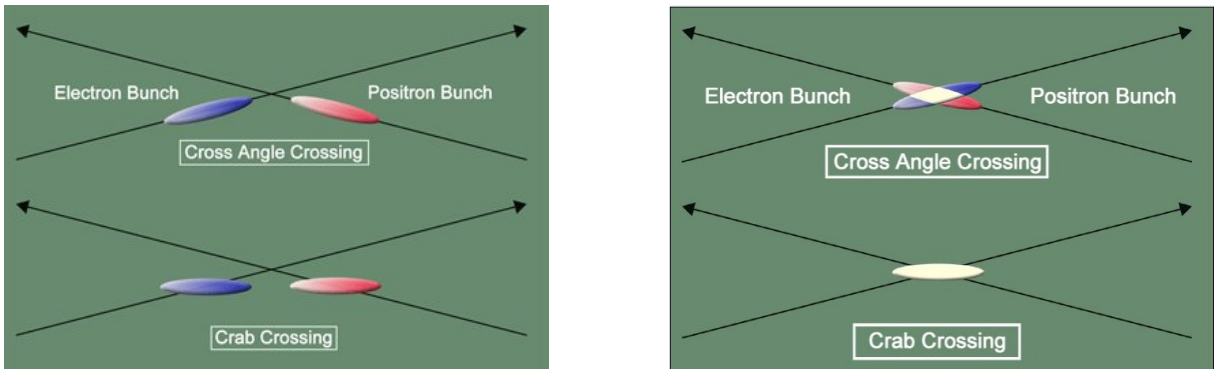

Figure 2.6: Crossing of bunches at a crossing angle (top) and at a Crab angle (bottom) [124].

The r.m.s. transverse beam sizes can be expressed as function of the beam emittance ϵ and the beta-function[1] $\beta(s)$, s being the arc length, describing the beam envelope:

$$\sigma_x = \sqrt{\epsilon_x \beta_x}. \tag{2.5}$$

This allows for rewriting the formula for the Luminosity:

$$\mathcal{L} = \frac{f_{\text{rev}} \gamma n_b N_b^2}{4\pi \epsilon_n \beta^*} F(\phi), \tag{2.6}$$

where $\epsilon_n = \gamma\epsilon$, the normalized beam emittance, γ is the Lorentz factor and β^* is the beta function at the interaction point. The beam emittance is the space and momentum phase-space (x, $\dot{x}$) area containing a certain fraction (in hadron colliders: 95%) of all particles. It is a measure of the spatial and angular spread of the beam. The normalized emittance ϵ_n is constant during the lifetime of the beam and the goal during the injection is to introduce a beam with the lowest beam emittance. A low emittance beam is a beam where the particles within a bunch are confined to a small distance and have nearly the same momentum [123]. At nominal operation the normalized beam emittance is $\epsilon_n = 3.75\,\mu$m and the beta function at the interaction point is $\beta^* = 0.55$ m.

During 2010 pp-running, the instantaneous luminosity increased over 7 orders of magnitude, starting with a low intensity beam of 10^{10} protons reaching an instantaneous luminosity of $\mathcal{L} = 10^{25}\,\text{cm}^{-2}\text{s}^{-1}$ for the first beams on March, 30$^{\text{th}}$ to $\mathcal{L} = 10^{31}\,\text{cm}^{-2}\text{s}^{-1}$ at the end of August 2010 with 48 bunches colliding. After commissioning bunch trains, allowing more than 56 bunches to be filled, twice the 2010 goal for the instantaneous luminosity was reached with 348 bunches colliding. This resulted in a peak luminosity of $\mathcal{L} = 2 \cdot 10^{32}\,\text{cm}^{-2}\text{s}^{-1}$ on the 29th of October 2010. Table 2.1 gives an overview of the machine parameters at the end of each of the different data taking periods in 2010, in 2011 and compared to the design parameters for nominal running. Figure 2.7 shows the steep increase of the luminosity integrated over time delivered by the LHC and recorded by the CMS experiment in 2010 and 2011.

Beam intensity, and hence instantaneous luminosity, decays during the operation of an accelerator in colliding mode. After these parameters become too small for efficient operation, the

[1]The β function is expressed in [m] and expresses the distance required for the increase of the envelope of the beam with a factor e^{-1}. Stated otherwise, the β function gives the distance required to decrease the beam envelope with a factor e.

Table 2.1: The LHC machine parameters at the end of each data taking period in 2010 and 2011, together with the design parameters for nominal operation.

		Run 2010A Sept 2010	Run 2010B Nov 2010	Run 2011A Sept 2011	Run 2011B Nov 2011	Design (Nov 2016?)
Machine and Beam						
Proton Energy	[TeV]			3.5		7
Lorentz factor $\gamma = \frac{E}{m_p c^2}$	[-]			3730		7461
Centre-of-Mass Energy $\sqrt{s}$	[TeV]			7		14
Dipole Field	[T]			4.17		8.33
Revolution Frequency	[Hz]			11 245		11 245
Bunch separation	[ns]	150	50	50	50	25
No. of Bunches	[-]	48	368	1380	1380	2760
No. of Bunches colliding	[-]	45×45	348×348	1318×1318	1331×1331	2662×2662
No. of Particles per Bunch	[-]	$1.15 \cdot 10^{11}$	$1.15 \cdot 10^{11}$	$1.45 \cdot 10^{11}$	$1.45 \cdot 10^{11}$	$1.15 \cdot 10^{11}$
Collisions						
σ^*	[μm]	60	60	23	18	16.7
β^*	[m]	3.5	3.5	1.5	1.0	0.55
ϵ_n	[μm]	3.75	2.75	2.4	2.4	3.75
Luminosity						
Peak Luminosity	[$cm^{-2}s^{-1}$]	10^{31}	$2 \cdot 10^{32}$	$3.29 \cdot 10^{33}$	$3.65 \cdot 10^{33}$	$1 \cdot 10^{34}$
Average collisions / BX	[-]	1.5	2.7	7	12	25

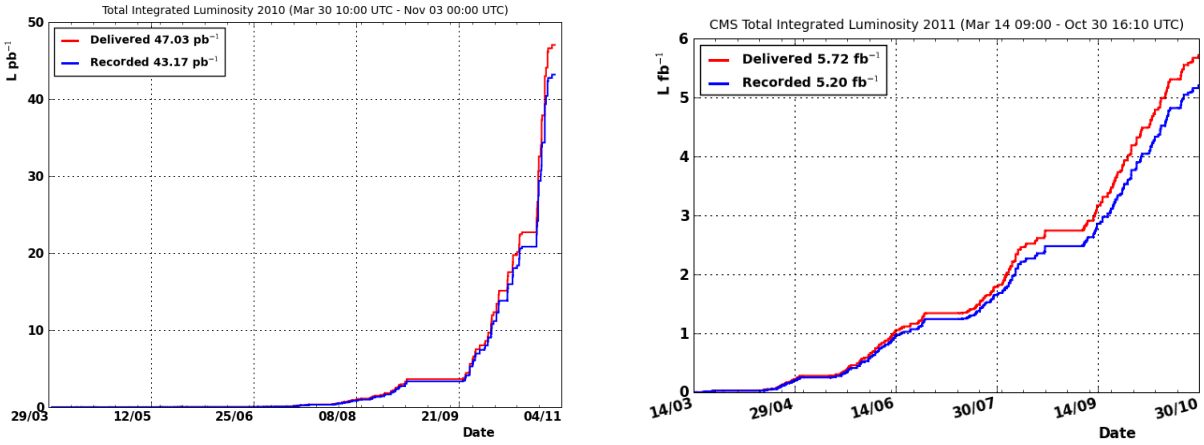

Figure 2.7: Integrated luminosity of proton-proton collisions versus time delivered to (red), and recorded by (blue) CMS during stable beams at 7 TeV centre-of-mass energy in 2010 (left) and 2011 (right). Figure taken from Reference [125].

beams are discarded using the beam abort system, and a new fill of proton beams needs to be prepared, injected and accelerated. One of the main and unavoidable causes of reductions in beam intensity is the collisions inside the detectors themselves. Particles are also lost due to beam-gas interactions and through perturbations and resonances in the proton motion that deflect particles away from the design orbit. These are generated, for example, at the collision points, where a particle in one beam is exposed to the Coulomb field of the opposing beam, or by field imperfections in the main magnets. Thanks to the focussing mechanism of the quadrupole magnets, these deflections do not lead directly to particle losses but, initially, just to an oscillation around the design orbit. Consecutive perturbations can add up coherently if the particle losses are in resonance with the revolution frequency, in which case the oscillation amplitudes can grow until the particles are lost when they are cleaned by the collimation system [115]. Including the above effects, the net estimate of the luminosity lifetime is $\tau = 14.9$ hours

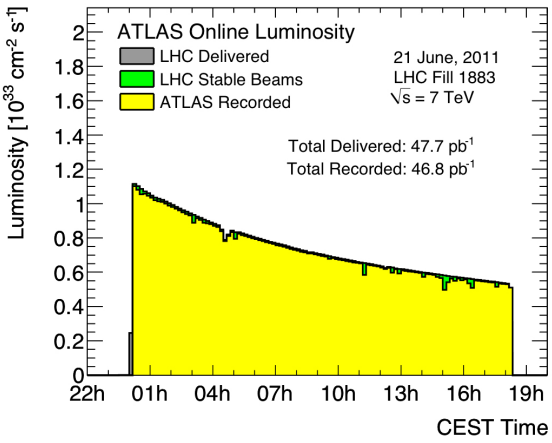

Figure 2.8: Instantaneous luminosity profile of LHC Fill 1883 as measured by the ATLAS detector. The beam had a lifetime of ~ 19 hours. Figure taken from Reference [126].

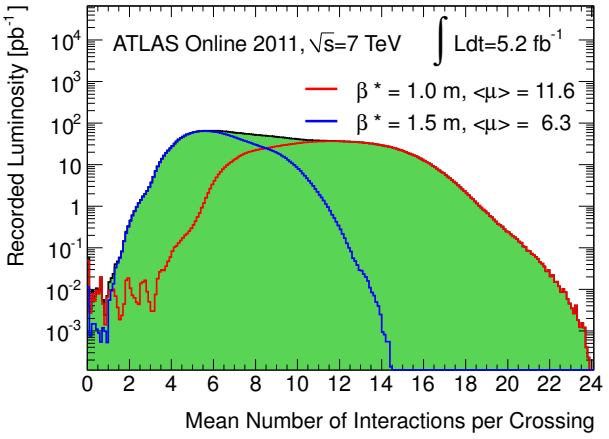

Figure 2.9: The distribution of reconstructed vertices in the ATLAS detector during 2011, before (blue) and after (red) the September technical stop where the beams were squeezed from $\beta^* = 1.5\,\text{m}$ to $\beta^* = 1.0\,\text{m}$. Figure taken from Reference [127].

[114]. The decrease of the instantaneous luminosity can then be described by:

$$\frac{\mathrm{d}\mathcal{L}}{\mathrm{d}t} = \mathcal{L}_0 e^{-\frac{t}{\tau}}, \tag{2.7}$$

with $\mathcal{L}_0$ the luminosity at the start of the run. Integrating the luminosity over the entire length of the run (T_{run}) yields:

$$\mathcal{L}_{\text{int}} = \int_0^{T_{\text{run}}} \mathcal{L}(t)\mathrm{d}t = \mathcal{L}_0 \cdot \tau \cdot \left(1 - e^{-\frac{T_{\text{run}}}{\tau}}\right). \tag{2.8}$$

In 2011 runs of well over 18h were recorded, integrating more than $40\,\text{pb}^{-1}$. This is more than the total amount of data recorded in 2010. Figure 2.8 shows the luminosity profile of such a run, recorded by the ATLAS detector. Running at higher luminosity leads to many proton proton collisions during one bunch crossing. Figure 2.9 shows the number of reconstructed vertices during the 2011 run of LHC: ~ 6 before the squeeze of the beams to $\beta^* = 1.0\,\text{m}$, and ~ 12 afterwards. Figure 2.10 shows a $Z(\mu\mu)$ event in the ATLAS detector in an event with 20 reconstructed vertices.

2.4 The CERN accelerator complex

The accelerator complex at CERN, shown in Figure 2.11 is a sequence of machines that deliver particle beams with increasingly higher energy. Each machine brings the beam to a higher energy and then injects it into the next one. The last element in the chain is the Large Hadron Collider, where beams can be accelerated up to 7 TeV.

The proton beams of the LHC start in a 50 MeV linear accelerator, Linac 2, and are then passed to a 157 m circumference multi-ring boosted synchrotron, the Booster, for an acceleration to

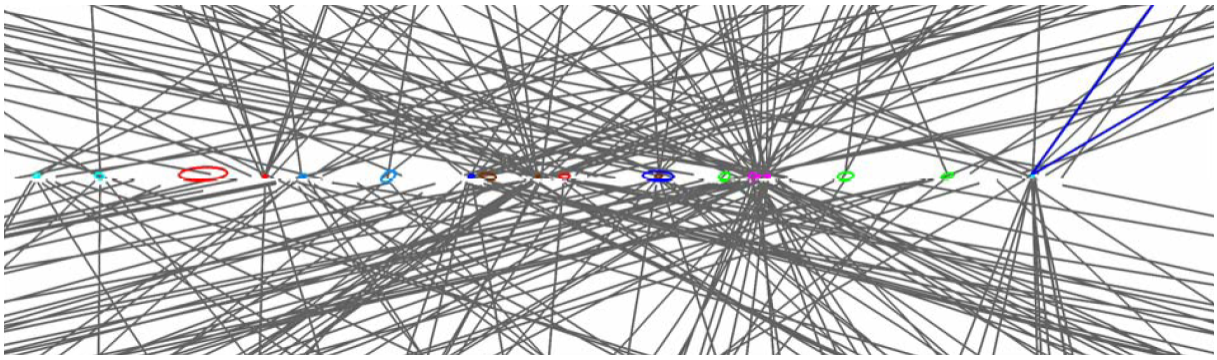

Figure 2.10: A detail of the interaction region of the ATLAS detector, showing an event with 20 reconstructed vertices, of which one is a $Z(\mu\mu)$ event (blue tracks) [128].

1.4 GeV. Next, they are transferred to the 628 m circumference Proton Synchrotron (PS) to reach a beam energy of 26 GeV. The PS also prepares the required bunch pattern and bunch spacing needed for the LHC. A final transfer is made to the 7 km circumference Super Proton Synchrotron (SPS), where the beam is accelerated to 450 GeV. This first step of the injection takes 20 s and creates a bunch train with a total kinetic energy of more than 2 MJ, which is 8% of the beam needed to fill the LHC entirely. Therefore the whole cycle must be repeated 12 times per ring [115].

The second step is the most delicate: the injection of the beam into LHC. The 450 GeV beam has already sufficient energy to damage the LHC and the transfer involves the use of fast kicker magnets to abruptly change the trajectory of the beam. Therefore injection always starts with the insertion of a low-intensity "pilot beam" to measure and adjust the machine parameters before the full-intensity injections are allowed. The injection of the complete beams (both in clockwise and anti-clockwise direction) takes 8 minutes to fill the LHC completely, during which the complete pattern for each of the two beams is generated. Finally the LHC will accelerate the beams for 9 minutes, with a kick of 0.5 MeV/turn, to the beam energy of 3.5 TeV used in 2010 (it takes 20 minutes to reach the design energy of 7 TeV) [115].

2.5 Future prospects for LHC running

With LHC up and running, preparations for the next years have already been started. A technical plan for the operation of LHC over the next two decades was released by CERN [129]. The original schedule is already outdated, since the running period was extended to the end of 2012 (or at least until 15 fb^{-1} of data is recorded by the experiments), with an increase of the centre-of-mass energy from 7 TeV to 8 TeV. The twenty year period can roughly be divided in two periods of equal length: **Phase I** (2010–2020) and **Phase II** (2020–2030), discussed in the next paragraphs. A preliminary schedule of the CERN 10 year technical plan, adapted to the extension of the running period to 2012, is shown in Figure 2.13.

2.5.1 Phase I: CERN 10 year technical plan

During Phase I, the LHC will ultimately reach its design energy (14 TeV centre-of-mass collisions) and luminosity ($2 \cdot 10^{34}\,\text{cm}^{-2}\text{s}^{-1}$). Two major long shutdowns, LS1 and LS2, of at least each a year will be needed to accomplish these objectives, LS1 from January 2013 to probably

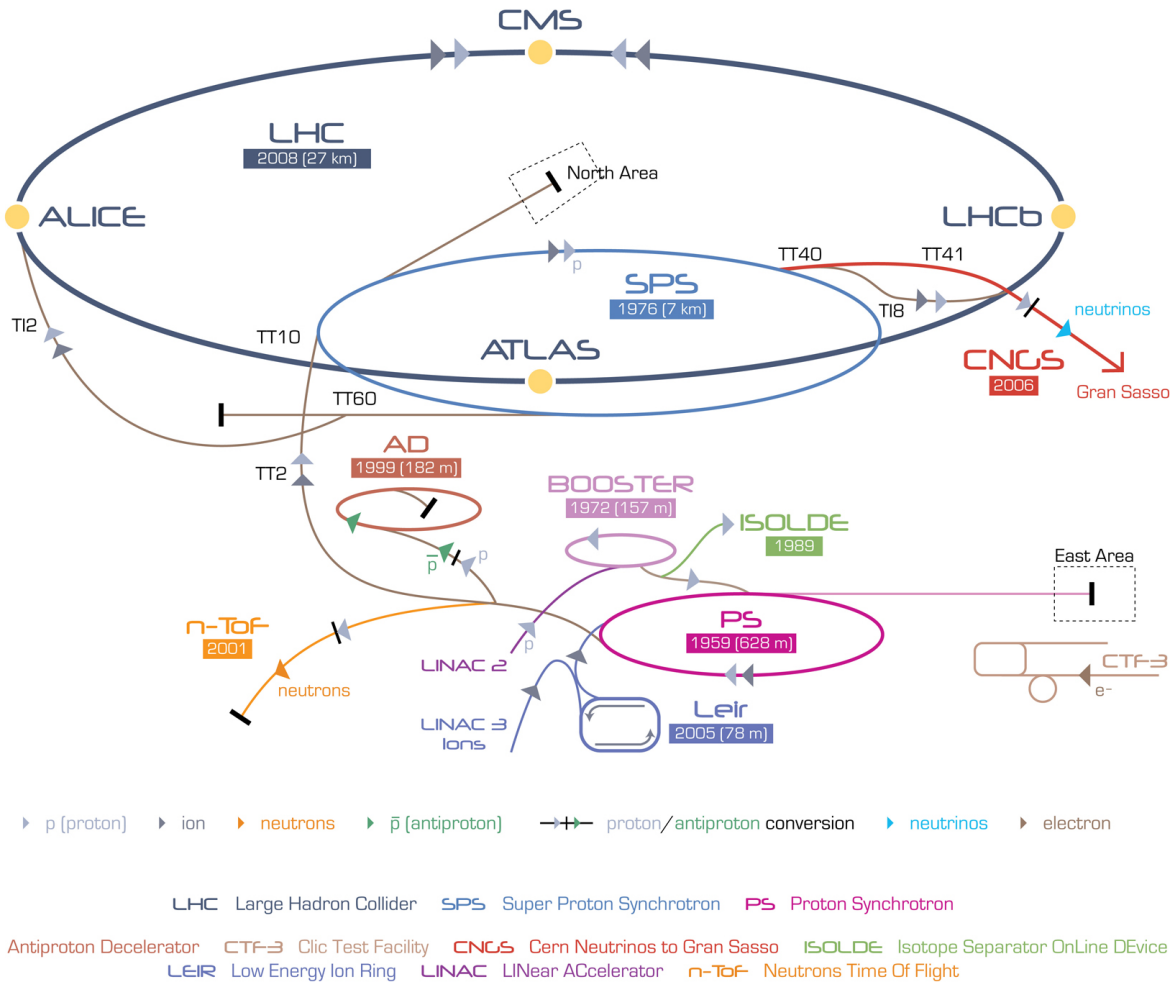

Figure 2.11: Overview of the CERN Accelerator Complex. The LHC injection chain for protons consists of Linac 2, the Booster, PS and SPS.

August 2014 and LS2 probably 2017–2018. These shutdowns will be needed to accomplish these objectives:

Long Shutdown 1 (LS1) to repair the magnet interconnections ("splices") to allow the LHC to operate safely at 14 TeV (requiring 13 kA currents in the dipole magnets to obtain field strenghts of 8.3 T).

Long Shutdown 2 (LS2) to improve the collimation system of the LHC. This is necessary for the addition of Crab cavities in Phase II and to reach the ultimate design luminosity. Linac 4, discussed in the next paragraph, is scheduled to be included to the LCH injector complex, while the PS Booster will be upgraded to reduce the beam emittance.

In the meanwhile experiments will have access to their detectors for maintenance and improvements. For instance in CMS, additional muon chambers will be installed during LS1 and a new silicon pixel detector will be installed during LS2. In between Phase I and Phase II there will be a third long shutdown, LS3, in which CMS will install a new silicon strip tracker.

2.5.2 Phase II: Super LHC

The Phase II project will not start earlier than 2020 and aims at a tenfold increase in luminosity for 14 TeV pp collisions to $\mathcal{L} = 10^{35}\,\mathrm{cm}^{-2}\mathrm{s}^{-1}$, allowing the multi-purpose experiments to integrate $\sim 500\,\mathrm{fb}^{-1}$ of data per year. The luminosity gain will be obtained mostly by a new injection chain. This comes as no surprise, considering that the existing injection was never designed for the LHC and contains elements older than 50 years. It is actually surprising that these old accelerators, that have been repaired and patched time and again, are still doing a great job delivering protons to the LHC.

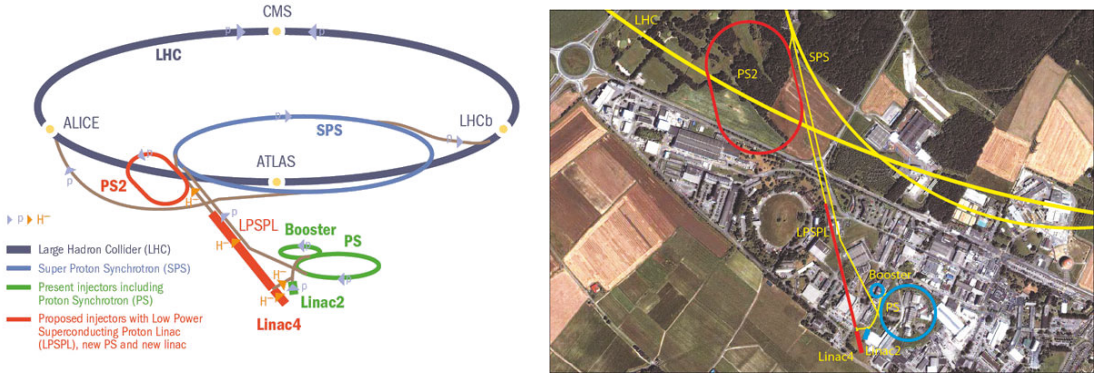

(a) (b)

Figure 2.12: Schematic (a) and aerial (b) view of the new injection chain for Super LHC.

The injection chain for the SLHC will consist of a new linear accelerator: Linac 4, which is a Low-Power Superconducting Proton Linac (LPSPL); PS2 (a new machine); and the existing SPS. Figure 2.12 shows a schematic and aerial view of where the different constituents of the new injector will be built on the CERN site. Accelerating H^- particles in Linac 4 instead of protons (as in Linac 2), followed by injection in the Booster where the excess electrons are removed will result in a first major upgrade of the beam brightness (the beam current within a given emittance), which translates directly into a luminosity increase in the LHC. Next bottlenecks are the Booster and the PS which are currently running at their maximum luminosity and suffer reliability problems after many years of service. They will be replaced by the Low-Power Superconducting Proton Linac and a new 50 GeV synchrotron, called PS2. The building housing Linac 4 has been finished in October 2010, and is presently being equipped with services (electricity, cooling, ventilation); at the end of 2012 the installation of the accelerator components will start. Construction works for the buildings and tunnels of LPSPL and PS2 are now in full swing. Finally, at the LHC another luminosity gain of a factor 2 can be obtained by installing new focussing triplets with larger aperture that allow a reduction of the beam size in the interaction point.

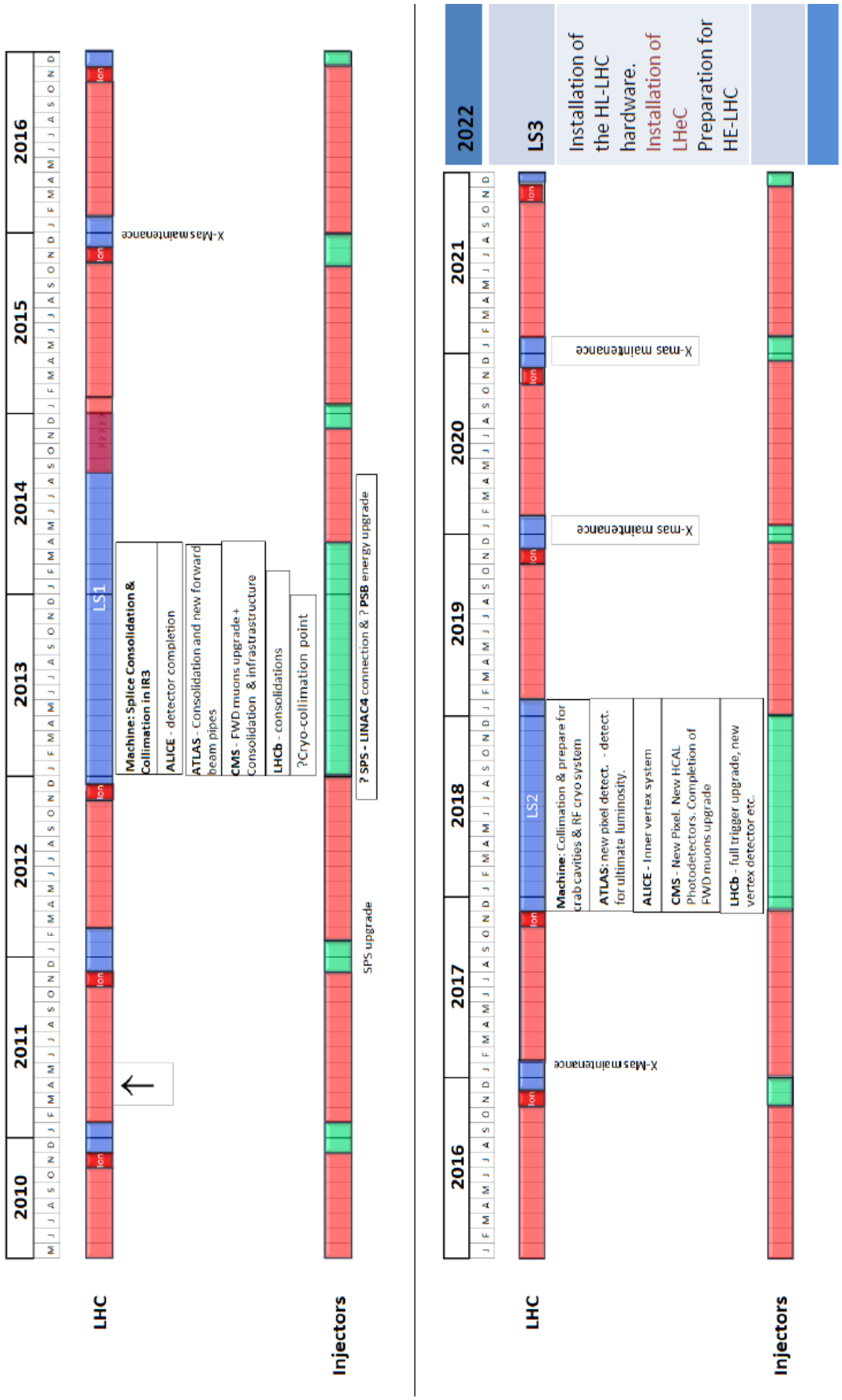

Figure 2.13: Preliminary schedule of the CERN 10 year technical plan, as of August 2011 [130].

Chapter 3

The Compact Muon Solenoid

The CMS detector is a general purpose detector built to explore physics at the TeV scale and is described in detail in References [67, 131–144]. Figure 3.1 shows the CMS detector, which has an overall length of 21.6 m, a radius of 7.5 m and a total weight of 12 500 ton.

CMS uses a right-handed coordinate system with the origin at the nominal interaction point (IP), which is in the centre of the detector. The coordinate system is determined by the z-axis, which is parallel to the counterclockwise beam direction. The x-axis then points to the center of the LHC ring and the y-axis is orthogonal to the xz-plane and points upwards. The LHC tunnel is inclined at max 1.41% (at CMS at 1.23%) with respect to the horizontal line because of construction advantages [145]. The azimuthal angle ϕ is measured with respect to the x-axis in the xy-plane and the polar angle θ is defined with respect to the z-axis. The pseudorapidity was defined earlier as $\eta = -\ln[\tan(\theta/2)]$.

The design of the CMS detector is driven by the p_{T} measurement of the muons with a precision of 10% or better of 1 TeV/c muons, for which a strong magnetic field is required. Therefore, the central feature of the CMS apparatus is a superconducting solenoid, of 6 m internal diameter, that produces a magnetic field of 3.8 T, which is discussed in section 3.1.

The magnetic flux generated by the solenoid is returned via the surrounding steel return yoke with a thickness of $\sim$ 1.5 m, arranged as a 12-sided cylinder, and closed at both ends by endcap disks. The steel return yoke is instrumented with gas detectors used to identify muons, detailed in section 3.2. The barrel yoke is subdivided in 5 wheels (YB0, YB±1 and YB±2) and each endcap yoke is subdivided in three disks (YE±1, YE±2, and YE±3).

The precise measurement of the muons is driven by a precise track measurement in the center of the detector. Within the magnetic field volume of the solenoid a silicon pixel and strip tracker are installed. These two detectors are discussed in detail in section 3.3.

CMS is a multi-purpose experiment that needs a good and hermetic calorimetry and an almost 4π coverage to enable missing momentum measurements. The barrel and endcap calorimeters are inside the magnetic field volume of the solenoid (up to $|\eta| < 3.0$) and consist of a crystal electromagnetic calorimeter (ECAL) and a brass scintillator hadronic calorimeter (HCAL), both described in section 3.4. Outside the field volume, in the forward region ($3.0 < |\eta| < 5.0$) there is an iron/quartz-fiber hadronic calorimeter, detailed in section 3.5.

The beams colliding inside CMS are very intense and energetic. To protect the precious and vulnerable tracker, beam radiation monitoring (BRM) systems are installed to monitor the beams. In case of danger, these systems can abort the beams. The BRM system is briefly discussed in

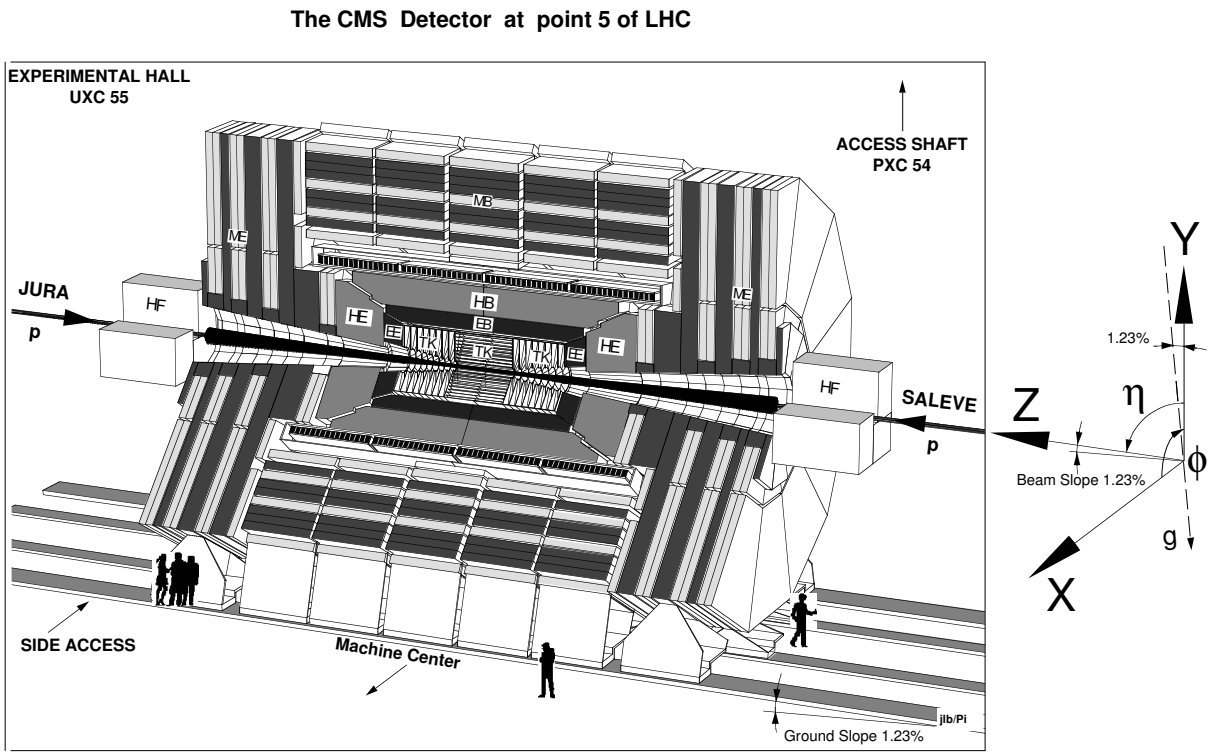

Figure 3.1: Overall view of the CMS detector. From the inside out, CMS consists of a silicon tracker (TK), an electromagnetic calorimeter (EB and EE), hadronic calorimeters (HB, HE and HF) and a muon system (MB and ME). The x-axis points to the middle of the LHC machine, the z-axis is parallel to the counterclockwise beam, causing the vertical y-axis to be 1.23% pointing off with respect to the true vertical due to the inclination of the LHC tunnel. Figure taken from Reference [139].

section 3.6.

The CMS experiment collects data using a two-level trigger system, a first level hardware trigger (L1) and a high-level software trigger (HLT) explained in sections 3.8 and 3.9. A final note concerns the CMS computing model that allows physicists to access, calibrate and analyze the data in section 3.10 and a short overview of the commissioning of the detector in section 3.11.

Figure 3.2 shows the CMS detector during the underground commissioning in April 2008. A more complete description of the CMS experiment and its subdetectors is given in the detector Reference [131] and the Technical Design Reports [67, 132–144]. The working principles of several subdetectors are explained in detail in Reference [147], while the choices made for the design of the CMS and ATLAS experiment are discussed in Reference [148]. People interested in the elementairy principles of particle detection and signal creation should have a look at the excellent lectures of Werner Riegler [149, 150] given at CERN.

3.1 The CMS Solenoid

The superconducting magnet for CMS has been designed to reach a 4 T field at a nominal current of 19.14 kA, in a free bore of 6 m diameter and 12.5 m length with a stored energy of 2.6 GJ at full power. The flux is returned through a 10 000 ton yoke, comprising 5 wheels and 2 endcaps,

Figure 3.2: CMS in open position being visited during the LHC open day in April 2008 [146].

each composed of three disks. The magnet consists of a 4-layer winding made from a stabilized reinforced NbTi superconducting cable [131]. The magnet is embedded in a cryogenic vessel, weighing about 220 ton, which is called the cold mass. A more detailed description is given in the Technical Design Report [136], while a short but still detailed description can be found in Reference [131].

The CMS collaboration has decided to operate the magnet at a central magnetic flux density of 3.8 T. After the first years of operation, once the ageing of the coil is better understood, the collaboration may decide to operate the magnet at 4 T [151].

The inner coil radius is big enough to accomodate the inner tracker and the full calorimetry. Figure 3.3 shows the magnet and iron return yoke before the installation of any detector inside or around. The magnetic flux is returned by a 1.5 m thick nearly saturated iron yoke, instrumented with four stations of muon chambers. The third iron disk (of the endcap) and first barrel ring (cylinder inside the wheels closest to the magnet) are about 30 cm thick (~ 2 interaction lengths), while the first and second disk and second and third barrel rings are about 60 cm thick, summing up in total to 1.5 m of steel. The CMS magnet is thus the backbone of the CMS experiment as all subdetectors are supported by it. On one hand, the thickness of the CMS yoke is kept as small as possible to avoid radiative muon losses, while on the other hand kept thick enough to absorb all hadrons that might punch through the hadron calorimeter and the magnet.

For accurate simulation and reconstruction of physics events, a detailed map of the magnetic field is required in both the inner tracking region inside the solenoid as in the large and complex iron return yoke, which is instrumented with the muon chambers. The field in the inner tracker

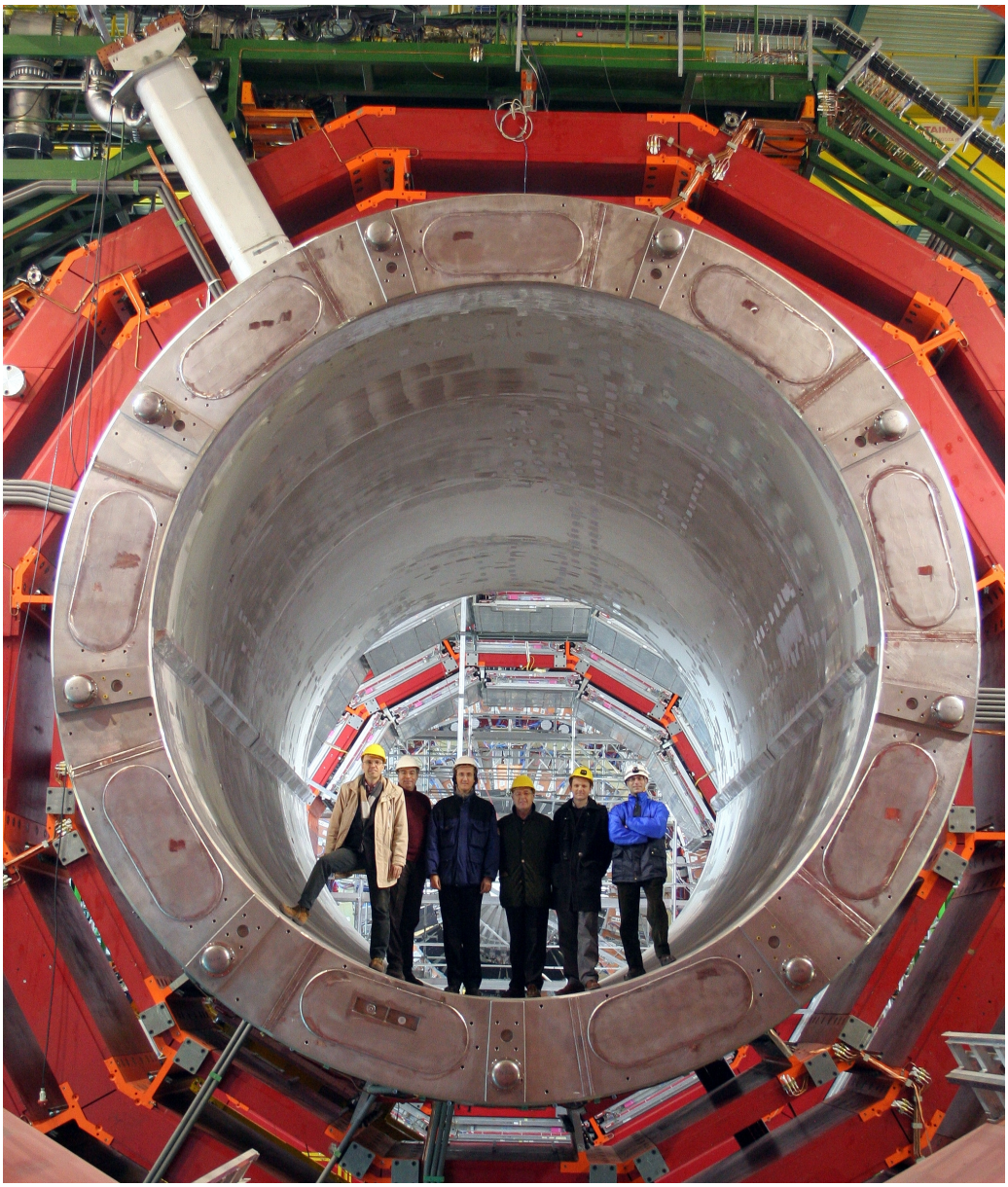

Figure 3.3: View of the magnet and iron return yoke before the installation of any detector. The pockets for the muon stations in the barrel return yoke are clearly visible, as well as the two side rails in the inner vacuum vessel for the support of the hadronic barrel calorimeter [152].

region has been measured with a magnetic field mapper and is known at the 0.1% level. The field in the iron return yoke has been determined using a large collection of cosmic muon events recorded in fall 2008 (CRAFT, see section 3.11) [151] and imprecisions have been spotted. Figure 3.4 shows an improved finite-element map of the magnetic field, which compares well to measurements made with cosmic ray muons. Approximately two thirds of the magnetic flux returns through the barrel yoke, half of which enters directly into the barrel without passing through the endcap disks. One third of the total flux escapes radially, returning outside the steel yoke [151]. The return of the magnetic flux outside the return yoke was found to be higher than predicted by the initial simulations. The origin was found to be the limited volume in which the CMS detector was placed. By increasing the simulation grid around the CMS detector, results

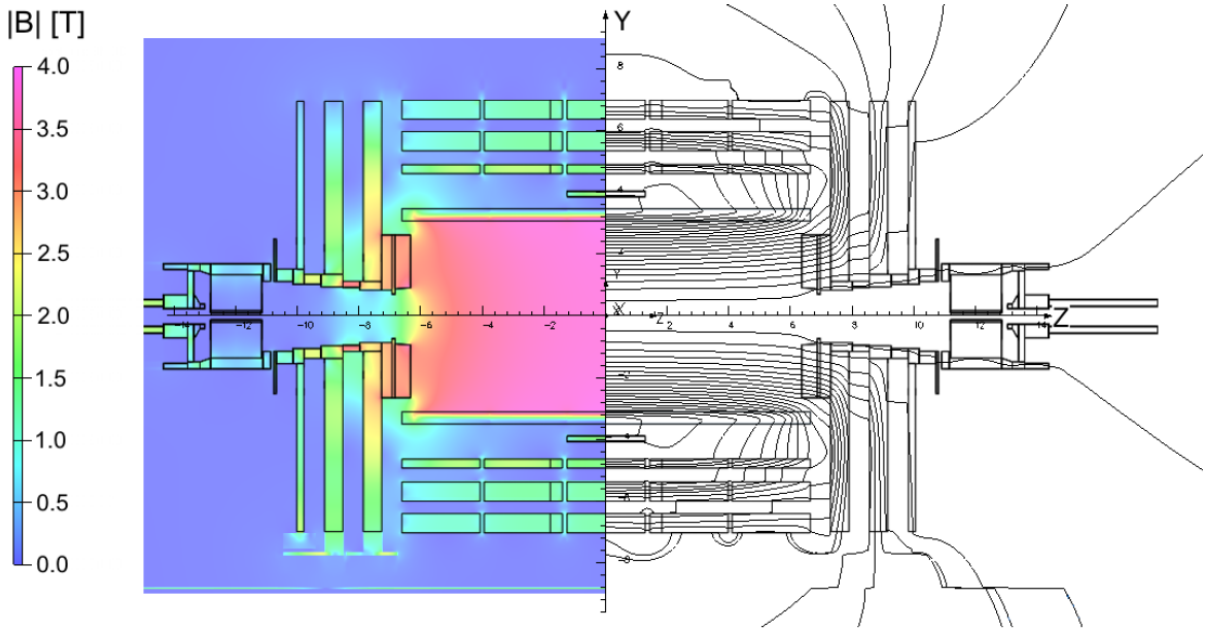

Figure 3.4: Value of the magnetic field (left) and the field lines predicted on a longitudinal section of the CMS detector, at a central magnetic flux density of 3.8 T [151].

in agreement with the measurements were found.

3.2 The CMS Muon system

The CMS muon detection system, shown in longitudinal view in Figure 3.5 and transversal view in Figure 3.6, has 3 functions: muon identification, momentum measurement, and triggering. Good muon momentum resolution in both the reconstruction (measurement) and selection (trigger) are provided by the high-field solenoidal magnet and the flux-return yoke, which also serves as a hadron absorber that improves the muon identification. CMS uses 3 different particle detectors for muon identification. Because of the central solenoidal magnet, it is natural to have a cylindrical, barrel region and planar endcaps. The muon detectors have to be inexpensive, reliable and robust, since they have to cover a large area and will be only accessible during extended (year-long) technical stops [153].

This section presents the muon detectors and their working principles briefly; a more complete description can be found in Reference [131]. For precision measurements, two types of gas detectors are used: drift chambers based on circular electric fields for precision position measurements and planar parallel plate counters based on parallel electric fields for precision timing measurements. Drift tubes (DTs) and cathode strip chambers (CSCs) are the implementation of the first type, whereas the resistive plate chamber (RPC) is an implementation of the second type. After discussing the features those different detectors have in common, the DT and CSC detectors are discussed in detail, while the RPC detectors are detailed in a separate chapter. Finally, the local reconstruction of a muon track inside the individual DT and CSC chambers is discussed.

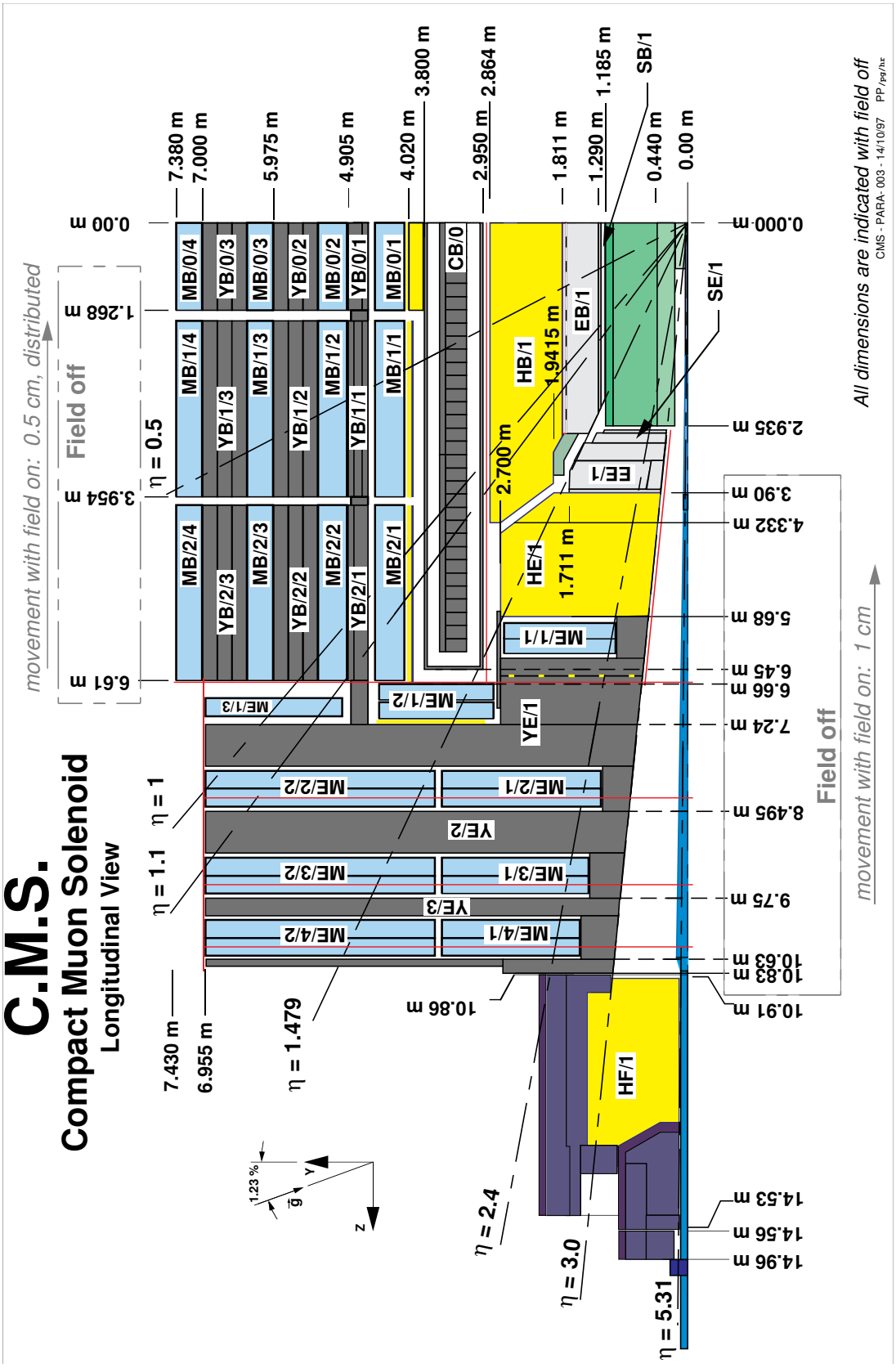

Figure 3.5: Longitudinal view of one quarter of the CMS detector [138].

Charged particles can be detected by gas detectors because they ionize the gas along their flight pad. The required energy to ionize a gas is very small, typically a few keV/cm, and is provided by their kinetic energy [154]. Amplification of this signal inside the gas volume allows for readout of electrical pulses induced by these moving charges on electrodes placed inside the gas volume. This so-called "gas gain" is obtained by applying a high electric field, which accelerates the ionization electrons, and gives them in turn enough energy to further ionize the gas, leading to an "avalanche" of electric charge.

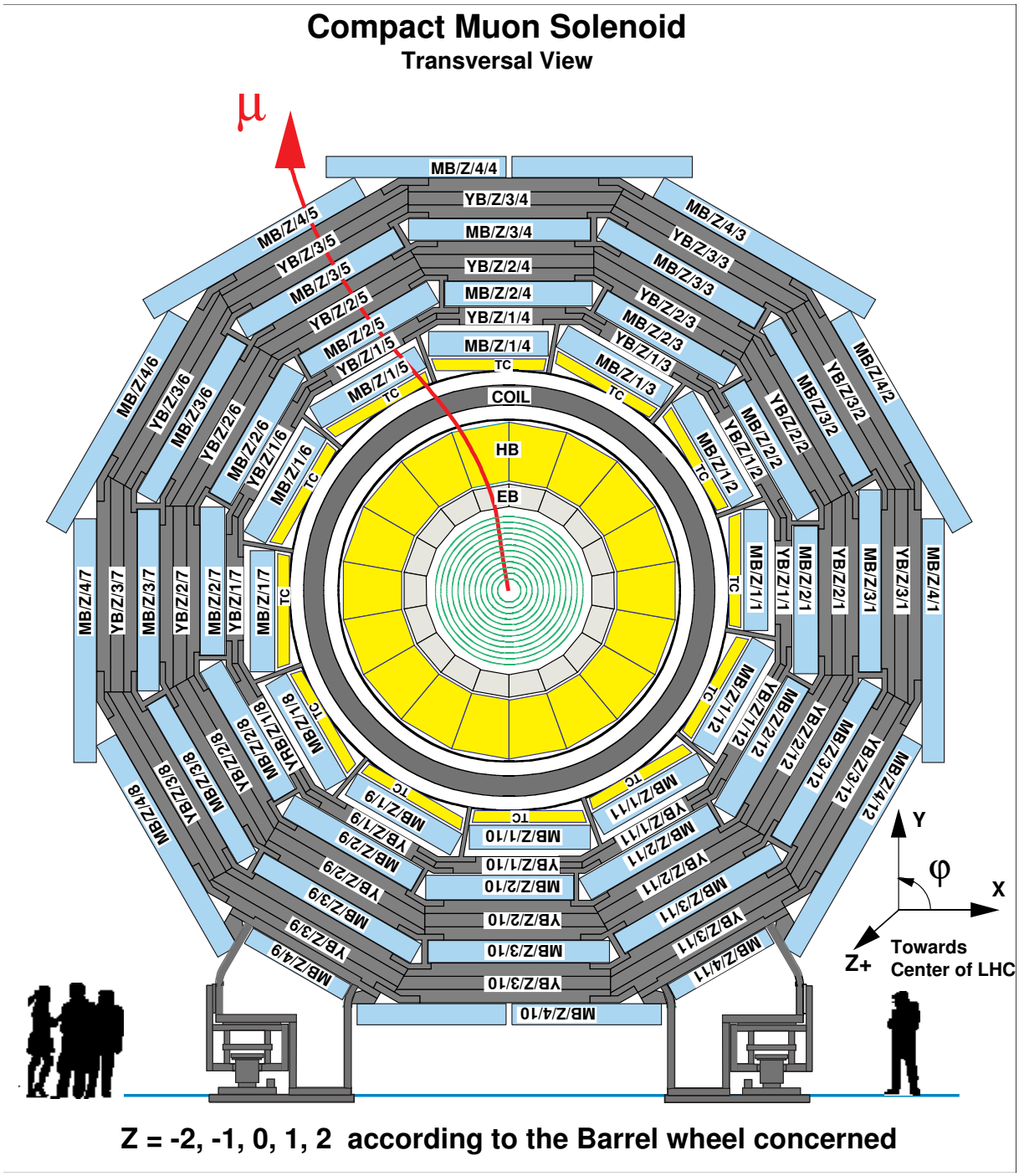

Figure 3.6: Transverse view of the CMS detector [138].

3.2.1 Gas detectors

Moving charges in a drift chamber give rise to electrical signals on the electrodes that can be read out by amplifiers. The electrons created in the avalanche close to a wire will move[1] to the wire surface, within a time typically much less than a nanosecond, resulting in a short signal pulse. The ions created in the avalanche move away from the wire with a velocity about a factor 1000 smaller, which results in a signal with a long tail of typically several hundred microseconds duration. The movement of these charges induces a signal not only on the wire but also on the other electrodes in the chamber, so for the purpose of coordinate measurements, the cathode can be subdivided into several parts, a technique used inside Cathode Strip Chambers (CSCs) [154].

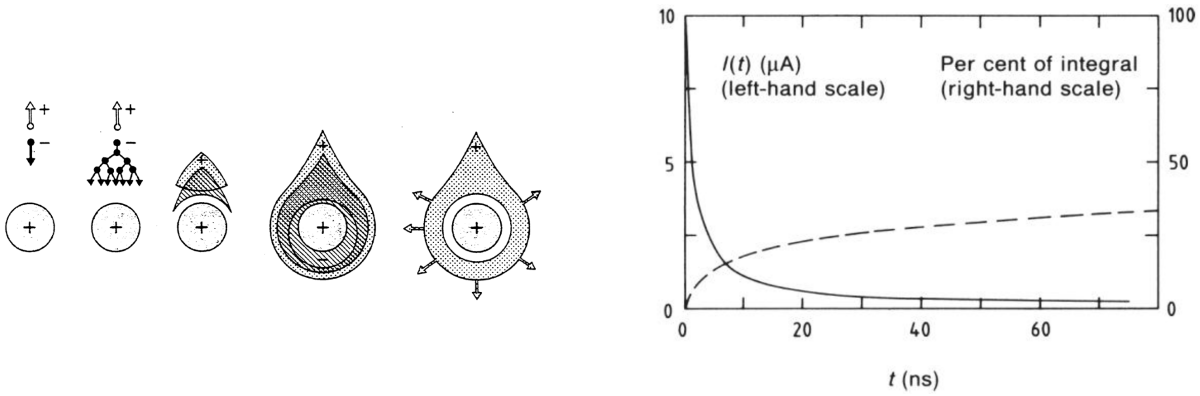

Figure 3.7: The development of a charge avalanche near an anode wire in a drift chamber (a) and the induced current on the anode (b). The currents induced on other electrodes inside the Faraday cage of the detector are such that the sum of all induced currents at each moment equals zero [149, 150, 155].

Figure 3.7 shows the development of a charge avalanche near an anode wire and the resulting induced current. The electron avalanche happens close to the wire, typically at a distance twice the wire radius. For a typical wire radius of $10\,\mu$m and an electric field at the wire radius of 150 kV/cm, the electrons move to the wire surface typically faster than 1 ns, while ions drift much slower to the cathodes, at times $O(100)\,\mu$s. The signal is characterized by a very fast spike due to the fast electron movement and a very long tail because of the slow ion drift. The total charge induced by the electrons, i.e. the charge of the current spike due to the short electron movement amounts to 1 to 2% of the total induced charge [149]. Since this charge is typically too low to be detected, particle detectors have to integrate also part of the ion induced current, slowing down the signal creation.

It is a common misunderstanding that electrical signals are due to the collection of the charge at the electrodes. Electrical signals are induced by the movement of charges towards the electrode. An electric signal starts when a charge starts moving and stops when the charge is not moving anymore, i.e. when it arrives at the electrode. The Shockley - Ramo theorem [156, 157] allows for easy calculation of instantaneous electric current induced by a moving charge in the vincinity of an electrode. Concerning the signal creation it states:

> The current induced in an electrode is due to the instantaneous change of electro-

[1] Assumed that the wire is at a positive potential with respect to the other electrodes.

static flux lines which end on the electrode, not the amount of charge received by the electrode per second.

3.2.2 Barrel precision chambers

In the barrel region where the muon rate is low, the neutron background (detailed in section 5.3) is relatively small (except in the outermost station MB4), and the magnetic field is mostly uniform and less than 0.4 T, drift chambers [154] with standard rectangular cells and sophisticated electric field shaping are employed.

The barrel muon detector, shown in Figure 3.6, consists of 250 chambers embedded in the steel yoke, which are arranged in four muon stations, named, starting from the interaction point, MB1, MB2, MB3 and MB4. The steel yoke is divided along the beam direction in five wheels, numbered from -2 to +2, each one with 12 sectors in the transverse plane, sector 1 being at $\phi = 0$. Figure 3.5 shows a longitudinal view of a quarter of the CMS detector. The barrel drift tube (DT) chambers cover the pseudorapidity region $|\eta| < 1.2$ and consist of 172 000 readout channels.

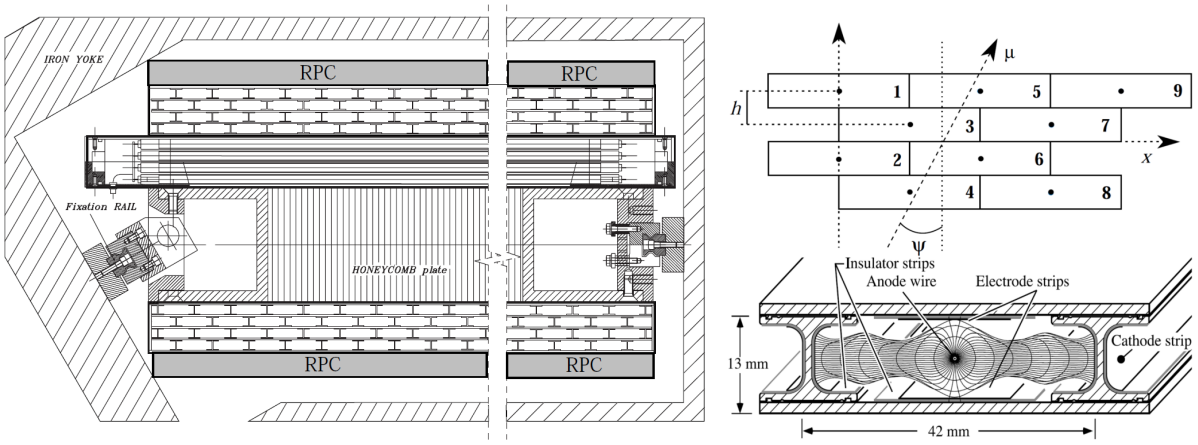

(a) (b)

Figure 3.8: (a) Cross section of a DT chamber with RPCs attached both on top and and at the bottom. The two superlayers measuring the ϕ coordinate are perpendicular to the plane of the figure and are at the bottom and at the top of the chamber. The superlayer measuring the η-coordinate is in the middle, above the honeycomb plate separating the two ϕ-superlayers. (b) Bottom: A Drift Tube cell and its complexly shaped electric field inside. (b) Top: The hit pattern of a muon passing through a superlayer [138, 141].

The layout of a DT chamber is shown in Figure 3.8(a). Each chamber consists of 8 layers of tubes measuring the (bending) ϕ-coordinate, and 4 layers measuring the longitudinal η-coordinate. Four such layers make up a superlayer (SL). The two superlayers measuring the ϕ-coordinate are separated by a 20 cm thick aluminium honeycomb plate that supplies the chamber with the required stiffness. It also provides a lever arm in the bending plane, improving the angular resolution and permits a good measurement of the muon in the second superlayer in case an electromagnetic shower was initiated inside the iron return yoke. The fourth station (MB4) differs from the others, since it does not have a superlayer measuring the η-coordinate, but the distance between the two superlayers measuring in the bending plane is kept the same.

Figure 3.8(b) (bottom) illustrates the design of a drift cell, including 5 electrodes: the anode wire, 2 field shaping strips (electrode strips) and 2 cathode strips (attached to the I-beams separating the different drift cells). The adjusted electric field structure improves the uniformity of the electric field inside the drift tube at distances far from the anode wire, where a high circular electric field is imposed. This improves the linearity of the space-to-drift time relation, which results in an improved spatial resolution [5].

When a charged particle passes through the cell, it ionizes the gas and the liberated electrons will travel towards the anode wire. The maximum pathlength inside a drift cell is 21 mm, leading to a maximum 380 ns drift time in the Ar/CO_2 85/15 gas mixture. Close to the wire, in the strong electric field, the electrons are multiplied and this moving charge avalanche will induce a fast signal, O(ns), on the anode wire. The cathode strips, nor the field shaping electrodes are read out.

Drift tubes estimate the longitudinal position of a track by extrapolating the arrival time of electrons at the anodes, if the time of interaction is known. Requiring at least three subsequent layers, staggered half a drift tube as shown in Figure 3.8(b)(top), both the time and the position of the track can be determined precisely. Within a superlayer, an angular resolution of 20 mrad, spatial resolution of 1.5 mm and a time resolution of a few ns are obtained. The latter allows for a good bunch crossing resolution determination, although this BX identification signal is delayed by the 380 ns (> 15BX) to allow all four drift cells to read out their electric signals.

Figure 3.9 shows a $B_s \rightarrow \mu\mu$-candidate. The event display shows two muons passing through the muon system. The double measurement of the ϕ-coordinate and single measurement of the η-coordinate within a single DT chamber is clearly visible. The fourth and outermost layer consists only of two superlayers, which are both dedicated to the measurement of the ϕ-coordinate of the muon track.

3.2.3 Endcap precision chambers

In the endcap regions of CMS, where the muon rates and background levels are high, and the magnetic field is strong and non-uniform, CMS uses cathode strip chambers. These chambers have a fast response time (because of the very short drift path), fine segmentation, and relative immunity to the non-uniformity of the field. In total 468 CSC chambers are installed in the two endcap regions. Each endcap has 4 stations of chambers mounted on the faces of the endcap steel disks: ME1, ME2, ME3 and ME4. The 72 ME4/2 chambers were not constructed and hence not installed for the early years of LHC running. The CSCs cover $0.9 \leq |\eta| \leq 2.4$.

CSCs are multiwire proportional chambers that consist of 6 layers and each layer consists of a cathode plane divided in strips and orthogonal anode wires. The cathode strips run radially outward and provide a high-precision measurement of the ϕ-coordinate in the bending plane. The wires run orthogonal to the strips and are optimized for bunch crossing identification with high efficiency and provide also a coarse measurement in the η direction.

The CSC system consists of 220 000 cathode readout strips and about 2 million anode wires. To reduce the amount of readout channels, the wires are hard-wired together at the readout in groups of 10-15 wires, leading to 180 000 anode wire readout channels. The nominal gas mixture consists of 40% Ar, 50% CO_2 which is a quencher to achieve high gas gains, and 10% CF_4 preventing polymerisation at the wires.

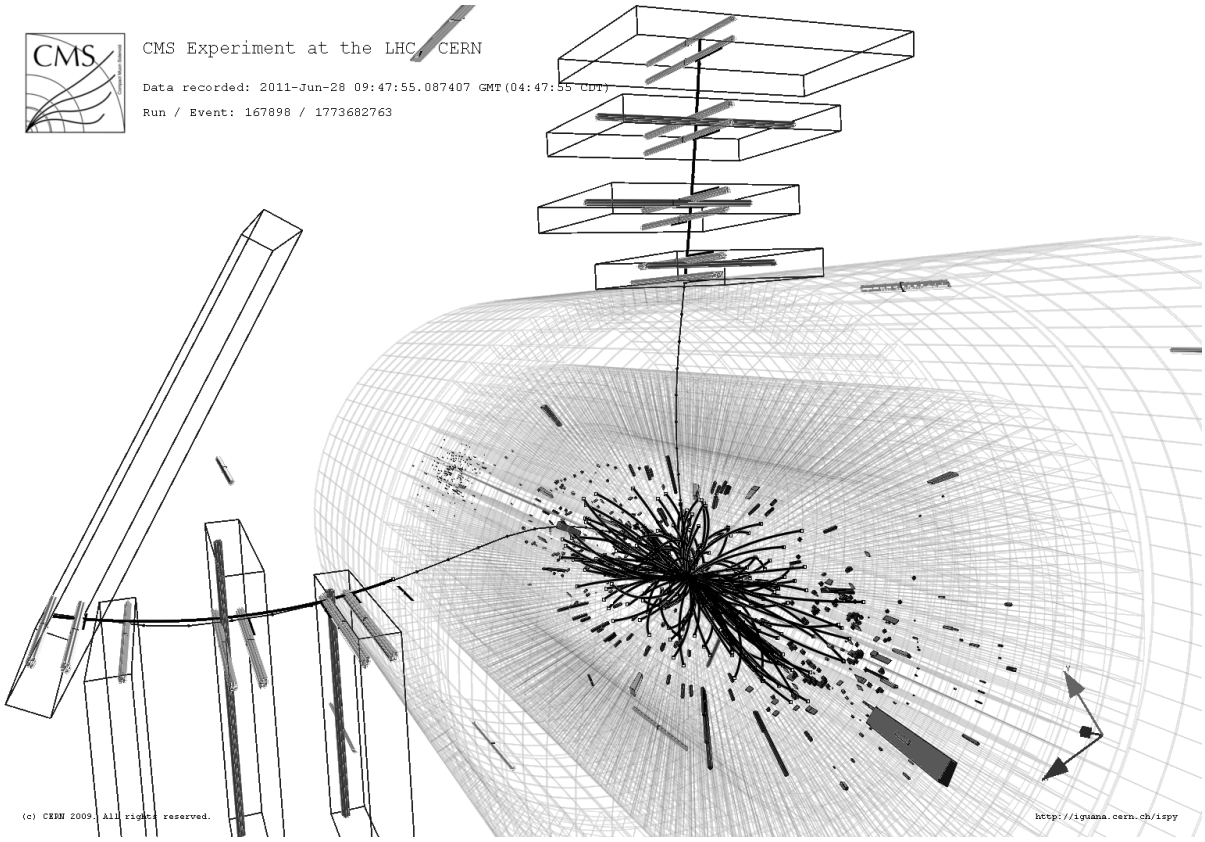

Figure 3.9: Event display of a $B_s \rightarrow \mu\mu$-candidate of event 1 773 682 763 recorded in run 167 898. Two particles identified as muons emerge from the tracker and leave hits in the DTs and RPCs [158].

A charged particle passing through a layer of the CSC detector, ionizes the gas. The ionized electrons drift to the anode wire, where a charge multiplication will develop. The movement of the charge avalanche induces a fast signal on the anode wire and the cathode strips. The wires are spaced 3 mm apart, leading to a drift time that can extend up to 50 ns, but which is still much shorter than the drift time for the drift tubes. Signals obtained at the cathode strips are amplified and shaped to have a length of 100 ns, and use about 8% of the avalanche charge.

Unlike the other CSC chambers, the 72 ME1/1 chambers are inside the CMS solenoid and are subject to the strong and uniform 4 T axial magnetic field, which influences charges drifting to the anodes. Therefore the ME1/1 chambers have a slightly different design, with wires not running azimuthally, but tilted by an angle $\alpha_L = 29°$ to compensate for the Lorentz-force, which is illustrated in Figure 3.10.

3.2.4 A dedicated muon trigger detector

Crucial properties of the DT and CSC systems are that they can each identify the collision bunch crossing that generated the muon, and trigger on the p_T of muons with good efficiency and high background rejection (by asking spatial and temporal coincidences) independent of the rest of the detector. In addition to these tracking detectors, CMS has added a complementary, dedicated trigger detector with excellent time resolution to improve the measurement of the correct beam-crossing time at the highest LHC luminosities: Resistive Plate Chambers.

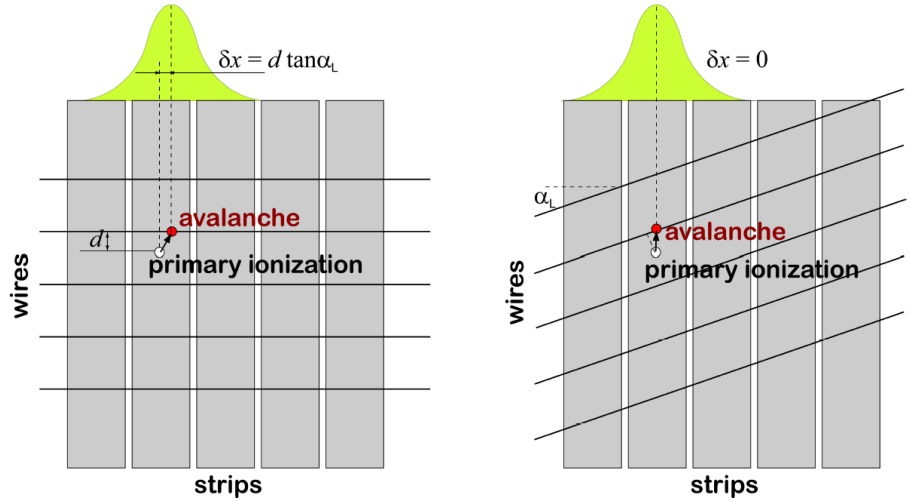

Figure 3.10: Left panel: if the ME1/1 wires were not tilted, ionization electrons, as they drift toward the anode wires in the strong magnetic field normal to the plane of the drawing, would drift sideways due to the Lorentz force. The direction and size of the shift would depend on whether the electrons drift upward or downward and on how far away they were from the wires to begin with. These sideways displacements would spread the charge over the cathode strips. Right panel: by tilting the wires at the Lorentz angle α_L, all ionization electrons arrive near the same point [131].

The RPCs are located in both the barrel and endcap regions, and they can provide a fast, independent trigger with a lower p_T-threshold over a large portion of the rapidity range ($|\eta| < 1.6$). A total of 6 layers of RPCs are embedded in the barrel muon system, 2 in each of the inner 2 stations and 1 in each of the outer 2 stations. The redundancy in the first 2 stations allows the trigger to work even for low-p_T tracks that may stop before reaching the outer 2 stations. In the endcap region, RPCs are installed in the first 3 stations.

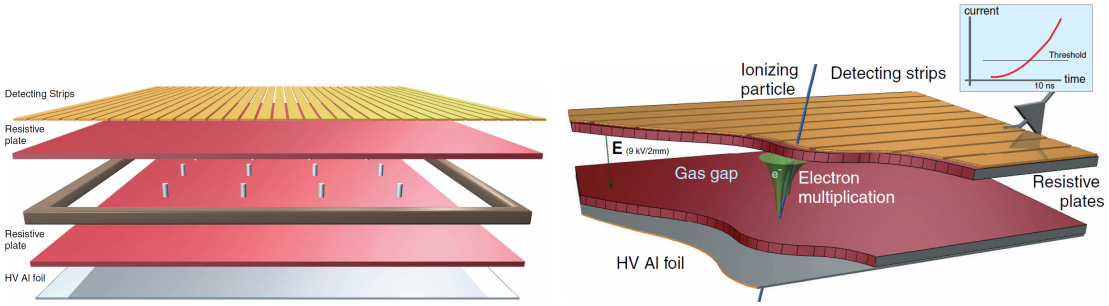

(a) (b)

Figure 3.11: (a) Drawing of the different layers an RPC is made of and (b) an illustration of the RPC detection principle [138].

The RPCs are double-gap chambers, operated in avalanche mode to ensure good operation at high rates. Figure 3.11(a) shows the different layers an RPC is made of: strips run on top of a bakelite resistive plate that is used as electrode, but is transparant to the fast discharge channel coupled into the strips. The CMS RPC system and RPC working principles are detailed in chapter 5. The RPC is the only muon detector able to produce an electronic signal within 25 ns of the passing of a muon through a chamber. This enables the RPC-trigger to assign

unambiguously the right bunch crossing to a muon track, even at high-rate and in environments with huge background.

3.2.5 Local track reconstruction

The muon hits in the different layers are read out by the chamber electronics to perform a local reconstruction of a charged track, which is used for triggering purposes and is hence called the "local trigger". These local charged tracks (LCTs), also called "muon segments", are used by the reconstruction to identify and combine the relevant tracker information with the hits of the muon detector. Hits of both tracker and muon system are then used in a global fit to reconstruct muons and determine their momentum with high precision. This is discussed in more detail in section 4.7.2.

The large number of layers in each tracking chamber is exploited by a local process that generates local track segments with a precision sufficient to set sharp p_T thresholds at the Level-1 trigger level up to 100 GeV/c, and to tag with very good time resolution the parent bunch crossing. A suitably sharp momentum threshold is obtained by requiring a local space resolution of the segments on the order of a couple of millimeters. This resolution is necessary to guarantee a high trigger efficiency and it defines a lower limit on the accuracy that must be reached by the alignment of the chamber positions.

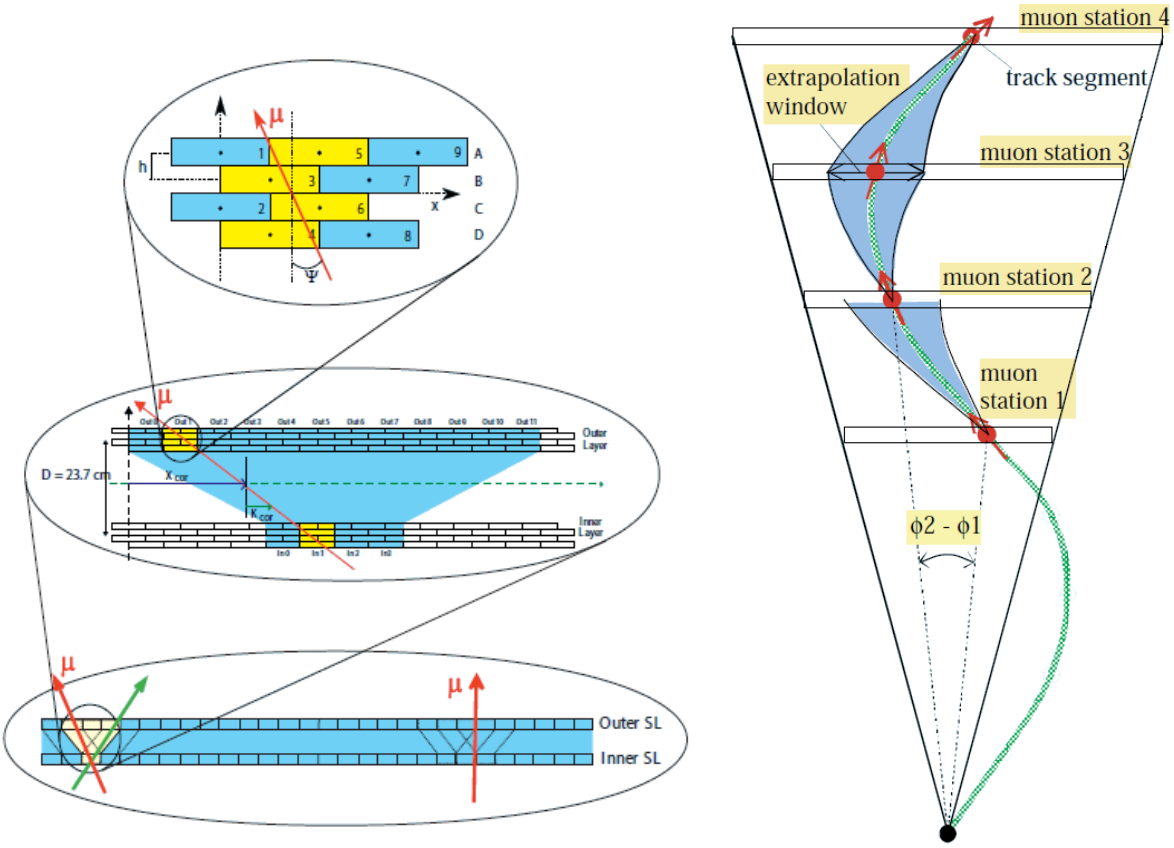

Figure 3.12: The DT local trigger 3.12(a) and the Track Finder extrapolation scheme (b) [131, 141].

3.2.6 Local track reconstruction in the drift tubes

The reconstruction of a local charged track inside the drift tube system starts with the search of coincident aligned hits in the four planes of staggered drift tubes in each chamber superlayer. The association of hits is based on the fact that there is a fixed relation between the drift times of any three adjacent planes. From the associated hits, track segments defined by position and angular direction are determined, with an angular resolution better than 60 mrad and a position resolution of 1.5 mm [131]. These 2D-segments, 2 for the ϕ-coordinate and 1 (except for MB4) for the η-coordinate are correlated and merged into a 4D-segment, combining 3D spatial information with the fitted value of the arrival time of the muon in the chamber. The superlayer providing the η-coordinate measurement is configured such that only candidates originating from the interaction point are considered. The long lever arm between the outer and inner superlayer improves the angular resolution to 10 mrad, while maintaining the position resolution at 1.5 mm. Figure 3.12(a) illustrates the muon segment reconstruction within a DT chamber.

The muon segments are then sent to the Drift Tube Track Finder (DTTF). The DTTF finds a muon track by extrapolation from a source track segment in one muon station to a possible target segment in another station according to a pre-calculated muon trajectory that originated at the vertex. If a compatible target segment is found, it is linked to the source segment. Up to four segments out of four muon stations are joined to form a complete track, to which parameters are then assigned. Figure 3.12(b) illustrates the extrapolation principle.

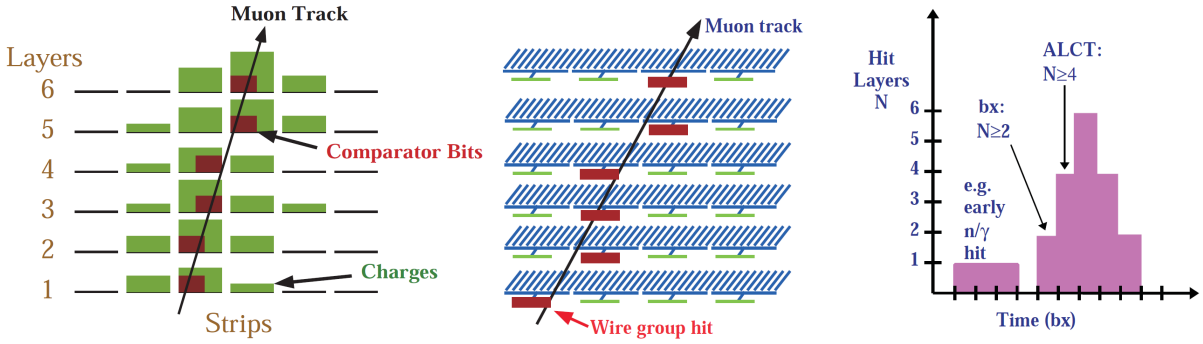

(a) CLCT (b) ALCT

Figure 3.13: The CSC local trigger: (a) Cathode LCT information from the strips, (b) Anode LCT information from wire group hits and the bunch crossing assignment [131, 141].

3.2.7 Local track reconstruction in the cathode strip chambers

The CSC local trigger uses the six layer redundancy of the CSC chambers to provide precise position information as well as high rejection power against backgrounds. Muon tracks segments, also known as Local Charged Tracks (LCTs), are determined separately in the nearly orthogonal anode and cathode views. These Anode Local Charged Tracks (ALCT) and Cathode Local Charged Tracks (CLCT) are then correlated in time and in the number of layers hit.

The cathode signals are used to determine precisely the position of the track in the bending plane. The most precise measurement of the track position is obtained by charge digitization and precise interpolation of cathode strip charges. A simpler, faster and more robust method is used for the CSC CLCT to achieve half-strip localization of the charged track in each cathode layer, which is illustrated in Figure 3.13(a). This is done with a “comparator” comparing the

amplified and shaped signals from adjacent strips. If a strip signal is found to be larger than that of its neighbours, a hit is assigned to the strip. Simultaneous comparison of left versus right neighbour strip signals allows assignment of the hit to the right or left side of the central strip, effectively improving the resolution with a factor 2 [141]. Up to two CLCTs per bunch crossing are provided per chamber.

In the non-bending plane such precision is not required and instead the electronics are optimized to identify the bunch crossing. The wires of a CSC chamber are much shorter (and thus faster) than the cathode strips. In addition, all charge is induced on a single wire instead of being smeared over several strips. Therefore, bunch crossing identification is based on signals obtained from the anode wires, which have a 30 ns shape after amplification, suppressing the tail due to the slow ion drift. About 12% of the total avalanche charge is used to create the anode signal. Since the drift time can exceed 25 ns, a multi-layer coincidence technique in the ALCT electronics is used to identify the bunch crossing. A spatial coincidence in two layers is used to establish timing, whereas a higher coincidence of four layers is used to establish the existence of a muon track. This coincidence technique efficiently cuts the neutron background[2] that typically creates hits in only a single layer. Figure 3.13(b) illustrates the spatial coincidence of wire groups used to identify the coarse η-position of the track, while the timing coincidence is used to separate real muon tracks from neutron background hits. The total time needed to build an ALCT including drift time, is 225 ns and up to two ALCT triggers per bunch crossing are provided per chamber.

Finally, the track segments of the cathode and anode electronics are combined to form three dimensional LCTs. They consist of a high precision ϕ-coordinate, a measurement of the incident angle ϕ_b, a rough η-coordinate and a bunch crossing number. The best two LCTs are sent to the regional CSC trigger, the CSC Track Finder (TF). The CSCTF receives muon segments from one muon station and extrapolates them to the next station. Hence, a muon track is matched to segments in different CSC stations. It is worthwile to mention that the finding of trigger primitives (LCTs) also affects the readout of the hits. If no LCT is found, no raw hits will be readout upon a Level-1 Accept (L1A) signal.

3.3 The CMS Tracker

3.3.1 The CMS Tracker subdetector

The CMS Tracker, shown in Figure 3.14, consists of two main detectors: a silicon pixel detector, covering the region from 4 to 15 cm in radius, and 49 cm on either side of the collision point along the LHC beam axis, and a silicon strip detector, covering the region from 25 to 110 cm in radius, and within 280 cm on either side of the collision point along the LHC beam axis [159].

The CMS silicon pixel detector has 66 million active elements imstrumenting a surface area of about 1 m^2. It is designed to provide the determination of three high precision three-dimensional points on track trajectories. The detector consists of three concentric cylindrical barrel layers and four fan-blade disks which close the barrel ends. The barrel layers have an active length of 53 cm and are located at average radii of 4.3, 7.3, and 10.2 cm. The endcap disks instrument

[2]Neutrons induce nuclear interactions that produce photons, which in turn can create electrons that ionize the CSC gas. The neutron background is discussed extensively in section 5.3.

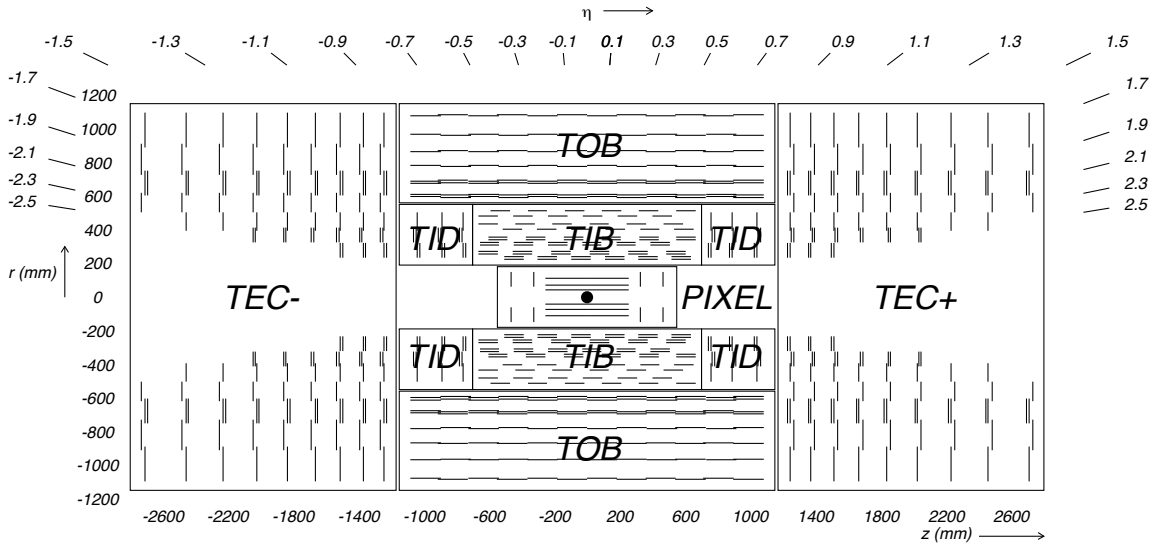

Figure 3.14: Schematic cross section through the CMS tracker. Each line represents a detector module. Double lines indicate back-to-back modules which deliver stereo hits. The strip detector region of the CMS Tracker consists of four main subsystems: the four-layer Tracker Inner Barrel (TIB), the six-layer Tracker Outer Barrel (TOB), and, on each side of the barrel region, the three-disk Tracker Inner Disks (TID), and the nine-disk Tracker End Caps (TEC) [159].

the regions between radii 4.8 and 14.4 cm at mean longitudinal distances of 35.5 and 48.5 cm from the interaction point. The system provides efficient three-hit coverage in the region of pseudorapidity $|\eta| < 2.2$ and efficient two-hit coverage in the region $|\eta| < 2.5$. The active elements are $100\,\mu$m×$150\,\mu$m pixels [131], which are oriented with the smaller pitch in the azimuthal direction in the barrel and the radial direction in the disks [159].

The 3.8 T magnetic field in CMS causes significant azimuthal Lorentz drift of the collected electrons in the pixel barrel which enhances the azimuthal charge sharing and therefore improves the resolution in that direction. The blades of the endcap disks are rotated by 20 degrees about their radial axes with respect to the disk planes to produce azimuthal charge sharing and radial Lorentz drift which enhances the radial charge sharing. The charge sharing improves the endcap resolution in both planes [159].

The CMS silicon strip detector has 9.3 million active elements instrumenting a surface area of 198 m^2. The detector consists of three large subsystems. The Tracker Inner Barrel and Disks (TIB/TID) are composed of four barrel layers and three disks at each end composed of $320\,\mu$m thick silicon microstrip sensors. The TIB/TID strips are oriented parallel to the beam axis in the barrel and are oriented radially in the disks. The strip pitch ranges from $80\,\mu$m to $120\,\mu$m in the TIB and varies between $100\,\mu$m and $141\,\mu$m in the TID. The TIB/TID is enclosed within the Tracker Outer Barrel (TOB), which consists of six barrel layers of $500\,\mu$m thick microstrip sensors with strip pitches of $122\,\mu$m in the first four layers and $183\,\mu$m in the last pair of layers.

The Tracker EndCaps (TEC) are composed of nine disks that are instrumented with up to seven rings of radial-strip silicon detectors. The sensor thicknesses are $320\,\mu$m in the inner four rings and $500\,\mu$m in the outer three rings; the average radial strip pitch varies from $97\,\mu$m to $184\,\mu$m. The inner two layers of the TIB and TOB, the inner two rings of the TID and TEC, and the

fifth ring of the TEC include a second microstrip detector module that is mounted back-to-back at a stereo angle of 100 mrad and that enables a measurement of the orthogonal coordinate. Assuming fully efficient planes and not counting hits in stereo modules, there are from 8 to 14 high precision measurements of track impact points for $|\eta| < 2.4$ and 4 measurements at $|\eta| = 2.5$ [159].

3.3.2 Track and vertex reconstruction

The track reconstruction algorithms rely on a good estimate of the proton-proton interaction region, referred to as the beamspot. The beamspot is measured using a sample of reconstructed tracks using the previous beamspot measurement. During the 2009 data-taking, a beamspot was fitted during each LHC fill. Starting from the location of the beamspot, an initial round of track and vertex reconstruction is performed using only pixel hits. The standard track reconstruction at CMS is performed by the combinatorial track finder (CTF) [160]. Tracks are seeded from either triplets of hits in the tracker or pairs of hits with an additional constraint from the beamspot of pixel vertex, yielding an initial estimate of the trajectory and its uncertainty. The seed is then propagated outward in a search for compatible hits. As hits are found, they are added to the trajectory and the track parameters and uncertainties are updated [159].

The current implementation of the CTF performs six iterations. Between each iteration, hits that can be unambiguously assigned to tracks in the previous iteration are removed from the collection of tracker hits to create a smaller collection that can be used in the subsequent iteration. At the end of each iteration, the reconstructed tracks are filtered to remove tracks that are likely fakes. The filtering uses information on the number of hits, the normalized χ^2 of the track and the compatibility of the track originating from a pixel vertex. Tracks that pass the tightest selection are labelled "highPurity". The first two iterations use pixel triplets and pixel pairs as seeds to find prompt tracks with $p_{\mathrm{T}} > 0.9\,\mathrm{GeV}/c$. The next iteration uses pixel triplets to reconstruct low-momentum prompt tracks. The following iteration uses combination of pixel and strip layers as seeds, and is primarily intended to find displaced tracks, i.e. tracks not pointing toward the IP. The final two iterations use seeds of strip pairs to reconstruct tracks lacking pixel hits [159].

After reconstructing the tracks of a pp-collision, these tracks are used for the reconstruction of the primary interaction vertex of the event. The tracks are clustered, based on the z-coordinate of the track at the point of closest approach to the beamline. The clusters are used as input for an adaptive vertex fitting procedure [161], where tracks in the vertex are assigned a weight between 0 and 1 based on their proximity to the common vertex. For a track consistent with the common vertex, its weight is close to 1. The number of degrees of freedom is defined as $n_{\mathrm{dof}} = 2\sum_i^{n_{\mathrm{tracks}}} w_i - 3$, where w_i is the weight of the i^{th} track [159, 162].

The performance of the track and primary vertex reconstruction is obtained using $1.1\,\mathrm{nb}^{-1}$ of minimum bias events collected at centre-of-mass energies of 7 TeV. Due to the relatively low LHC luminosity, the CMS readout was triggered by dedicated Minimum Bias triggers, detailed in section 3.6 covering Beam Radiation and Monitoring. The transverse impact parameter d_{xy} is the closest approach between the track and the reconstructed primary vertex in the transverse plane. The longitudinal impact parameter d_z is the smallest distance between the track and the reconstructed primary vertex in the longitudinal direction. The distributions of d_{xy} and d_z are shown in Figure 3.15.

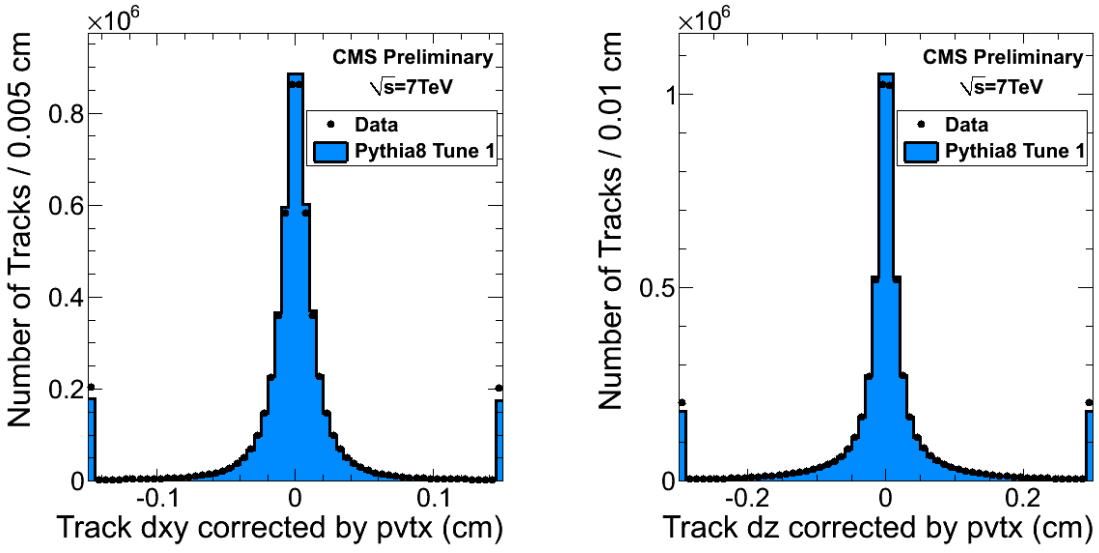

(a) (b)

Figure 3.15: Data/Simulation comparison for the track transverse impact parameter (a) and longitudinal impact parameter (b) measured w.r.t. the reconstructed primary vertex [162].

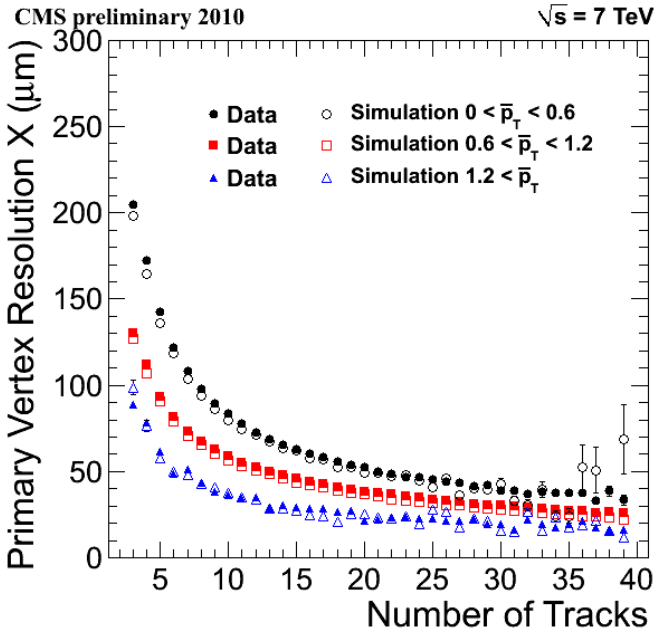

Figure 3.16: Primary vertex resolutions in the x-direction for different average transverse momentum $\overline{p_{\mathrm{T}}}$ as a function of the number of tracks of the fitted vertex [162].

The primary vertex resolution depends strongly on the number of tracks assigned to the vertex in the fit and the p_{T} of these tracks [162]. Figure 3.16 shows the measured primary vertex resolutions in the x-direction as a function of the number of tracks for different average transverse momentum $\overline{p_{\mathrm{T}}}$ of tracks in the vertex. Results are shown both for data and simulation, the latter being able to describe the data fairly well.

A dedicated study [163] was performed to investigate the amount of material in the tracker. For the detector simulation it is of utmost importance that all material in the tracker (silicon detectors, cables, cooling, etcetera) are well described in the simulation geometry. This study was performed using converted photons and nuclear interactions, for which two additional iterations were added on top of the six existing iterations of the track reconstruction, dedicated to reconstruct low-p_T tracks with largely displaced vertices.

With the first data only the pixel barrel (PXL) and the inner tracker barrel (TIB) could be studied. The resulting material distributions for photon conversions and nuclear interactions are shown in Figure 3.17. The plots in Figure 3.17 clearly demonstrate a very good agreement between data and simulation for both photon conversions and nuclear interactions, showing that the description of the Tracker material in the simulation is well under control. Overall the observed relative agreement is of the order of ~10%, except a localized larger discrepancy in the region between the TIB and the Tracker Outer Barrel (TOB) [163].

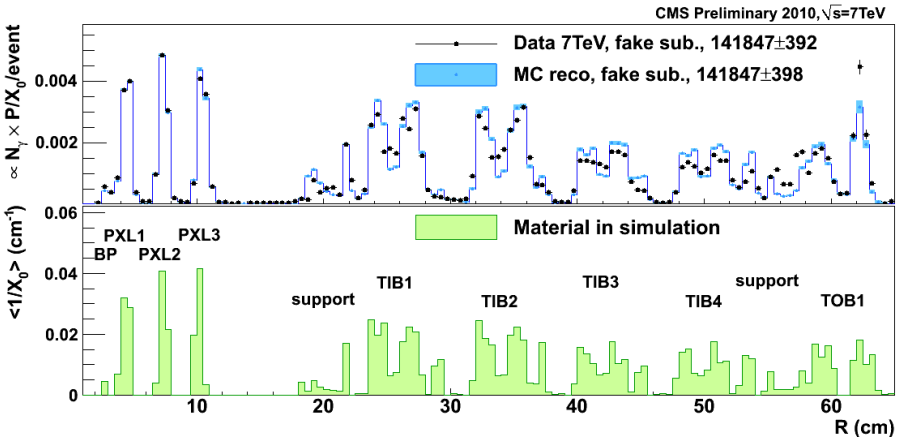

(a)

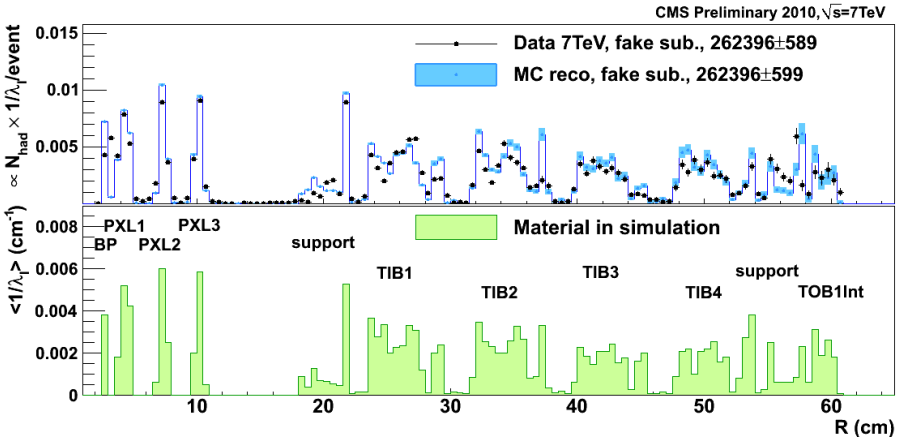

(b)

Figure 3.17: Material distribution versus the radius estimated from reconstructed photon conversions (a) and nuclear interactions (b). As a comparison, the histogram in the bottom panel represents the material distribution in the simulation in average X_0^{-1} per bin (a), and in average λ_I^{-1} per bin (b) [163].

3.4 The CMS Calorimeters

3.4.1 The CMS Calorimeter subdetectors

The CMS Calorimeter system consists of subdetectors optimized for electromagnetic and hadronic energy measurements in the central (barrel), forward (endcap) and very forward region. Figures 3.18 and 3.19 show a quarter of the electromagnetic and hadronic calorimeters. Photons and electrons loose their energy predominantly by radiative processes in the electromagnetic calorimeter. The distance scale is governed by the (material dependent) radiation length, X_0, defined as the mean free path for radiative processes. Hadrons loose their energy by nuclear interactions in the hadronic calorimeter. Here, the typical distance scale is set by the (material dependent) interaction length, λ_I, the mean free path length for hadronic interactions. 100 GeV electrons and photons loose almost all their energy in $\sim 20\, X_0$ of material, while $9\, \lambda_I$ of hadronic absorber stops most of the hadrons.

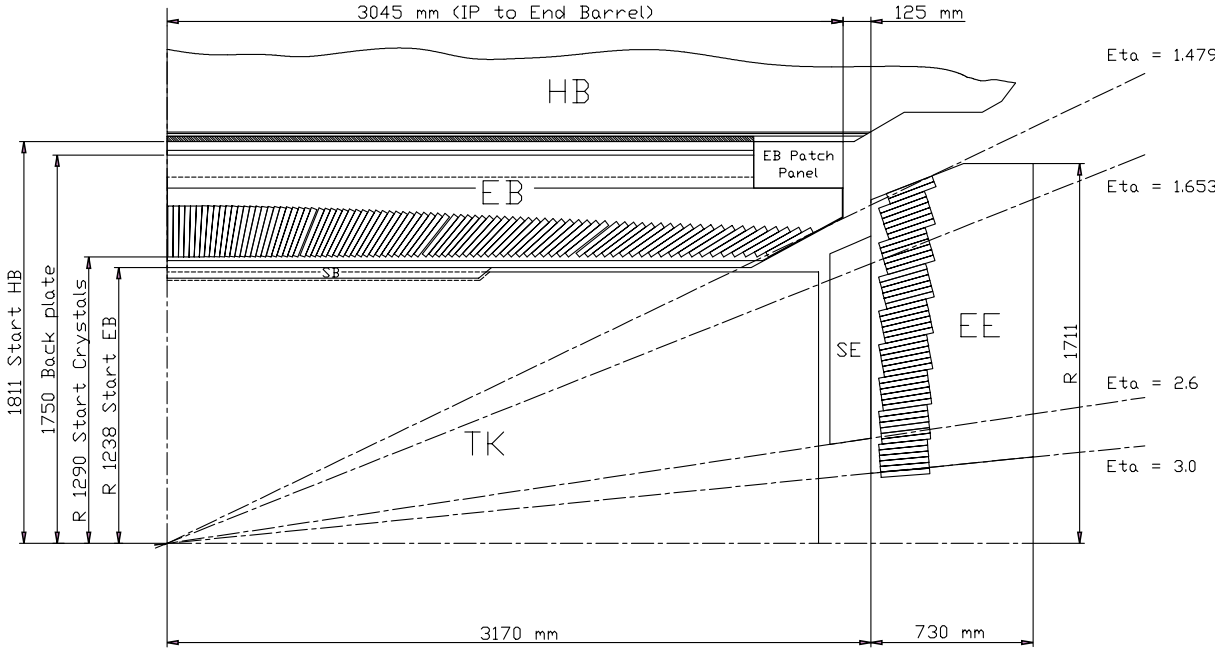

Figure 3.18: Longitudinal section of one quadrant of the electromagnetic calorimeter: showing the barrel (EB), endcap (EE) and preshower (SE, nowadays called ES). Note that the crystals have an angle of 3° with respect to lines at constant η to prevent particles traveling exactly in between two crystals [139].

The electromagnetic calorimeter (ECAL) is made of $PbWO_4$ crystals and can be divided in a barrel (EB) section and two endcaps (EE). Avalanche photodiodes (APDs) are used to detect the scintillation light in the barrel region, while vacuum phototriodes (VPTs) are used in the endcap region [164].

The EB contains 61 200 lead tungstate crystals, arranged in 170 η-rings of 360 crystals each (one crystal covers 1° in ϕ). It is subdivided in 36 supermodules and provides coverage in pseudorapidity up to $|\eta| < 1.479$. The two ECAL endcap (EE) subsystems consist of four half-disk, so-called "Dees", each containing 3 662 crystals. The EE provides a coverage of $1.479 < |\eta| < 3.0$. The $PbWO_4$ crystals are characterized by a high density ($\rho = 8.28\,\mathrm{g/cm^3}$), short radiation length ($X_0 = 0.89\,\mathrm{cm}$) and small Molière radius ($r_\mathrm{M} = 2.2\,\mathrm{cm}$). The crystals are

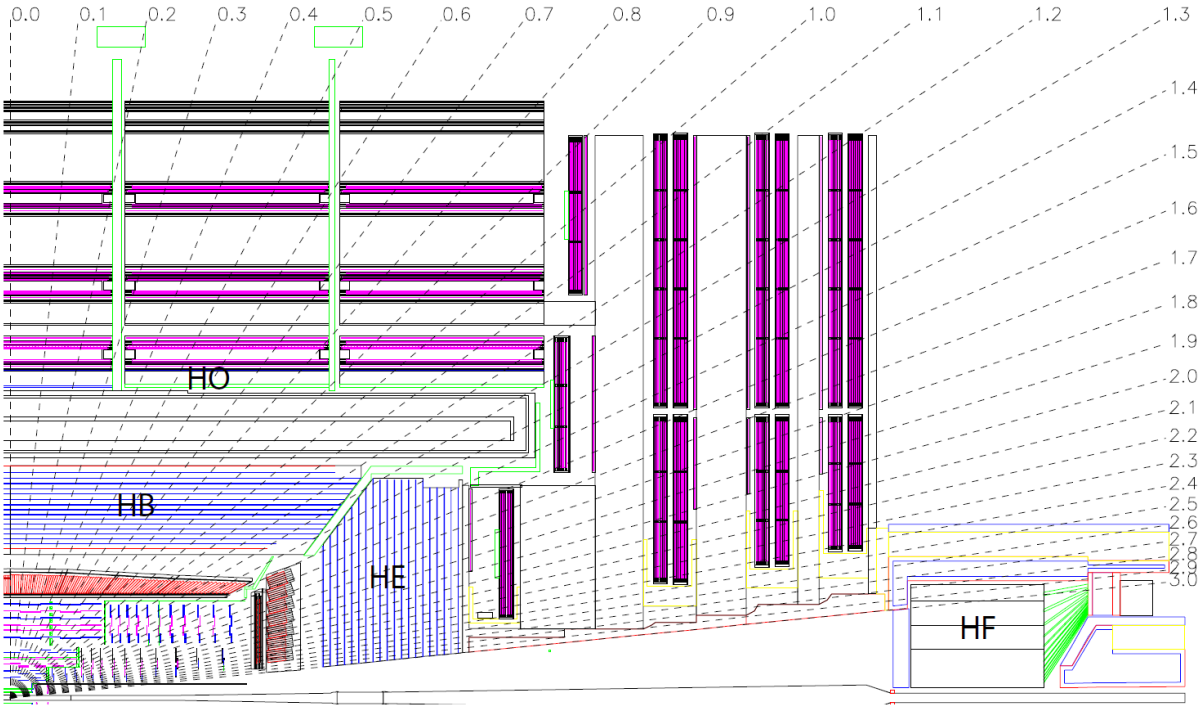

Figure 3.19: A view in (r, z) of a quarter of the different parts of the Hadron Calorimeter: Barrel (HB), Endcap (HE), Outer (HO) and Forward (HF). The different trigger towers of the central ($|\eta| < 3.0$) part of the calorimeter are indicated [131].

25.8 X_0 long in the barrel and 24.7 X_0 long in the endcaps [164].

In the barrel region, the transverse distance from the interaction point to the front face of the crystals, with a size of $22 \times 22\,\text{mm}^2$, is 1.29 m, corresponding to a granularity of $\Delta\eta \times \Delta\phi = 0.0174 \times 0.0174$. In the endcap region, the frontface of the crystals is $26.82 \times 26.82\,\text{mm}^2$ and the distance to the interaction point to the front face is 3.15 m.

A preshower detector is located in front of the ECAL endcaps, covering $1.653 < |\eta| < 2.6$. It is a a high-granularity photon-sensitive detector and consists of two planes of silicon strip sensors that are interleaved with a total of $3\,X_0$ of lead ($2\ X_0$ in front of and $1\ X_0$ behind the first silicon plane) [164]. The goal of the preshower detector is to distinguish the rare prompt γ production from the copiously produced π^0 decays to two closely spaced γ's. The angle between the two photons depends on the energy and the direction of the pion, with very small angles for pions directed at the endcaps. The granularity of the endcap crystals is not sufficient to distinguish single photons from two closely spaced photons from π^0-decay. The energy deposited in the radiators (Pb) slightly decreases the energy resolution, but is not significantly worse than without preshower detector.

Figure 3.20 shows the simulated electromagnetic showers of a prompt photon (Figure 3.20(a)) and a neutral pion (Figure 3.20(b)) incident on the preshower detector and the ECAL endcap detector. Although the showers in the endcap detectors are very similar, the signals in the preshower detector differ as shown in Figure 3.20(c) and allow to distinguish neutral pions from photons.

At the time of the design of the ECAL, a preshower detector was also foreseen for the barrel. In

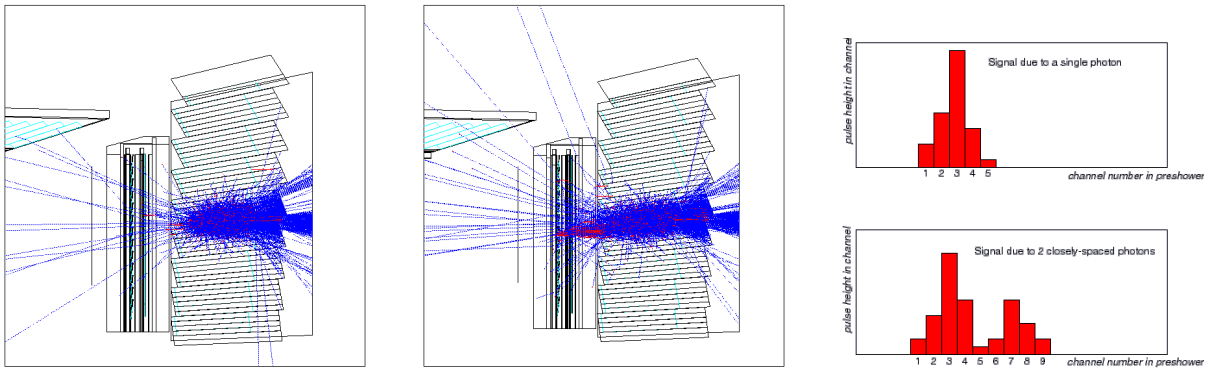

(a) (b) (c)

Figure 3.20: Simulated electromagnetic showers for a prompt photon (a) and a neutral pion (b) in the preshower and ECAL endcap detector. The preshower detector is able to distinguish the single photon (top) and double photon (bottom) signature (c). Figure taken from Reference [165].

the barrel the neutral pion energy is lower (for the same transverse momentum p_T) and hence the photons are separated more. Simulations have shown that the granularity of the EB is sufficient to separate prompt photons from neutral pions with sufficient efficiency. Recent simulations also showed that the determination of the photons' primary vertex can be done with high efficiency, even with high pile-up, such that an additional measurement with a barrel preshower detector became obsolete.

The ECAL energy resolution has been measured in test beams to be [131]:

$$\frac{\sigma(E)}{E} = \frac{2.8\%}{\sqrt{E[\,\mathrm{GeV}]}} \oplus \frac{12\%}{E[\,\mathrm{GeV}]} \oplus 0.3\% \tag{3.1}$$

for electron beams with momenta between 20 and 250 GeV/c. The energy was reconstructed by summing 3×3 crystals. This energy resolution is valid for energies below 500 GeV, where shower leakage from the rear of the calorimeter starts to become significant. The three contributions correspond to the stochastic, noise and constant terms, respectively. This result was obtained in the absence of a magnetic field, with almost no inert material in front of the calorimeter and with the beam pointing to the centres of the crystals. Figure 3.21 shows the resoluton as a function of incident energy. For 120 GeV/c electrons, an energy resolution better than 0.45% was obtained, while for a beam not restricted to the center of the crystals (not shown in Figure 3.21), a resolution of 0.5% was found [131, 166].

The ECAL is surrounded by a brass/scintillator sampling hadronic calorimeter (HCAL) with a coverage up to $|\eta| < 5.0$, shown in Figure 3.19. The HCAL is comprised of four subdetectors: a barrel detector (HB) covering $|\eta| < 1.3$; two endcap detectors (HE) covering $1.3 < |\eta| < 3.0$; and the HCAL Outer (HO) calorimeter, which is a scintillator "tail catcher" placed outside the coil covering $|\eta| < 1.3$; and the HCAL Forward (HF) covering $2.9 < |\eta| < 5$. The HCAL is subdivided into towers with a segmentation of $\Delta\eta \times \Delta\phi = 0.087 \times 0.087$ at central rapidity ($|\eta| < 1.74$) and 0.09×0.174 to 0.35×0.174 at forward rapidity ($1.74 < |\eta| < 3.0$).

Each HB and HE tower has 17 scintillator layers (except near the interface of HB and HE). The scintillation light is collected by wavelength-shifting fibres that are read out with hybrid photodiodes (HPDs). The HO calorimeter comprises layers of scintillators placed outside the solenoid

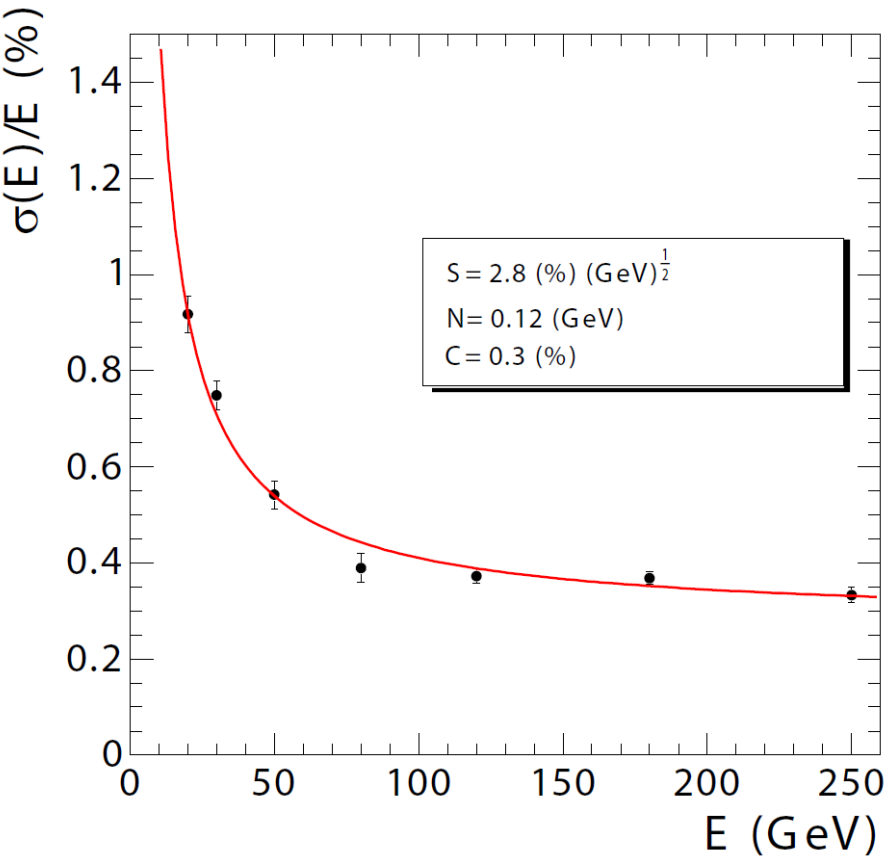

Figure 3.21: ECAL energy resolution, $\sigma(E)/E$, as a function of electron energy as measured from a beam test. The energy was measured in an array of 3×3 crystals with an electron impacting the central crystal. The points correspond to events taken restricting the incident beam to a narrow $4 \times 4\,\text{mm}^2$ region. The stochastic (S), noise (N), and constant (C) terms are given [131].

cryostat to catch the energy leaking out of the HB, extending the overall thickness to more than 10 interaction lengths (λ_I) everywhere. In the η - ϕ plane and for $|\eta| < 1.479$, the HCAL cells map onto 5×5 ECAL crystal arrays to form calorimeter towers (Calo towers) projecting radially outward from close to the nominal interaction point. At larger $|\eta|$, the size of the towers increases and the matching ECAL arrays contain fewer crystals. The HCAL, when combined with the ECAL, measures hadrons with an energy resoluton $\Delta E/E \approx 100\% \sqrt{E[\,\text{GeV}]} \oplus 5\%$ [167].

The Hadronic Forward (HF) calorimeters (shown in Figure 3.22) are installed behind the endcap disks, one on either side of CMS, and the front faces of each calorimeter are at a distance of 11.2 m from the interaction point. The calorimeters consist of iron absorbers and embedded radiation-hard quartz fibres, providing a fast collection of Cherenkov light. The collected light is detected using radiation hard photomultiplier tubes (PMT). The HF calorimeters are segmented longitudinally by the use of long fibres, which run over the full depth of the absorber (165 cm $\approx 10\,\lambda_I$) and short fibres, which start at a depth of 22 cm from the front of the detector. Each set of fibres is read out separately. The different length of the fibres makes it possible to distinguish electromagnetic showers from hadronic ones [168]. The HF tower segmentation in η and in azimuthal angle ϕ (expressed in radians) is 0.175×0.175, except for $|\eta|$ above 4.7 where the segmentation is 0.175×0.35 [169].

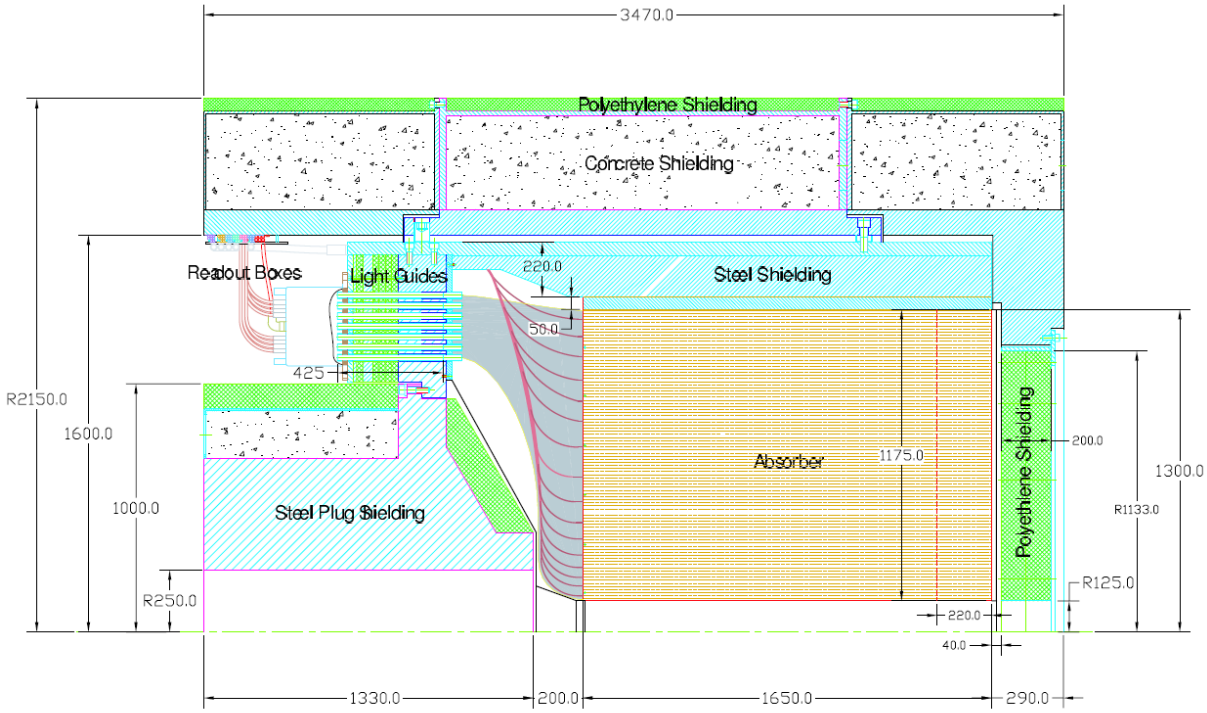

Figure 3.22: A cross section through the HF calorimeters. The sensitive volume is the absorber, extends from 125 mm to 1300 mm radially and has a length of 1650 mm. The fibers are bundled and routed to air-core light guides that penetrate through a steal-lead-polyethylene shielding matrix. The light is detected by PMTs housed in the Readout BoXes. The outer muon stations of the endcap are protected from the highly-radioactive HF by a polyethylene shield. The cavern is shielded from HF by steel (blue shaded) and concrete (gray) and polyethylene (green)[131].

3.5 The CMS Very Forward Region

The central detectors of the CMS experiment have an acceptance in pseudorapidity η, of roughly $|\eta| < 2.5$ for tracking information (muon, strip and pixel detectors) and $|\eta| < 5$ for calorimeter information. Figure 3.23 shows the expected pseudorapidity distribution of the charged particles and of the energy flow at the LHC [144]. This plot shows that with an acceptance limited to $|\eta| < 5$ most of the energy of the collision (carried by the proton fragments emitted with small angles with respect to the beamline) will not be absorbed in the central detectors of CMS, but that most of the tracks (due to a hard scatter) will be reconstructed. For instance, the tracker coverage of $|\eta| < 2.5$ was limited by the radiation damage expected from the high energies in the forward region [148]. Three detectors are installed in the very forward region of CMS ($|\eta| > 5$) of which two are part of CMS: CASTOR and ZDC, and one is an independent experiment aiming at measuring the total elastic pp-collision cross section: TOTEM [92]. The locations of TOTEM and CASTOR are shown in Figure 3.24. In the very forward region dedicated shielding is installed to reduce the radiation, which is detailed in section 5.3.1.

CASTOR is a quartz-tungsten sampling calorimeter, installed around the beam pipe, behind HF, at the $z < 0$ side of the IP, commonly known as the "minus side" and it covers the pseudorapidity range $-6.6 < \eta < -5.2$. The calorimeter is radiation hard, has a fast response and is compact, which makes him suitable for the very forward region at the LHC. CASTOR was installed in

CMS during the data taking of 2010 and 2011, but is removed for the high-luminosity running of LHC.

The two Zero-Degree-Calorimeters (ZDC), with pseudorapidity coverage of $|\eta| > 8.3$, aimed at the detection of neutral particles, are designed to complement the CMS very forward region for pp-diffractive studies. Two identical ZDCs are installed between the two LHC beam pipes at ≈ 140 m on each side of the CMS interaction region. The ZDCs are located inside the neutral particle absorber (Target Neutral Absorber, TAN) that shields the dipole magnets of the LHC against high-energetic neutral particles.

The TOTEM experiment consists of 2 tracking telescopes, T1 and T2, and Roman Pot (RP) stations. The T1 and T2 telescopes consist of Cathode Strip Chambers (CSCs) and Gas Electron Multiplier (GEM) chambers and will detect particles in the η regions $3.2 < |\eta| < 5$ (T1) and $5 < |\eta| < 6.6$ (T2). The TOTEM RP stations are placed at a distance of ± 147 m and ± 220 m from the interaction point. TOTEM T1 is installed after the 2011 data taking period, below the endcap muon system, while the T2 was already installed during the 2010 data taking period, and is in front of CASTOR, as shown in Figure 3.24.

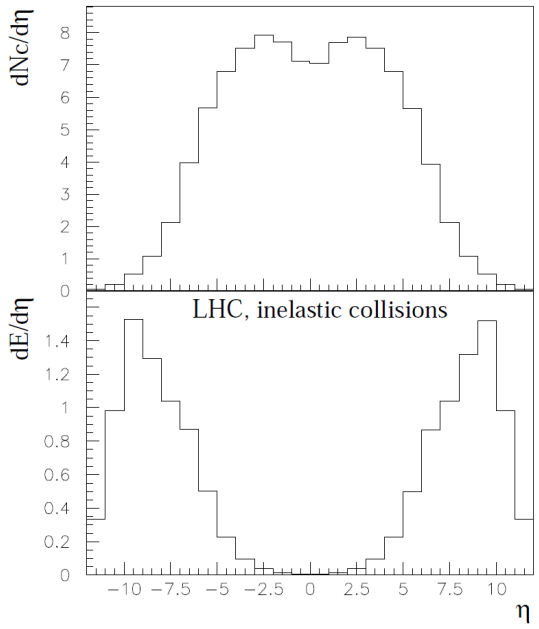

Figure 3.23: Pseudorapidity distribution of the charged particles and of the energy flow at the LHC, energy is expressed in units of TeV [144].

Track finding in T1 and T2 for triggering purposes is optimized to select beam-beam events with charged tracks that point back to the IP, while rejecting beam-halo tracks. These triggers are sent to the CMS Level-1 Global Trigger. The Roman Pot detectors are aimed to detect protons in diffractive interactions of $pp \rightarrow p + X$ and $pp \rightarrow p + X + p$. Interesting phenomena such as hard diffractive scattering can be studied in conjunction with the central CMS detector, where the system X can consist of jets, W and Z and γ bosons, $t\bar{t}$ or even the Higgs particle [144].

3.6 The CMS Beam Radiation Monitoring Systems

The proton beams colliding in CMS are very energetic (360 MJ at design luminosity) and can cause a lot of damage when lost in the detector. Especially during the startup of a new collider, when parameters are still being tuned by the accelerator physicists, it is very important to have adequate beam monitoring systems. Moreover, these systems can provide some technical triggers to investigate the detector performance when beams are passing through.

The Beam Radiation Monitoring (BRM) systems perform both a monitoring and a protection function for CMS [131]. The BRM systems, shown in Figure 3.24, are installed along the beam line and give online feedback about the beam structure and about radiation conditions

within the experimental cavern. The main components are the Beam Pick-up and Timing for eXperiments (BPTX), located at ±175 m from the interaction point, Beam Scintillation Counters (BSC) located at ±10.86 m (BSC1) and ±14.4 m (BSC2) from the interaction point and the Beam Condition Monitors (BCM) at ±1.8 m (BCM1) and ±14.4 m (BCM2) from the interaction point.

Both BCM detectors are the only protection systems foreseen for initial LHC operation. BCM1 is a diamond detector installed very close to the beam pipe at $z = \pm 1.8$ m. BCM2 consists also of diamond detectors on either side of the IP behind the TOTEM T2 telescope at z-values of ±14.4 m. Signals from the BCMs are used to protect the tracking detectors from potentially dangerous beam backgrounds. In severely pathological conditions, they are capable of triggering an abort of the LHC beams.

The two BSC1 detectors are located at a distance of 10.86 m from the nominal interaction point, on either side, covering the $|\eta|$ range from 3.23 to 4.65. Each BSC consists of a set of 16 scintillator tiles mounted on both front faces of the HF Calorimeters. They provide information on hits and coincidence signals with an average detection efficiency of 96.3% for minimum ionizing particles and a time resoluton of 3 ns, compared to a minimum inter-bunch spacing of 25 ns for data.

The two BSC2 detectors are located behind the TOTEM T2 Telescope at ±14.4 m from the IP and consists of two scintillator tiles surrounding the beampipe. The primary function of the BSC2 is to distinguish between ingoing and outgoing particles along the beamline, as there is a 8-ns time difference between them. The particles detected at this location can therefore be tagged as to whether they are incoming (beam halo only) or outgoing (collision products and beam halo).

The two BPTX devices are radio frequency pickups, designed to provide precise information on the structure and timing of the LHC beams, with a time resolution better than 0.2 ns. They are installed around the beam pipe at a distance of ±175 m from the IP. RADMON and Passives are systems that give calibrated information on the radiation field within the CMS cavern, which is of utmost importance to allow physicists access to the CMS experiment when no beams are circulating in LHC.

The BRM are sensitive to changes at the 25 ns level, although the deployed protection systems will react in times of the order $O(3-40)\,\mu$s. The BSC and BPTX sensitivity at the 25 ns level is exploited as technical trigger inputs into the global CMS trigger for the zero- and minimum-bias triggers. The BPTX can determine exactly which BX two bunches are crossing each other in the center of CMS, while the BSC identifies inelastic pp-collisions. The former is therefore used as zero-bias trigger, while the combination of the former and the latter determines a Minimum Bias interaction.

3.7 Overview of the event selection and data collection

The Trigger and Data Acquisition (DAQ) system of an experiment at a hadron collider plays an essential role because both the collision and the overall data rates are much higher than the rate at which data can be written to mass storage. At the LHC, the proton beams cross each other at a frequency of 40 MHz at the design luminosity of $\mathcal{L} = 10^{34}\,\mathrm{cm}^{-2}\mathrm{s}^{-1}$. Every

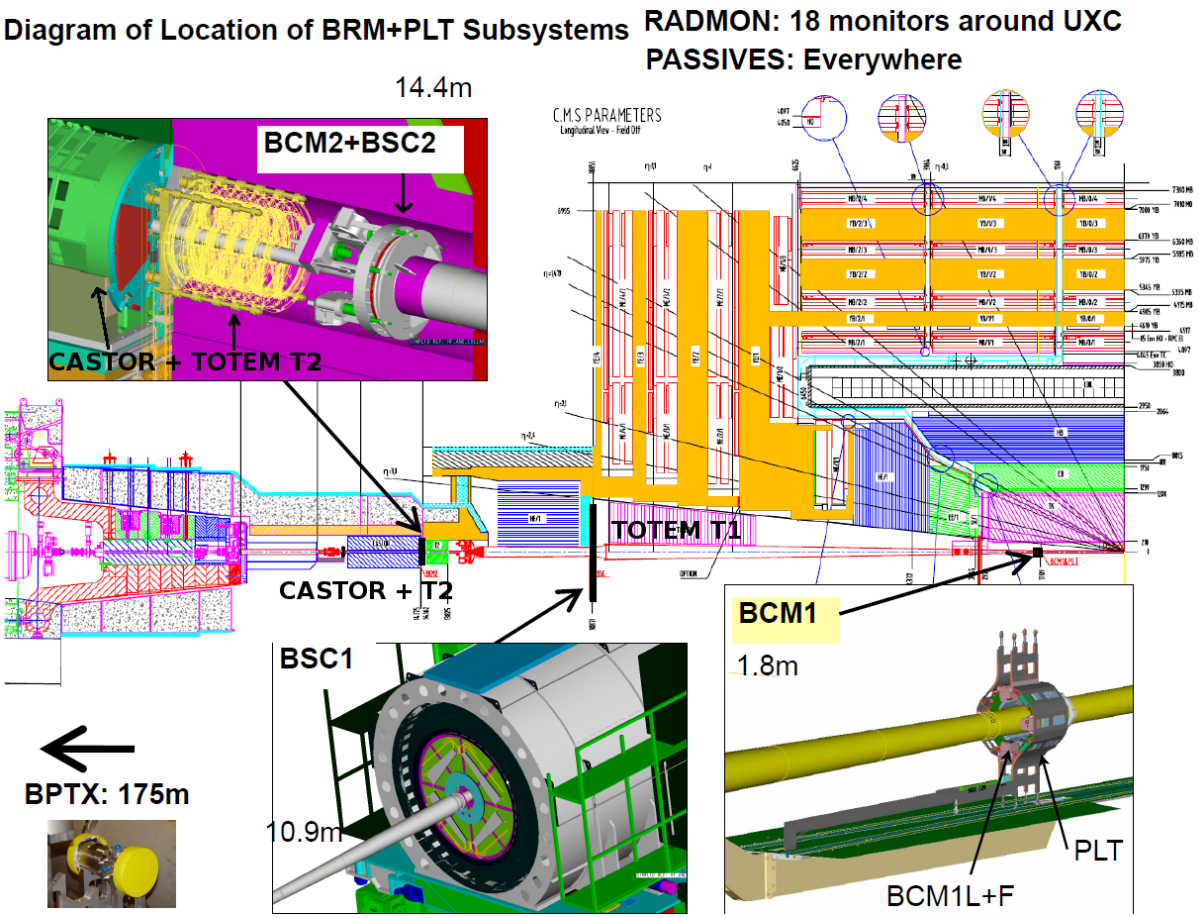

Figure 3.24: Layout of a quarter of the CMS detector and the very forward region. The different BRM sub-systems are shown, in addition to the TOTEM T1 and T2 telescopes and the CASTOR calorimeter [131].

bunch crossing will contain on average $\sim$ 25 inelastic pp-collisions, leading to 1 MB of zero-suppressed[3] data. This would result in a data rate of $\sim$ 40 TB/s, which is many orders of magnitude higher than the currently available storage capability. Therefore this data rate needs to be reduced to O(1 GB/s), which leads to a maximal event rate of O(300 Hz) that can be written to tape. This rate is three times higher than the originally designed O(100 Hz) [142] due to improvements in network technology and safety-margins considered in the design. The rate is more limited by the reconstruction speed at the central computing farm (Tier-0) than by the available storage capacity.

The trigger selects the events and this selection is based on the physics one wants to study, and the very basic and very well known physics processes that are used to monitor and calibrate the detector. Cross sections of phenomena studied at the LHC span many orders of magnitude, as is illustrated in Figure 3.25. Due to the high cross section of a.o. jet and $b\bar{b}$ production, the trigger system has to select efficiently a few interesting events among millions of background ones. The trigger is the start of the physics event selection process.

The CMS Trigger and DAQ are designed to inspect the detector information at full LHC cross-

[3]Literally: removal of redundant zeros. Here: readout of all channels above a certain programmable noise threshold.

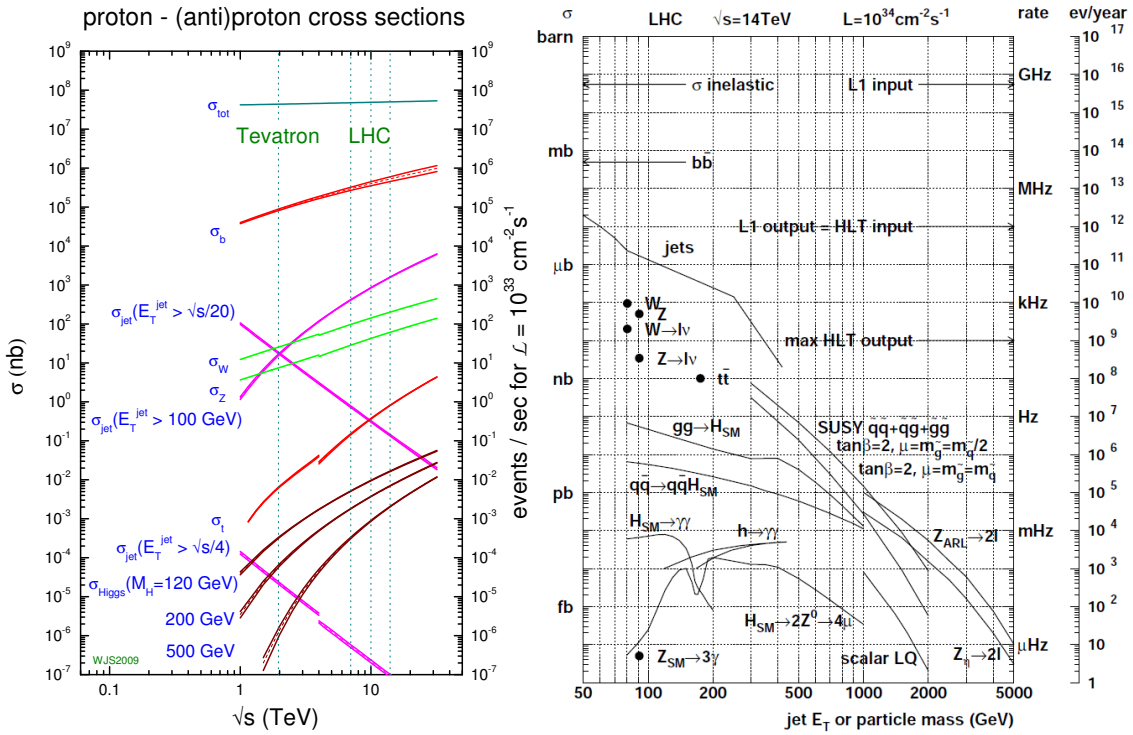

Figure 3.25: Cross sections for specific physics processes as a function of $\sqrt{s}$ [100] (left) and for $\sqrt{s} = 14$ TeV as a function the jet E_T or particle mass [141] (right). The dotted lines on the left plot show the design energies of the Tevatron at 1.96 TeV and the LHC at 7, 10 and 14 TeV. The cross sections are calculated for $p\bar{p}$-collisions, in the 1 - 4 TeV range, and calculated for pp-collisions, in the 4 - 30 TeV range. For processes where gluon fusion is the dominant process, the transition is smooth, while for processes proceeding through $q\bar{q}$-annihilation, such as vector-boson production, the curves show a discrepancy.

ing frequency and to select events at a maximum rate of $O(300\,\text{Hz})$ for storage and physics analysis later on. The required rejection power of $O(10^5)$ is too high to be achieved in a single processing step and is therefore split into two steps. The first step (Level-1 Trigger or L1) is designed to reduce the rate of events to less than 100 kHz, while the second step (High-Level Trigger or HLT) is designed to reduce this rate to a final output rate of 300 Hz [142].

The L1 system is based on custom electronics, while the HLT system relies upon commercial processors. Due to the strict timing requirements of accepting a new event every 25 ns and producing an accept-or-decline signal at most 3.2 μs later, the L1 system is limited to use only coarsely segmented data from calorimeter and muon detectors, while holding all the high-resolution data in pipelined memories in the front-end electronics. The HLT has access to the complete readout data and can therefore perform complex calculations similar to those made in physics analysis if required for particularly interesting events. A software system, the Trigger Supervisor (TS), controls the configuration and operation of the trigger components.

The design of the CMS Trigger and Data Acquisition system is illustrated in Figure 3.26. Every 25 ns the **front-end electronics** of each subdetector process and shape the electrical signals they receive and store it in pipelined memories. Upon a **L1 Accept (L1A) signal**, the detector frontend electronics are read out in parallel by multiple units (**Readout Systems**) that format and store the data in deep buffers. These buffers are connected to the processors in the HLT farm

by the large switching network (**Builder Network**). Two systems complement this flow of data from the front ends to the processor farm: the **Event Manager**, responsible for the actual data flow through the DAQ and the **Control and Monitor System**, responsible for the configuration, control and monitoring of all the elements. The HLT algorithms are then executed on the **Filter Systems** once the processors were provided with a "full" event by the readout. **The Computing Services** include a host of monitoring services, storage and the interface of the DAQ to the "offline" environment, where physicists perform data analyses.

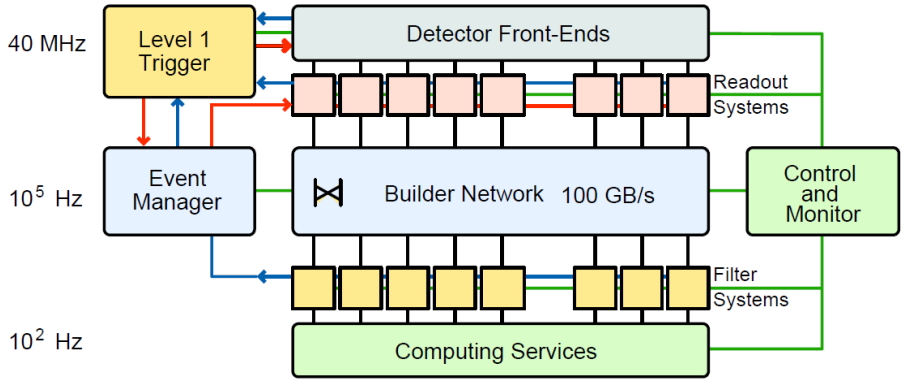

Figure 3.26: Layout of the CMS Trigger and Data Acquisition System. Data is arriving both at the Level-1 Trigger and the Detector Front-Ends at a rate of 40 MHz and needs to be reduced to $\mathcal{O}(100\,\text{Hz})$ that can be written to tape [131].

3.8 The CMS Level 1 Trigger

The CMS L1 Trigger system design and implementation is detailed in Reference [141], while Reference [170] describes the performance of the L1 trigger during commissioning with cosmic ray muons and beams. The L1 Trigger is designed to process information from the CMS detector at a bunch-crossing rate of 40 MHz. The frontend electronics, located on the detectors, read out the electrical signals and store them in 128 BX (3.2 μs) pipelined memories. Within these 3.2 μs, a decision has to be made by the L1 trigger whether to send this event to the High Level Trigger or not. The decision taking occurs in 25 ns steps, and every 25 ns the event is passed to the next step, such that every 25 ns a new event can enter the buffer and every 25 ns a decision (keep or reject) for an event that occured 3.2 μs earlier is taken.

Figure 3.27 illustrates the latency of the Level-1 trigger. The pipelined memories, located on the front end electronics of the detectors inside CMS can store 128 BX in their buffers. During these 3.2 μs, coarsely segmented data from the calorimeters and muon detectors is sent to the L1 Trigger and an accept/reject signal is sent back. An accept is followed by a readout of that specific event by the Readout Systems of the DAQ. Most of these 3.2 μs are spent on signal transmission from and to the control room and synchronization delays (for information coming from the "far side"[4] of the detector. The actual processing of the Level-1 Trigger algorithms on the coarse event data proceeds in about a 1 μs.

[4]The part of the detector nearest to the counting room (UCS55) is called the "near side", while the opposite part is called the "far side". The x-axis of the CMS reference frame points toward the centre of the LHC, therefore the "near side" is the side at positive x, the "far side" is the side at negative x.

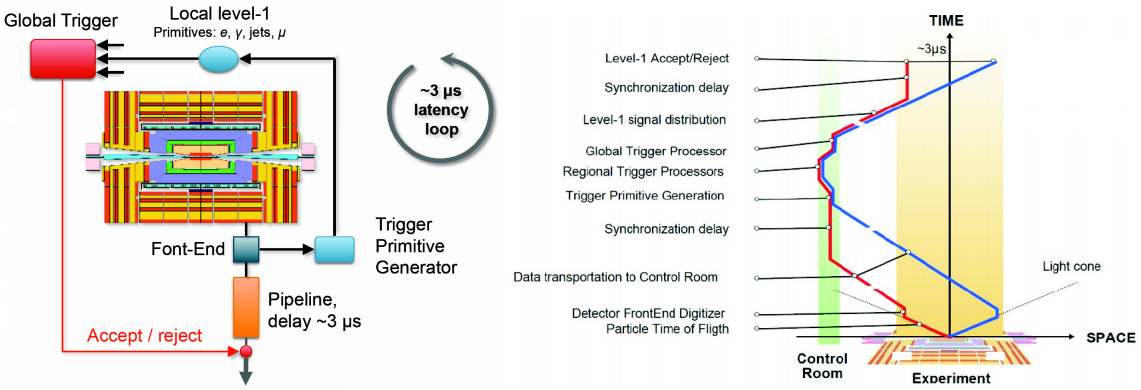

(a) (b)

Figure 3.27: Illustrations of the Trigger Latency of the Level 1 Trigger [131].

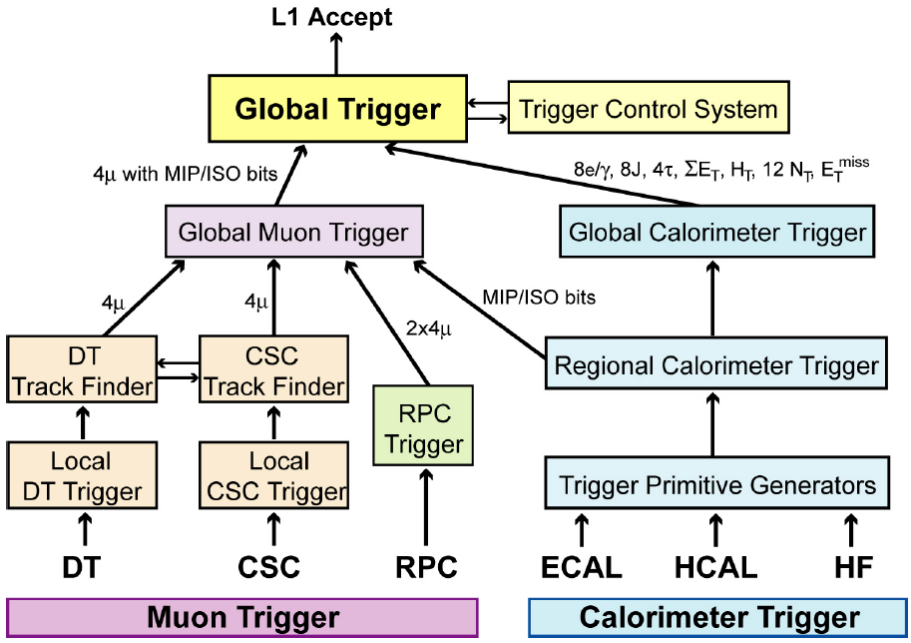

Figure 3.28: Architecture of the Level 1 Trigger [131].

The L1 Trigger has local, regional and global components. A schematic view of the CMS L1 Trigger system is presented in Figure 3.28. Track segments or hit patterns in the muon chambers and local energy deposits in calorimeter trigger towers are processed into Trigger Primitive Generators. Regional Triggers combine these primitives and use pattern recognition logic to create regional triggers, which are sorted according to their rank. The rank is a function of energy or transverse momentum and quality and reflects the level of confidence attributed to the L1 parameter measurements. The global Calorimeter and Global Muon Triggers determine the highest rank objects and pass them on to the Global Trigger. The latter takes the decision to reject or accept an event for further evaluation by the HLT.

3.8.1 The Level 1 Muon Trigger

The primary function of the CMS muon system is to identify muon tracks. The triggering scheme relies on two independent and complementary triggering technologies: one based on

the precise tracking detectors in the barrel and endcaps, and the other based on the RPCs. The tracking detectors provide good space and time resolution, while the RPC system provides excellent timing with somewhat lower spatial resolution. For values of p_T up to 200 GeV/c, the spatial resolution (and hence the p_T resolution) is dominated by the large multiple scattering caused by the steel combined, in the endcaps, with the effects of the complicated magnetic field caused by the bending of the field lines returning through the barrel yoke. At higher energies, the radiative processes start to dominate the p_T resolution. This environment allowed the design of robust, multilayered chambers in which the good spatial resolution needed for accurate momentum determination is obtained with a modest resolution per layer [153].

Three different muon detectors are used within CMS, each with their own trigger system. Both DT and CSC detectors have a chamber-based local trigger, that creates track segments using hit patterns as input, as detailed in section 3.2.5. Segments are only accepted if they point back to the interaction point. Up to two (three) trigger primitives per DT (CSC) chamber and per bunch crossing are produced by the on-chamber electronics and sent to the Drift Tube Track Finder (DTTF) or Cathode Strip Chamber Track Finder (CSCTF). DDTF and CSCTF receive trigger primitives from both systems in the barrel - endcap transition region. The Track Finders perform a track matching and assign a quality code, η, ϕ, charge and transverse momentum values to the track. Both DTTF and CSCTF deliver up to four muon candidates to the Global Muon Trigger. In the CSC system, track segments parallel to the beamline were used to identify tracks from "halo muons", which has proven to be very useful for alignment of the tracker and muon detectors.

The RPCs have excellent timing resolution, of the order of 1 ns, and their main purpose is to identify the bunch-crossing in which the detected muon was emitted. The RPC trigger is based on the spatial and temporal coincidence of hits in several layers. The Pattern Comparator trigger logic (PAC) compares signals from all four stations to predefined hit patterns in order to find muon candidates. Muon p_T, η, ϕ and quality code are assigned according to the matched pattern and the number of coincident hits. Analog signals of the chambers are digitized by the Front End Boards (FEBs), assigned to the proper bunch crossing and sent to the Trigger Boards in the underground counting room. Finally, eight muon candidates (four in the barrel, four in the endcaps) are sent to the Global Muon Trigger.

The Global Muon Trigger (GMT) receives up to four candidates from DTTF and CSCTF and up to eight candidates from the RPC Trigger. The GMT combines the candidates identified by more than one sub-detector and assigns a quality code. The four highest quality muon candidates are forwarded to the Global Trigger (GT).

3.8.2 The Level 1 Calorimeter Trigger

The CMS Calorimeter System consists of the Electromagnetic Calorimeter and the Hadron Calorimeter. The electron/photon and jet candidates are identified by their energy deposition patterns in the calorimeter trigger towers, i.e. a rough η,ϕ- segmentation used at trigger level. The candidate transverse energy (E_T) is obtained by summing the energy deposits in those towers. A trigger primitive is generated for each tower in ECAL and HCAL up to $|\eta| = 3.0$. The towers have the same η,ϕ-segmentation in ECAL and HCAL. Trigger primitives from the

forward region $3.0 < |\eta| < 5.0$ are used for jet and energy sum ($\sum E_T$) triggers[5] only.

The Trigger Primitive Generators (TPG) make up the first or local step of the Calorimeter Trigger. The ECAL TPG starts by summing the energy of each crystal in a strip of five in the ϕ-direction (at constant η) and converting the result to E_T, taking into account the electronic gains and calibration coefficients. The E_T-values from five adjacent strips in η are then summed and the E_T-estimate for the trigger tower is transferred to the Regional Calorimeter Trigger. A fine-grain veto is set for each trigger tower if the two adjacent strips with the highest energy contain less than 90% of the total E_T. This gives some indication of the lateral shower shape and can be used to reject L1 e/γ candidates that result from jets. The HCAL TPG starts by linearising the received signal, using Look-Up-Tables (LUTs) that are programmed to account for individual channel gains and pedestals. The energies from separate longitudinal readout channels are summed and sent to the Regional Calorimeter Trigger.

The Regional Calorimeter Trigger (RCT) receives ECAL and HCAL trigger primitives in 18 electronics crates, each covering half of the detector in z and 40° in ϕ. e/γ candidates are identified up to $|\eta| \sim 2.5$ and are classified as isolated or non-isolated according to the ECAL trigger primitive fine-grain information and the ratio of HCAL to ECAL E_T. Information relevant for muons about isolation and compatibility with minimally ionizing particles is also calculated and transferred to the Global Muon Trigger. Each RCT crate transmits up to 4 isolated and four non-isolated e/γ candidates to the Global Calorimeter Trigger (GCT), where they are sorted based on E_T. The highest four isolated and highest four non-isolated candidates are then sent to the Global Trigger (GT). Apart from e/γ candidates, the GT also determines jets, total transverse energy, missing transverse energy, jet counts and H_T (the scalar transverse energy sum of all jets above a programmable threshold).

3.8.3 The Level 1 Global Trigger

The main task of the Global Trigger is to reject or to accept events for readout and further processing by the High-Level Trigger. It first receives and synchronizes the muon and calorimeter input data and sends it to the Global Trigger Logic (GTL) board that is programmed to provide a menu of up to 128 algorithms, which transform logical combinations of L1 trigger objects (muons, e/γ, jets, $H_T, \not{E}_T$) with selection criteria (energy/momentum thresholds) into decision bits. These bits can be enabled to contribute to a final decision which determines whether the data are read out. Additionally, random triggers (using a random number generator) and 64 technical triggers are added to the final decision. The Timing Trigger and Control (TTC) system controls the delivery of the Level-1 Accept (L1A) signals to the front end electronics of the detectors.

Besides combining and propagating triggers from subdetectors, the GT (or GTP[6]) provides a throttling mechanism to assure that all triggered events can be completely recorded by the DAQ system. Part of this Trigger Throttle System (TTS) is the application of programmable Trigger Rules, which prevent accumulation of triggers in short time intervals. The rules are: no more than 1 trigger in 3 BXs, 2 in 25, 3 in 100, and 4 in 240 [170]. Moreover front-end buffers of subdetectors can signal to the GT that they are filling up, which results in GT interrupting

[5] In energy sum triggers the E_T of the jets is summed and they provide a measure of the energy (or mass) scale of the event.

[6] Global Trigger Processor

trigger activity until the buffers are emptied and the flag is removed. Counters in the GT record the overall trigger rate and the individual rate of each trigger algorithm and technical trigger, as well as the dead time counters that record the amount of time during which triggers were inhibited [170].

3.9 The CMS Data Acquisition System

The CMS Data Selection system is divided into two parts: L1 and HLT. While the first is implemented with custom electronics, the latter is fully software based and runs on a commercial processor farm. In order to decide whether to keep the event or not, the HLT requires access to the full event data, which is enabled by the DAQ. The DAQ is responsible for the readout of the detector and the collection of all data fragments, recorded during a bunch crossing, into one single event, and to make it available to the HLT. The HLT runs sophisticated reconstrution algorithms to decide whether to keep the event or not. In the functional breakdown of the DAQ system, one can identify four stages:

- A detector readout stage, storing the event data in $\sim$ 700 buffers;
- An event building stage, in which all the data corresponding to a single event are collected from the different buffers;
- A selection stage, in which the event is processed by the High-Level Trigger in a processor farm;
- An analysis/storage stage in which the events selected by the HLT are forwarded to the computing services for further processing and storage.

The first three points: readout, event building and event selection, are the subject of the next three sections, while the discussion of the computing services is moved to a separate section 3.10. The architecture of the CMS DAQ was already shown schematically in Figure 3.26 and is given in more detail in Figure 3.29.

3.9.1 The Readout System

The Global Trigger Processor (GTP), sends the synchronous L1A signal, via the Timing Trigger and Control (TTC) system, to the Front-End Drivers (FEDs). The FEDs extract the data from the frontend buffers located on the detector. The data from the $\sim$ 700 FEDs are then read into the $\sim$ 512 Front-end Read-out Links (FRLs), that are able to merge data from two FEDs and generate so-called "event fragments" with an average size of $\approx 2\,\text{kB}$. The FED and FRL electronics are located in the underground counting room (USC) and they send those 512 fragments, belonging to the same event, to the FED Builders in the surface control room (SCX) by optical Data Links.

3.9.2 The Event Builder

The task of the Event Builder is to assemble all 512 separate "event fragments" sent by the optical links to the surface control room and make the assembled event available to the HLT algorithms that are running on the computing farm. CMS opted for a geometry that is modular and scales easily. Therefore a design based on eight 64×64 switches was favoured with respect to a single massive 512×512 switch. The eight 64×64 switches, the so-called Readout Builders (or "slices"), are connected to sixty-four 8×8 switches, the so-called FED Builders. The two

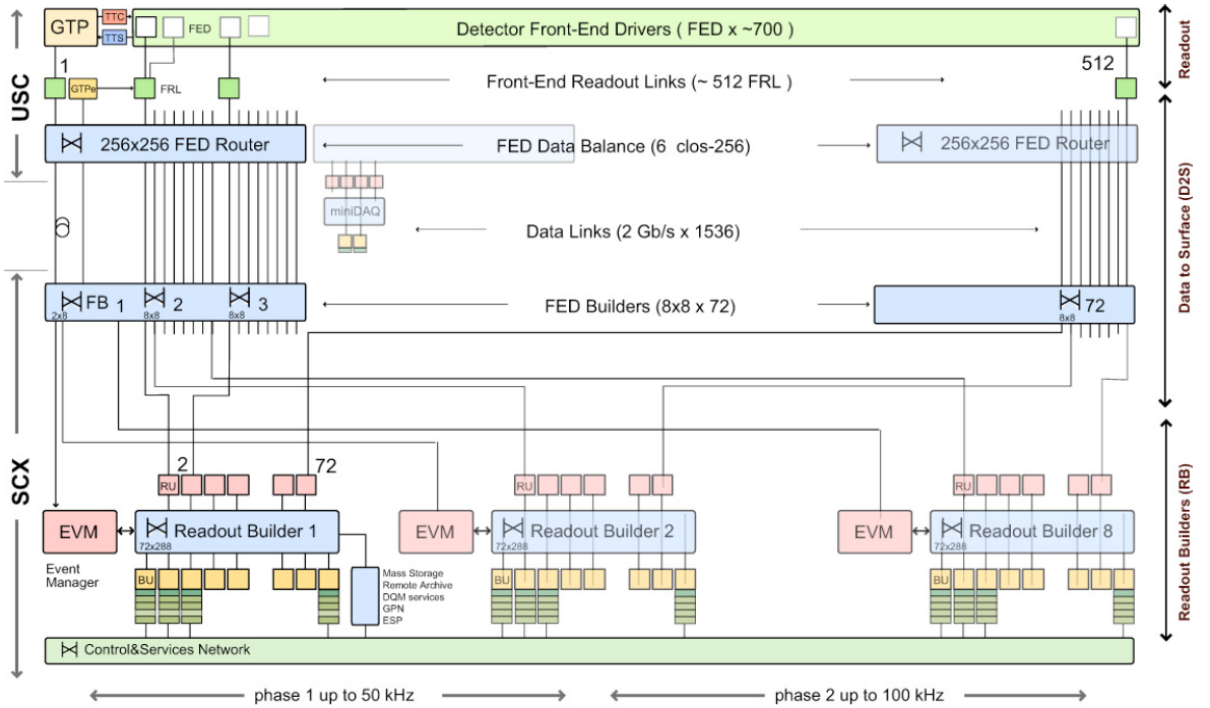

Figure 3.29: Design of the CMS DAQ, showing the multiplicity of all parts. Up to eight Readout Builders will be installed when LHC is working at design luminosity. The route the data takes, starting from the Front-End Drivers (FEDs) in the underground service cavern (USC) over the 2GB/s Data Links to the Readout Builders (RBs) in the service control room (SCX) is shown. Figure taken from [131, 142].

Event Builder options are shown in Figure 3.30, with on the right hand side the 3D switch design chosen by CMS.

The Event Builder (shown in full glory in Figure 3.29 and shown in detail for one slice in Figure 3.31) assembles the event fragments belonging to the same L1A from all FEDs into a complete event and transmits it to one Filter Unit (FU) in the Event Filter for further processing. The Event Builder is implemented in two stages, the FED-builder (a 8×8 switch) and the RU-builder (a 64×64 switch). The FED-builders are located in the surface control building (SCX) and receive the event fragments from the FRL electronics located in the underground counting room (USC). The event fragments are assembled into 72 super-fragments and then stored in large buffers in Read-out Units (RUs), waiting for the second stage of the event building in the Readout Builders. There are 8 Readout Builders, or DAQ-slices, each of which is a nearly autonomous system, capable of handling a 12.5 kHz event rate.

Each FED-builder is in charge of assembling fragments into super-fragments and distributing them, on an event-by-event basis, to the RU-builders and ensures that all super-fragments belong to one and only one DAQ slice, and are read out by one Builder Unit (BU) of the RU-builder network. A schematic overview of the dataflow through the Readout System and the Event Builder is shown in Figure 3.32. The dataflow within a DAQ-slice is supervised by the Event Manager (EVM). The complete event is then assembled by the Builder Unit (BU) and passed to a single unit of the Event Filter, the Filter-Units, where the HLT algorithms are executed to select the events to be kept for offline processing.

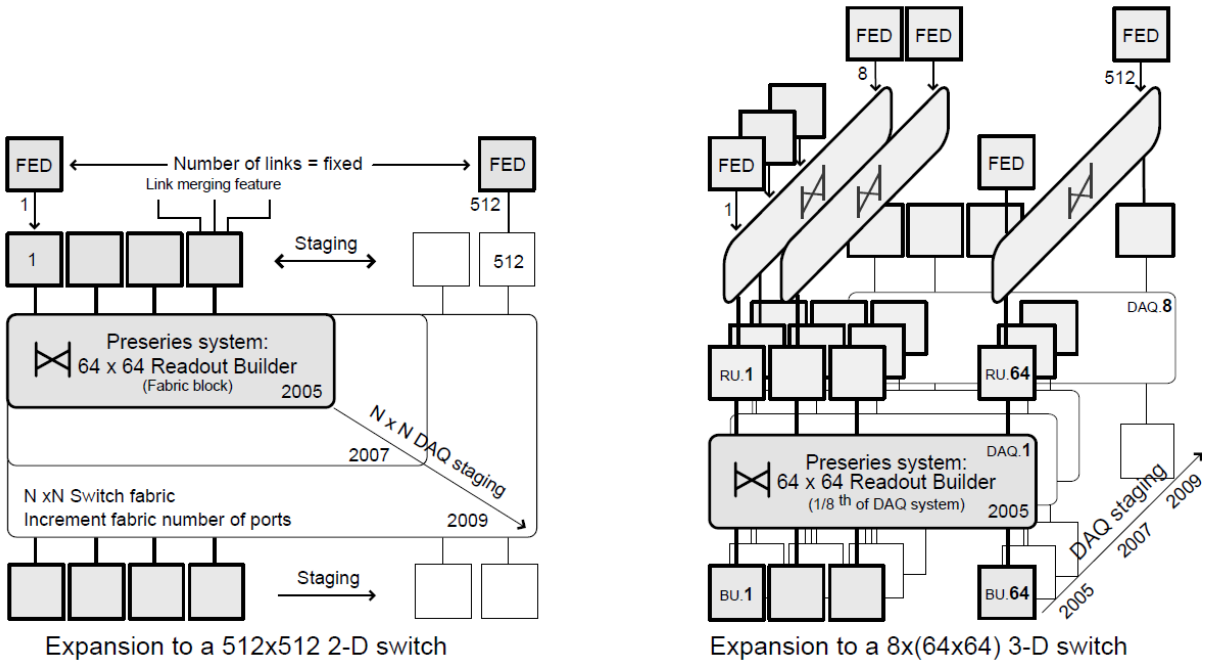

Figure 3.30: The two DAQ Event Builder designs: a massive 512 × 512 switch (left) versus eight 64 × 64 switches (right). Figure taken from Reference [142].

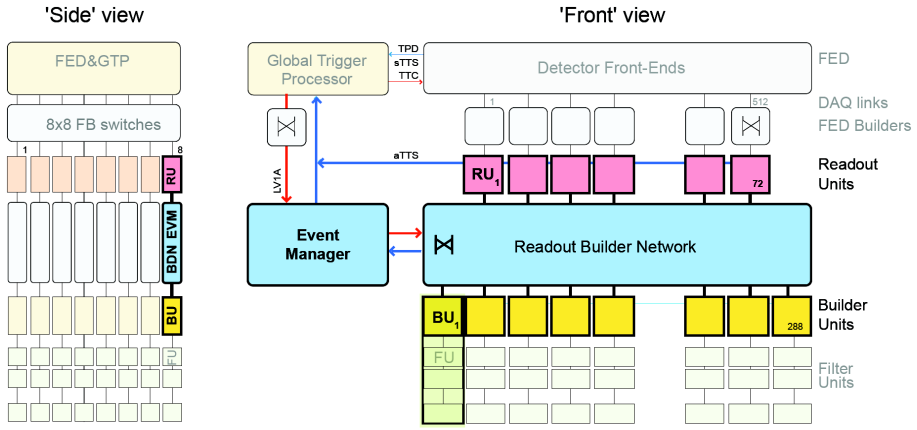

Figure 3.31: Detailed view of a Event Builder or DAQ-slice. On the right hand side, the front view of the 3D Event Builder is shown (simplified version provided in Figure 3.26). On the left hand side, a schematic view of the entire Event Builder is shown from the side, showing the eight slices. The eight Readout Builders are connected to the FEDs via small 8 × 8 switches, called the FED Builder switches. Figure taken from Reference [131].

3.9.3 The Filter System and High-Level Trigger

The Event Filter consists of hundreds of Filter Units, implemented as a farm of commercial processors where the HLT algorithms are executed. The HLT algorithms read the Level-1 trigger information, unpack the data in the region of interest and perform a regional reconstruction of the trigger objects. If the reconstructed object (or a combination of reconstructed objects) passes some programmed thresholds on quality and transverse momentum, the event is kept and the Filter-Unit is prepared to accept a new event. Typically, the HLT algorithms have to process the event in 50 to 100 ms, depending on the L1 input rate and the amount of DAQ slices

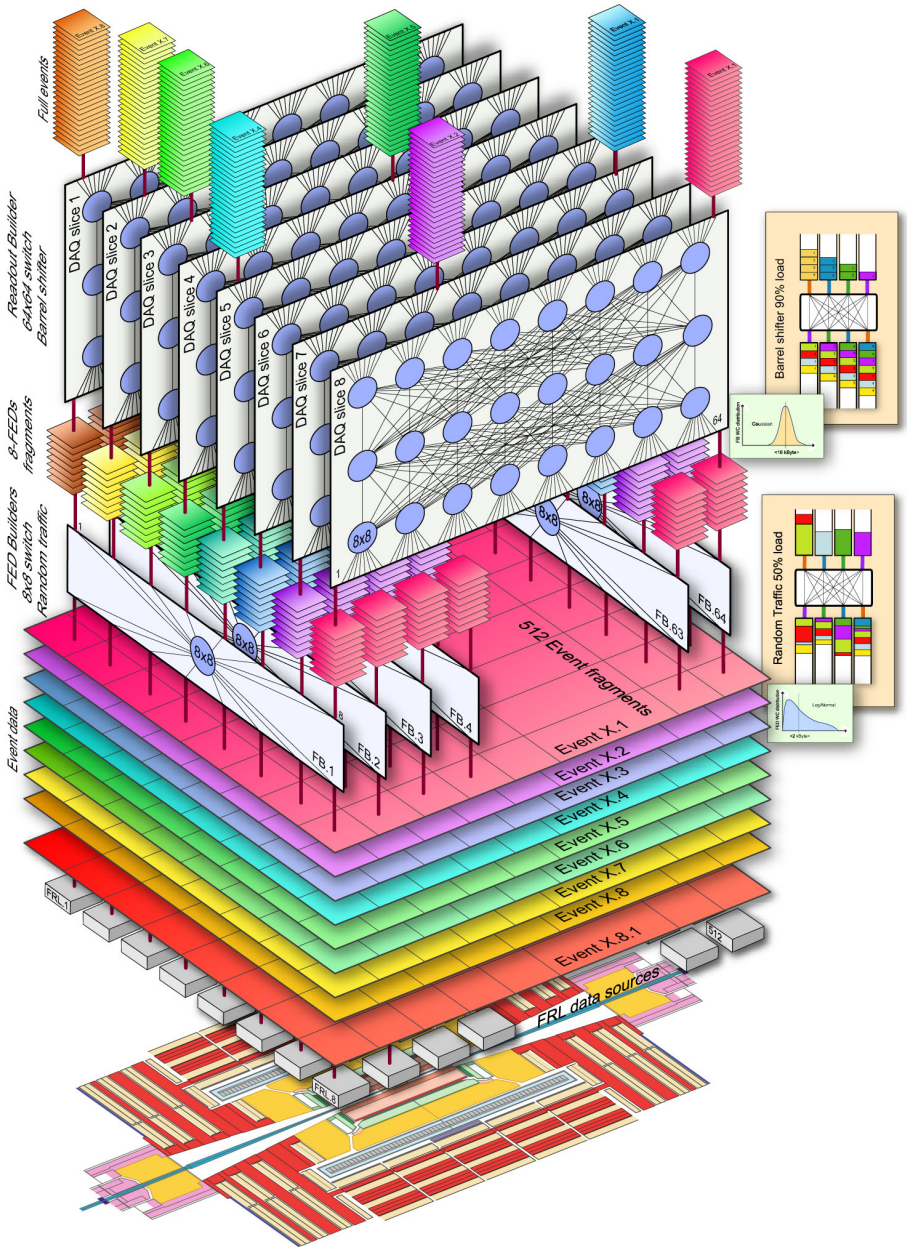

Figure 3.32: Example of the assembly of an entire event, starting at the bottom with the different event fragments collected by the FEB Builder switch into super-fragments. The Readout Builder then assembles all super fragments into one single event accepted by the Builder Unit (not shown) [171].

that are in use. Data Quality Monitoring (DQM) information is generated during online event processing in the HLT. This is the so-called "DQM Online" that is processed on a subset of the total data. During the reconstruction, the full DQM algorithms are run on the data, resulting in the so-called "DQM Offline". Both DQM Online and Offline are used to verify the quality of the data and the integrity of the detector and DAQ during (DQM Online) and after (DQM Offline) datataking.

3.9.4 The HLT during 2010 data taking

The algorithms executed on the HLT computing farm are close to the final offline reconstruction of the data, discussed in chapter 4 and this will not be discussed here. Trigger algorithms were implemented for single objects such as electrons and photons, muons, jets, $E_{\mathrm{T}}^{\mathrm{miss}}$, and taus, but also for composite objects such as di-electron, di-muon, di-photon, electron + tau, ... A p_{T} threshold was set for each of these objects, which increased during data taking because of the increased instantaneous luminosity.

The HLT trigger configuration consists of a so-called "trigger menu". This menu is a list of different algorithms, a so-called "trigger paths", together with a list of prescales. The trigger algorithms used for physics analysis are unprescaled, since one wants to collect, reconstruct, and investigate every single event. Other algorithms are used as cross checks, to measure the backgrounds for a give physics analysis, to measure the efficiency and the performance of triggers, to debug the detector, ... These trigger paths have, on average, rather low (p_{T}) thresholds, which would result in huge trigger rates. Therefore, these algorithms are prescaled to reduce the amount of events: for instance only every 10^{th} event or only every 100^{th} event would be kept, the other events would be rejected. A short list of trigger algorithms from the last (2E32) trigger menu, for some important unprescaled physics objects is shown in Table 3.1, together with the L1 trigger path that served as a seed. Events passing this L1 trigger are then given to the corresponding HLT triggers. Those events are stored for offline reconstruction if they also pass one of these HLT trigger paths.

Table 3.1: Some HLT trigger paths for some frequently used physics objects from the 2E32 trigger menu, shown together with their L1 trigger seed. The p_{T} or E thresholds are mentionned in the trigger names, for jets only uncorrected energies are used [172].

	HLT Path	L1 Seed
Electron	HLT_Ele22_SW_TighterEleId_L1R_v3	L1_SingleEG8
	HLT_DoubleEle17_SW_L1R_v1	L1_DoubleEG5
	HLT_IsoEle12_PFTau15_v3	L1_SingleEG8
Jet	HLT_Jet180U_v3	L1_SingleJet60U
	HLT_DiJetAve140U_v3	L1_SingleJet60U
Muon	HLT_Mu15_v1	L1_SingleMu7
	HLT_DoubleMu3_v2	L1_DoubleMuOpen
	HLT_Mu5_Ele13_v2	L1_SingleMuOpen AND L1_SimpleEG8
	HLT_Mu8_Ele8_v1	L1_SingleMu3
Multijet	HLT_150U_v3	L1_HTT50
	HLT_QuadJet25U_v3	L1_QuadJet8U
Photon	HLT_Photon70_Cleaned_L1R_v1	L1_SingleEG8
	HLT_DoublePhoton22_L1R_v1	L1_DoubleEG5

During the 2010 data taking period, approximately 12 different trigger menus had been implemented, each one adapted to the instantaneous luminosity delivered by the LHC at that time. These menus covered an increase of five orders of magnitude in instantaneous luminosity: $\mathcal{L} = 2 \cdot 10^{27}\,\mathrm{cm}^{-2}\mathrm{s}^{-1}$ (1E27) to $\mathcal{L} = 2 \cdot 10^{32}\,\mathrm{cm}^{-2}\mathrm{s}^{-1}$ (2E32). A menu was developed for roughly each twofold increase in instantaneous luminosity: 1E29, 2E29, 4E29, 8E29, 1.6E32, ..., 6E31, 2E32. At any given time in 2010, when a certain trigger menu was developed, the menu for the double of the instantaneous luminosity was already ready and tested, while several

other menus were under development for data taking the next months. Due to the very smooth operationof the LHC machine, CMS had learnt not to rely on the machine schedules and was always ready for a twofold or threefold increase of the instantaneous luminosity.

The low luminosity menus (1E29, 2E29, 4E29, ...) consisted of rather simple algorithms, using only threshold cuts on the reconstructed objects at the HLT. The high luminosity menus (2E31, 6E31, 2E32) consisted of more elaborate paths, requiring the reconstructed objects to be isolated and identified. At the end of the 2010 run, the trigger menu consisted of more than 150 different trigger paths. During the 2010 running, also a large fraction of the trigger bandwidth, $\sim$ 30%, was spend on calibration and alignment triggers, Minimum and Zero Bias triggers to ensure the complete understanding of the CMS detector and the L1 and HLT triggers.

3.10 The CMS Computing System and the Grid

The CMS offline computing system is arranged in four tiers and is geographically distributed around the world, according to the distribution of the members of the CMS Collaboration. The tiered computing system consists of a Tier-0 at CERN that accepts data from the Storage Manager of the DAQ and writes the raw data on tape. The Tier-0 is located at the CERN Computing center and performs a first reconstruction of the raw data. Thereafter, it distributes both raw and processed data to a set of Tier-1 centres located in CMS collaborating countries. These centers provide services for data archiving, reconstruction, calibration, skimming and other data-intensive analysis tasks. More abundant are the Tier-2 centres, which are smaller and provide CPU capacity for physics analysis by end-users and are responsible for the Monte-Carlo simulation productions. Furthermore, there is a smaller number of Tier-3 centres that provide resources to end-users. Additionally, there is a CMS Analysis Facility (CAF) at CERN that provides fast computing services to the experiment. More details on the tiered structure of the CMS Computing System is provided in Reference [143].

The CMS design performance can only be reached with very well aligned and calibrated subdetectors. The exact location of all tracker modules and muon chambers must be known up to very high precision (sub-mm) to achieve the design momentum resolution for charged hadrons, electrons and muons. Calibration defines the ultimate performance of the CMS crystal calorimeter. The potential discovery of the intermediate mass Higgs boson in the channel H$\rightarrow \gamma\gamma$ depends upon an excellent energy resolution of the ECAL. Calibration of all calorimeter channels and Aligment of all tracker modules and muon gas chambers is based on *in situ* measurements with physics events. An Alignment and Calibration system, based on several data streams, was designed in order to handle calibration and alignment data in an efficient way. A dedicated calibration stream serves all calibration algorithms and is built on a specific event selection. The bandwidth of this stream is kept low by restricting the event content to for example only data from one subdetector.

In figure 3.33 the overall CMS processing workflow relevant for alignment and calibration is illustrated. Data originate from the HLT and are split in different streams by the Storage Manager. Then the data are sent to the Tier-0. The "Physics stream" is split in multiple "Primary Datasets" and is the main stream for physics analysis. About 10% of these events are redirected to the "Express stream", which is reconstructed within a few hours for fast feed-back. Events for detector calibration, collected by dedicated calibration triggers and with a reduced event

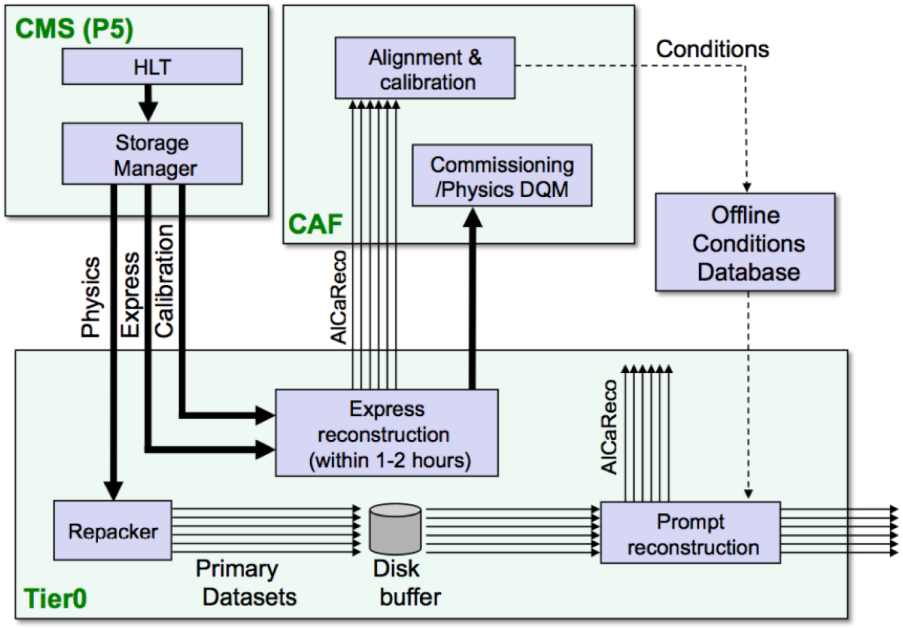

Figure 3.33: Offline work flow for calibration and alignment.

content to save bandwidth, are sent by the Calibration Stream to the Express reconstruction. The events from the Express and Calibration streams are processed within hours and are sent to the Alignment and Calibration algorithms packed in a dedicated "AlcaREco" dataset. The alignment and calibration constants obtained by those algorithms are stored in the "Offline Conditions Database", and are used by the prompt reconstruction of all data in the physics stream at Tier-0.

The Grid connects computers that are scattered all over the world to share computing power and storage capacity, using the analogy to the electric grid where end-users receive electricity without having to care where it comes from. The Worldwide LHC Computing Grid (WLGC) provides a global computing resource to store and analyse the huge amounts of data ($\sim$ 15 PB/year) collected by the LHC experiments. Data from the LHC experiments are distributed around the globe to the Tier-1, Tier-2 and Tier-3 centres, while a primary back-up is recorded at the Tier-0 at CERN. The Grid depends on the underlying architecture of the internet: computers and communication networks, but is novel in the way that it provides software that enables the users to acces the computers distributed over the network. More than 8000 scientists worldwide can access the Grid, identify where the data is they want to analyze, and run their analysis on this data remotely using the Grid software [173].

3.11 A brief history of the commissioning of CMS

The large solenoid of CMS was fully tested for the first time, from August to November 2006, while it was still in the surface assembly hall. The exercise, called the Magnet Test and Cosmic Challenge (MTCC), provided important commissioning and operational experience for both the different subdetectors, and CMS as a whole. About 7% of the muon detection systems, 22% of HCAL, 5% of ECAL, a pilot silicon strip tracker ($\sim$ 1% of the full tracker) and the global trigger and DAQ were successfully operated together [174].

The lowering of the heavy elements of CMS into the experimental cavern began in November 2006, starting with the forward calorimeters. Shortly after came the $+z$ endcap disks and barrel wheels, with muon detectors and services installed. In February 2007, the central yoke wheel (YB0) that houses the cryostat was lowered. The last heavy elements of the $-z$ endcap were successfully lowered into the cavern by January 2008. The weight of the fifteen loads was between 250 tons (forward calorimeters) and 1920 tons for YB0. Lowering these heavy elements 100 m at an average speed of 10 m/h took about 10 hours. The campaign to connect services for the detectors within the central portion of CMS included the installation of more than 200 km of cables and optical fibres and more than 20 km of cooling pipes and lasted more than 6 months [174].

In the underground cavern, the detectors were connected to the necessary services: low voltage, high voltage, (water)cooling, gas, and the necessary readout and control cables were installed. Monthly or bimonthly, global commissioning exercises, including all commissioned detectors were performed. A series of four week-long exercises, each known as Cosmic RUn at ZEro Tesla (CRUZET) were conducted to accumulate sizeable samples of cosmic muon events, which were used to study the overall detector performance. In the fourth CRUZET exercise in August 2008, the complete silicon pixel tracker was introduced, along with the ECAL endcaps. The preshower detector for the electromagnetic calorimeter was the only major subsystem not installed prior to the 2008 LHC run. These global runs did not only test the readiness of the subdetectors but also exercised the full data flow from the DAQ system at the experimental site to the reconstruction facility (Tier-0) at the CERN IT centre, followed by the subsequent transfer of the reconstructed data to all seven of the CMS Tier-1 centres [174].

The CMS experiment was operational and recorded triggers associated with activity from the first LHC beams in September 2008. This activity included single shots of the beam on to a collimater 150 m upstream of CMS, which yielded sprays (so called "beam splashes") containing $O(10^5)$ muons crossing the cavern synchronously and beam-halo particles associated with the first captured orbits of the beam on September 10 and 11. On 19 September 2008, a fault occured in an electrical bus connection between two LHC magnets, causing major mechanical damage. The repair took more than 12 months. The LHC resumed operations in November 2009 with 450 GeV beams (the injection energy of SPS), culminating in the first collisions at $\sqrt{s} = 7$ TeV, March 30$^{\text{th}}$ 2010, shortly after 12 p.m. This event was covered by media worldwide and was the kick-off of the 2010 data taking campaign for pp-collisions that lasted until 30$^{\text{th}}$ of October.

The integration and commissioning of the different subdetectors of CMS, starting with the Magnet Test and Cosmic Challenge in 2006 up to (but not including) the first collisions at injection energy in November 2009 is described in detail in Reference [174] and a brief summary was given above.

Chapter 4

Event Reconstruction

The CMS event reconstruction is a complex software framework, programmed by many physicists during many years. Their expertise range from event generation, detector simulation to reconstruction algorithms. This software framework is subject to continuous improvement and evolves with the understanding of the detector during collisions. The CMS event reconstruction uses information from all subdetectors to obtain a global description of an event. An event in CMS typically contains leptons (electrons, muons, taus) and jets being the signature of quarks and gluons. Neutrinos cannot be detected directly but missing transverse energy reveals the passage of weakly interacting particles through the detector. Electrons and muons are reconstructed by combining hits in the tracker and the energy deposited in ECAL, or by hits in the muon stations. Since the physics analysis discussed in this work depends only on photons, jets and missing energy, the reconstruction of leptons will only be covered briefly. Photons are objects that can be reconstructed with high precision and are therefore widely used in detector calibration and estimation with high accuracy of Standard Model processes involving massive vector bosons.

For jets and missing transverse energy, different algorithms are developed in CMS depending on the way the information from different subdetectors are combined:

- Fully calorimeter based: Calo jets and Calo$\not\!\!E_{\mathrm{T}}$;
- Calorimeter based but corrected with information from the tracker: Jet-Plus-Track (JPT) jets and Track Corrected (TC)$\not\!\!E_{\mathrm{T}}$;
- By following each particle produced in a collision: Particle-Flow.

The first two reconstruction techniques are rather well established and widespread amongst collider experiments. Particle-flow was pioneered by ALEPH [175] and was only used on a limited scale in hadron collider experiments at the Tevatron, for tau reconstruction by matching calorimeter clusters to tracks [176, 177]. Particle-flow combines information from all subdetectors of CMS and is the only reconstruction algorithm providing a consistent description of the event. For instance, in the calorimetric approach, there is an overlap between the photon and the jet collection, since photons are jets with a very high electromagnetic fraction. Furthermore, heavy-flavour jets, where the b- or c-quark decays to a muon and a neutrino have a bad energy resolution in the calorimetric approach, since there the jet is only built from the calorimetric energy. In the particle-flow algorithm, the non-isolated muon is summed in the jet energy, leading to an improved energy resolution. For these (and many more) reasons, particle-flow is widely adopted in CMS by various analyses. After a brief introduction to particle-flow in the first section, the particle-flow event reconstruction will be discussed in detail in the second section. The

third section discusses the removal of anomalous signals in the calorimeters while the fourth and fifth section deal with the jet reconstruction and the missing transverse energy, which are the key components in the jets + missing transverse momentum search for new physics. In the sixth section the photon reconstruction is detailed and the seventh section, finally, contains a short introduction to lepton reconstruction.

4.1 Introduction to Particle-Flow

The particle-flow event reconstruction [178] aims at reconstructing and identifying all stable particles in an event. An optimal determination of energy and direction for electrons, muons, taus, photons, charged hadrons and neutral hadrons is obtained by combining the information provided by the different CMS subdetectors in a particular way. The output of the particle flow is a particle list, just as being produced by a Monte-Carlo event generator. The improved reconstruction obtained by particle-flow can be understood by looking both at the **composition of the objects** one wants to reconstruct as well as the p_{T} **distribution of the particles**.

Consider, for example, jets with $p_{\mathrm{T}} > 25\,\mathrm{GeV}/c$, investigated with the first $6.2\,\mathrm{nb}^{-1}$ of data, recorded with Minimum Bias triggers [179] . The jet constituents were classified into seven types: electrons, photons, muons, charged and neutral hadrons and electromagnetic and hadronic energy deposits in HF. The jet energy fraction was calculated as the fraction of the jet energy carried by a certain class of particles. Figure 4.1 shows the mean jet energy fraction for the various particle types for data and for Monte-Carlo simulation. In the region covered by the tracker, 65 % of the jet energy fraction was carried by hadrons, 25 % by photons and 10 % by neutral hadrons.

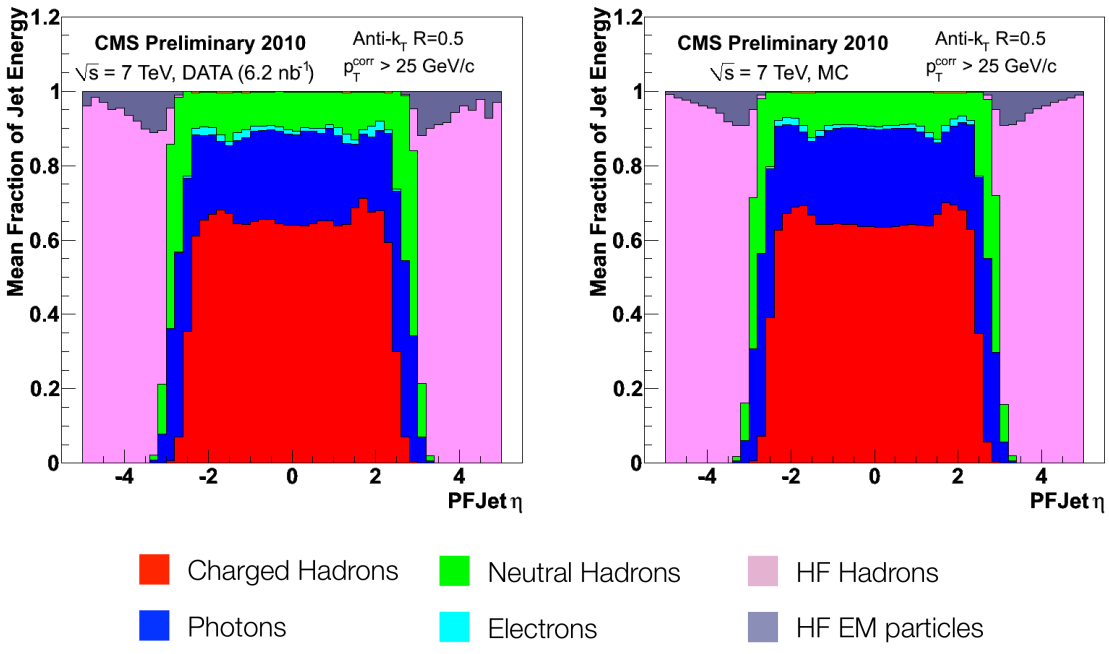

Figure 4.1: Reconstructed jet energy fractions as a function of pseudorapidity in $6.2\,\mathrm{nb}^{-1}$ of data (left) and in Monte-Carlo simulation (right) [179].

In pp-collisions, most stable particles produced have rather low p_{T}. For instance, for a 500 GeV/c jet, the average p_{T} of the constituents of the jet is $O(10\,\mathrm{GeV}/c)$, while for a 100 GeV/c jet, the p_{T} of the particles is roughly a few GeV/c [179]. Additionally, two-thirds of the particles produced in pp-collisions are charged hadrons, where the reconstruction is improved by the use of the superior angular and energy resolution of the tracker, which outperforms the hadronic calorimeters for particles with transverse momenta up to $O(300\,\mathrm{GeV}/c)$.

The particle-flow algorithm was developed in first place for the reconstruction of hadronically decaying taus and for an improved jet and $\not\!\!E_{\mathrm{T}}$ reconstruction, where the information from the tracker is not ignored (Calo-objects) or used as a correction (JPT-jets, TC-$\not\!\!E_{\mathrm{T}}$) but as a fundamental part of the reconstruction. Therefore the emphasis was put on the reconstruction of rather low energy photons, charged and neutral hadrons, which are the main constituents of jets and hadronic tau decays. The key detectors in the particle-flow algorithm are the Tracker, that reconstructs tracks with momenta as low as 150 MeV/c and ECAL which has an excellent energy resolution, also for low energy photons. The high granularity of the ECAL allows to separate photons from charged particle energy deposits within jets. This enhances the detection of low energy photons inside jets. The hadron calorimeter collects energy deposits of charged and neutral hadrons. The granularity of the hadron calorimeter is 25 times coarser than that of the ECAL, which does not allow to separate charged and neutral hadron energy depositions inside jets with transverse momenta of $O(100\,\mathrm{GeV}/c)$. However the combined ECAL + HCAL energy resolution of $O(10\,\%)$ for jets with 100 GeV/c transverse momenta allows for this separation: neutral hadrons can be recognized as energy excess on top of the energy deposit of charged hadrons.

Later on, when it became clear that CMS wanted to go for an overall adoption of particle-flow in its analyses, the need for incorporation of high-energy photons, electrons and muons became obvious. While for the latter two the standard reconstruction algorithms could easily be adopted, this was less obvious for the high-energy photon objects. For the analysis of the 2010 data, the particle-flow photon reconstruction was not commissioned and could not be used, hence the standard photon reconstruction was used in this thesis and will be discussed in this chapter. For future data-taking, the particle-flow algorithm should be working properly and the use of particle-flow photons is encouraged [180, 181].

4.2 Particle-Flow Event Reconstruction

Particle-flow event reconstruction is based on very efficient **tracking** and on smart **clustering** of calorimetric energy deposits, exploiting the high granularity of the ECAL. Thereafter, the tracks and clusters are connected by a **link algorithm**. These links are then sent to the **particle-flow algorithm**, analyzing the links and producing a list of reconstructed particles. Each of the steps will be described in more detail below, with the aid of an example jet, shown in Figure 4.2. The particle-flow event reconstruction is described in detail in Reference [178]. A summary of the particle-flow machinery and key components is given below, more elaborate overviews can be found in References [182, 183].

To illustrate the basic principles of the particle-flow event reconstruction, an example is taken from Reference [178]. Figure 4.2 shows the simulated and reconstructed tracks and the calorimeter deposits of a 65 GeV/c hadronic jet that consists of four particles: π^+, π^-, π^0 and a K^0_{L},

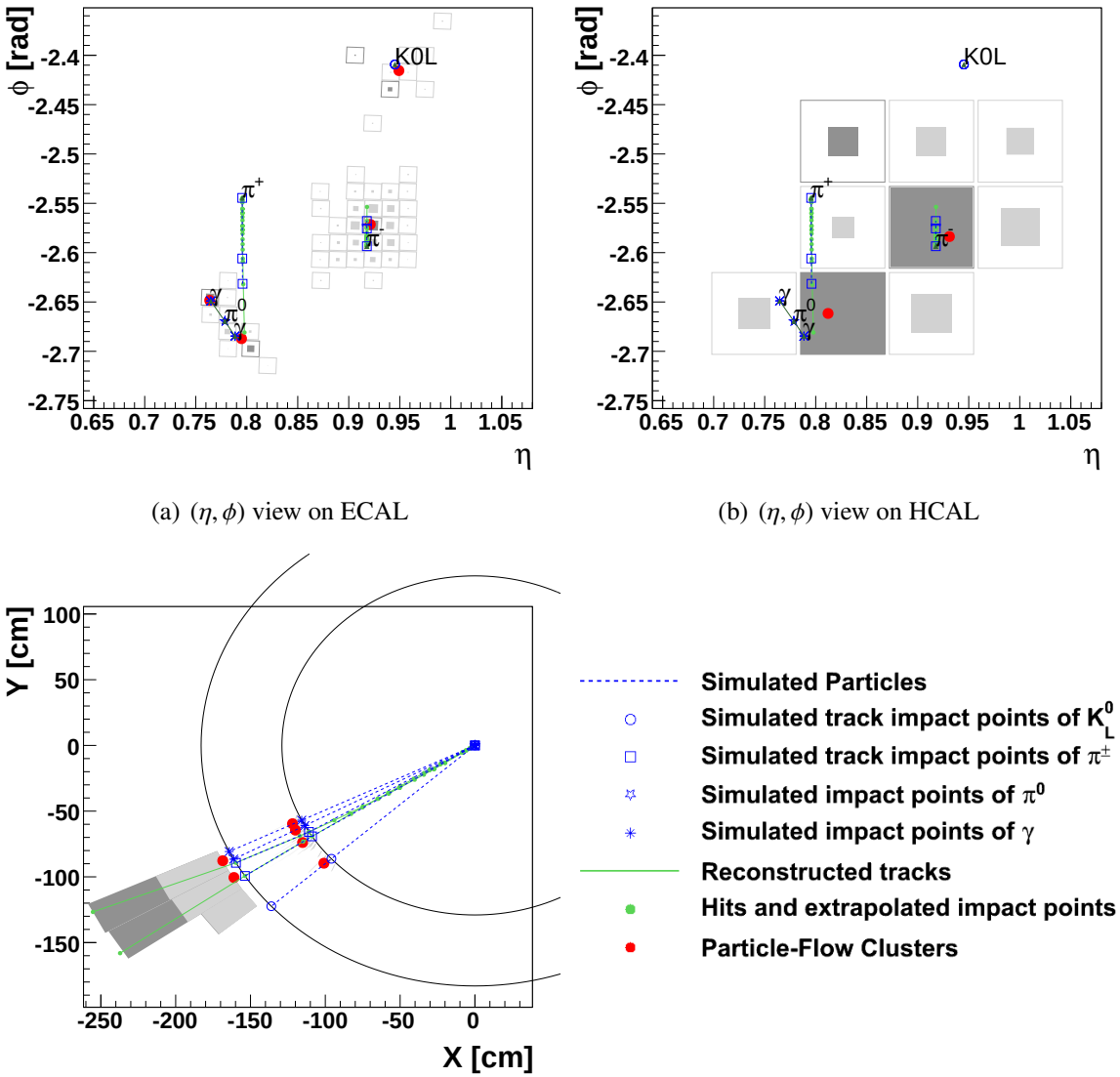

(a) (η, ϕ) view on ECAL

(b) (η, ϕ) view on HCAL

(c) (x, y) view

(d) legend

Figure 4.2: An event display of a hadronic jet in the (η, ϕ) view on the ECAL surface (a), on the HCAL surface (b) and in the (x, y) view (c). The simulated lines are shown as a blue dashed line, while reconstructed tracks are shown in green solid lines [178].

with the neutral pion decaying to two photons. Three views are provided: an η, ϕ-view on the ECAL and HCAL calorimeters and one transverse view in the x, y-plane, where the ECAL and HCAL surfaces are represented as the two concentric circles around the interaction point (IP).

In Figure 4.2, the blue dashed lines represent the simulated particle tracks. The blue markers represent the IP and the impact points of the simulated particles on the ECAL and HCAL surfaces: squared markers denote charged hadrons, circles denote neutral hadrons and asterisks denote photons. The star marker shows the IP for the neutral pion, which can be considered as decayed at the vertex, since its mean decay length $c\tau = 25.1\,\text{nm}$. Information about the reconstructed objects will be given in the separate sections of the particle-flow reconstruction described below.

4.2.1 Iterative Tracking

The performance of the particle-flow algorithm depends dramatically on the reconstruction of the charged hadrons with a much better energy resolution than the hadronic calorimeter. The track reconstruction must therefore be extremely efficient and with very high purity. Additionally, the tracker provides a precise measurement of the direction of the charged particles at the production vertex, allowing reconstruction of pile-up events. Very pure and efficient tracking was obtained by the "Iterative Tracking" algorithm [184]. The first step consists of track seeding and reconstruction with high quality, resulting in a moderate tracking efficiency but negligible fake rate. The hits unambiguously assigned to these tracks are removed, before a new track iteration is started. Progressively loosening the track seeding criteria, increases the tracking efficiency in the subsequent iterations, while the fake rate remains low due to the reduced combinatorics. The fourth and fifth iteration are dedicated to reconstruction of secondary particles from photon conversions, nuclear interactions in the tracker or the decay of long-lived particles such as K^0's or Λ's. This iterative technique allows tracking efficiencies higher than 90 % for charged particles in jets and reconstructs charged particles with as little as three hits, a p_{T} as small as 150 MeV/c and a vertex more than 50 cm away from the beam axis, with a fake rate of the order of one percent.

In Figure 4.2 the reconstructed hits in the tracker are represented by green dots and fitted to those hits are the green tracks, belonging to the π^+ and π^- particles. Since those particles have an opposite charge, they are bent in a different direction. In the η, ϕ-view of the ECAL, the π^+ track runs down, while the π^- track goes up. Furthermore, the π^+ is less energetic then the π^-, since the latter has a straighter track in the x, y-view, while the former shows a longer path length in the η, ϕ-view. The extrapolated hits on the ECAL and HCAL surface are also shown in Figure 4.2(c). The two photons and the neutral hadron K_L^0 did not leave a trace in the tracker.

4.2.2 Calorimeter Clustering

Particles entering the calorimeters will deposit energy in different cells. If one wants to reconstruct the energy of an incident particle, one has to sum (cluster) the energy of all hit cells together. The clustering algorithm developed for particle-flow aims at high detection efficiency even for low energy particles and a good separation of close energy deposits. The clustering is performed separately in each subdetector: Preshower (PS), ECAL barrel (EB) and endcap (EE) and the three hadronic subdetectors: HCAL barrel (HB), endcap (HE) and forward (HF). Each cell can belong to more than one cluster. The cluster position in η and ϕ is calculated by weighing the contributing calorimeter cells. A new iteration of the cluster algorithm is performed starting from the previous cluster position until the list of contributing cells remains unchanged. Calorimeter cells can still contribute to more than one cluster after the last iteration. Clustering at subdetector-level is a main difference between particle-flow and the standard Calorimetric clustering, preserving the much finer ECAL granularity.

The K_{L}^0, the photons and the π^- of the example shown in Figure 4.2 are detected as four well separated ECAL clusters, while the π^+ left no energy in the ECAL. The separation of these clusters (shown in the η, ϕ-view of the ECAL in Figure 4.2(a)) is possible thanks to the high granularity of the ECAL. The HCAL clusters are shown in Figure 4.2(b) and are not well separated and overlap because of the much coarser segmentation and the HCAL. The clustering algorithm allows for energy-sharing of HCAL cell, according to the cell-cluster distance. The

position of the ECAL and HCAL particle-flow clusters is denoted with a red dot.

4.2.3 Link Algorithm

Several particle-flow elements such as tracks, ECAL and HCAL clusters are then connected to a "block" by the link algorithm. The quality of the link is expressed as the distance in (η, ϕ) between the two linked elements. A charged particle track is linked to a given cluster if the extrapolated position is within the cluster boundaries. These boundaries can be enlarged to account for cracks in the detector, uncertainty in the position of the shower maximum and multiple scattering. A link between two calorimeter clusters is established when the cluster of the more granular calorimeter (PS or ECAL) is within the cluster envelope of the coarser calorimeter (ECAL or HCAL).

In Figure 4.2, the charged tracks of the $\pi^{\pm}$ are linked to their ECAL and HCAL clusters. Links are only made between clusters and tracks of different subdetectors. The interpretation of two close-by ECAL clusters to belong to the $\pi^0 \rightarrow \gamma\gamma$ decay is left for the physicist analyzing data, since their separation in two single photons does not improve the particle-flow reconstruction.

4.2.4 Particle-Flow Algorithm

The reconstruction and identification of particles is performed by the "particle-flow algorithm". This algorithm analyzes the particle-flow blocks produced in the linking step and distills a final list of particles. Muons and electrons are reconstructed first, after which their corresponding tracks and clusters are removed from further processing. Muons are reconstructed starting from global muons (see section 4.7.2) and are allowed to pick up possible energy loss in the calorimeters. Electrons have low mass and thus suffer large Bremsstrahlung losses. Tangents to reconstructed tracks are extrapolated to ECAL, starting from the intersection points of the track and each of the tracker layers, to collect the energy of Bremsstrahlung photons. Charged hadrons suffer less from radiation losses in the tracker and tighter quality criteria are applied to the remaining tracks. The difference between the measured p_{T} in the tracker and in the calorimeters is required to be smaller than the calorimetric energy resolution, allowing the best energy measurement (this time given by the calorimeter) for badly reconstructed tracks. In rare cases where the total calibrated calorimetric energy is smaller than the total track momentum by more than three standard deviations, a relaxed search for muons and fake tracks is performed. If the calibrated energy of the closest ECAL and HCAL clusters is much bigger than the charged track p_{T} and the relative energy excess is higher than the calorimeter energy resolution, particle-flow photons and particle-flow neutral hadrons are reconstructed. Remaining non-linked ECAL and HCAL clusters are reconstructed as particle-flow photons and particle-flow neutral hadrons.

4.3 Calorimeter Noise Cleaning

The CMS ECAL and HCAL occasionally record anomalous signals that correspond to particles hitting the transducers. Anomalous signals in HCAL can also be produced by rare random discharges of the readout detectors. Some of these effects had already been observed during past test beam and cosmic data taking [185]. Detailed studies of these effects have continued with the 7 TeV data taking, and are documented in detail in [186] for the HCAL, and in [187, 188] for the ECAL. For some types of anomalous energy deposits, the number of affected channels

is small and the event can still be used in the physics analysis after removal of the anomaly. We refer to the removal process as "cleaning" the event. If a large number of channels are affected, "filters" instead tag the event as not suitable for use in physics analysis.

Anomalous energy deposits in EB are associated with particles striking the sensors where very occasionally secondaries are produced that cause large anomalous signals through direct ionization of the silicon of the Avalanche Photo Diodes (APDs). Three main types of noise have been identified in HF: scintillation light produced in the light guides that carry the light from the quartz fibers to the photomultipliers; Cherenkov radiation in the photomultiplier tube (PMT) windows; and punch-through particles hitting the PMTs. In HB and HE electronics noise from the Hybrid Photo Diode (HPD) and Readout BoX (RBX) occurs at low rate and at random times, so the overlap with pp interactions is very low at the bunch spacings of the 2010 run.

The existence of this high-energy calorimeter noise can cause the particle-flow algorithm to reconstruct fake neutral particles, ultimately leading to significant fake missing transverse energy. The effect of noise cleaning was therefore evaluated with a sample of $7.5\,\mathrm{nb}^{-1}$ minimum bias events recorded at 7 TeV [179]. Substantial progress had already been achieved in cleaning such noise effects with $0.00375\,\mathrm{nb}^{-1}$ of data recorded in 2009 at lower center of mass energies ($\sqrt{s} = 900\,\mathrm{GeV}$) [189] by rejecting from further processing:

- high-energy deposits in single ECAL crystals surrounded by little or no energy in the four neighbouring crystals;
- high-energy deposits in HF short fibers, not backed up by some energy in the long fibers of the same HF tower;
- high-energy deposits in HF long fibers surrounded by little or no energy in the short fibers of the same HF tower and in the short and long fibers of the four neighbouring HF towers;
- high-energy deposits in large groups of HCAL towers from a single HPD or RBX.

Because of the increased statistics and larger occupancy, many spurious high-energy deposits were found not to be cleaned in 7 TeV collisions by the procedures developed in 2009 and new strategies were pioneered by particle-flow [179, 189] and adopted by the standard event reconstruction later on. The basic strategy for the identification and removal of anomalous signals (cleaning) is based on information such as unphysical charge sharing between neighbouring channels in η-ϕ and/or depth, and timing and pulse shape information. The shapes of the pulses for signals that develop from energy deposits in the calorimeters are different than those from anomalous noise signals. Once a "hit" in an HCAL tower or ECAL crystal is determined to be unphysical, it is excluded from the reconstruction of particles in particle flow and hence excluded from higher-level objects such as jets or$\vec{\not{E}}_{\mathrm{T}}$. We thus arrive at a reconstruction of jets and $\vec{\not{E}}_{\mathrm{T}}$ that is consistently "cleaned" of anomalous detector effects. Various studies indicate that the amount of energy removed from real particles produced in pp-collisions is negligible [167].

The effect of the particle-flow cleaning procedure is shown in Figures 4.3 and 4.4, where the missing transverse energy distribution is displayed at different cleaning stages. Starting from the top curve in Figure 4.3, the inclusive raw distribution exhibits a peak at around 280 GeV. This peak corresponds to the energy deposit in a single 5×5 crystal area in the ECAL that detected the laser calibration signal of the previous (empty) bunch crossing. This short data taking period was declared a "bad run" by the data-certification team. By using only runs certified for data

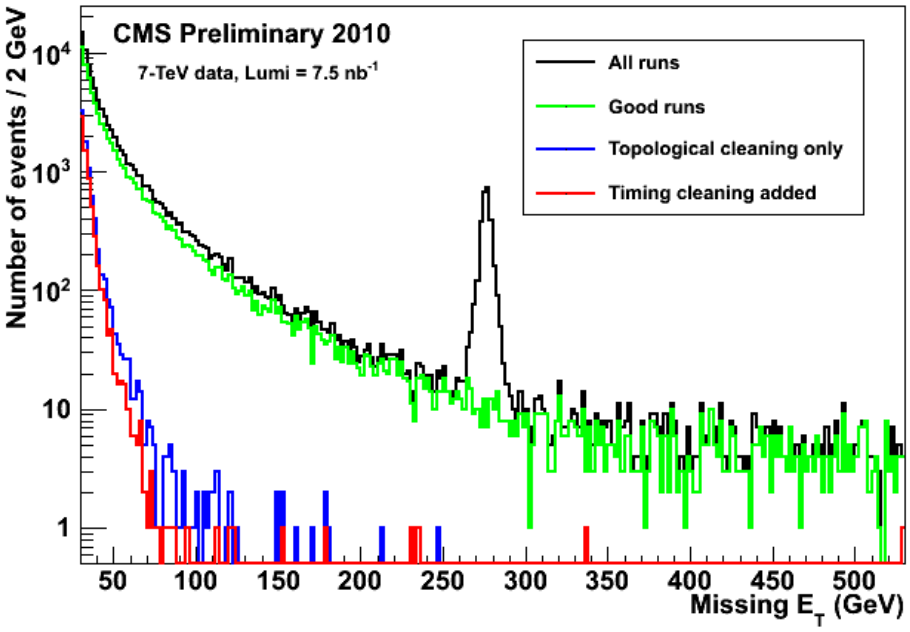

Figure 4.3: Distribution of missing transverse energy above 30 GeV, for 100 million collisions recorded at 7 TeV. From top to bottom: before any cleaning (black); for the subset of these collisions in the "good runs" (green); with the topological cleaning applied (blue) and with the timing cleaning procedure included (red). Most events with a missing transverse energy larger than 30 GeV before cleaning move below 30 GeV after cleaning [179].

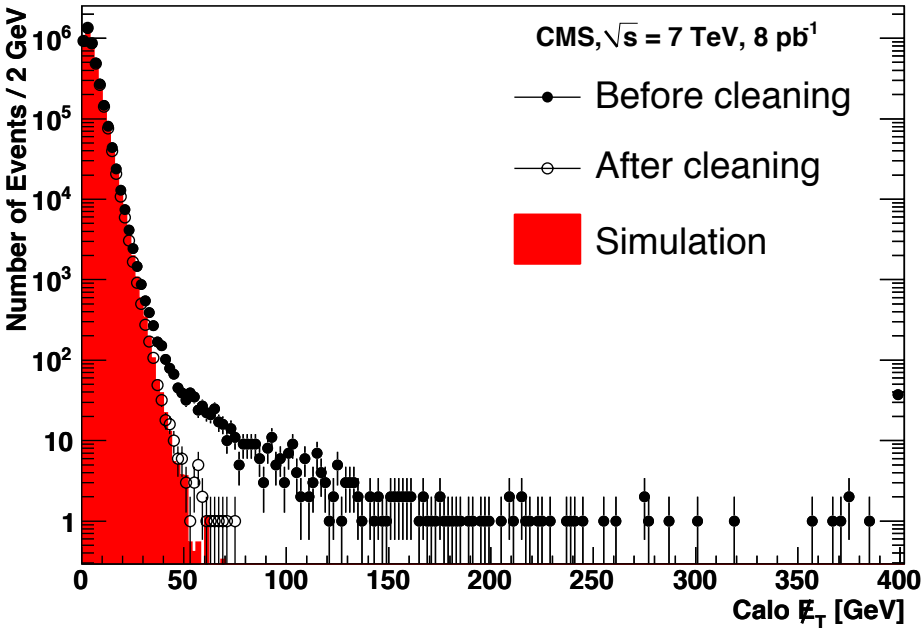

Figure 4.4: Calo $\not\!\!E_{\mathrm{T}}$ distributions in a minimum bias data sample without (black dots) and with (open circles) cleaning and filters compared to simulation. Figure taken from Reference [167].

analysis ("good" runs), the peak disappears as can be seen from the second distribution in this figure. The effect of the topological cleaning (see section 4.6.5) developed for the 2009 data, applied on $7.5\,\mathrm{nb}^{-1}$ of data recorded in 2010 is shown in the third distribution, reducing the tail many orders of magnitude. Finally, the fourth and cleanest distribution includes the use of timing information added in the 2010 cleaning version. With this upgraded cleaning procedure, applied to $8\,\mathrm{pb}^{-1}$ of data recorded in 2010 shown in Figure 4.4, the missing transverse energy distribution obtained from data is described well by the Monte-Carlo simulation [189].

4.4 Jet Reconstruction

This section summarizes the use of jets within CMS and draws heavily upon an overview reference on jet finding by Salam [190] and a recently published article of CMS on Jet Energy Corrections and Jet Energy Resolutions [191]. First, the different jet clustering algorithms will be discussed. These algorithms cluster particles or energy deposits in calorimeter towers into jets. Then, the anti-k_t algorithm used in this thesis is detailed, followed by a discussion of the different reconstructed jets in CMS. These jet types rely on the different objects (calorimeter deposits or particle-flow particles) that can be clustered into a jet. Thereafter the jet energy scale (JES) and jet energy resolutions (JER) are discussed.

4.4.1 Jets and Partons

Quantum Chromodynamics describes the strong interaction between hadrons such as protons and neutrons in atomic nuclei in terms of quarks and gluons. Yet quarks and gluons are never visible in their own right due to the confinement that coloured charged particles have to obey. Almost immediately after being produced, a quark or gluon fragments and hadronises leading to a collimated spray of energetic hadrons – a jet. Jets are obvious structures when looking at event displays and by measuring their energy and direction, one can get close to the idea of the original **parton**, but there is no one-to-one correspondence.

However, the relation between jet and parton is very ambiguous, and not just because partons are an ill-defined concept. Two partons originating from boosted W or Z boson decays may be so collimated by the boost that they will appear as a single jet. On the other hand, the radiation of gluons can cause one parton to be reconstructed as two jets. To come to a useful description of an event, one must introduce a prescription for defining what exactly one means by a jet. Jets are defined through a **jet definition**: a set of rules for how to group particles into jets and how to assign a momentum to the resulting jet. A good jet definition can be applied both to experimental measurements (**recojets**) as well as to the output of parton-showering Monte-Carlo simulation programs (**genjets**).

4.4.2 Jet Clustering Algorithms

A jet definition consists of two parts: a jet algorithm with its parameters and a recombination scheme. A **jet algorithm** provides a set of rules for grouping particles into jet, involving one or more parameters that indicate how close two particles must be for them to belong to the same jet. The **recombination scheme** explains what momentum should be assigned to the combination of two particles. The simplest is the sum of the four-momenta, the so-called "E-scheme". Two families of jet algorithms exist: "Cone Algorithms" catching the energy flow in a cone and

"Sequential Recombination Algorithms" that repeatedly combine the closest pair of particles according to some (p_T-dependent) distance measure.

Most of today's widely used cone algorithms are **"iterative cones" (IC)**. In such algorithms a seed particle i sets some initial direction, and one sums the momenta of all particles j within a circle ("cone") of radius R around i in azimuthal angle ϕ and rapidity y (or pseudorapidity η), i.e. taking all j such that:

$$\Delta R_{ij}^2 = (y_i - y_j)^2 + (\phi_i - \phi_j)^2 < R^2, \tag{4.1}$$

where y_i and ϕ_i are respectively the rapidity and azimuth of particle i. The direction of the resulting sum is then used as a seed for a new direction, and one iterates the procedure until the direction of the resulting cone is stable (i.e. the set of particles of the jet remains unchanged).

To be fully defined, Iterative Cone algorithms should specify what seeds they use and how they deal with overlapping cones (i.e. cones sharing particles). Depending on different approaches two broad classes of iterative cone algorithms can be defined. One way to deal with overlapping cones is by "progressively removing" (IC-PR) particles already assigned to a jet. Jet reconstruction is started with the seed (particle or calorimeter tower) with the highest p_T. Once one has found a stable cone around that seed, it is called a jet and the corresponding particles are removed from the set. Then again, one takes the hardest particle/tower from the remaining set and repeats the procedure. Another way is the "split-merge" (IC-SM) approach, where the cones are merged if a certain fraction of the softer cone's transverse momentum is contained by particles shared with the harder cone, or otherwise the particles are assigned to the cone they are closer to.

Infrared and collinear (IRC) safety is the property that if one modifies an event by a **collinear splitting** or the addition of a **soft emission**, the set of hard jets that are found in the event should remain unchanged [190]. Cone algorithms have been plagued by issues related to IRC safety. IC-PR algorithms suffer from collinear unsafety: collinear splitting of the first seed results in the clustering algorithm starting with another seed, leading to a different set of final jets. IC-SM algorithms are prone to infrared unsafety: the added soft particle can act as a new seed, causing the iterative process to find a new stable cone, also resulting in a different set of final jets. Figure 4.5 illustrates the modification of an event by a collinear splitting: a high-p_T parton is split into two partons with smaller p_T. For a collinear safe algorithm (left: Figures a&b) this leads to exactly the same set of jets, while for a collinear unsafe algorithm (right: Figures c&d) a different set of jets is obtained. This illustrates the sensitivity of a jet algorithm on its seeding. Figure 4.6 illustrates the modification of an event by a soft emission. This soft gluon is a higher-order diagram, so the corresponding loop-diagram should also be considered for a correct matrix element calculation. Whether the gluon was a soft loop-particle or a tree-level-particle will result in a different set of jets obtained by an infrared unsafe jet algorithm.

The IRC unsafety of the IC-PR and IC-SM algorithms in fact leads to their failure to find all stable cones. One full solution to the IRC safety issue avoids the use of seeds and iterations and finds all stable cones through some exact procedure and is called the "exact seedless cone" (SC) algorithm.

Another category of jet algorithms are **"sequential recombination" (SR) schemes**, clustering particles or energy deposits based on a distance measure. The advantage of these algorithms

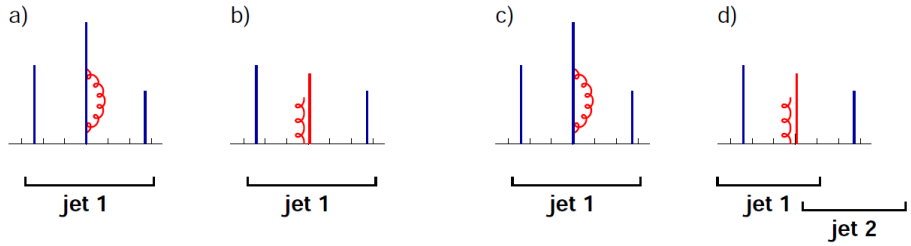

Figure 4.5: Illustration of a collinear safe jet algorithm (left: Figures a&b) and a collinear unsafety jet algorithm (right: Figures c&d). The collinear splitting of a parton leads in the right situation to a different set of jets. Figure taken from Reference [190].

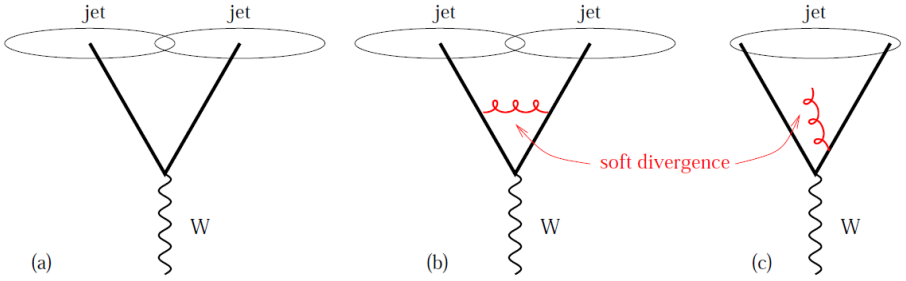

Figure 4.6: Illustration of infrared unsafety with an W-event decaying in two hard partons. Left picture shows the leading-order diagram, middle and right pictures show the addition of a soft gluon in a loop-diagram (middle) or in a tree-level-diagram (right). Obviously a different set of jets is obtained whether the soft gluon was a loop particle or not. Figure taken from Reference [190].

is that they go beyond jet finding and implicitly assign a "clustering sequence" to an event, which is often closely connected with the approximate probabilistic pictures that one may have for parton branching. This feature made those algorithms attractive to use in the much cleaner e^+e^- collision experiments, where they had their roots. These algorithms are IRC safe but have often irregular shapes in η, ϕ-space, which is shown in Figure 4.7(a). This, together with the fact that sequential recombination algorithms are computationally slow lead in the past to the adoption of cone algorithms in the much busier pp or $p\bar{p}$ collision environments. Experimentalists prefer circular (conical) jets since those regular jets are easily identified to be within the fiducial volume of a detector: if it is at least a distance R away from the detector boundary, the jet will be fully contained in the detector. Recently a new sequential recombination algorithm, anti-k_t, is introduced which abolishes previous drawbacks: it results in circular jets, shown in Figure 4.7(b), and is computationally competitive. Therefore, and because it is IRC safe, the anti-k_t algorithm is the most widespread jet algorithm in CMS[1].

[1]Several different jetalgorithms are used by CMS, for instance in the search for jet substructure. Further on, the use of the IC-PR algorithm was widespread in the HLT algorithms used in 2010. Since the anti-k_t was found to have equal or better computation speed, this was changed in the HLT in 2011. This lead to improved trigger turn-on curves with respect to anti-k_t jets reconstructed offline.

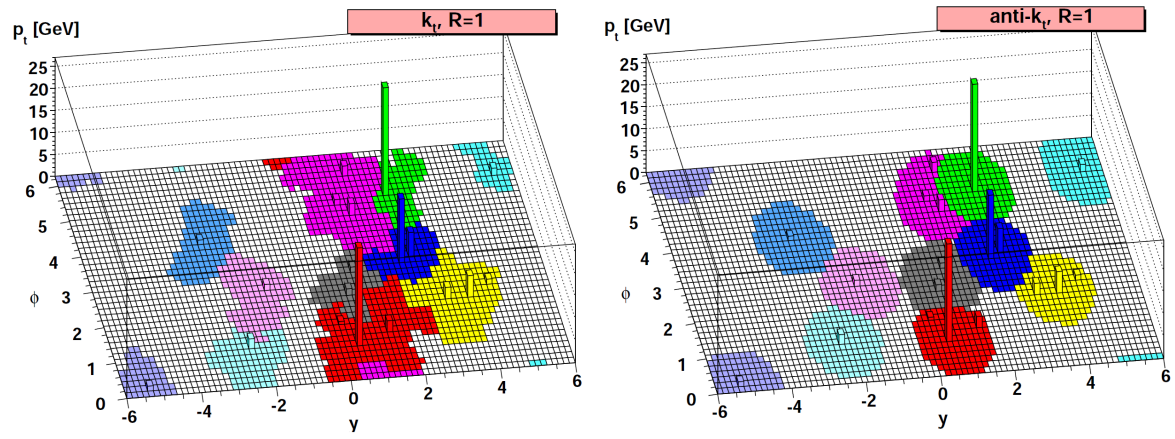

(a) Event clustered by the k_t-algorithm.

(b) Event clustered by the anti-k_t-algorithm.

Figure 4.7: A simulated event clustered by the k_t- (left) and the anti-k_t-algorithm (right) resulting in different jets denoted by different colours. Note the irregular shapes of the sequential recombination algorithm (left), while the anti-k_t-algorithm results in regular jet shapes. Figure taken from Reference [190].

4.4.3 The anti-k_t algorithm

The jet clustering algorithm used in this work is the anti-k_t algorithm, and will be discussed below. Consider the distance between two particles i, j as:

$$d_{ij} = \min(p_{\mathrm{T}i}^{-2}, p_{\mathrm{T}j}^{-2})\frac{\Delta R_{ij}^2}{R^2}, \qquad \Delta R_{ij}^2 = (y_i - y_j)^2 + (\phi_i - \phi_j)^2, \tag{4.2}$$

and the distance between a particle i and the beam as:

$$d_{iB} = p_{\mathrm{T}i}^{-2}. \tag{4.3}$$

The algorithm proceeds as follows:

1. Work out all d_{ij} and d_{iB} according to formulas 4.2 and 4.3.
2. Find the minimum of the d_{ij} and d_{iB}.
3. If it is d_{ij}, recombine i and j into a single new particle and return to step 1.
4. Otherwise if it is d_{iB}, declare i to be a jet and remove it from the list of particles. If the list of particles is not empty, return to step 1.
5. Stop when no particles remain.

The question what gets called a jet is determined by R. If a particle i has no other particles within a distance R then d_{iB} will be smaller than d_{ij} for any particle j and the particle i will thus become a jet. The anti-k_t algorithm favours the clustering of hard particles rather than soft particles. This means that jets grow outwards around hard "seeds". The result is an IRC safe algorithm that gives circular hard jets, making it an attractive replacement for cone-type algorithms. Unlike original sequential recombination algorithms such as the k_t algorithm, no

substructure classification can be usefully related to QCD branching since the latter algorithms start clustering the soft particles instead of the hard particles.

4.4.4 Jet Types

Three different approaches to reconstruct jets are available in CMS: a calorimeter based approach, the "Jet-Plus-Track" approach which improves the measurement of calorimeter jets by using ad-hoc information from the tracker and the "Particle-Flow" approach which is a more consistent approach to use information from all subdetectors to reconstruct jets;

- **Calorimeter jets** (Calo-jets) are reconstructed starting from calorimeter towers which are a simple sum of the HCAL energy of one or more cells and the energy of the corresponding ECAL cells.
- **Jet-Plus-Track jets** (JPT-jets) are reconstructed calorimeter jets whose energy response and resolution are improved by replacing calorimeter energy by measurements of the track p_{T} where possible [192]. Each Calo-jet is geometrically associated with a set of tracks. Each track can be either "in-cone" or "out-of-cone", depending of the extrapolation of the track to the calorimeter surface points within or outside the geometric jet cone. The p_{T} of the "in-cone" tracks are added to the jet momentum, while for each track the average calorimeter particle response is subtracted. The "out-of-cone" tracks are simply added to the jet momentum. Furthermore, every track is weighted by $1/\epsilon_{\mathrm{tracking}}$, including the lost tracks artificially.
- **Particle-Flow jets** (PF-jets) are reconstructed by clustering the four-momentum vectors of the particle-flow candidates produced by the particle-flow algorithm discussed in detail in section 4.2.

The particle-flow jets have an improved energy resolution with respect to the Calo-jets and JPT-jets, demonstrated in section 4.4.6. Therefore only particle-flow jets will be used in this thesis. The jet reconstruction results (such as the energy response and energy resolution) for the other two jet types are only shown for comparison.

4.4.5 Jet Energy Scale

The jet energy calibration relates the energy of the jet measured in the detector to the corresponding true particle jet. In simulation, the true particle jet is made by clustering the Monte-Carlo simulated particles originating from the fragmenting parton as well as the particles of the underlying event. To obtain the calibrated four-momentum of the jet, a factorized multi-level correction was designed for CMS [193, 194], consisting of an **offset** correction (**L1**), **relative** (η) correction (**L2**) and an **absolute** (p_{T}) corrections (**L3**).

After removing pile-up and noise effects with the L1 correction, the L2 correction corrects jets at arbitrary η relative to a control region where the absolute calibration is easier. The L3 correction, finally, is the absolute calibration of the jets in that control region, consisting of the barrel calorimeters with full tracker coverage. The bulk of the relative and absolute jet energy corrections are determined using Monte-Carlo simulation, while small residual corrections are measured in data. Therefore those corrections are calculated together (L2L3) and split into a Monte-Carlo calibration factor and two residual calibration factors, one for the relative (η) correction, the other for the absolute (p_{T}) correction.

The calibrated four-momentum of a jet is then obtained by a correction factorized in the offset correction (C_{offset}), the Monte-Carlo simulated calibration factor (C_{MC}) and the relative and absolute residual calibration factors (C_{rel} and C_{abs}) that correct for small differences between data and Monte-Carlo simulation:

$$p_{\text{T}}^{\text{cor}} = C_{\text{abs}}(p_{\text{T}}'') \cdot C_{\text{rel}}(\eta) \cdot C_{\text{MC}}(p_{\text{T}}', \eta) \cdot C_{\text{offset}}(p_{\text{T}}^{\text{raw}}) \cdot p_{\text{T}}^{\text{raw}},$$

equation with:

$$p_{\text{T}}' = C_{\text{offset}} \cdot p_{\text{T}}^{\text{raw}} \qquad \text{and} \qquad p_{\text{T}}'' = C_{\text{rel}} \cdot C_{\text{MC}} \cdot p_{\text{T}}'. \tag{4.5}$$

All correction factors except the Monte-Carlo calibration factor are measured with $\sim 36\,\text{pb}^{-1}$ of data recorded in 2010.

- The **offset correction** removes the extra energy clustered into the jet due to pile-up and detector noise. In CMS, three different methods were developed to measure the offset correction on data, which are in agreement with each other.
- The **Monte-Carlo simulated correction** corrects the energy of the reconstructed jet such that it equals on average the energy of the generated jet. The Monte-Carlo simulated correction is a function of p_{T} and η and removes the bulk of the non-uniformity of the detector response (defined as $\mathcal{R} = p_{\text{T}}^{\text{reco}}/p_{\text{T}}^{\text{gen}}$) in η and the non-linearity of the detector response in p_{T}. The Monte-Carlo simulated correction is the largest contribution to the total jet energy correction shown in Figure 4.8. The two peaks can clearly be identified as the barrel - endcap interface, where a less precise determination of the jet p_{T} is possible. The correction falls steep in the forward region because the jet energy response depends more on the energy than on the transverse momentum of the jet ($E \approx p_{\text{T}} \cosh\eta$). Calo jets require a much larger correction factor than JPT and PF jets due to the low response of the CMS Hadron Calorimeter. JPT and PF jets benefit from the accurate measurement of the charged particles in the jets by the tracker.
- The **relative residual correction** measures the response of a jet at any given η with respect to the jet energy response in the central region of the detector ($|\eta| < 1.3$). The central region is chosen as a reference because of the uniformity of the detector, the small variations of the jet energy response and because it provides the highest jet p_{T}-reach. It is also the easiest region to calibrate using γ+jet and Z+jet events. The measurement is performed in a dijet sample extrapolated to zero third-jet activity.
- The **absolute residual correction** is measured with jets in $|\eta| < 1.3$ using jets balanced by a γ or Z boson of which the momentum can be determined with high precision in ECAL (γ and $Z \to e^+e^-$) or the tracker and muon system ($Z \to \mu^+\mu^-$).

All correction factors can be convoluted in one single total jet-energy-scale correction factor $C_{\text{tot}}(p_{\text{T}}^{\text{raw}}, \eta)$:

$$p_{\text{T}}^{\text{cor}} = C_{\text{tot}}(p_{\text{T}}^{\text{raw}}, \eta) \cdot p_{\text{T}}^{\text{raw}}, \tag{4.6}$$

which is shown in Figure 4.8 as a function of η for two different corrected jet p_{T}'s [191]. The offset and residual corrections are rather small (order of a percent), such that the shape is mainly determined by the Monte-Carlo simulated correction. The JPT-jets require smaller JEC because the JPT-algorithm corrects explicitly for the tracking inefficiency: every track is weighted with $1/\epsilon_{\text{tracking}}$ [195]. Therefore the lost tracks are artificially included, where the particle-flow algorithm only reconstructs charged hadrons if the track is found. If it is lost, a neutral hadron

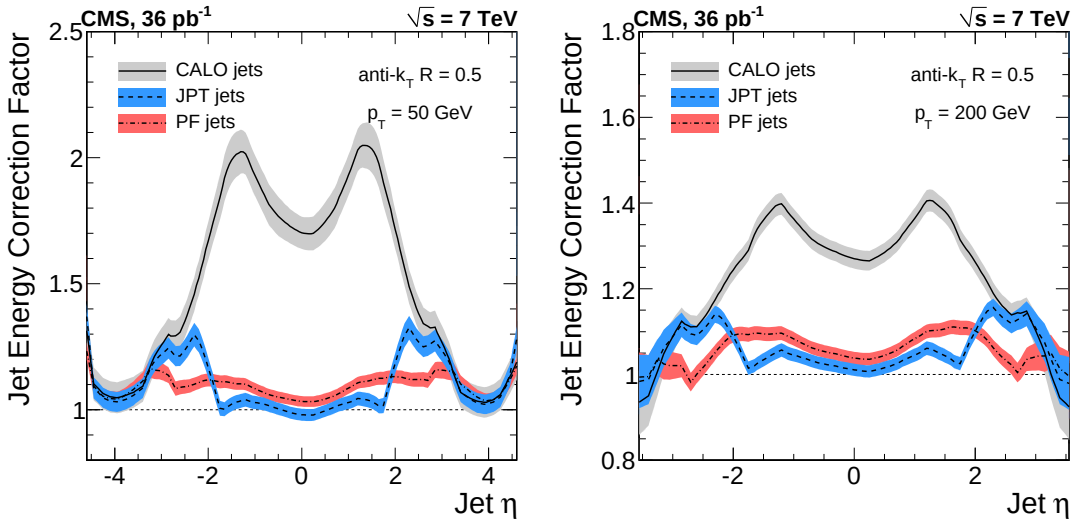

Figure 4.8: Total jet-energy-scale correction factor, as a function of jet η for a corrected jet $p_{\mathrm{T}} = 50\,\mathrm{GeV}/c$ (left) and a corrected jet $p_{\mathrm{T}} = 200\,\mathrm{GeV}/c$ (right). Figure taken from Reference [191].

is reconstructed. This leads to a smaller correction factor, but does not improve the resolution, where particle-flow has a better performance, as will be shown in the next section. Figure 4.9 shows the uncertainties on the jet-energy-scale correction factor as a function of p_{T} for four different η values. The uncertainty is dominated by the relative energy scale uncertainty at low p_{T}, while it becomes negligible at high p_{T}. In general PF jets have the smallest systematic uncertainty on the jet energy scale, while Calo jets have the largest [191].

4.4.6 Jet Energy Resolutions

After having calibrated the jet energy, one is interested in **the accuracy of the jet energy** measurement. The width of the distribution of corrected jet transverse momentum is interpreted as the jet energy p_{T} resolution $\sigma(p_{\mathrm{T}})$ and is a function of p_{T} and η. The jet energy resolutions are measured in data. As a benchmark the jet energy resolutions are also extracted from Monte-Carlo simulation. Figure 4.10(a) shows an example of $p_{\mathrm{T}}^{\mathrm{reco}}/p_{\mathrm{T}}^{\mathrm{gen}}$ distribution for Calo-jets in $|\eta| < 0.5$ and with $250 < p_{\mathrm{T}}^{\mathrm{gen}} < 320\,\mathrm{GeV}/c$. The Calo-jet energy resolution is fitted by a double-sided Crystal-Ball function[2] [196, 198]. The jet energy resolution function has tails on both sides of the distribution: the so-called "lower-tail" and "upper-tail". The main contributions to the lower-tail in the jet resolution distributions are muons and neutrinos from semi-leptonic decays of heavy flavour jets. In PF-jets, such muons are clustered into the jets leading to smaller

[2]The Crystal-Ball function is a function modeling radiative energy loss processes and consists of a Gaussian core and a power-law tail. The double-sided Crystal-Ball is defined as:

$$f(u; N, \mu, \sigma, a_1, p_1, a_2, p_2) := N \cdot \begin{cases} A_1(B_1 - u)^{-p_1} & : \quad u < -a_1 \\ e^{-\frac{-u^2}{2}} & : \quad -a_1 \leq u < a_2 \\ A_2(B_2 + u)^{-p_2} & : \quad u \geq a_2 \end{cases}, \tag{4.7}$$

where $u := \frac{x-\mu}{\sigma}$, $A_i := \left(\frac{p_i}{|a_i|}\right)^{p_i} \cdot e^{-\frac{a_i^2}{2}}$, $B_i := \frac{p_i}{|a_i|} - a_i$ and N is a normalization factor. The Gaussian parameters μ and σ are determined from a Gaussian-only fit and then fixed when determining the additional four parameters of the tails: a_i and p_i [196]. The function is named after the Crystal Ball collaboration who used it for the lineshape of the detector (NaI(Tl) crystals) response to Bhabha scattering ($e^+e^- \to e^+e^-$) at the J/ψ resonance [197].

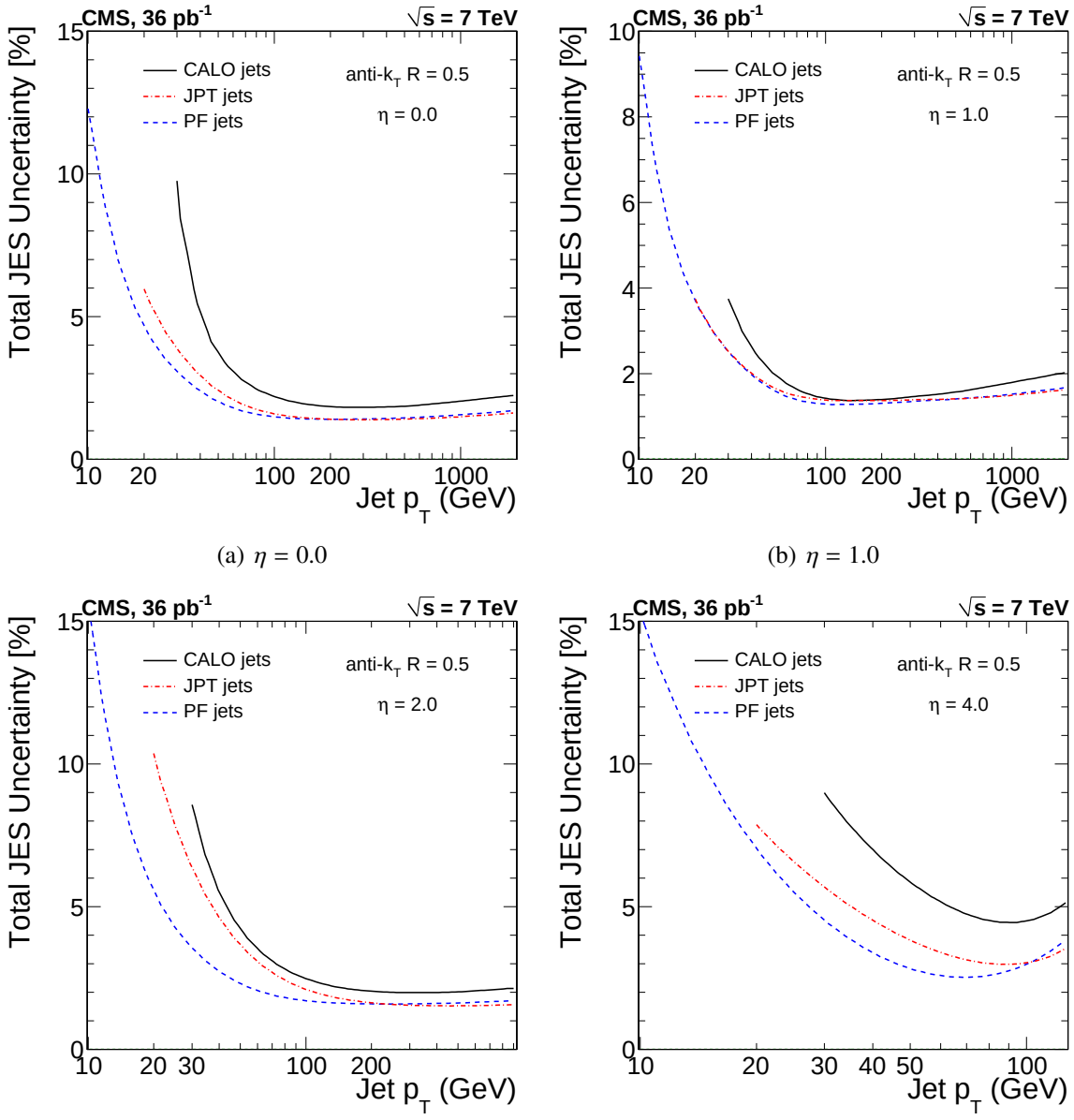

(a) $\eta = 0.0$ (b) $\eta = 1.0$

(c) $\eta = 2.0$ (d) $\eta = 4.0$

Figure 4.9: Total jet-energy-scale uncertainty, as a function of corrected jet p_{T} for various η values: $\eta = 0.0$, 1.0, 2.0 and 4.0. Figures taken from Reference [191].

tails, since only neutrinos deteriorate the resolution. Another contribution comes from masked or dead ECAL cells. The upper-tail consists of jets with reconstructed energy higher than the simulated energy, most likely because of the clustering noisy (higher-energy) channels into the jet.

The jet p_{T} resolution is measured from two different samples, in both data and MC samples, using dijet and γ + jets events:

- The **dijet asymmetry method** exploits the momentum conservation in the transverse plane of the dijet system. The idealized topology of two jets with exactly compensating transverse momenta is spoiled by the presence of extra activity from

additional soft radiation and the underlying event. The additional soft radiation often results in a third jet, below or above certain p_T threshold. Consequently, the resulting asymmetry distributions are broadened and the jet p_T resolution is systematically underestimated. As a measure of the extra activity, the ratio of the transverse momentum of the third jet in the event over the dijet average transverse momentum: $p_T^{\text{Jet3, rel}} = p_T^{\text{Jet3}}/p_T^{\text{ave}}$ is used.

To account for soft radiation in dijet events, the measurement of the asymmetry in each η and $p_T^{\text{ave}} = (p_T^{\text{Jet1}} + p_T^{\text{Jet2}})/2$ is carried out multiple times, for decreasing amounts of extra activity. The jet p_T resolution is then extracted by extrapolating the extra event activity to zero. Unfortunately, calculating the dijet asymmetry removes the separate access to the low and high tails.

- The γ+**jet balance method** exploits the balance in the transverse plane between a well measured photon and a recoiling jet. Due to the limited number of γ+jet events, this measurement serves only as an independent and complementary cross check of the dijet asymmetry results and a reasonable agreement is observed between the two measurements.

The final results are obtained with the dijet asymmetry method and are shown in Figure 4.11 for all three types of jets in the central region. The resolution obtained from generator-level MC and corrected for the measured discrepancy between data and simulation is shown by the solid red line and represents the best estimate of the jet p_T resolution in data. The systematic uncertainty on the MC resolution is shown as a yellow band. The black dots are the measurements in data, which are found to be in good agreement with the MC within statistical and systematic uncertainties.

The dashed red line is the uncorrected generator-level MC resolution. Already at particle level an imbalance in jet p_T is introduced by out-of-cone radiation and addition of the underlying event. To account for the particle-level imbalance contribution to the measured jet p_T resolution, the asymmetry method is applied to the generated MC particle jets. Then the extrapolated particle level resolution is subtracted in quadrature from the measurement.

One of the most promising signatures of physics beyond the standard model involves events with multiple jets and a large missing transverse energy $\not{E}_T$. A search for new physics with this signature is discussed in this thesis, in chapters 6, 7 and 8. A particular huge background with exactly the same signature is expected to come from QCD multijet production where / E_T can originate e.g. from fluctuations in the detector response to jets. One way to estimate the QCD background in the high$\not{E}_T$ signal region is to smear particle-level multijet events with parametrization of the full jet-p_T-resolution functions that model both the Gaussian core and the tails of the distributions. The non-Gaussian component of the jet p_T resolution is quantified for PF-jet reconstruction, since it provides the best jet p_T resolution and is adopted in the primary physics analyses most sensitive to the impact of the jet p_T resolution tails. Both dijet and γ+jet events are used to study the tails but only results for dijet are shown, since the γ+jet method is limited by the small amount of events available.

The full resolution functions are derived using the generator-level MC information in the simulation. The MC simulation description of the p_T-resolution tails are validated using the $\sim 36\,\text{pb}^{-1}$ of data available at the end of 2010. The fractional number of events in the tail regions of the dijet p_T asymmetry distributions are compared between data and simulation and

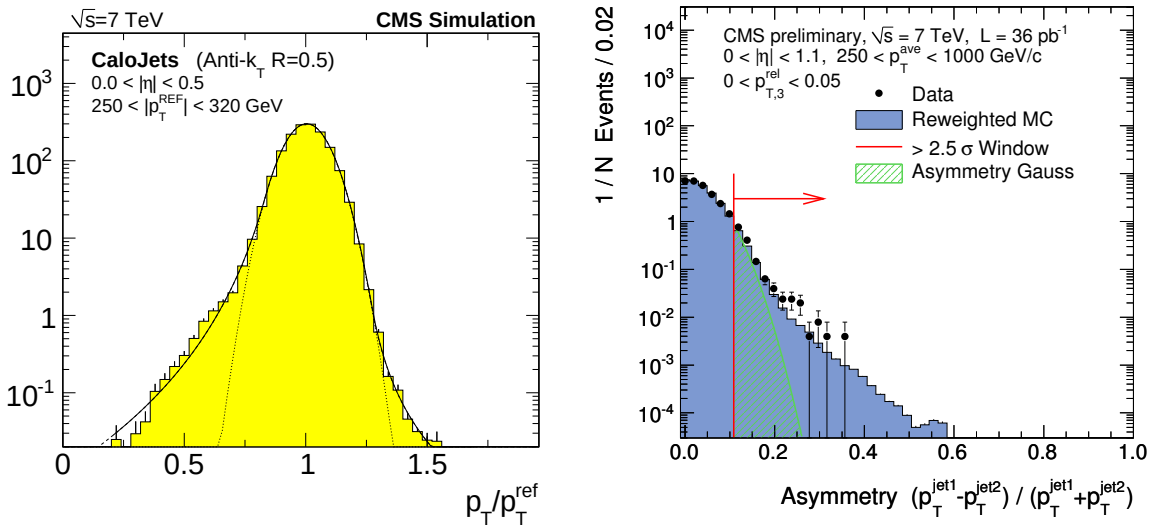

(a) (b)

Figure 4.10: (a) Distribution of the simulated Calo jet response $p_{\mathrm{T}}^{\mathrm{reco}}/p_{\mathrm{T}}^{\mathrm{gen}}$, in a particular $|\eta|$ and $p_{\mathrm{T}}^{\mathrm{gen}}$ range. Fit examples with a Gaussian and a double-sided Crystal-Ball function are shown [191]. (b) Dijet asymmetry for adjusted simulation and for data. The area starting from the red line defines the window which is kept fixed during the extrapolation to $p_{\mathrm{T,3}}^{\mathrm{rel}} = 0$. For comparison the green shaded area shows the fraction of events in the asymmetry window under the hypothesis of a purely Gaussian shape [199].

a difference is observed in the central core widths. The adopted strategy is to adjust the MC response distributions to have the same Gaussian core resolutions in MC simulations as in data in a window of $0 - 2.5\sigma$, as is shown in Figure 4.10(b). Then, the fraction of events in a given asymmetry window in the tail of the distribution ($2.5\sigma - \infty$) is calculated with both data and MC samples. These fractions are observed to depend on the threshold on the third-jet p_{T}, and are therefore extrapolated to zero: $p_{\mathrm{T,3}}^{\mathrm{rel}} = 0$. The measured ratio between data and MC fractions from asymmetry is used to correct the fraction from generator-level MC in the form of a scaling factor. Figure 4.12 shows the final results for the scaling factors and demonstrate that the observed data over MC ratios of the resolution tails are within a factor of 1.5 and that the uncertainty is dominated by the limited statistical precision of the sample.

4.5 Missing Transverse Energy

Neutral weakly-interacting particles, such as neutrinos, escape from typical collider detectors without producing any direct response in the detector elements. The presence of such particles must be inferred from the imbalance of total momentum. The vector momentum imbalance in the plane perpendicular (transverse) to the beam direction is particularly useful in pp and $p\bar{p}$ colliders, and is known as missing transverse momentum, here denoted as $\vec{\not{E}}_{\mathrm{T}}$. Its magnitude is called missing transverse energy, and is denoted $\not{E}_{\mathrm{T}}$. From now on, the term missing transverse momentum ($\vec{\not{E}}_{\mathrm{T}}$) will be used when the direction of the missing momentum is important, such as in the reconstruction, else missing transverse energy ($\not{E}_{\mathrm{T}}$) will be used.

Missing transverse energy is one of the most important observables for discriminating leptonic

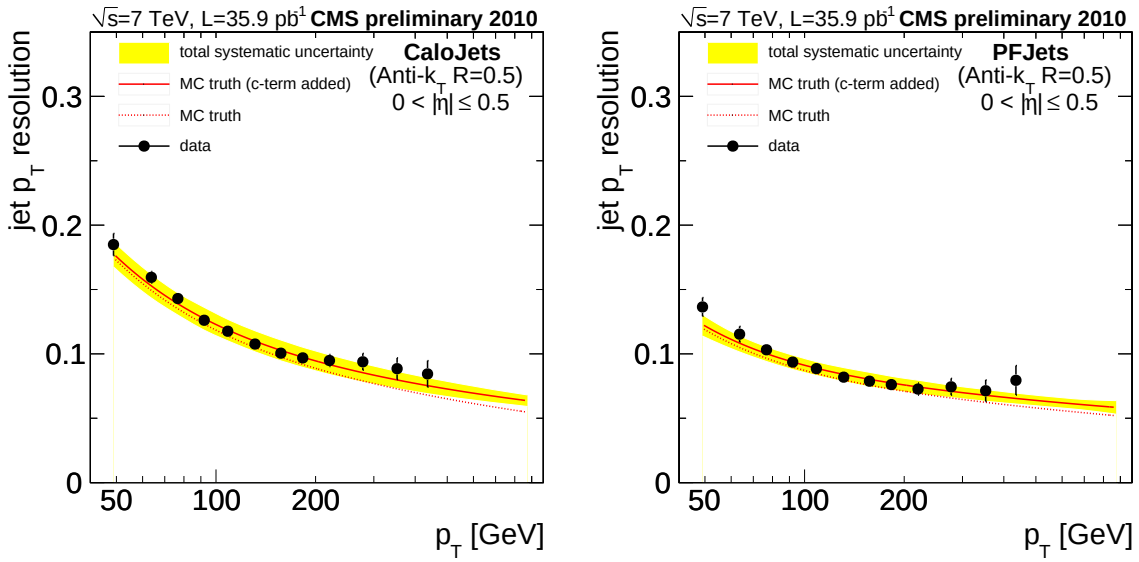

Figure 4.11: Bias-corrected data measurements, compared to the generator-level MC (denoted as MC-truth) p_{T} resolution before (red-dashed line) and after correction for the measured discrepancy between data and simulation (red-solid line) for Calo- (left) and PF-jets (right) in $0.0 \leq |\eta| \leq 0.5$ [191].

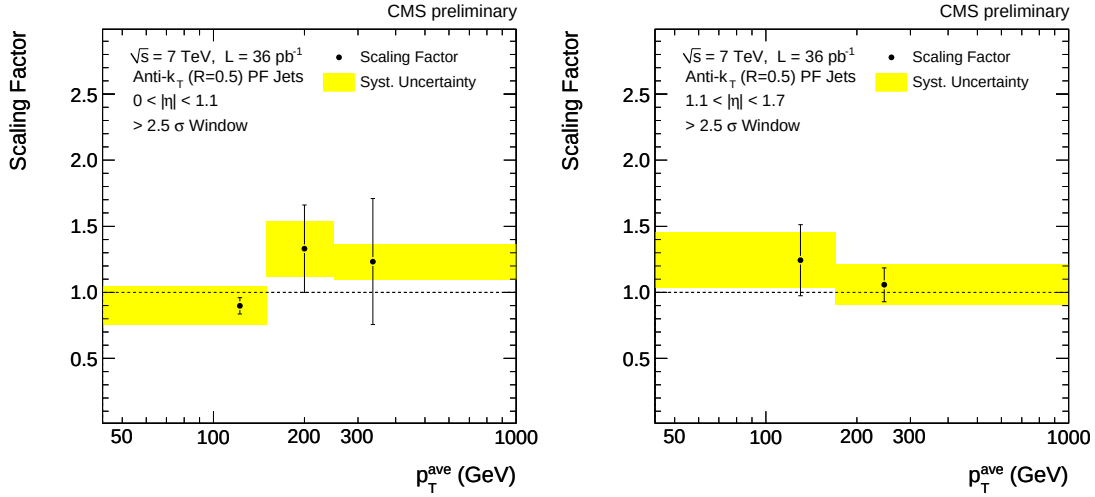

Figure 4.12: The data/MC scaling factors for the tails of the resolutions observed in the dijet samples for different η and p_{T} bins, using the $> 2.5\sigma$ window [191].

decays of W bosons and top quarks from background events which do not contain neutrinos, such as multijet and Drell-Yan events. It is also an important variable in searches for new weakly interacting, long-lived particles. Many beyond-the-standard-model scenarios, including supersymmetry, predict events with large $\not\!\!E_{\mathrm{T}}$. The reconstruction of $\vec{\not\!\!E}_{\mathrm{T}}$ is very sensitive to particle momentum mismeasurements, particle misidentification, detector malfunctions, particles impinging on poorly instrumented regions of the detector, cosmic-ray particles, and beam-halo particles, which all may result in artificial $\not\!\!E_{\mathrm{T}}$.

Three distinct algorithms to reconstruct $\vec{\not\!\!E}_{\mathrm{T}}$ were developed in CMS:

- PF$\vec{\not{E}}_{\mathrm{T}}$, which is calculated using a complete particle-flow technique;
- Calo$\vec{\not{E}}_{\mathrm{T}}$, which is based on calorimeter energies and the calorimeter tower geometry;
- TC$\vec{\not{E}}_{\mathrm{T}}$ which corrects Calo$\vec{\not{E}}_{\mathrm{T}}$ by including the p_{T} of the tracks reconstructed in the inner tracker and removing the expected calorimetric energy deposit of each track.

PF$\vec{\not{E}}_{\mathrm{T}}$ is calculated as the negative vectorial sum of the $\vec{p}_{\mathrm{T}}$ of the reconstructed PF-particles:

$$\mathrm{PF}\vec{\not{E}}_{\mathrm{T}} = -\sum_i \vec{p}_{\mathrm{T}}(i). \tag{4.8}$$

PF-sum-E_{T} (PF-$\sum E_{\mathrm{T}}$) is the associated scalar sum of the (visible) transverse energies of the PF-particles:

$$\text{PF-sum-}E_{\mathrm{T}} = \sum_i |\vec{p}_{\mathrm{T}}(i)|. \tag{4.9}$$

Similar variables, such as Calo$\vec{\not{E}}_{\mathrm{T}}$ and TC$\vec{\not{E}}_{\mathrm{T}}$ are constructed in the same way, but by summing calorimeter towers (and correcting them by including tracks), instead of summing PF-particles [167].

4.5.1 Large missing transverse energy due to misreconstruction

Anomalous energy deposits in the calorimeters can cause large artificial $\vec{\not{E}}_{\mathrm{T}}$. Procedures adopted both in particle-flow and in standard event reconstruction guarantee reconstructed jets and $\vec{\not{E}}_{\mathrm{T}}$ to be consistently "cleaned" of anomalous detector effects.

Machine-induced backgrounds, especially muons when beam protons suffer collisions upstream of the detector ("beam halo") can cause anomalous large $\vec{\not{E}}_{\mathrm{T}}$. Muons traveling parallel to the beam line can pass trough the calorimeters, radiate photons and cause large local energy deposits leading to large $\not{E}_{\mathrm{T}}$ when superposed on a pp collision event. Cathode Strip Chambers (CSCs) have good reconstruction performance for both muons originating from the middle of the detector as well as muons traveling parallel to the beam pipe and are used to tag events for removal. Figure 4.13 shows an event display of a halo muon passing through both CSCs and depositing a lot of energy in the barrel calorimeter.

Particles traversing poorly instrumented regions of the detector can be another cause of apparent $\vec{\not{E}}_{\mathrm{T}}$. While generally hermetic, the CMS calorimeter does have uninstrumented areas (cracks) at the boundary between the barrel and endcap sections, and between the endcap and forward calorimeters. The gap between the barrel and endcap sections is about 5 cm and contains various services, including cooling, power cables and readout cables for the tracker [167]. The gap is not projective to the interaction point, i.e. particles originating from the IP will follow straight trajectories in η, while the gap is not at constant η. Therefore energies of particles traversing these cracks are still measured, but with degraded resolution [167].

In addition, about 1% of the ECAL crystals are either not operational or have a high level of electronic noise and they are masked in reconstruction. The η-ϕ distribution of these crystals for the barrel and the x-y distribution for the endcaps is shown in Figure 4.14. While the impact of the cracks is small, analyses sensitive to events with large $\not{E}_{\mathrm{T}}$ need to take the ECAL masked channels into account. About 70% of the ECAL channels that are masked during offline reconstruction have a useful measurement of their energy from the separate readout of the L1

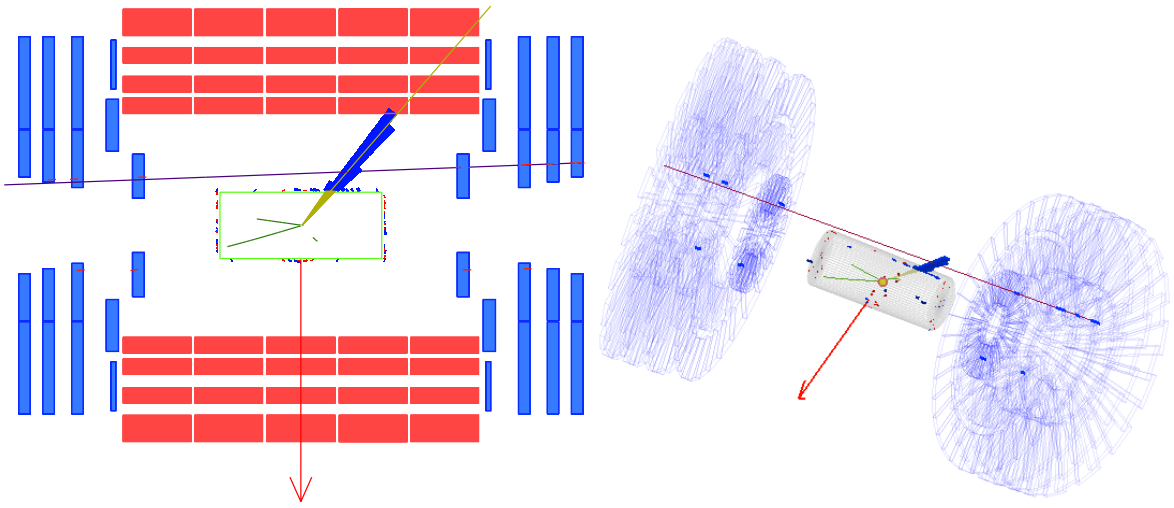

Figure 4.13: Event display in $r - z$ (left) and in 3D (right) of the halo-tagged event 15 564 358 in lumisection 92 of run 135 535. Muon hits in the CSC system are shown in red (left) and blue (right). The muon deposited energy in the hadron calorimeter, resulting in Calo-$\not\!\!E_{\mathrm{T}}$ of 224 GeV [200, 201].

trigger. Although the trigger readout saturates at 64 GeV[3], it can be used to recover energies smaller than the saturation value and to identify (and remove) events that had more than this amount of energy in a masked channel.

4.5.2 Missing transverse energy resolution

The performance of $\vec{\not\!\!E}_{\mathrm{T}}$ was studied using events with an identified Z boson or isolated photon. While there is no genuine $\not\!\!E_{\mathrm{T}}$ in these events, it can be introduced by removing the vector boson. By comparing the momenta of the well-measured vector boson to the $\vec{\not\!\!E}_{\mathrm{T}}$ introduced this way, the energy scale and resolution of $\vec{\not\!\!E}_{\mathrm{T}}$ is measured. Because the $\not\!\!E_{\mathrm{T}}$ resolution has a strong dependence on the associated $\sum E_{\mathrm{T}}$, it is presented as a function of $\sum E_{\mathrm{T}}$. The $\vec{\not\!\!E}_{\mathrm{T}}$ resolution is characterized using the standard deviation of a Gaussian fit to the distribution of the $\vec{\not\!\!E}_{\mathrm{T}}$ x and y components: $\vec{\not\!\!E}_{\mathrm{x,y}}$. For $\sum E_{\mathrm{T}}$, the PF-$\sum E_{\mathrm{T}}$ is used as measurement by the particle-flow algorithm for all types of $\not\!\!E_{\mathrm{T}}$, as it gives the best estimate of the true $\sum E_{\mathrm{T}}$, and hence is an accurate evaluation of the event activity. Figure 4.15 shows the calibrated $\vec{\not\!\!E}_{\mathrm{x,y}}$ Gaussian core resolution versus the calibrated PF $\sum E_{\mathrm{T}}$ for different $\not\!\!E_{\mathrm{T}}$ reconstruction algorithms in events containing at least two jets with $p_{\mathrm{T}} > 25$ GeV/c. The inclusion of the tracker information clearly leads to improvements in the $\not\!\!E_{\mathrm{T}}$ resolution with PF-$\not\!\!E_{\mathrm{T}}$ yielding the smallest $\not\!\!E_{\mathrm{T}}$ resolution.

[3] Increased to 128 GeV during the 2011 data taking.

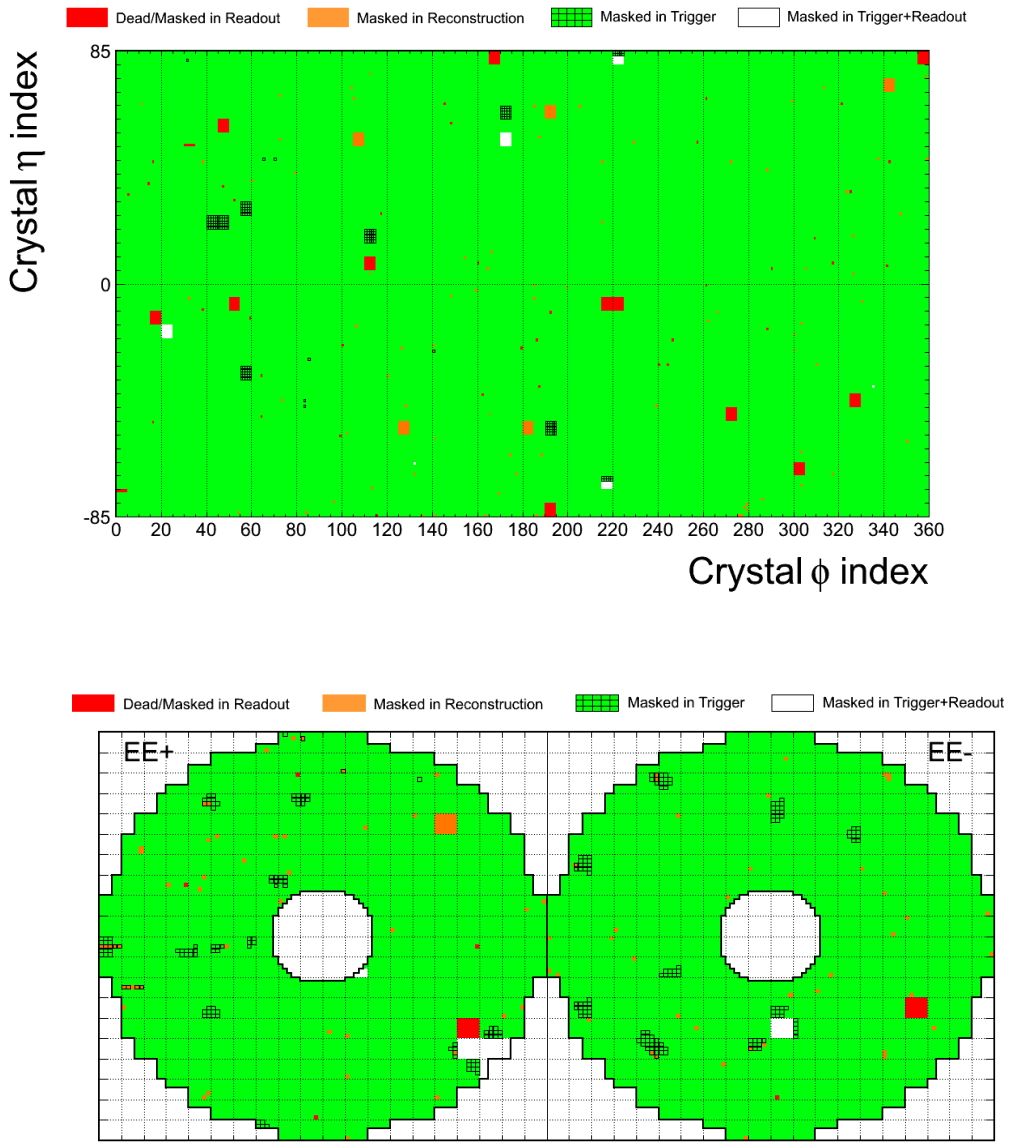

Figure 4.14: Distribution of masked ECAL channels in the barrel: $\eta - \phi$ view of 170×360 individual crystals (top) and in the endcaps: $x - y$ view of 2×7400 individual crystals [167].

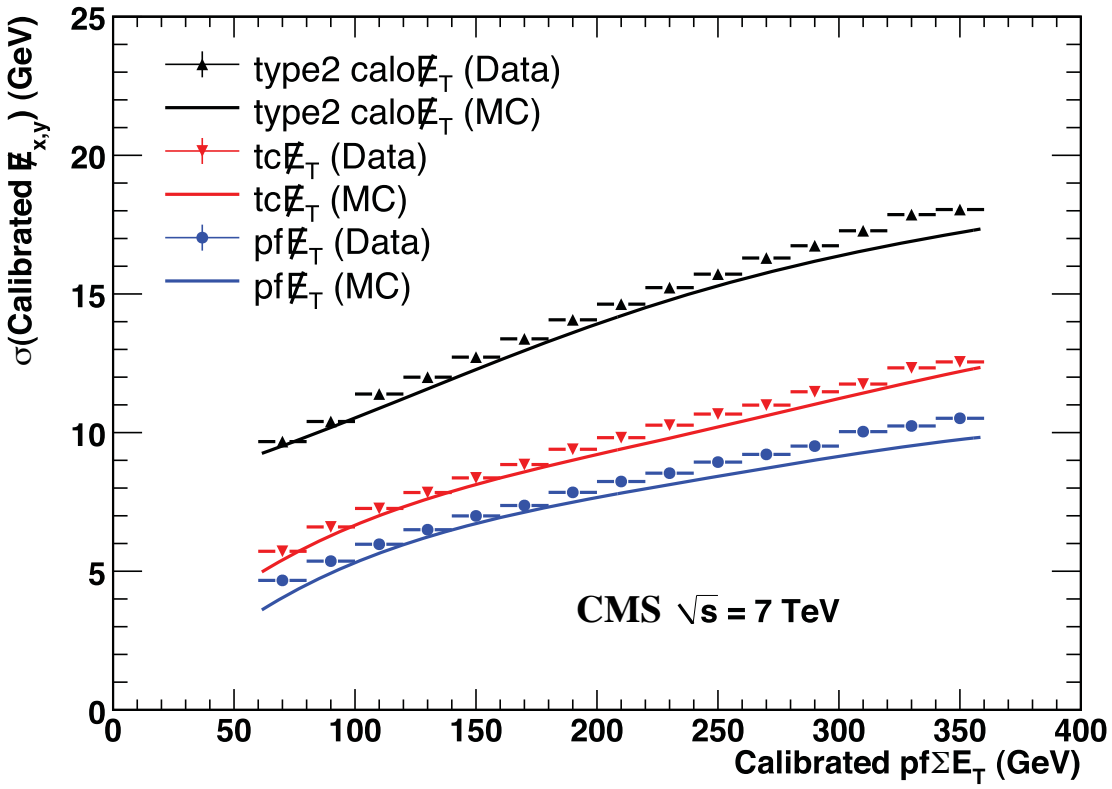

Figure 4.15: Calibrated $\vec{\not\!\!E}_{x,y}$ resolution versus calibrated PF-$\sum E_T$, for Calo-E_T (black), TC-E_T (red) and PF-E_T (blue) in data and simulation [167].

4.6 Photons

Photons and electrons behave very similar when interacting with material. At high energies, pair production and Bremsstrahlung are the dominating energy loss mechanisms. Electrons will radiate photons and photons will convert to electron-positron pairs. Combination of both processes in the dense material of calorimeters leads to electromagnetic showers. These showers are very similar for photons and electrons[4], therefore the energy reconstruction in the ECAL is similar for both particles. The description of the photon reconstruction and identification discussed in this section is based on the CMS Physics TDR [144] and early Physics Analysis Summaries (PAS) describing the photon reconstruction and identification [202] and the isolated photon identification [188].

4.6.1 Supercluster reconstruction

Electron and photon showers deposit their energy in several crystals in the ECAL. Approximately 94% of the incident energy of a single electron or photon is contained in 3×3 crystals, and 97% in 5×5 crystals. Summing the energy measured in such fixed arrays gives the best performance for unconverted photons (or electrons when using beam tests) [144].

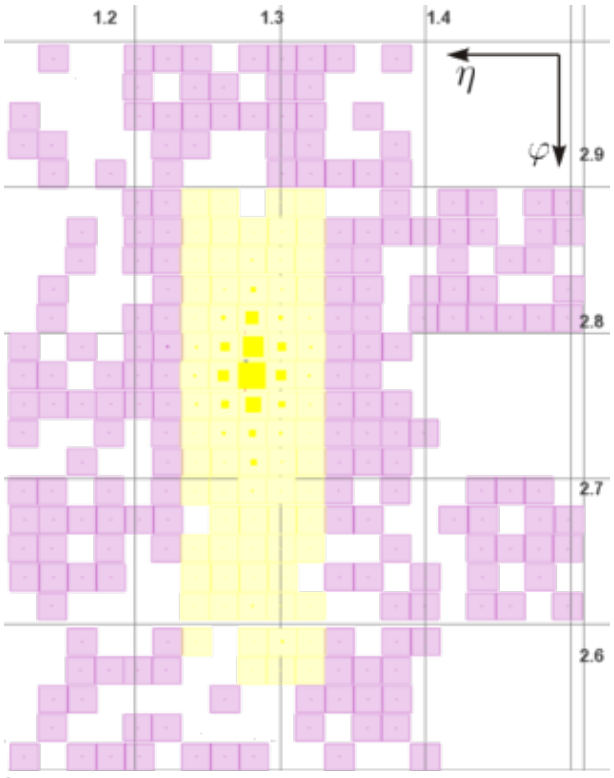

Figure 4.16: An η-ϕ view of a part of the ECAL, with crystals above readout threshold. The crystals inside the supercluster are shown in yellow, unclustered crystals are shown in plum.

The presence of material in front of the calorimeter can cause conversion of photons and Bremsstrahlung from electrons and positrons. Because of the strong magnetic field the energy flow associated to primary electrons or converted primary photons then spreads in ϕ with increasing distances from the collision vertex within the tracker volume. To collect the photon energy in the ECAL, local deposits (adjacent crystals with energy above a certain threshold, so-called "basic clusters") are clustered into superclusters (SC), shown in Figure 4.16, which are extended in ϕ.

Two different cluster algorithms have been designed due to the different mechanical layout of EB and EE and are detailed in Reference [203]. The clustering algorithm used in EB, called the "hybrid" algorithm, searches for different basic clusters along a road 5 crystals wide in η and max. 35 crystals long in ϕ [204]. Figure 4.16 shows such a supercluster, 17 crystals long in η. Superclustering in EE and ES proceeds similarly, but uses a

[4] A distinction between photons and electrons can only be made by placing a tracking device (such as a silicon strip detector: e.g. the preshower detector) in front of the electromagnetic calorimeter. This detector will be able to make a distinction between photons and electrons, because electrons will leave a track, while photons won't.

slightly different algorithm, the "Multi5x5", which adds together fixed 5×5 crystal basic clusters. EE cluster positions are extrapolated to the ES where ES clusters are built. The total endcap basis cluster energy is the sum of cluster energies in EE and ES.

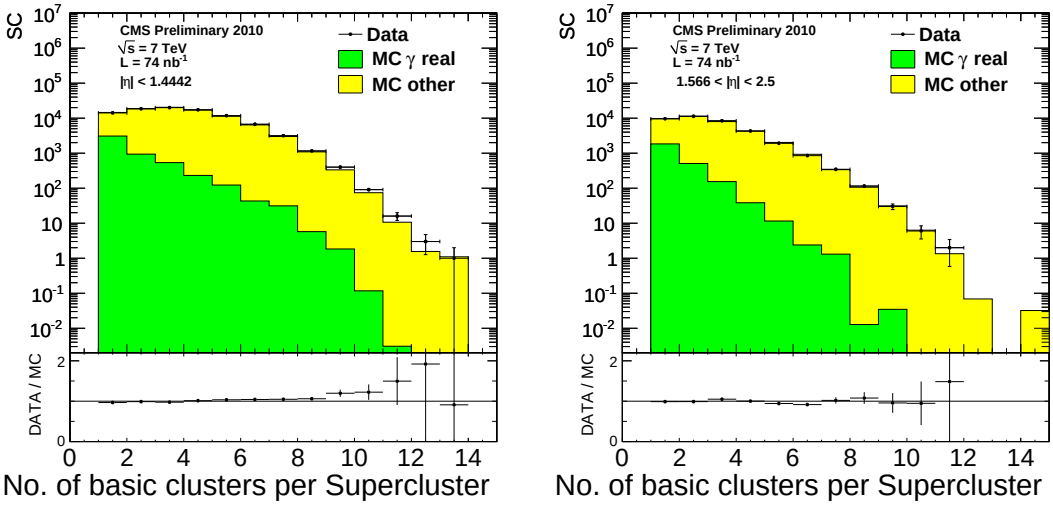

Figure 4.17: Number of basic clusters included in EB (left) and EE (right) superclusters. The Monte-Carlo results are normalized separately for each plot to the number of entries in the data histogram. Figure taken from Reference [202].

Figure 4.17 shows the number of basic clusters included in superclusters for both data and Monte-Carlo simulation. Figure 4.18 shows the distribution of the uncorrected transverse energy of reconstructed superclusters. The supercluster E_T spectrum is well reproduced by the simulation over a wide range. For the Monte-Carlo simulation of the signal and background, two processes generated with Pythia are used: one that contains mostly photons produced in the initial parton interaction, and a second one generated with di-jets that will contain both fragmentation and decay photons. Fragmentation photons are photons radiated at small angle from a parton line, as discussed in section 7.5. Neutral mesons such as π^0 and η decay to two collimated photons. For high energy mesons the opening angle is small such that those two photons will be clustered in the same supercluster, leading to a "fake" photon. Isolated direct and fragmentation photons are treated as signal (indicated as "MC γ real", while all other photons are considered to be background (refered to as "MC other").

4.6.2 Supercluster energy corrections

Energy corrections have been developed using Monte-Carlo simulation to take into account the interactions with the material in front of ECAL and shower containment. The corrections are parametrised as a function of cluster size, E_T and η and are on average 1% [205]. The corrections include following steps:

- To compensate for the η dependence of the lateral energy leakage, arising from the 3° offpointing of the EB crystals. This correction is applied only to EB superclusters.
- A correction to compensate for energy loss due to interactions with material in front of ECAL. Since these interactions spread energy only in the ϕ direction, this loss can be parametrised as function of the ratio of the supercluster size in ϕ to its size in η.

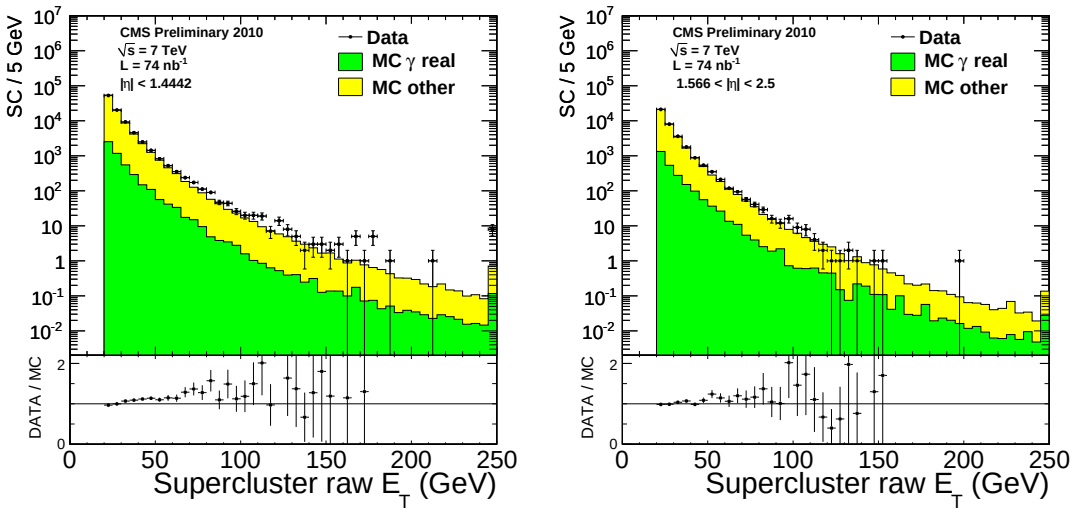

Figure 4.18: Uncorrected transverse energy spectra for EB (left) and EE (right) superclusters. The Monte-Carlo results are normalized separately for each plot to the number of entries in the data histogram. Figure taken from Reference [202].

- A residual correction which is a function of the supercluster E_{T} and η, to compensate for variations along η in the amount of tracker material and the dependence on E_{T} of the Bremsstrahlung and conversion processes.

4.6.3 Photon reconstruction

Photon candidates are reconstructed from the corrected superclusters. The energy (E_γ) of each photon candidate is estimated based on an observable called $r9$, which is the ratio of the energy contained within the 3×3 array of crystals centered on the seed crystal of the photon candidate's supercluster to the total energy contained in the supercluster:

$$r_9 = \frac{E_{3\times3}}{E_{\mathrm{SC}}}. \tag{4.10}$$

The quantity is used to determine if the photon is converted or unconverted. If the $r9$ of the candidate is above 0.94 (0.95) in the barrel (endcap), the photon is unconverted and the energy of the 5×5 crystals around the highest energy crystal is used. Otherwise, the supercluster energy is used. The candidate transverse momentum (p_{T}^{γ}) is calculated with respect to the location of the reconstructed primary vertex. If multiple vertices are reconstructed, the vertex with the largest scalar sum of the transverse momenta of the associated tracks ($\sum p_{\mathrm{T}}$) is selected. The timing of ECAL signals is required to be consistent with that of collision products [206].

On average there is one radiation lenght of material in front of the ECAL. The relatively massive CMS Tracker leads to a large probability of photon conversion and electron Bremsstrahlung radiation in the tracker volume. Conversion finding based on standard tracking [159, 163] optimizes the reconstruction of soft conversions which hardly reach the ECAL. To optimize the reconstruction of converted isolated photons, an ECAL-driven conversion track finding algorithm is used [207]. The conversion reconstruction algorithm combines calorimetric and tracking information to achieve high efficiency throughout the CMS tracker volume.

Conversion candidates are built from superclusters and the constituting basic clusters are used as starting points for an inward conversion track search, using the E_T of basic clusters as an initial guess for the trajectory of the track. If a pair of matching hits are found in the outer three layers of the tracker, they are used to re-evaluate the track parameters. Track finding then proceeds inward, considering the mean energy loss experienced by electrons in the tracker material. Once the inward ECAL-seeded tracks are built, their innermost hits are used as starting points for the other arm of the conversion. Inside-out tracks are then built outwards, again considering the mean energy loss for an electron. The possible combinations of oppositely charged tracks are selected and combined to form conversion candidates. A detailed description of the method is given in Reference [207]. Figure 4.19 shows a detailed view of the superclusters of an unconverted and converted photon.

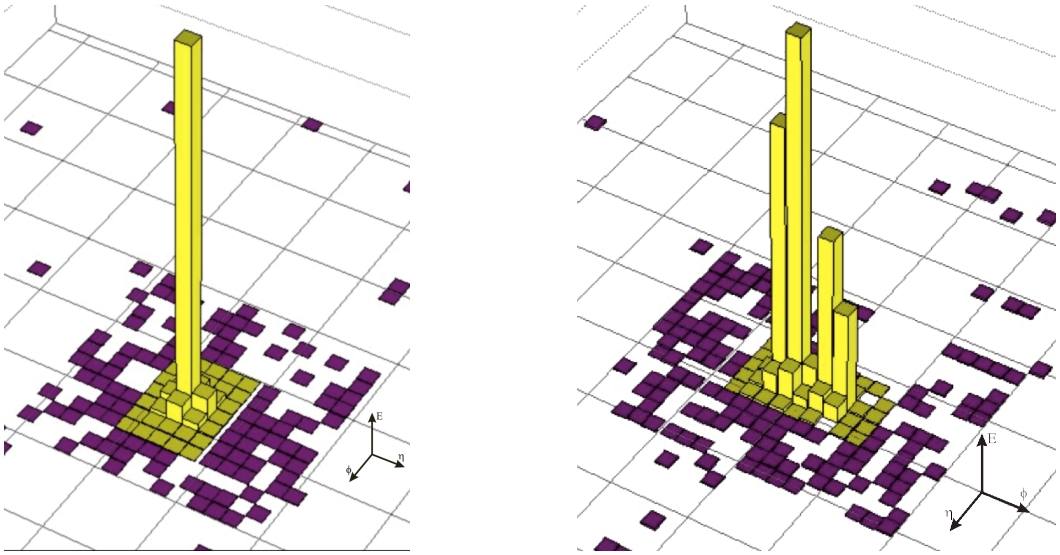

(a) unconverted photon (b) converted photon

Figure 4.19: (a) Detailed view of a photon candidate in event 222 480 885 of run 139 103. Clustered ECAL crystals are shown in yellow, unclustered energy in violet. The candidate has $r9 > 0.94$ and is considered to be unconverted [202]. (b) Detailed view of a photon conversion candidate in event 28 236 360 of run 135 175, the double peak signature is clearly visible.

Photon conversions are characterized by a pair of oppositely charged tracks with small opening angle and consistent with zero invariant mass. Variables that are used to separate the conversion candidates from long-lived particles and vertices from mis-reconstructed tracks are the angular separation measured at the production vertex between the conversion electrons in the transverse plane ($\Delta\phi$) and in the longitudinal plane ($\Delta \cot\theta$), and the χ^2 of the vertex fit. Figure 4.20 shows the relevant distributions for the raw conversion candidates before any additional selection is performed. The selection then requires $|\Delta\phi| < 0.2$, $|\Delta \cot\theta| < 0.3$ and a valid vertex with χ^2 probability greater than 5×10^{-4}.

4.6.4 Photon Identification

The sample of reconstructed photons contains a large background due to π^0 and η mesons decaying to two photons. As can be seen from Figures 4.17 and 4.18, "fake" photons from meson decay prevail over the prompt photons at more than one order of magnitude if no additional

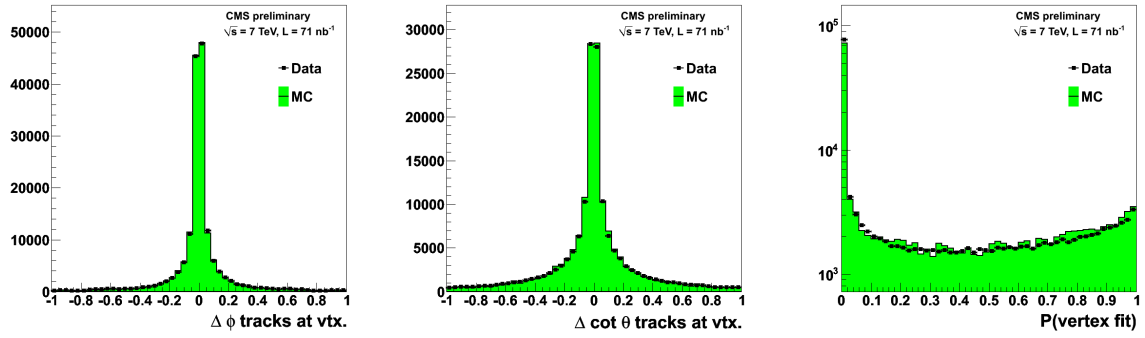

(a) (b) (c)

Figure 4.20: Angular separation between the conversion electrons measured in the longitudinal plane (a) and in the transverse plane (b). χ^2 probability for the conversion vertex fit (c).

identification criteria are required. To increase the purity of the photon sample, additional isolation and identification requirements were applied. The selection criteria and cut values have been adjusted on the basis of Monte-Carlo simulation [204], in absence of a data-driven control sample, aiming to maximize the background rejection while keeping the efficiency flat as a function of η and E_{T}. This is a robust selection, intended to be used for commissioning and early data analysis. This isolation scheme is – by design – very similar to the isolation scheme used for electrons, such that photon identification efficiencies can be measured on an electron control sample in data. The photon selection is based on the following variables [188]:

- **H/E**: The fraction of hadronic over electromagnetic energy inside a cone of $\Delta R = 0.15$ around the photon;
- **Showershape** in η direction: $\sigma_{\eta\eta}$[5] is the transverse shape of the electromagnetic cluster computed as:

$$\sigma^2_{\eta\eta} = \frac{\sum_{k=1}^{25} w_k(\eta_k - \bar{\eta})^2}{\sum_{k=1}^{25} w_k}, \quad w_k = \max(0, 4.7 + \ln(\frac{E_k}{E})), \tag{4.11}$$

  where η_k and E_k are the pseudorapidity and the energy of the k^{th} crystal within the 5×5 group of crystals centred on the one with the highest energy. E is the total energy of the group and $\bar{\eta}$ the average η weighted by w_k in the same group.

  For calorimeters which are segmented in the lateral direction, weighting with log energy gives an unbiased estimate of the ECAL position of the supercluster, as opposed to a simple energy weight, which would yield a position biased towards the core of the shower [210].
- **Tracker Isolation ($\mathbf{Iso_{TRK}}$)** is computed as the sum of the tracks in a hollow cone in

[5] In the CMSSW software, both $\sigma_{i\eta i\eta}$ and $\sigma_{\eta\eta}$ are defined. Here the notation $\sigma_{\eta\eta}$ is used to refer to the $\sigma_{i\eta i\eta}$ variable, to avoid confusion for people not familiar with the photon object in CMS, since this notation is also used in the first CMS paper describing the photon reconstruction: Reference [208]. The difference between $\sigma_{i\eta i\eta}$ and $\sigma_{\eta\eta}$ in the CMSSW software is that the calculation of $\sigma_{i\eta i\eta}$ is based on the use of the crystal index $\hat{\eta}_i$ of crystal i: $\eta_i = \hat{\eta}_i \times \delta\eta$, $\delta\eta = 0.0174$, where $\sigma_{\eta\eta}$ uses the CMS geometry to determine the position of the crystals. In the photon identification $\sigma_{i\eta i\eta}$ is used to describe the showershape, since it is more regular across the different boundaries within the ECAL. More details can be found in the detailed technical break out of the photon object [209].

the tracker. A strip[6] $2\Delta\eta \times 2\Delta\varphi$ is excluded from the sum to avoid misidentification of converted photons. Only tracks with a transverse (longitudinal) impact parameter < 0.1 (0.2) cm with respect to the photon vertex are summed in the Tracker Isolation sum. The values of the cone radii and strip lengths are defined in Table 4.1 while the cone geometry is sketched in Figure 4.21.

- **Ecal Isolation ($\mathbf{Iso_{ECAL}}$)** is computed as the sum of the transverse energy deposits inside a hollow cone in the electromagnetic calorimeter. A strip $2\Delta\eta \times 2\Delta\varphi$ is excluded to avoid misidentification of converted photons. This allows us to define exactly the same isolation cones for electrons and photons, although the former can emit Bremsstrahlung and the latter can convert into an e^+e^- pair. This allow for the use of $Z(ee)$ events as a source of pure photons at the level of the calorimeter.
- **Hcal Isolation ($\mathbf{Iso_{HCAL}}$)** is computed as the sum of the transverse energy in a hollow cone of the hadron calorimeter.

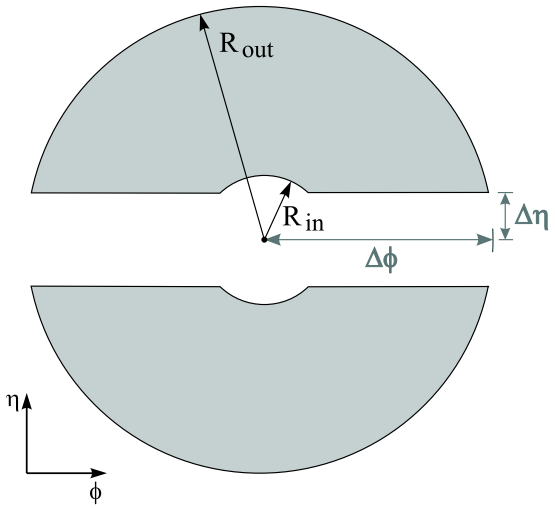

Figure 4.21: Sketch illustrating the isolation cones for the ECAL- and HCAL-E_T and Tracker-p_T deposits.

Table 4.1: Values of the Photon Identification Variables [212].

	R_{out}	R_{in}	$\Delta\eta$	$\Delta\varphi$	`reco::Photon` method
Iso_{TRK}	0.4	0.04	0.015	0.4	`trkSumPtHollowConeDR04`
Iso_{ECAL}	0.4	0.0609 (3.5 crystals)	0.0435 (2.5 crystals)	0.4	`ecalRecHitSumEtConeDR04`
Iso_{HCAL}	0.4	0.15	-	-	`hcalTowerSumEtConeDR04`
H/E	0.15	-	-	-	`hadronicOverEm`

Currently four different Photon Identifications exist, all based on the variables defined above. The Loose and Tight Identification are the "vanilla" Identification, the former with a high efficiency ($\sim 90\,\%$) and minimal impact on the systematics, the latter with a more powerful background rejection and hence higher purity and relatively high efficiency ($\sim 70\,\%$) [213]. The photon identification for the QCD Photon production cross section measurement differs from the Loose Identification in the isolation variables in the Tracker, ECAL and HCAL, where a

[6] In CMSSW the strip excluded from the isolation cone is implemented by variables denoting half of the strip width $\Delta\eta$, and half of the strip length $\Delta\varphi$ [211].

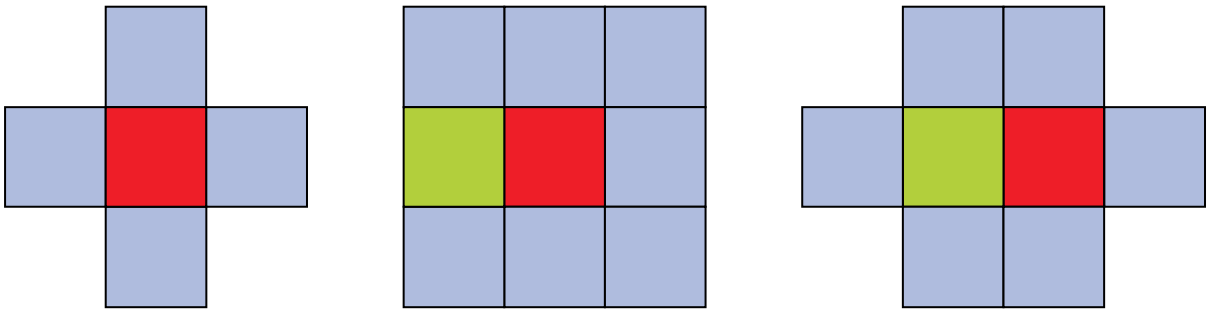

(a) E_1/E_4 (b) E_2/E_9 (c) E_2/E_6

Figure 4.22: Illustration of the topological cleaning variables: the "Swiss Cross" (left), E_2/E_9 (middle) and E_2/E_6 (right). The highest energy crystal (seed crystal) is shown in red, the next-highest in green.

factor relative to the photon p_T is allowed. This relative isolation is the one used in this thesis. Further identifications were defined for searches in CMS looking for high energetic photons. The factors relative to the photon p_T were added to obtain flat identification efficiencies for high p_T γ. A fifth definition was designed for the $H \to \gamma\gamma$ decay, meeting the needs of a very strong background rejection, since this is one of the most challenging diphoton searches performed at relatively low energy. The values for the Isolation Variables for the four Photon Identities are tabulated in Table 4.2.

Table 4.2: Different photon identification criteria in CMS.

Variable	Loose		Tight		QCD		Exotica / SUSY		$H \to \gamma\gamma$	
	Barrel	Endcap	Barrel	Endcap	Barrel	Endcap	Barrel	Endcap	Barrel	Endcap
pixel seed	require none		require none		require none		require none		require none	
Iso_{TRK}	$< 2.0\,\text{GeV}$		$< 0.9\,\text{GeV}$		$< 2.0\,\text{GeV} + 0.001\times p_T^\gamma$		$< 2.0\,\text{GeV} + 0.0010\times p_T^\gamma$		$< 1.5\,\text{GeV} + 0.0010\times p_T^\gamma$	
Iso_{ECAL}	$< 4.2\,\text{GeV}$		$< 2.4\,\text{GeV}$		$< 4.2\,\text{GeV} + 0.003\times p_T^\gamma$		$< 4.2\,\text{GeV} + 0.0060\times p_T^\gamma$		$< 2.0\,\text{GeV} + 0.0060\times p_T^\gamma$	
Iso_{HCAL}	$< 2.2\,\text{GeV}$		$< 1.0\,\text{GeV}$		$< 2.2\,\text{GeV} + 0.001\times p_T^\gamma$		$< 2.2\,\text{GeV} + 0.0025\times p_T^\gamma$		$< 2.0\,\text{GeV} + 0.0025\times p_T^\gamma$	
H/E	< 0.05		< 0.03		< 0.05		< 0.05		< 0.02	
$\sigma_{i\eta i\eta}$	< 0.01	< 0.03	< 0.01	< 0.028	< 0.01	< 0.03	< 0.013	< 0.03	< 0.01	< 0.028

4.6.5 Cleaning of anomalous energy deposits

Possible anomalous signals in ECAL are a source of background in the selected photon sample. A detailed description of this phenomenon, which occurs only in the barrel detector, can be found in Reference [187, 214]. At reconstruction level, anomalous calorimeter signals, "spikes", are rejected by the "Swiss Cross" topological cleaning shown in Figure 4.22(a). The sum of the energy in the four adjacent crystals surrounding the central crystal should be at least 5% of the central crystal's energy: $(1 - E_4/E_1) < 0.95$ and the central crystals' energy should exceed 3 GeV. Figure 4.23 shows the distribution of the quantity $(1 - E_4/E_1)$ for data and simulation for the channel with the highest reconstructed energy ($E > 3\,\text{GeV}$) in each event. The unphysical peak near 1 are the spikes and are only visible in data and are not described by the detailed Monte-Carlo simulation. A cut on $(1 - E_4/E_1) < 0.95$ removes most of the spikes.

Although this selection removes a large fraction of the anomalous events, a small fraction of spikes remains. The residual spike contribution was tackled using the reconstruction time of the most energetic crystal in the supercluster (t_{seed}) and the E_2/E_9 variable, shown in Figure 4.22(b). The latter is defined as the ratio of the sum of the energy of the most energetic crystal and its

highest energy neigbour crystal over the sum of the energy in the nine-crystal (3×3) region around the most energetic crystal. Figure 4.24 shows the scatter plot of the reconstructed time of the most energetic crystal in the supercluster (t_{seed}) vs. the E_2/E_9 variable.

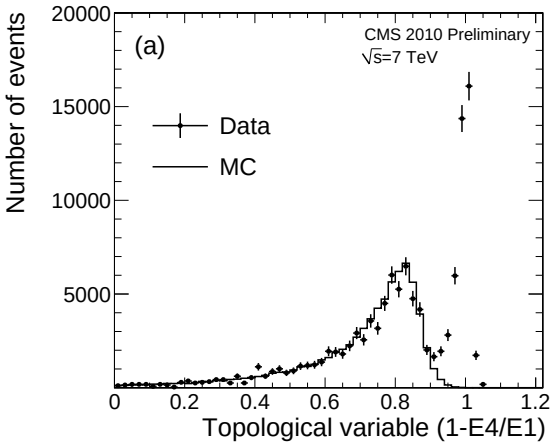

Figure 4.23: Distribution of the "Swiss Cross" topological variable ($1 - E_4/E_1$) for data and simulation. Only deposits with $E_{\text{T}} > 3\,\text{GeV}$ are plotted [187].

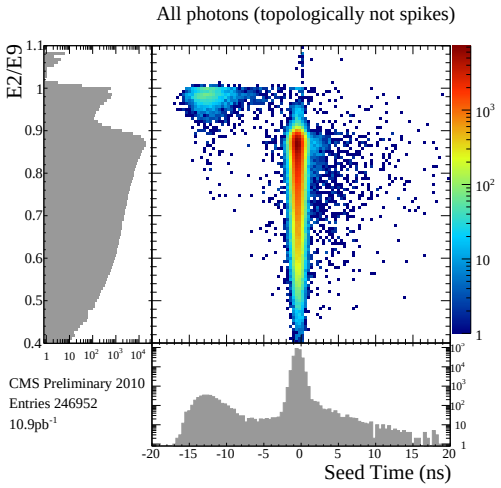

Figure 4.24: The scatter plot of the measured seed crystal timing (t_{seed}) and the E_2/E_9 variable, for photon candidates with $E_{\text{T}} > 3\,\text{GeV}$ and "Swiss cross" topological cleaning applied [188].

The seed time of the cluster is required to be $|t_{\text{seed}}| < t_0$ (where $t_0 \approx 3.6\,\text{ns}$ is the amplitude dependent parameter which corresponds to 5σ of the ECAL time resolution) for seed energies of $E_1 < 130$ GeV. For higher energies ($E_1 \geq 130$ GeV) $t_{\text{seed}} > 0$ is requested, since the time reconstruction is biased due to a non-linear response of the ECAL electronics in case of a gain switch. E_2/E_9 is required to be lower than 0.95, which allows for a slightly stronger spike-rejection [215] than the $\sigma_{i\eta i\eta}$ and $\sigma_{i\phi i\phi} > 0.001$ requirements used in [188, 216]. In 2011 data the E_2/E_6 variable, shown in Figure 4.22(c) will be used, since it has even stronger spike-rejection capabilities than E_2/E_9 [217, 218].

The seed time of the cluster and $(\sigma_{i\eta i\eta}, \sigma_{i\phi i\phi})$ are used to estimate the remaining spike contamination with a so-called "ABCD-method" shown in Figure 4.25, which is detailed in References [188, 215]. Figure 4.25 shows the seed crystal timing distribution measured in $10.9\,\text{pb}^{-1}$ of data (indicated with the black line). Applying the topological cut $(\sigma_{i\eta i\eta}, \sigma_{i\phi i\phi}) > 0.001$ (indicated with the orange line) removes most of the spikes, but a "shoulder" with negative crystal seed times remains. This shoulder is estimated from the distribution without the topological cut (shown as the blue solid line). Scaling down this distribution to the candidates with the topological cut in the range of $[-12\,\text{ns}, -7\,\text{ns}]$ (indicated with the blue dashed line) reveals an estimation of the spikes in the photon candidates sample defined by $(\sigma_{i\eta i\eta}, \sigma_{i\phi i\phi}) > 0.001$ and $t > -3.5\,\text{ns}$. The remaining contribution of spikes is 75.3 ± 2.7 events, corresponding to $0.0305 \pm 0.0011\%$. Applying the same procedure but using the $E_2/E_9 < 0.95$ topological cut instead, the remaining contribution of spikes is 33.3 ± 1.8 events, corresponding to $0.0137 \pm 0.0007\%$ [215]. The latter topological cut is used in the jets-plus-$\not{E}_{\text{T}}$ analysis presented in chapters 6, 7, and 8.

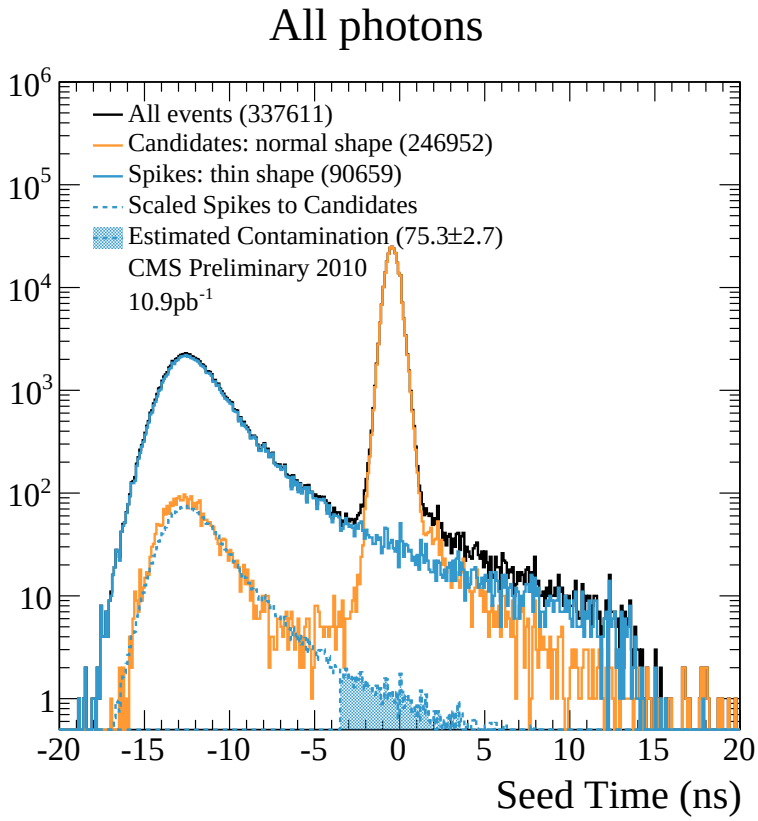

Figure 4.25: Distribution of the measured seed crystal timing (t_{seed}) for all photon candidates are shown by the black solid line, photon candidates with topological cut $(\sigma_{i\eta i\eta}, \sigma_{i\phi i\phi}) > 0.001$ are shown by the orange solid line. "Spikes" are selected by requiring $\sigma_{i\eta i\eta}$ or $\sigma_{i\phi i\phi} < 0.001$ and are indicated by the solid blue line. This blue line is scaled down to the distribution of candidates that passed the topological cut in the range $[-12\,\text{ns}, -7\,\text{ns}]$. The filled histogram shows the estimated contamination in the photon candidates sample with $(\sigma_{i\eta i\eta}, \sigma_{i\phi i\phi}) > 0.001$ above $t > -3.5\,\text{ns}$ [188, 215].

4.7 Leptons

The detection of charged leptons is very important at hadron colliders, since they are typically produced in events with large momentum transfer, such as W- and Z-production, and in the production of heavier (new?) states decaying through W- and Z-particles. Charged leptons come in three flavours: e, μ and τ, which have a very different mass scale, spanning more than three orders of magnitude: 511 keV, 105 MeV and 1.8 GeV, leading to very different signatures inside the CMS detector.

Although the analysis presented here is a jets-plus-$\not{E}_{\text{T}}$ based search, leptons are used in this analysis to veto events from W- and Z-decays and to create background control regions. The use of leptons in the analysis is discussed in chapter 6, while a brief summary of their reconstruction is presented here.

4.7.1 Electrons

The signature of electrons inside CMS consists of a track matched to an electromagnetic cluster. Figure 4.26 shows an event with 4 electrons, represented as four red tracks pointing to four electromagnetic clusters. Electron tracks are reconstructed using an algorithm that accounts for possible energy loss due to Bremsstrahlung in the tracker layers [219] and is based on a Gaussian Sum Filter (GSF) [220]. The electron reconstruction uses two complementary algorithms at the track seeding stage: "Tracker-driven" seeding, more suitable for low-p_{T} electrons and electrons inside jets, and the "ECAL-driven" seeding [221]. The latter starts with the reconstruction of ECAL superclusters with $E_{\mathrm{T}} > 4\,\mathrm{GeV}$ and is optimized for isolated electrons from W and Z decays [221]. Above 20 GeV, the energy resolution of the electron is essentially determined by the ECAL cluster energy, while the momentum direction is determined by the p_{T} of the reconstructed track [219]. Particles misidentified as electrons are suppressed by requiring a tight match between the η- and ϕ-coordinates of the track trajectory extrapolated to the ECAL surface and the η- and ϕ-coordinates of the ECAL cluster, and also by limiting the HCAL energy measured around the ECAL cluster. Electrons from converted photons are suppressed by requiring the track to have a hit in the innermost pixel layer. Furthermore, if there is a "partner-track" to the electron track consistent with a photon conversion, based on the opening angle and the separation in the transverse plane, the electron is also rejected [221].

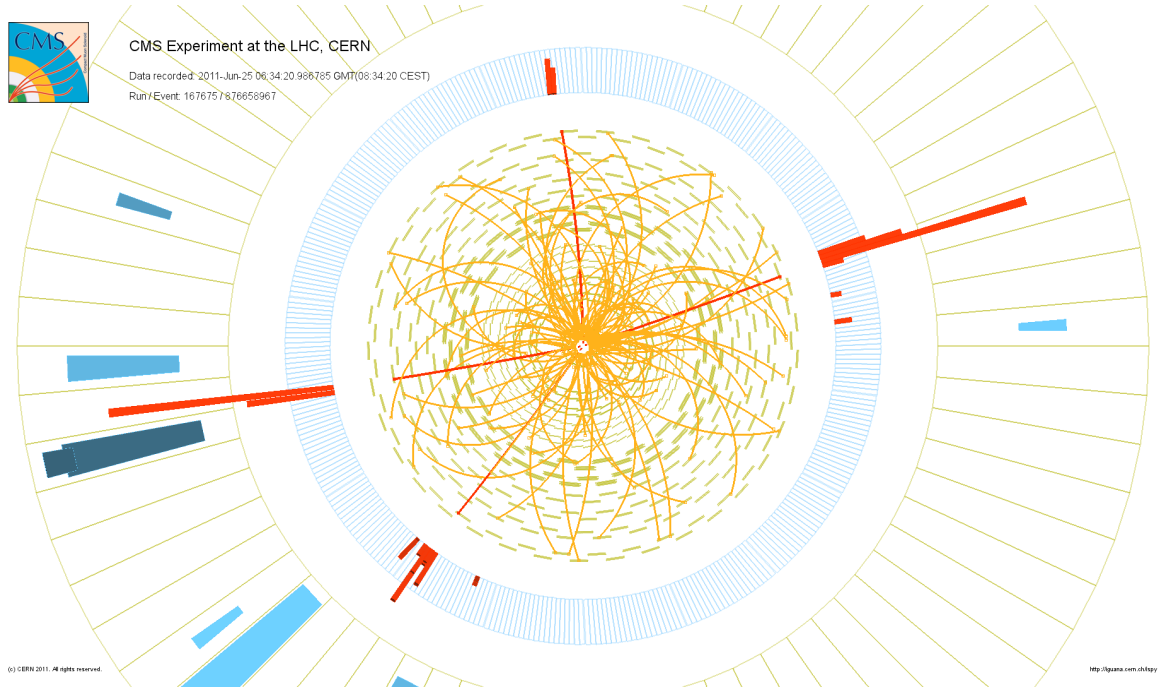

Figure 4.26: Event display of a $ZZ \rightarrow 4e$-candidate of event 876 658 967 recorded in run 167 675. Tracks are reconstructed in the tracker (inner circle), which is surrounded by the electromagnetic calorimeter (with fine segmentation) and the hadron calorimeter (outer ring).

4.7.2 Muons

The muon detector elements, discussed in section 3.2, cover the full pseudorapidity interval $|\eta| < 2.4$ with no acceptance gaps, ensuring good muon identification over a range corresponding to $10^\circ < \theta < 170^\circ$. Offline reconstruction efficiency for the muons is typically 96%–99%. Because

of the large amount of material before the first muon station, punch-through of $\pi^{\pm}$ and $K^{\pm}$ (in jets) is small.

For muons with momentum below 200–300 GeV/c the spatial resolution is dominated by the large multiple scattering caused by the steel, combined with the effects of the complicated magnetic field in the endcaps. This environment intrinsically limits the spatial resolution. The best resolution is obtained by the central tracker, after matching with muon data. At higher values of p_{T} the muon chamber resolution allows the muon and tracker system data to be combined, exploiting the full bending of the CMS central solenoid to achieve the ultimate performance in the TeV/c region. The geometry of CMS has a deep influence on the performance of the muon system. The changing direction of the magnetic field in the return yoke causes the curvature of the muon trajectory to reverse. Therefore, the first muon detector stations (ME1, MB1) in both the barrel and endcap regions are critical, and provide the largest sagitta and, hence, the most important contribution to the measurement of muon momentum up to momenta of a few hundred GeV/c. For higher momenta the role of the outer stations increases as multiple scattering effects become less important.

In standard CMS reconstruction for pp collisions, tracks are first reconstructed independently in the silicon tracker (**tracker track**) and in the muon spectrometer (**stand-alone-muon track**). Based on these, two reconstruction approaches are used [222], while dedicated methods exist for high-p_{T} muons.

1. **Global Muon reconstruction (outside-in):** starting from a *stand-alone-muon track* in the muon system, a matching tracker track is found and a *global-muon track* is fitted combining hits from the tracker track and stand-alone-muon track. At large transverse momenta ($p_{\mathrm{T}} \gtrsim 200$ GeV/c), the global-muon fit can improve the momentum resolution compared to the tracker-only fit [144, 222, 223].

2. **Tracker Muon reconstruction (inside-out):** in this approach, all tracker tracks with $p_{\mathrm{T}} > 0.5$ GeV/c and $p > 2.5$ GeV/c are considered as possible muon candidates and are extrapolated to the muon system, taking into account the expected energy loss and the uncertainty due to multiple scattering. If at least one muon segment (i.e. a short track stub made of DT or CSC hits) matches the extrapolated track, the corresponding tracker track qualifies as a *tracker-muon track*. At low momentum (roughly $p < 5$ GeV/c) this approach is more efficient than the global muon reconstruction, since it requires only a single muon segment in the muon system, whereas global muon reconstruction is designed to have high efficiency for muons penetrating more than one muon station [222].

The majority of muons from collisions (with sufficient momentum) are reconstructed either as a global muon or a tracker muon, and very often as both. However, if both approaches fail and only a **stand-alone-muon track** is found, this leads to a third category of muon candidates:

3. **Standalone-muon track only**: this occurs only for about 1% of muons from collisions, thanks to the high tracker-track efficiency [224]. On the other hand, the acceptance of this type of muon track for cosmic-ray muons is a factor 10^2 to 10^3 larger, thus leading to a collision muon to cosmic-ray muon ratio that is a factor 10^4 to 10^5 less favourable than for the previous two muon categories. These cosmic muons are recorded in runs without beam to test the detector [222].

The results of these three algorithms are merged into a single collection of muon candidates, each one containing information from the standalone, tracker, and global fit, when available. Candidates found both by the tracker muon and the global muon approach that share the same tracker track are merged into a single candidate. Similarly, standalone-muon tracks not included in a global muon are merged with a tracker muon if they share a muon segment. The combination of different algorithms provides a robust and efficient muon reconstruction. The expected muon momentum resolution when using either only the muon system, or only the inner tracker, or using both sub-detectors is shown in Figure 4.27 for both simulation (in barrel and endcap) [131] and cosmic ray muon data (only in barrel) [222]. The momentum resolution is dominated by the tracking system up to $\sim$ 100 GeV/c, at higher momenta the muon system contributes as well. Up to 1 TeV the muon momentum resolution stays below 10%.

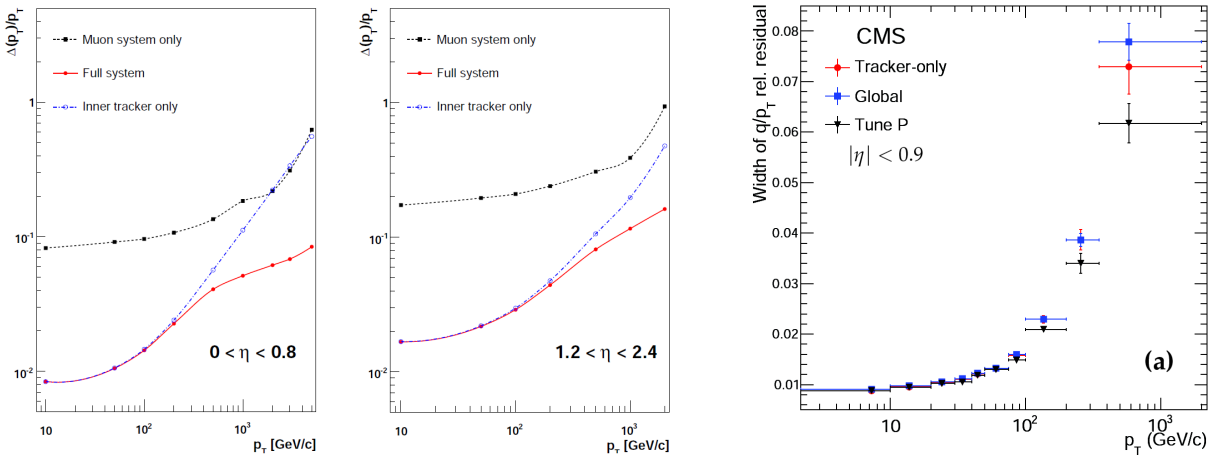

Figure 4.27: Left and Middle: The muon transverse momentum resolution obtained in simulation, as a function of the transverse momentum, p_{T}, using the muon system only, the inner tracking only, or both, for $0 < |\eta| < 0.8$ (left) and $1.2 < |\eta| < 2.4$ (middle) [131]. Right: Muon resolution for tracker-only, for a global fit and for a dedicated "Tune-P" algorithm described in Reference [222], as a function of the transverse momentum p_{T}, obtained from cosmic ray muon data [222]. Figures taken from Reference [131, 222].

4.7.3 Taus

The τ lepton is the charged lepton of the third generation and has the largest lepton mass, making it an important player in the searches for the standard model (SM) Higgs boson, especially in the mass region below two times the W-boson mass [225]. Models of new physics also predict increased couplings to the third-generation charged fermions. Lepton universality ensures that one third of W and Z-boson leptonic decays give rise to τ leptons. When measuring rare processes, this contribution becomes substantial, making a strong case for the development of τ-reconstruction and identification.

The τ lepton has a short lifetime, 0.29 ps, leading to a $c\tau = 87.11\,\mu$m. The τ lepton can decay either into purely leptonic final states: $\tau \rightarrow e\bar{\nu}_e\nu_\tau$ or $\tau \rightarrow \mu\bar{\nu}_\mu\nu_\tau$, or into hadronic final states denoted by "τ_{h}", consisting of a hadronic system and a ν_τ. Constrained by the τ mass, 1776.84 ± 0.17 MeV/c^2, the hadronic system is characterized by a low particle multiplicity and a highly collimated jet which allows a τ_{h} signal to be separated from the large QCD jet backgrounds [226]. In two thirds of the cases, τ leptons decay hadronically, typically in one or three charged

mesons (predominantly π^+, π^-), often accompagnied by neutral pions (decaying via $\pi^0 \to \gamma\gamma$), and a ν_τ [225]. Figure 4.28 illustrates both the leptonic and the hadronic decay of τ leptons. Table 4.3 gives a rough overview of the branching ratios of the different τ decays. The h stands for both π and K hadrons, but in the τ reconstruction, the π mass is always assigned since it is the dominant charged particle [5, 225].

Table 4.3: Branching Ratio (BR) of the leptonic and the dominant hadronic decays of the τ lepton [5, 225].

Decay mode	BR[%]
$\tau \to e\bar{\nu}_e\nu_\tau$	17.9%
$\tau \to \mu\bar{\nu}_\mu\nu_\tau$	17.4%
$\tau \to h^-\nu_\tau$	11.6%
$\tau \to h^-\pi^0\nu_\tau$	26.0%
$\tau \to h^-\pi^0\pi^0\nu_\tau$	9.5%
$\tau \to h^-h^+h^-\nu_\tau$	9.8%
$\tau \to h^-h^+h^-\pi^0\nu_\tau$	4.8%
Other	3.0%
Total leptonic	35.3%
Total hadronic	64.7%

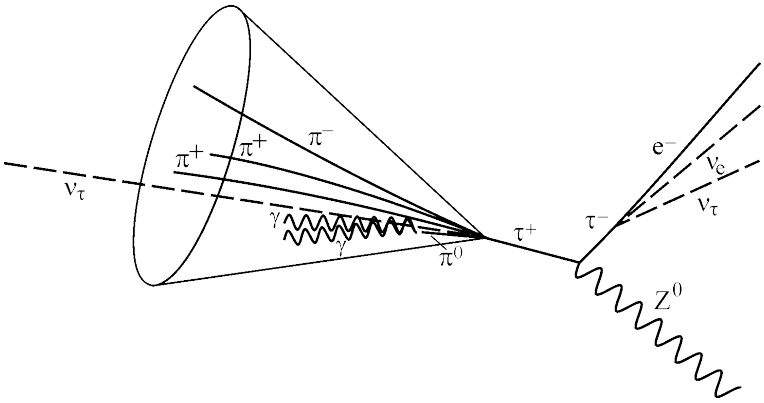

Figure 4.28: Illustration of a semi-hadronic $Z^0 \to \tau^+\tau^-$ decay. The τ^--lepton decays leptonically to an electron and two neutrino's. The τ^+-lepton decays hadronically to $\pi^0\pi^+\pi^-\pi^+$ and a neutrino. Figure adapted from Reference [227].

Unlike at LEP, where the centre-of-mass of a collision was precisely known, and hence muons and electrons from τ decays were identified as leptons whose p_T sum is smaller than the centre-of-mass energy, the leptonic τ decay cannot be identified at LHC. The $Z \to \tau^+\tau^-$ measurement [226] uses a multivariate likelihood ratio technique based upon, amongst others, the distance of the closest approach between the two muon tracks, to suppress the Drell-Yan background $Z/\gamma^* \to \mu^+\mu^-$. Muons from Drell-Yan events should point back to the same primary vertex, while muons from τ-decays should be displaced from the primary vertex, since the τ has a short lifetime.

Thanks to the excellent particle-flow reconstruction, hadronic taus can be reconstructed at CMS. CMS has developed two algorithms for identifying τ_h decays, based on the classification of the τ_h decay channels through the reconstruction of intermediate resonances: the Tau Neural Classifier (TaNC) and the Hadron Plus Strips (HPS) algorithms [225]. Both algorithms start the reconstruction of a τ_h candidate from a PF jet, whose four-momentum is reconstructed using the algorithm with a distance parameter $R = 0.5$. Using a PF jet as an initial seed, the algorithms first reconstruct the π^0 components of the τ_h, then combine them with charged hadrons to reconstruct the tau decay mode and finally calculate the tau four-momentum and isolation quantities [225].

Figure 4.29 shows the signal shapes and background yields for the mass distributions of the $\tau_\mu\tau_\mathrm{h}$, $\tau_e\tau_\mathrm{h}$, $\tau_\mu\tau_e$ and $\tau_\mu\tau_\mu$ final states of Z-boson decay. The identified lepton in the semi-leptonic channel helps to identify the hadronic tau decay. The opposite-flavor channel is the most pure, while discriminating the $\tau_\mu\tau_\mu$ final state from the Drell-Yan $Z/\gamma^* \to \mu^+\mu^-$ is clearly challenging. No attempts are made to also discover the $\tau_e\tau_e$ and $\tau_\mathrm{h}\tau_\mathrm{h}$ final states, since they are experimentally unaccesible with the current techniques. Note that the visible mass distributions peak below the Z-boson mass, since one or two neutrino's can have a non-negligible p_T. The $\tau_e\tau_\mathrm{h}$ final state

shows a clear contamination of $Z/\gamma^* \rightarrow e^+e^-$, where one of the electrons is mis-identified as a jet. This contamination pops up at the Z mass, indicating that no neutrino's participate in the subsequent decay of the Z-boson decay products. The plots demonstrate the capability of the CMS detector to correctly reconstruct and identify the very difficult final state signature of the τ-decays.

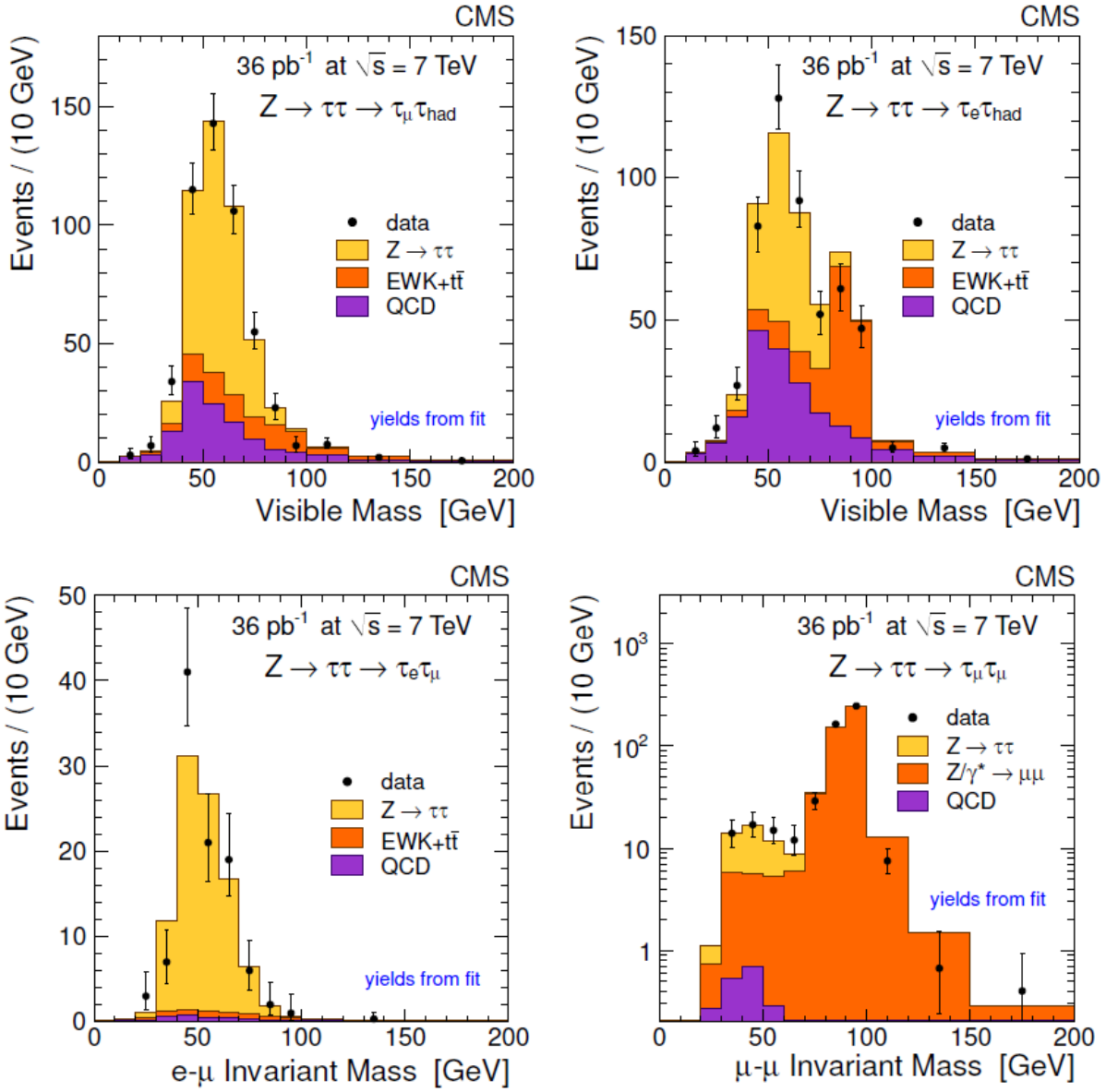

Figure 4.29: Visible mass distributions of the $\tau_\mu\tau_h$ (top left), $\tau_e\tau_h$ (top right), $\tau_\mu\tau_e$ (bottom left) and $\tau_\mu\tau_\mu$ (bottom right) final states [226].

CMS is able to reconstruct and identify the three charged leptons very well. This is very important since they are an important signature of events with large momentum transfer. In conclusion the event reconstruction of CMS as a whole is working very well and the reconstructed events, consisting of charged leptons, photons, jets and missing energy, can be used to measure Standard Model physics processes or search for new particles in, for instance, the jets-plus-$\not\!\!E_T$ channel as described in chapters 6, 7, and 8.

Part II

Detector Work

Chapter 5

RPC Upgrade Simulation Studies

Figure 5.1 shows a R–Z cross-section[1] of a quadrant of the present CMS detector. Compared to the detector foreseen in the Technical Design Report [138], the fourth muon station is not fully installed. The CSC detectors of the fourth station close to the beam line (ME4/1) are installed, but the CSCs at higher distance (ME4/2) are not. Also the RPC system is far from complete. Only three layers (in green) were built and installed on both endcaps. The fourth layer is missing. Furthermore, the RPC detectors are only installed up to a pseudorapidity of $|\eta| \leq 1.6$, while the original design included RPCs up to $|\eta| \leq 2.1$.

Due to financial reasons, the high-η chambers and all chambers of the fourth station were "descoped" (i.e. removed from the installation schedule). The RPC-system installed was restricted to the minimum necessary for the first years of low luminosity running of the LHC. Furthermore, it was not certain if the RPC technology would be able to withstand the high rates expected at $1.6 \leq |\eta| \leq 2.1$. For the $|\eta| \leq 1.6$ region, the RPC technology has been subjected to extensive tests for several years, in order to validate the RPC technology, gas mixture and operational characteristics. The RPCs have proved to be a mature technology for particle rates $\leq 10\,\mathrm{Hz/cm^2}$. For the high-$\eta$ region of the muon system, however, much higher particle rates are expected. Although RPCs might be able to handle rates as high as $1\,\mathrm{kHz/cm^2}$, ageing issues due to the high amount of deposited charge on components of the detectors could severely shorten its lifetime. Therefore dedicated studies are pursuing micro pattern gas detectors (MPGDs), and these seem to be a promising technology to instrument the forward region of the muon system of CMS ($1.6 \leq \eta \leq 2.1$). Installing detectors with these, or similar, technology is only envisaged during Phase-II of the Upgrade, scheduled currently to be later than 2021.

In the past, a modification to the RPC design in CMS was proposed to enhance the trigger efficiency and lower the trigger rate [228] in the endcaps of the RPC system. Installing five layers instead of four would yield more or less the same trigger efficiency by requiring 4-out-of-5 coincidences instead of 3-out-of-4 coincidences, but would provide a better measurement of the transverse momentum and would be less vulnerable to "fake" muons. In this way the trigger rate could be lowered sufficiently. Unfortunately, an independent fifth layer was not feasible in the endcap, but the idea was modified to a double second station, where one could reduce the fake rate by asking for coinciding hits.

The effect of such a modified geometry is studied with respect to the original geometry described in the TDR. In the first section, the working principle of the RPC detectors is explained,

[1] With R the polar coordinate $R := \sqrt{x^2 + y^2}$ instead of the spherical coordinate $r := \sqrt{x^2 + y^2 + z^2}$. For the longitudinal coordinate z, both upper-case and lower-case letters are used.

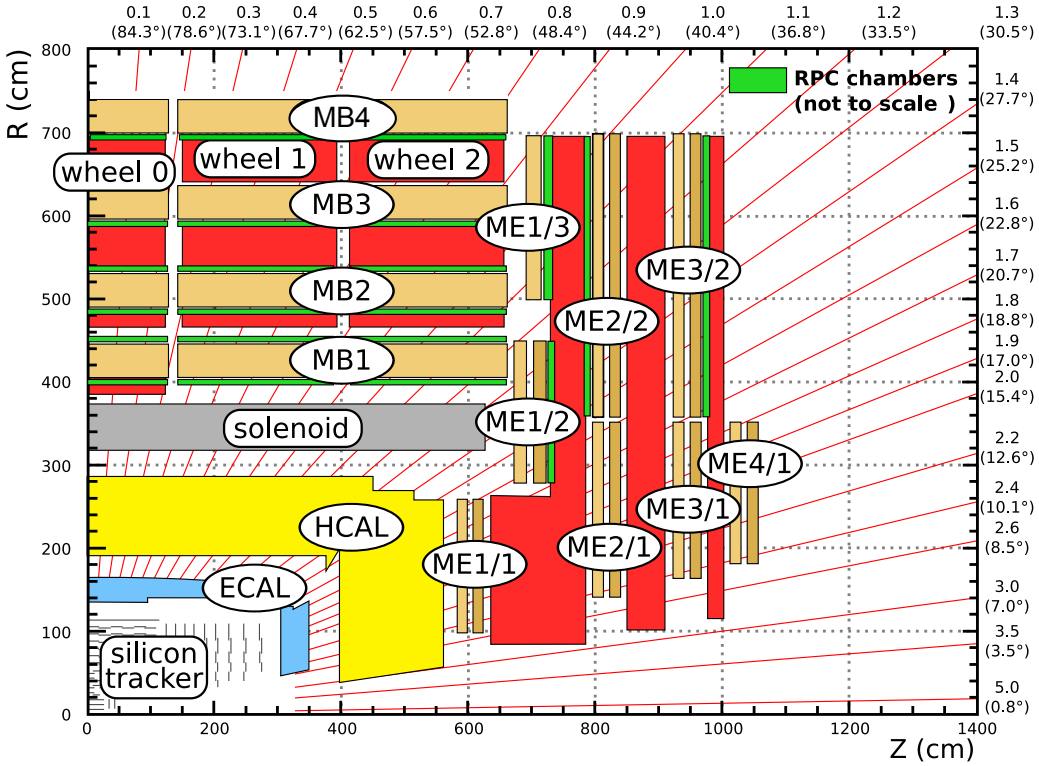

Figure 5.1: An R–Z cross-section of a quadrant of the CMS detector with the axis parallel to the beam (z) running horizontally and radius (r) increasing upward. Lines of constant-η are also shown, the η-values (and the equivalent θ-angles) are shown at the top and right. The interaction region is at the lower left corner. Shown are the locations of the various muon stations and the steel disks (red areas). The four drift tube (DT) stations are labeled MB ("muon barrel") and the cathode strip chambers (CSC) are labeled ME ("muon endcap"). Resistive plate chambers (RPC, in green) are in both the barrel and the endcaps of CMS [153].

followed by the discussion of the RPCs inside CMS and their ability to trigger muons. Thereafter the backgrounds to muon detection are discussed in detail. Sections four and five discuss the simulation of the RPC detectors within CMS and discuss the performance of the RPC trigger for several possible geometries.

5.1 RPC working principle

Resistive Plate Chambers (RPCs) were developed [229, 230] as a low cost alternative to fast, large area scintillator detectors by Santonico and Cardarelli and proposed [231] and investigated [232] as a fast "tracking" L1 muon trigger for the LHC experiments. A resistive plate chamber, shown in Figure 5.2(a), consists of two parallel plates with a high resistivity, with a small gap in between that is filled with gas slightly above atmospheric pressure. A high electric field is applied over the gas volume, thereby multiplying (by secondary ionization) the ionization electrons caused by the passage of a charged particle, and this electric signal is picked up by readout strips on top of the gas gap.

Many different configurations exist. CMS has opted for a double-gap design, shown in Fig-

ure 5.2(b), where each gap consists of 2 mm thick bakelite (phenolic polymer) plates with a bulk resistivity of $1–6 \cdot 10^{10}\,\Omega$cm, and a gas gap of 2 mm. The plates are separated by means of spacers that are placed on a 10 cm × 10 cm grid. The whole chamber is made gas tight and the outer surface of the bakelite plates is coated with a thin conductive graphite layer to form the high voltage (HV) and ground electrodes. The graphite coat has a surface resistivity[2] of $10^5\,\Omega/\square$.

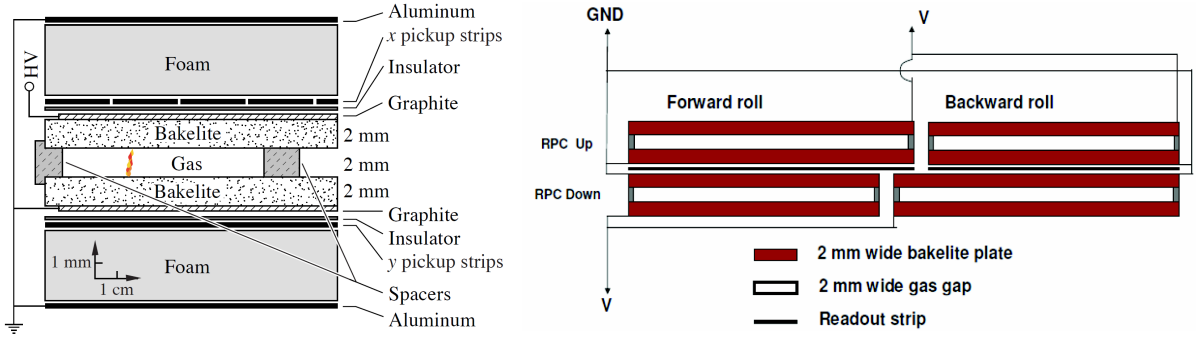

(a) Babar single gap RPC (b) CMS double gap RPC

Figure 5.2: A cross section of the BaBar single gap RPC with two layers of readout strips (left) [5] and a simple sketch of the layout of the double gap RPC installed in the barrel of CMS (right) [233].

Figure 5.2(a) shows a single-gap RPC with strips in x and y direction routed on top and below the gas gap. The readout strips are electrically insulated from the graphite coating that distributes the high voltage uniformly over the resistive bakelite plates. When a charged particle passes through an RPC, it will ionize the gas, and due to the high electric field an avalanche will be created in $\sim$ 10 ns. The avalanche induces image charges on the readout electrodes on both sides of the gas gap and these can be read out by for instance an oscilloscope. In CMS the read out is performed by a custom designed chip on the front end board (FEB) that contains a zero-crossing discriminator and pulse shaper [234].

Historically, RPCs were first operated only in streamer[3] mode. In streamer mode, the electric field inside the gas gap is so intense that passing charged particles generate limited discharges. This allows for a detection efficiency $> 95\%$ and time resolution of $\sim$ 1 ns but does not allow for rate capability exceeding 200 Hz/cm^2, since the charges of the streamers are large. On one

[2]Surface resistance R_s and surface resistivity ρ_s have the same dimension (Ω), the former because it follows from Ohm's law: $R_s = U/I_s$, the latter since bulk resistivity has the unit of Ωcm, hence surface resistivity has Ω. Therefore one has adopted to use $\Omega/\square$ for surface resistivity to distinguish it from the (surface) resistance. This assignment is however often mixed up, and sometimes one finds surface resistance in terms of $\Omega/\square$ and surface resistivity in terms of Ω. It is important to note that both have the same dimension and $\square$ does not represent any unit (such as "unit area" or the like).

[3]A streamer is a thin ionized (conducting) channel that grows fast along the positively charged trail left by an intense primary avalanche. The avalanche generates photons, which in turn initiate numerous secondary avalanches in the vicinity of the primary avalanche. The electrons of the secondary avalanches are pulled by the strong electric field into the positively charged trail of the primary avalanche, creating a streamer [235]. The streamer can propagate through the gas, and if not quenched, it can finally connect the two electrodes, resulting in an electric arc. The latter is also called streamer breakdown, and is the very same mechanism one observes during lightning. The electric arc is only visible when a conducting channel has been established between two clouds on a different potential or between a cloud and the earth. More details about streamers and streamer formation are in Reference [236] and references therein.

hand, this results in high output pulses $\sim$ 300 mV, but on the other hand also to longer recharge times for the bakelite electrodes and hence larger dead time. Furthermore, increased charge deposited on the inside of the detector also means faster ageing of the detector. Searching for high-rate regimes, the avalanche mode was discovered independently by Cardarelli et al. [237] and Crotty et al. [238] and pioneered further in References [239, 240] for use at LHC detectors. When operated in avalanche mode, lower electric fields of O(5 kV/mm) can be used to reduce the size and charge of the avalanches, leading to an improved rate capability of about $\sim$ 1 kHz and longer lifetime [241]. In the avalanche mode the electric signals induced on the strips are $\sim$ 1 mV and dedicated electronic amplifiers are necessary to compensate for the loss of gas amplification to process the signals.

Using electric fields of 5 kV/mm puts some constraints on the electrodes: they should be very smooth to prevent discharges at sharp edges or irregularities on the surface. Therefore the bakelite electrodes are treated with linseed oil to improve their smoothness. Serious problems have been reported by both the BaBar [242, 243] and Belle [244, 245] experiments, where temperatures inside the RPC rose too high and the linseed oil melted, forming droplets leading to local increases of the electric field. This lead to serious degradation of the detection efficiency of the chamber. Improved techniques for smoother bakelite production were promising for building RPCs without linseed oil treated bakelite. This was considered for the construction of the CMS RPCs at the time of the Muon TDR [138] at the price of higher intrinsic noise O(100 Hz/cm^2) due to a less smooth surface with respect to the linseed oil treated bakelite. Improvements in the linseed oil polymerization process resulted in improved linseed attachment to the bakelite and finally this technology was preferred [246].

An intense program of R&D was started in 1992 and lasted for almost 20 years, leading to the first production tests. A new generation of RPCs suitable for LHC operation was delivered. The RPC design for the CMS experiment is shown in Figure 5.2(b) and consists of a double gas gap with readout strips in between, operated in avalanche mode. The electric signal of both gas gaps is coupled into the strips and the sum of both signals is read out. Depending on the charge threshold of the readout electronics, one can more or less require the RPC to have a well-developed avalanche in both gas gaps (high threshold), or only one good avalanche or two avalanches having electric signals that would not pass the threshold individually, but passes the threshold when summed (low threshold). Low thresholds allow for high efficiency, while high thresholds reduce the background (for instance neutrons that only provide a hit in one of the two gas gaps, see section 5.3 and intrinsic noise of random discharges due to surface impurities of the bakelite). The RPCs of CMS are operated at $\sim$ 220 mV optimized for intrinsic noise suppression.

5.1.1 Simplified electric model of the RPC

In a simplified view the RPC can be seen as a series of three capacitors, described by the capacitance of the bakelite, C_b, and the capacitance of the gas, C_g, as shown in Figure 5.3. The capacitance for each of the materials is described by their dielectric permittivity $\varepsilon = \varepsilon_0\varepsilon_r$, often expressed as the product of the relative permittivity ε_r with respect to the vacuum, and the permittivity of the vacuum ε_0. The capacitance between two surfaces A at a distance d, is described by:

$$C = \varepsilon_0\varepsilon_r\frac{A}{d}. \tag{5.1}$$

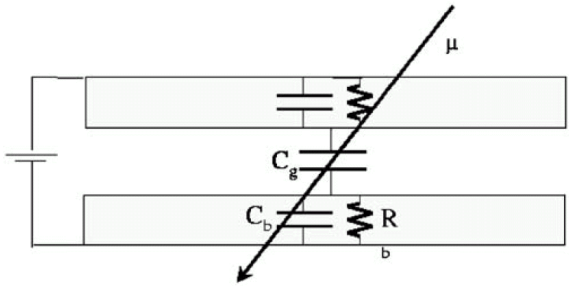

Figure 5.3: Simple layout of the electric circuit describing the discharging and recharging of an RPC. Figure taken from Reference [247].

The bakelite electrodes are also resistive, so they are better described by a RC-circuit, with the resistance R determined by the bulk resistivity ρ:

$$R = \rho \frac{d}{A}, \tag{5.2}$$

where A is the surface of the resistor and d is the depth or the length of the resistor, in the direction of the flow of the electric current. The time constant of a bakelite plate is given by $\tau = RC = \rho\varepsilon$, and is independent of the surface A and depth d. This is the time scale[4] governing the recharge of the capacitive and resistive bakelite electrode: $\tau_{\text{recharge}} = \rho\varepsilon \sim 10\,\text{ms}$.

A charged particle passing through a material will create electron-ion pairs. This process is called ionization. Using gasses, the electrons and ions can drift if an electric field is applied to them. These single electrons and ions will only induce very small currents on the electrodes, therefore they need to be amplified. This can be done inside the gas by imposing a high electric field. The electrons will accelerate and ionize even more atoms, leading to an avalanche. The movement of the free charges will induce a current on the electrodes as the electrons drift towards the positively-charged anodes and the positive ions drift towards the negatively-charged cathodes. The current consists of a fast component due to the high drift velocity of the electrons, and a slow component, due to the low drift velocity of the ions.

Using a simplified model, where only the contribution of the current induced by the movement of the electrons is considered, the current induced by an avalanche is described qualitatively by Townsend [235]:

$$I = I_0 \exp\left[(\alpha - \beta)x\right], \tag{5.3}$$

with x the length of the avalanche, α the first Townsend coefficient describing the number of electron-ion pairs created per unit length and β the second Townsend coefficient describing the (re)attachment of electrons and ions to neutral atoms. Using the effective Townsend coefficient: $\eta = \alpha - \beta$, and expressing the distance as a function of time: $x = v_d \cdot t$, with $v_d = \mu \cdot E$ the drift velocity of electrons in an electric field E, the current reads:

$$I = I_0 \exp\left(\eta \cdot v_d \cdot t\right) = I_0 \exp\left(\frac{t}{\tau}\right), \tag{5.4}$$

with $\tau^{-1}_{\text{avalanche}} = v_d \cdot \eta \sim 1\,\text{ns}$ the timescale of the avalanche. Snapshots of cosmic ray induced signals in an RPC read out with an oscilloscope are shown in Figure 5.4. This figure shows also

[4] A more elaborate time constant governing the whole system (bakelite – gas – bakelite) is given in Reference [247], the physics is (still) governed by the time constant of the bakelite electrode.

the transition in the signal waveform from avalanche to streamer mode operation, where more charge is freed inside the avalanche and hence a larger electric signal is induced on the readout strips.

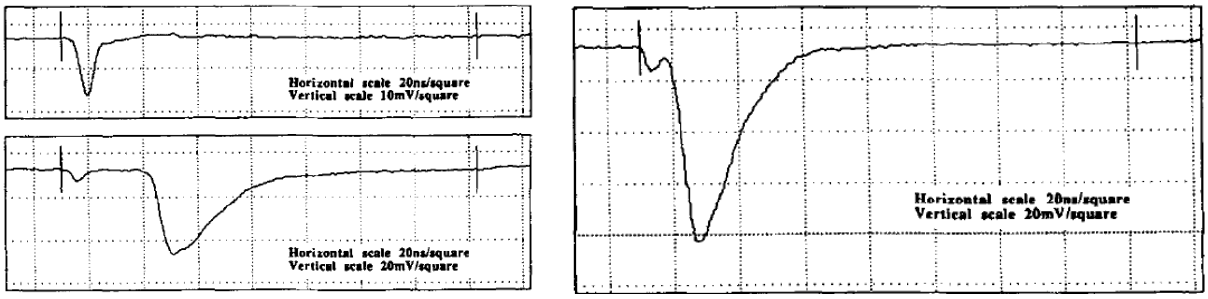

Figure 5.4: Signal waveforms at different operating voltages. The avalanche signal at 9.4 kV (top left) has a typical duration of 4–5 ns Full Width at Half Maximum (FWHM). A streamer signal follows the avalanche with a delay of 38 ns at 9.6 kV (bottom left). At higher voltages (10.2 kV) the delay between avalanche and streamer becomes gradually shorter (right) and they will eventually merge in a single pulse at even higher potential. The horizontal scale is 20 ns per decade (square) and the vertical scale is 10 mV (top left) and 20 mV (bottom left and right) per decade (square). Figures taken from Reference [240]

As is shown in Figure 5.4, the streamer signal is always preceded by an avalanche signal, which is called the "precursor" and is typical for streamer formation. First an avalanche creates electrons and ions. These recombine by emitting a photon, and these photons start new avalanches at a certain distance from the initial avalanche. This leads to a set of avalanches, merging into a streamer, causing a much larger voltage drop than the initiating avalanche. By increasing the voltage, the delay between avalanche and streamer shortens, and eventually the two signals merge. The larger charge of the streamer leads to a larger voltage drop and this is the origin of the lower rate capability. Figure 5.5 shows the effective voltage a second particle experiences when passing through a detector. In case of an avalanche, the effective voltage is high enough to generate again an avalanche and hence a detectable signal. In case of the streamer, the voltage drop was larger, requiring a larger recharge time, and the effective voltage is not high enough to generate an avalanche. The particle will not be detected.

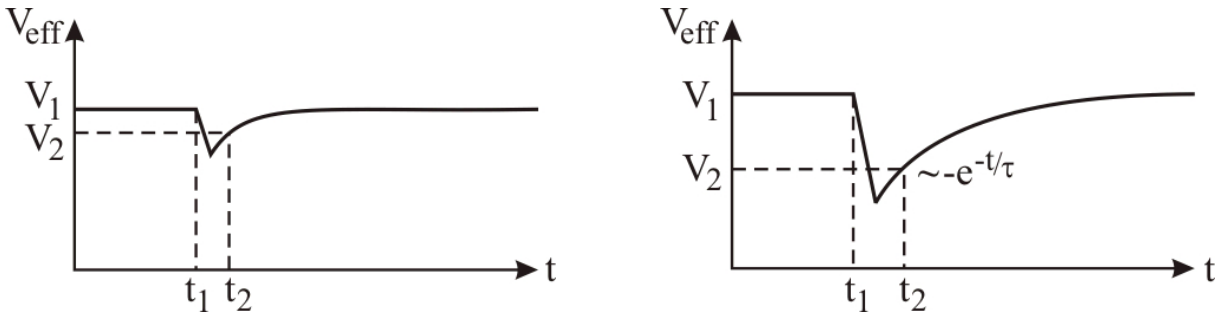

Figure 5.5: The voltage drop due to an avalanche (left) and a streamer (right) at time t_1. A second charged particle passing through the gas gap at t_2 experiences a different effective voltage V_2. In case of the avalanche the effective voltage is high enough to produce an avalanche, while in case of the streamer, the effective voltage is to low to create an avalanche and the detector is inefficient.

These two simplified models for the electrode discharge and the signal generation can explain the basic physics of the operation of RPC detectors. If the timescale to recharge the resistive electrodes is much larger than the timescale to have a discharge due to the avalanche creation, the discharge will therefore be snuffed out. This leads to a limited electric discharge when a particle passes, such that the rest of the detector stays sensitive. This limits the dead time of the detector to a limited region of a few cm^2 and for $\tau_{\text{recharge}} \approx 10\,\text{ms}$, until the electrode has been fully recharged to restore the electric field [248].

The charge pulse created by the avalanche inside the gas gap has to be coupled to the readout strips on top of the bakelite electrodes. This can be understood if one looks at the readout strips as being capacitively coupled to the bakelite electrodes, which act as high-pass filter due to their high resistivity. The bakelite electrode and the graphite coating on top are highly resistive and hence transparent to the high-frequency components of the induced signal. Figure 5.6 shows a slightly more complicated electric model of the RPC [249], taking into account the surface resistance of the bakelite (R_s) and the graphite layer (R_c) and the capacitive coupling of the signal in the $50\,\Omega$ terminated strips C_c, sent through coaxial cables (in this figure[5]) to the operational amplifiers of the front end electronics. Since no strips are underneath the gas gap, the electric signal is coupled (C_a) into the ground of the detector.

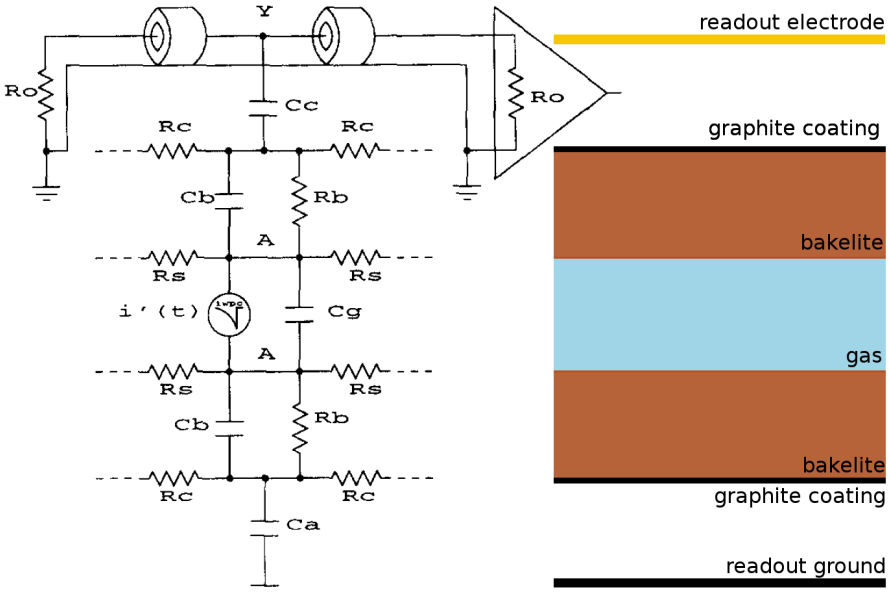

Figure 5.6: Local electric model of the RPC [249] (left) illustrated with the main components of the RPC detector (right).

While the rise time of the signal is $\sim$ 1 ns, the pulse is shaped by the front end electronics to have a length of 100 ns to mask second pulses due to reflections of the signal at the end of the readout electrodes [250]. This implies at the LHC, when a strip is hit, it cannot record other hits in the following three bunch crossings. This introduces dead time for the detector, but this is insignificant for normal LHC running since the muon rate is expected to be low. The pulse shaping in the front end electronics preserves the fast rise time of the signal, which is crucial to the role of the detector in fast triggering [250].

[5] In the barrel RPCs of CMS capton foil is used to propagate the signals from the read out strips to the front end electronics. In the endcap RPCs of CMS coaxial cables are used.

Although the RPCs installed in CMS have only strips running in the η-direction (for a rather precise measurement of the ϕ-coordinate), a second coordinate (determining where exactly along the strip the muon passed) could be obtained if the pick-up strip was read out at both ends, by calculating the time difference between the two pulses. The strips are, however, only read out at one side, and the other side is terminated with a 50 Ω resistor. This termination is necessary, since the propagation time along the strip is much longer than the rise time of the induced signal ($\sim$ 1 ns) and transmission line effects, such as reflections, would appear. Due to this termination, half of the signal picked up by the readout strip is lost. In the endcap it was mechanically impossible[6] to properly terminate the readout strips, but here the transmission line effect is less important since the strips are much shorter [253]. The reflections in this case add to the initial pulse, but do not deteriorate the times measured by the detectors. Only the timing is of importance, since there is no attempt to integrate the waveform in order to obtain information on the energy deposited by the charged particle.

5.1.2 Detailed simulation of resistive plate chambers

A detailed, quantitative, description of the physics of resistive plate chambers, starting with the generation of primary ion-electron clusters due to the ionizing particle, up to using the Shockley-Ramo theorem [156, 157] to calculate the current induced on the pick-up electrodes, is elaborated in Reference [254]. The model describes the charge induced on the electrodes q_{ind} as:

$$q_{\text{ind}}(x = g) = \frac{k}{\eta g} \sum_{\text{clusters}} q_e n_0 M k \left[e^{\eta(g - x_0)} - 1 \right], \tag{5.5}$$

where q_e is the electron charge; η is the effective Townsend coefficient; g is the gap width; x_0 is the initial distance between the cluster and the anode; and n_0 is the initial number of electrons in the considered cluster. The avalanche gain fluctuation factor M is described by a Polya distribution[7] and k is a geometrical factor, that takes into account that not the whole charge can actually be read out by the pick-up electrodes: $q_{\text{ind}} = k \cdot q_{\text{d}}$, where $q_{\text{d}}(t) = q_{\text{d}}(x/v_d)$ is the drifting charge and v_d is the electron drift velocity in the gas.

The induced charge is the core observable described by the simulation and is used to determine all derived quantities, such as the induced charge calculated by the Ramo-Shockley theorem:

$$i_{\text{ind}}(t) = -q_{\text{ind}}(x/v_d)\vec{v}_d \cdot \vec{E}_w, \tag{5.7}$$

with $\vec{E}_w$ the weighting field, the electric field inside the detector if the charge is removed and the considered electrode is put to unit voltage, while the other electrodes are grounded[8].

[6] Due to the particular design of the endcap RPC chambers, there is no access to back end of the read out strips, see figures in References [251, 252].

[7] M accounts for the stochastic fluctuations of the exponential growth of the avalanche and for large values of the reduced electric field E/p, and is obtained by drawing a number from a Polya distribution:

$$P(n) = \left[\frac{n}{N}(1 + \theta) \right]^{\theta} \exp\left[-\frac{n}{N}(1 + \theta) \right], \tag{5.6}$$

and dividing this number by N. The value $\theta = 0.5$ has been chosen [254] and $N = n_0 e^{\eta(g - x_0)}$, the number of electrons produced after a path length $g - x_0$ as described by Townsend.

[8] For a more detailed discussion of the use of the weighting field, see for instance References [149, 150, 154, 255].

The charge spectra and detection efficiencies predicted by these detailed simulations are in good agreement with measurements on various kinds of chambers, as shown in Figure 5.7 [241]. Although the description of streamers requires more detailed simulations taking into account space charges screening, those simulations are able to provide rough streamer probabilities using the criterion that avalanches with gain exceeding $e^{20} \approx 4.85 \times 10^8$ [-] can be considered streamers [254]. At first, only static models were simulated, thereafter also the dynamic behaviour, where the rate of incident particles is not negligible, were investigated in References [247, 256].

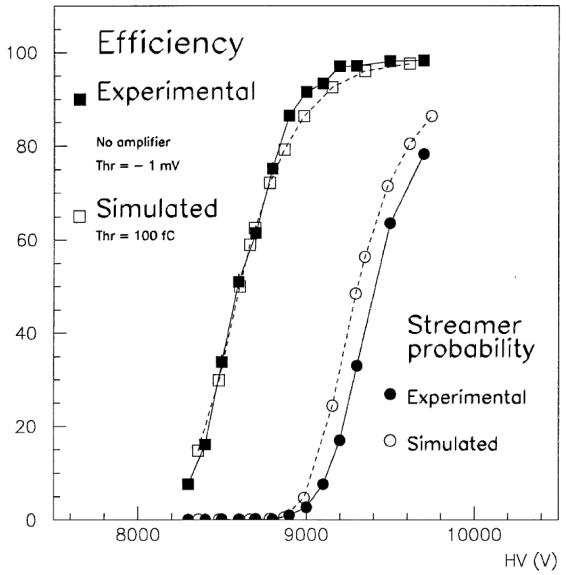

Figure 5.7: Simulated and experimental detection efficiency and streamer probability for a single 2 mm gap RPC with a 90/10 $C_2H_2F_4$/i-C_4H_{10} mixture. Figure taken from Reference [241].

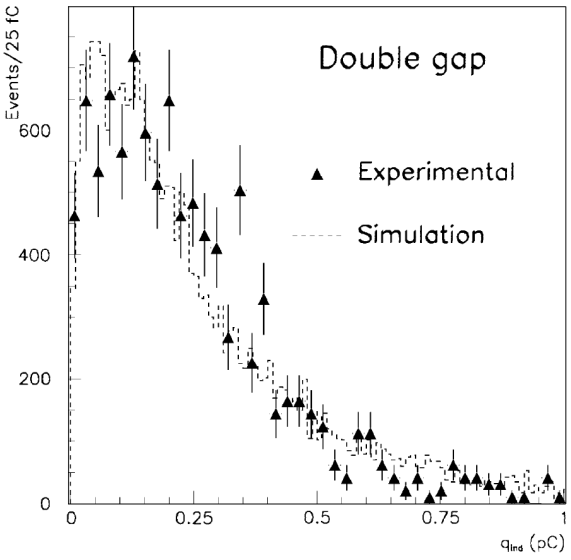

Figure 5.8: Simulated and experimental charge distributions for a 2 mm double gap RPC with a 90/10 $C_2H_2F_4$/i-C_4H_{10} mixture. Figure taken from Reference [241].

These simulations were used in addition to experimental data obtained for different RPC geometries to design the RPCs for the CMS experiment. Two important parameters for a high detection efficiency and a small time resolution are the width of the gas gap and the composition of the gas mixture. On one hand, a small gas gap will lead to a fast signal, on the other hand the probability for creating ionization decreases. The number of primary clusters generated by the ionizing particle per unit length, λ, follows a Poisson distribution and for most RPC gas mixtures it has a typical value of $\lambda \approx 5.5\,\mathrm{mm}^{-1}$ [254]. Therefore a minimum gap width is necessary to keep high efficiency. The need for a gas mixture with high λ is twofold. First, it allows for a high detection efficiency with the same gas gain. Second, the use of lower gas gain reduces the streamer probability, which increases with higher gas gain.

A gas gap of 2 mm was found to be the compromise between a detection efficiency greater than 98%, and a time resolution of 2 ns. Furthermore, a double-gap design was adopted, where the electric signals of two gas gaps are picked up by the same set of readout strips. This again allows for higher efficiency and lower gas gain, reducing the streamer probability. This reduction of the streamer probability increases the lifetime of the chamber, the rate capability and the spatial resolution, since streamers have higher charge and larger spatial extension. Freon ($C_2H_2F_4$) was found to have superior properties with respect to other gasses (for example Argon) and was chosen to be the main constituent of the gas mixture.

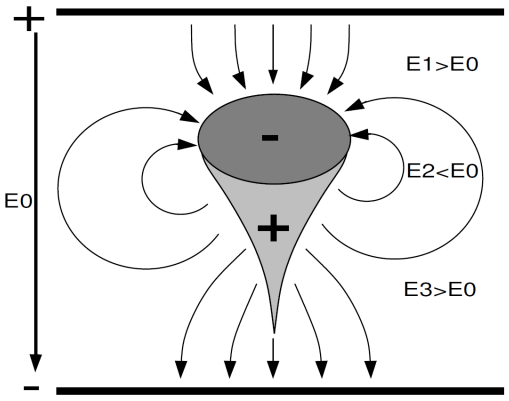

Figure 5.9: Schematic picture of avalanche and electric field deformation caused by the avalanche charge carriers. Figure taken from Reference [257].

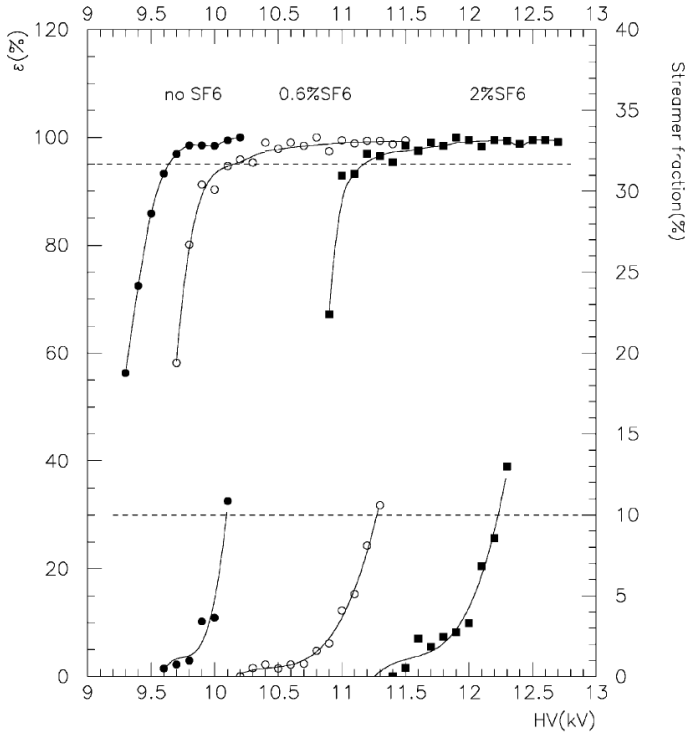

Figure 5.10: Experimental detection efficiency (top) and streamer probability (bottom) for a double 2 mm gap RPC with a $C_2H_2F_4$/i-C_4H_{10} mixture without SF_6 (filled circles), with 0.6% SF_6 (open circles), and with 2% SF_6 mixture. Figure taken from Reference [258].

The experimental charge spectra were well described overall by the simulation, but the events with avalanche charges below 0.15 pC were largely overestimated by the simulation, especially for small gas gaps. The detectors proved to have higher efficiencies measured experimentally [259] than predicted in simulation [249]. While this discrepancy was not of major concern for the trigger RPCs as used by CMS and ATLAS, they were to the ALICE collaboration, using multi gap resistive plate chambers (MRPCs) [260, 261] operated with lower charge inside the avalanches. Therefore the effects of space charge [257, 262–264] were simulated by dividing the avalanche development into time steps and by calculating the electric field inside the avalanche at each step. Figure 5.9 shows the deformations of the avalanche and the electric field due to the charge carriers of the avalanche. At the tip and the tail of the avalanche the electric field was found to be increased, while in the center of the avalanche the electric field was decreased [263]. Most of the electrons of the avalanche are in the center and hence experience only little multiplication, while in the tip and tail the electric field in the avalanche reached twice the value of the externally imposed electric field. This results in the observed small charges of a few pC [263] in the ALICE MRPCs.

5.1.3 Gas mixture, bakelite resistivity and other operating issues

The CMS and ATLAS RPC detectors are operated with a three component, non-flammable gas mixture that consists[9] of 95.2% Freon (R134a, $C_2H_2F_4$), 4.5% isobutane (iC_4H_{10}) and 0.3% sulphur hexafluoride (SF_6). After mixing, water vapour is added to obtain a mixture with a relative humidity of 40–50%. R134a, the main component of the gas mixture, was pioneered in References [249, 259], where it was found to be an adequate gas for operation at LHC. It has a high electron drift speed, allowing for excellent timing properties [249]. During the R&D phase of the RPC detectors, a dedicated effort was made to find an environmentally friendly gas with a negligible ozone-depletion power. In 1998, R134a was found to be an environment friendly, non-flammable gas, and was therefore selected for use in the trigger RPCs of the LHC experiments. Furthermore, R134a has some attractive features such as a high density, and therefore high primary ionization, a low cost and it is easy to find, as its use is established in industry. Freon is a higly electronegative gas, further reducing the size of the discharge inside the detector [265].

Isobutane was added to the gas mixture to absorb UV photons. The concentration is kept low to keep the gas mixture below the flammable limit. The emission of UV photons during avalanche development leads to a transverse growth of the avalanche, deteriorating the spatial resolution. Moreover, secondary avalanches initiated by UV photons increase the charge, therefore limiting the rate capability and the detector lifetime. The addition of a small amount of sulphur hexafluoride, SF_6, was motivated by its strong effect in suppressing streamers [266]. The effect of the addition of a small amount SF_6 can be seen as a shift of the streamer probability curve, as seen in Figure 5.10, such that the plateau efficiency can be reached for very small values of the streamer probability. A lower streamer probability leads to smaller deposited charge, and hence a smaller electric signal induced by the avalanche on the pick-up strips. On the other hand, the lifetime of the chamber is roughly inversely proportional to the deposited charge, so smaller deposited charge increase the lifetime of the chamber.

The dependence of the operation of RPCs on temperature [267] and pressure [268] is related to two issues: the gas density and the plate resistivity. In plasma physics, the reduced electric field (the electric field strength divided by the pressure) E/p is often used to express the influence of the gas density on the electric field, since the drift velocity of free charge carriers depends on the density [154, 235]. In experimental setups, the dependence of the resistivity of the bakelite on humidity and temperature was studied and variations by a factor ten were observed [269]. The resistivity of the electrodes of the RPC is of utmost importance to limit the discharge related with the passage of an ionizing particle, and hence in the rate capability of the detector. Therefore it is important to stabilize the temperature and humidity inside a detector as well as to record the temperatures and humidity conditions in which the detectors are operated.

The Townsend ionization coefficient α is related to the drift velocity of the electrons in the gas,

[9]The gas mixture in CMS has been 96.2% Freon ($C_2H_2F_4$ known as R134a), 3.5% isobutane (i-C_4H_{10}) and 0.3% sulphur hexafluoride (SF_6) for almost twenty years, from the time of the Muon TDR up to the pp-run of 2010. At the begin of the 2011 pp-run, CMS decided to increase the concentration of isobutane by 1%, and now the CMS and ATLAS gas mixtures are identical. This increase of the isobutane component was motivated by a possible elonged lifetime of the detector. Therefore it was decided to increase the isobutane component to the maximum allowed concentration, which is limited by the flammable limit, which is 5%. The 1% reduction of Freon will result in a shift of the efficiency plateau with 50–75 V to lower voltages, since Freon is more electronegative than isobutane.

which is inversely proportional to the density of the gas. Therefore α is often presented as depending on the reduced electric field: $\alpha/p = f(E/p)$. The following semi-empirical model is known as the "Korff approximation" for the Townsend reduced coefficient [155]:

$$\frac{\alpha}{p} = A \exp\left(-\frac{B}{E/p}\right), \tag{5.8}$$

with A and B parameters tabulated for different gasses at different magnitudes of the reduced electric field. The high voltage V_{eff} that is relevant for the development of the avalanche needs to be corrected for fluctuations in the gas density. Therefore the following equation is proposed:

$$V_{\text{eff}} = V \cdot \frac{p_0}{p} \cdot \frac{T}{T_0}, \tag{5.9}$$

with V the applied power voltage, and p_0 and T_0 arbitrary chosen to be $p_0 = 1010\,\text{mbar}$ and $T_0 = 293\,\text{K}$ as the reference pressure and temperature [267, 268]. Figure 5.11 shows the influence of the temperature on the efficiency. Applying a temperature-based correction factor T/T_0 to the applied high voltage results in a unified efficiency curve. Figure 5.12 shows the influence of the pressure on the efficiency. Since the amplification process in the gas is in principle only a function of the reduced electric field E/p, the efficiency curves are also plotted versus HV/p. At lower gas pressure, lower efficiency plateaus are obtained, which can be understood from the lack of ion-electron pairs to start the avalanche [268]. Further on, at lower gas pressure, also higher effective voltages are required to obtain the plateau efficiency. This is due to the pressure dependence of the first Townsend coefficient α, as shown in Equation (5.8), leading to an additional term $\propto \ln \frac{p}{p_0}$ to Equation (5.9) [265].

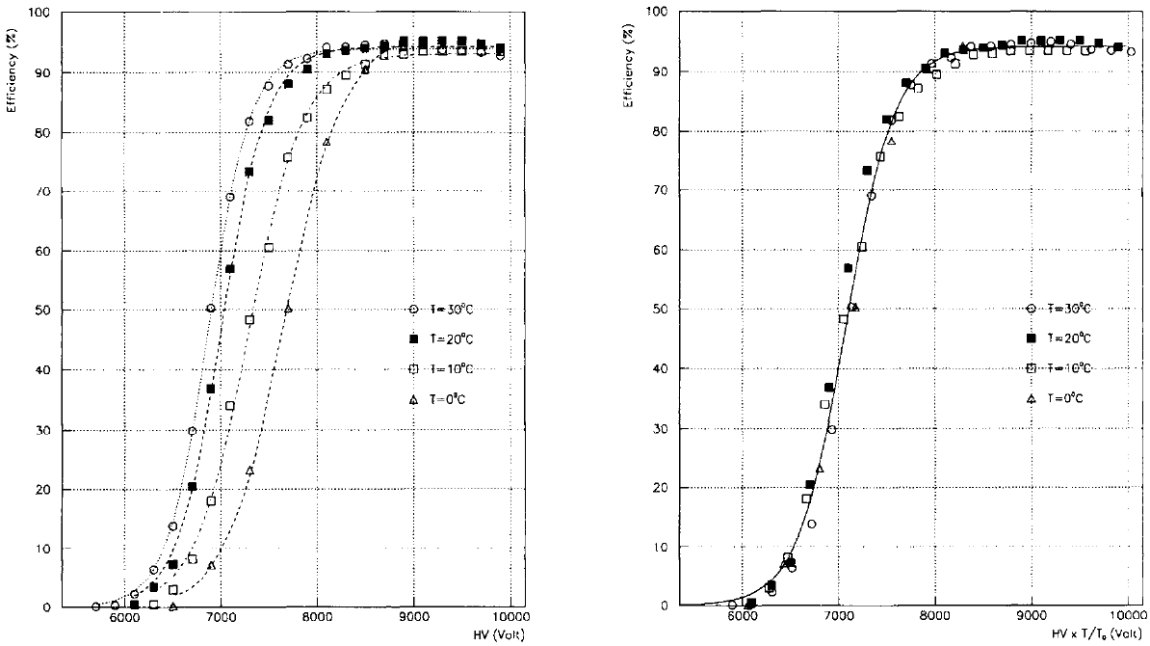

Figure 5.11: Efficiency for RPCs operated at 0, 10, 20 and 30°C as a function of their operating voltage (left) and as a function of a temperature corrected voltage $T/T_0 \cdot \text{HV}$, with $T_0 = 293\,\text{K}$. The RPC was a double-gap RPC with gas gaps of 2 mm and a 58/40/2 Argon/Butane/Freon (CF_3Br) gas mixture was used. Figure taken from Reference [267].

Both the temperature and the pressure effects are combined in Equation 5.9 to obtain the effective voltage. Only the effective voltage is relevant for operating the RPC at full efficiency. When RPCs are operated at the knee of their efficiency curve, small differences in pressure and temperature will be reflected in large efficiency variations. When being operated at a high voltage in the plateau region, small fluctuations will not affect the detection efficiency of the RPC. Unfortunately this plateau region requires higher values of the applied power (HV) leading to higher charges in the avalanche and higher streamer probability.

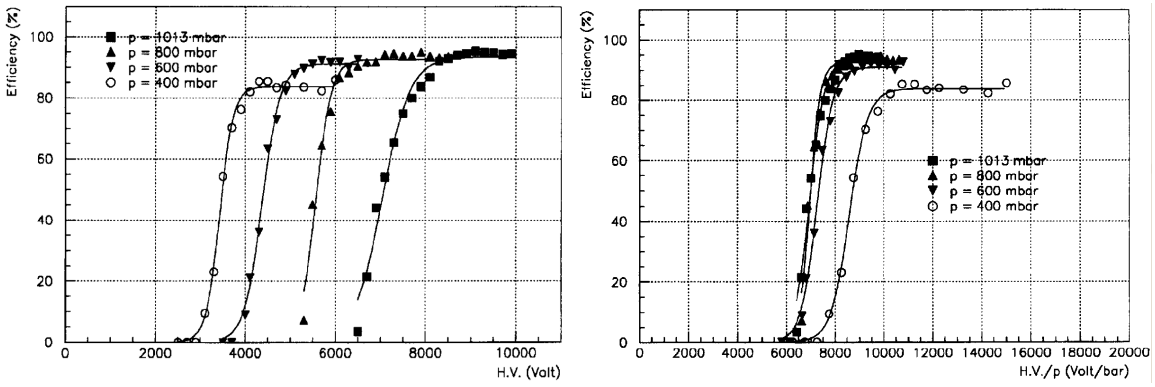

Figure 5.12: Efficiency for RPCs operated at 1013, 800, 600 and 400 mbar as a function of their operating voltage (left) and as a function of a pressure corrected voltage HV/p. The RPC was a double-gap RPC with gas gaps of 2 mm and a 58/40/2 Argon/Butane/Freon (CF_3Br) gas mixture was used. Figure taken from Reference [268].

The resistivity of the electrodes also depends on the temperature, but this is less well understood [247, 267, 269, 270]. It is known that the rate capability of the RPC depends on the charge in the avalanche on the one hand, and on the electrode resistance on the other hand. The recharge time scale $\tau = \varepsilon \cdot \rho$ is proportional to the bulk resistivity ρ and hence higher resistivity will lead to lower rate capability. The resistivity of bakelite plates has been observed to increase when in contact with a circulated dry gas. Therefore a relative humidity of 40-50% is maintained to avoid a degradation of the RPC system under high background rates.

5.2 RPC as a dedicated muon trigger detector in CMS

5.2.1 RPC detectors in CMS

Although the RPC system is not fully installed, as discussed earlier, a short overview of the design RPC system is given here. Keep in mind that currently only three stations are installed in both endcaps and that the RPC system is only installed up to $|\eta| \leq 1.60$ instead of the foreseen $|\eta| \leq 2.10$. It is important to have an overview of the full RPC system, since the proposed changes are largely based on the TDR design and since the RPC based muon trigger is designed for a 4 station RPC system.

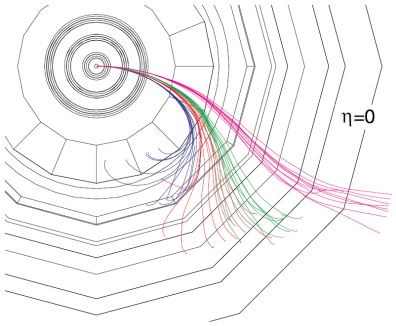

Figure 5.13: Simulated muons at $\eta = 0$, with different p_T [271].

The RPC based muon trigger of the CMS experiment relies on four RPC **stations** RB1-4 in the barrel and 4 stations RE±1-4 in the endcaps and it covers the pseudorapidity region $|\eta| \leq 2.10$. The barrel consists of five **wheels**, while the endcaps comprise three **disks** on which three muon stations are installed. In the barrel, the stations are approximately concentric cylinders, while in the endcap a station is a circular disk.

Figure 5.14 shows the layout of **the RPC system in the barrel**. The thick muon chambers are the DTs, while RPC chambers are much thinner and installed on top of and below the DTs. Muons with transverse momentum p_T between 3 and 6 GeV/c in the barrel region are not able to reach the outer stations RB3 and RB4, as shown in Figure 5.13. Therefore, additional layers are inserted in each of the inner stations RB1 and RB2, raising the total amount of sensitive layers in the barrel to six: RB1in, RB1out, RB2in, RB2out, RB3 and RB4.

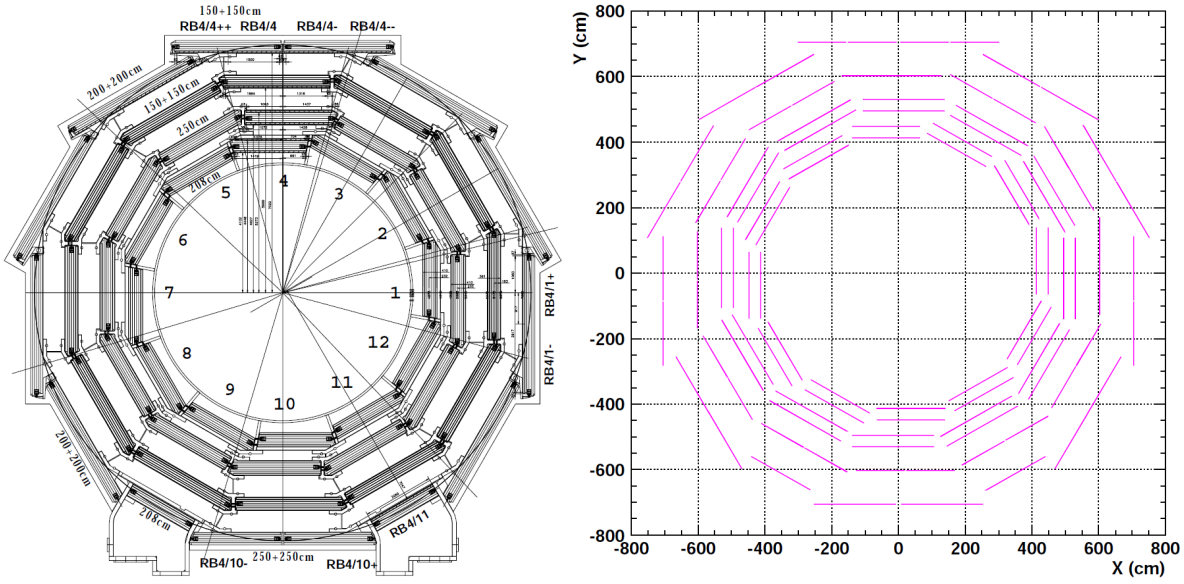

Figure 5.14: General layout of the RPC system in the barrel: a technical drawing (left) [272] and the implementation in GEANT 3.21 in early versions of the CMS software (CMSSIM 118 & ORCA 4.2) (right) [273].

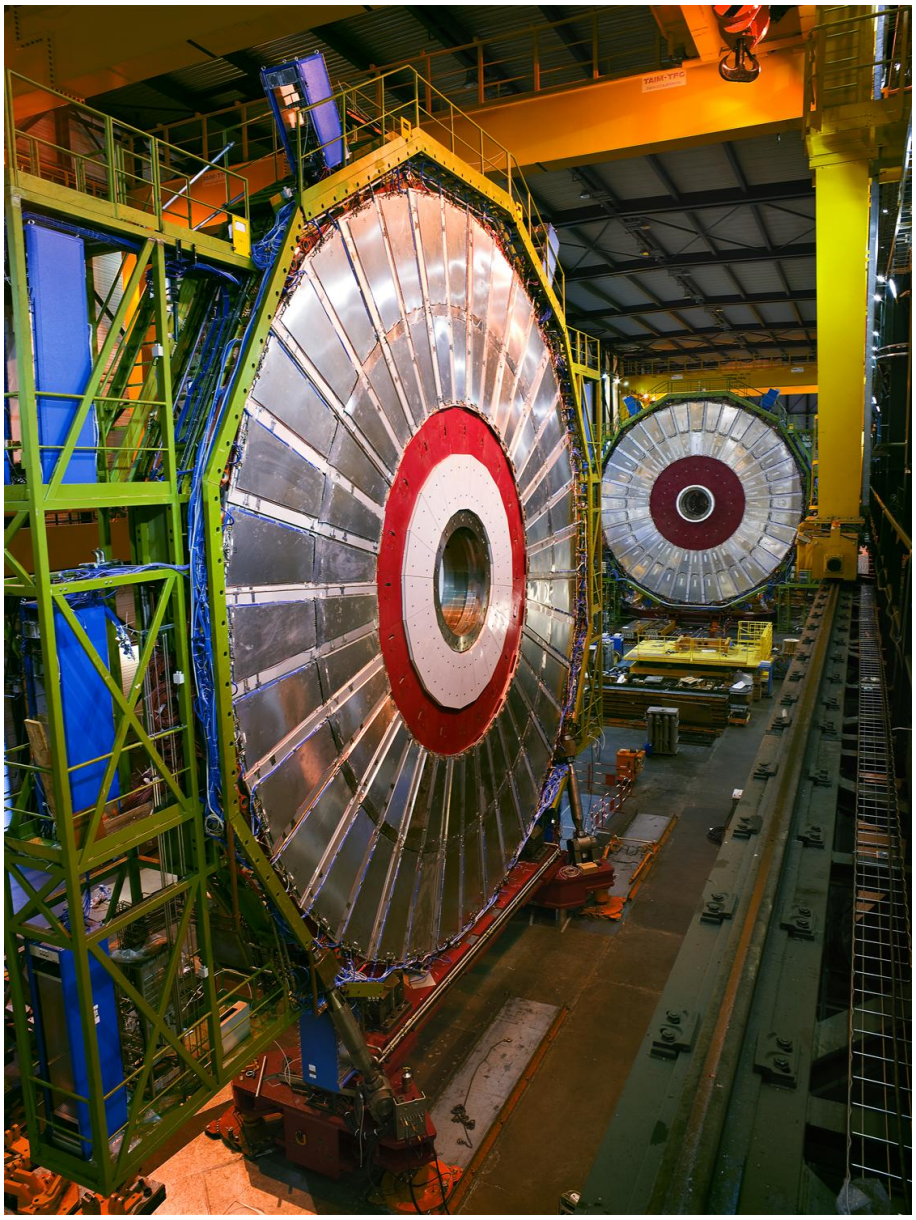

Figure 5.15: View of the front side (Positive side) of YE-3 (front) and the back side (Negative side) of YE-1. Picture taken November 2007 during the "waltz of the endcaps", where the large 400 tonne endcap disks were moved along each other, prior to lowering to the experimental cavern.

Each barrel wheel is divided into twelve 30° sectors (RB/y, y = 1–12), The counting starts at the "Near" side, which is the side close to the service cavern, at the inside of the LHC ring. The "Far" side consists of sectors 4–9, the "Near" side of sectors 10–3. The smallest mechanical structure containing RPCs is called a chamber. In the barrel these chambers consist of a mechanical structure with two or three η partitions. For trigger purpose reasons, which will be explained in the next section, RB2in of wheel 0 and ±1 and RB2out of wheel ±2 consist of three η partitions, called "rolls", while all other chambers consist of two rolls. The RPCs installed in the barrel, have various widths of 1.5 m up to 2.5 m and all have a length of 2.455 m, which is the length of a barrel wheel. The barrel RPC system consist of 1020 rolls, covered with 68 136 strips and has a total sensitive area of $22.8575 \times 10^6\,\mathrm{cm}^2$, or $2\,285.75\,\mathrm{m}^2$, roughly half of a football field.

Within the 30° sectors, the outermost stations RB3 and RB4 consist of 1,2 or 4 chambers. All sectors except sectors 4, 9 and 11 consist of two chambers, typically denoted with a + or - sign: for example: RB4/1- and RB4/1/+ shown in Figure 5.14. The largest RPC coverage is needed in station 4, sector 4 which consists of 4 chambers: RB4/4–, RB4/4-, RB4/4+, RB4/4++. The smallest RPC coverage is required in sectors 9 and 11, located in the wheel supports ("feet"), with just a single chamber. Note that the y-axis is a symmetry axis, but that there is no azimuthal symmetry in the barrel RPC system. The rolls are instrumented with projective readout strips with rectangular geometry in the barrel, running parallel with the beam line: the strips of RB1 have a pitch of 23-24 mm, while strips of RB4 have a pitch of 41 mm. Each "roll" can have up to 36 to 90 strips, depending on the strip width and width of the chamber.

The RPC system in the endcaps consist of four stations on each side, numbered RE±1–4. These stations are installed on the front and back of the yoke endcap disks YE±1 and YE±3, only CSCs are attached to the YE±2 disks, see Figure 5.1. Figure 5.15 shows RE-3 in front and RE-2 in the back of the picture. The azimuthal symmetry of the endcap RPC system is clearly visible. Each station can be divided in three *rings* (RE/y, $y = 1, 2, 3$) which are a set of 36 RPC *chambers* in the same station with the same distance r to the beam pipe. These rings are divided in six 60° sectors. The mechanical structure of an RPC (a chamber) in the endcap contains three or four "rolls", which are the η partitions. The rolls are instrumented with projective readout strips with a trapezoidal shape and directed radial with respect to the beam line. The endcap RPC system consist of 2304 rolls, covered with 82 080 strips and has a total sensitive area of $9.96937 \times 10^6\,\mathrm{cm}^2$.

As is visible in Figure 5.15, only the two outer rings (RE/y, $y = 2, 3$) of the RPCs are installed in the endcaps. Further on, only the first three stations are installed at each side of the barrel, RE±4 is not yet built, as already discussed above.

5.2.2 RPC PAC trigger

The RPC system is segmented into 33 so-called trigger towers in pseudorapidity (covering $|\eta| \leq 2.10$, while only 3 stations up to $|\eta| \leq 1.6$ are currently installed), schematically shown in Figure 5.16. Each of the trigger towers is subdivided in azimuth in 144 logical units [141]. Each trigger processor covers a geometrical region $\Delta\eta \times \Delta\phi = 0.1 \times 2.5°$ (8 strips) in the reference RPC plane, called segment. The barrel reference plane is RB2in in wheel -1,0,1 and RB2out in wheel -2,2, whereas in the endcap the reference plane is station RE2. Towers -7 to 7 are the barrel towers since their reference plane is situated in the barrel, for towers -16 to -8 and 8 to

16 the reference plane is RE±2 and are therefore called the endcap towers.

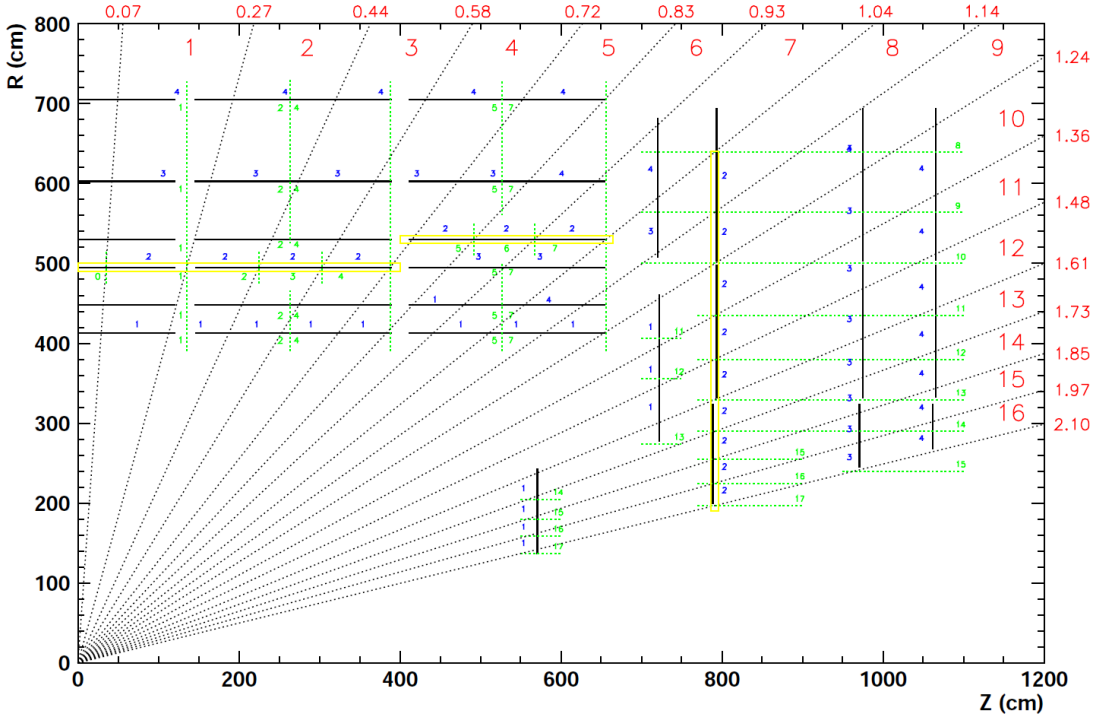

Figure 5.16: The segmentation of the RPC system in a quarter of the CMS experiment for the TDR design ($|\eta| \leq 2.10$ and 4 stations in the endcap). Lines of constant η are drawn and the η boundary values of the trigger towers and their numbering are printed in red (dark gray). The reference plane is marked yellow (light gray). Figure taken from Reference [274].

The trigger principle relies on the magnetic field in the return yoke, which can be as high as 1.8 T. Muon tracks are bent in the r, ϕ plane, while having constant η. A muon traveling through the detector fires readout strips and generates a pattern of hits that carries information about the bending of the track and thus about the p_{T} of the muon. Trigger processors compare the observed pattern within one segment with predefined patterns corresponding to certain p_{T} values. The PAttern Comparator Trigger (PACT) allows for coincidences of 4 hits out of 4 stations (4-out-of-4 or 4/4) and 3 hits out of 4 stations (3/4). The latter are assigned with a lower quality ($Q = 0$) with respect to the former ($Q = 1$). In the barrel $Q = 2$ and $Q = 3$ are also possible, referring to 5/6 and 6/6 coincidences. If multiple patterns match the produced hits, the muon candidate with highest quality and highest p_{T} is selected. All candidates are first sorted in quality, then in p_T and the L1 RPC Regional Trigger delivers the 4 best muons in the barrel and the 4 best muons in the endcap to the Global Muon Trigger (GMT).

Segments have a conical shape and are uniquely defined in the reference station. An example of a segment is shown in Figure 5.17, along with one of his neighbouring segments. Strips from other stations are copied to multiple segments, creating ghosts in segments near that which contains a true muon. Ghost busting algorithms are applied but are not 100% efficient, allowing fake triggers. The CSC system, the other muon detector in the endcaps is even more vulnerable to ghost hits due to their orthogonal read out pattern of strips and wires. Especially at high particle fluxes, the CSCs will be overloaded with these ghost hits and need information from the RPC system to eliminate them efficiently.

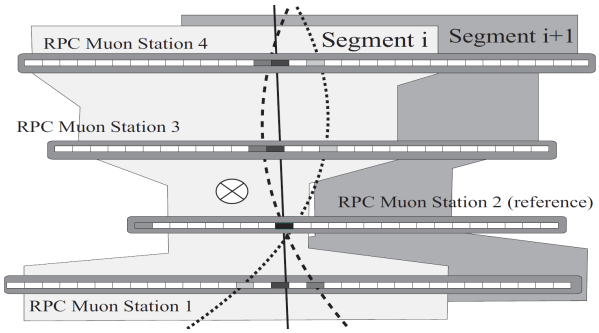

Figure 5.17: Illustration of pattern matching in a PAC segments. A high p_{T} muon is matched to collinear hits (the straight solid line). Due to a combination of real and background hits, two low-p_{T} muons are also matched. The strip widths are exaggerated with respect to the distances between the muon stations. Figure taken from Reference [141].

The working point of the trigger is determined by a trade-off between high trigger efficiency and low trigger rate. Since the L1 trigger is responsible for a reduction of the data rate to 100 kHz, the GMT has a limited bandwidth of 12.5 kHz (applying a safety factor of two). Therefore the p_T threshold which keeps the single-muon trigger rate below 10.0 kHz is 25 GeV/c at a luminosity of $\mathcal{L} = 10^{33}\,\mathrm{cm}^{-2}\mathrm{s}^{-1}$ [141].

An earlier trigger algorithm study [228] shows an improved trigger performance in the endcap for 4/5 coincidences with respect to 3/4 and 4/4 coincidences. However, this study was carried out with an independent 5$^{\mathrm{th}}$ plane, which highlighted the need for a new study with a double 2$^{\mathrm{nd}}$ station (RE2bis).

The pattern comparator (PAC) is based on a programmable ASIC chip and finds the highest-p_{T} candidate for a given trigger segment area ($\Delta\eta\times\Delta\phi = 0.1\times2.5°$). In the barrel there are six RPC planes, to provide low- and high-p_{T} candidates, whereas in the endcaps we have only four RPC planes, fed with only one set of patterns. Figure 5.17 shows two neighbouring segments. These segments are defined at the level of the reference muon station, where the strip assignment to the segment is unique. The reference segment contains eight strips. In other muon stations, the segment areas in the other, non-reference stations are much bigger and overlap with other segments. The set of strips in non reference stations, connected to the reference strip is called a "cone" [141].

Hits in the overlapping stations can give rise to fake track candidates, called "ghosts". For example in Figure 5.18, three hits are also belonging to the cone of the right segment, causing a 3/4 coincidence (not drawn). Almost all ghosts are due to the 3-out-of-4 logic, which allows for a missing hit in one layer, often the reference layer. These 3/4 coincidences have a lower quality assigned than the high quality 4/4 ones. The quality code takes preference over the p_{T} code in the sorting of the candidates. However, the high quality tracks often have higher momenta, since their trajectories have smaller curvature. Sophisticated algorithms have been developed and implemented to reduce the ghost rate, nevertheless a small fraction might remain, since too strong ghost busting leads to the rejection of real dimuon events, where the muons are close due to the boost of the original particle. The latter happens for instance with a J/ψ ($c\bar{c}$) which has rather low mass.

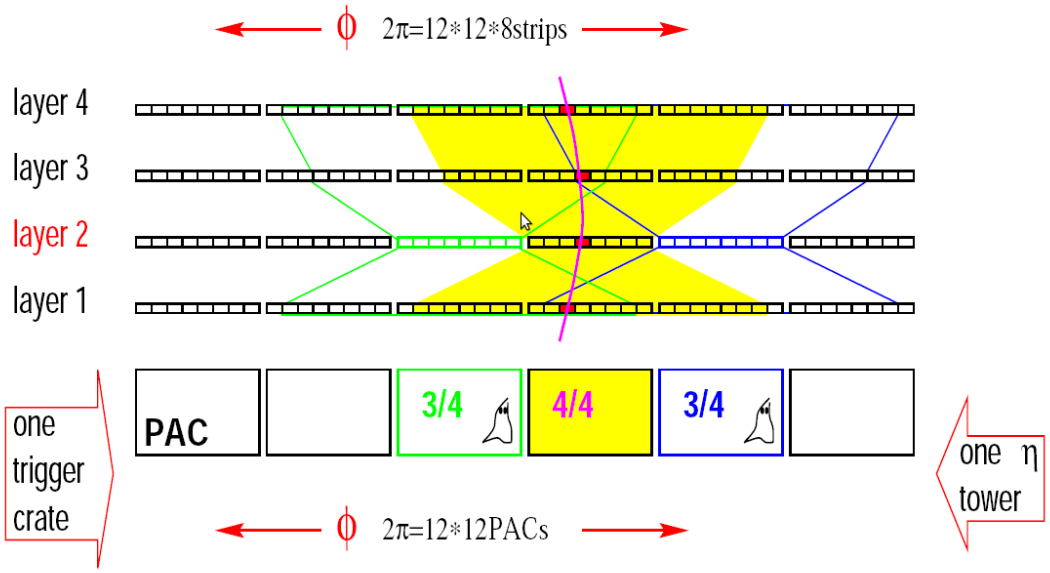

Figure 5.18: Illustration of ghost creation in nearby PAC segments due to overlap between the hour-glass shaped set of strips (cones): A 4/4 trigger induces 3/4 ghosts in the neighbouring segments. Figure taken from Reference [141].

5.2.3 Performance of the RPC detectors during cosmic runs and first collisions

After the LHC accident in September 2008, a dedicated cosmic run with the fully powered 4 T CMS magnet was performed during October and November 2008 and more than 300 million events were recorded. These were used to study detector alignment and efficiency. The RPC barrel was fully operational at that time and the performance of the detector was reported in Reference [233]. The RPCs were operated at 9.2 kV, corresponding to an effective voltage of 9.6 kV, being at 95% of the maximum plateau efficiency. This operational regime at "the knee" of the efficiency plateau is a conservative operation mode, which does not permit the detector to reach its maximum efficiency. This approach was chosen to maintain safe operation. The working conditions were maintained within strict ranges: the temperature had to remain below 24°C and the humidity of the gas mixture had to be within 40-50% [233].

The detector performance of the barrel has been studied as a function of the cluster size, the position resolution and the detection efficiency. A cluster is defined as a consecutive set of strips, each of them collecting a charge above the discrimination threshold of 180 fC (230 mV). The number of strips within a cluster is called the cluster size and depends on the pitch (width) of the readout strips, the impact point position with respect to the strip and the track crossing angle. Figure 5.19 shows the fraction of events having cluster sizes corresponding to 1, 2, 3 and 4 and more strips for the different layers in the barrel [233]. More than 60% of the muons fire a single hit, and as expected this increases with larger strip pitch.

For the study of the position resolution and detection efficiency, muon segments provided by nearby DT stations were used to extrapolate a hit in the RPC system. The residual distance between the impact point determined from the extrapolation of the DT-segment and the center

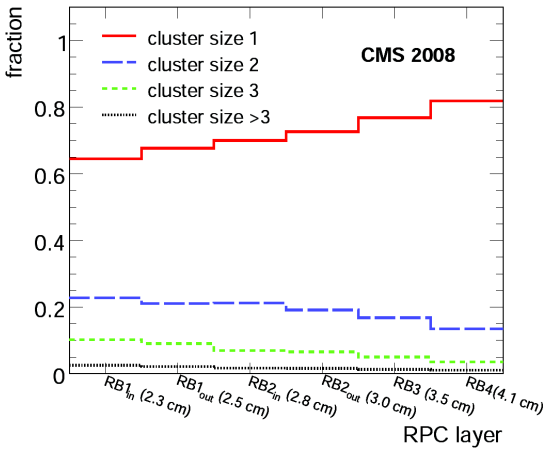

Figure 5.19: Fraction of the reconstructed clusters with size equal to 1, 2, 3 and 4 and more strips for each RPC layer in the barrel as measured during the cosmic run at the end of 2008 [233].

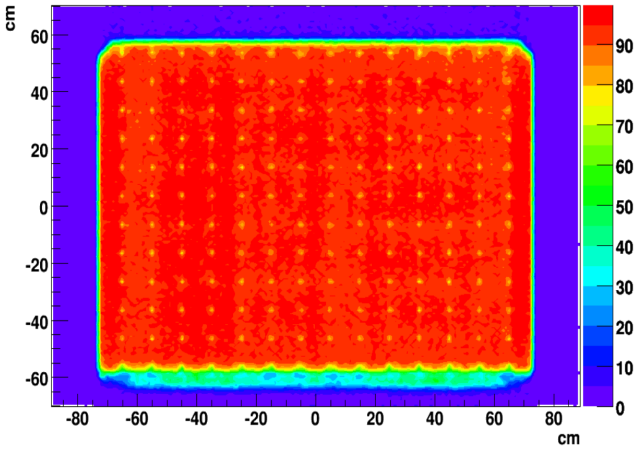

Figure 5.20: Local efficiency map during LHCs first run in 2010, for all RB3 backward rolls (in the barrel). The low efficiency points correspond to the location of spacers in the gas gap [153].

of the cluster (the reconstructed RPC hit) was used to study the position resolution and discover misalignments. This "segment extrapolation" was also used to study the efficiency of the RPC rolls. Figure 5.20 shows the efficiency map of all RB3 backward rolls, for the data recorded during the 2010 pp-collision run [153]. For the collision runs, the (uncorrected) high voltage was increased to 9.35 kV in the barrel and 9.55 kV in the endcap. The RPCs have been performing very well during the cosmic-ray- and collision-data-taking and their performance is detailed in Reference [153].

In CMS both muon precision detectors, DTs and CSCs have bunch crossing assignment at trigger level[10]. Initially [135], only RPCs were foreseen to provide the trigger for the muon chambers. Later on the CSCs and DTs were designed such that, although they have long signal integration time on their detectors, they could provide a bunch crossing determination at trigger level. Due to their long signal integration time, their bunch crossing assignment is vulnerable to background hits and multiple muons passing through the same chamber in the large ($\sim$ 9BX) time window. Here the advantage of the RPC system becomes clearly visible. Its signal resolution is 2 ns, much smaller than the time between two bunch crossings. Therefore the RPCs can assign the correct bunch crossing unambiguously, especially at very high luminosities. A correct bunch crossing assignment at L1 trigger level is of the utmost importance. It is the L1 Accept signal (L1A), broadcast to all subdetectors, that initiates the readout of the event. If a trigger assigns the wrong bunch crossing to the muon, it forces the readout of the entire detector in the wrong BX. Moreover, the RPC system provides redundancy to the muon system. If a muon fails to get detected in one of the muon precision chambers, the hits recorded in the RPC system improves the muon reconstruction, and sometimes they are even indispensable for the reconstruction of muons.

[10]In ATLAS, also drift tubes (MDT) and CSCs are used, but the trigger depends entirely on the RPCs in the barrel and thin gap chambers in the endcap. The precision chambers were not provided with the appropriate electronics to determine their bunch crossing identification at trigger level.

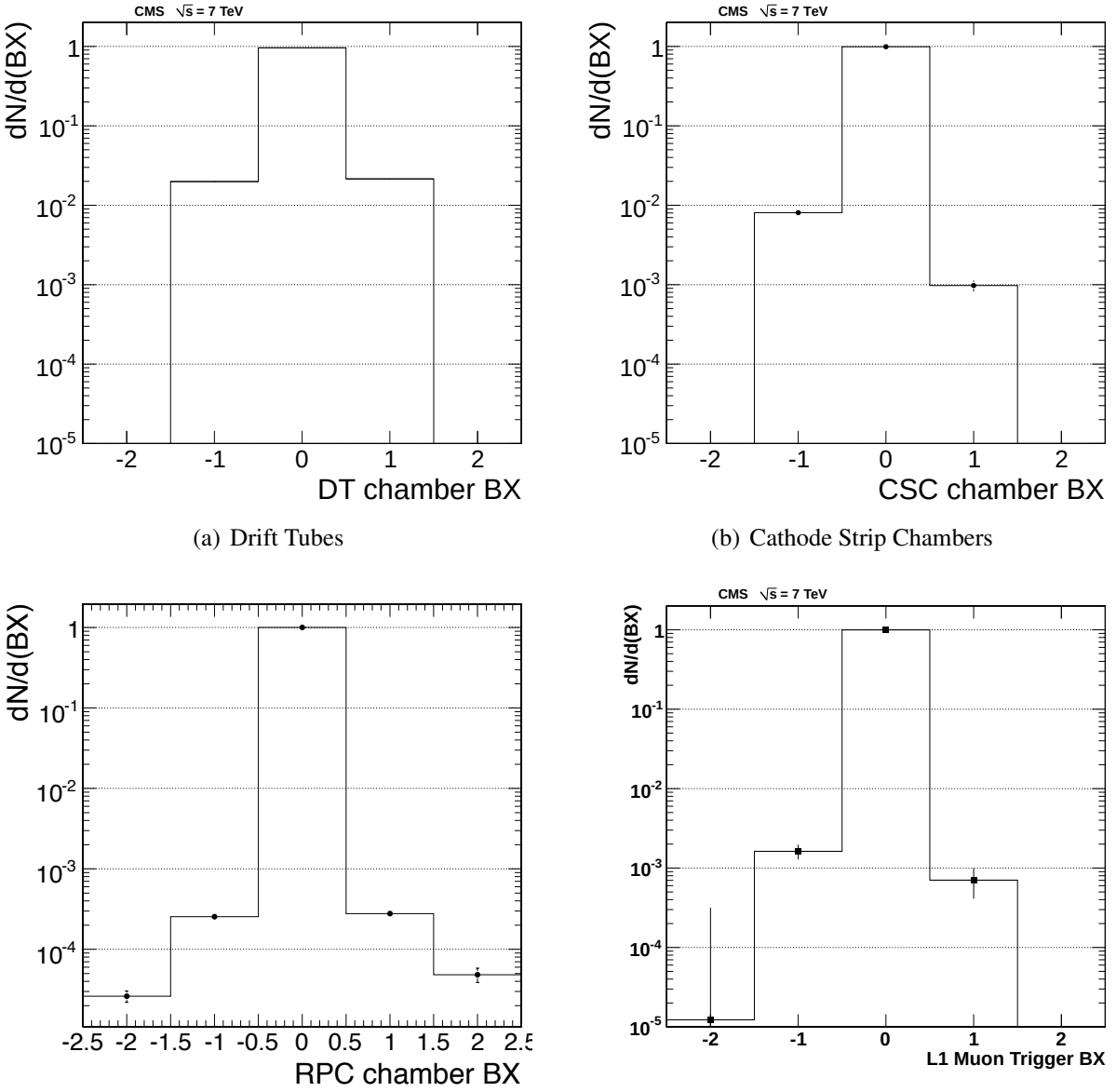

(a) Drift Tubes

(b) Cathode Strip Chambers

(c) Resistive Plate Chambers

(d) Level-1 Trigger Accept

Figure 5.21: Time distributions for the chamber level (a) DT and (b) CSC (ALCT) trigger primitives, and (c) RPC hits relative to the true event BX. In each distribution, data from all chambers were summed to show the overall subsystem synchronization. (d) Distribution of the combined L1 single-muon trigger. Figures taken from Reference [153].

Although the instantaneous luminosities during the *pp*-collision run in 2010 were relatively low, the RPC detector contributed to the assignment of the correct bunch crossing, as can be seen in Figure 5.21. This figure shows the time distributions for the DT, CSC, RPC triggers with respect to the reconstructed (true) event BX. The contribution of the RPC bunch crossing determination could be seen in the plot for the trigger timing at L1 Accept (L1A) level. It decreased the contribution of the DT and CSC triggers with BX±1 to the L1A.

5.3 Radiation Environment

5.3.1 Shielding of the endcap muon station and the forward region

In pp-collisions a significant amount of energy is emitted in the very forward direction which would be absorbed by the LHC magnets, leading to magnet quenches, if not properly shielded. To protect the magnets, a copper collimator, the Target Secondary Absorber (TAS), is installed in front of the first quadrupole. A second collimator, the Target Neutral Absorber (TAN), is installed behind the quadrupole magnets to provide additional protection to the vulnerable dipole magnets [114]. The collimator is hit by highly energetic particles with energies of $O(1\,\text{TeV})$, causing intense hadronic cascades. These hadronic cascades, together with interactions in the beam pipe and hadronic showers leaking out the forward hadronic calorimeter (HF) give rise to a huge radiation background in the experimental area. Special shielding in the whole forward region suppresses the background to a rate at which the muon system can operate [275–282].

Figure 5.22 shows the detailed design of the forward shielding. From left to right one may observe the high-η part of the outer muon chambers (ME4/2), the forward hadron calorimeter (HF), the locations for vacuum pumps around the beam pipe, the TAS and the last quadrupole magnet (Q1) the beam passes before entering the detector. For access purposes the shielding around the vacuum pumps and the TAS consists of a rotating collar made of concrete, which is attached to the concrete block house. This provides important constraints for the shielding, since the mechanical structure is only supported at one point, the block house, and it should protect the very vulnerable beam pipe, which has its own delicate support structure.

Sources of intense radiation in the forward region are the places where the beam pipe changes geometry, the front, top and back of the forward calorimeter (HF), the vacuum pumps and the front and top of the TAS. Particles traveling at fixed η, parallel to the conical beam pipe, will interact when the beam pipe changes from a conical to a straight geometry. Particle showers are sometimes not completely contained within the absorbing HF (punch through) or are scattered backward (back splash). Back splash is also the main mechanism for radiation induced by the TAS. The TAS is by far the most intense source of background and thus requires the most efficient shielding. Within the rotating shielding, the TAS is supported (and shielded) by a fixed iron nose.

Starting at the beam pipe, the forward shielding consists of steel around the beam pipe and the TAS, covered by borated (0.5%) concrete and a 5 cm thick coating of borated polyethylene. The boron was added to the concrete and the polyethylene because of its high neutron capture cross section and the desired feature that it gives rise to only low energy photons ($\sim$ 487 keV) after neutron capture. These low energy photons are less harmful than the 2.2 MeV photons originating from hydrogen or the 7.8 MeV photons emitted after neutron capture by an iron nucleus [281]. Borated polyethylene is even more effective at absorbing neutrons, but also more expensive than concrete. This is used as a final coating on top of the borated concrete. To model the radiation backgrounds in the region, the detailed geometry and shielding materials were integrated in FLUKA [283], a radiation simulation program.

To protect the muon chambers at high-η, dedicated shielding is used at the $\eta = 3$ cone and next to and below the high-η ends of the muon chambers. Figure 5.23 shows the geometry as implemented in the radiation simulation program as well as the actual implementation on the endcap disks. The endcap disks are part of the magnetic flux return yoke and hence have to be

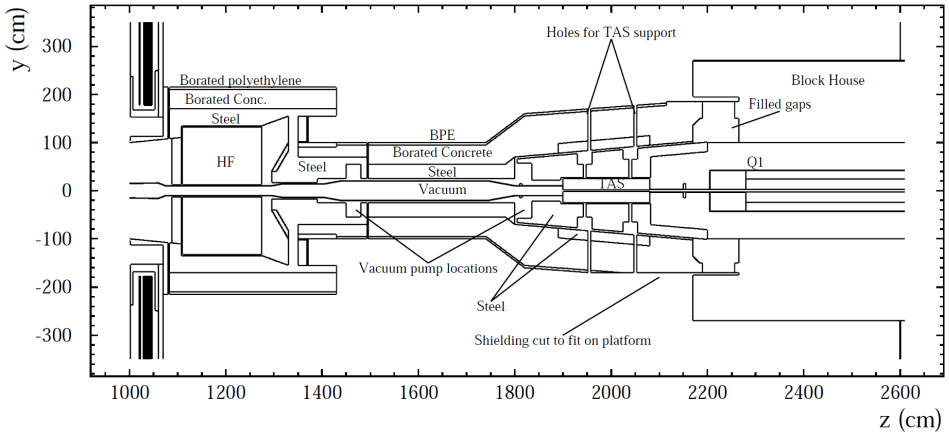

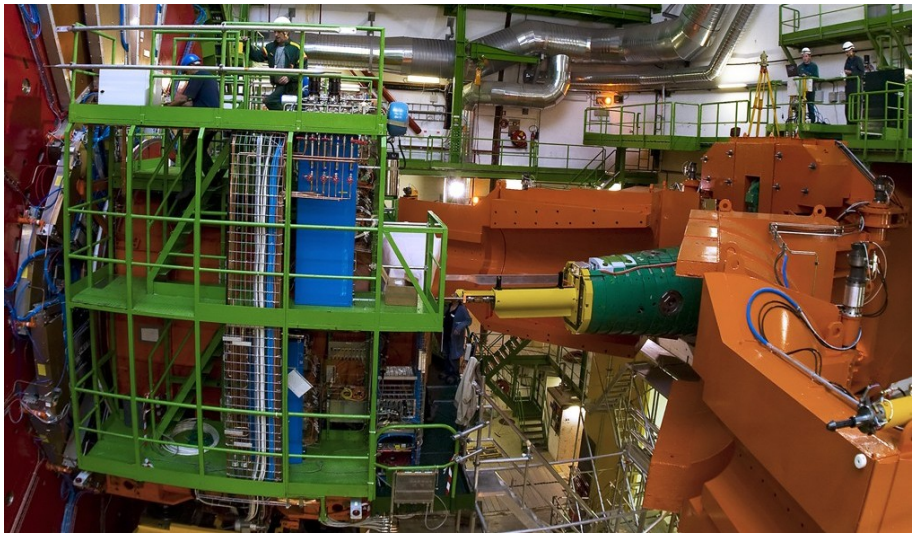

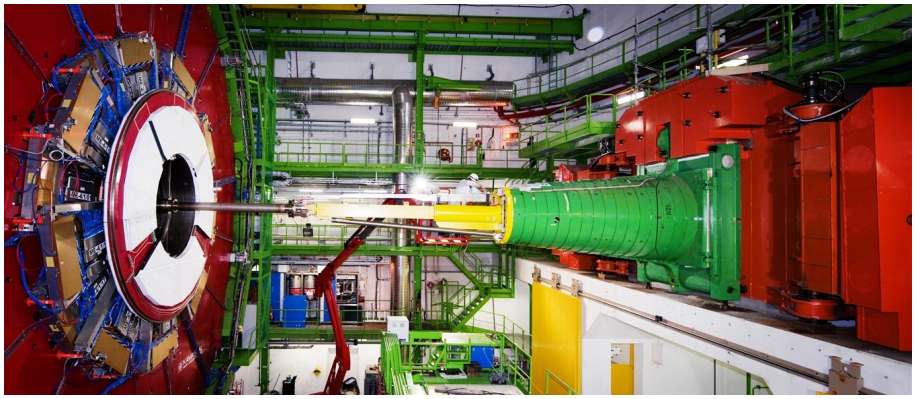

Figure 5.22: Longitudinal view of the beam pipe and the optimized shielding in the forward region as described in the FLUKA simulation (top) [280] and as realized in the experimental cavern at the Positive side ($+z$) (middle) and the Negative side ($-z$) (bottom). The scheme shows on the left side, the outer muon chambers (ME4/2) and HF, and on the right side the conical shielding holding inside the TAS which in turn protects the first quadrupole magnet (Q1) in the block house. The middle picture shows the HF at the left and the opened rotating shielding. The rotating collar (orange) consists of concrete and covers the iron nose (green) with inside (not visible) the TAS. In the bottom picture the HF is removed and the outer muon chambers (ME4/2) and the beam pipe are clearly visible.

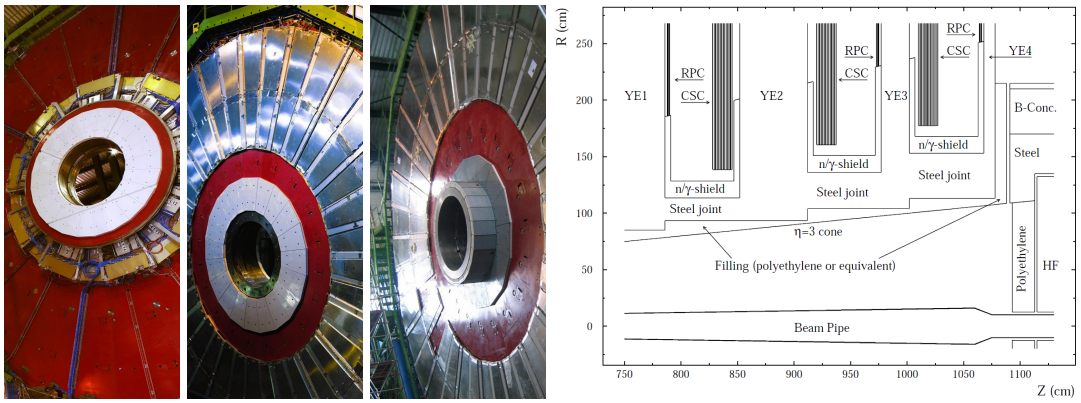

Figure 5.23: From left to right: Shielding near the $\eta = 3$ cone attached on the endcap yokes: YE+3 (back), YE+3 (front) and YE+1 (back) and described in the radiation simulations [281].

connected at their inner radius with 20 cm thick steel joints, which are visible on the pictures of the back of YE+1 and the front of YE+3 in Figure 5.23. On top of these joints 15 cm of hydrogenated material was added to absorb low-energy neutrons, which penetrate the iron relatively easily. In the shielding design, this hydrogenated material continued as a 5 cm thick layer along both faces of the CSCs, down to $\eta = 2.15$. Lead-boron-polymer was considered as a first candidate for the hydrogenated material, but was later found to have possible health risks and it was replaced by layers of borated polyethylene and lead [281]. Remember that the space starting at $\eta = 2.10$ is foreseen for RPC or RPC-like detectors that have not yet been installed. At the inner radius of the iron joints, another thin layer of hydrogenated shielding was foreseen, but is not installed. At the back of YE+3, after installation of the ME4 CSC detectors, an iron disk and additional shielding are attached that screen the forward hadron calorimeter, as can be seen on the picture of the back of YE+3 in Figure 5.23. Although the geometry of the shielding design seen in Figure 5.23 (right) is intended to have symmetric shielding on both sides of the CSC chamber, this is actually not possible because the CSCs are attached to the steel of the yoke and there is no space for shielding between the CSCs and the steel. The shielding is only on the side of the yoke where the RPCs are attached [281].

5.3.2 Sources of background in the muon system

Background hits in the CMS muon system arise from three main sources [141]: pp-interactions themselves; loss of beam particles in the LHC, interacting with collimators and other aperture limiting devices along the LHC lattice; and cosmic rays. Furthermore, the proton beams can also interact with the very few particles left in the vacuum of the beam pipe, which is called beam-gas interaction. The flux of cosmic rays at sea-level is typically 200 Hz m^{-2}. Since CMS is located 100 m underground, a reduction factor of $\sim$ 100 is determined [174] leading to a rate of only 2 Hz m^{-2}. Although this rate is very low, it has turned out to be very useful for the calibration and alignment of the detector. Several processes give rise to muons, charged hadrons and thermal neutrons:

- **Muons** originate from pp-collisions in decays of W and Z bosons or from b and c quark decays. These are often called *prompt muons* because they are produced at (or very close to) the pp-interaction point. Muons can also arise from the decays of π and K mesons, either directly produced in the pp-collisions (so-called "decays

in flight") or from hadronic showers in the calorimeters. Muons also arise from π/K decays in cosmic-ray showers, and from beam halo. Beam-halo muons are produced when protons deviating from the beam center interact with machine elements, producing secondaries which decay finally to muons.

- **Charged Hadrons** can give hits in the muon system. Charged hadrons in the muon system can arise from punch-through (hadronic showers that are not completely contained in the hadronic calorimeter), and from back-splash. In very forward detector elements (HF, beam pipe, forward shielding, ...) particles can be emitted at very large angles with respect to the incoming particle, causing hits in the forward muon systems, called back-splash.
- The very last product of hadronic showers are **thermal neutrons**, which are very penetrating and can cause a hit in the muon detectors by elastic (n,p) collisions. This has, however, a rather low probability with respect to neutron capture by a nucleus. Thermal neutrons can be captured by a nucleus, leading to an unstable nucleus emitting photons during de-excitation. Typical energies of these de-excitation photons are 7-8 MeV, the binding energy of a nucleon in the nucleus. These photons produce electrons by Compton scattering, the photo-electric effect or pair production. Since the n-capture cross section depends on the specific isotopes composing the nuclei of all materials involved, realistic simulation is complex and time-consuming. On average the cross section is proportional to $1/\sqrt{E_{\text{kin}}}$ and is highest for thermal neutrons ($E_n < 0.5\,\text{eV}$). These cross sections are very low, leading to long time-of-flights (TOF). Therefore processes must be simulated down until very low energies and up to very long times after the collision. Figure 5.24 shows a Minimum Bias event simulated up to 1 s after the pp-collision. The regions near the beam pipe and the forward calorimeter have the highest number of hits. Neutrons (black dashed lines) are "evaporated" by the forward calorimeter and forward shielding. With approximately 10^9 collisions per second at the nominal LHC luminosity of $10^{34}\,\text{cm}^{-2}\text{s}^{-1}$ (40 MHz collision rate $\times$ 25 pile-up interactions per BX), the CMS detector is effectively embedded in a "neutron gas", where neutrons overlapping a given bunch crossing were produced by particles from millions of earlier collisions.

If one looks more closely at the various signatures these processes leave in the muon detectors, one can discriminate among three types: hits, track segments and tracks, where hits can be separated into two classes, those due to muons (and other processes related to a real muon passing by, such as a Bremsstrahlung electron) and those due to background processes. Before going into more detail, it might be useful to review shortly the different muon detectors of CMS: the precision chambers (DTs and CSCs) have several sensitive layers (8-12 for DTs, 6 for CSCs), while the trigger detectors, RPCs, have two sensitive layers, but only one readout plane. So, from the reconstruction point of view, they can be treated as single layers, while from the background point of view, they have two layers.

- A **correlated hit** is caused by a muon, or its secondaries, passing through a detector layer. A muon can produce high-momentum electrons by Bremsstrahlung or δ-rays can be produced in the ionization process.
- An **uncorrelated hit** is a hit not correlated to a muon passing through the detector. It is mainly caused by a low-energy electron giving a hit in a single detector layer.

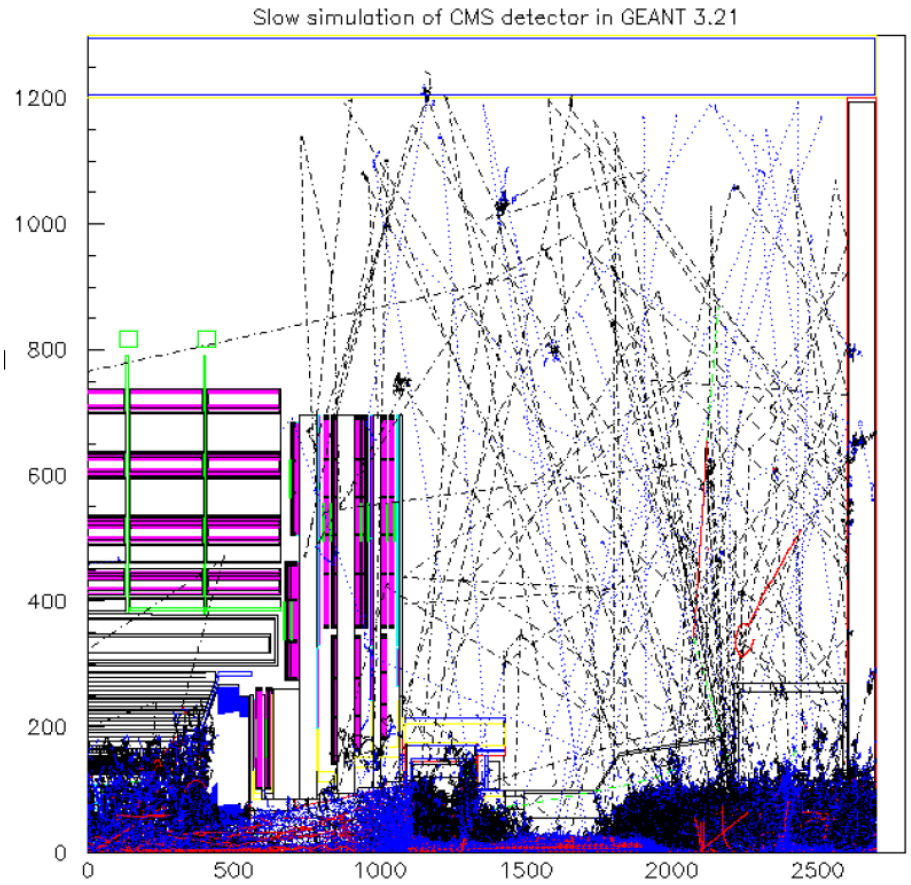

Figure 5.24: Event display of a Minimum Bias event simulated up to 1 s after the pp-collision. Photons are denoted with blue dotted lines, neutral hadrons and neutrinos are indicated with black dashed lines, muons are shown as green dashed lines, while all other charged particles are denoted with a red solid line. Figure taken from References [284–286].

The electron typically originated from a photon emitted by the capture of a thermal neutron by a nucleus.

- A **track segment** is a set of aligned hits within a muon station. Track segments are the main signature of muons passing through a multi-layered detector, but can also be induced by hadrons, originating from punch-through and back-splash of high energetic particles.
- A **track** is a set of aligned track segments in several muon stations. Prompt muons give rise to tracks in the muon system, but those tracks can also be caused by low p_T muons, produced by b and c quark decays and in decay in flight of π and K mesons.

In the following sections only background hits (due to neutrons) and to signal hits (muon hits) will be discussed.

5.3.3 Fluxes and hit rates in the muon system

Two studies have been performed to determine the background fluxes in the CMS experiment. One study targeted the background from pp-collisions inside CMS, while the other discussed the background due to the operation of the LHC. **Particle fluxes originating from pp-collisions**

were simulated with FLUKA for an idealized detector baseline shielding[11] [275] and are presented and discussed in the Muon TDR [138]. Because of the approximations in the geometry description and the extrapolation of the pp-cross section to 14 TeV, systematic uncertainties are dominant but are believed credible to within a factor of three [138]. **An accelerator related background study** [276, 277] pointed out that the main accelerator induced background are muons whose flux is comparable to the muon flux caused by pp-collisions, while other machine induced backgrounds (n, γ, charged hadrons) are much smaller than the pp-induced backgrounds.

While fluxes are independent of the chamber geometry, calculations of the hit rates are much more complicated because they depend on the specific sensitivity of the chamber to the particles, and this depends on the chamber geometry, the materials used inside the chamber and the particle's energy. A crude parametrization of the hit rate was obtained by using a very schematic chamber geometry and roughly estimated material responses (sensitivity factors) to the neutron (Φ_n) and photon flux (Φ_γ) [275]:

$$\text{Rate} = 10^{-4} \times \Phi_n + 10^{-2} \times \Phi_\gamma + \Phi_{\text{charged}}. \tag{5.10}$$

It was thus assumed that the probability of a charged hadron to give a hit was equal to 1.

The predicted hit rates for various backgrounds [141, 287] are shown in Figure 5.25. These hit rate calculations are based[12] on the sum of the predicted pp-induced fluxes [275] and the simulated LHC induced fluxes [276]. They are computed in the old trigger η-segmentation, in which the RPC-system was implemented up to $\eta = 2.4$ and was divided into 39 trigger towers [287], while the implemented geometry consists of 33 towers and ranging to $\eta = 2.1$ [141].

Hit rates were obtained by summing the charged flux with the photon and neutron fluxes multiplied by their respective sensitivity factors, as done in Equation 5.10. For rough estimates the electron flux causing hits is $O(100)$ times lower than the photon flux, which is in turn $O(100)$ times lower than the neutron flux. The probability for a neutron to produce a signal by the (n, p) recoil mechanism is of the order of $O(10^{-4})$. The calculated rates shown in Figure 5.25 agree reasonably well with older calculations; small differences are due to different muon fluxes and the consideration of LHC-induced background. Since the systematic uncertainty on the simulated particle fluxes is a factor of three, this factor should also be taken into account as a systematic uncertainty on the predicted hit rates.

A realistic forward shielding model resulted in an increase of the estimated background by a factor of two. Efforts were needed to recover the TDR/idealized shielding performance and an optimized shielding design resulted in essentially the same particle fluxes as before [280]. This implies that the results presented in Figure 5.25 are still valid, however they are based on rough estimates for the neutron-capture cross section in the GEANT 3 detector simulation.

More recently, experiments on the neutron and photon sensitivity factors of RPC detectors were performed. Distinguishing hits due to (n,p) recoil or due to a neutron capture producing a photon is experimentally impossible. However, the sensitivity to photons only can be determined by γ irradiation tests, while the sensitivity to both neutrons and photons can be measured by n-

[11] Later on, a realistic shielding design was first tested and later on improved. Simulations in this optimized design predict particle fluxes similar to those obtained in the idealized shielding design [280].

[12] Muon fluxes were taken from other references, see Reference [287] for more details.

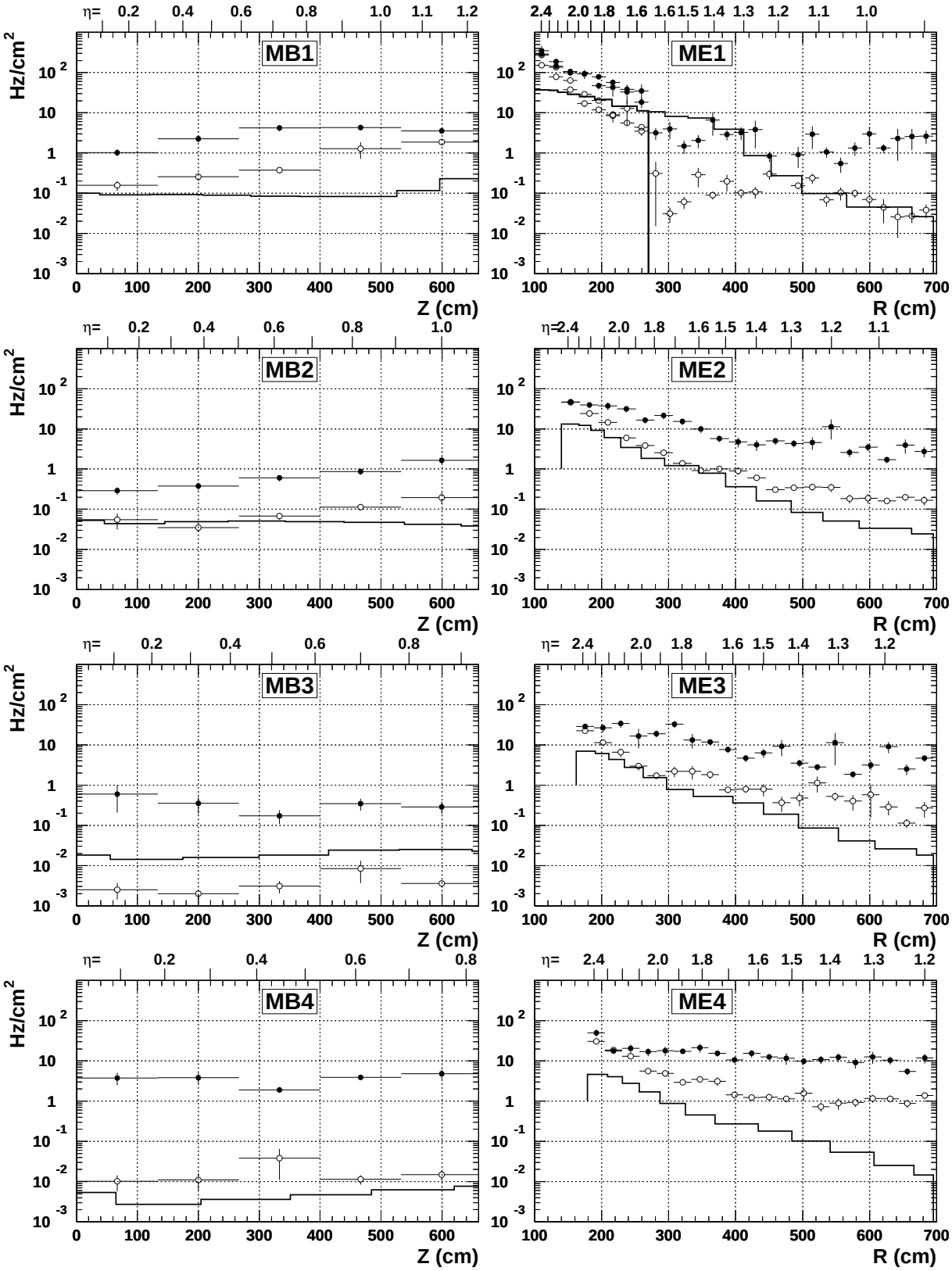

Figure 5.25: Hit rates in muon chambers due to muons (solid line), hadronic punch-through and back-splash (open circles), and thermal neutrons (filled circles) originating from pp-collisions and LHC induced background. Figure taken from References [141, 287].

irradiation tests. The sensitivity to neutrons only can then be calculated afterwards and both sensitivities (to n and to γ's) should be used in Equation (5.10). A sensitivity of $(0.63 \pm 0.02) \times 10^{-3}$ was obtained for neutrons, while for photons a sensitivity of $(1.40 \pm 0.02) \times 10^{-2}$ was measured. Both results were confirmed by a GEANT 3 simulations [288]. Given that these numbers were obtained for a specific beam energy, they seem to have the right order of magnitude. Hence, the hit rates obtained in Reference [287], shown in Figure 5.25, are correct, within a systematic uncertainty of a factor of three.

5.3.4 Neutron simulation studies for SLHC

At very large luminosities, the correct simulation of neutron hits is very important to estimate precisely the trigger rates and trigger efficiencies. Thermal neutrons ($E_n < 0.5\,\text{eV}$) can travel (scatter) through the detector for times to up to 1 second. Therefore the neutrons produced several million collisions ago can contribute to the hits in the current bunch crossing. The CSC detector group within CMS started long ago looking into the influence of neutrons on the CSC performance [284–286]. The GEANT simulation implemented in CMSSW had to be modified to take neutrons into account: the simulation time was increased from 250 ns to 1 s and special physics lists were used that correctly describe the behaviour of thermal neutrons [289]. While more details about the simulation of neutron events are provided here, the digitization and their contribution to the trigger will be discussed later on in section 5.4.

Figure 5.26 shows the simulated hit (simhit) time vs. the hit energy deposition (E_{kin}) for all simulated particles by GEANT for the DT and CSC system and for the RPC barrel and endcap detectors. The simulation time was extended from 250 ns to 0.1 s. There is a huge contribution from electrons (electron hits with TOF $<$ 250 ns), while there are also a lot of hits due to electrons originating from non-prompt neutrons (electrons hits with TOF $>$ 250 ns), which we will call the neutron background. It's worth mentioning that the number of hits arising from the neutrons depends sensitively on the neutron cross sections of the materials in the detectors[13] The electron hits due to neutrons are typically low energetic (keV to a few MeV). As expected from background studies, there are significantly more neutron hits in the endcap detectors, than in the barrel detectors. Even so, there are more hits in the CSC system than in the RPC system, which can be explained by the difference in number of detection layers. The low-energy cutoff that is observed most clearly in the CSC plot comes from the e^+e^- pair creation threshold of 2×0.511 keV. The highest energies are 7-8 MeV, the typical energy of photons emitted from nuclei excited due to neutron capture.

Figure 5.27 shows the comparison between the rough estimates for the hit rates in the endcap muon stations as reported in the L1 Trigger TDR and the hit rates obtained with detailed neutron simulation in the CSC system [292]. The results in the TDR were obtained with GEANT 3 rough estimates for the muon chamber sensitivity and rough estimates for the neutron-capture cross section process, while the newest results were calculated with GEANT 4 and the full CMS simulation. It is remarkable to see that the 15 year old predictions hold up rather well. The version of GEANT 4 has had 15 years of development and these results are surely more reliable than those done back than. As a rough estimate of the neutron rate at the nominal LHC luminosity of $\mathcal{L} = 2 \times 10^{34}\text{cm}^{-2}\text{s}^{-1}$ and for $\eta \leq 1.6$ a rate of $10\,\text{Hz/cm}^2$ is predicted.

[13] E.g. at one time there was a bug in the GEANT 3 cross sections for the RPC material which made these plots look like the RPCs were going to be completely overwhelmed with hits [284].

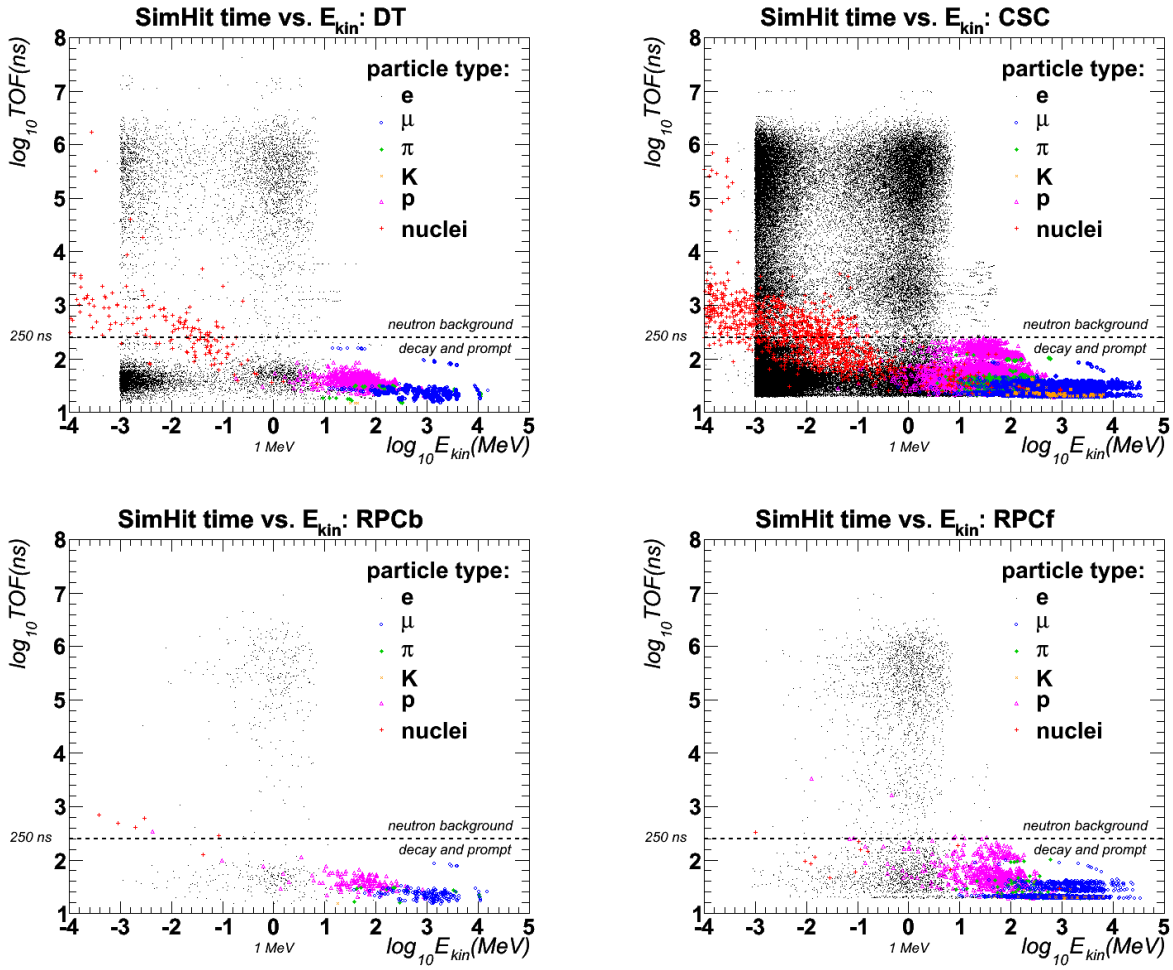

Figure 5.26: Simulation of the interaction of particles produced in Minimum Bias interactions up to 1 s (only shown up to 0.1 s) instead of the normal 250 ns. The particle time of flight before interaction (simhit time) is plotted versus the energy deposit in the Drift Tube detectors (top left), Cathode Strip Chambers (top right), and RPC barrel (bottom left) and endcap (bottom right). Figures taken from Reference [289], based on plots made by Yuri Fisyak and Tim Cox [285, 286, 290, 291].

5.3.5 Measurement of the radiation background

The 2010 *pp*-collision data provide an opportunity to measure the radiation backgrounds at several different (low) luminosities, and to compare these results to the simulations that strongly influenced the design of CMS. Since CSCs consists of 6 sensitive layers, while RPCs consist only of two layers, the trigger rates are expressed in units of Hz layer^{-1} cm^{-2} for the CSCs and Hz gap^{-1} cm^{-2} for the RPCs, denoting clearly that a RPC roll consists of two gas gaps and the rates are expressed for a single gas gap[14]. Both CSC and RPC rates increase linearly with the luminosity and decrease with the distance r to the beam line [153], except for ME4/2 chambers which are at the outer edge of the detector and are not shielded from the neutron flux

[14] Although the noise rates in the RPC system are measured by roll, the results were reported for each gas gap and hence divided by two. There is, however, more to the picture than meets the eye, since the rates are inclusive (cosmics, collisions and neutron background), where the cosmics and collisions cause hits in both gas gaps, while neutron hits only cause single hits. More details on this discussion can be found in Reference [294].

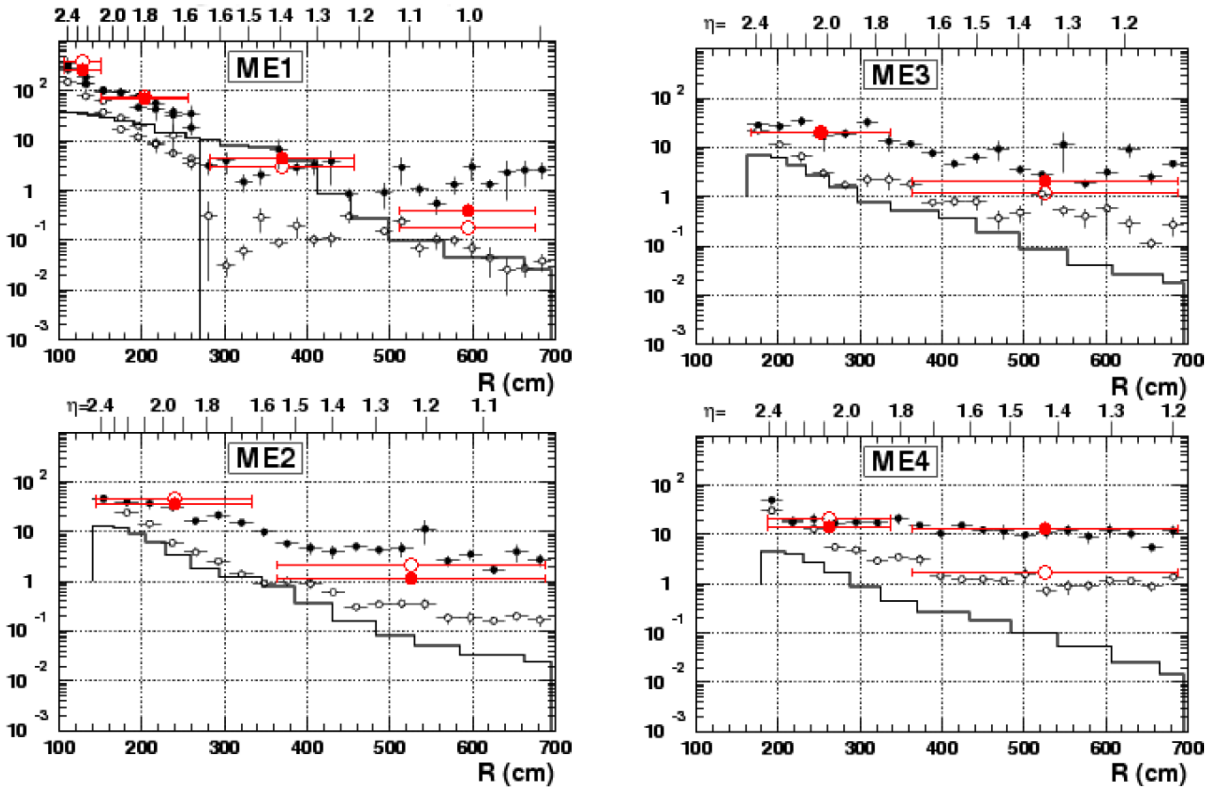

Figure 5.27: Comparison of the hit rates obtained in the CSC system with a detailed GEANT simulation to the hit rates shown in Figure 5.25 obtained in the L1 Trigger TDR [141]. In the TDR plot, the minimum bias muon rate is denoted with a continuous black line, the punch through charged hadrons with open black circles and neutron hits (either direct or indirect by photons) by fulled black circles. The new result sums the punch through and the muon rate into a single minimum bias, shown as open red circles, while the neutrons are shown as filled red circles. Figure taken from Reference [293].

in the cavern, since the YE4 shielding wall is not yet installed. The measurements of the CSCs and RPCs are in good agreement with each other, with RPC rates of $\sim$ 0.1 Hz gap^{-1} cm^{-2} for collisions at an instantaneous luminosity of $1.6{\cdot}10^{32}$ cm^{-2}s^{-1} [153]. Extrapolations to the design luminosity 10^{34} cm^{-2}s^{-1} are smaller than the rates predicted by the simulations made more than 10 years ago, shown in Figure 5.25, although the difference in centre-of-mass energy has to be taken into account: 7 TeV for the measurements, while all simulations were performed for 14 TeV.

5.4 RPC simulation and trigger emulation

The simulation chain explored here starts with generating muons, and tracking them through the detector, followed by the reconstruction of the hits, which are then sent to the trigger electronics, that create the L1 muon regional candidates:

1. **Event generation:** During this step the $pp \rightarrow X$ event (depending on the physics process under study) is generated at the collision point. The output consist of all long-lived particles ($e^{\pm}$, $\mu^{\pm}$, $\pi^{\pm,0}$, $K^{\pm,0}$, p, n, γ). This part contains roughly speaking all physics that

happens inside the beam pipe and gives as an output the particles that can travel through (parts of) the detector. Particles used and produced at this stage of the simulation are called the "GenParticles".

For the study of the RPC trigger, a sample of 10^6 single muons was generated with the *RandomFlatPtGun* of the PYTHIA generator in the CMS software release CMSSW_2_2_10. The muons were generated according to a flat distribution in the region $-2.10 \leq \eta \leq 2.10$ and $0 \leq \phi \leq 2\pi$ with p_T distributed uniformly between 10 and 200 GeV/c.

2. **Vertex smearing:** The luminous region, where two beams cross, is not exactly in one point in the middle of the detector, but more a region of half a meter, centered in the middle of the detector. The position of the vertex is rather smeared over this region.

3. **Pile-Up:** At very high luminosities there will be multiple pp-collisions in each bunch crossing. Each bunch-crossing is read out as being an event and hence consists of several pp-collisions, of which most are "soft" (i.e with low energy-transfer), and only rarely an interesting "hard" event with high-energy transfer occurs. The vertices of the additional soft interactions are also smeared and the pile-up module finally mixes these different interactions with the generated interesting hard event.

4. **Particle propagation** through the detector (EVENT SIMULATION): The long lived particles from the event generator and the pile-up are tracked through the CMS detector, taken into account energy loss, multiple scattering, bending of charged tracks due to the magnetic field and the production of secondary particles. Energy deposits in different *sensitive* volumes of the detector (e.g. the gas volumes of the RPCs) are measured together with the precise point of impact and the time-of-flight of the particle. Additional processes that particles undergo when interacting with matter, such as Bremsstrahlung and pair production are simulated and the daughter particles are also tracked through the detector. These particles are called the "SimParticles" having "SimTracks". Their energy deposits in sensitive layers of the detector, together with their points of impact and exit of the sensitive volume, are called "simhits". The tracking of the particles was performed with GEANT, also incorporated in the CMS Software.

   Not every aspect of a detector needs to be fully and precisely specified in this geometry. RPCs are implemented as simple rectangular or trapezoidal shapes, with a certain thickness, of Aluminium, Bakelite and gas, where the gas consists of the right mixture and is referred to as the sensitive volume. Details such as the thin Copper readout electrodes, cables, electronics, gas pipes and cooling piping are not implemented. Even more important to note is that the RPCs, actually consisting of two gas gaps, are only implemented in the simulation as single gas gaps[15] and also the spacers are not implemented, although they are responsible for 1-2% of inefficiency.

5. **Detector simulation (Digitization):** The simhits have to be translated into physical quantities, such as charge, time and positions that are recorded by the DAQ of the real detectors. This level of simulation is detector specific. The goal of this simulation is to model

[15] Work is currently ongoing to have a more detailed RPC simulation, with double gaps, such that the small effect of non-overlap of the gas gaps can be taken into account properly. The gas volume in the barrel also consists of one single gap, while they actually consist of multiple gaps, leading to small regions where there is no overlap between the two gas gaps.

at least the most important aspects of the detector and electronic signal processing. This simulation can be fairly elaborate, as for the CSC detectors, or rather simplified as for the RPC detectors.

The digitization of the RPC detector is based on a random generation technique to account for the detection efficiency ($\sim 95\%$) and to create a set of fired strips ascribed to a certain bunch crossing and a certain "roll". This "roll" is the smallest possible RPC detector element in η, ϕ. The size of the set of fired strips is called the cluster size and this value is sampled from a distribution taken from data. The cluster size parametrizes several physical effects in a single detector observable: the angle at which the muon passes through the detector, the extent of the avalanche created by the ionization electrons and cross talk between strips. The cluster size is centered around the strip closest to the impact point of the simulation. The bunch crossing assignment is corrected for the signal propagation time, from the IP to the RPC roll. Hits due to noise are simulated using a Poisson distribution. This noise includes all sources of noise: electronics, gap noise and background hits due to neutrons. All hits (signal and background) are kept separately for each roll and consist of a strip number and a BX assignment, and are called "digis". Digis created due to simulated hits are kept in a "DigiSimLink" collection, such that the trigger performance can be studied afterwards.

Different RPC digitization models can be used to digitize the simulated hits, ranging from a very simple simulation of the RPC detector response to a more detailed one where all parameters could be set strip by strip. The most important models are:

- **RPCSimParam:** A parametric simulation of the RPCs: noise, efficiency and the cluster size distribution are equal for all rolls.
- **RPCSimAverageNoiseEff:** A detailed simulation of the RPCs: noise and efficiency could be set strip by strip, while the cluster size is sampled from an exponential distribution.

Although the latter model is adopted (which is a very parametrized approach), the results of the simulation are in very good agreement with the data [153].

Previous simulation studies [274] assumed non-oiled chambers, which have an intrinsic noise rate of 50 Hz/cm^2, due to discharges of the electric field at irregularities in the electrode surface. The RPCs built for the CMS detector are oiled chambers, which gives rise to much smaller intrinsic noise rates. The average intrinsic noise rate was considered to be 0.05 Hz/cm^2, which is rather optimistic, but simulations have shown that the RPC trigger is rather robust with respect to a difference between a realistic noise rate of 1 Hz/cm^2 and 0.05 Hz/cm^2.

The noise due to neutral (and charged) particle background is simulated in exactly the same way as the intrinsic noise. The read out of an event consists of 9 bunch crossings (BXs), ranging from -4 to +4, where the simulated muon is embedded in BX = 0 and the number of noise hits are distributed over all 9 bunch crossings according to a Poisson distribution whose average is the nominal noise rate (expressed in Hz/cm^2). The noise hits are then uniformly distributed over the surface of the roll.

6. **Trigger emulation:** The digis are the input to the custom electronics of the RPC Trigger. The logic implemented on these electronic boards is simulated by the "Trigger emulator". The emulator matches the pattern of the digis to the strip pattern of muons saved in the

Look Up Tables. If a match is found, the properties of the muon (η, ϕ, p_T) is propagated as the *regional muon candidate*.

In the barrel, two sets of patterns are used to match the digis to a muon track: a low p_T pattern based on the first two stations, having two layers each (RB1in, RB1out, RB2in and RB2out), and a high p_T pattern, using all six layers of the RPC system. A quality code is assigned to these regional muon candidates, according to the number of digis matched to the pattern of the muon: A muon with digis from three different layers has quality 0, while a muon with digis of all six layers (only possible in the barrel), is well measured, and has quality 3.

There can be more than one *regional muon candidate* related to a set of fired strips, which is called a *ghost muon*. An algorithm for ghost busting has been implemented to eliminate this behaviour as much as possible. All muon candidates of barrel and endcap are sorted, first in quality, then in p_T and the four best candidates of both barrel and endcap are returned to the Global Muon Trigger (GMT).

To study the L1 RPC regional trigger, the regional muon candidates were compared with the simulated tracks to compute the trigger efficiency and the ghost rate:

- The **trigger efficiency** is defined as the probability of triggering a muon of a given generated p_T and assigning a p_T above the p_T^{cut} to the regional muon candidate [274].
- The **ghost probability** is defined as the probability of reconstructing two muons if only one muon is simulated.

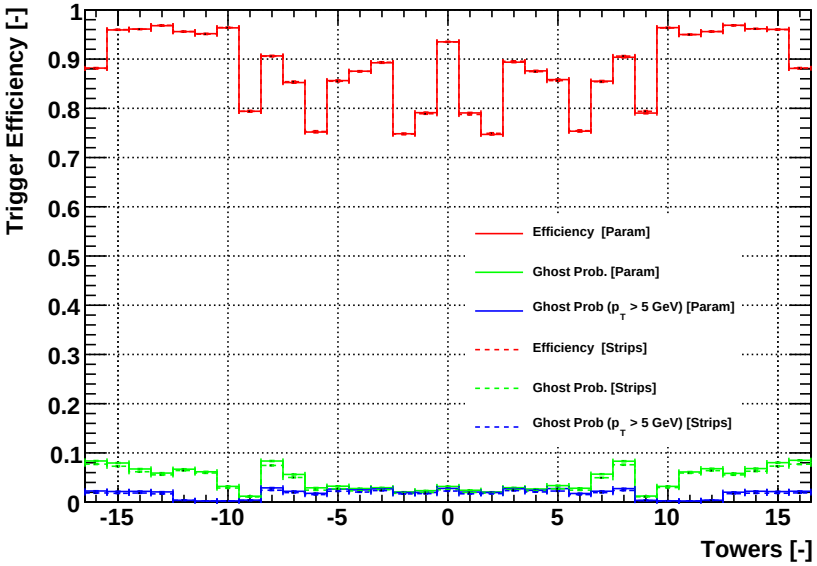

Figure 5.28: Trigger efficiencies and ghost probabilities vs. towers in the TDR geometry for the two different RPC Digitization models described above. Differences between the two models are within statistical uncertainties.

The trigger efficiency obtained with two different RPC digitization models, *RPCSimParam* [Param] and *RPCSimAverageNoiseEff* [Strips] is shown in Figure 5.28, along with the ghost

rate and the rate of ghosts with $p_T > 5$. The simulation was performed for the TDR geometry, with all RPC chambers installed. The efficiency of the RPC detectors was implemented to be 95 % while the noise rate was implemented to be as low as $0.05\,\mathrm{Hz\,cm^{-2}}$. The difference between the two models is hardly visible and within the small statistical uncertainty of the simulation. These results are, taking into account the changes in detector design (non–oiled chambers vs oiled chambers) and a more detailed and realistic detector geometry, consistent with earlier studies [141, 274].

A first check was performed by understanding the shape of the efficiency curves. This can be done using Figure 5.14 showing the x, y layout of the barrel RPC system and Figure 5.16 showing the η trigger towers in the R, z layout for the whole RPC system. Figure 5.14 shows considerable gaps in ϕ between the RPC chambers, while the ϕ-coverage in the endcaps is rather hermetic. Furthermore the RPC system in the barrel suffers from η-gaps in between the barrel wheels, while for the endcaps, only one such gap is at the place where z-stops are installed to keep the endcap disks at a certain distance from the barrel wheels. These effects lead to the high overall efficiency in the endcap towers (±10–16), where the lower efficiency of tower ±16 is due to a small fraction of muons falling out of acceptance. Towers ±8 and ±9 use RPC planes from both barrel and endcap, but are assigned to the endcap, since the reference station is in the endcap. The z-stops cause lower efficiency in tower ±9, while endcap towers ±8 suffer from gaps in ϕ in the barrel.

An explicit check was obtained by comparing the trigger efficiencies in Figure 5.29 obtained by this simulation and a previous study [295] made for the L1 Trigger TDR [141]. Fair agreement was obtained in the barrel region, while even better agreement can be observed in the region where all reference segments are defined in the endcap: towers 8–16 in Figure 5.16, or $1.04 \leq |\eta| \leq 2.1$. The difference can be due to an improvement in the patterns.

The tremendous effect of the gap between wheel 0 and wheel ±1 on the RPC trigger efficiency is not visible in the plots in the L1 Trigger TDR [141], while it has been confirmed in the more recent studies [292]. The gap at $1.14 \leq |\eta| \leq 1.24$ is due to the z-stops, where no RPC coverage is possible in RE1. All lower efficiency regions can be pointed back to "cracks" in the detector, where muons can pass one or more layers without being detected. The lower efficiency in the barrel can be brought back to "cracks" in the $r - \phi$ geometry, as shown in Figure 5.14.

The region in between the first barrel wheels YB0 and YB±1 ($0.15 \leq \eta \leq 0.4$) has a particularly bad acceptance for several reasons. First, all signal cables and services coming from the detectors installed inside the solenoidal magnet are routed on top of the cylindrical magnet and are guided to the periphery of the detector in between YB0 and YB±1. Second, two chimneys for the magnet cryogenics had to be carved out of the yoke of YB±1, reducing the size of the muon detectors, both RPC and DT, in that sector. The location of those two chimneys is clearly visible in Figure 5.30 showing the acceptance (here: the average amount of simulated hits caused by a muon track passing through the detector) and trigger efficiency in the η,ϕ plane. The separation between the different barrel wheels is obviously visible for the central three wheels, while the influence of the gap between the second and third wheels on each side appears as a slightly more complex structure, showing areas of higher and smaller acceptance. The coverage in the endcap region is very uniform and nearly everywhere 4 simhits could be obtained, resulting in a high overall efficiency.

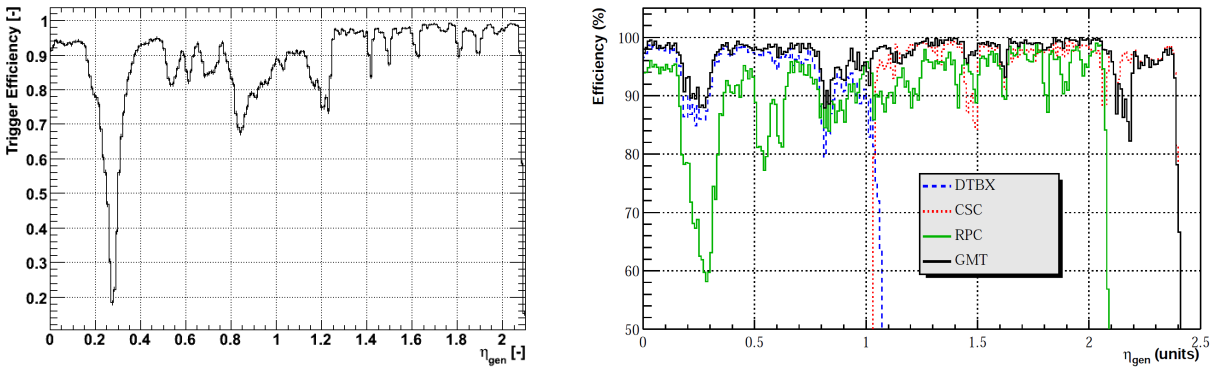

Figure 5.29: Left: RPC trigger efficiency obtained with CMSSW_2_2_10 in the fully restored TDR geometry (four layers in the endcap and $\eta \leq 2.10$). Right: The "reference" trigger efficiencies for DT, CSC, RPC and GMT in the TDR geometry, obtained in studies [295] performed for the L1 Trigger TDR [141] in 2000.

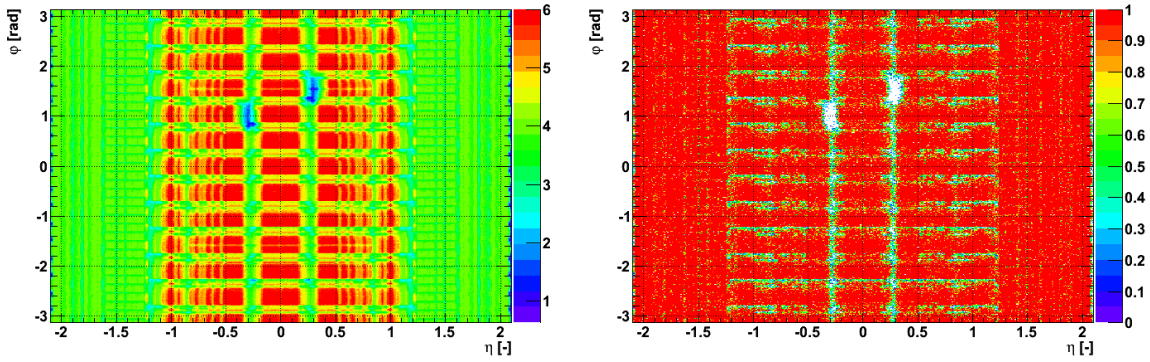

Figure 5.30: The acceptance, expressed as the average amount of simulated hits a simulated muon track leaves in the detector geometry, and trigger efficiencies for the RPCs in the TDR geometry.

Triggers matched to hits in more layers yield better p_T measurements and hence are assigned higher quality than triggers with less matched hits. In tower 9, only three planes are available for measuring muons, leading to very low quality ($Q = 0$) hits and lower trigger efficiency. Hits are often missed because of the muons passed through cracks in the detector, but they could also be due to detector inefficiencies. Figure 5.31 shows the contribution of the high and low quality triggers to the RPC Trigger efficiency, as a function of the continuous η (left) or as function of the different trigger towers (right).

The quality of the triggers is important for the Global Muon Trigger. The GMT compares the triggers of the different muon systems and looks for matches between them, which are assigned the highest (GMT) quality. Triggers not confirmed by the other muon systems can only pass if they have the highest quality assigned within their own trigger system.

Figure 5.32 shows the RPC trigger turn-on curves for different p_T cuts. Steep turn-on curves are very important to keep low trigger rate. Since the low p_T muons have much higher abundance, they might, when mismeasured, pass tighter p_T cuts and fill the trigger with low-p_T muons.

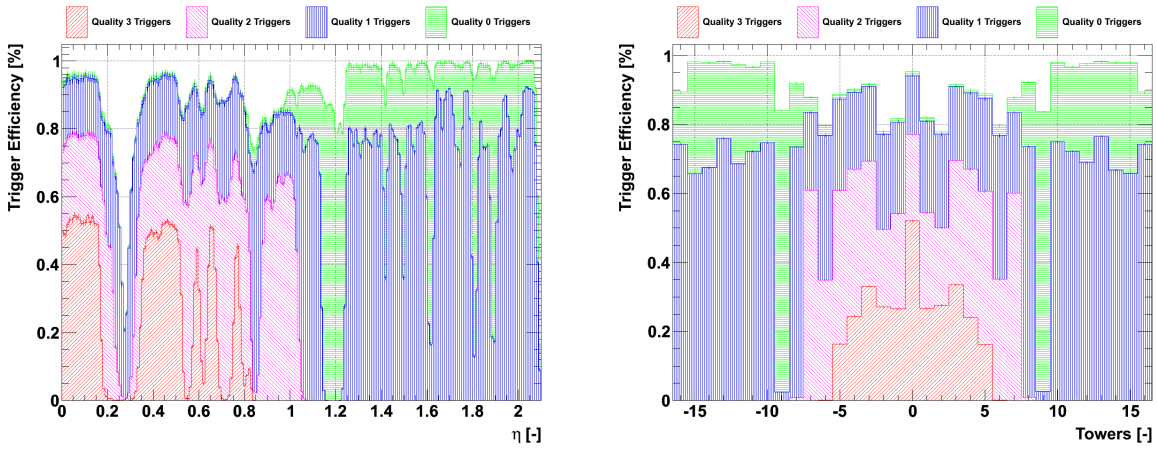

Figure 5.31: The quality of the triggers contributing to the trigger efficiency calculation with the TDR geometry as a function of η (left) and the trigger towers (right).

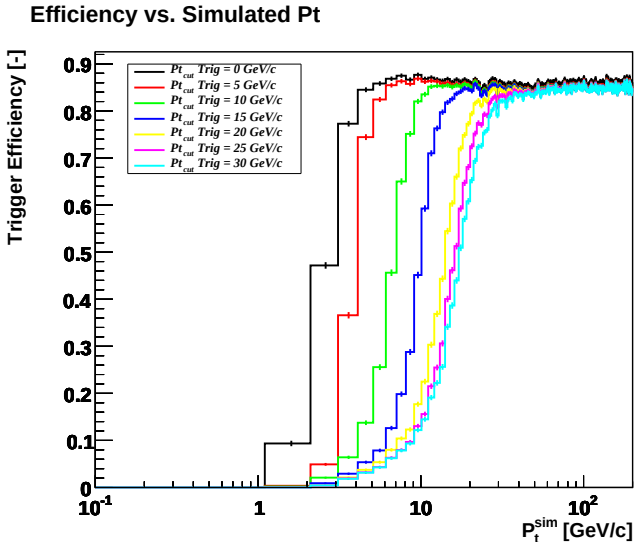

Figure 5.32: The RPC trigger turn-on curves as a function of simulated muon p_{T} for different thresholds using the TDR geometry.

A small probability to mismeasure low-p_{T} muons as being high-p_{T} muons, leads to seriously higher trigger rates.

5.5 Trigger performance study

The RPC system in the endcap is not fully constructed and installed and several modifications to complete the RPC system have been proposed in the past. A study performed in 2001 [228] suggested that the addition of a fifth layer would improve the muon trigger efficiency and trigger rate by requiring 4 hits out of 5 stations passed by a muon. Unfortunately, from the detector integration point of view, it was impossible to have a completely independent fifth station installed. Independent means a separate readout of the signal and a certain lever arm with respect

to the other RPC stations, for which separate services (HV, LV, gas, cooling) would be required and push op the price tag. Therefore, suggestions were made to replace the second RPC station with a double station, killing the high background rate by asking for coincident muons. This is clearly not an independent measurement, but rather a confirmation of the hit in the second muon station. The second muon station was chosen, since it is the muon reference station, uniquely defining the trigger segment the muon passed through. In the beginning of the development of the PAC electronics, this chamber was indispensable, since it was the muon "seed" station. The PAC trigger started with the hit in this chamber to look for a match in the Look Up Tables. A missed hit in this station would immediately have led to missing the muon trigger. Later on, the trigger electronics were changed so that the muon seed station is changed when the hit in the second RPC station is missed.

To investigate this double second station, four possible scenarios for the restoration of the RPC system were considered. All have been simulated up to $|\eta| \leq 2.10$ unless stated otherwise:

- The system as it exists now: three planes in the endcap up to $|\eta| \leq 1.61$ [StartUp/3Pl].
- The system as described in the TDR: four planes in the endcap [TDR/4Pl].
- The TDR system completed with a double station in RE2 [RE2bis].
- The TDR system completed with a double station in RE4 [RE4bis].

5.5.1 Simulation of a double RPC station

The double stations were not implemented in the geometry, but were instead mimicked by appropriate conditions of the RPC parameters for the rolls of those special stations. To deal with different values for different rolls, the *RPCSimAverageNoiseEff* digitization was used. The double station was considered as a single station with the efficiencies and noise rates of a double station. To compute the latter quantities, we started from two RPCs with same length x, width y (in cm) and strips n but with respective efficiencies ϵ_1 and ϵ_2 and noise rates R_1 and R_2 (in Hz/cm^2) to obtain a coincident efficiency of:

$$\epsilon_{\text{AND}} = \epsilon_1 \epsilon_2. \tag{5.11}$$

The probability for a coincidence in strip i is the probability P_1 to have a hit in strip i of the first station multiplied by the probability P_2 to have a hit in the very same strip i of the second station. This strip i could be chosen n times, therefore the probability for the coincidence of the two stations is $P_{\text{AND, station}} = n \cdot P_1 \cdot P_2$. The probability for a strip to have a hit is given by the rate in Hz/cm^2 multiplied by the strip area $A_i = \frac{x \cdot y}{n}$:

$$P_{\text{AND, station}} = n \cdot R_1 \frac{xy}{n} \cdot R_2 \frac{xy}{n}. \tag{5.12}$$

The coincident rate is then obtained by evaluating how often this coincident probability occurs per station area $x \cdot y$ in a bunch crossing interval of 25 ns, or stated in another way, how often this coincident probability occurs at a $40 \cdot 10^6$ Hz bunch crossing frequency:

$$R_{\text{AND}} = \frac{P_{\text{AND, station}} \times 40 \cdot 10^6}{xy}. \tag{5.13}$$

This leads to a coincident noise rate of:

$$R_{\text{AND}} = R_1 R_2 \frac{xy}{40\,10^6 n}. \tag{5.14}$$

As a check of this analytical formula, a toy Monte-Carlo simulation was written, generating hits on both layers following a two-dimensional uniform distribution. The coincident rate, for firing exactly the same strips at a frequency of 40 MHz was extracted. Figure 5.33 shows the coincident noise rate given by the toy Monte-Carlo model (red triangles) describing exactly the coincident noise rate R_{AND} predicted by the analytical model (red dashed line). The plot also shows the gain in reducing noise one obtains by asking for a coincidence with a second station. This "Noise Reduction Rate" is defined as the rate divided by the coincident rate: R_1/R_{AND} and is shown as a blue dotted line. One sees that two stations, both with random noise of 100 Hz/cm^2 have a coincident rate of less than 0.1 Hz/cm^2, which is a reduction of more than a factor 1000, and that two chambers with 1 kHz of random noise only has a coincident rate of $\sim$ 10 Hz, a reduction of $\sim$ 100. The analytical formula, however, is not valid for very high noise rates, where the probability to have two hits on the same strip within the same chamber in the same bunch crossing is not negligible. A modified toy Monte-Carlo simulation took this into account and is plotted as the green dashed line. For noise rates above 10 kHz saturation occurs.

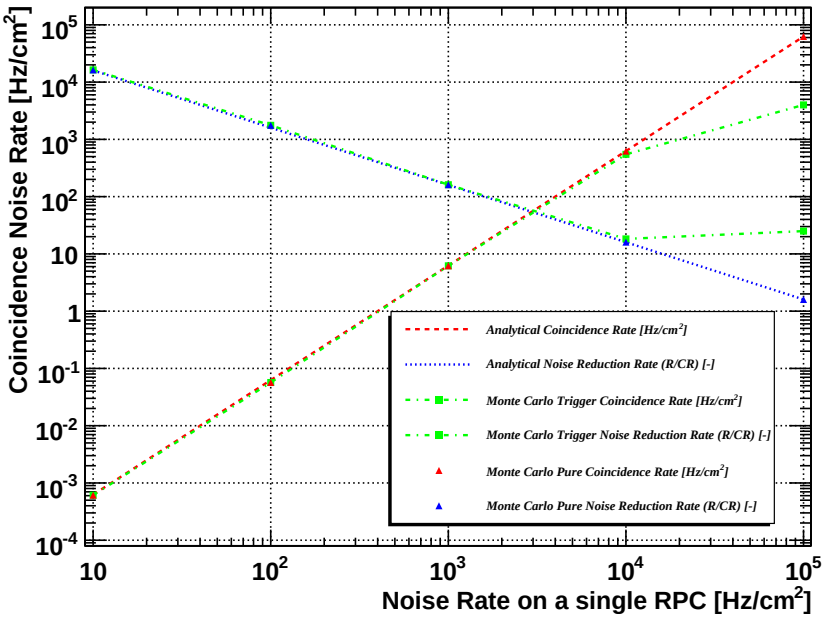

Figure 5.33: The noise rate and the noise reduction rate using the analytical formula (red dashed line, resp. blue dotted line) and for the toy Monte-Carlo simulation (filled red triangle, resp. filled blue triangle). A modified toy Monte-Carlo simulation was made to take multiple hits on the same strip into account (green dashed line with green marker). There is excellent agreement between the analytical formula and the modified Monte-Carlo simulation for rates $\leq 10^4$ Hz/cm^2.

As a rule of thumb for the simulation of RE2bis, the coincident rate of two chambers of 10 Hz/cm^2 and 100 Hz/cm^2 was assumed to be negligible (zero), while the coincident rate of two 1000 Hz/cm^2 chambers was set to 10 Hz/cm^2. To check if the noise rates were properly simulated in the CMS software, 100 000 events were simulated with a single muon with p_{T} lower than the acceptance for the muon system and counted the hits in the RPC system due to the noise setting of 100 Hz/cm^2, both for barrel and endcap. Figure 5.34 shows the distribution

of the noise rate for 100 000 events, simulated with a noise of 100 Hz/cm^2. The distribution is described very well by a Gaussian distribution and the corresponding fit shows that there is no offset and the distribution has a standard deviation of $\sigma = 4.4$ in the barrel and $\sigma = 6.7$ in the endcap. This proves the noise implementation in the RPC simulation to be bug free.

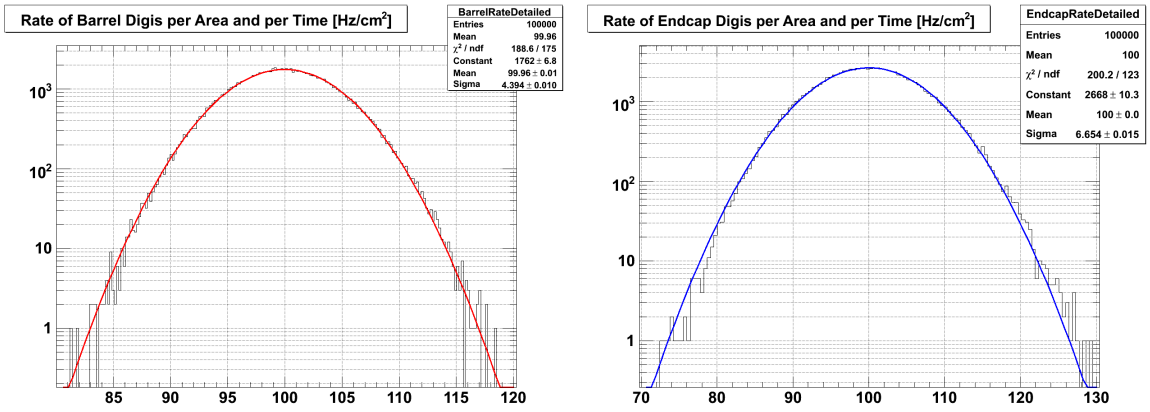

Figure 5.34: Noise hits simulated in the RPC system: barrel (left) and endcap (right). The plots show the amount of events as a function of the different measured noise rates, in Hz/cm^2.

5.5.2 Trigger efficiency result

The result of the improved trigger efficiency for the TDR design, with respect to the currently installed RPC system, in the pseudorapidity region $1.04 \leq |\eta| \leq 2.10$, is shown in Figure 5.35. Although the study only had to evaluate the upgrade of the RPC system for $|\eta| \leq 1.6$, the study was performed up to $|\eta| \leq 2.10$, since that allowed for comparison to earlier studies. The trigger efficiencies for the RE2bis and RE4bis scenario were also studied and were found to have similar behaviour but were slightly lower, due to the lower chamber efficiency of the second and fourth chamber respectively, which is 90% instead of 95%.

In the four layer TDR geometry a 3-out-of-4 trigger is possible, whereas in the currently installed system the trigger logic is 3-out-of-3, not allowing for a muon to have a detection inefficiency in an RPC chamber or passing through an uninstrumented region, thereby missing an RPC chamber. An improvement of nearly 20% is visible due to the upgrade. Building a fourth station would bring the RPC system to a full trigger detector, restoring the redundancy as described in the original TDR proposal.

As a first check the results of the present simulation study were confronted with the results obtained in 2001 [228]. Figure 5.36 compares the original results (full lines) for the trigger efficiency versus the trigger rate at a p_T cut of 25 GeV/c to the results obtained in the new CMS software (dashed lines). The plot was created by performing two independent studies for each point in the (discrete) space spanned by the RPC chamber efficiency (95% and 98%) and noise rate (50 Hz/cm^2 and 100 Hz/cm^2). A sample of 1 000 000 muons with $1.04 \leq |\eta| \leq 2.10$ and $10 \leq p_T \leq 200$ GeV/c was used to determine the trigger efficiency of the RPC endcap system and provided the y-axis coordinate, while a sample of 40 000 000 events with muon $1.04 \leq |\eta| \leq 2.10$ and $p_T = 1$ GeV/c and noise rates of 50 Hz/cm^2 and 100 Hz/cm^2 were used to determine the trigger rate due to random noise, which is the x-axis coordinate. This procedure results in four points showing the RPC trigger efficiency as function of the trigger rate. For

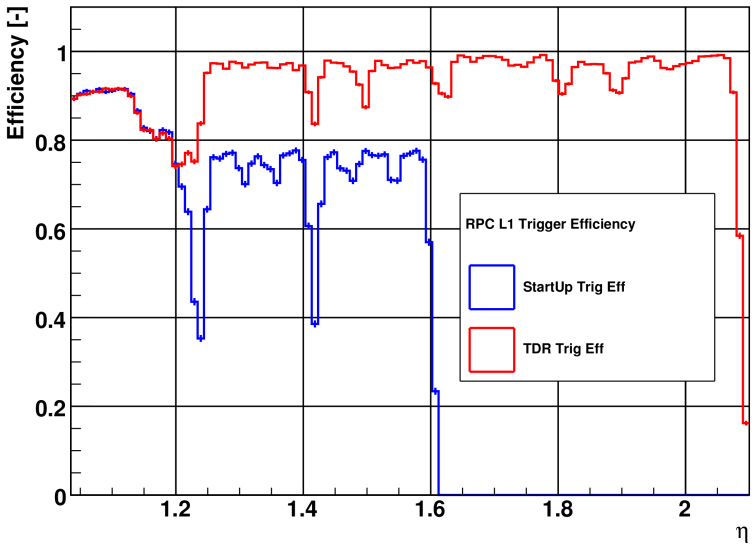

Figure 5.35: Trigger efficiency using 4 RPC stations in $1.04 \leq |\eta| \leq 2.10$ ("TDR", red) compared to the currently installed three station RPC system in $1.04 \leq |\eta| \leq 1.60$ ("StartUp", blue).

these plots only noise was generated (no signal muons) and this trigger rate shows the rate that a random combination of noise hits makes up a pattern matching the trigger patterns with $p_T > 25\,\text{GeV}/c$. The red boxes show trigger efficiency vs. trigger rate for 3-out-of-4 triggers, while the blue boxes are for 4-out-of-4 coincidences.

Apart from the software change, there were improvements in the RPC simulation geometry and the RPC patterns were updated to tighter patterns allowing for better high-p_T assignment but lower efficiency for low-p_T muons. Furthermore, the previous study was performed for non-oiled chambers, which have an intrinsic noise rate of 100-150 Hz/cm^2. Therefore, the four points were simulated again, but now with 150-200 Hz/cm^2 noise rate (dotted lines). The good agreement for the 4 out of 4 triggers was lost, while a slight improvement in reproducing the old results in the 3 out of 4 triggers was obtained. Finally, it was concluded within the RPC Detector Performance Group that it would be impossible to reproduce the old plots and that the trigger simulation was reliable enough to study the difference between the different "upscope" geometries.

For the study of the different upgrade geometries, simulations were performed for the full endcap ($1.04 \leq |\eta| \leq 2.10$) and for nine points in the 2D space RPC chamber efficiency vs. noise: efficiencies of 90%, 95% and 98% are simulated for intrinsic noise rates of 10, 50 and 100 Hz/cm^2. The results are shown in Figure 5.37 for the 3-out-of-4 logic applied to the current situation, in which only three layers are installed in the endcap. The red trapezium shows the result for the 3-out-of-4 triggers in the current geometry, where a maximum trigger efficiency of 80% is reached for 98% efficient RPC chambers. The trigger rate due to noise ranges from less than 10 Hz up to almost 10 kHz. The green rectangle shows the 4 out of 4 triggers in the three layer geometry. This is possible, since the trigger segments up to $|\eta| \leq 1.24$ use hits from the barrel and do not use hits from the fourth station. This can be seen clearly in Figure 5.16.

The TDR design was simulated as well, resulting in the dark blue box for the 3-out-of-4 triggers

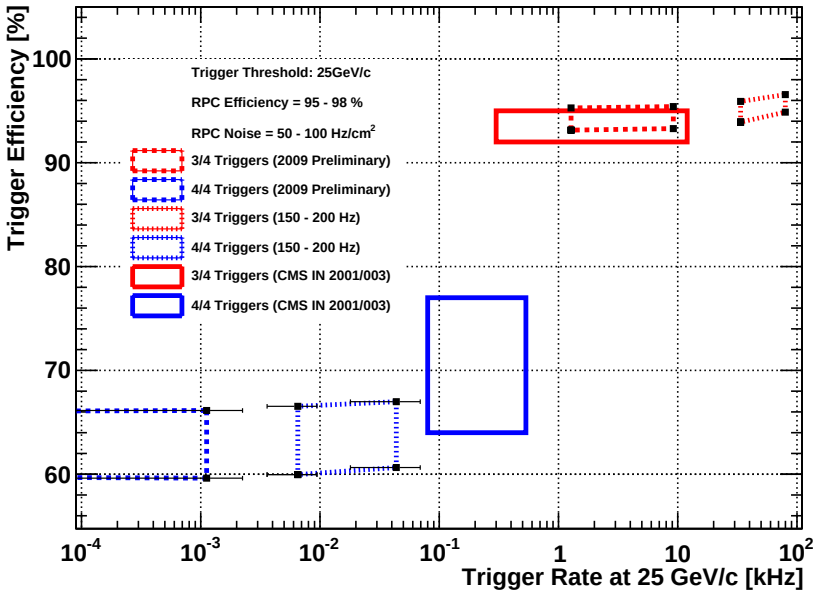

Figure 5.36: Reference plot for Trigger efficiency vs. trigger rate for different geometries at a trigger threshold p_T of 25 GeV/c.

and the yellow box for the 4-out-of-4 triggers. The 3-out-of-4 trigger boxes for the double station at the second station, RE2bis (labelled RE2 in the legend of the plot) and RE4bis (denoted RE4 in the legend) are the cyan blue, respectively the dark green box. The 3-out-of-4 triggers are the most important ones for this study. To study the 4-out-of-4 triggers, the 40 000 000 events impinging on the endcaps were not sufficient to simulate trigger rates of the order of 10^{-3}kHz or lower.

The important part of the plot is the comparison between the TDR geometry and the RE2bis and RE4bis geometries for the 3-out-of-4 triggers. Adding a fifth independent plane improves a lot with respect to the random noise trigger rate, while Figure 5.37 shows only a marginal improvement for the RE2bis and RE4bis geometries. Background rates of 10 Hz/cm^2 are most realistic and they result in the three left most dots of the trapezoidal structures (one point for each efficiency setting: 90%, 95% and 98%). They show an rate improvement of a factor $\sim$ 5 for RE2bis with respect to the TDR design, which is rather low compared to the rate improvement of factor $\sim$ 30 obtained for the independent 5$^{\text{th}}$ plane in the original study [228].

5.5.3 Trigger rate result

Apart from the RPC system, also the CSC system has not been installed completely: the 72 ME4/2 chambers are missing. While the aim of the RPC upgrade is to increase the trigger efficiency to more than 90% overall, the upgrade for the CSC system is motivated by a trigger rate reduction. The current CSC track finder (CSCTF) uses a 2-out-of-3 coincidence, which has high efficiency due to the high CSC chamber efficiency[16] [153], but has rather poor p_T resolution. With a fully installed fourth station, the CSCTF can require a much tighter 3-out-

[16]The CSC local trigger, discussed in section 3.2.7 requires at least four hits out of the six detection layers of the CSC, resulting in a high efficiency of the CSC chambers for the detection of muon tracks.

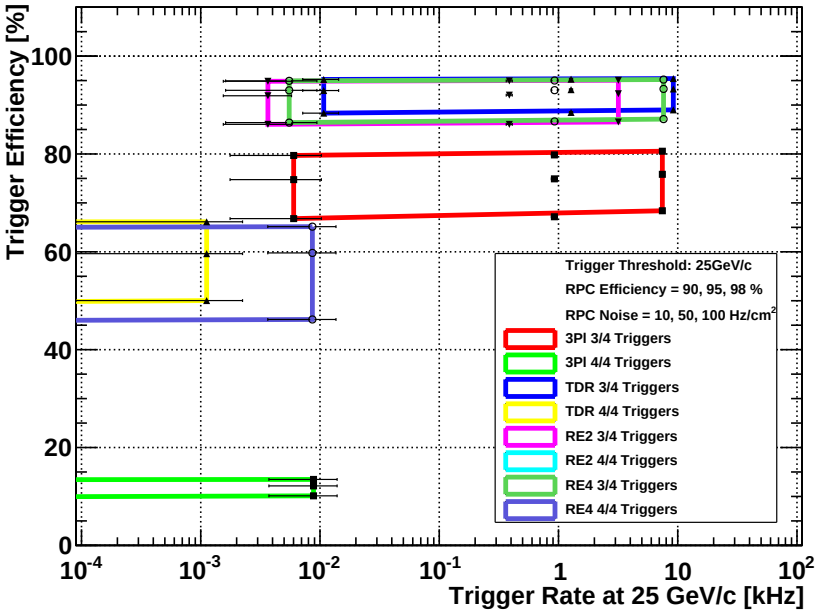

Figure 5.37: Trigger efficiency vs. trigger rate for the current RPC geometry and for different upgrade geometries.

of-4 coincidence, leading to a better p_T estimation and hence lower trigger rate.

The trigger rate reduction due to the addition of the fourth CSC station (ME4/2) is shown in Figure 5.38(a). The 3-out-of-4 coincidence gives only a slightly higher efficiency, but especially improves the p_T measurement of muons with one lost track stub, mainly due to a "crack" in the detector. One big crack is right at the position of the z-stop, which keeps the first yoke disk (YE±1) at a fixed distance of the second barrel wheel (YB±2) and is located in between ME1/2 and ME1/3. A second smaller crack occurs between ME2/1 and ME2/2. The addition of the fourth station also helps in correctly identifying scattered low energy muons, that appear to have a much straighter track (and hence higher p_T) than they should have. Both aspects help to improve the p_T estimate for the muon at L1 trigger level and reduce the rate drastically. In order to stay below the target L1 trigger rate of 5 kHz, one has to apply a p_T cut of 47 GeV/c if no ME4/2 CSCs are installed, and this can brought back to 18 GeV/c if ME4/2 CSCs are installed.

Although it is not the primary goal of the RPC upgrade to obtain a trigger rate reduction, the trigger rate for the upgraded RPC system is also simulated and compared to a simulation of the trigger rate of the existing RPC system. To investigate the RPC trigger rate reduction, a flat muon sample was generated, similar to the sample used by the CSC group, with $3 < p_T < 100$ GeV and $1.25 < \eta < 1.9$, of which the $1.25 < \eta < 1.6$ subset was used. The flat spectrum was weighted according to a formula parametrizing the muon rate in Reference [287], which was in preparation for the L1 Trigger TDR [141]. This parametrization describes the muon rate due to prompt muons from W and Z decay, and minimum bias muons due to the decay of b and c quarks as well as secondary muons from pion and kaon decays. The formulae from

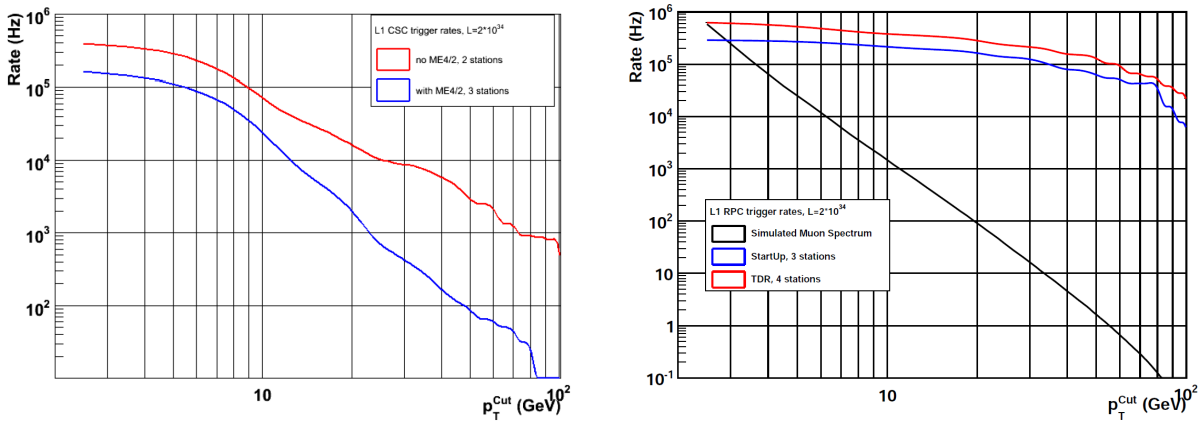

(a) L1 CSC trigger rates

(b) L1 RPC trigger rates

Figure 5.38: L1 Trigger rates for different geometries in the CSC system (left) [296] and the RPC system (right) at the design luminosity ($\mathcal{L} = 2 \times 10^{34}\,\mathrm{cm}^{-2}\mathrm{s}^{-1}$) and centre-of-mass energy ($\sqrt{s} = 14\,\mathrm{TeV}$). The generated muon spectrum used in both figures is shown at the right. For the CSC system the trigger rates were calculated for a system with and without the ME4/2 chambers [296]. For the RPC system, the trigger rate was simulated with and without RE4. For both 10 Hz of random noise was added everywhere.

Reference [287] were integrated over η and read:

$$N_{\mathrm{prompt}}(p_{\mathrm{T}}^{\mathrm{sim}}) = 1.3084 \cdot 10^6 \times \exp\tfrac{1}{2}\left(\frac{^{10}\log p_{\mathrm{T}}^{\mathrm{sim}} + 0.725}{0.4333}\right)^2, \tag{5.15}$$

$$N_{\mathrm{decay}}(p_{\mathrm{T}}^{\mathrm{sim}}) = 3 \cdot 10^7 \times 4.19 \times \left(p_{\mathrm{T}}^{\mathrm{sim}}\right)^{-5.19}. \tag{5.16}$$

The RPC trigger rate simulation is shown in Figure 5.38(b), where the trigger rate with and without the fourth station (RE4) is shown. Instead of a rate reduction, as in the CSC system, a small rate increase was obtained, because of an efficiency improvement of $\sim 20\%$ and mostly because of the increased amount of possible combinations for ghosts, upgraded (low p_{T}) muons and fakes. A very precise p_{T} estimation is the "conditio sine qua non" for reducing the trigger rate. Without precise p_{T} measurement, the triggers are overwhelmed by the low p_{T} muons, and assigning high p_{T} to even a small fraction of low p_{T} muons leads to huge trigger rates. This is a well-known effect, shown in Figure 5.39(a), where the RPC trigger rate reaches a "plateau", while the muon spectrum follows a $1/\hat{s}$ spectrum.

One would like to understand the effect of the RPC upgrade on the Global Muon Trigger rate. This required the inclusion of the CSC detectors in the RPC study, but this was not straightforward since CSCs and RPCs have a totally different approach to the simulation of background hits. In the RPC simulation, the total noise, consisting of hits from cosmic rays, noise due to electronics and due to spontaneous discharges in the gas gaps and neutron hits are modelled by a single Poissonian distributed noise value, defined by the central value of noise per strip. In contrast, the CSC are described by a pretty complete simulation of the charge collection, and amplification, shaping and signal readout in the CSC electronics. The different steps inside the CSC simulation results in different sources of noise (e.g noise related to the creation of a signal on the wires and on the strips, noise related to electronics, noise due to neutron background),

which are all simulated separately. To have a realistic simulation in the RPCs, the background hits due to neutrons should be treated the same way as was done in the CSCs. Therefore the strategy was adopted to use the RPC noise parameter only for the intrinsic noise related to electronics and dark current, but to simulate the neutron background noise separately, as was done in the CSC system. This has the advantage that all sources of noise independent of the instantaneous luminosity are treated as a single parameter, while the noise proportional to the instantaneous luminosity is taken into the simulation. This makes sense for the production of huge Monte-Carlo simulation samples for physics analysis.

As a first check the rate in the RPC system was simulated at $\mathcal{L} = 2 \cdot 10^{34}\,\mathrm{cm^{-2}s^{-1}}$ and scaled by a factor ten to compare to the RPC trigger rate in the Physics TDR [144] obtained for $\mathcal{L} = 2 \cdot 10^{33}\,\mathrm{cm^{-2}s^{-1}}$. Figure 5.39(a) shows the RPC trigger rate of the Physics TDR overlaid with the scaled RPC trigger rate with and without RE4. The TDR trigger rate compares rather well to both rates, and a slightly higher trigger rate was obtained for the upgraded RPC system, hereby confirming the qualitative result of Figure 5.38(b). As a second check the trigger rates with noise uniformly distributed over the RPC system were simulated in Figure 5.39(b) for a luminosity of $\mathcal{L} = 2 \cdot 10^{33}\,\mathrm{cm^{-2}s^{-1}}$. A uniform noise rate of 25-120 Hz/cm^2 increases only slightly the RPC trigger rate. A quantitative difference of a factor ten is observed when compared to Figure 5.38(b), where a uniform noise rate of 10 Hz/cm^2 was applied, and its origin is not firmly established. This, however, has no impact on the RPC trigger upgrade, since the main motivation is to restore the high efficiency. Furthermore, the global muon trigger relies heavily on the precise p_T estimation of the CSC system to remain below the allowed 5 kHz output rate, as will be shown later on.

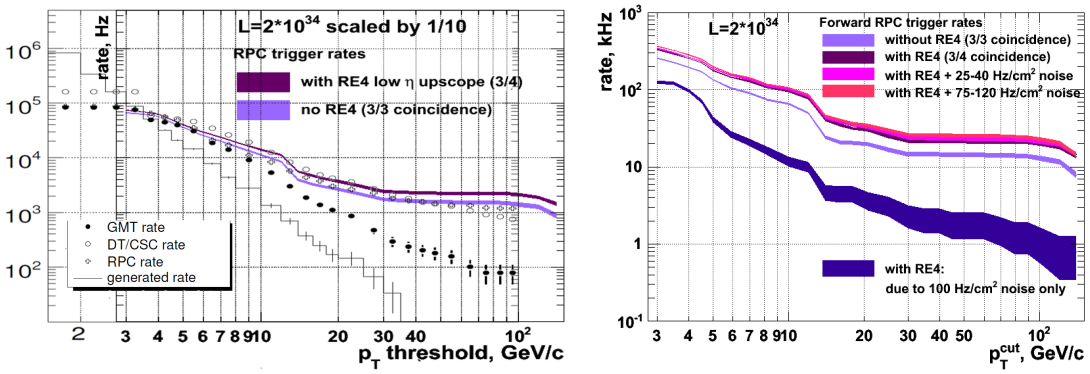

Figure 5.39: Figures taken from [144, 292]. Left: Validation of the obtained RPC trigger rates against RPC trigger rates at $\mathcal{L} = 2 \cdot 10^{33}\,\mathrm{cm^{-2}s^{-1}}$ by overlaying the RPC trigger rates (scaled by a factor 1/10, since it was obtained at $\mathcal{L} = 2 \cdot 10^{34}\,\mathrm{cm^{-2}s^{-1}}$). Right: RPC trigger rate for several noise rates.

The detailed neutron simulation was implemented for the RPC system, as it was done earlier in the CSC system. Neutron events were created by continuing the simulation of minimum bias events up to 1 second after the primary interaction and without p_T cuts by the GEANT program (see Figure 5.26). The simhits with time-of-flight greater than 250 ns (10 BX) were taken to be due to neutrons. Since it is very time consuming ($\sim$ 20 minutes) to simulate a single event up to 1 s and since the CMS simulation does not digitize hits outside the 9 BX window, neutrons were treated in the same way soft pile-up events are mixed into the event. A neutron pile-up sample, with neutron hits within the BX wide time interval, was added to the

mixing module. This mixing module mixes the simhits from the hard interaction under study (for instance $pp \rightarrow \mu + X$) with the simhits originating from the soft pile-up interactions and the simhits due to neutrons and ships this set to the detector simulation that digitizes the detector response to these hits [293, 297]. The number of simhits mixed into the signal events depend on the luminosity one is simulating. Briefly summarized the Neutron simulation works as follows:

- In special, separate, simulation runs, generate minimum bias events in GEANT but let it simulate up to 1 second after the collision, rather than stop at 250 ns as is done normally.
- Save the resulting simhits in the CSC, DT and RPC detectors, storing them event-by-event, such that any correlations within an event are maintained (e.g. if a neutron-originated electron penetrates several CSC layers and gives a track segment, that pattern will be maintained).
- Use this bank of events-containing-neutron-originated-simhits as the source for mixing on top of singal events, when running the singal simulation.
- Add an appropriate number of these neutron-simhit-evetns onto the signal event, depending on the instantaneous luminosity.

Including a detailed simulation of the neutrons in the RPCs, GMT trigger rates could be investigated. A study performed by the SLHC CSC group is discussed below. Figure 5.39(a) compares the L1 trigger rate for the RPCs with respect to trigger rate simulations performed for the Physics TDR [144]. This figure proves that the RPC trigger rate obtained in the Physics TDR is very well described by the new RPC simulation. In Figure 5.39(b) shows the influence of different noise rates on the RPC trigger rate. At the design luminosity of $\mathcal{L} = 2 \cdot 10^{34}\,\mathrm{cm}^{-2}\mathrm{s}^{-1}$, the influence of higher background rates is rather negligible, while at higher luminosities ($\mathcal{L} = 8 \cdot 10^{34}\,\mathrm{cm}^{-2}\mathrm{s}^{-1}$), a non-linear rise of the RPC trigger rate is observed [292].

Figure 5.40 compares the L1 trigger rates in the endcap for the upgraded RPC system, requiring 3 out of 4 hits coincidence and the current CSC system with a 2 out of 3 coincidence and the phase-I upgraded CSC system where a 3 out of 4 hit can be asked. For both scenarios the Global Muon Trigger is shown, which has to stay below 5 kHz. While in the not-upgraded CSC system this is only possible at a muon p_T threshold of $\sim$40 GeV/c, in the upgraded CSC geometry this can be as low as $\sim$20 GeV/c. Due to the superior momentum resolution, the trigger rate for the CSCs is much lower than for the RPCs. The GMT combines the triggers of the CSC and RPC system and is dominated by the high quality triggers of the CSC system. Nevertheless, a small improvement can be seen, where the RPC system helps the CSC system recover a few lost triggers.

5.5.4 Robustness of the RPC regional trigger

As shown before, the improvement of the background rate rejection with a double RPC system is too small to afford the necessary extra efforts with respect to a single RPC station. Another reason for a double RPC station could be an improvement of the robustness of the RPC Regional Trigger. The second RPC station, RE2, is the trigger reference station where the trigger segments are defined uniquely and the trigger needs the hit in RE2 to exclude ghost muons. Therefore it is important to know the consequences for the trigger performance if RE2 is removed from the trigger logic due to failure or because the operating conditions are not safe to

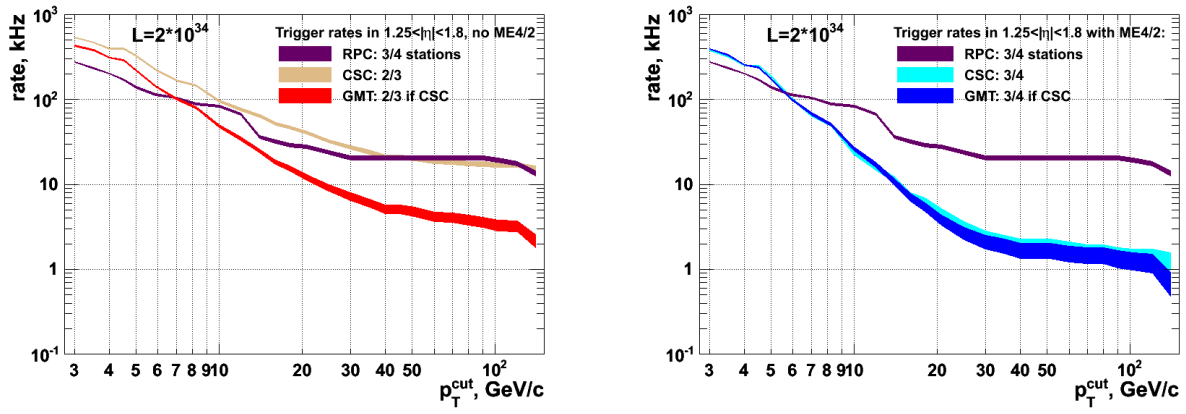

Figure 5.40: L1 Trigger rates for the upgraded RPC system (3/4) and for the current CSC system (2/3) at the left side, and for the upgraded CSC system (3/4) at the right side. Figures taken from [129, 293].

switch it on. If the impact on the trigger performance is dramatic, it might be better to build a double station to have a backup in case the original station is switched off.

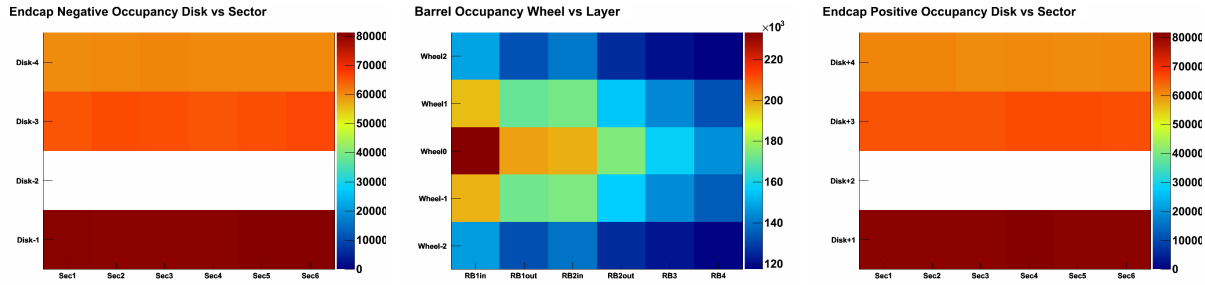

Figure 5.41: DQM plots showing the occupancy (in hits) in the negative endcap (left), barrel (middle) and positive endcap (right), where the second station in the endcaps was switched off.

The influence of RE2 on the trigger performance was simulated by switching off RE2: $\epsilon_{RE2} = 0$, $R_{RE2} = 0\,\mathrm{Hz/cm^2}$. The relative impact of RE2 on the trigger was investigated by studying the RPC Regional Trigger with switching off one of the other stations: RE1, RE3 or RE4. A module used in the data quality monitoring was used to check the simulation for properly switching on and off certain layers in the detector. Figure 5.41 shows the occupancy in the barrel and the endcaps when the second station was switched off.

Figure 5.42 shows the trigger efficiency for the different η-bins (trigger towers). The black solid line is the efficiency when all stations are switched on and is shown as reference. The trigger efficiencies when RE1, RE2, RE3 and RE4 are switched off are indicated by the red, green, blue and magenta solid lines, respectively. To interpret these results correctly consult of Figure 5.16 is indispensable,

Towers -5 to 5 show no difference, since barrel towers are not affected by changes in the endcap. Tower 6 has a small difference, that is due to small amount of muons which were simulated in the vertex with an η–value in tower 6 but due to multiple scattering were triggered in tower ±7. In towers (±)7-8 only a difference in trigger efficiency for removing RE1 and RE2 is observed, because RPCs in RE3 and RE4 do not contribute to this trigger tower, as can be seen in Figure

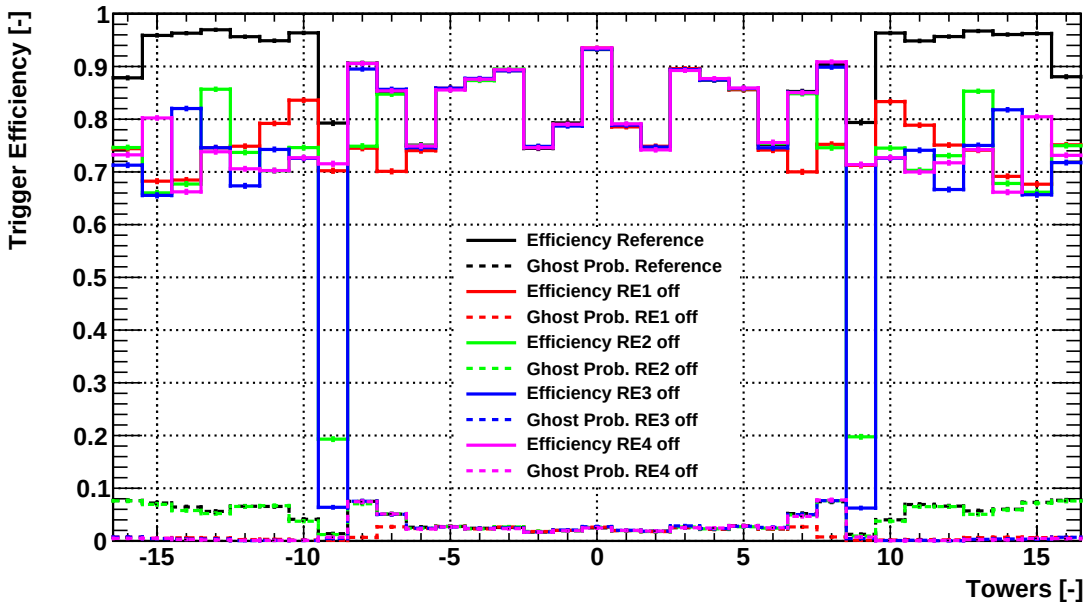

Figure 5.42: Trigger efficiencies (solid lines) and ghost probabilities (dashed lines) vs. towers for the TDR lay-out and for the different scenarios with one station switched off.

5.16.

Removing RE1 or RE4 has almost no influence on the trigger efficiency in tower ±9. On the other hand, switching off RE2 or RE3 drasticaly reduces the trigger efficiency because tower ±9 is the tower with the worst geometrical acceptance. It has only three layers of RPCs, which is the strict minimum, as only 3/3 coincidences are accepted by the trigger algorithm. The trigger efficiency is not exactly zero due the multiple scattering of the muons.

For towers (±)10–16 a 15 to 20 % lower trigger efficiency is observed. The differences in trigger efficiency for switching off different stations is due to geometrical acceptance as can be understood from Figure 5.16. For instance taking out RE2 leaves tower 13 with a higher efficiency, because there is a small gap between RE2/1 and RE2/2. Tower 14 has a higher efficiency if RE3 is taken out, because the gap between RE3/1 and RE3/2 occurs exactly in that tower. The same arguments hold for tower 15 and the gap between RE4/1 and RE4/2.

The dashed lines in Figure 5.42 show the ghost rates. It is clearly visible that the ghost rate is governed by copying the fired strips in stations 1, 3 and 4. Switching off RE2 has no influence on the probability to trigger a ghost muon, because most ghosts miss a hit in RE2. Switching off another station reduces the ghost rate drastically since most of them already missed the hit in RE2, leaving only two hits to trigger, which is impossible since 3/4 and 4/4 coincidences are required.

The probability of assigning a wrong p_T to a simulated muon is even more important. RE1 and RE2 are the endcap stations that are in the highest magnetic field. Missing the measurement of one of them will influence the measurement of the bending of the muon track. This will lead to straighter patterns and thus incorrectly assigning higher p_T to the muon trajectories. The assignment of high p_T to high p_T muons will probably not be influenced. In contrast, it will be

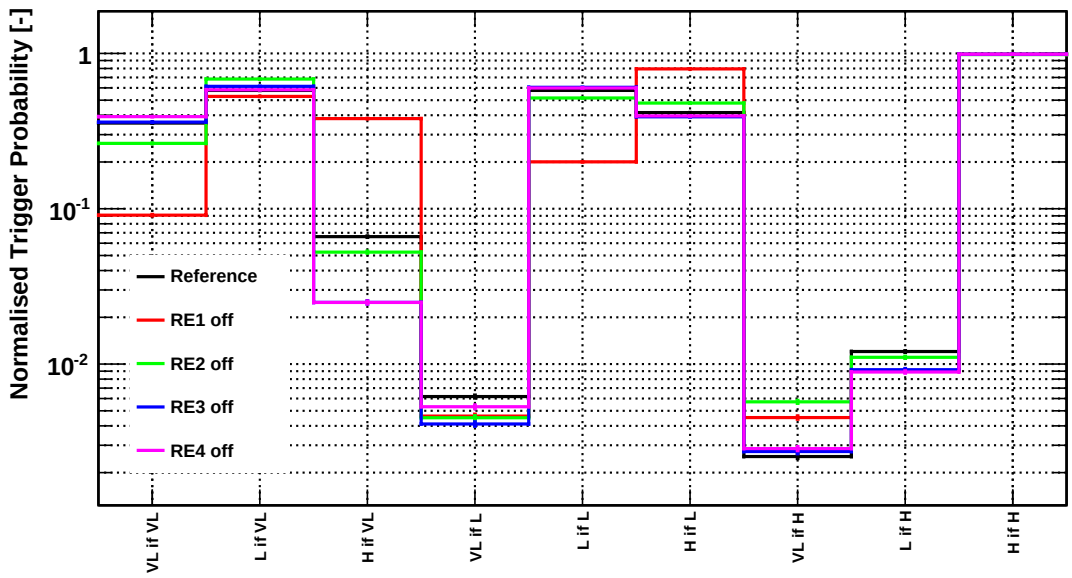

Figure 5.43: Bin 1–3: The probability to trigger very low-p_T muons (VL), low-p_T muons (L) or high-p_T muons (H) if only very low-p_T muons are simulated. Bin 4–6: The probability to trigger very low-p_T muons, low-p_T muons or high-p_T muons if only low-p_T muons are simulated. Bin 7–9: The probability to trigger very low-p_T muons, low-p_T muons or high-p_T muons if only high-p_T muons are simulated. Very low-p_T muons are $0.0 < p_T < 4.5\,\text{GeV}/c$, low-$p_T$ muons are $4.5 < p_T < 14\,\text{GeV}/c$, while high-$p_T$ muons are $14 < p_T < 140\,\text{GeV}/c$.

in particular the low energetic muons which will be upgraded to high p_T muons filling the small bandwidth of the muon trigger with uninteresting events.

To distinguish between the widths of patterns (more strips OR-ed in φ) different set of patterns were made for different p_T values of the muon:

VL: $0.0 < p_T < 4.5\,\text{GeV}/c$: Very Low p_T;
L: $4.5 < p_T < 14\,\text{GeV}/c$: Low p_T;
H: $14 < p_T < 140\,\text{GeV}/c$: High p_T;

Figure 5.43 shows the probability to assign very low (VL), low (L) or high-p_T (H) to muons with very low-, low- or high-p_T respectively. The effect of a missing station RE1 seems much more severe than missing station RE2. To have a higher robustness of the trigger, it would be better to build a back–up station for RE1 than for RE2. For this study an additional sample of 10^6 muons with $1 \leq p_T \leq 10$ was simulated to improve the coverage of the low p_T simulation.

5.5.5 Conclusions

The results shown in this chapter prove that the RPC simulation is working fine and could be used to study different upgrade geometries. The simulation of the different geometries showed that the proposed double second station geometry (RE2bis) contributed a small decrease in fake trigger rate, but this comes at the price of a slightly lower efficiency and much higher con-

struction costs. It also showed that the installation of the fourth RPC station is really necessary to reach the design trigger efficiency. Furthermore, the correct implementation of the neutron background in the RPC simulation is necessary to obtain the correct trigger rates. The impact of RE2 on the trigger performance was also studied and it was shown that the impact of the first RPC station, RE1, is much more fundamental, since this station is indispensible to measure the bending (and hence the p_{T}-assignment) of the muon correctly.

The results of these studies have been used to judge the different scenarios for the RPC upgrade. The trigger rate improvement brought by the double second station was found too little, compared to the overall cost and risk for the CMS detector. Hence, the CMS Collaboration has opted for the design geometry, consisting of the installation of the fourth layer of RPC detectors.

Part III

Search for Supersymmetry

Chapter 6

Inclusive Jets plus Missing Transverse Momentum Search

Supersymmetry is a good candidate to describe phenomena beyond the Standard Model. At hadron colliders, new particles are expected to be produced in pairs (assuming R-parity), mainly by the strong interaction. Generally, these particles can decay to one or more jets (depending on their colour charge) or leptons, plus a Lightest Supersymmetric Particle (LSP) which interacts only very weakly with matter. Final states consist of leptons, visible transverse momentum (H_{T}) due to the jets, plus missing transverse momentum ($\not{H}_{\mathrm{T}}$) from the LSP. With index i running over all jets J_i of an event, the visible transverse momentum and missing transverse momentum for that event are defined as:

$$H_{\mathrm{T}} := \sum_i |\vec{p}_{\mathrm{T}}(J_i)| \quad \text{and} \quad \not{H}_{\mathrm{T}} := |-\sum_i \vec{p}_{\mathrm{T}}(J_i)|. \tag{6.1}$$

Scenarios in which the Supersymmetry breaking is mediated by the GMSB mechanism expect photons to be produced, associated with jets and missing transverse momentum. Figure 6.1 shows an example SUSY-event in which two gluinos are produced, decaying through off-shell squarks to quarks and a neutralino or a chargino. The neutralino and chargino decay further on, producing more quarks and a lightest supersymmetric particle (LSP / $\tilde{\chi}_1^0$).

In 2010 the SUSY searches in CMS were classified according to the number of leptons or photons:

- **All-hadronic searches**: In 2010 three different zero-lepton searches were performed: the kinematic α_{T}-search [298]; the jets-plus-missing-transverse-momentum search [299]; and the Razor search[1] [300].
- **Lepton searches:** the single-lepton search [301]; the same-sign-dilepton [302], the opposite-sign-dilepton [303] and the Z-plus-$E_{\mathrm{T}}^{\mathrm{miss}}$-plus-jets search [304]; and the multi-lepton search [305].
- **Photon searches:** the diphoton [306]; and the photon-plus-lepton search [307].

The α_{T}-search was also repeated with b-tagging [308]. In this thesis a search for Supersymmetry in the zero-lepton channel is performed, with the jets plus missing transverse momentum search [299]. In most of the SUSY models the all-hadronic channel is believed to be the most

[1] Although the Razor search was lodged in the all-hadronic searches, it actually combined a all-hadronic search with searches with leptons.

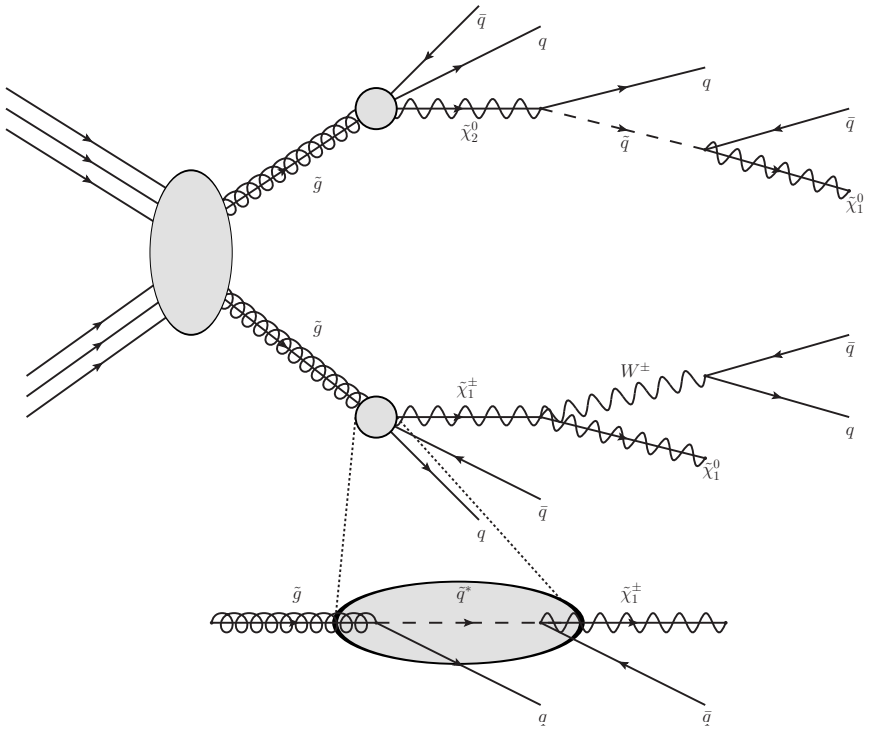

Figure 6.1: Example SUSY event: $\tilde{g}\tilde{g}$-production, where the $\tilde{g}$ decays through an off-shell $\tilde{q}^*$ (detailed below) to two jets and a $\tilde{\chi}_1^\pm$ (top) or $\tilde{\chi}_2^0$ (bottom). Finally two LSPs ($\tilde{\chi}_1^0$) were produced, causing missing transverse momentum in the detector.

sensitive channel, since the QCD-coupling to squarks and gluinos is much stronger than the electroweak coupling required for the production of heavy flavour quarks and leptons. Although there are other SUSY scenarios in which the coupling to leptons is enhanced, such that final states with leptons would prevail. An all-hadronic search is in many scenarios one of the most sensitive searches. Furthermore, the jets and missing transverse momentum search is one of the most sensitive searches in this channel due to its inclusive nature explained later on. Unfortunately, Standard Model processes have similar signatures with $\not{H}_\mathrm{T}$ introduced by vector bosons decaying to leptons or jet mismeasurements in QCD multijet events. The quest for Supersymmetry observation in events with this final state is challenging due to the large background.

A search for Supersymmetry was performed with the first 7 TeV data recorded by the CMS detector in 2010. Three analyses approached the jets plus missing transverse momentum signature in a different way. The α_T-search [298] concentrated on an early discovery in an inclusive dijet data sample, with a strong QCD background rejection. This strong rejection came at the prize of a loss in signal efficiency. The "inclusive jets plus missing transverse momentum" analysis, described in this thesis, is complementary to the previous search. It investigated high missing transverse momentum in an inclusive multijet sample, requiring three or more jets and a loose selection to predict rather than to avoid the Standard Model backgrounds, leading to a higher signal efficiency. The "razor" search [300] uses a totally different method, testing events against the hypothesis of pair production of heavy particles in an inclusive dijet data sample.

The work described in this thesis is part of the "inclusive jets plus missing transverse momen-

tum" search. This chapter follows the flow of the relevant CMS paper [299], public analysis summary [199] and supporting internal analysis notes [309]. The "inclusive jets plus missing transverse momentum" search adopted the particle flow event reconstruction, while the search was originally designed for the standard event reconstruction [310]. The first section (6.1) discusses the strategy developed for this analysis and the data selection, starting with the online selection (6.1.1), followed by the cleaning of the data sample (6.1.2), the actual event selection (6.1.3) and a data - simulation comparison (6.1.4). Thereafter the estimation of all but one of the Standard Model backgrounds to this search are discussed: Section 6.2 discusses the W and top background, while section 6.3 deals with the QCD background. The estimation of one peculiar Standard Model background was the main topic of this thesis, contributing to this search for new physics, and is discussed in chapter 7. Chapter 8 will then detail the results obtained and interpret these results in terms of Supersymmetry models.

6.1 Search strategy and data-event selection

In the CMS large emphasis was put on developing techniques to estimate the Standard Model background processes from data. The key backgrounds for the jets plus missing momentum search are the associated production of jets and vector bosons, and multijet events with large missing transverse energy due to leptonic decays of heavy flavor hadrons inside jets, jet energy mis-measurements or instrumental effects such as noise and dead detector regions.

- Z + jets $\rightarrow \nu\bar{\nu}$ + jets is an irreducible background. The neutrinos will pass the detector without notice and the Z boson cannot be reconstructed, leading to missing transverse momentum.
- W + jets $\rightarrow \ell\bar{\nu}$ + jets with $\ell = e$ or μ, including the leptonic decays of τ. W + jets events can be produced prompt or as a decay product of $t\bar{t}$ events, where each top quark decays to a W and a b-quark. If the W decays leptonically, and the muon or electron is not identified or the tau lepton undergoes a hadronic decay, one or more neutrinos will provide a true source of missing momentum.
- QCD Multijet production has a huge cross section, many orders of magnitude higher than the sought BSM-signal, and thus promotes jet mis-measurements to a dominant source of artificial $\not{H}_{\mathrm{T}}$. Jet mis-measurements can be due to calorimetric noise, uninstrumented or dead detector regions or leptonic decays of heavy flavor quarks inside jets, where a neutrino runs away with a part of the jet momentum.
- Diboson (WW, WZ, ZZ, $W\gamma$, $Z\gamma$) and single-top production with at least one leptonic decay have very small cross sections with respect to the single boson and QCD multijet cross section. Their contribution is estimated to be small and hence not covered by the data driven background estimations.

The event selection for this search aims to be inclusive, such that it can detect new physics from any model yielding a high-multiplicity hadronic final state with high missing transverse momentum [299]. The discriminating variables of the search are H_{T} and $\not{H}_{\mathrm{T}}$, where $\not{H}_{\mathrm{T}}$ is preferred over $E_{\mathrm{T}}^{\mathrm{miss}}$, since the $\not{E}_{\mathrm{T}}$ variable was not yet commissioned at the time of the analysis reported here. $\not{H}_{\mathrm{T}}$ is easier in usage for the estimation of the QCD background [311]) and is similar to $\not{E}_{\mathrm{T}}$, since it calculates the transverse missing momentum based on jets above a certain threshold instead of single calorimetric energy deposits. The choice of the observables and applied

background suppression cuts aim for minimal kinematic bias facilitating the characterization of new physics in case of a discovery. This means that the selection was not optimized to select as much signal events over background, since we don't (want to) know where to expect signal. The cuts are optimized to cut Standard Model background, in a very general way, to avoid cutting on possible signal from any kind of BSM physics and to limit the amount of different Standard Model backgrounds. This section describes the event selection, starting with the online event selection in the High-Level Trigger, discussing the cleaning of the event sample and the data - simulation comparison for some of the event selection steps.

6.1.1 Trigger selection

The analysis is performed using the full data sample recorded by the CMS detector between March 30$^{\text{th}}$ and November 3$^{\text{rd}}$ 2010. The data was re-reconstructed after the 2010 pp-collisions run had ended, with improved calibration and alignment constants. Only officially certified data from the November 4$^{\text{th}}$ reprocessing campaign were used.

The events used in the analysis are collected on the multi-jet H_{T} trigger as reported in Table 6.1. The SUSY group opted for the H_{T} triggers for several reasons: the target (SUSY) signal is not defined in terms of jet multiplicity nor as a function of jet spectra or total visible or invisible energy. The H_{T} trigger provides high acceptance for a wide range of hadronic SUSY and non-SUSY signals, while keeping acceptable rates for 2010 data taking.

The single jet triggers could not be used since the high QCD cross section leads to very high rates. These high rates were reduced by a very high p_{T} threshold: 140 GeV/c uncorrected, making it an inefficient trigger for low mass SUSY scenarios. The MET/$\not{H}_{\text{T}}$ triggers have acceptable rates and efficiencies, but are selecting on the very same variable as used offline to discriminate between signal and background. The aim of the inclusive jets plus missing momentum search is to estimate all backgrounds from data, and therefore it needs low$\not{H}_{\text{T}}$ control regions to predict backgrounds in the high-MHT search regions [310]. This might seem an conservative approach, but the first data of a new detector have to be investigated with care. Further on, the rather small amount of integrated luminosity in 2010 (in comparison with 2011 and the years to come) allowed for recording a lot of less interesting low$\not{H}_{\text{T}}$ events, which in turn allowed for using a low$\not{H}_{\text{T}}$ control region.

The HLT trigger is based on the scalar sum of uncorrected Calo jets:

$$H_{\text{T}}^{\text{trig}} = \sum p_{\text{T}}(J_i), \quad \text{with } p_{\text{T}}(J_i) > 20\,\text{GeV}/c \text{ and } |\eta(J_i)| < 5.0.$$

The jets reconstructed in the High-Level Trigger were built using the Iterative Cone (ΔR = 0.5) jet algorithm applied to energy deposits in the calorimeter (Calo towers). The trigger was seeded by the Level-1 trigger L1_HTT50, which is an H_{T}-trigger, summing transverse energy of all uncorrected L1-jets with $E_{\text{T}} > 10\,\text{GeV}$ and with an H_{T}-threshold of 50 GeV/c. The L1-jets were built by summing energy deposits in rectangular η-ϕ regions. Due to the increase of instantaneous luminosity over time, the rates of the triggers went up and the H_{T} threshold of the triggers needed to be increased from 100 GeV/c, over 140 GeV/c, to 150 GeV/c. The latest threshold was maintained up to the end of data taking, giving a rate of 70 Hz at an instantaneous luminosity of $\mathcal{L} = 2 \times 10^{32}\,\text{cm}^{-1}\text{s}^{-1}$.

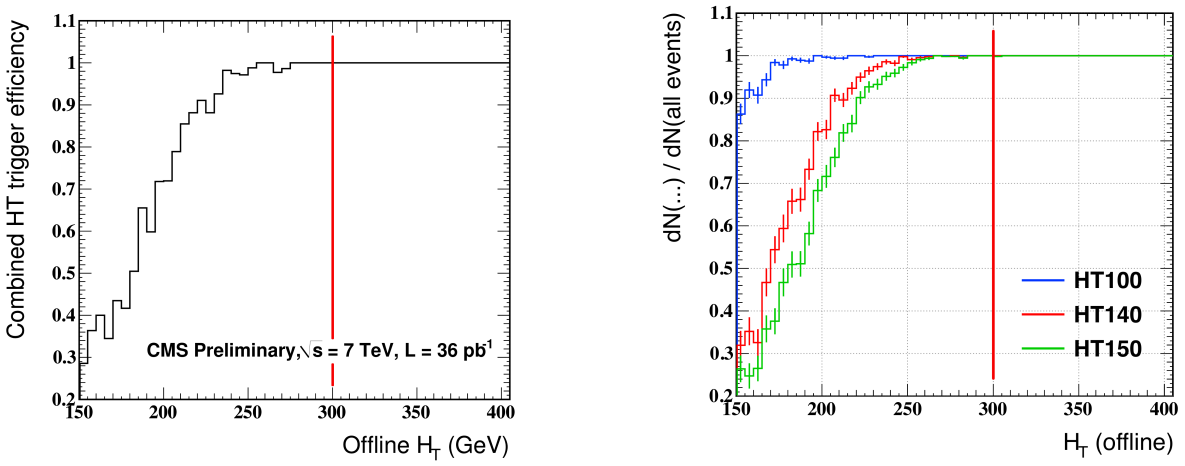

Figure 6.2: Trigger efficiency curves as function of the H_T computed offline, measured in data (left), and in simulation for the LM1 benchmark signal for three different triggers (right). The red line indicates the analysis requirement $H_T > 300\,\text{GeV}/c$, showing that the HLT trigger is 100% efficient for the event selection of the analysis [199].

Table 6.1: Datasets used in the analysis, the third column gives the integrated luminosity $L = \int \mathcal{L} dt$, while the fourth column shows the peak instantaneous luminosity at the start of that range of runs. The date corresponds to the time the first run within the range was recorded. Note that more than 75% of the data were recorded during the last month of data taking (October 3rd - November 3rd).

Dataset	Run range	Start date	L_{int} [pb^{-1}]	$\mathcal{L}_{\text{peak}}$ [$\text{cm}^{-2}\text{s}^{-1}$]	HLT path
JetMETTau_Run2010A-Nov4ReReco_v1	136 033 - 141 882	2010-05-22	0.285	1E28	HLT_100U
JetMET_Run2010A-Nov4ReReco_v1	141 956 - 144 114	2010-07-28	2.895	1E31	HLT_100U
Jet_Run2010B-Nov4ReReco_v1	146 428 - 147 116	2010-09-21	5.057	5E31	HLT_100U
MultiJet_Run2010B-Nov4ReReco_v1	147 196 - 148 818	2010-10-03	9.471	1E32	HLT_140U
MultiJet_Run2010B-Nov4ReReco_v1	148 819 - 149 294	2010-10-23	18.436	2E32	HLT_150U_v3
Total			36.144		

The L1 and HLT trigger efficiency were studied simultaneously using a prescaled trigger[2] with a single jet requirement: HLT_Jet15U seeded by L1_SingleJet6U. The HLT path requires only a single calo jet reconstructed in the HLT with uncorrected $p_T > 15\,\text{GeV}/c$.

The trigger efficiency is measured by evaluating how many events were triggered by the logic (HLT_100U || HLT_140U || HLT_150U) && L1_HTT50 in a sample collected by the combination HLT_Jet15U && L1_SingleJet6U. The trigger efficiency of the latter was determined using a data sample selected by Minimum Bias triggers in References [312, 313]. Table 6.1 shows the datasets and runs used for this analysis, while the combined trigger efficiency curves for L1 and HLT triggers are shown in Figure 6.2. This figure shows that for events with $H_T > 300\,\text{GeV}/c$ the HLT trigger is 100% efficient.

[2] Although more statistics could be accumulated by using multiple prescaled triggers, the combination of those triggers is very difficult.

6.1.2 Cleaning of the data sample

The CMS experiment is designed such that the actual physics final state of the pp collision at the interaction point can be reconstructed. During data taking, several sources can contaminate the recorded electronic picture and bias the measurement of one of the final state objects or even prevent the full reconstruction of the event. These contaminations can be due to real particles, such as particles from beam-backgrounds, particles hitting the PMT windows of the ECAL barrel causing "spikes" (as discussed in section 4.6.5) or cosmic muons passing through the interaction region. Other contaminations are due to instrumental (electronic) noise, often introducing fake energy deposits in the calorimeters. A short list of all different contaminations is given below. CMS standarized the procedure to remove effects from these contaminations, known as the "standard event cleaning" [314].

Standard event cleaning:

- **beam-gas interactions** Protons in the LHC beams do not only collide with each other, but also with the residual gas atoms in the beam pipe vacuum. These interactions are highly boosted and hence the produced particle sprays are very collimated and make only a small angle with respect to the beamline. This leads to many hits in the pixel detector, giving rise to many fake tracks or even leading to track reconstruction failure. Those PKAM[3] events were studied in early 2009 and 2010 collisions [315] and a thourough understanding is provided by Reference [316]. To clean the event samples from this background, a **PKAM-filter** was developed and at least one **good primary vertex** was required. A good primary vertex has at least 25% high purity tracks. If there are less than ten tracks in the event, a good primary vertex was no longer required to keep high efficiency on exceptional events such as $ZZ \rightarrow 4\mu$ [314]. In this way one keeps high efficiency on events with very small track multiplicity, such as a $ZZ \rightarrow 4\mu$ event.
- **beam-halo muons** Beam losses, such as beam-gas interactions and beam-beam effects, cause beams to loose protons. Most of them are cleaned out by the collimation system, but sometimes they interact in the shielding in front of the detector. Muons created in these interactions, so called halo muons, can traverse the detector in time with the beam. Though the rate is rather low and reduces with distance to the beamline, these halo muons give rise to genuine tracks in the muon chambers and, more importantly, energy deposits in the calorimeters when radiating a high energy photon. Since they travel nearly parallel to the beam and their timing is, in at least half of the detector, not in time with particles coming from the collision vertex, they can be efficiently suppressed. Detailed studies have been performed in CMS on real data, described in Reference [201] and a **beam-halo filter** was developed.
- **cosmic muons** Another source of muons are the particle showers in the atmosphere induced by cosmic rays. These cosmic muons contribute in two different ways. They can on the one hand pass through the luminous region: $z \leq 25\,\text{cm}$, $r \leq 2\,\text{cm}$, which is within the constraints for tracks coming from the interaction point. They will then be reconstructed both by the tracker and the muon system, leading to high quality muon objects. When coinciding with collisions, these muons can contaminate the event by

[3]Previously Known As Monster. These events with a large amount of pixel clusters were named "Monster" events before their origin was elucidated.

adding a track and by depositing energy in the calorimeters. On the other hand, those cosmic muons can also miss the central part of the detector, in which case they will only be reconstructed by the muon system and not by the tracker. These muons can contaminate collision events when radiating energy in the calorimeters. Fortunately, cosmics have been studied in great detail in CMS [174] and the phenomena described above can be tagged and removed [222], and "in-time" cosmic muons can be estimated from "out-of-time" control samples. Requiring the muon impact parameter to be close to the primary vertex and additional timing requirements lead to a negligible rate.

- **ECAL noise** When first collisions (at $\sqrt{s} = 900\,\text{GeV}/c$ and $\sqrt{s} = 2360\,\text{GeV}/c$) were recorded in CMS, an unexpected instrumental effect was observed in the ECAL barrel, leading to so-called ECAL spikes. These isolated high-energy signals turned out to arise from direct interaction of soft particles in the APD readout diode [187, 214]. Timing and cluster shape information, as discussed in section 4.6.5 were used to supress those fake energy deposits.
- **HB/HE noise** Electronic noise from photodiodes (HPDs) and readout boxes (RBX) is related rather to instrumentation issues. A **HB/HE noise filter** was developed to remove these events. More details can be found in section 4.3 and are provided in References [185, 186].
- **HF noise** Direct hits on the PMT readout transducer in the forward calorimeters (HF) can induce fake energy deposits. This so-called PMT window noise can be identified by comparing energy deposits in neighbouring short and long fibres. This noise is removed by default in the CMS event reconstruction. More details can be found in section 4.3 and is provided in Reference [186].

Detailed analysis cleaning:

In addition to the above, events were rejected in which a significant amount of energy is lost in the approximately 1% of non-functional crystals of the ECAL that are masked in reconstruction. Such losses were identified either by exploiting the energy measured through a parallel readout path used for the trigger, or by measuring the energy deposited around masked crystals, when information from this parallel readoutpath is not available[4] [299]. Figure 6.3 shows an η, ϕ view of such an event, the $\not{H}_{\text{T}}$ (denoted as a line constant in η)is pointing to a jet in the event, where a group of 25 crystals is missing. This effect introduces a small inefficiency for signal events, which is taken into account for the results presented in chapter 8.

After application of the standard event cleaning recipe and the baseline event selection (detailed in section 6.1.3), a visual scan of the remaining events was performed to ensure that large $\not{H}_{\text{T}}$ was not due to instrumental effects or mis-reconstruction. Artificial $\not{H}_{\text{T}}$ can easily be introduced by jet mis-measurements and wrong p_{T}-assignment to muons[5]. Investigation of data and Monte-Carlo simulation samples lead to improvements of the particle-flow muon reconstruction, which was not finalized at the time the analysis was performed [318]. Hence, events with poorly measured muons were rejected for analysis. A fully detailed report is presented in Reference [318].

[4] Events with a potentially large amount of energy lost in the missing ECAL crystals were removed by a "Trigger Primitive" filter (TP-filter) and a "Boundary Energy" filter (BE-filter), discussed in Reference [317].

[5] These wrongly reconstructed PF-muons were removed by the "inconsistent muon" and "greedy muon" filters detailed in Reference [318].

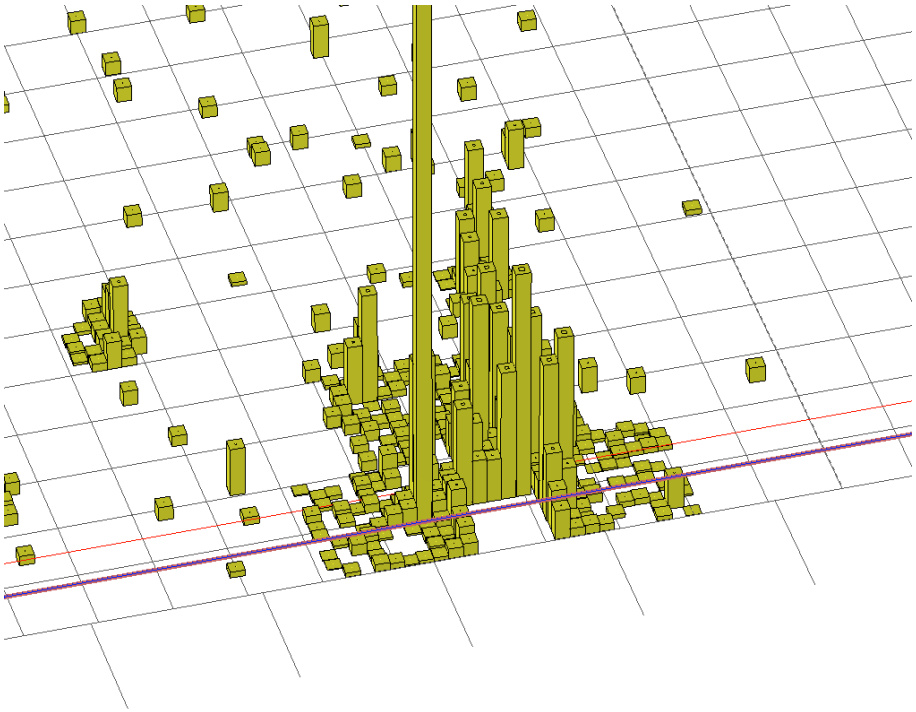

Figure 6.3: η, ϕ projection of the fourth jet in event 646 130 594 in luminosity section 621 of run 149 291. A full ECAL tower, corresponding to 25 crystals, is missing in the core of the jet and the $\not{H}_T$, represented as a thick line (constant in η) points to this tower [318].

As an example, two instrumental effects are discussed below, illustrating the level at which the high-energy tail of the $\not{H}_T$ distribution should be understood. A final breakdown of all analysis cleaning cuts is shown in Table 6.2. These cleaning cuts were applied on the data shown in Table 6.1, after requiring the events to have at least one good primary vertex and the PKAM filtered events rejected. Furthermore the events were required to have at least three PF-jets with $p_T > 50\,\text{GeV}/c$ and $|\eta| \leq 2.5$ summing up to a $H_T > 300\,\text{GeV}/c$ and to have a missing transverse momentum $\not{H}_T > 150\,\text{GeV}/c$, which are some of the first selection criteria discussed in the next section (section 6.1.3).

The first instrumental effect is due to the filling of the bunches in the injection chain of LHC. Figure 6.4(a) shows an event where the hard collision did not happen in the central part of the detector, between two "nominal" bunches, but rather between one nominal bunch and one satellite bunch, (created in the SPS [319]), at 5 ns of a nominal bunch. Since the two beams are counter rotating, the nominal bunch crosses a satellite bunch of the other beam at 2.5 ns after the crossing of the nominal bunches, resulting in a 75 cm displacement from the nominal interaction point. A "tracking failure" filter was developed, requiring the events to have the ratio of the sum of the p_T of all tracks of the primary vertex and the H_T of all jets greater than 10%. Figure 6.4(b) shows the small amount of events removed by this filter (events at the left side of the cut-value). The H_T is defined as in formula 6.1.3, resulting in a large tail of the $\sum p_T(\text{tracks from PV})/H_T$ distribution due to events with a jet failing the $p_T > 50\,\text{GeV}/c$ and $|\eta| < 2.5$ criteria.

The second effect illustrated here, is noise correlated across subdetectors. Figure 6.5(a) shows an event with huge energy deposits in the ECAL endcaps only, along with activity in the muon

Table 6.2: Detailed analysis cleaning cuts applied on the data reported in Table 6.1 and after requiring at least one good primary vertex, PKAM rejection, HB/HE noise filtered. Furthermore, events were required to have least three PF-jets with $p_T > 50\,\text{GeV}/c$ and $|\eta| < 2.5$ summing up to a $H_T > 300\,\text{GeV}/c$ and a $\not{H}_T > 150\,\text{GeV}/c$.

Consecutive cuts	Events in 36.1 pb^{-1}
$H_T > 300\,\text{GeV}/c$ & $\not{H}_T > 150\,\text{GeV}/c$:	603
H_T-Triggered:	601
μ-veto:	539
e-veto:	496
EE noise filtered:	495
bad reconstructed PF-μ:	475
beam halo filtered:	474
tracking failure filtered:	462
HB/HE noise filtered	461
masked ECAL-crystals filtered:	379

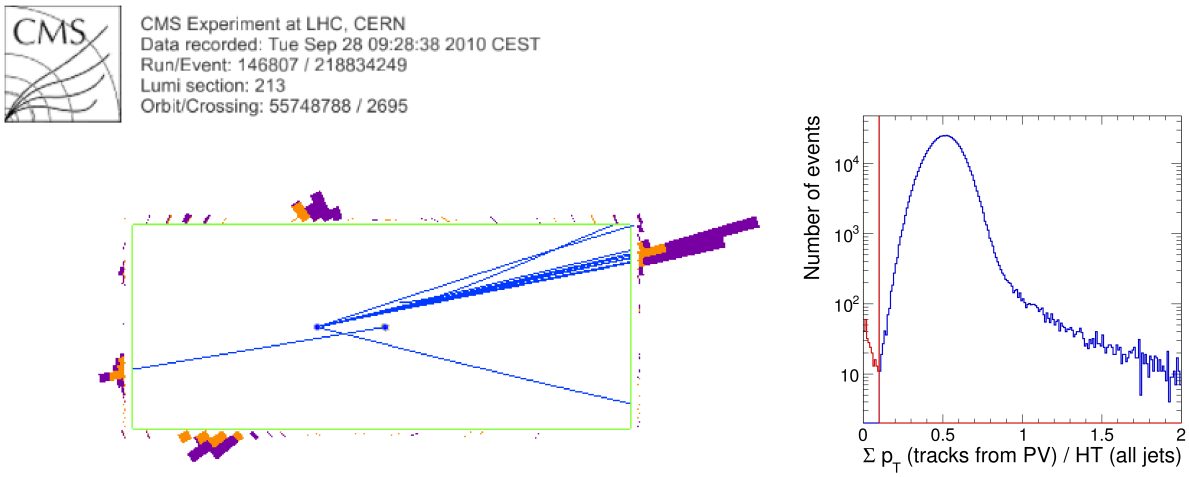

(a) (b)

Figure 6.4: (a) Event 218 834 249, in luminosity section 213 of run 146 807 exhibits a hard interaction displaced by 75 cm (to the left in this view) and was most likely a collision between a nominal bunch and a satellite bunch. Some tracks are reconstructed, but the majority fails the tracking requirements for being reconstructed. (b) Discrimination variable to reject events with tracking failure. The cleaning cut is placed at 10% and rejects events with a low value of the discriminator [318].

system. The event exibits almost no energy in the ECAL barrel or in the HCAL barrel and endcap detectors. Figure 6.5(b) shows the number of reduced ECAL Rechits (reconstructed ECAL hits used in the event reconstruction) for the 2010 data sample reported in Table 6.1. Two "ring-of-fire"events can clearly be identified by the amount of RecHits in the event. Events with more than 2000 rechits were rejected for the 2010 analysis, while this particular type of noise will be investigated when more similar events are recorded.

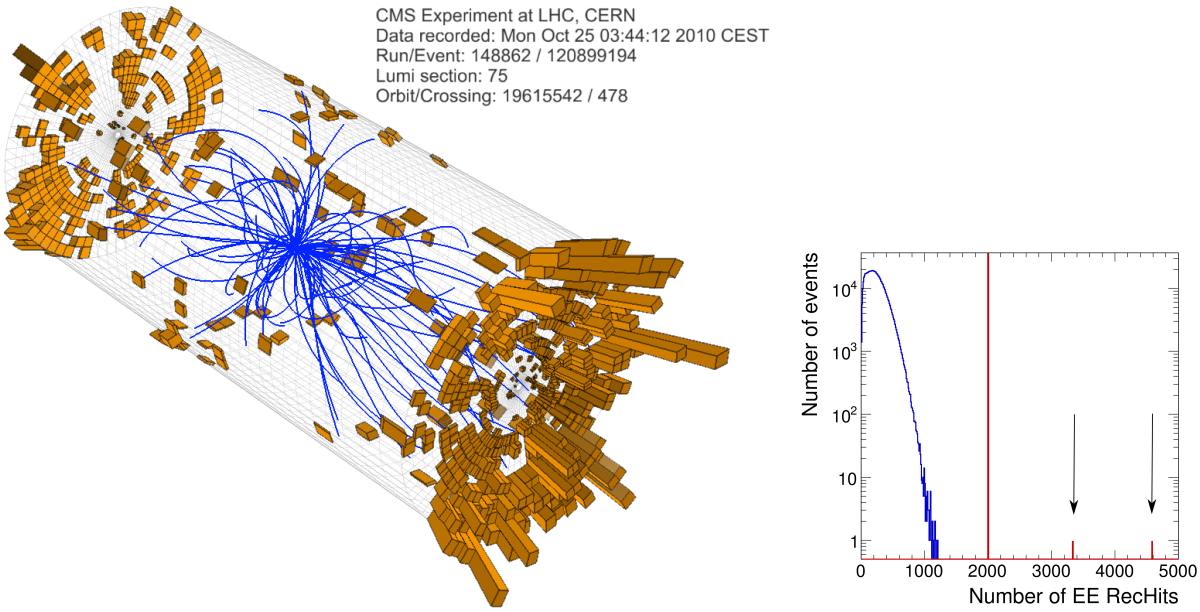

(a) (b)

Figure 6.5: (a) Event 120 899 194, in luminosity section 75 of run 148 862 exhibits the ECAL ring-of-fire noise (left). Number of hits in the ECAL endcaps for events passing all selection criteria except$\not\!\!H_{\mathrm{T}} > 150\,\mathrm{GeV}/c$ (right). (b) A filter was developed to remove all events with more than 2000 ECAL Rechits [318].

6.1.3 Event selections

For the event reconstruction, the full event description delivered by the particle-flow algorithm, as described in sections 4.1 and 4.2, was used. The analysis selection is based on a loosely selected sample of events, called the **baseline selection**. Search selections were defined requiring higher values of the visible transverse momentum (H_{T}) or requiring higher values of the missing transverse momentum ($\not\!\!H_{\mathrm{T}}$). The baseline selection requirements are summarized below:

- Events were first selected by the L1 and HLT trigger. Since different prescaled and unprescaled HLT paths collect data that all go in the same Primary Dataset, events were explicitly required to pass the HLT triggers shown in Table 6.1.
- Events should contain at least three particle-flow jets:

$$p_{\mathrm{T}}(J_i) > 50\,\mathrm{GeV}/c; \quad |\eta(J_i)| < 2.5.$$

  Jets are clustered with the anti-kt algorithm in a cone with $R = 0.5$. The three central jets with highest-p_{T} (J_1, J_2, J_3) are called the "leading jets".
- The scalar sum of the p_{T} of the jets defined above should exceed 300 GeV/c:

$$H_{\mathrm{T}} = \sum p_{\mathrm{T}}(J_i) \qquad p_{\mathrm{T}}(J_i) > 50\,\mathrm{GeV}/c; \quad |\eta(J_i)| < 2.5.$$

  This is called the transverse momentum of the event, named H_{T}. The threshold is chosen to be above the HLT trigger turn-on, shown in Figure 6.2, ensuring 100% trigger efficiency.

- The negative vector sum of particle flow jets with $p_T > 30\,\text{GeV}/c$ and $|\eta| < 5.0$, known as the missing transverse momentum, should exceed $150\,\text{GeV}/c$:

$$\vec{\not{H}}_T = -\sum \vec{p}_T(J_i) \qquad p_T(J_i) > 30\,\text{GeV}/c; \quad |\eta(J_i)| < 5.0.$$

  The jet definition used for the missing transverse momentum was enhanced to reduce the high $\not{H}_T$ tails from QCD multijet events. The probability for an event with one or more jets falling below threshold to promote the event to have a missing transverse momentum greater than $150\,\text{GeV}/c$ is higher for $50\,\text{GeV}/c$ jets than for $30\,\text{GeV}/c$ jets, therefore the p_T-threshold was lowered to $30\,\text{GeV}/c$. Also, the requirement for the jets to be within the tracker coverage ($|\eta| < 2.5$), implicitly assuring a good momentum measurement, was dropped, since forward jets ($3.0 < |\eta| < 5.0$) have a non-negligible contribution to the missing transverse momentum.
- The distance in azimuth between the three leading jets and the missing transverse momentum should exceed respectively 0.5, 0.5 and 0.3:

$$\left|\Delta\phi(\vec{J}_n,\vec{\not{H}}_T)\right| > 0.5, \quad n = 1,2 \quad \text{and} \quad \left|\Delta\phi(\vec{J}_3,\vec{\not{H}}_T)\right| > 0.3.$$

  This requirement removes most of the mismeasured jets. If the leading jet is mismeasured, the $\vec{\not{H}}_T$ will be anti-aligned to this jet and aligned to the next-to-leading jet. The value of $\Delta\phi = 0.5$ was chosen to be equal to the jet conesize, while the looser cut at 0.3 was chosen to maintain high signal efficiency.
- Events were required not to contain an isolated electron or muon. This will remove most of the leptonic decays of W/Z + jet and $t\bar{t}$ events. Muons and electrons are required to have $p_T > 10\,\text{GeV}/c$, and a good quality track that is matched to the primary vertex within $200\,\mu$m transversely and 1 cm longitudinally. They must also be isolated, requiring a relative isolation variable to satisfy:

$$\frac{\sum_{\Delta R=0.4} p_T^{\text{charged hadron}} \sum_{\Delta R=0.4} p_T^{\text{neutral hadron}} \sum_{\Delta R=0.4} p_T^{\text{photon}}}{p_T^{\text{lepton}}} < 0.20,$$

  where $p_T^{\text{charged hadron}}$, $p_T^{\text{neutral hadron}}$, and p_T^{photon} are the momentum of charged hadrons, neutral hadrons, and photons, respectively, in the event within a distance $\Delta R = 0.4$ in η-ϕ space of the lepton. Muons are required to have $|\eta| < 2.4$, whereas electrons must have $|\eta| < 2.5$, excluding the barrel-endcap transition region $1.4442 < |\eta| < 1.566$ [299].

6.1.4 Data-simulation comparison

Throughout the analysis, several Monte-Carlo simulation samples were used, produced with a detailed CMS detector simulation based on GEANT [320]. Samples of QCD multijet, $t\bar{t}$, W/Z + jets, γ + jets , diboson and single-top events were generated with the PYTHIA [104] and MADGRAPH [107] generators, using the CTEQ6.1L [96] parton distribution functions. For the $t\bar{t}$ background an approximate next-to-next-to-leading-order (NNLO) cross section of 165 pb [321] is used, while the cross sections for $W(\ell\nu)$+jets (31 300 pb) and $Z(\nu\nu)$+jets (5 769 pb) are derived from an NNLO calculation with FEWZ [322].

While already excluded by the earlier α_T-analysis [298], the LM1 CMSSM point is used as a benchmark for new physics in this search. This point has a cross section of 6.5 pb at NLO, calculated with PROSPINO [323]. It is defined to have a universal scalar mass $m_0 = 60\,\text{GeV}/c^2$, universal gaugino mass $m_{1/2} = 250\,\text{GeV}/c^2$, universal trilinear soft SUSY-breaking-parameter $A_0 = 0$, the ratio of the vacuum expectation values of the two Higgs doublets $\tan\beta = 10$, and the sign of the Higgs mixing parameter sign(μ) positive. The squark and gluino masses for LM1 are respectively 559 GeV/c^2 and 611 GeV/c^2, and the LSP mass is 96 GeV/c^2.

The event yields in the data and the simulated samples after two loose versions of the baseline selection, the baseline selection itself, and the two different search-event selections are summarized in Table 6.3, where the simulated event yields correspond to an integrated luminosity of 36 pb^{-1}. The $\not{H}_T$ and H_T distributions for data and MC simulation are compared in Figure 6.6 after the baseline selection, except the $\not{H}_T$ and H_T requirements, respectively. In the following sections, however, all the backgrounds in this search are estimated directly from data.

Table 6.3: Event yields in data and simulated samples were produced for five different selection criteria. The latter are normalized to an integrated luminosity of 36 pb^{-1}. All simulated samples were generated with the PYTHIA and MADGRAPH generators. The row labeled LM1 gives the expected yield for the benchmark point described in the text.

	Baseline no $\Delta\phi$-cuts no e/μ-veto	Baseline no e/μ-veto	Baseline selection	High-$\not{H}_T$ selection	High-H_T selection
LM1	71.2	60.4	45.0	31.3	33.8
QCD multijet	222.0	27.0	24.6	0.2	9.9
$Z(\nu\nu)$+jets	26.7	21.1	21.1	6.3	5.7
$W(\ell\nu)$+jets	93.9	57.8	23.5	4.7	7.6
$t\bar{t}$	57.5	40.1	21.9	2.6	5.7
WW+WZ+ZZ+tW +Wγ+Zγ+Z/γ^*	6.1	3.4	2.1	0.2	0.2
Total MC background	406	149	93	14	29
Data	482	180	111	15	40

6.2 W and $t\bar{t}$ background estimation

The leptonic decays of W and $t\bar{t}$ were estimated together, since the top quarks have a 100% BR to decay to a W-boson and a b-quark. Both processes have at least one leptonically-decaying W-boson and contribute to the search backgrounds, because the neutrino creates missing transverse momentum. Fortunately, the weak decay of the W boson produces a charged lepton, allowing for an easy tag of this type of events. W+ jets and $t\bar{t}$ events, however, are not rejected by the lepton veto if the lepton is outside the kinematic ($p_T^{\text{lepton}} < 10\,\text{GeV}/c$) or geometric acceptance ($|\eta^\mu| > 2.4$ for the muon and $|\eta^e| > 2.5 \cup 1.4442 < |\eta^e| < 1.566$ for the electron), or the lepton is not reconstructed or not isolated. These three cases are denoted as "lost lepton". Another failure of the lepton veto to exclude W+jets and $t\bar{t}$ events from the selection is due to tau leptons decaying hadronically, denoted as τ_h.

The estimation of the remaining background due to W+ jets and $t\bar{t}$ events is performed using a technique predicting the amount of "lost leptons" and another method to predict the amount

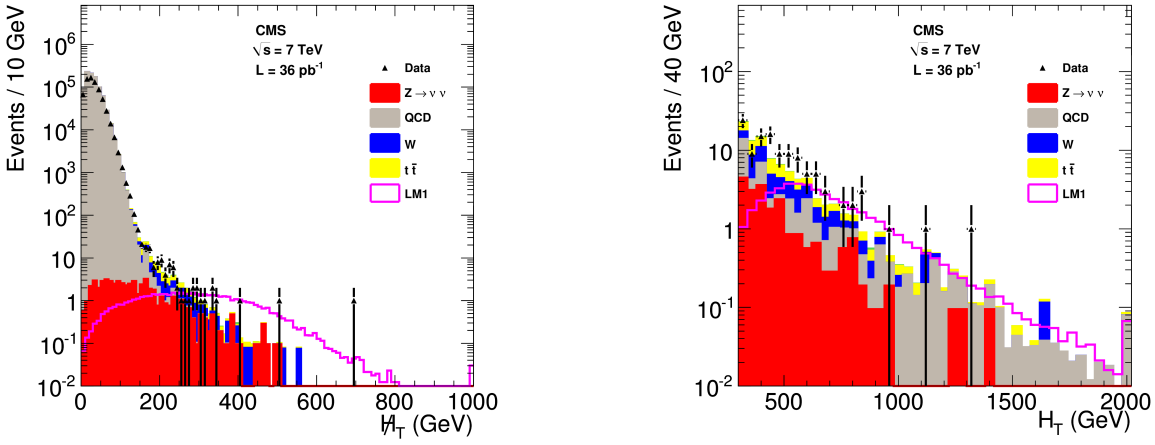

Figure 6.6: The $\not{H}_T$ (left) and H_T distributions (right) for the data and MC simulation samples with all baseline selection cuts applied except the $\not{H}_T$ and H_T requirements, respectively. The distributions for the different backgrounds are shown as stacked histograms, while the SUSY LM1 signal is overlaid for illustrative purposes [299].

of hadronically decaying tau leptons. The sum of both methods yields the estimate for the sum of the W+ jets and $t\bar{t}$ background. The $t\bar{t}$ background is also measured separately from a b-tagged control sample. Using the W to $t\bar{t}$ ratio, the result is found to be consistent with the other methods [299].

6.2.1 The $W/t\bar{t} \rightarrow e, \mu + X$ background estimation

The background from W+ jets and $t\bar{t}$ events, where a W-boson decays into a muon or an electron that is not rejected by the explicit lepton veto, is measured using a muon control sample. This control sample is collected using the same H_T triggers and the selection requires exactly one muon that is isolated and passes the identification and isolation requirements as discussed in section 6.1.3. Simulation indicates that more than 97% of these muons are due to W+ jets and $t\bar{t}$ events. The remaining 3% is due to QCD, $Z \rightarrow \mu^+\mu^-$ with one lost muon and diboson events resulting in one and only one isolated and identified muon. The number of events in the signal region that are either identified but not isolated, or are not identified at all, are estimated reweighing the muon control sample with the correct weights. Consider the whole μ + jet sample (N_{tot}) which is unknown, and consists of identified muons (N_{ID}) and not identified muons ($N_{\overline{\text{ID}}}$):

$$N_{\text{ID}} = \epsilon_{\text{ID}} N_{\text{tot}}, \tag{6.2}$$

$$N_{\overline{\text{ID}}} = (1 - \epsilon_{ID}) N_{\text{tot}}. \tag{6.3}$$

The identified muons, N_{ID}, are split in the identified and isolated muons, $N_{\text{ID\&ISO}}$, and the identified and not isolated muons, $N_{\text{ID\&}\overline{\text{ISO}}}$:

$$N_{\text{ID\&ISO}} = \epsilon_{\text{ISO}} \epsilon_{\text{ID}} N_{\text{tot}} \tag{6.4}$$

$$N_{\text{ID\&}\overline{\text{ISO}}} = (1 - \epsilon_{\text{ISO}}) \epsilon_{\text{ID}} N_{\text{tot}} \tag{6.5}$$

Only the identified and isolated muons are known together with the isolation and identification efficiencies, ϵ_{ISO} and ϵ_{ID} respectively. The identified, but not isolated muons can than be

rewritten as:

$$N_{\mathrm{ID}\&\overline{\mathrm{ISO}}} = (1-\epsilon_{\mathrm{ISO}})\epsilon_{\mathrm{ID}}N_{\mathrm{tot}} = \frac{1-\epsilon_{\mathrm{ISO}}}{\epsilon_{\mathrm{ISO}}}(\epsilon_{\mathrm{ISO}}\epsilon_{\mathrm{ID}}N_{\mathrm{tot}}) = \frac{1-\epsilon_{\mathrm{ISO}}}{\epsilon_{\mathrm{ISO}}}N_{\mathrm{ID\ \&\ ISO}}, \tag{6.6}$$

while the non identified muons can be written as:

$$N_{\overline{\mathrm{ID}}} = (1-\epsilon_{ID})N_{\mathrm{tot}} = \frac{1}{\epsilon_{\mathrm{ISO}}}\frac{1-\epsilon_{ID}}{\epsilon_{\mathrm{ID}}}(\epsilon_{\mathrm{ISO}}\epsilon_{\mathrm{ID}}N_{\mathrm{tot}}) = \frac{1}{\epsilon_{\mathrm{ISO}}}\frac{1-\epsilon_{ID}}{\epsilon_{\mathrm{ID}}}N^{\mu}_{\mathrm{ID\ \&\ ISO}}. \tag{6.7}$$

While we dropped the muon-index on the isolation efficiency ϵ_{ISO} and the identification efficiency ϵ_{ID}, the muon- and electron-index are now introduced to extend the formulas given above for electrons. Since muons can be identified and isolated with higher efficiency than electrons, only a muon control sample has been used. Therefore **the identified, but not isolated leptons** (electrons and muons) are given by:

$$N^{e}_{\mathrm{ID}\&\overline{\mathrm{ISO}}} = \frac{\epsilon^{e}_{\mathrm{ID}}}{\epsilon^{\mu}_{\mathrm{ID}}}\cdot\left(\frac{1-\epsilon^{e}_{\mathrm{ISO}}}{\epsilon^{\mu}_{\mathrm{ISO}}}\right)\cdot N^{\mu}_{\mathrm{ID\ \&\ ISO}} \qquad \text{and} \qquad N^{\mu}_{\mathrm{ID}\&\overline{\mathrm{ISO}}} = \left(\frac{1-\epsilon^{e}_{\mathrm{ISO}}}{\epsilon^{\mu}_{\mathrm{ISO}}}\right)\cdot N^{\mu}_{\mathrm{ID\ \&\ ISO}}, \tag{6.8}$$

and **the non-identified leptons** (electrons and muons) are given by:

$$N^{e}_{\overline{\mathrm{ID}}} = \frac{1}{\epsilon^{\mu}_{\mathrm{ISO}}}\cdot\left(\frac{1-\epsilon^{e}_{ID}}{\epsilon^{\mu}_{\mathrm{ID}}}\right)\cdot N^{\mu}_{\mathrm{ID\ \&\ ISO}} \qquad \text{and} \qquad N^{\mu}_{\overline{\mathrm{ID}}} = \frac{1}{\epsilon^{\mu}_{\mathrm{ISO}}}\cdot\left(\frac{1-\epsilon^{\mu}_{ID}}{\epsilon^{\mu}_{\mathrm{ID}}}\right)\cdot N^{\mu}_{\mathrm{ID\ \&\ ISO}}. \tag{6.9}$$

The lepton isolation efficiencies ($\epsilon^{\ell}_{\mathrm{ISO}}$, $\ell = e,\mu$) are measured from $Z \to \ell^{+}\ell^{-}$ events ($\ell = e,\mu$), using a tag-and-probe method as a function of lepton p_{T} and the angular distance between the lepton and the nearest jet. The lepton identification efficiency ($\epsilon^{e}ll_{\mathrm{ID}}$) is also determined with a tag-and-probe method, on the same sample of events, and parametrized as a function of lepton p_{T} and η.

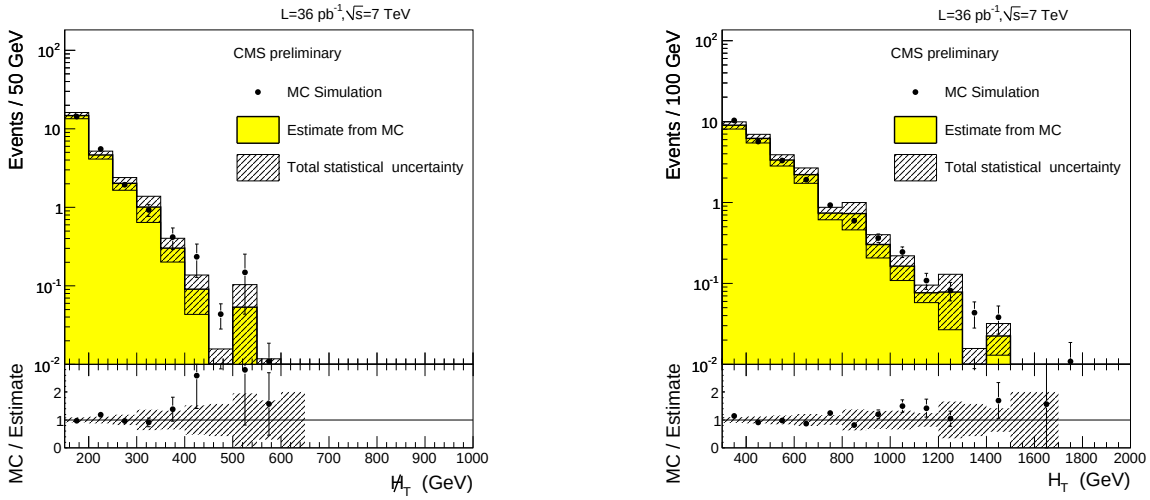

Figure 6.7: Application of the lost lepton method to Monte-Carlo simulated samples of W + jets and $t\bar{t}$. This, so-called "closure test" of the lost lepton method shows the W + jets and $t\bar{t}$ contribution to the $\not{H}_{\mathrm{T}}$ (left) and H_{T} distributions (right) for the baseline selection [199].

Leptons out of the kinematic or geometric acceptance form about half of the total e,μ contribution, which is not unexpected since the $\not{E}_T$ requirement prefers the subset of events where the neutrino(s) gets the highest momentum from the boosted W. The ratio R_{accept} of events with out-of-acceptance leptons to those within acceptance is determined using simulation and is applied to the same muon control sample described above, corrected for isolation and identification efficiencies:

$$N_{\overline{\text{accept}}} = \frac{N_{\text{tot}}}{R_{\text{accept}}} = \frac{N_{\text{ID \& ISO}}}{\epsilon_{\text{ISO}}\epsilon_{\text{ISO}} \cdot R_{\text{accept}}}. \tag{6.10}$$

Dominant uncertainties arise from the statistical uncertainties on the muon control sample and the Z sample used for measuring the lepton efficiencies. The residual presence of QCD, Z or diboson events (3%) is taken into account as a systematic uncertainty. A total systematic uncertainty of 18% is obtained [299].

This method is also applied to a Monte-Carlo simulated muon sample, shown in Figure 6.7, where the method could be tested with the same information one obtains from data, the "data-like MC-information", and checked afterwards with the so-called "Monte-Carlo truth", since one knows what has been simulated. This procedure is called a "Monte-Carlo Closure" test. The MC-obtained prediction (the data-like MC) reproduces within the uncertainties the expectation from the simulation (the MC truth), as could be seen in Figure 6.7. Using the prediction from data after the baseline selection, about 50% more events are predicted than expected from Pythia and Madgraph simulated samples. The difference is due to the parameter tune of Pythia, which describes the shape of the distributions measured in data, but fails to predict the right amount of data. More details on this method are given in References [199, 324].

6.2.2 The $W/t\bar{t} \to \tau_h + X$ background estimation

Hadronically decaying tau leptons constitute an important second component of the W and $t\bar{t}$ background, since $\approx$ 65% of the tau decays are hadronic and only $\approx$ 35% are leptonic. Jets from τ leptons are characterized by a low multiplicity of particles and their reconstruction was briefly discussed in section 4.7.3. Since the reconstruction efficiency for hadronic-τ's is not high enough, no τ-veto was applied, such as was done for muons and electrons, but instead the background was estimated from data. The hadronic-τ background is estimated by substituting a muon from a μ+jets control sample by a τ jet. These events are mainly composed of $W(\mu\nu)$+jets and $t\bar{t}(\mu\nu)$ events and are selected with single muon triggers for reasons that will later become obvious. Events are required to have exactly one muon with $p_T > 20\,\text{GeV}/c$ and $|\eta| < 2.1$ and to satisfy the identification and isolation requirements as described in section 6.1.3.

Lepton universality ensures us identical hadronic properties in $pp \to \mu X$ and $pp \to \tau X$ events, except for the fraction of the τ-jet energy deposited in the calorimeters (since a neutrino is produced in the hadronic τ-decay). To account for this difference, each muon in the control sample is replaced by a τ-jet. The momentum of this τ jet is obtained by scaling the muon momentum by a factor obtained from a simulated energy response distribution that models the fraction of visible momentum as a function of the true τ momentum [299]. By selecting events with single muon triggers, the hadronic properties of the events are identical for events with an hadroniccally decaying τ, and events of the muon control sample. The extra jet is then taken into account when applying selection cuts to obtain the hadronic-τ prediction from these modified events. To probe the full response distribution of the τ_h, this procedure was repeated

multiple times for each event [299]. The increase of the H_{T} of the event by the μ-τ substitution justifies the use of single muon triggers, since the use of H_{T} triggers would yield events with $H_{\mathrm{T}} > p_{\mathrm{T}}^{\mu} + 300\,\mathrm{GeV}/c$ instead of $H_{\mathrm{T}} > 300\,\mathrm{GeV}/c$.

Finally, corrections are applied for the kinematic and geometric acceptances of the muons, the muon trigger, reconstruction and isolation efficiencies and the relative branching fraction for W decaying into muons or hadronic τ jets. The main source of SM background contamination in the muon control region comes from $W \to \tau\nu + X \to \mu\nu + X$, estimated to be 10% of the total control sample and is subtracted using Monte Carlo simulation. More details on this method are given in References [199, 325].

6.3 QCD background estimation

Multijet events are events where several jets were produced by the strong interaction, which does only couple to quarks and gluons. Therefore these events are called QCD multijet events and they have the nice feature that, at the production vertex (i.e. before any measurement), the event is completely balanced in the transverse plane, since no neutrinos or other invisible particles are produced. However, jet mismeasurements will obscure the obvious balancing of the event and introduce missing transverse momentum. The knowledge, that if an event is a QCD multijet event, then the true jets should be balanced, is a strong feature to tackle this QCD background.

QCD multijet production is the most difficult background to model for new-physics searches in the all-hadronic channels. Current theoretical knowledge of the spectrum of jets has large uncertainties when probing phase-space regions with high-H_{T} and high jet multiplicity. Therefore two different methods were designed to estimate the contamination of QCD multijet events from data:

- The "Rebalance-and-Smear"(R&S) method estimates the multijet background directly from data. This method predicts the full kinematics in multijet events. Crucial inputs to this method are the jet energy resolutions, which are measured from data, including the non-Gaussian tails, as discussed in section 4.4.6. A summary of the method, based on Reference [299] is given below. More details can be found in References [299, 309–311, 326].
- The "factorization method" provides an alternative prediction for the QCD multijet background, based on the extrapolation from a low-$\not{H}_{\mathrm{T}}$ control region to the high-$\not{H}_{\mathrm{T}}$ search region using the correlation between $\not{H}_{\mathrm{T}}$ and an angular variable. This method will not be discussed here, but details can be found in References [299, 327].

The data sample used for the QCD estimation was collected on jet or H_{T} triggers. It is an inclusive data sample: there is no requirement nor veto on missing transverse momentum in the event. This choice will be clear later on, after the discussion of the R&S method.

6.3.1 The rebalance-and-smear method

QCD multijet events can have large missing transverse momentum when one or more jets in the event are mismeasured, i.e. the jet has a jet energy response far from unity, and hence the event is not balanced anymore, hereby introducing . The jet energy response is the ratio of the jet-p_{T} of

the reconstructed jet over the jet-p_{T} that would result from measuring perfectly (truely) the four-momenta of the particles in the jet, a so called "particle jet": $\mathcal{R} = p_{\mathrm{T}}^{\mathrm{reco}}/p_{\mathrm{T}}^{\mathrm{true}}$. For Monte-Carlo simulated events, those "particle jets" are genjets and the jet energy response is defined as $\mathcal{R} = p_{\mathrm{T}}^{\mathrm{reco}}/p_{\mathrm{T}}^{\mathrm{gen}}$, as discussed in section 4.4.6. The R&S method is essentially a simplified simulation, where a sample of "seed events" is smeared by the jet energy resolution function. The "seed events" are well-balanced QCD multijet events obtained from data and consist of "seed jets" that are good estimators of the true particle-jet momenta. The smearing with the jet energy resolution will introduce mis-measurements, leading to large missing transverse momentum, in a similar way as observed in real data.

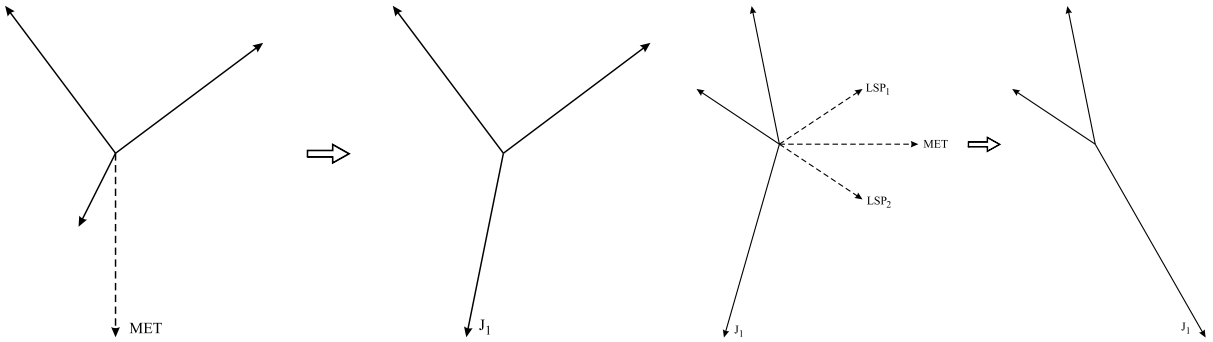

(a) Rebalancing of a mismeasured QCD multijet event

(b) Rebalancing of a SUSY event with genuine $\not\!\!E_{\mathrm{T}}$

Figure 6.8: Illustration of the rebalancing procedure, each arrow represents a jet of an event. (a) A QCD multijet event, where the leading jet is mismeasured, leading to large $\not\!\!H_{\mathrm{T}}$ aligned with one of the jets. The rebalancing procedure yields a perfectly balanced event. (b) A tiny contribution from BSM events leads also to perfectly balanced QCD multijet events.

The "rebalance" step, shown schematically in Figure 6.8, allows one to bypass the need for precise theoretical understanding of the QCD jet production at centre-of-mass energies scanned by the LHC by using real data as input, namely an inclusive multijet sample. This is mostly made up of QCD multijet events, but has tiny contributions from fully hadronic W, Z and $\mathrm{t\bar{t}}$ events and even tinier contributions from possibly new physics events. None of these contributions matter because of the overwhelmingly large QCD cross section. The seed events are constructed in the rebalance step by adjusting the jet momenta in events with n jets given the likelihood $\mathcal{L} = \Pi_{i=1}^{n} r(p_{\mathrm{T},i}^{\mathrm{reco}}|p_{\mathrm{T},i}^{\mathrm{true}})$. $p_{\mathrm{T},i}^{\mathrm{reco}}$ and $p_{\mathrm{T},i}^{\mathrm{true}}$ are the reconstructed and true jet transverse momentum, respectively, and r is the resolution probability distribution. The likelihood is maximized as a function of $p_{\mathrm{T},i}^{\mathrm{true}}$, within the constraint of the transverse momentum balance: $\sum_{i=1}^{n} \vec{p}_{\mathrm{T},i}^{\,\mathrm{true}} + \vec{p}_{\mathrm{T,soft}}^{\,\mathrm{true}} = 0$. Here, all clustered objects with $p_{\mathrm{T}} > 10\,\mathrm{GeV}/c$ are classified as jets and $\vec{p}_{\mathrm{T,soft}}^{\,\mathrm{true}}$ is the sum of all particles not included in the jets and is approximated by the measured quantity $\vec{p}_{\mathrm{T,soft}}^{\,\mathrm{reco}}$. In other words, in the rebalancing step all of the jet momenta of an event are adjusted, in a manner consistent with the expected measurement uncertainties, to return the event back into approximate transverse momentum balance. This forces events with genuine high $\not\!\!H_{\mathrm{T}}$ from neutrinos or other undetected particles to be similar to well-balanced QCD-like events. While Figure 6.8(a) shows the rebalancing of a QCD multijet event, Figure 6.8(b) shows how a BSM event with genuine $\not\!\!H_{\mathrm{T}}$. $\mathrm{t\bar{t}}$, W + jets and Z + jets events and also contributions from new physics, if any, have negligible impact on the background prediction since their production rate is orders of magnitude smaller than the QCD multijet production rate.

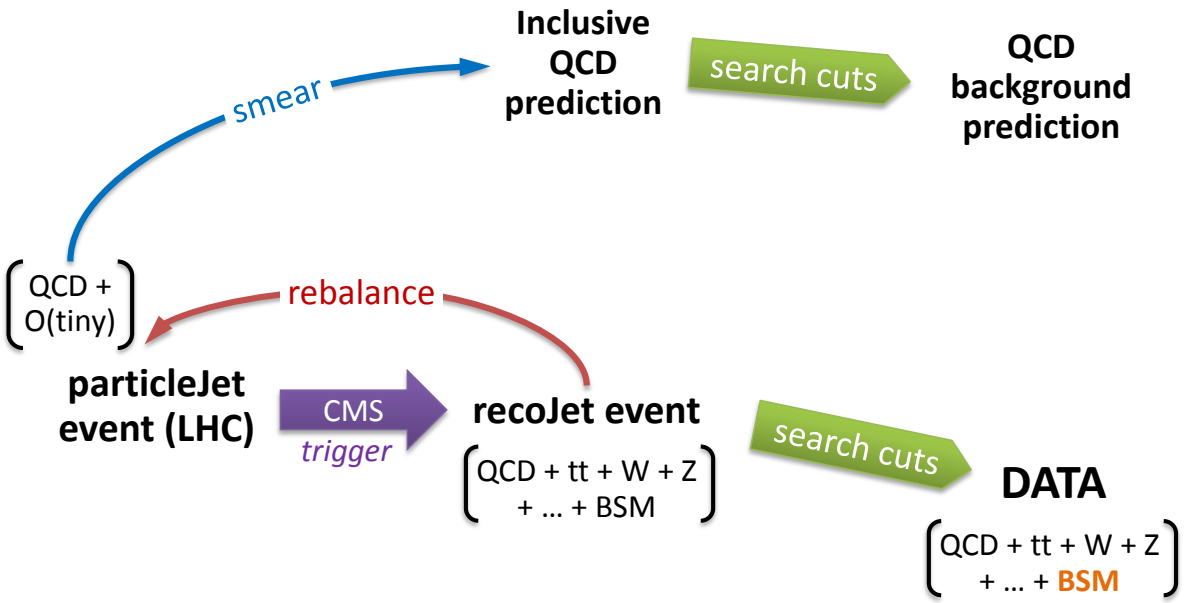

Figure 6.9: Overview of the R&S method [199].

Figure 6.9 shows the procedure of the R&S method, starting with pp collisions delivered by the LHC. The pp collisions provide the "true" spectrum of particle jets, while the data selected by jet and H_{T} triggers was used to reconstruct the original final state to the best possible extent: these are reco jets. While for QCD processes particle jets are perfectly balanced in the transverse plane, this is often not the case for the reco jets description. By rebalancing these reco jets, the real QCD events are "unfolded" back to particle jet level, while the non-QCD events are stripped of their characteristic $E_{\mathrm{T}}^{\mathrm{miss}}$. The resulting pure QCD multijet sample is the desired seed event sample. Next, the momentum of each seed jet of these seed events is smeared using the jet energy resolution distribution. The search requirements can then be applied to predict all event-by-event jet kinematic properties. The distributions predicted by the R&S procedure are compared with those from Monte-Carlo simulation in Figure 6.10. Notice that in the left plot, it is the MC truth that is running out of statistics, while the R&S method has high statistical accuracy.

It has now become clear why an inclusive data sample, i.e. events selected without any requirement on the missing transverse momentum, was required for this method. Supressing contamination of non-QCD events with high $E_{\mathrm{T}}^{\mathrm{miss}}$ by rejecting events with significant $E_{\mathrm{T}}^{\mathrm{miss}}$, one undesirably depletes the high-H_{T} region of the QCD phase-space, since high-$\not{H}_{\mathrm{T}}$ is always correlated with high-H_{T} in an event. The outcome would then be a bias in which one underestimates the contribution of the high$\not{H}_{\mathrm{T}}$ tail.

6.3.2 Jet response distributions

The rebalance step was shown to be almost insensitive to tails in the resoluton functions, and can hence be limited to the Gaussian core. For smearing, and therefore the prediction of the $\not{H}_{\mathrm{T}}$ spectrum, the full resolution functions including the non-Gaussian tails are used. The tails of the jet response function are of particular importance for the prediction of the QCD multijet background at high$\not{H}_{\mathrm{T}}$.

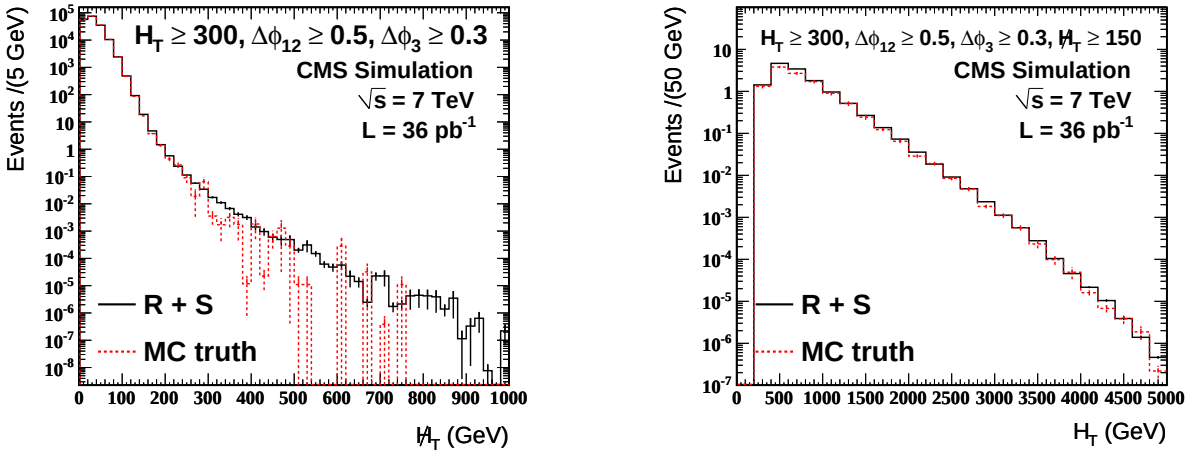

Figure 6.10: The $\not{H}_T$ (left) and H_T (right) distributions from the R&S method applied to simulation events, compared to the actual Monte Carlo simulated distribution (MC truth), for events passing ≥ 3 jets, $H_T \geq 300\,\text{GeV}/c$, and $\Delta\phi(, J_{1-3})$ selections and additionally $\not{H}_T > 150\,\text{GeV}/c$ for the right plot [299].

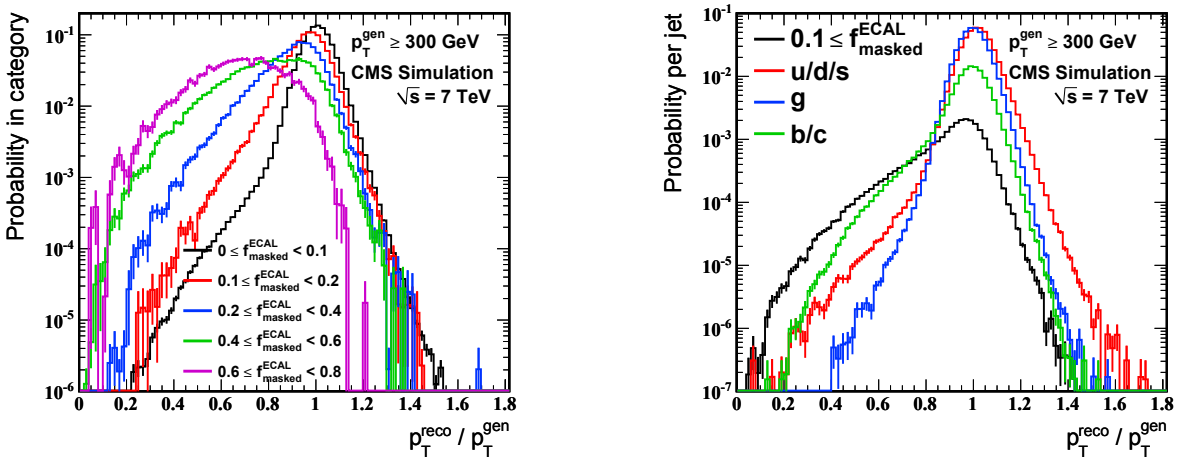

Figure 6.11: Ratio of the reconstructed jet transverse momentum to the generated transverse momentum for jets with $p_T^{gen} \geq 300\,\text{GeV}/c$. Distributions are shown for different values of f_{masked}^{ECAL} (left) and gluons and different quark flavours (right) [299].

The jet momentum resoluton functions are parametrized using simulated PYTHIA dijet samples and adjusted to match the measurements from data, as described in section 4.4.6. The response distributions are parametrized with respect to p_T and η. Furthermore, an exceptionally low response arises at specific η - ϕ locations where ECAL channels have been masked. This effect is taken into account by parametrizing the jet response as a function of the fraction of jet momentum lost in the masked area of the detector, computed using a template for the p_T-weighted distribution of particles as a function of the distance in η and ϕ to the jet axis. The dependence of the jet resolution on f_{masked}^{ECAL} is shown in Figure 6.11 (left). Finally, heavy flavour b- or c-quarks and also gluons exhibit different jet resolution shapes than light jets, as shown in Figure 6.11 (right). At high jet p_T, decays of heavy flavour hadrons into charged leptons and

neutrinos become one of the dominant sources of significant jet energy loss. The jet resolution functions are determined for bottom, charm, gluon, and light-flavour quarks separately. The flavour dependence is then accounted for by using these resolution functions in the smearing procedure according to the flavour fractions from simulation [299].

The measurement of the jet energy resolution functions contains two separate parts: a Gaussian core and non-Gaussian tails, and was detailed in section 4.4.6. The measurements of the Gaussian core resolution as a function of jet η were found to be 5 - 10% larger in data than in simulation, with systematic uncertainties of similar size as the deviation. No significant dependence on the p_{T} of the jet is observed. The measurement of the non-Gaussian resolution tails is compatible within uncertainties with the simulation. Correction factors were developed to adjust the Monte-Carlo simulated resolution.

6.4 Conclusion

In this chapter the design of the search for Supersymmetry, based on jets and missing transverse momentum is discussed. This search relies on the precise estimation of the Standard Model backgrounds. Two of these backgrounds: W/top and QCD are discussed here, while the production of a Z boson associated with jets, followed by the decay of the Z boson into neutrinos, is the third and last background. This background is an irreducible background and is detailed in chapter 7 and constitutes the main physics result of this thesis. The results of the three different Standard Model backgrounds will then be presented in chapter 8 and interpreted in the context of a specific SUSY model: mSUGRA and in terms of more general models for new heavy particle production: the simplified model spectra (SMS).

Chapter 7

Datadriven Z($\nu\nu$) prediction

7.1 Introduction to the invisible Z background

The associated production of a Z boson and jets, followed by the decay of the Z boson into neutrinos, constitutes an irreducible background to a jets-plus-missing-momentum search. This background can be estimated from the data using three methods, which provide important cross-checks of each other. All three methods are based on selecting a control sample containing one of the three electroweak vector bosons (γ, W or Z) and use the electroweak correspondence to predict the invisible Z background. Apart from the three-way correspondence, these three methods are also affected by most anticipated new-physics signals in different ways, thus providing a handle on the problem of signal contamination of lepton and γ control samples.

The first method corresponds to the use of $Z(\mu\mu)$ + jets events, interpreting the momentum of the pair of muons as missing momentum. Removing the muon pair automatically introduces missing momentum into the event. The downside of this very obvious and simple method is the lack of $Z \to \mu\mu$ +jets events passing the selection criteria in the early stages of the LHC. Taking into account the ratio:

$$R = \frac{Z \to \nu\bar{\nu}}{Z \to \mu\mu} = \frac{(20.00 \pm 0.06)\%}{(3.366 \pm 0.007)\%} = 5.942 \pm 0.022$$

this method suffers from a large statistical uncertainty. Further uncertainties are the acceptance and identification efficiency of the muons. The present analysis is performed on the dataset recorded in 2010, which has very few Z + jets events decaying to a muon pair, preventing this method from being used in this analysis.

For the second and third method, the electroweak correspondence between the Z

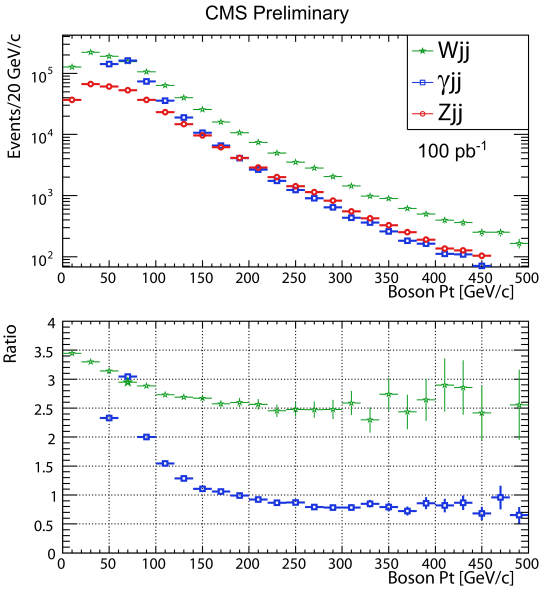

Figure 7.1: Figure taken from Reference [328]. Top: Monte-Carlo generator event yields for the vector boson + two parton process, for the γ, W and Z vector bosons. The events are calculated by MADGRAPH at generator level at $\sqrt{s} = 14$ TeV and for 100 pb^{-1} of integrated luminosity. Bottom: ratio of the W (top) and γ (bottom) yields relative to the Z.

boson and either the W or γ is exploited.
As shown in Figure 7.1, above a boson p_{T} of roughly $\sim 150\,\mathrm{GeV}/c$, the ratios of W and γ with respect to Z production depend mostly on the electroweak couplings of the participating particles of the events. In the high mass range, differences in the electroweak couplings of W, γ and Z bosons to quarks will lead to small corrections. The hadronic part of the event is expected not to depend upon whether the boson is a Z, W, or γ. The ratios of W or γ to Z production are thus relatively robust to variations in analysis selection criteria, such as multiplicity and transverse energies of jets. In the absence of large contributions from new physics to these samples, they therefore can provide a robust prediction of the missing momentum spectrum for invisible Z's at high p_{T}.

While the mass difference between the W and Z boson is much smaller than between the photon and Z boson, the W method has one drawback. It is rather complicated to select a prompt sample of W-bosons, since the W-boson is also produced in the decay of $t\bar{t}$ events, while Z bosons are not. Therefore it is important to estimate the $t\bar{t}$ background properly. The $t\bar{t}$ contribution can be identified by requiring b-tags, introducing systematic uncertainties from b-tag efficiency and purity.

In this chapter the correspondence between γ and Z production at high boson p_{T} is used to predict the $\mathrm{Z} \to \nu\bar{\nu}$ background to the "inclusive jets plus missing transverse energy" analysis. The missing momentum spectrum is obtained by removing the identified photon, and correcting for residual phenomenological and experimental differences between the selected γ sample and invisible Z events. The proof of concept of this method on Monte-Carlo simulation was documented previously in Reference [329]. Section 7.2 provides background on γ and Z bosons and their correspondence. Section 7.4 gives an overview of the event selection, while section 7.5 discusses the various backgrounds to the photon sample. In section 7.6 the correspondence between photons and Z bosons is investigated, followed by a prediction of the $\mathrm{Z}(\nu\bar{\nu})$ + jet events in section 7.3, the estimation of the systematic uncertainty in section 7.7 and discussion of the final result in section 7.8.

7.2 Photons and Z bosons

In the Standard Model, Z bosons decaying to muons can be produced at $O(\alpha)$ by quark-antiquark annihilation. The massless photon can only be produced at $O(\alpha \cdot \alpha_{\mathrm{S}})$ through an off-shell quark, to preserve energy-momentum conservation. Virtual photons decaying to the same final states as the Z-boson are produced copiously. These two processes cannot be disentangled and are considered together as the Drell-Yan process. The Feynman-diagram of the $q\bar{q} \to Z/\gamma^* \to \mu^+\mu^-$ is shown in Figure 7.2, and leads to a continuous spectrum of the dilepton invariant mass shown in Figure 7.3. The invariant mass of the opposite sign muon pairs shown in Figure 7.3 is recorded by the CMS experiment in 2010. Due to prescaled triggers, the $1/\hat{s}$ behaviour of the Drell-Yan cross section is only visible for $M(\mu\mu) \geq 30$ GeV/c^2. The continuous spectrum comes from processes mediated by virtual photons, while the peaks are due to particular decays of particles, such as cc (J/ψ) or bb (Υ), into two muons. Most of the events at the Z mass peak are from events mediated by the Z-boson, although a small background comes from events mediated by virtual photons.

The events with two charged leptons in the final state, mediated by a virtual photon, do not

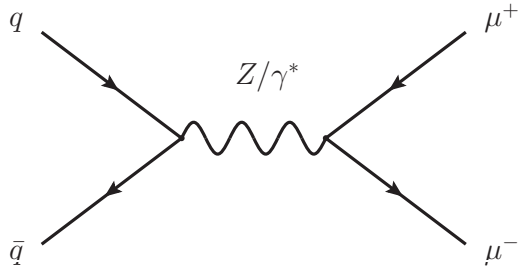

Figure 7.2: The Drell-Yan process $q\bar{q} \rightarrow \mu^+\mu^-$, mediated by a Z-boson or a virtual photon γ^*.

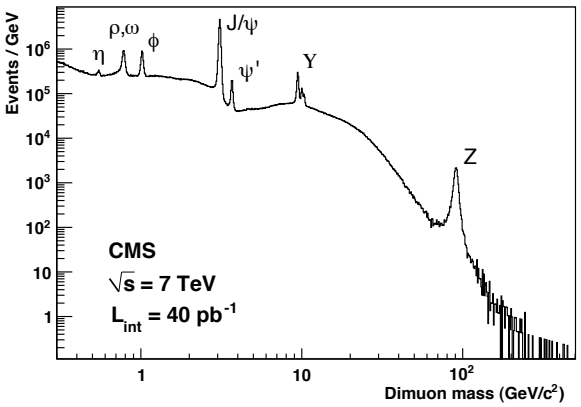

Figure 7.3: Invariant mass spectrum of opposite sign muon pairs. The continuous spectrum is due to the interference of the Z and the virtual photon.

have a counterpart in the final state with two neutrinos, since photons do not carry weak charge and hence do not couple to neutrinos. A restriction on the invariant mass of the dilepton pairs will lead to an acceptable pure Z + jets $\rightarrow \ell^+\ell^-$ + jets sample that can be used to estimate the Z + jets $\rightarrow \nu\bar{\nu}$ + jets events.

Although there is no correspondence between photons and Z bosons at $O(\alpha)$, this difference, however, is of no interest to this analysis, since at least three hard jets are required. Requiring at least one jet, photons and Z bosons are produced by the same processes, as shown in Figure 7.4: Compton scattering: $qg \rightarrow Vq$ in both s- and t-channel and quark-antiquark annihilation: $q\bar{q} \rightarrow Vg$ in the t-channel, where V can be either a Z-boson or a photon.

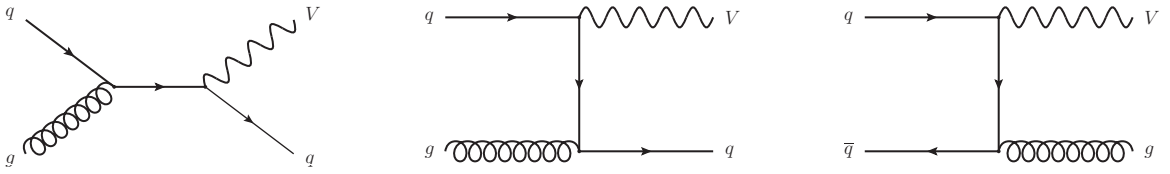

(a) qg Compton scatt. : s-channel (b) qg Compton scatt. : t-channel (c) $q\bar{q}$ annihilation: t-channel

Figure 7.4: Leading order processes for V + jet production, with $V = \gamma$ or Z: quark-gluon Compton scattering (in s- and t-channel) and quark-antiquark annihilation (t-channel). The u-channel diagrams to the corresponding t-channel diagrams are not shown.

The hadronic content of events with associated production of a Z-boson and jets is identical to events with associated production of a photon and jets. Both bosons need to be produced off a (virtual) quark, since gluons only couple to particles with colour charge. Figure 7.5 shows two example diagrams for the NLO production of photons and Z bosons associated with three jets, illustrating the similar hadronic content.

Although γ and Z production properties are very different at energies below or of the order of the Z mass, the impact of the mass difference is expected to become negligible with large boson transverse momenta. Apart from some mass and electroweak coupling effects, the production of γ's and Z bosons should exhibit similar characteristics at high energies at the LHC, particularly in regard to the hadronic jets in the events. This correspondence between γ's and Z bosons is

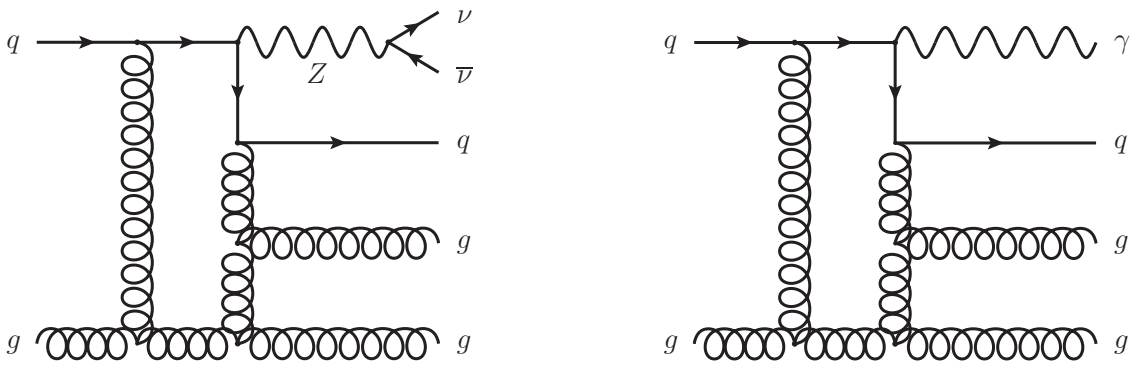

Figure 7.5: Example Feynman diagrams of $Z(\nu\overline{\nu})$ + 3 jets (left) and γ + 3 jets production (right) at Next-to-Leading Order.

interesting for early physics at the LHC since there is no branching ratio cost for γ's as compared to $Z \rightarrow \mu\mu$.

The first distinction between Z and γ production is due to the different electroweak coupling effects. Unlike the Z boson, the photon does not carry weak charge and hence will couple differently to u and d quarks. Since the parton distribution functions for u and d quarks have different x-dependence, the Z/γ ratio will also be a function of x. In the Standard Model the coupling of photons and Z bosons to quarks are (at a vertex with index μ):

$$\frac{i}{\hbar} e\gamma^{\mu} \qquad \text{vs.} \qquad \frac{i}{\hbar} e(\rho_V + \rho_A\gamma^5)\gamma^{\mu}, \tag{7.1}$$

with e, $e\rho_V$ and $e\rho_A$ the strength of respectively the QED γ-fermion coupling, and the vector- and axial-vector Z-fermion coupling. This difference is discussed in detail in a phenomenological Leading Order study for the ATLAS SUSY searches in Reference [330], but this only appeared after the finalization of the study discussed in this chapter. In the present study a Z/γ ratio was obtained from Monte-Carlo simulation, averaged over the u and d parton distribution functions.

Another, more important, distinction between Z and γ production arises from the lack of mass of the γ, hence it can be emitted arbitrarily close to a parton. Experimentally, an isolation criterion is necessary to select a pure sample of photons, as discussed in section 7.4.3. The isolation allows the radiation of soft gluons close to the photon and hence is infrared safe. However, it is not collinear safe, since it prohibits the collinear radiation of massless quarks in a finite region of phase-space. Theoretically, this could be omitted by the use of a continuous isolation criterion, the so-called Frixione isolation [331]. This Frixione isolation reduces the prohibited region for collinear radiation for massless quarks to a singularity, where the photon and the parton are exactly aligned.

7.3 Invisible Z + jets estimation from the photon sample

The initial aim of the analysis was to estimate $Z(\nu\nu)$ + jets events in the search regions by γ + jets events, using a conversion factor obtained from theory. This theoretical factor had to be corrected for the photon acceptance and the reconstruction and selection efficiency to estimate

the full γ + jets production cross section observed in the data. From that yield all possible backgrounds need to be subtracted. The amount of $Z(\nu\nu)$ + jets events ($N^{\text{DATA}}_{\text{Z}(\nu\bar{\nu})+\text{jet}}$) would then be estimated as follows:

$$N^{\text{DATA}}_{\text{Z}(\nu\bar{\nu})+\text{jet}} = \left(\frac{\text{Z}(\nu\bar{\nu})+\text{jet}}{\gamma+\text{jet}}\right)_{\text{THEORY}} \times \frac{\text{Purity}}{\epsilon_{\text{RECO,ID}} \times \text{Acceptance}} \times N^{\text{DATA}}_{\gamma+\text{jet}}. \tag{7.2}$$

The first factor is the theoretical correspondence between Z-bosons decaying to neutrinos and photons, which includes the correction for the $Z(\nu\nu)$ branching ratio, the effect of the masslessness of the photon relative to the large mass of the Z, and the differences in electroweak couplings of photons and Z's. The second factor consists of the purity correction (background removal) in the denominator and the reconstruction and selection efficiency ($\epsilon_{\text{RECO,ID}}$) of the photon object and the acceptance of the photon in the numerator. The selection and reconstruction factor corrects for the amount of real photons that are lost because of failing the selection criteria (such as being emitted to close to a jet) and reconstruction failure. The acceptance factor corrects for the fact that photons can only be reconstructed inside the tracker coverage of the detector ($\eta < 2.5$), else no distinction between electrons and photons can be made, and that the transition region between ECAL barrel (EB) and ECAL endcap (EE) is excluded from the reconstruction because of their bad energy resolution. Applying these corrections to the observed amount of photon plus jet events $N^{\text{DATA}}_{\gamma+\text{jet}}$ leads then to the predicted amount of $Z(\nu\nu)$ + jets events ($N^{\text{DATA}}_{\text{Z}(\nu\bar{\nu})+\text{jet}}$).

Although the BlackHat collaboration recently published next-to-leading order calculations of vector boson plus 3-jet calculations [332, 333] and Z + 4 jets [334], the γ + 3 jets calculations are not yet finished. Instead, the BlackHat collaboration performed a study comparing $Z+2$ jets to $\gamma+2$ jets events at Next-to-Leading Order, which was of direct use to the three jets case [335], as will be discussed in section 7.6.

Since the theoretical correspondence factor is not available, we opted to use the MadGraph Monte-Carlo simulated samples calculated at leading order and their corresponding leading order cross sections, to obtain the phenomenological correction factor translating γ + jets event yields into $Z(\nu\nu)$ + jets. Furthermore, since at generator level no isolation is applied, the photon can be arbitrarily close to the genjet, while at reconstruction level this is prohibited due to the isolation requirement. Since an estimate of this effect is not yet available, a phenomenological factor obtained at reconstruction level will be used. This phenomenological factor is determined after detector simulation and reconstruction and hence absorbs the photon reconstruction and identification efficiency ($\epsilon_{\text{RECO,ID}}$) and the detector acceptance, leaving only the purity factor to be implemented. Further on, the difference between the selection efficiency in data and the selection efficiency in Monte-Carlo simulated events is taken into account by a scale factor ($\text{SF}_{\text{DATA/MC}}$). The purity correction is split two factors:

- a factor due to secondary photons (determining the purity of the prompt photons):

$$\epsilon^{prompt}_{\text{DATA}} = \frac{\text{prompt}\,\gamma}{\text{all}\,\gamma}; \tag{7.3}$$

- a factor correcting for the fragmentation photons (determining the purity of the direct

photons):

$$\epsilon_{\mathrm{MC}}^{direct} = \frac{\mathrm{direct}\,\gamma}{\mathrm{prompt}\,\gamma}. \tag{7.4}$$

The former is measured on data, the latter has been obtained at generator level. The distinction between prompt photons (consisting of direct photons and fragmentation photons, discussed in section 7.5) and non-prompt or secondary photons (originating from meson decays) is discussed briefly in section 7.4.4 and more extensively in section 7.5. The formula used to estimate the $Z(\nu\nu)$ + jets events in data becomes:

$$N_{\mathrm{Z}(\nu\bar{\nu})+\mathrm{jet}}^{\mathrm{DATA}} = \left(\frac{\mathrm{Z}(\nu\bar{\nu})+\mathrm{jet}}{\gamma+\mathrm{jet}}\right)_{\mathrm{MC}} \times \epsilon_{\mathrm{MC}}^{direct} \times \mathrm{SF}_{\mathrm{DATA/MC}} \times \epsilon_{\mathrm{DATA}}^{prompt} \times N_{\gamma+\mathrm{jet}}^{\mathrm{DATA}}. \tag{7.5}$$

The different factors of formula 7.5 are discussed in the following sections. Section 7.4 deals with the event selection and the data/Monte-Carlo scale factor ($\mathrm{SF}_{\mathrm{DATA/MC}}$), while section 7.5 determines both purity corrections ($\epsilon_{\mathrm{MC}}^{direct}$ and $\epsilon_{\mathrm{DATA}}^{prompt}$). Section 7.6 discusses the correspondence between Z-bosons and photons and determines the Monte-Carlo correction factor after detector reconstruction and identification. All these corrections, along with some possible effects in the event selection, bring in phenomenological and experimental systematic uncertainties. Section 7.7 details the estimation of the systematic uncertainties. This allows to make the final estimation of the amount of $Z(\nu\nu)$ + jets events ($N_{\mathrm{Z}(\nu\bar{\nu})+\mathrm{jet}}^{\mathrm{DATA}}$) and the uncertainty on this estimation in section 7.8.

7.4 Selection of the photon sample

7.4.1 The modified event selection

The baseline selection of the inclusive jets plus missing transverse energy search is described in detail in section 6.1.3. Since the photon will be removed to create the $\not{H}_{\mathrm{T}}$, the baseline selection must undergo a modification before it can be applied to select a photon + jets sample. The $\not{H}_{\mathrm{T}}$ is calculated as the negative vectorial sum of the transverse momentum of jets recoiling against the photon, which is the quantity directly comparable to the $\not{H}_{\mathrm{T}}$ in $\mathrm{Z} \to \nu\bar{\nu}$ events. The QCD-suppression cuts on the angles between $\not{H}_{\mathrm{T}}$ and jets are also defined using the azimuthal angle of this "$\not{H}_{\mathrm{T}}$-like" quantity. Figure 7.6 illustrates the modification. The particle flow jet connected to the photon is removed from the $\not{H}_{\mathrm{T}}$ calculation, introducing artificial $\not{H}_{\mathrm{T}}$. The $\not{H}_{\mathrm{T}}$ vector is pointing exactly at the photon in the transverse plane, while this is not necessarily so in the 3D view, since the momentum is only conserved in the transverse plane.

The selection of the analysis is based on particle-flow reconstruction of collision events. For what concerns photons, the integration of photon identification and isolation within the particle-flow framework is not in a mature state yet in CMS. Therefore standard reconstructed photons are used, and a match between those and the nearest PF jet in a $\Delta R = 0.1$ cone is sought to remove the PF jet corresponding to the photon from the PF jet list. This, because of the particle flow algorithm uses all particles (charged hadrons, neutral hadrons, muons, electrons, photons, ...) as an input to the clustering algorithm.

However, it is not 100% guaranteed that the photon is reconstructed as a single particle flow jet. Therefore the probability for a photon to be reconstructed as two or more particle flow

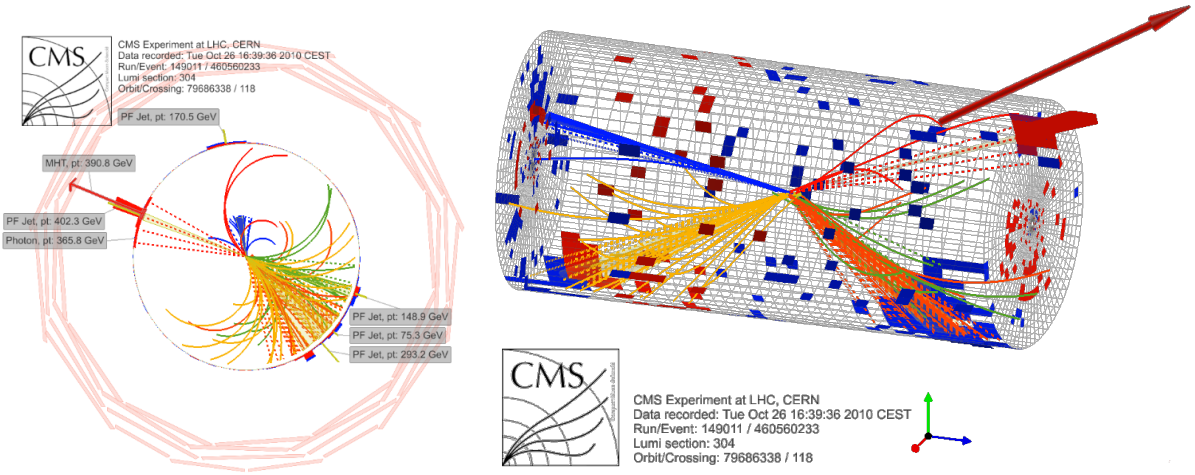

Figure 7.6: Illustration of the photon removal procedure for Event 460 560 233 in lumi section 304 of Run 149 011. The event has three central jets of 293, 149 and 75 GeV/c, one forward jet of 171 GeV/c, which are indicated by the spray of charged particles reconstructed within the tracker volume and the energy depositions in the calorimeter indicated by towers. The event contains a photon of 366 GeV/c, indicated as the red tower without tracks pointing at it. This photon is also reconstructed as a particle flow jet of 402 GeV/c. Removing the photon leads to a $\not{H}_T$ of 391 GeV/c, indicated with an arrow, allowing this event to pass both the high-H_T and the high-$\not{H}_T$ selection.

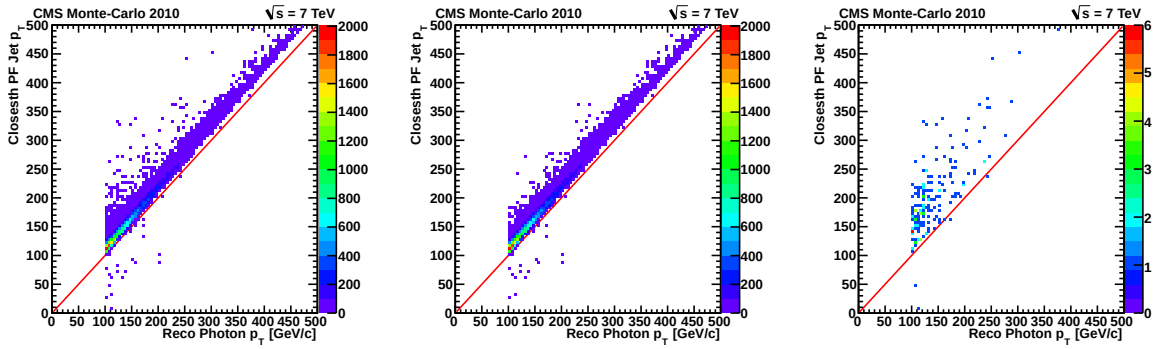

Figure 7.7: Transverse momentum of the reconstructed particle flow jet vs. the transverse momentum of the reconstructed photon for all events (left), for all events with $\Delta R_{\gamma\text{jet}} < 0.1$ (middle) and for events with $0.1 < \Delta R_{\gamma\text{jet}} < 0.4$ (right).

jets, contributing to H_T and $\not{H}_T$ calculations, was investigated. It was found to be negligible. In both data and Monte-Carlo only 1 jet with $p_T > 30$ GeV/c was found to be inside either a $\Delta R < 0.1$ cone or a $0.1 < \Delta R < 0.4$ hollow cone. Figure 7.7 shows the transverse momentum of the reconstructed particle flow jet vs. the photon for a high-p_T photon sample[1]. The $\sim 0.4\,\%$ fraction of events that do have a jet within $0.1 < \Delta R < 0.4$, contain a jet with on average more transverse momentum than the photon, due to clustering of additional energy deposits. Removing the jet in these events would lead to an over-estimation of the $\not{H}_T$. Therefore, the jet was not removed, leading to events with no significant $\not{H}_T$, not passing the selection criteria,

[1] The GJETS_HT_200 sample, see Table 7.1.

which is equivalent to removing that event from the Monte-Carlo sample. To ensure the samples to be free of noise and other problems, event cleaning, as discussed in section 7.4.5 is applied to the data, as well as to the MC samples where applicable.

7.4.2 Samples and triggers

The analysis is based on selecting a γ + jet control sample of high purity. Apart from the γ + jet events, also QCD multijet, electroweak and top samples are studied to estimate the backgrounds to prompt photons. In Table 7.1 the different samples used from the CMS `Fall10` MC production are summarized with their respective Leading Order (LO), Next-to-Leading Order (NLO) or Next-to-Next-to-Leading Order (NNLO) cross sections, the total number of events in the Monte-Carlo samples and their equivalent integrated luminosities. The NNLO and NLO cross sections for the heavy vector boson and $t\bar{t}$ samples were used, unless otherwise mentionned. Unfortunately, higher-order cross sections for the photon and QCD samples were not available.

Table 7.1: Properties of the MC Samples used in the analysis. All samples were produced using MADGRAPH and PYTHIA generators with the D6T tune in the CMSSW_3_6_4 and reconstructed using the CMSSW_3_8_X series of the CMS reconstruction software assuming start-up conditions for detector simulation, calibration and alignment.

Dataset	σ [pb]			# Events	L [pb^{-1}]
GJets_HT-40To100	23620	[LO]		$2.2171{\cdot}10^6$	94.
GJets_HT-100To200	3476	[LO]		$1.0616{\cdot}10^6$	305.
GJets_HT-200	485	[LO]		$1.14217{\cdot}10^6$	2355.
QCD_HT-100To250	$7 \cdot 10^6$	[LO]		$1.00226{\cdot}10^7$	1.432
QCD_HT-250To500	171000	[LO]		$4.67507{\cdot}10^6$	27.3
QCD_HT-500To1000	5200	[LO]		$7.35123{\cdot}10^6$	1414.
QCD_HT-1000	83	[LO]		$1.71332{\cdot}10^6$	20642.
WJets	31300	[NNLO]	(24380 [LO])	$1.48182{\cdot}10^7$	478.
DYJets	3100	[NNLO]	(2289 [LO])	$2.49374{\cdot}10^6$	804.
TTJets	165	[NLO]	(95 [LO])	$1.39455{\cdot}10^6$	8452.
ZinvJets	5760	[NNLO]	(4500 [LO])	$2.16732{\cdot}10^6$	376.

The photon-plus-jets and QCD multijets samples were binned in H_T at generator level (H_T^{gen}), where all high-p_T objects are summed. The cross section for physics processes typically follows a $1/\hat{s}$ spectrum. The H_T^{gen} binning ensures that for each H_T bin an appropriate amount of events was generated. The photon-plus-jets sample was split in three bins: $40 < H_T^{gen} < 100\,\text{GeV}/c$, $100 < H_T^{gen} < 200\,\text{GeV}/c$ and $200 < H_T^{gen} < \infty\,\text{GeV}/c$, and the p_T^{gen} spectrum is shown in Figure 7.8(a). The γ + jets sample (signal) is also shown along with all backgrounds expected in the 2010 analysis in Figure 7.8(b).

The data samples used for this analysis, taken from the November 4 reprocessing of the 2010 run data, are listed in Table 7.2, along with the run range used and the integrated luminosity. Good runs were selected by the JSON-file[2], which bookkeeps the good data recorded in 2010. In Table 7.3 the single-photon triggers and their thresholds are detailed as they evolved throughout the 2010 run.

[2] `Cert_136033-149442_7TeV_Nov4ReReco_Collisions10_JSON.txt`

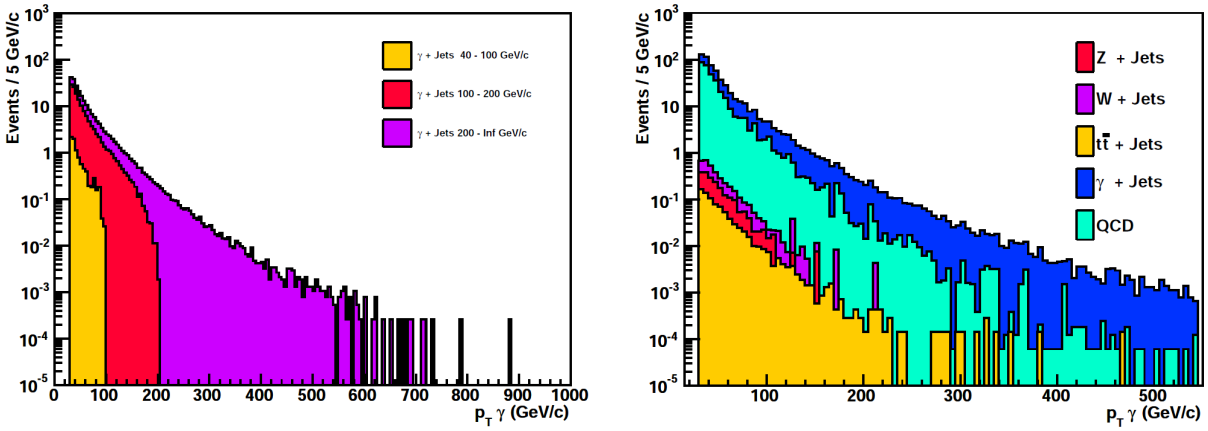

(a) γ + jets (b) signal and background

Figure 7.8: Monte-Carlo simulated p_{T} spectrum of the combined γ+jets sample (left) and of all signal (γ+jets) and background (QCD multijets, W+jets, Z+jets and $\mathrm{t\bar{t}}$+jets) samples (right), for $p_{\mathrm{T}}^{\gamma} > 70\,\mathrm{GeV}/c$. Both samples are scaled to leading-order cross sections for an integrated luminosity of $1.2\,\mathrm{pb}^{-1}$.

Table 7.2: Datasets used in this analysis. All data were reconstructed using CMSSW_3_8_6 version of the CMS reconstruction software.

Run Range	Dataset	L_{int} [pb^{-1}]
136033-144114	/EG/Run2010A-Nov4ReReco_v1	3.18
146417-149442	/Photon/Run2010B-Nov4ReReco_v1	32.96

Table 7.3: Trigger names and thresholds for the different run ranges used in this analysis.

Run Range	HLT Path	L1^{thr} [GeV]	HLT^{thr} [GeV]
136033-137028	HLT_Photon20_L1R	8	20
138560-143962	HLT_Photon20_Cleaned_L1R	8	20
144010-144114	HLT_Photon25_Cleaned_L1R	8	25
146428-147116	HLT_Photon30_Cleaned_L1R	8	30
147196-148058	HLT_Photon50_Cleaned_L1R_v1	8	50
148819-149442	HLT_Photon70_Cleaned_L1R_v1	8	70

Since in this analysis high-p_{T} photons are selected to mimic Z bosons with high momentum, it is expected that the triggers listed in Table 7.3, due to their relatively low thresholds, will be fully efficient. In Reference [221] it is shown that for a photon p_{T} of only 1 GeV above the HLT threshold the photon triggers become fully efficient. The event selection does not cut on the photon p_{T} directly though, but rather on the $\not\!\!H_{\mathrm{T}}$-like variable. To check for a possible trigger inefficiency, the efficiency of the $\not\!\!H_{\mathrm{T}}$ cut, as last cut in the baseline event selection, is measured in simulation as a function of the boson p_{T}. Figure 7.9(a) shows that the amount of photons with $p_{\mathrm{T}} < 100\,\mathrm{GeV}$ passing the $\not\!\!H_{\mathrm{T}}$ requirement is negligible. Therefore 100 GeV is further chosen as a pre-selection requirement on the photon samples, i.e $p_{\mathrm{T}}^{\gamma} > 100\,\mathrm{GeV}/c$. In Figure 7.9(b) the same $\not\!\!H_{\mathrm{T}}$ efficiency plot is shown for simulated Z bosons decaying into neutrinos.

Figures 7.9((a)&(b)) show the turn-on curve for the probability of an event with boson-$p_{\mathrm{T}} > 150\,\mathrm{GeV}/c$ to pass the $\not\!\!H_{\mathrm{T}} > 150\,\mathrm{GeV}/c$ criterium. $Z(\nu\nu)$-boson or a photon with $p_{\mathrm{T}} > 150\,\mathrm{GeV}/c$ does not automatically translate into a $\not\!\!H_{\mathrm{T}} > 150\,\mathrm{GeV}/c$, because the jet-$p_{\mathrm{T}}$ threshold in the $\not\!\!H_{\mathrm{T}}$

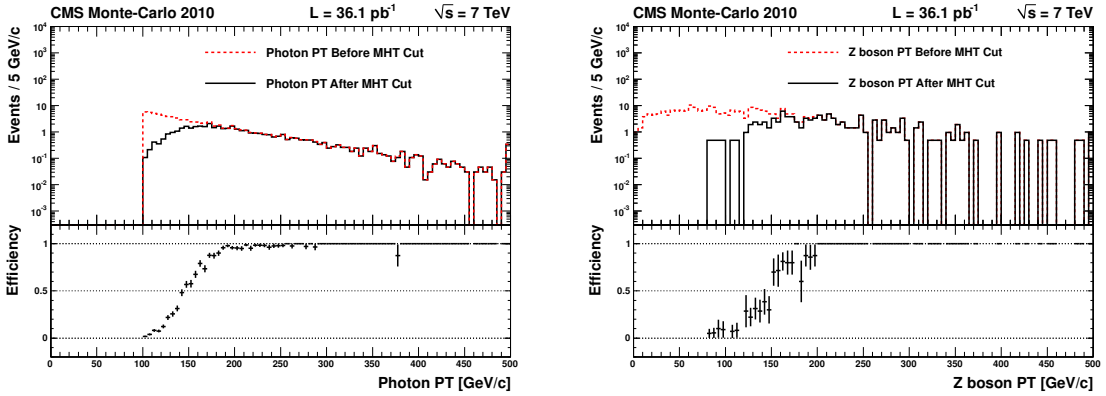

(a) γ + jets sample (b) $Z(\nu\nu)$ + jets sample

Figure 7.9: Efficiency in simulation of the $\not{H}_T > 150$ GeV cut in the baseline event selection as a function of (a) the photon p_T in a γ+jets sample, and (b) the Z boson p_T, taken from the generator information, in a $Z \to \nu\bar{\nu}$ sample.

calculation leads to a small but not vanishing $\not{H}_T$ in perfectly balanced events. The vector sum of the intrinsic $\not{H}_T$ and the boson-p_T is than the actual $\not{H}_T$ of the event and has the form of a turn-on curve as a function of the boson-p_T. Both the Photon and $Z(\nu\nu)$-boson have the same turn-on curve, the latter a bit obscured in Figures 7.9 because of the low statistics of the $Z(\nu\nu)$ sample.

7.4.3 Isolated photon selection

After applying the cleaning criteria, the selection of the photon-plus-jets sample starts by collecting prompt photon candidates with a pre-selection cut of $p_T > 100$ GeV. Photons are rejected if their ECAL superclusters are also used in the reconstruction of an electron. In this context the presence of a pixel seed is used to discriminate photons from electrons. The photon candidates do not have a pixel seed and are required to pass isolation cuts. Photons are selected in both barrel and endcap. The seed crystal is required to be outside a $\Delta\eta = 0.1$ ($\sim$ 6 crystals) region around the interface between barrel and endcap ($|\eta| = 1.479$).

To select a photon sample with a high purity, isolation requirements are added to the photon identification. Different groups in CMS optimized the photon selection criteria for their search, depending on different event topologies: single photon, double photon, additional jets and additional missing transverse energy. In the present analysis, the photon selection is based on the selection made by the isolated photon cross section measurement, published in Reference [208], which was the first result using photon objects in CMS. The purity was increased with a cut on the shower shape variable $\sigma_{i\eta i\eta}$, which is defined in section 4.6.4. The isolated photon selection criteria are shown in Table 7.4 and were designed for an optimal signal extraction [204]. These criteria on reconstructed photons are equivalent to a 5 GeV isolation imposed on simulated photons [208]. Several variations on these selections exist, by removing one of the selection criteria, enabling a fitting procedure to determine signal and background.

The photon isolation is computed in a hollow cone of $\Delta R_{\text{out}} = 0.4$. An inner cone and a η-slice were not included for tracker and ECAL isolation to avoid misidentification of converted photons. The properties of the Isolation Variables are briefly summarized in Table 4.2 of section 4.6.4 and a more detailed explanation can be found in Reference [188]. Requiring the

Table 7.4: The photon identification criteria used in the present analysis.

Variable	Loose	
	Barrel	Endcap
pixel seed	require none present	
Tracker Isolation ($\mathrm{Iso}_{\mathrm{TRK}}$)	$< 2.0\,\mathrm{GeV}/c + 0.001 \times p_{\mathrm{T}}^{\gamma}$	
ECAL Isolation ($\mathrm{Iso}_{\mathrm{ECAL}}$)	$< 4.2\,\mathrm{GeV}/c + 0.003 \times p_{\mathrm{T}}^{\gamma}$	
HCAL Isolation ($\mathrm{Iso}_{\mathrm{HCAL}}$)	$< 2.2\,\mathrm{GeV}/c + 0.001 \times p_{\mathrm{T}}^{\gamma}$	
H/E	< 0.05	
$\sigma_{i\eta i\eta}$	< 0.01	< 0.03

transverse energy in a cone around the photon to be smaller than a fixed amount of additional energy is motivated by the fact that most of the additional energy within the isolation cone results from the pile-up of collisions and the underlying event and is hence independent of the photon energy. The small amount of energy proportional to the photon energy (the so-called "proportional term", e.g. $0.001 \times p_{\mathrm{T}}^{\gamma}$ for $\mathrm{Iso}_{\mathrm{TRK}}$) allowed in the isolation cone maintains a flat selection efficiency curve for high-energy photons.

Anomalous signals in the ECAL barrel detector were removed as discussed earlier in section 4.6.5. The cleaning consists of a topological selection at both trigger and reconstruction level with a "Swiss Cross" cut. Triggers with a topological cleaning are named "Cleaned" and require the ratio of the energy of the most energetic crystal over the surrounding 3×3 crystal matrix to be smaller than 0.98. Additionally, the t_{seed} and E_2/E_9 variables, as defined in section 4.6.5 were used. We require the t_{seed} to be within $5\,\sigma$ of the collision time for seed energy $E_1 < 130$ GeV, for higher energies $t_{\mathrm{seed}} > 0$ is requested, since the time reconstruction is biased due to a non-linear response of the electronics in case of a gain switch. E_2/E_9 is required to be lower than 0.95, which is allows for a slightly stronger spike rejection [215] than the $\sigma_{i\eta i\eta}$ and $\sigma_{i\phi i\phi} > 0.001$ requirements used in [188, 208].

Figure 7.10 shows the distributions for the isolation variables used in the photon selection: for a preselected sample (left) and for the baseline selection (right). The preselected sample requires one photon with $p_{\mathrm{T}} > 100\,\mathrm{GeV}/c$ and at least two central particle flow jets with $p_{\mathrm{T}} > 50\,\mathrm{GeV}/c$ and $|\eta| < 2.5$ and are the left plots of Figure 7.10. Figure 7.10(right) shows the distributions for the γ + jet events passing the baseline selection criteria. The simulated events are categorized either by their origin (i.e. the underlying physics process), detailed in Table 7.5 or by the Monte-Carlo sample tabulated in Table 7.6. The Monte-Carlo simulation described the shape of the data curve rather well, but underpredicts the amount of data. The plots show an excess of data with respect to the simulation, which is due to the tune of the Monte-Carlo simulation. The PYTHIA Z2 Tune predicts $\sim 30\%$ more events than the D6T Tune and describes the data better [325], but the D6T Tune had to be used since no Z2 Tune for both Photons and $Z(\nu\nu)$ Monte-Carlo samples existed.

The selection of the photon is almost identical to the loose isolated photon selection of Reference [188], with the only difference that high energy photons are allowed to have a slightly higher isolation value due to the term relative to p_{T}^{γ}. To check this difference, tracker, ECAL and HCAL isolation sums are shown in Figure 7.10 after isolation. Almost no events have $\mathrm{Iso}_{\mathrm{TRK}} > 2\,\mathrm{GeV}/c$, $\mathrm{Iso}_{\mathrm{ECAL}} > 4.2\,\mathrm{GeV}$ or $\mathrm{Iso}_{\mathrm{HCAL}} > 2.2\,\mathrm{GeV}$. The deviation due to the term propor-

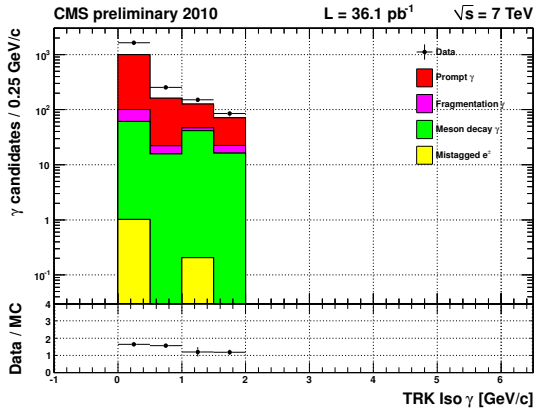

(a) Iso_{TRK} for $\gamma + 2$ jets

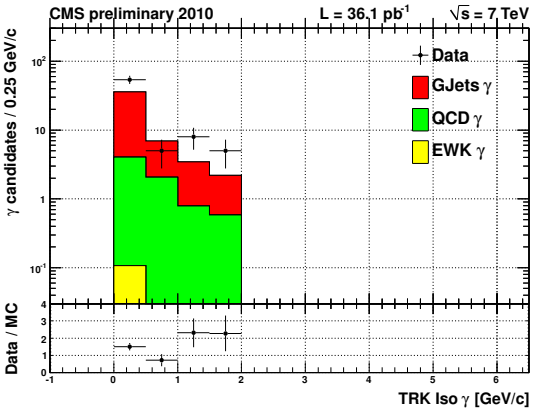

(b) Iso_{TRK} for RA2 selection

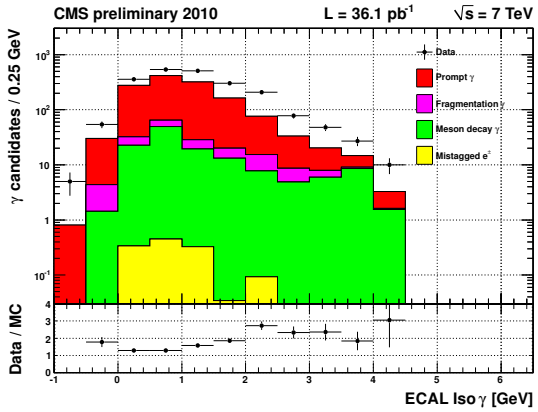

(c) Iso_{ECAL} for $\gamma + 2$ jets

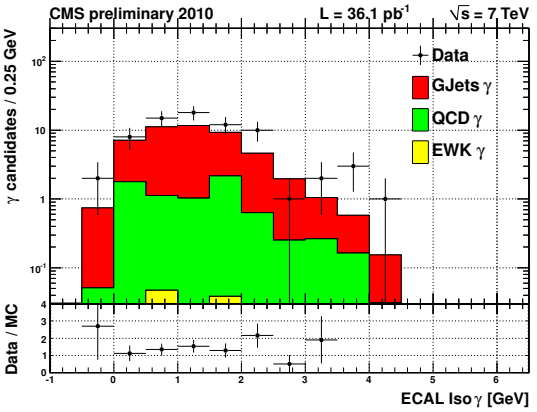

(d) Iso_{ECAL} for RA2 sel

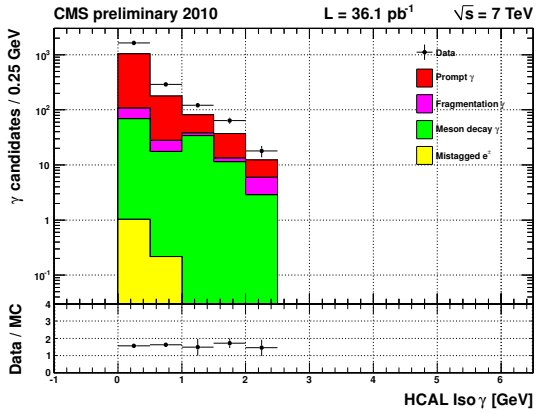

(e) Iso_{HCAL} for $\gamma + 2$ jets

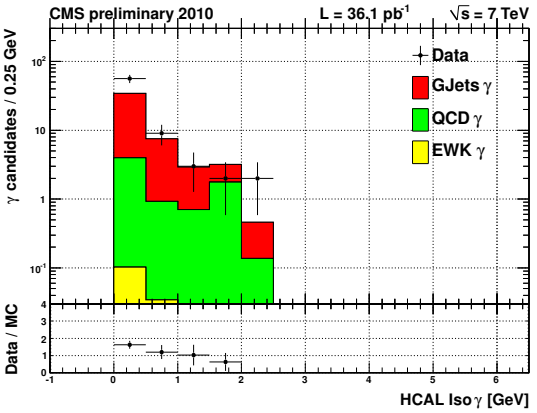

(f) Iso_{HCAL} for RA2 selection

Figure 7.10: Isolation variables for events with isolated photons passing the preselection criteria (left) and the RA2 selection criteria (right): Iso_{TRK} (a)&(b), Iso_{ECAL} (c)&(d) and Iso_{HCAL} (e)&(f). The simulated events are categorized according to the origin of the photon.

tional to the photon-p_{T} is negligible and the selection efficiency obtained in Reference [188] for the loose selection can be applied to this study.

7.4.4 Event selection results

In Table 7.5 the detailed breakdown is given for the different steps in the event selection for data and Monte-Carlo samples. Table 7.6 distinguishes different sources of photons: direct photons from the matrix element calculation, fragmentation photons produced close to or within a jet and surviving isolation, photons from high-energy meson decays in multijet events. Photons of the first two categories both originate at the vertex and are therefore named **prompt photons**, the latter emerge from the decay of neutral mesons in hadronic showers and are often refered to as **secondary photons**. A fourth category of photons is formed by electrons without a pixel seed. These are labeled as mis-tagged electrons. At generator level the distinction was made using the Particle Data Group Identification (`pdgId`):

- a **direct photon** is a reconstructed photon, matched to a generated photon with a status[3] 3 mother that is a photon (`pdgId() == 22`);
- a **fragmentation photon** is a reconstructed photon, matched to a generated photon with a status 3 mother that is a parton (`pdgId() < 25 && pdgId() != 22`);
- a **secondary photon** is a reconstructed photon, matched to a generated photon with a status 2 mother that is a meson (`pdgId() > 100`);
- a **mis-tagged electron** is a reconstructed photon, matched to a generated electron in the final state (status 1).

The matching procedure is based on a $\Delta R < 0.2$ match between a generated photon and a reconstructed photon, implemented in the PAT framework. The distinction between photons originating from the matrix element calculation on the one hand and fragmentation photons, secondary photons and mis-tagged electrons on the other hand is made because only the former are related to the production of Z bosons in a multijet environment. The latter are therefore refered to as "background" to the direct photon sample.

Table 7.5: Signal and background expected for 36.1 pb^{-1} after various steps in the selection for data and MC simulation organized by sample.

	Data	GJets	QCD	Electroweak
Boson + Jets ≥ 2:	2136±46	1166.0±7.6	190±28	2.14±0.31
Boson + Jets ≥ 3:	337±18	188.2±2.0	43.7±5.8	0.82±0.16
$H_{\text{T}} > 300$ GeV/c:	175±13	100.4±1.2	21.8±2.4	0.52±0.12
QCD Angular Cuts:	133±12	78.1±1.1	14.1±1.9	0.43±0.11
Baseline Selection:	72±8.5	40.92±0.80	7.3±1.9	0.162±0.026
High H_{T} Selection:	22±4.7	10.21±0.40	1.26±0.17	0.056±0.015
High$\not{H}_{\text{T}}$ Selection:	16±4.0	10.25±0.40	0.79±0.14	0.026±0.010

To obtain a better control over the photon selection, a looser preselection only requiring two central jets instead of three increased the photon statistics. Figure 7.11 shows the photon p_{T} and η distribution, as well as the number of jets in events with at least 2 central jets.

[3] In Pythia the status is used to determine the origin of the particle:
- The particles used inside the matrix-element generator of Pythia (only $2 \to 2$ processes) or MadGraph (up to $2 \to 5$ processes), then those particles have status 3;
- Non-stable particles (often mesons) that decay have status 2
- All stable final state particles have status 1.

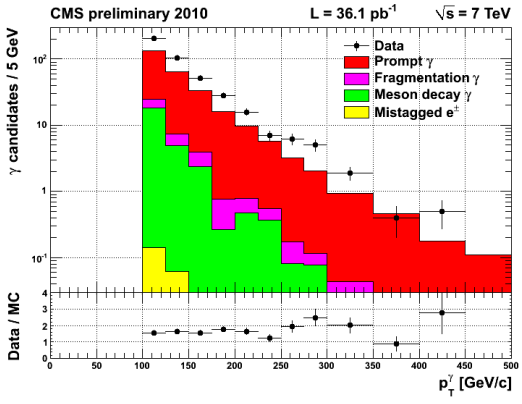

(a)

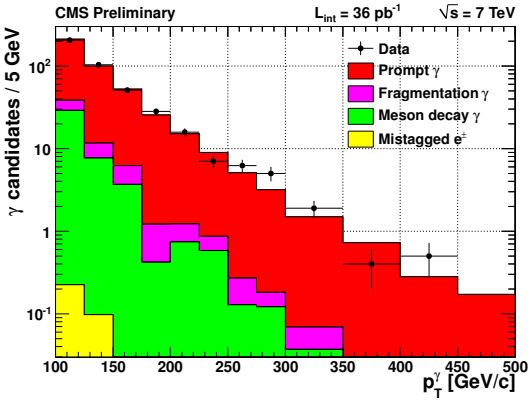

(b)

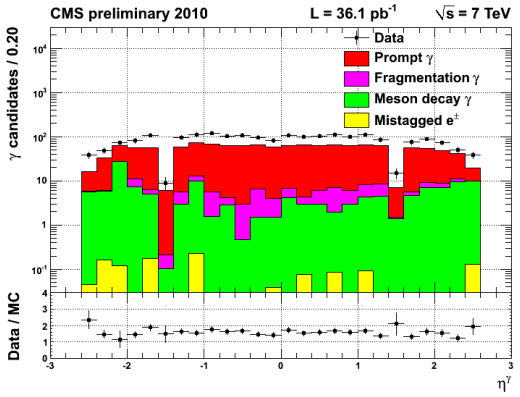

(c)

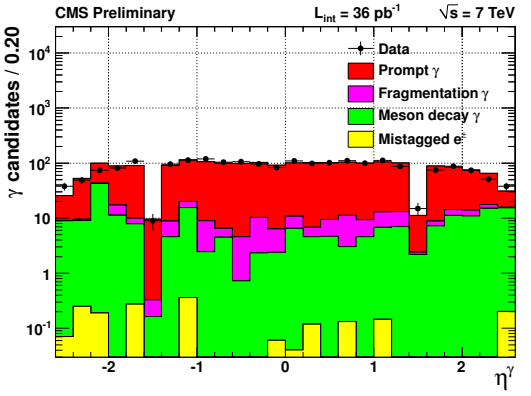

(d)

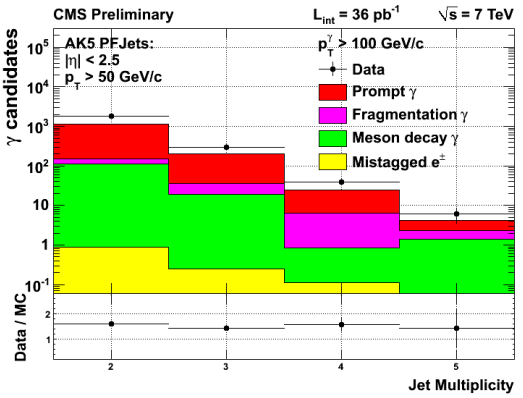

(e)

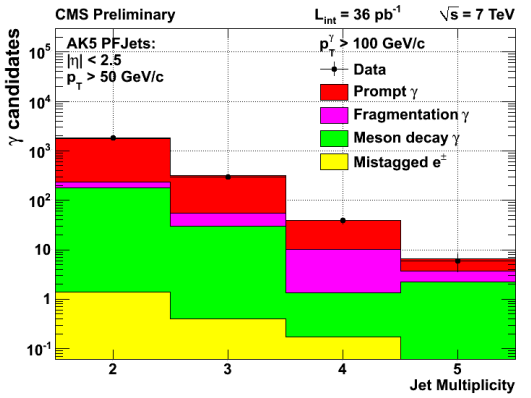

(f)

Figure 7.11: Photon p_{T} (a), η (c) and number of jets (e) distribution of events with 2 or more jets and γ with $p_{\mathrm{T}} > 100$ GeV/c. Photon and QCD are scaled by their LO cross sections as listed in Table 7.1. Figures (b), (d) and (e) show the same distributions, but with all Monte-Carlo samples scaled to the number of events observed in data.

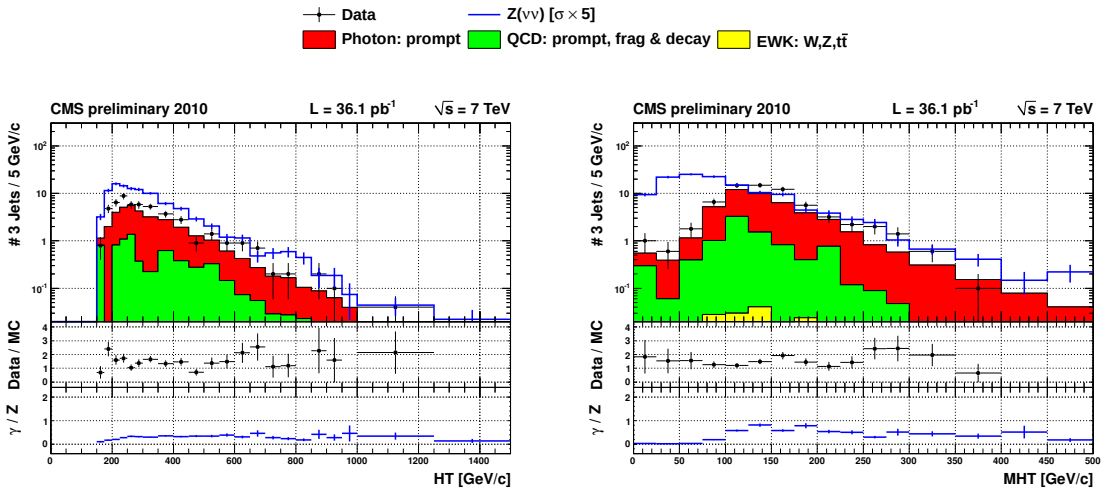

(b) H_{T} distribution for Jets ≥ 3

(c) $\not{H}_{\mathrm{T}}$ distribution for Jets ≥ 3

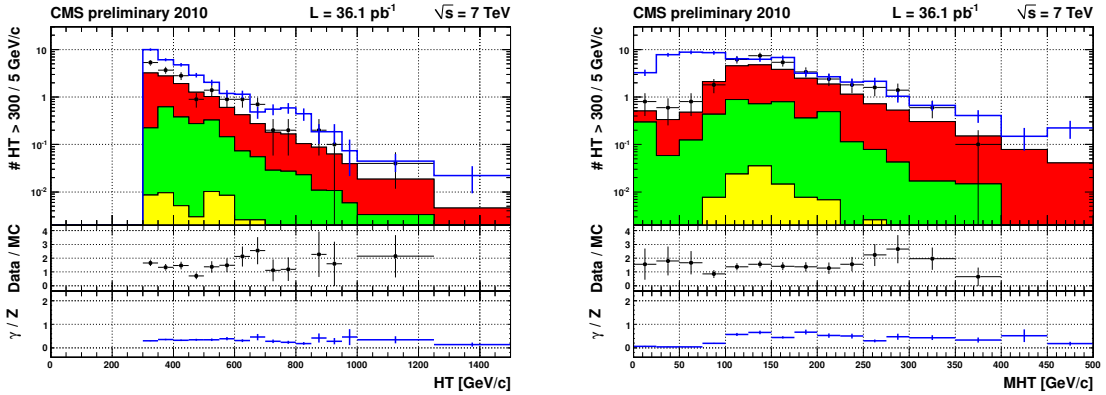

(d) H_{T} distribution for $H_{\mathrm{T}} > 300$ GeV/c

(e) $\not{H}_{\mathrm{T}}$ distribution for $H_{\mathrm{T}} > 300$ GeV/c

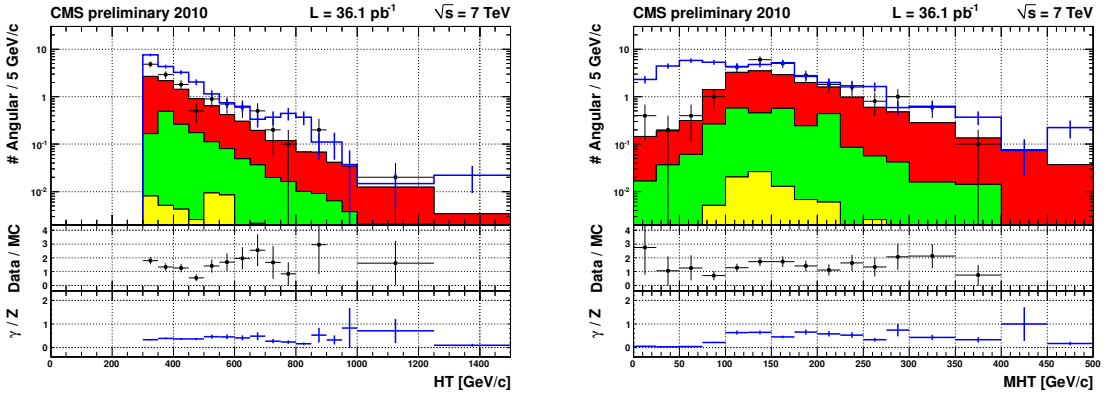

(f) H_{T} distribution after $\Delta\varphi(\not{H}_{\mathrm{T}}, J_{1,2,3})$ cuts

(g) $\not{H}_{\mathrm{T}}$ distribution after $\Delta\varphi(\not{H}_{\mathrm{T}}, J_{1,2,3})$ cuts

Figure 7.12: Consecutive plots during the baseline selection: as function of H_{T} (left) and $\not{H}_{\mathrm{T}}$ (right). The simulated (at LO) Z($\nu\bar{\nu}$) + jet distributions are shown for comparison. They are scaled to the total Z + jet cross section ($\sigma_{\mathrm{Z+jet}} = 5 \times \sigma_{\mathrm{Z}(\nu\bar{\nu})+\mathrm{jet}}$). Top: Event Selection (isolated Photon with $p_{\mathrm{T}} > 100$ GeV/c and 3 Jets). Middle: $H_{\mathrm{T}} > 300$ GeV/c. Bottom: $\Delta\varphi(\not{H}_{\mathrm{T}}, \mathrm{jet}_j)$ ($j = 1, 2, 3$).

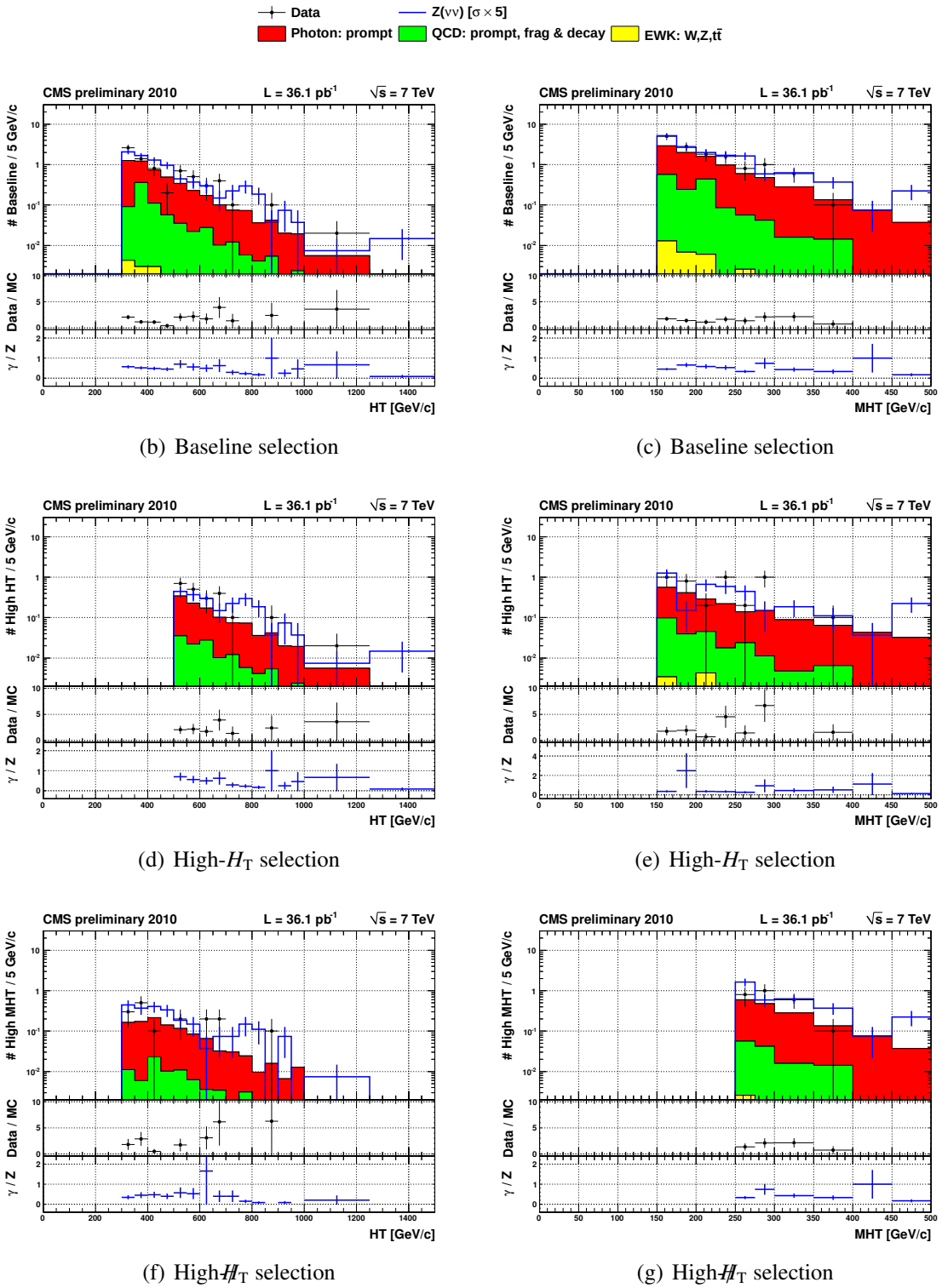

(b) Baseline selection

(c) Baseline selection

(d) High-H_T selection

(e) High-H_T selection

(f) High-$\not{H}_T$ selection

(g) High-$\not{H}_T$ selection

Figure 7.13: Baseline and search selection plots: as function of H_T (left) and $\not{H}_T$ (right). The simulated Z($\nu\bar{\nu}$) + jet distributions are shown for comparison. They scaled up the total Z + jet cross section ($\sigma_{Z+jet} = 5 \times \sigma_{Z(\nu\bar{\nu})+jet}$). Top: Baseline event selection. Middle: High-H_T Search Region. Bottom: High-$\not{H}_T$ Search Region.

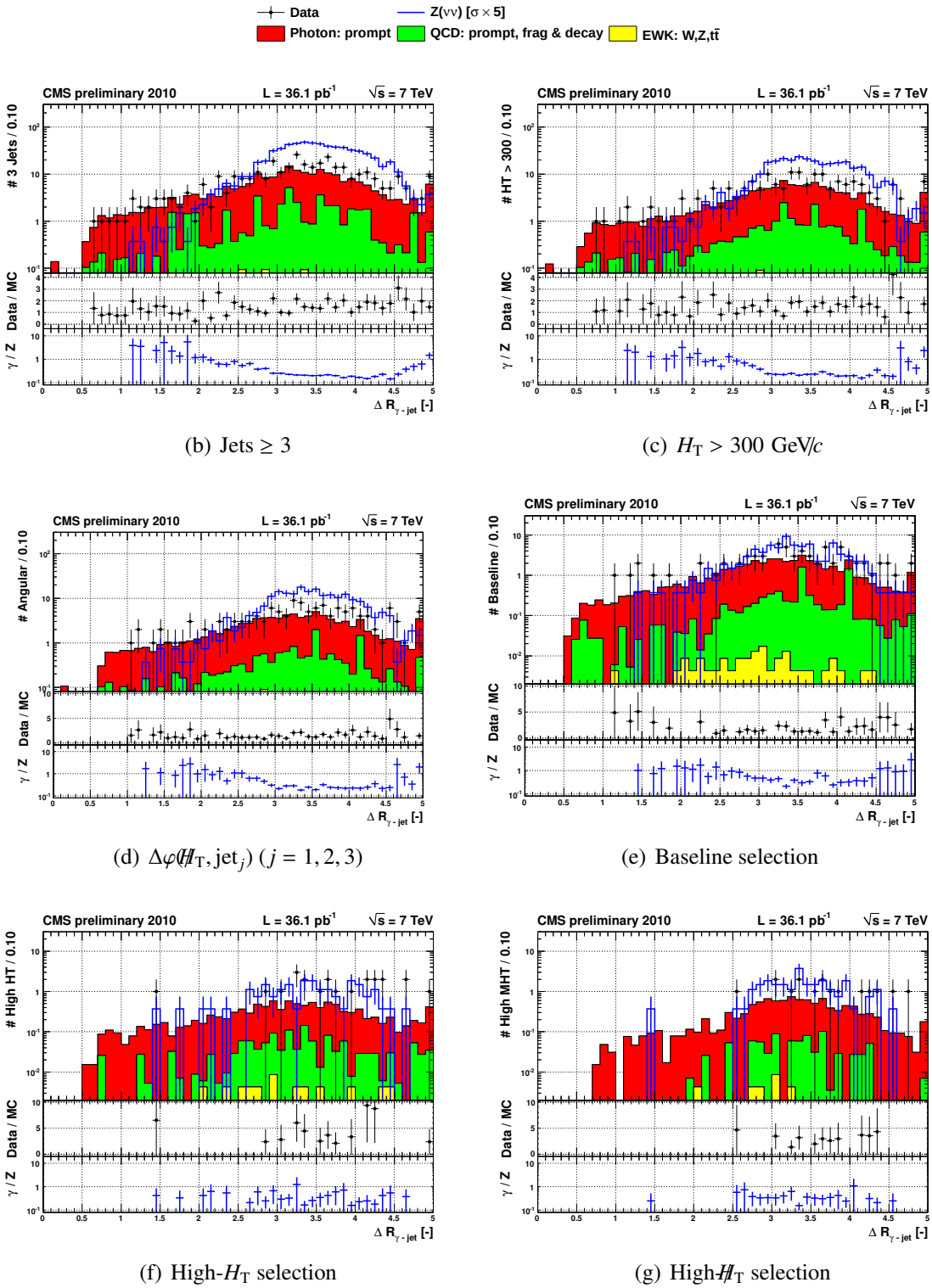

(b) Jets ≥ 3 (c) $H_{\mathrm{T}} > 300$ GeV/c

(d) $\Delta\varphi(\not{H}_{\mathrm{T}}, \mathrm{jet}_j)$ $(j = 1, 2, 3)$ (e) Baseline selection

(f) High-H_{T} selection (g) High-$\not{H}_{\mathrm{T}}$ selection

Figure 7.14: $\Delta R(\gamma, \mathrm{jet})$ plots at different stages of the event selection. The simulated $\mathrm{Z}(\nu\bar{\nu})$ + jet distributions are shown for comparison. They are scaled up to the total Z + jet cross section ($\sigma_{\mathrm{Z+jet}} = 5 \times \sigma_{\mathrm{Z}(\nu\bar{\nu})+\mathrm{jet}}$).

Table 7.6: Signal and background expected for 36.1 pb^{-1} after various steps in the selection for data and MC simulation ordered by origin.

	Data	Direct γ	Frag. γ	Sec. γ	Mistag. $e^{\pm}$
Boson + Jets $\geq$ 2:	2136±46	1166.0±7.6	57.6±6.5	134±28	1.27±0.27
Boson + Jets $\geq$ 3:	337±18	188.2±2.0	23.3±3.3	21.0±4.8	0.37±0.14
$H_{\mathrm{T}} > 300$ GeV/c:	175±13	100.4±1.2	14.71±0.60	7.5±2.3	0.24±0.12
QCD Angular Cuts:	133±12	78.1±1.1	8.94±0.47	5.5±1.9	0.19±0.11
Baseline Selection:	72±8.5	40.95±0.80	3.41±0.28	4.09±1.9	0.021±0.096
High H_{T} Selection:	22±4.7	10.22±0.40	1.00±0.14	0.318±0.085	0.0043±0.0043
High $\not{H}_{\mathrm{T}}$ Selection:	16±4.0	10.25±0.40	0.54±0.11	0.271±0.081	0.0043±0.0043

Also here, the $\sim$ 30% difference is visible. Figures 7.11(b) and 7.11(d) show the same data, but with the Monte-Carlo simulation scaled to the number of events observed in data. The relative contribution of the different background remained unchanged during this scaling. Overall a good agreement exists between the shape of the Monte-Carlo and Data distributions. The Pythia D6T tune is able to describe the kinematical observables rather good, but fails to give the correct normalization. Fortunately this is of no importance for the analysis. A slight increase of events is observed for photons with $250 < p_{\mathrm{T}}^{\gamma} < 300\,\mathrm{GeVc}$. This has been discussed extensively with experts[4] and is considered as a statistical fluctuation. Low level photon observables as timing, energy were investigated along with plots of $\Delta R(\gamma, \mathrm{MET})$ but no smoking gun could be found.

Figures 7.12 and 7.13, showing the H_{T} and $\not{H}_{\mathrm{T}}$ plots through the event selection, the baseline and the search selections, also indicate that this "excess" does not influence the observables of the analysis. Figure 7.14 shows the distance between the photon and the closest jet, $\Delta R(\gamma, \mathrm{jet})$, during the consecutive steps of the event selection. Although dominated by low statistics, this distribution has the same shape for both γ + jets and $Z(\nu\bar{\nu})$ + jets for the baseline and search selections.

7.4.5 Photon selection efficiency

Apart from knowing the amount of photons surviving the event selection, it is also very important to know the selection efficiency. How many "fake" photons are selected and how many good photons are not selected. While the former is discussed in the next section, detailing the backgrounds, the latter will briefly be discussed here. The photon selection efficiency can be factorized into two parts: the photon reconstruction efficiency, which is nearly 100% and the photon identification efficiency. Photon identification is driven to a large extent by the isolation criterion.

To estimate the photon reconstruction and identification efficiency on data, no pure sample of prompt photons can be selected at the startup of the LHC without using the isolation properties themselves. In the 36.1 pb^{-1} of recorded data, a few hundred photons produced in $Z + \gamma$ and $W + \gamma$ events were observed [336], but their p_{T} is limited by the (relatively) small mass of the massive vector bosons.

As an alternative, a data-driven method, called "tag-and-probe" is employed to measure the detection efficiency. The method measures the efficiency for an electromagnetic object to pass

[4] https://hypernews.cern.ch/HyperNews/CMS/get/egamma/934.html

the photon selection criteria. No source of pure photons was available. Instead, the decay of W and Z bosons provides a very pure source of high-p_T electrons, which have identical electromagnetic shower development in ECAL, as discussed in section 4.6. They can be distinguished from photons by the straight (high-p_T) track pointing to the electromagnetic cluster. Since electrons are much easier to identify than missing transverse energy, electron pairs from Z-boson decays were used as "photons" in the tag-and-probe method.

The **tag-and-probe** method requires a well identified electron ("tag") and allows for the investigation of all successive photon selection criteria (as tabulated in Table 7.4) on a second electromagnetic object ("probe"). The tag and probe have to match to the Z mass within a $50 < M_{ee} < 120\,\text{GeV}/c^2$ window. The probe photon has to match pixel hits consistent with a track from the interaction point to reduce the background. The efficiency is then computed as the ratio of reconstructed Z decays with a probe passing all selection criteria and all events with a reconstructed Z decay ($50 < M_{ee} < 120\,\text{GeV}/c^2$). The selection efficiency was measured in Reference [188] in $2.9\,\text{pb}^{-1}$ of data. Figure 7.15 shows the invariant mass of di-electron events within the Z-boson mass window, for probes passing all selection criterias ("passing probe") and probes failing one of the selection criteria ("failing probes"). The measurement was performed for the ECAL barrel (EB) and endcap (EE) detectors separately. The mass peak of the Z-boson is visible in both the "passing probe" as the "failing probe" histograms. This indicates that the $Z(ee)$ sample used for the study is very pure. The events failing the probe requirements are clearly $Z(ee)$ events, and no background events, where the quality of the reconstruction was not high enough to pass the selection criteria.

Table 7.7: Photon efficiency measured in $Z(ee)$ data and the Monte-Carlo simulation correction factor measured in Reference [188] and the final corrected photon efficiency.

	p_T^γ	$Z(ee)$ DATA	MC Ratio γ/e	Corrected
Barrel	$45 - \infty$	$89.04 \pm 1.83\%$	1.005 ± 0.005	$89.5 \pm 1.9\%$
Endcap	$45 - \infty$	$91.06 \pm 3.23\%$	1.013 ± 0.005	$92.2 \pm 3.3\%$

Differences in the isolation properties might occur due to Bremsstrahlung and multiple scattering in the CMS tracker. Therefore, a correction factor that accounts for the difference between electrons and photons is obtained from simulation by comparing the identification criteria in γ + jets to $Z(e^+e^-)$. Table 7.7 shows the selection efficiency measured in data with a $Z(ee)$ sample and the Monte-Carlo simulation correction factor obtained by comparing simulated photon events to simulated electron events. The measured and corrected photon efficiency for $p_T^\gamma > 45$ GeV/c photons is 89.5 ± 1.9 % in the barrel and 92.2 ± 3.3 % for the endcaps [188].

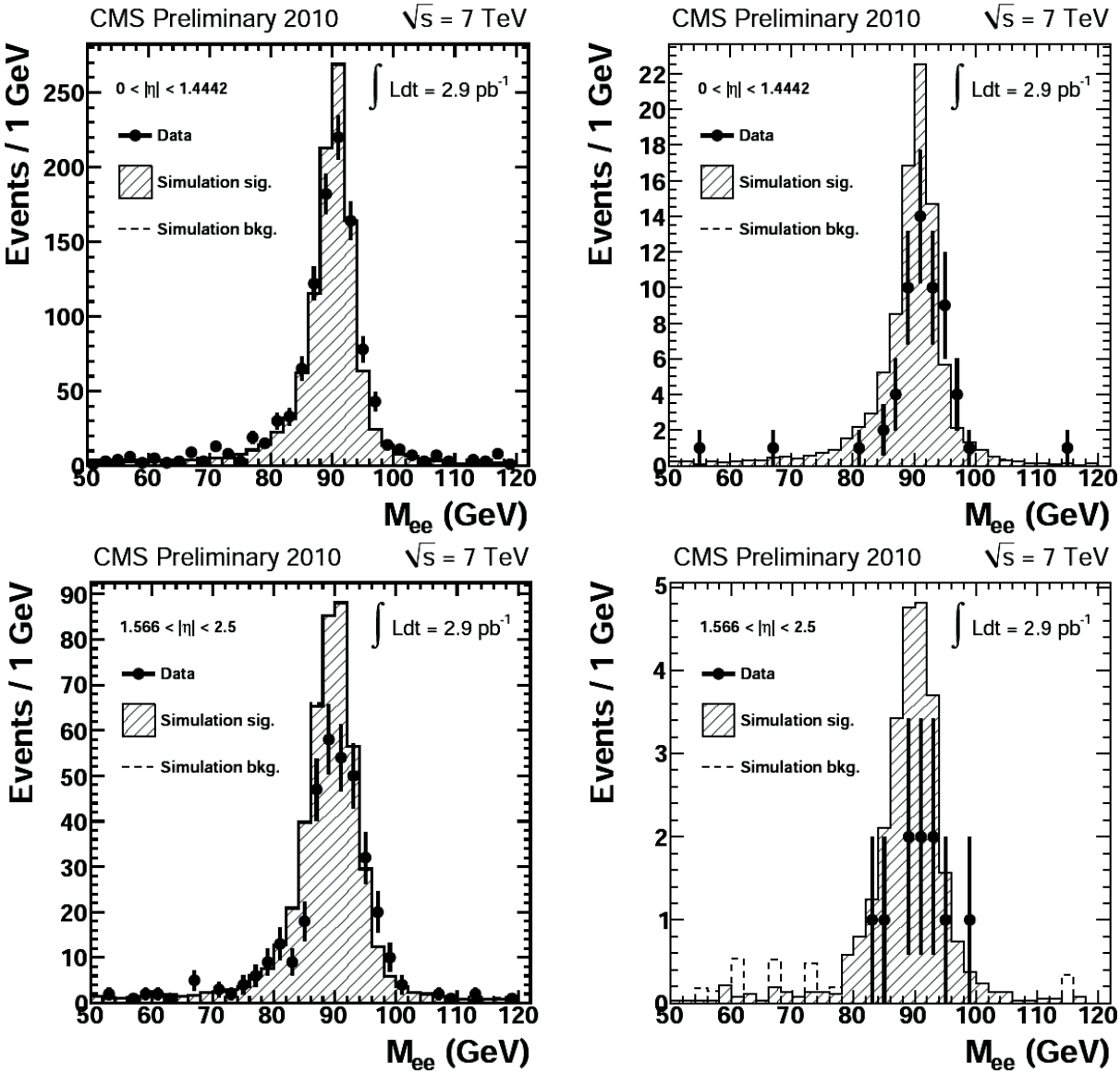

Figure 7.15: Figure from [188]. Invariant mass of the $Z(ee)$ events for passed (left) and failed (right) probe selections, for the barrel (top) and endcap (bottom) regions.

7.5 Backgrounds to the photon sample

In this analysis prompt photons are referred to as the sum of direct photons from the matrix element calculation and fragmentation photons arising during the fragmentation of partons. When making the prediction of the $Z \to \nu\bar{\nu}$ background from the γ+jet sample, only the direct photons should be taken into account, since the fragmentation photons, arising from the collinear and infrared divergence of the massless photons, do not have a counterpart in the massive Z boson production. Three different backgrounds to direct photons can be distinguished: the aforementioned fragmentation photons, photons from mesons produced in QCD jets and electrons for which no electron track is reconstructed.

7.5.1 Fragmentation photons

At lowest order in the electromagnetic and strong coupling constants $O(\alpha\alpha_s)$, the production of prompt photons proceeds via two mechanisms: "direct" (D) photon production and collinear "fragmentation" (F) of a parton into a photon. The direct production occurs either through quark-gluon Compton scattering ($qg \to \gamma q$) or quark-antiquark annihilation ($q\bar{q} \to \gamma g$), which are illustrated in Figure 7.16(a) and (b). In the fragmentation mechanism, a photon is radiated collinearly from a coloured parton from a QCD process, as shown in Figure 7.16(c) and (d).

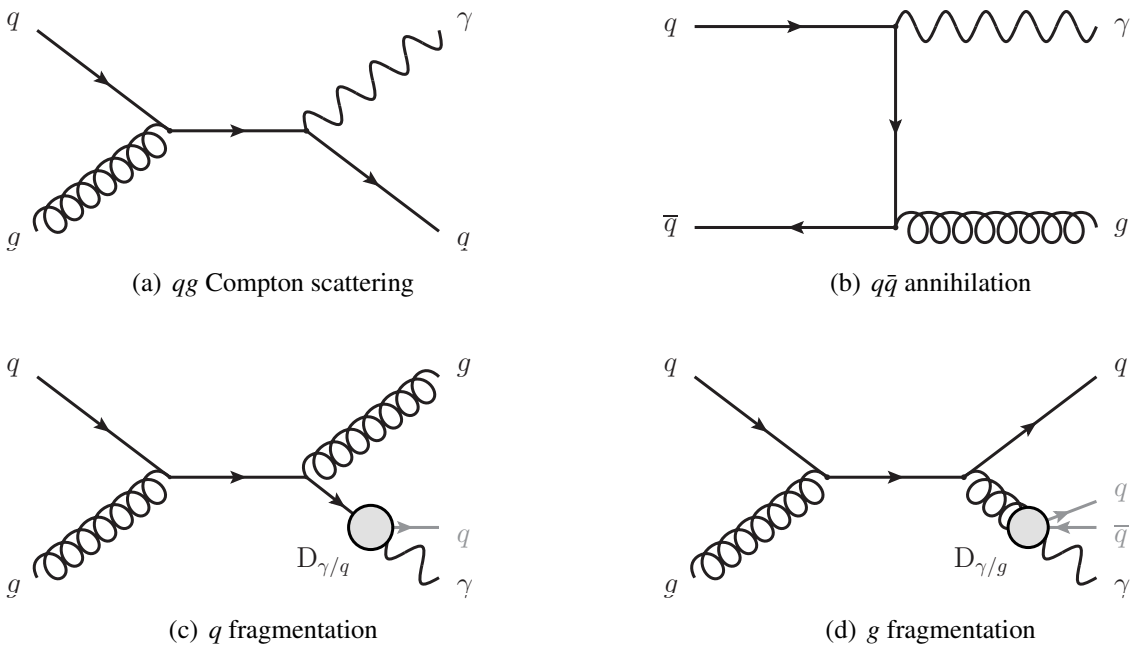

Figure 7.16: Top: Leading order processes for direct photon production: quark-gluon Compton scattering (a) (only s-channel shown) and quark-anti-quark annihilation (b). Bottom: Photon fragmentation of a quark (c) and gluon (d).

Fragmentation photons can be seen as the higher order corrections to direct photon (D) production. This fragmentation process is a non-perturbative QCD process and is calculated with fragmentation functions $D_{\gamma/k)}$ describing the probability for a parton of type k to fragment in a

photon γ. The photon production cross-section can be written as:

$$\sigma_\gamma = \sigma^{(D)}(\mu_R, \mu_F, \mu_f) + \sum_{k=q,\bar{q},g} \sigma_k^{(F)}(\mu_R, \mu_F, \mu_f) \otimes D_{\gamma/k}(\mu_F) \tag{7.6}$$

where $\sigma^{(D)}$ describes the direct photon production and $\sigma_k^{(F)}$ describes the production of a parton k in a hard collision, while the fragmentation functions $D_{\gamma/k}$ describe the probability for a parton k to fragment into a photon γ. The distinction between the direct and the fragmentation contributions is arbitrary and only the sum is physically observable. This distinction is governed by the arbitrary parameter μ_f, called the fragmentation scale. μ_R is the renormalization scale of the QCD running coupling constant α_s, while μ_F is the factorization scale used by the arbitrary splitting between the perturbative QCD (pQCD) and non-perturbative QCD calculations.

A fragmentation photon is in fact a Bremsstrahlung photon radiated collinearly of a parton during the fragmentation processes in the non-perturbative regime when hadrons are formed. Only photons and gluons can be radiated collinearly, since they are massless. This is a production mechanism for photons, not open to massive Z-bosons and it is therefore important to distinguish the fragmentation process. The relative contribution of each of the prompt photon production mechanisms is shown in Figure 7.17(a) as a function of the photon E_{T}^{γ} for $\sqrt{s} = 14\,\mathrm{TeV}$ collisions at the LHC. At a photon E_{T}^{γ} of 100 GeV, approximately 60% of the photons come from the direct (Compton and annihilation) processes, while no less than 40% is due to fragmentation processes. Applying an isolation criterion, requiring the surrounding hadronic energy to be less than 10% in a cone of $\Delta\mathrm{R} = 0.4$ around the photon, reduces the fragmentation component drastically, as can be seen in Figure 7.17(b). Thus allowing 10 GeV hadronic energy around a 100 GeV photon, only 10% of the photons are produced in fragmentation processes.

For the inclusive photon cross section measurement at CMS [208], a similar estimate of the fragmentation component was made with the JetPhox NLO matrix element event generator [338] for collisions at $\sqrt{s} = 7\,\mathrm{TeV}$. Generated photons were required to have less than 5 GeV hadronic energy in a cone of $\Delta\mathrm{R} = 0.4$. The calculations predicted a fraction of fragmentation photons of 8 % for photons with $85 < p_{\mathrm{T}}^{\gamma} < 120\,\mathrm{GeV}/c$ and 5 % for photons with $120 < p_{\mathrm{T}}^{\gamma} < 300\,\mathrm{GeV}/c$ [338]. An uncertainty on this estimation was conservatively estimated to be 20% [337].

The fragmentation contribution could also be extracted from the LO Madgraph events fed in the Pythia parton shower (ME+PS) used in the CMS simulation, tabulated in Table 7.6. In the baseline selection, the ratio direct to prompt photons is 92.3 ± 1.8 %, while in the high H_{T} search region 91.0 ± 3.7 % is obtained and in the high $\not{H}_{\mathrm{T}}$ search region the ratio is calculated as 95.1 ± 4.0 %. The uncertainties are only statistical.

In future analyses, more advanced techniques are envisaged to suppress the presence of the fragmentation photons. The so-called Frixione [331] isolation uses a smoothly growing isolation cone to regularize the collinear divergence of the photon cross section near a jet. The ongoing NLO calculations for the photon + 3 jets process are based on such an isolation [339]. To use it in the experiment, further study is required on the interplay with detector effects and to take into account the effects of discretization in a real detector.

7.5.2 Secondary photons

Neutral mesons are omnipresent in jets and decay in pairs of so called "secondary" photons. The angular separation between the photons in the laboratory frame is $\sim 1/E_{\mathrm{meson}}$, approach-

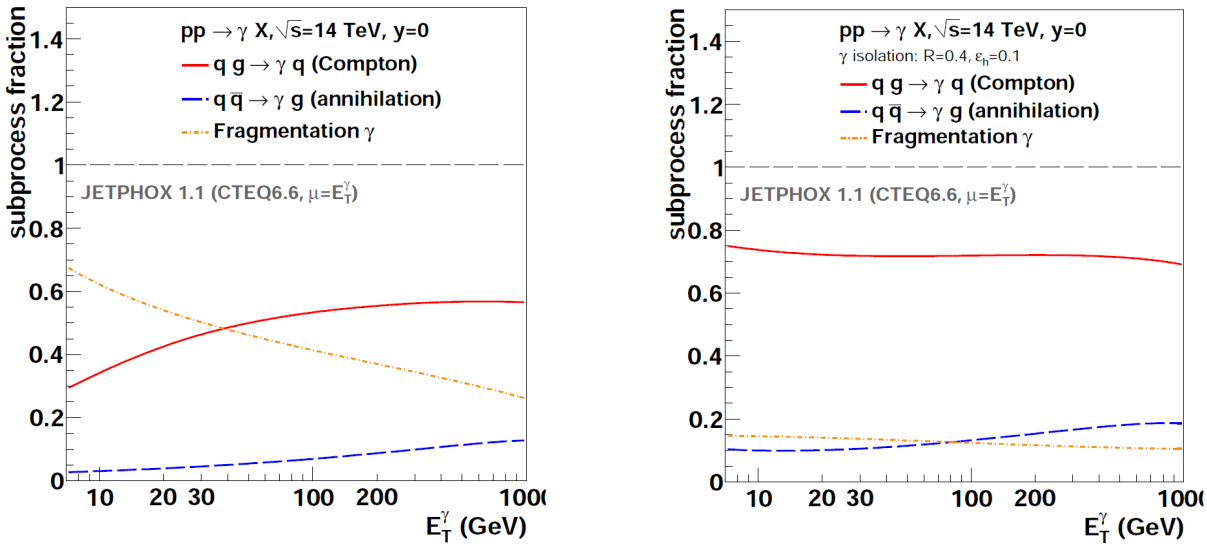

Figure 7.17: Relative contributions of the quark-gluon Compton scattering, $q\bar{q}$ annihilation and fragmentation subprocesses in NLO photon production at $\sqrt{s} = 14\,\text{TeV}$ at central rapidity $y = \eta = 0$. Left: prompt photon production without isolation constraints, right: isolated prompt photon production, requiring the hadronic energy in a cone of $\Delta R = 0.4$ to be smaller than 10% of the photon energy. The photon events are simulated with the NLO JetPhox using CTEQ6.6 pdfs, $\mu = E_T^\gamma$ and BFG-II fragmentation functions. Figure taken from Reference [337].

ing the ECAL granularity for 20 GeV/c neutral pions. Photon identification with an isolation requirement is very effective in rejecting secondary photons, since they are inside hadronic jets. The photon identification may fail when a parton fragments almost exclusively into a single neutral meson, carrying almost all energy inside a jet. Although event-by-event discrimination becomes impossible, a separation of signal and background on statistical basis is possible.

The secondary photon background was determined for the measurement of the inclusive isolated photon cross section [208] in the first $3\,\text{pb}^{-1}$ of data recorded in 2010. Reference [188] reports on two methods for measuring this secondary photon background, both using extended maximum likelihood fits. The first method fits the showershape in the η direction: $\sigma_{i\eta i\eta}$, and is documented in References [216, 340]. The second method fits the combined isolation variable, and is documented in Reference [341]. These measurements were used to determine the photon purity in the $\gamma+3$ jets sample selected for the $Z(\nu\nu)+3$ jets estimation. In the next paragraph the purity measurements are briefly discussed, more information can be found in the corresponding References [188, 208, 216, 340, 341]. The resulting photon purity measurements are tabulated and compared in Table 7.8.

For the present analysis, first the purity determined in $3\,\text{pb}^{-1}$ using the showershape (the first method) was used. Later on the purity determined by fitting the combined isolation variable (second method) was updated for the full 2010 dataset comprising $36\,\text{pb}^{-1}$, and this measurement was used for the final determination of the $Z(\nu\nu)$ + jets background. The two methods are first discussed, and compared, for the $3\,\text{pb}^{-1}$ measurement. Thereafter the purity of the photons selected by the present analysis is discussed, using the $36\,\text{pb}^{-1}$ measurement.

Photon purity measurement in 3 pb^{-1} using the showershape variable

The first photon purity measurement used a binned extended maximum likelihood fit with two components to fit to the showershape distribution in the η direction ($\sigma_{i\eta i\eta}$) in data. The signal component shape ($\mathcal{S}(\sigma_{i\eta i\eta})$) is a histogram obtained from simulated photon events and corrected for differences between data and simulation observed in an electron control sample ($Z(ee)$). The background shape ($\mathcal{B}(\sigma_{i\eta i\eta})$) was derived from data by taking the $\sigma_{i\eta i\eta}$ of a "side-band" data sample. This sideband data sample was obtained by requiring the events to pass all selection criteria, except for the track isolation. Instead the track isolation was required to be: $2 < \mathrm{Iso}_{\mathrm{TRK}} < 5\,\mathrm{GeV}/c$ in the barrel and $2 < \mathrm{Iso}_{\mathrm{TRK}} < 3\,\mathrm{GeV}/c$ in the endcap, while for the real event selection the track isolation was required to be $\mathrm{Iso}_{\mathrm{TRK}} < 2\,\mathrm{GeV}/c + 0.001 \times p_{\mathrm{T}}^{\gamma}$. Each photon E_{T} bin was then fit with a weighted sum of the signal and background component shape:

$$f(\sigma_{i\eta i\eta}) = N_{\mathcal{S}}\mathcal{S}(\sigma_{i\eta i\eta}) + N_{\mathcal{B}}\mathcal{B}(\sigma_{i\eta i\eta}), \tag{7.7}$$

where $N_{\mathcal{S}}$ and $N_{\mathcal{B}}$ are the estimated total number of signal and background events. A fit was then performed using a binned extended maximum likelihood function:

$$\mathcal{L} = \frac{e^{-(N_{\mathcal{S}}+N_{\mathcal{B}})}(N_{\mathcal{S}}+N_{\mathcal{B}})^{N}}{N!}\prod_{i=1}^{n}\left(N_{\mathcal{S}}\mathcal{S}_i + N_{\mathcal{B}}\mathcal{B}_i\right), \tag{7.8}$$

where n is the number of bins and $\mathcal{S}_i$ and $\mathcal{B}_i$ are the respective content of the i^{th} bin of the signal and background. More details are provided in References [188, 208, 216, 340]. Figure 7.18 shows the showershape $\sigma_{i\eta i\eta}$ distribution for photons measured in data with overlaid the histograms of the two-component fit of signal and background in the barrel and endcap region.

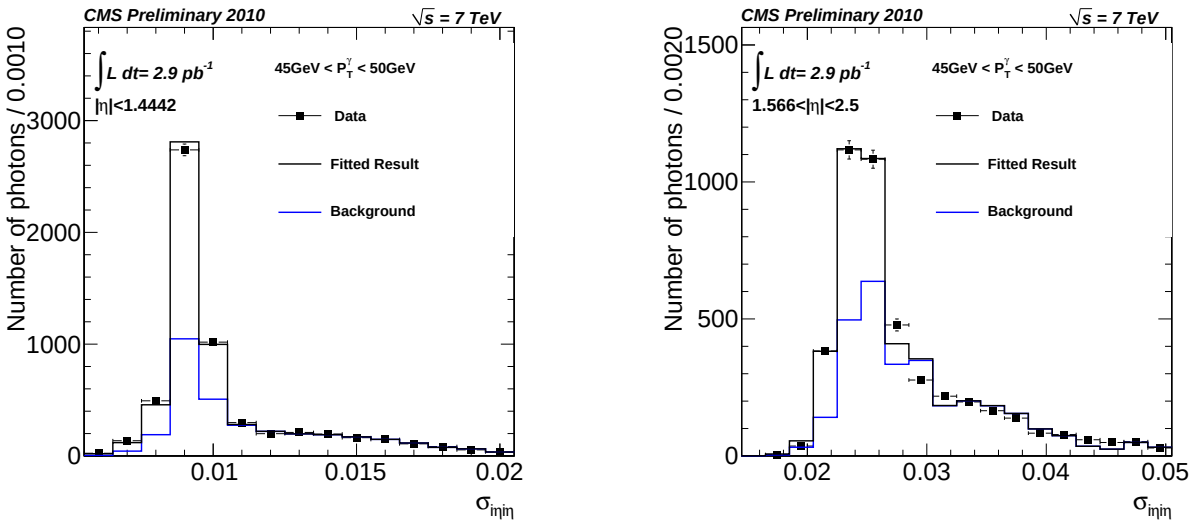

Figure 7.18: Figure taken from Reference [188]. The measured showershape $\sigma_{i\eta i\eta}$ distribution for photons with $45 < p_{\mathrm{T}}^{\gamma} < 50\,\mathrm{GeV}/c$ in the barrel (left) and endcap (right) region (datapoints with error bars). The binned extended maximum likelihood fit of both signal and background (black histogram) and the fitted background only (blue histogram) are overlaid [188].

Photon purity measurement in 3 pb^{-1} using the combined isolation variable

The photon purity was also measured using an unbinned extended maximum likelihood two-component fit to the combined isolation distribution. The combined isolation is the sum of isolation variables in the tracker and the electromagnetic and hadronic calorimeter:

$$\mathrm{Iso} = \mathrm{Iso}_{\mathrm{TRK}} + \mathrm{Iso}_{\mathrm{ECAL}} + \mathrm{Iso}_{\mathrm{HCAL}}. \tag{7.9}$$

By summing both tracker p_{T} and calorimeter energy, the energy of charged hadrons is counted twice. The signal and background component are parametrized with analytic functions, for the signal a Gauss convoluted with an exponential function:

$$\mathcal{S}(x) = \frac{1}{\sqrt{2\pi\sigma}} \exp\left[\frac{(x-\mu)^2}{2\sigma^2}\right] \exp\left[-\alpha x\right], \tag{7.10}$$

while for the background a threshold function was used:

$$\mathcal{B}(x) = [1 - p_1(x - p_0)]^{p_2} \times [1 - e^{p_3(x-p_0)}]. \tag{7.11}$$

The unbinned extended maximum likelihood function L is then defined by:

$$\mathcal{L} = \frac{e^{-(N_{\mathcal{S}}+N_{\mathcal{B}})}(N_{\mathcal{S}} + N_{\mathcal{B}})^N}{N!} \prod_{i=1}^{N} \left(N_{\mathcal{S}}\mathcal{S}(x_i) + N_{\mathcal{B}}\mathcal{B}(x_i)\right), \tag{7.12}$$

where x_i is the Iso variable computed for the i^{th} event and the product is over all events N. The exponential tail of the signal component (α) was obtained by a fit to events from a $Z(ee)$ sample, while μ and σ were floated in the maximum likelihood fit. For the background component, the parameters p_0 corresponding to the background starting point and p_3 related to the turn-on power were extracted from a fit to the simulated background component and corrected for differences between data and simulation. p_1 and p_2 were floated in the maximum likelihood fit. Figure 7.19 shows the distribution of the combined isolation for photons measured in data with the histograms of the two-component fit of signal and background in the barrel and endcap region.

Comparing the different photon purity measurements in 3 pb^{-1}

The resulting photon purity measurements are tabulated in Table 7.8. The photons in the γ+3jets selection are weighted according to the purities obtained in the methods for specific η and p_{T} bins. The columns of Table 7.8 show the photon purity for a certain η and p_{T} range and the event yields in the baseline, high-H_{T} and high-$\not{H}_{\mathrm{T}}$ selection. These event yields are then weighted according to the purity measured in either of the two methods, resulting in a global purity estimation for the entire baseline, high-H_{T} and high-$\not{H}_{\mathrm{T}}$ selection for the "combined isolation method" (upper half of the table) and the "showershape method" (lower half of the table).

At the bottom of the table, both methods are compared with each other and compared to the estimation from simulation. When comparing both methods, one observes that the "combined isolation method" predicts lower purity than the "showershape method". However, the uncertainty on both methods is of the order of 13% and the predictions agree within systematic uncertainties [188]. For the simulation purity, only statistical uncertainties are shown. As we

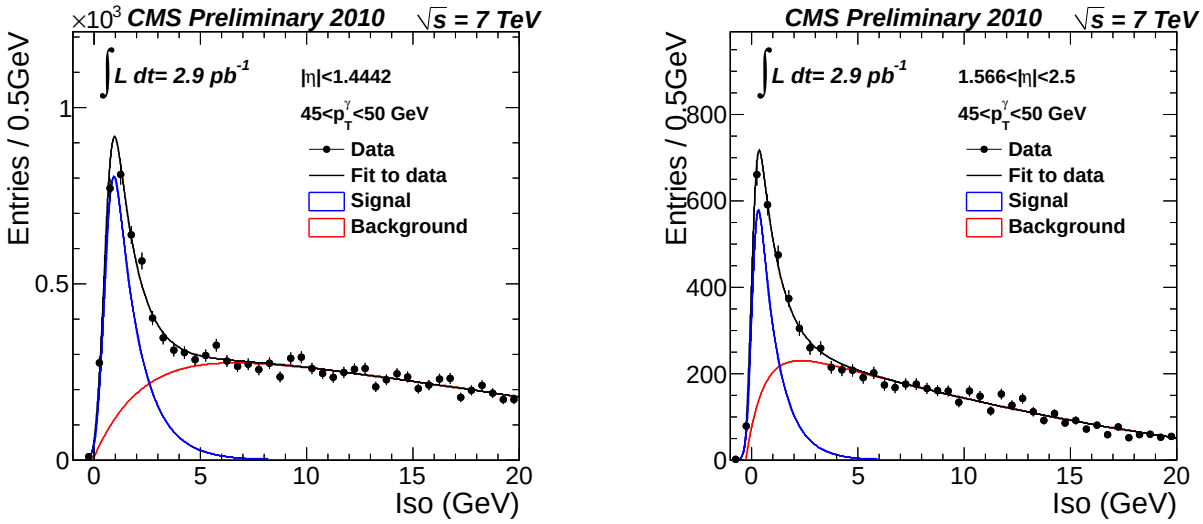

Figure 7.19: Figure taken from Reference [188]. The measured combined isolation (Iso) distribution for photons with $45 < p_{\mathrm{T}}^{\gamma} < 50\,\mathrm{GeV}/c$ in the barrel (left) and endcap (right) region (datapoints with error bars). The unbinned extended maximum likelihood fit of both signal and background (black histogram) and the fitted signal (red histogram) and background (blue histogram) are overlaid [188].

do not want to rely on simulation, the latter result is not used. The showershape method was preferred to calculate this background, since it was the central method in the photon cross section determination and has powerful background rejection, even at high p_{T}^{γ}. However, a recent update of the combined isolation method on 36.1 pb^{-1} became available [164] and allowed us to make a more precise purity estimation.

Photon purity measurement in 36 pb^{-1} using the combined isolation

Using the full 2010 pp set of certified data, the photon purity estimation with the combined isolation template method was updated for 36 pb^{-1} in Reference [164]. Figure 7.20 shows the distribution of the combined isolation for photons measured in data with the histograms of the two-component fit of signal and background for four different η regions and for $120 < p_{\mathrm{T}}^{\gamma} < 200\,\mathrm{GeV}/c$. The photon purities relevant for this analysis are tabulated in Table 7.9, along with the event yields in the baseline and two search regions. The photons are then weighted according to the purity obtained in the different p_{T}^{γ} and η bins and the purity for the different selection regions was obtained. The use of the full 2010 dataset reduced the systematic uncertainty on the photon purity measurement from about 13% in 3 pb^{-1} to 10% in 36 pb^{-1}. The purity was also estimated from Monte-Carlo simulation (Table 7.6), resulting in a purity of 91.6 ± 0.9 % for the baseline selection, 97.2 ± 2.9 % for the high H_{T} selection and 97.5 ± 3.7 % for the high $\not{H}_{\mathrm{T}}$ selection (only statistical uncertainties).

Although the photon selection was performed requiring the combined isolation to be smaller than 5 GeV, this method was used in Reference [188] to state the purity of the loose photon selection. Also, when comparing the purity obtained in 3 pb^{-1} and 36 pb^{-1} in Table 7.10, one sees that these results are not only in agreement within uncertainties, but also that the central value of the purity obtained with combined isolation method on 36 pb^{-1} of data is close to

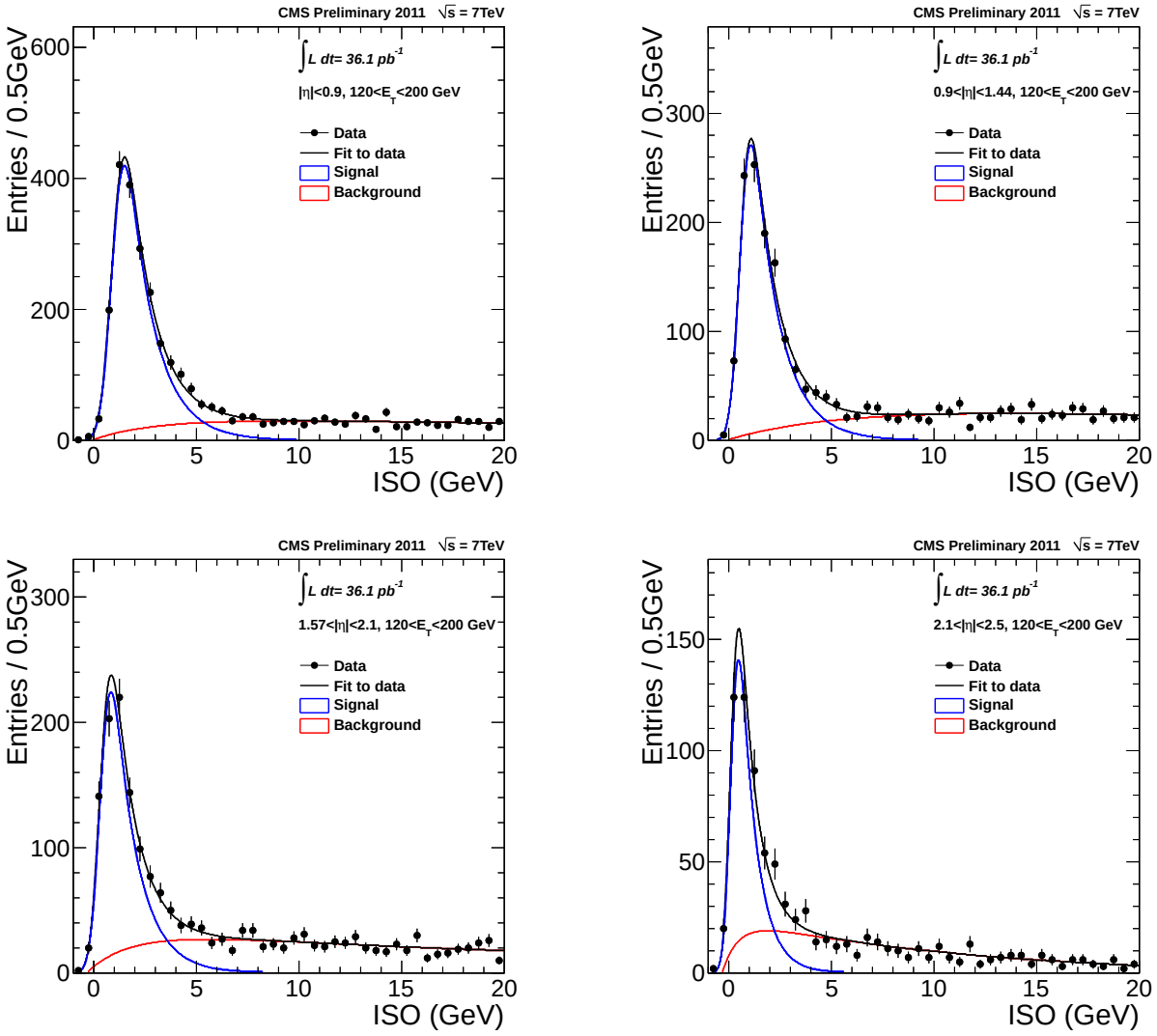

Figure 7.20: Figure taken from Reference [342]. The measured combined isolation (Iso) distribution for photons with $120 < p_{\mathrm{T}}^{\gamma} < 200\,\mathrm{GeV}/c$ in two barrel regions ($|\eta| < 0.9$ top left and $0.9 < |\eta| < 1.44$ top right) and two endcap regions ($1.57 < |\eta| < 2.1$ bottom left right and $2.1 < |\eta| < 2.5$ bottom right) regions (datapoints with error bars). The unbinned extended maximum likelihood fit of both signal and background (black histogram) and the fitted signal (red histogram) and background (blue histogram) are overlaid [164].

Table 7.8: Photon purity for the baseline, high H_T and high $\not{H}_T$ search regions determined with the photon purity measured with the Showershape resp. Isolation template in Ref. [188] and compared to Monte-Carlo. The event yield in this analysis is obtained in $(0 < |\eta| < 1.379) \cup (1.579 < |\eta| < 2.5)$, while the photon purity in Ref. [188] is obtained in $(0 < |\eta| < 1.442) \cup (1.566 < |\eta| < 2.5)$. For photons with $300 < p_T^\gamma < 450$ GeV/c, the purity of the $120 < p_T^\gamma < 300$ GeV/c bin was used.

p_T^γ [GeV/c]	Purity ±(stat)±(syst)	Baseline Yield [-]	High-H_T Yield [-]	High-$\not{H}_T$ Yield [-]
Shower Shape:				
$[0 < \|\eta\| < 1.4442]$				
$85 < p_T^\gamma < 120$	79.2 ± 2.6 ± 6.3	1	0	0
$120 < p_T^\gamma < 300$	95.2 ± 2.6 ± 7.7	47	13	9
$300 < p_T^\gamma < 450$	-	3	2	3
$[1.566 < \|\eta\| < 2.5]$				
$85 < p_T^\gamma < 120$	77.9 ± 6.6 ± 13.5	1	0	0
$120 < p_T^\gamma < 300$	96.5 ± 12.1 ± 16.7	18	6	2
$300 < p_T^\gamma < 450$	-	2	1	2
Total Yield [-]		72	22	16
Total Purity [%]		95.10 ± 12.04	95.61 ± 12.52	95.53 ± 11.58
Combined Isolation:				
$[0 < \|\eta\| < 1.4442]$				
$85 < p_T^\gamma < 120$	81.0 ± 4.6 ± 7.0	1	0	0
$120 < p_T^\gamma < 300$	90.2 ± 8.4 ± 8.7	47	13	9
$300 < p_T^\gamma < 450$	-	3	2	3
$[1.566 < \|\eta\| < 2.5]$				
$85 < p_T^\gamma < 120$	61.4 ± 5.4 ± 10.8	1	0	0
$120 < p_T^\gamma < 300$	69.3 ± 10.8 ± 10.3	18	6	2
$300 < p_T^\gamma < 450$	-	2	1	2
Total Yield [-]		72	22	16
Total Purity [%]		83.87 ± 12.83	83.55 ± 12.99	84.98 ± 12.80
Overview:		Purity [%]	Purity [%]	Purity [%]
Shower Shape:		95.10 ± 12.04	95.61 ± 12.52	95.53 ± 11.58
Combined Iso:		83.87 ± 12.83	83.55 ± 12.99	84.98 ± 12.80
MC Simulation:		91.6 ± 0.9	97.2 ± 2.9	97.5 ± 3.7

the central value of the purity obtained with the showershape method in $3\,\text{pb}^{-1}$. This gives us confidence that the purity measured with the combined isolation method on $36\,\text{pb}^{-1}$ can be used for this analysis. Possible residual differences are accounted for in the approximately 10% systematic uncertainty on the photon purity measurement.

When selecting photons using the combined isolation selection Iso < 5 GeV instead of discrim-

inating against each of the individual isolation sums as stated in Table 7.4.5, a slighthly higher event yield was obtained in the baseline and two search selections.

Table 7.9: Photon purity for the baseline, high H_{T} and high $\not{H}_{\mathrm{T}}$ search regions determined with the photon purity measured with the Isolation template in Reference [164]. The event yield in this analysis is obtained in $(0 < |\eta| < 1.379) \cup (1.579 < |\eta| < 2.5)$, while the photon purity in Reference [188] is obtained in $(0 < |\eta| < 1.442) \cup (1.566 < |\eta| < 2.5)$. For photons with $300 < p_T^{\gamma} < 450$ GeV/c, the purity of the $200 < p_T^{\gamma} < 300$ GeV/c bin was used.

p_{T}^{γ} [GeV/c]	Purity ±(stat)±(syst)	Baseline Yield [-]	High-H_{T} Yield [-]	High-$\not{H}_{\mathrm{T}}$ Yield [-]
Combined Isolation:				
$[0 < \|\eta\| < 0.9]$				
$100 < p_T^{\gamma} < 120$	91 ± 2 ± 6.4	0	0	0
$120 < p_T^{\gamma} < 200$	94 ± 2 ± 7.4	25	6	1
$200 < p_T^{\gamma} < 300$	97 ± 7 ± 7.7	12	4	8
$300 < p_T^{\gamma} < 450$	-	2	1	2
$[0.9 < \|\eta\| < 1.4442]$				
$100 < p_T^{\gamma} < 120$	88 ± 3 ± 6.2	1	0	0
$120 < p_T^{\gamma} < 200$	92 ± 3 ± 7.4	7	1	0
$200 < p_T^{\gamma} < 300$	92 ± 9 ± 7.4	3	2	0
$300 < p_T^{\gamma} < 450$	-	1	1	1
$[1.566 < \|\eta\| < 2.1]$				
$100 < p_T^{\gamma} < 120$	84 ± 3 ± 8.3	1	0	0
$120 < p_T^{\gamma} < 200$	75 ± 5 ± 7.9	13	4	0
$200 < p_T^{\gamma} < 300$	85 ± 13 ± 8.4	2	0	1
$300 < p_T^{\gamma} < 450$	-	1	1	1
$[2.1 < \|\eta\| < 2.5]$				
$100 < p_T^{\gamma} < 120$	69 ± 3 ± 7.0	0	0	0
$120 < p_T^{\gamma} < 200$	70 ± 4 ± 7.2	1	0	0
$200 < p_T^{\gamma} < 300$	80 ± 18 ± 8.8	2	2	1
$300 < p_T^{\gamma} < 450$	-	1	0	1
Total Yield [-]		72	22	16
Total Purity [%]		94.38 ± 8.81	90.32 ± 8.88	96.50 ± 10.44

Table 7.10: Comparison for the photon purity obtained with the showershape and combined isolation methods in 3 pb^{-1} and the combined isolation method in 36 pb^{-1} of data for the baseline and two search selections.

Purity [%]:	L_{int} [pb^{-1}]	Baseline	High-H_{T}	High-$\not{H}_{\mathrm{T}}$
Shower Shape:	3 pb^{-1}	95.10 ± 12.04	95.61 ± 12.52	95.53 ± 11.58
Combined Iso:	3 pb^{-1}	83.87 ± 12.83	83.55 ± 12.99	84.98 ± 12.80
Combined Iso:	36 pb^{-1}	94.38 ± 8.81	90.32 ± 8.88	96.50 ± 10.44

7.5.3 Electrons faking photons

At high p_T, the ECAL supercluster of an electron is indistinguishable from the photon ECAL supercluster. When track reconstruction fails, or there is an early occurrence of hard Bremsstrahlung (for instance in the first pixel layer), isolated electrons such as those from decays of primary W or Z bosons have a small probability to be misidentified as photons.

The contribution of electrons reconstructed as photons is estimated using a tag-and-probe technique as described in Reference [343] and the actual measurement was performed in Reference [213]. The probability to mistag an electron is $0.62 \pm 0.06(\text{stat}) \pm 0.65(\text{syst})$ % in the barrel and $1.13 \pm 0.13(\text{stat}) \pm 1.08(\text{syst})$ % in both endcaps [213]. The contribution of this background is negligible, first because the small mistag probability, secondly because the isolated photon rate is much higher than the isolated electron rate (which comes primarily from W and Z bosons). In the Monte-Carlo (Table 7.6) just one event survived in the photon + 2 jets sample and none survived the 3 jets requirement.

7.6 Phenomenological photon to Z correspondence

As stated earlier, the initial aim of the analysis was to estimate $Z(\nu\nu)$ + jets events in the search regions by γ + jets events, using a conversion factor obtained from theory. Next-to-leading order calculations are available for W- and Z-bosons, produced in association with up to four jets, but no next-to-leading order calculations were avaliable for associated production of photons and jets. Therefore, we opted to use the MadGraph Monte-Carlo simulated samples calculated at leading order and their corresponding leading order cross sections, both listed in Table 7.1 to obtain the phenomenological correction factor translating γ + jets event yields into $Z(\nu\nu)$ + jets. The BlackHat collaboration compared the ratio of Z + 2 jets to γ + 2 jets at next-to-leading order (NLO), leading order (LO) and leading order plus parton shower (LO+PS), which is the configuration used by experimental physicists at CMS [335]. This study was performed to estimate the scale uncertainty, i.e. the systematic uncertainty related to the fact that a leading-order comparison was used, while data is only described reasonably well at next-to-leading order. This is discussed further on in section 7.7, where the systematic uncertainties are presented.

The events containing photons were simulated in three H_T bins: 40-100, 100-200 and 200-∞ GeV/c, while for the sample for $Z(\nu\nu)$ was inclusive (0-∞ GeV/c). This generator-H_T is defined as the scalar sum of transverse momentum of all outgoing partons (including photons and neutrinos). Therefore the first two H_T bins of the photon sample were not useful for the final selection, since requiring a 100 GeV/c photon and three 50 GeV/c jets sums already up to H_T = 250 GeV/c. The third photon sample with H_T starting at 200 GeV/c contains events passing the modified baseline selection and has an integrated luminosity of 2 355 pb^{-1}, which is more than 50 times higher than the amount of analyzed data (36.1 pb^{-1}). When comparing data to simulation in less populated corners of phase space, containing only a few data events, it is useful to have a simulated sample with high statistics, as a large amount of events reduces the statistical uncertainty on the simulated sample. The high integrated luminosity of the photon sample is also useful in obtaining a Z/γ correction factor with small statistical uncertainty. Unfortunately, the integrated luminosity of the simulated $Z(\nu\nu)$ sample was only 376 pb^{-1}, roughly six times less than the high-H_T photon sample. Furthermore, this $Z(\nu\nu)$ sample is inclusive with only a small amount of events with $H_T > 200$ GeV/c. This constrains the possibilities to study

the correction factor in detail for the search selections.

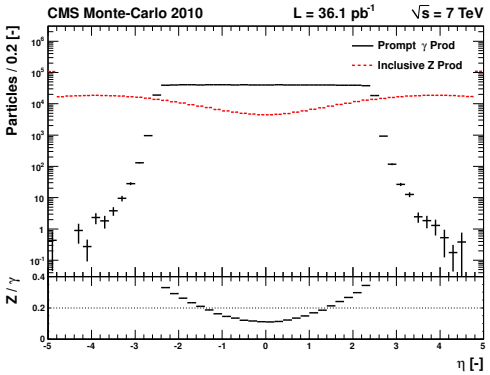

(a) ≥ 0 Jets, no p_{T} cut

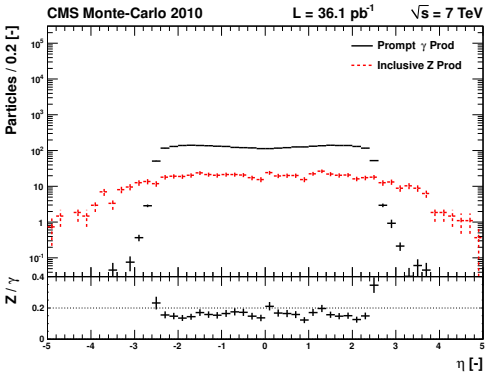

(b) ≥ 3 Jets, no p_{T} cut

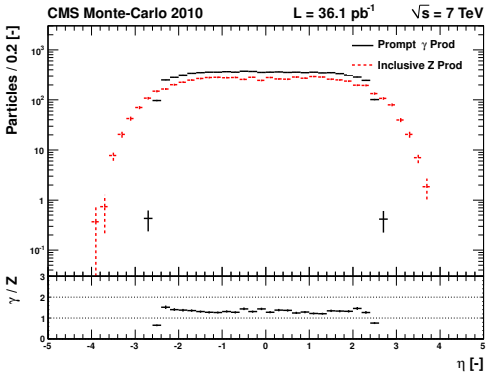

(c) ≥ 0 Jets, $p_{\mathrm{T}} > 100$ GeV/c

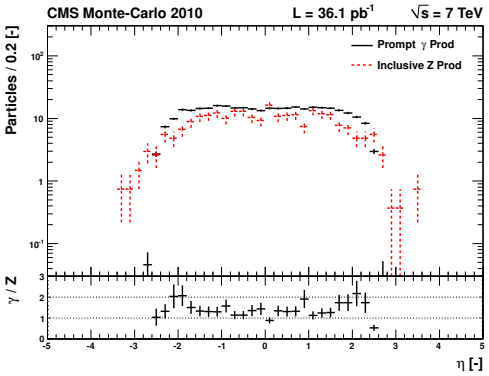

(d) ≥ 3 Jets, $p_{\mathrm{T}} > 100$ GeV/c

Figure 7.21: Generator level pseudorapidity distribution of Z and γ for all events (a), all events with 3 jets (b), all events with boson $p_{\mathrm{T}} > 100$ GeV/c (c) and all events with 3 jets and boson $p_{\mathrm{T}} > 100$ GeV/c (d). Only statistical errors are shown.

The photon and Z simulated samples were first studied at generator level, i.e. the anti-k_t jet algorithm was run on the final state particles, omitting the neutrinos of the Z-decay. Final state particles were obtained by running Pythia's parton shower simulation on the final state partons from the MadGraph matrix element calculation. Therefore the underlying event is taken into account. The η spectrum of γ + jets and Z + jets is shown in Figure 7.21. Figure 7.21(a) shows the inclusive (no jet requirements) spectrum of both samples, where clearly different distributions can be seen. While the photon events are rather flat in $-2.4 < \eta < 2.4$, the Z-boson events tends to be produced more at higher rapidities, $\eta > 3$. The "inclusive" Z production was obtained by dividing $\mathrm{Z} \to \nu\bar{\nu}$ by the branching ratio: $BR = (20.00 \pm 0.06) \times 10^{-2}$ [5], for both samples the LO cross sections were used. The simulated events are scaled to the amount of good data collected with CMS ($36.1\,\mathrm{pb}^{-1}$). The photon sample is only simulated with photons in $-2.5 < \eta < 2.5$, since the track information (necessary to distinguish photons from electrons) is only available up to $\eta = 2.5$. Therefore photons and Z-bosons cannot be compared to each other outside the $|\eta| < 2.5$ window. Requesting the boson to have $p_{\mathrm{T}} > 100$ GeV/c improves the agreement in η, as shown in Figure 7.21(c). Although no explicit p_{T} cut is applied to the Z boson, the requirement is hidden in the $\not{H}_{\mathrm{T}} > 150$ GeV/c cut, as shown in Figure 7.9. Requiring three high-p_{T} central jets ($p_{\mathrm{T}}^{\mathrm{gen}} > 50\,\mathrm{GeV}/c$ and $|\eta| < 2.5$) as in Figure 7.21(b), or requiring the γ

and Z boson to have a $p_T > 100$ GeV/c as in Figure 7.21(c) flattens both bosons' η spectrum and results in more centrally produced bosons. Requiring both criteria as in Figure 7.21(d) clearly highlights the limiting statistics of the $Z(\nu\nu)$ sample. Figure 7.21 shows that requesting the boson to have a p_T of at least 100 GeV/c or requesting additional jets results in events that have similar characteristics in η.

The generator level p_T correspondence between γ and Z events for events with boson $p_T >$ 100 GeV/c is shown in Figure 7.22. Figure 7.22(a) shows the p_T distribution of the inclusive sample, while Figures 7.22(b), 7.22(c) and 7.22(d) show the p_T spectrum for requiring additionaly 1, 2 and 3 central jets. Requiring the boson $p_T > 100$ GeV/c (see Figure 7.21(c)) reduces most of the high-η Z + jets events. The Z boson was not required to be produced in $|\eta| < 2.5$, since we wanted to estimate all $Z(\nu\nu)$ events, including all events outside the photon acceptance.

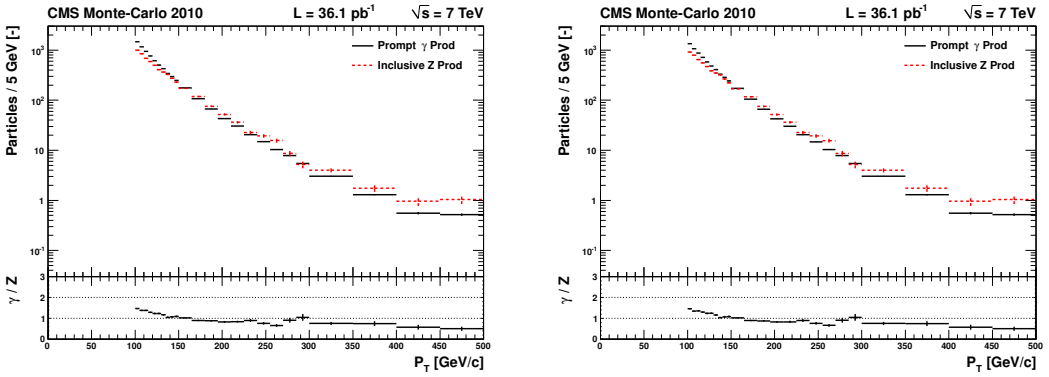

(a) ≥ 0 Jets (b) ≥ 1 Jets

(c) ≥ 2 Jets (d) ≥ 3 Jets

Figure 7.22: Generator level transverse Momentum distribution of Z and γ for events with $\geq 0-3$ jets and with boson $p_T > 100$ GeV/c (a) - (d). Only statistical errors are shown, the last bin contains the overflow.

At 100 GeV/c the photon yield is higher than the Z-boson yield and it decreases steeper than the Z-boson rate, becoming equal around 150 GeV/c. At around 300 GeV/c the Z-boson yield takes over and is higher than the photon rate. While the photon excess below 150 GeV/c is due to the mass difference between the Z-boson and the photon, the difference at high energy is because of different electromagnetic couplings. For the high-p_T region a constant conversion factor between γ + jets and Z + jets can be determined starting at $p_T > 300$ GeV/c. But also in the "intermediate p_T" region a conversion factor can be established, which is slightly higher.

Since the statistics used in this search is limited (both in data and simulation), we opted for a single conversion factor, averaged over all events in the baseline and the two search selections. This is justified since the analysis consists of a single cut and count method and does not predict the shape of the $Z(\nu\nu)$ + jets background.

The correction factor for the different cuts in the analysis is shown for Monte-Carlo simulation at generator level in Table 7.11 and after detector simulation and reconstruction in Table 7.12. No isolation at generator level was applied leading to the higher photon yield in the generated Monte-Carlo with respect to the reconstructed Monte-Carlo. The correction factor obtained from reconstructed Monte-Carlo simulation will be used in this analysis. In both Table 7.11 and 7.12 photons with $p_{\mathrm{T}}^{\gamma} > 100$ GeV/c are compared to Z bosons with $p_{\mathrm{T}} > 100$ GeV/c, since before the baseline selection the comparison between γ with p_{T} cut and Z events with arbitrary p_{T} would not make sense. For the actual background estimation we also want to predict the very small amount of $Z(\nu\nu)$ + jets with $p_{\mathrm{T}} < 100$ GeV/c, so the p_{T} requirement on the Z boson was removed for the baseline, high H_{T} and high$\not{H}_{\mathrm{T}}$ selections, while the $p_{\mathrm{T}}^{\gamma} > 100$ GeV/c requirement was maintained.

Table 7.11: γ to Z scaling factor in events with boson $p_{\mathrm{T}} > 100$ GeV/c for 36.1 pb^{-1} at generator level. The bottom three lines show the scaling factors if no p_{T} cut was applied to the Z boson. Only statistical uncertainties are shown.

Cut Flow	$Z \to \nu\bar{\nu}$	γ	$Z \to \nu\bar{\nu}/\gamma$	Z/γ
All Events:	158850±107	973609±802	0.16316±0.00017	0.81578±0.00087
Boson $p_{\mathrm{T}} > 100$ GeV/c:	1345.5±9.9	8095±29	0.1662±0.0014	0.8310±0.0068
Boson + Jets ≥ 1:	1283.0±9.6	7644±28	0.1678±0.0014	0.8392±0.0070
Boson + Jets ≥ 2:	260.3±4.3	1795.1±9.2	0.1450±0.0025	0.725±0.013
Boson + Jets ≥ 3:	49.3±1.9	322.4±2.5	0.1528±0.0060	0.764±0.030
$H_{\mathrm{T}} > 300$ GeV/c:	30.3±1.5	184.3±1.7	0.1644±0.0082	0.822±0.041
Angular Cuts:	23.0±1.3	120.5±1.3	0.190±0.011	0.953±0.055
Baseline Selection:	14.2±1.0	59.06±0.94	0.240±0.018	1.202±0.088
High H_{T} Selection:	3.91±0.53	15.36±0.48	0.255±0.036	1.27±0.18
High$\not{H}_{\mathrm{T}}$ Selection	4.85±0.59	13.97±0.46	0.348±0.044	1.74±0.22
No p_{T} cut on Z boson:				
Baseline Selection:	14.2±1.0	59.06±0.94	0.240±0.018	1.20±0.09
High H_{T} Selection:	3.91±0.53	15.36±0.48	0.254±0.035	1.27±0.18
High$\not{H}_{\mathrm{T}}$ Selection:	4.85±0.59	13.97±0.46	0.348±0.044	1.74±0.22

7.7 Systematic uncertainties

The total systematic uncertainty on the estimated $Z(\nu\bar{\nu})$ + jet process includes contributions from the photon purity (fragmentation and secondary photons), the photon mistag rate, the Z/γ-correction factor and the γ selection efficiency. The largest contributions are the theoretical uncertainty on the Z/γ-correction factor (7 – 10%) and the photon purity (9 – 10%). The total systematic uncertainty is estimated as 14 % in the baseline selection, 17% in the high H_{T} and 18 % in the high$\not{H}_{\mathrm{T}}$ search region.

Table 7.12: γ to Z scaling factors in events with boson $p_T > 100$ GeV/c for 36.1 pb^{-1} after detector simulation and reconstruction. The bottom three lines show scaling factors if no p_T cut was applied to the Z boson. Only statistical uncertainties are shown.

Cut Flow	$Z \to \nu\bar{\nu}$	γ	$Z \to \nu\bar{\nu}/\gamma$	Z/γ
Boson + Jets ≥ 3:	52.5±2.9	188.0±2.0	0.279±0.015	1.397±0.077
$H_T > 300$ GeV/c:	33.4±2.3	100.3±1.2	0.333±0.023	1.66±0.12
QCD Angular Cuts:	25.3±2.0	78.0±1.1	0.324±0.026	1.62±0.13
Baseline Selection:	16.4±1.6	40.92±0.80	0.400±0.040	2.00±0.20
High H_T Selection::	4.48±0.83	10.21±0.40	0.439±0.083	2.19±0.42
High $\not{H}_T$ Selection:	4.17±0.80	10.25±0.40	0.407±0.080	2.03±0.40
No p_T cut on Z boson:				
Baseline Selection:	16.5±1.1	40.92±0.80	0.402±0.028	2.01±0.14
High H_T Selection:	4.45±0.57	10.21±0.40	0.436±0.059	2.18±0.29
High $\not{H}_T$ Selection:	4.90±0.60	10.25±0.40	0.477±0.062	2.39±0.31

Photon Purity A measurement of the photon purity with the combined isolation method was performed on 36.1 pb^{-1} in Reference [342]. Table 7.9 lists the purity for different η and p_T^γ bins. Since the photon isolation does not allow for jets to be in the isolation cone, the requirement of additional central jets was not considered to influence the purity measurement. A possible influence of the jets on the mistag rate is discussed above in the context of additional primary vertices.

Fragmentation Contribution The contribution of fragmentation photons to the prompt photon sample is estimated to be 8 % for photons with $85 < p_T^\gamma \leq 120$ GeV/c and 5 % for photons with $p_T^\gamma > 120$ GeV/c [338]. An uncertainty on the Fragmentation Functions is conservatively estimated to be 20 % [344, 345], leading to a correction factor of 0.95 with an uncertainty of 1 %.

Photon Mistag Rate The efficiency of the pixel seed veto was studied using Monte-Carlo simulation in Reference [346] and estimated to be 96.65 ± 0.5 %. This was confirmed by another study in Reference [216] stating that the pixel efficiency is 97 ± 1 % due to early conversions in the beam pipe and the first pixel layer, while random coincidences between photons and tracks subtract 0.5 ± 1 % . A measurement of this last effect (in 3.1 pb^{-1} of data) as a function of additional vertices was dominated by background and thus no correction for pile-up was applied [216]. The photon mistag rate is absorbed in the Z/γ-correction factor, since Z bosons were related to reconstructed and identified γ's after detector simulation and reconstruction.

Z/γ Monte-Carlo Statistical Uncertainty The statistical uncertainty on the Z/γ correction factor determined using MadGraph simulated samples is dominated by the limited statistics of the Z + jets sample and is the largest uncertainty, ranging from 7% in the baseline selection to 13% in both the high-H_T and high-$\not{H}_T$ selection.

Z/γ Scale Uncertainty According to Blackhat theoreticians, the uncertainty on NLO/LO scale for the Z/γ correspondence factor will be smaller than ±10 % for the high $\not{H}_T$ search region and ±7 % for the high H_T search region [339]. The scale difference was treated as a

uniform uncertainty, the root-mean-square (RMS)[5] value is resp. 5.8 % and 4.0 %. Since no detailed NLO to LO comparison for photon + 2 jets was evaluated for the baseline selection, the higher value of the search regions: 10 % in a box was taken, corresponding to a 5.8 % RMS value.

The uncertainty was determined by comparing BlackHat leading order to next-to-leading order computations for the Z + 2 jets / γ + 2 jets ratio. Later on, final results for BlackHat leading-order and next-to-leading order computations were obtained and are tablulated in Table 7.13. This table contains also the BlackHat leading-order plus Sherpa parton shower computations and the MadGraph leading-order plus Phythia parton shower computations after detector simulation and reconstruction. The final results differ slightly from the results used in this analysis, but this should have little or no impact on the final result.

Table 7.13: Z + 2 jets / γ + 2 jets ratio for the MadGraph and BlackHat computations. The matrix element plus parton shower (ME+PS) method uses LO matrix element calculation and only the statistical uncertainty is shown, while for the leading-order and next-to-leading order matrix element computations, an uncertainty due to the scale variation is included. BlackHat and BlackHat + Sherpa numbers are obtained from Reference [335].

Z/γ (+ $\geq$ 2jets)	MadGraph (ME) + Pythia (PS) + sim & reco	BlackHat (ME) LO	BlackHat (ME) + Sherpa (PS)	BlackHat (ME) NLO
Baseline selection	0.202 ± 0.01	0.215 ± 0.107	0.211 ± 0.005	0.201 ± 0.046
High-H_{T} selection	0.238 ± 0.03	0.215 ± 0.103	0.194 ± 0.003	0.195 ± 0.026
High-$\not\!\!H_{\mathrm{T}}$ selection	0.258 ± 0.02	0.250 ± 0.122	0.214 ± 0.004	0.229 ± 0.027

Z/γ Acceptance A 5 % uncertainty is assigned to the acceptance uncertainty of the Z/γ ratio [347].

Selection Efficiency The selection efficiency accounts for the photon reconstruction, isolation and identification and is measured in Monte-Carlo simulation and 3.1 pb^{-1} of data [188]. The ratio of efficiencies obtained from data and Monte-Carlo simulation for prompt photons with $p_{\mathrm{T}} > 45$ GeV/c is 1.011 ± 0.019 in the barrel and 0.997 ± 0.032 in the endcaps. In Table 7.14 the efficiencies obtained in Reference [188] are shown together with the calculated scale factor ($\mathrm{SF_{data/mc}}$). Since these efficiencies are measured at the begin of data taking, pile-up is not taken into account. In Reference [213] the much tighter photon selection efficiency for H $\rightarrow \gamma\gamma$ is evaluated with and without and pile-up in Monte-Carlo simulation and the ratio of the selection efficiency with pile-up w.r.t. without pile-up in the barrel (endcaps) is 1.053 (1.013). In another study [346], where a slightly looser photon identification is used, no significant dependence on the number of primary vertices is observed and a systematic uncertainty of 1 % is assigned. Since our photon identification resembles more the latter, the same approach was used here.

In Table 7.15 the full list of corrections to be applied is summarized, along with the corresponding systematic uncertainties. The purity and fragmentation contributions were obtained

[5] The RMS of a uniform distribution of $1/(b-a)$ over an interval of $[a, b]$ is $(b-a)/\sqrt{12}$.

Table 7.14: Efficiency for $45 < p_{\mathrm{T}}^{\gamma} < \infty$ measured in data and simulation using the $Z \to e^+e^-$ control sample in the ECAL Barrel (EB) and ECAL Endcap (EE) [188]. The efficiency ratio for photons and electrons in Monte-Carlo simulation and the Scale Factor (SF) obtained by dividing the efficiency in Data by the efficiency in Monte-Carlo and corrected by the previous efficiency ratio are also included.

	$Z(ee)$ MC	$Z(ee)$ DATA	MC Ratio γ/e	$\gamma = Z(ee) \times \gamma/e$	$\mathrm{SF}_{\mathrm{data/mc}}$
EB	88.50 ± 0.23%	89.04 ± 1.83%	1.005 ± 0.005	89.5 ± 1.9%	1.011 ± 1.8%
EE	92.55 ± 0.26%	91.06 ± 3.23%	1.013 ± 0.005	92.2 ± 3.3%	0.997 ± 3.2%

by weighing the above mentioned values for events in different p_{T}^{γ} and η bins. The 7–10% theoretical uncertainty on the Z to γ correspondence is treated as a uniform uncertainty, hence the RMS is tabulated. The central values of the $Z(\nu\nu)/\gamma$-correction factor for the three selections are the tabulated values of the last three rows of Table 7.12: 0.402 ± 0.028 for the baseline selection; 0.436 ± 0.059 for the high-H_{T} selection; and 0.477 ± 0.062 for the high-$\not{H}_{\mathrm{T}}$ selection.

Table 7.15: Overview of all correction factors and corresponding systematic uncertainties. The correction factor is dimensionless [-], the uncertainty is expressed as a percentage [%].

	Contribution	Baseline [-]±[%]	High-H_{T} [-]±[%]	High-$\not{H}_{\mathrm{T}}$ [-]±[%]
1.	Fragmentation	0.95±1 %	0.95±1 %	0.95±1 %
2.	Photon purity	0.94±8.8 %	0.90±8.9 %	0.97±10 %
3.	Photon mistag	1.00±1.4 %	1.00±1.4 %	1.00±1.4 %
4.	±scale	±6 %	±4 %	±6 %
5.	Z/γ correction±acceptance	0.41±5 %	0.44±5 %	0.48±5 %
6.	±MC stat	±7 %	±13 %	±13 %
7.	Selection efficiency: data/MC ratio	1.01±2.4 %	1.01±2.4 %	1.01±2.4 %
	Total correction	0.37±14 %	0.38±17 %	0.45±18 %

Apart from the corrections listed above, we identified some other possible sources of systematic uncertainties, but these were determined not to have any effect on the analysis and are listed below for completeness:

ECAL Spikes The remaining fraction of spikes after the E_2/E_9 and t_{seed} cleaning is estimated on a 10.9 pb^{-1} prompt inclusive loose (as defined in Table 7.4) photon sample. The residual spike fraction is 0.0044 ± 0.044 % for $84 \leq p_{\mathrm{T}}^{\gamma} < 120$ and 0.0521 ± 0.0373 % for $120 \leq p_{\mathrm{T}}^{\gamma}$ [215]. The approach used in this analysis is inherent spike-proof, since a spike will introduce transverse momentum imbalance in the event. Removing the PF-jet related to the photon (containing a spike) yields a low-$\not{H}_{\mathrm{T}}$ event not passing baseline nor search selections. An even more rare event would be a γ + jet event where a relatively low energy spike is clustered in one of the jets and not in the photon. Given the good performance of the PF Spike cleaning the probability for these events is negligible. These rare events also appear in the $Z(\nu\bar{\nu})$ + jet sample we want to predict.

Photon Energy Scale Is estimated to be better than 1 % in the barrel and 3 % in the endcaps [348]. The photon scale does not enter directly in the selection, since the $\not{H}_{\mathrm{T}}$ is estimated from the jets excluding the photon.

ECAL Dead and Masked Cells The effect on the selected photon sample from the ~ 1% masked ECAL channels feeds automatically into the estimation of the acceptance, since a realistic masked channel map is applied in the reconstruction of the used MC samples. The influence of the ECAL Dead and Masked Cells for the RA2 analysis is detailed in Reference [317]. The existing small run-dependent differences between the MC map and the data map are a negligible second order effect.

Electron Mistag Rate The probability that an electron is misidentified as a photon in the barrel is 0.62 ± 0.06(stat)±0.65(syst) % while in the endcaps the electron misidentification is 1.13 ± 0.13(stat)±1.08(syst) %) [213]. Since the high p_T electron cross section is at least an order of magnitude below the photon cross section, this effect is negligible.

7.8 Results

7.8.1 Estimation of the $Z(\nu\nu)$ background

Application of the total correction factors of Table 7.15 for the three search selections allow us to obtain the final prediction for the Z($\nu\bar{\nu}$) + jet events. Table 7.16 summarizes the results of the $Z(\nu\nu)$ prediction from the γ + jet control sample. The amount of Monte-Carlo simulated Z($\nu\bar{\nu}$) + jet events (scaled to next-to-leading order cross section) passing the selection cuts is shown for comparison. This ~ 30% underprediction is expected, since the D6T tune was used, as discussed earlier.

Table 7.16: Estimation of $Z(\nu\nu)$ background using a correction factor obtained after detector simulation and reconstruction, correcting for the differences in γ and Z phenomenology, tabulated in Table 7.15. Monte-Carlo simulated $Z(\nu\nu)$ events are scaled to NLO cross section and are shown for comparison (MC Truth).

Selection Cuts	γ + jet Data Events	Z($\nu\bar{\nu}$) + jet Predicted Data Events	Z($\nu\bar{\nu}$) + jet MC Truth
$\not{H}_T$ > 150 GeV/c:	72±8.5	26.3±3.1(stat)±3.6(syst)	21.1±1.4
High H_T Search:	22±4.7	8.4±1.8(stat)±1.4(syst)	5.70±0.74
High$\not{H}_T$ Search:	16±4.0	7.1±1.8(stat)±1.3(syst)	6.27±0.78

7.8.2 Estimation of $W(\mu\nu)$ in the two jets channel

As a cross check, the muon yield for the method exploiting $W(\mu\nu)$ to predict $Z(\nu\nu)$ is estimated and compared to data. To increase the statistics this prediction is done in the two jets channel, whereas the actual search regions require three jets. The muon control sample was obtained in a way similar to the hadronic tau background (section 6.2.2). All baseline selection cuts were applied on a data sample containing exactly one isolated and identified muon, with $p_T > 20$ GeV/c and $|\eta^\mu| < 2.1$, as discussed in section 6.1.3, except for the three central jets requirement. Instead only two central $p_T > 50$ GeV/c jets were required and the angular separation cuts were reduced to the two leading jets.

The first step is to obtain the $W(\mu\nu)/\gamma$ conversion factor. Table 7.17 shows the LO scaling factors obtained by comparing a simulated sample W with leading-order cross section to a similarly simulated γ sample, also with leading order cross section, as was done for $Z(\nu\nu)$ in Table 7.12,

Table 7.17: $W(\mu\nu)/\gamma$ scaling factors for 36.1 pb^{-1} after detector simulation and reconstruction for some preselections, the RA2 cut flow and for the three search regions. Only statistical uncertainties are shown. LO cross sections are used for γ and W Monte-Carlo.

	W $\rightarrow \mu\nu$	γ	W $\rightarrow \mu\nu/\ \gamma$
2 Jets Channel:			
Boson + Jets $\geq$ 2:	1506±17	1165.2±7.6	1.293±0.017
$H_{\mathrm{T}} > 300$ GeV/c:	173.8±5.6	236.5±1.9	0.735±0.025
QCD Angular Cuts:	133.6±4.9	193.5±1.7	0.690±0.026
Baseline Selection:	34.2±2.5	108.5±1.3	0.315±0.023
High H_{T} Selection:	7.3±1.2	19.14±0.54	0.380±0.061
High $\not{H}_{\mathrm{T}}$ Selection:	12.0±1.5	33.49±0.72	0.359±0.045
3 Jets Channel:			
Boson + Jets $\geq$ 3:	190.3±3.7	188.0±2.0	1.012±0.022

but this time without a p_{T} cut on the bosons. Results for the associated production of a (W or γ) boson with three or more jets are shown for comparison.

The $W(\mu\nu)/\gamma$ correction factor obtained in Table 7.17 was then corrected for γ purity, fragmentation, pixel efficiency and the Data / Monte-Carlo simulation scale factor as was done before for the Z($\nu\bar{\nu}$) + jet prediction in Table 7.15. A very conservative ±30 % (uniform) uncertainty was assigned to the scale uncertainty of $W(\mu\nu)/\gamma$, since it was determined with LO cross sections, but will be applied at NLO level. This correction factor was used in Table 7.18 to predict the amount of $W(\mu\nu)$ + jets events that would have passed the same selections if the muon was not triggered, reconstructed, identified or isolated. The rightmost column shows the $W(\mu\nu)$ Monte-Carlo simulation. The agreement between the $W(\mu\nu)$ events predicted from data and the NLO-scaled Monte-Carlo simulated $W(\mu\nu)$ events is fair, keeping in mind that the MadGraph D6T Tune underpredicts the data by about 30 %.

Table 7.18: Estimation of W $\rightarrow \mu\nu$ using a correction factor obtained after detector simulation and reconstruction correcting for the differences in γ and W phenomenology. A MadGraph + (D6T) simulated sample of W $\rightarrow \mu\nu$ scaled to NLO is shown for comparison (MC Truth).

Selection Cuts	γ + jet Data Events	$W(\mu\nu)/\gamma$ Correction	$W(\mu\nu)$ Predicted Data Events	$W(\mu\nu)$ MC Truth (NLO)
2 Jets Channel:				
Boson + Jets $\geq$ 2:	2136±46	1.170±0.237	2499±54 ±505	1934±21
$\not{H}_{\mathrm{T}} > 150$ GeV/c:	202±14	0.305±0.067	61.6±4.3±13.5	43.9±3.2
High H_{T} Search:	35±5.9	0.357±0.094	12.4±2.1±3.3	9.3±1.5
High $\not{H}_{\mathrm{T}}$ Search:	66±8.1	0.373±0.092	24.6±3.0±6.1	15.4±1.9
3 Jets Channel:				
Boson + Jets $\geq$ 3:	337±18	0.918±0.187	309±17 ±63	244.3±4.8

To predict the muons observed in the data control sample, a muon efficiency correction is needed. The efficiency ϵ of the muon selection cuts determined on data can be factorised as follows:

$$\epsilon = \epsilon_{\mathrm{trig}} \times \epsilon_{\mathrm{reco+ID}} \times \epsilon_{\mathrm{iso}} \tag{7.13}$$

where $\epsilon_{\text{trig}} = 0.95 \pm 0.02$ is the efficiency to pass the single-muon trigger (L1+HLT), $\epsilon_{\text{reco+ID}} = 0.96 \pm 0.02$ is the reconstruction and identification efficiency and $\epsilon_{\text{iso}} = 0.85 \pm 0.05$ is the efficiency for a reconstructed muon to be isolated [325]. This results in a muon efficiency of $\epsilon = 0.78 \pm 0.06$. Applying this efficiency to the $W(\mu\nu)$ prediction in Table 7.18, one can predict the muon yield due to the $W(\mu\nu)$ process, as is tabulated in Table 7.19. The main contaminations for $W(\mu\nu)$ in the muon + 2 Jets sample are QCD, semi-leptonic $t\bar{t}$ and W $W \to \tau \to \mu$ as is shown Figures 1–3 in Reference [325]. The Data and Monte-Carlo simulated yields reported in Reference [325] agree with Table 7.19. Adding $\sim$ 400 QCD events (estimated in Figure 3(d) of Reference [325]) to the 1949 $W(\mu\nu)$ and 526 $t\bar{t}$ events compares rather well to the 3041 observed muon events. The QCD contamination to the 3 jets channel and to the search regions in the 2 jets channel is negligible. The prediction in the high statistics bins of the "Boson + Jets $\geq$ 2" selection and the "Boson + Jets $\geq$ 3" selection is rather good.

Table 7.19: Estimation of W $\to \mu\nu$ and the μ yield in data using a correction factor obtained after detector simulation and reconstruction correcting for the differences in γ and W phenomenology.

Selection Cuts	γ + jet Data	$W(\mu\nu)$ Pred. Data	μ Yield Pred. Data	$t\bar{t}$ Yield MC	μ Yield Data
2 Jets Channel:					
Boson + Jets $\geq$ 2:	2136±46	2499±54 ±505	1949±42 ±409	526.0±1.5	3041±55
$\not{H}_{\text{T}} > 150$ GeV/c:	202±14	61.6±4.3±13.5	48.0±3.4±11	27.8±0.3	70±8
High H_{T} Search:	35±5.9	12.4±2.1±3.3	9.7±1.7±2.6	5.80±0.16	13±4
High$\not{H}_{\text{T}}$ Search:	66±8.1	24.6±3.0±6.1	19.2±2.4±4.9	6.83±0.17	31±6
3 Jets Channel:					
Boson + Jets $\geq$ 3:	337±18	309±17 ±63	241±13 ±51	256.9±1.0	553±24

7.8.3 Estimation of the $Z(\nu\nu)$ background shape

Although the analysis presented here is a single "cut and count" analysis, in which events are counted in a simple bin and are compared to background estimations to obtain an upper limit on the amount of signal events, an attempt was made to compare the shape of the $Z(\nu\nu)$ prediction with a simulated $Z(\nu\nu)$ sample. Figure 7.23 shows the Z($\nu\bar{\nu}$) + jet prediction from the γ + jet control sample for H_{T} and$\not{H}_{\text{T}}$ for the three selection regions. The predictive power of the plots is limited by the small amount of events in the p_{T}^{γ} bins. The agreement is rather fair, given the low statistics of both data and Monte-Carlo simulated samples. Future analyses will implement comparisons of the shape in data with a predicted shape of the backgrounds, leading to the exclusion of a greater part of the CMSSM or the discovery of new physics.

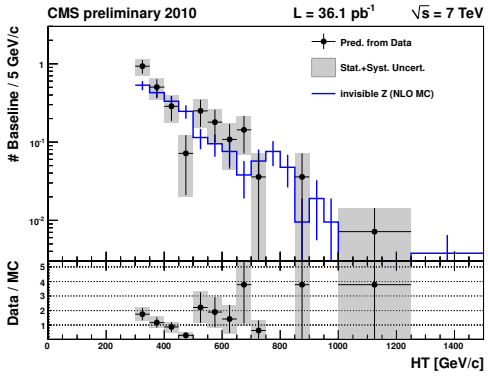

(a) Baseline selection

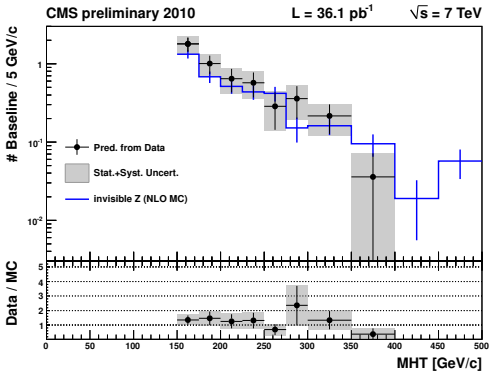

(b) Baseline selection

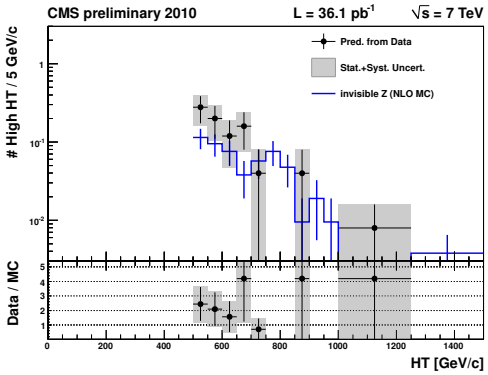

(c) High-H_{T} selection

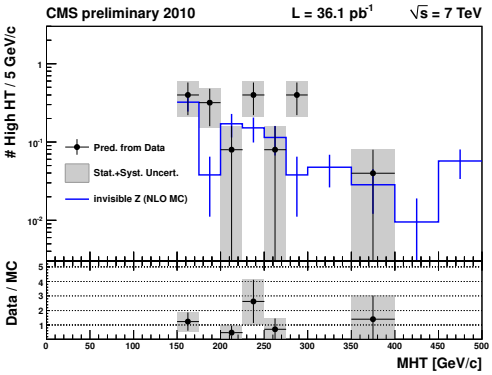

(d) High-H_{T} selection

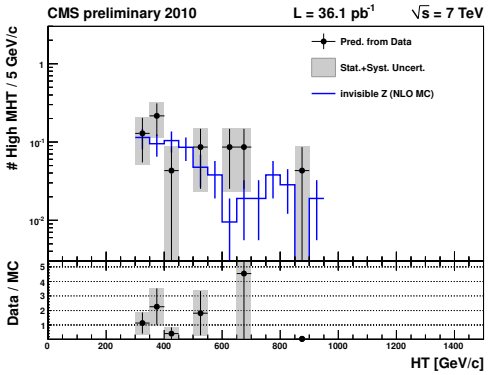

(e) High-$\not{H}_{\mathrm{T}}$ selection

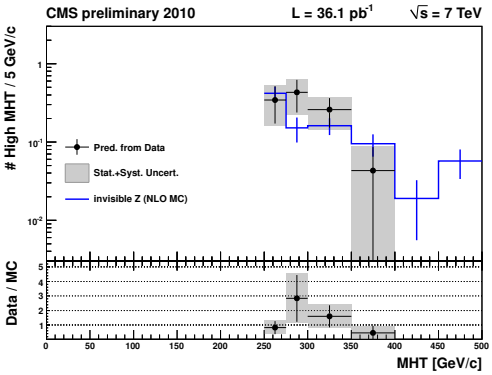

(f) High-$\not{H}_{\mathrm{T}}$ selection

Figure 7.23: Z($\nu\bar{\nu}$) + jet prediction from the γ + jet control sample for H_{T} (left) and $\not{H}_{\mathrm{T}}$ (right). Top: Baseline Event Selection, Middle: High-H_{T} search region, Bottom: High-$\not{H}_{\mathrm{T}}$ search region. Z($\nu\bar{\nu}$) + jet scaled to NLO cross sections is shown for comparison.

7.9 Initial State Radiation and signal contamination

Although the estimation of the $Z(\nu\nu)$ is now finished, some more information is needed for the jets and missing transverse energy search to use the predicted backgrounds to set limits. Effects such as signal contamination and uncertainties due to parton distribution functions and initial state radiation are discussed here.

7.9.1 Initial State Radiation

Additional radiation of gluons can enhance the jet multiplicity of an event. This radiation can occur off incoming partons: Initial State Radiation (ISR) and outgoing partons: Final State Radiation (FSR). Final State Radiation tends to be more central, since the gluons are radiated from centrally emitted partons and will be detected as additional jets within the CMS detector. Physically there is no distinction between an additional parton radiated in the final state or a next-to-leading-order parton being emitted. On the other hand, Initial State Radiation occurs on the incoming partons which have their momentum aligned with the beam axis, which leads to gluons radiated in more or less the same direction, resulting in far less central jets, not detected by CMS. The radiation of a high-energy parton leads to less energy available to the hard interaction, reducing the probability of the creation of jets-plus-$\not\!\!E_{\mathrm{T}}$ events with multiple central jets and high missing momentum.

The Initial State Radiation is taken into account in the event simulation, although some uncertainty on chosen parameters remains. Therefore the effect of a small change in these "ISR parameters" on the final result was investigated in the simulation. We would like to know if ISR enhances $Z(\nu\nu)$ events in a different way with respect to γ events. If both are enhanced in the same way, no correction would have been applied on the $Z(\nu\nu)/\gamma$ correction factor, even strengthening the case for a data-driven approach and the use of events to estimate the $Z(\nu\nu)$ process.

The ISR settings were adjusted such that no radiation was allowed with energy above the scale at which the parton distribution functions were probed. Reducing the ISR implies that more energy remains for the hard scattering, leading to slightly more energetic jets that can pass the selection criteria. The γ/Z ratio for events with three central jets is shown in Figure 7.24(a). A small difference due to the different ISR settings is visible in the η distribution of the events, resulting in a slightly higher event yield. When investigating the γ/Z ratio, the differences are within the statistical uncertainty, because of the low statistics of the $Z(\nu\nu)$ sample. Allowing more statistics by removing the three-jets criterion results in Figure 7.24(b). Although we are comparing apples to oranges here (the inclusive Z and inclusive γ sample have a different jet content, as discussed in section 7.2), the ratio of γ/Z for the two different ISR settings is constant in η. We thus expect the ISR to enhance the Z and γ events in the same way. We therefore expect a negligible influence of the modelling of the ISR on the final $Z(\nu\nu)$ estimation.

7.9.2 Parton Distribution Functions

Photons and Z bosons couple differently to u and d quarks, and therefore the choice of parton distribution functions in the event simulation also provides an uncertainty. This is an uncertainty that is also only affecting the $Z(\nu\nu)/\gamma$ correction factor. The PDFs used by the standard MadGraph + Pythia CMS simulation software are CTEQ6L1.

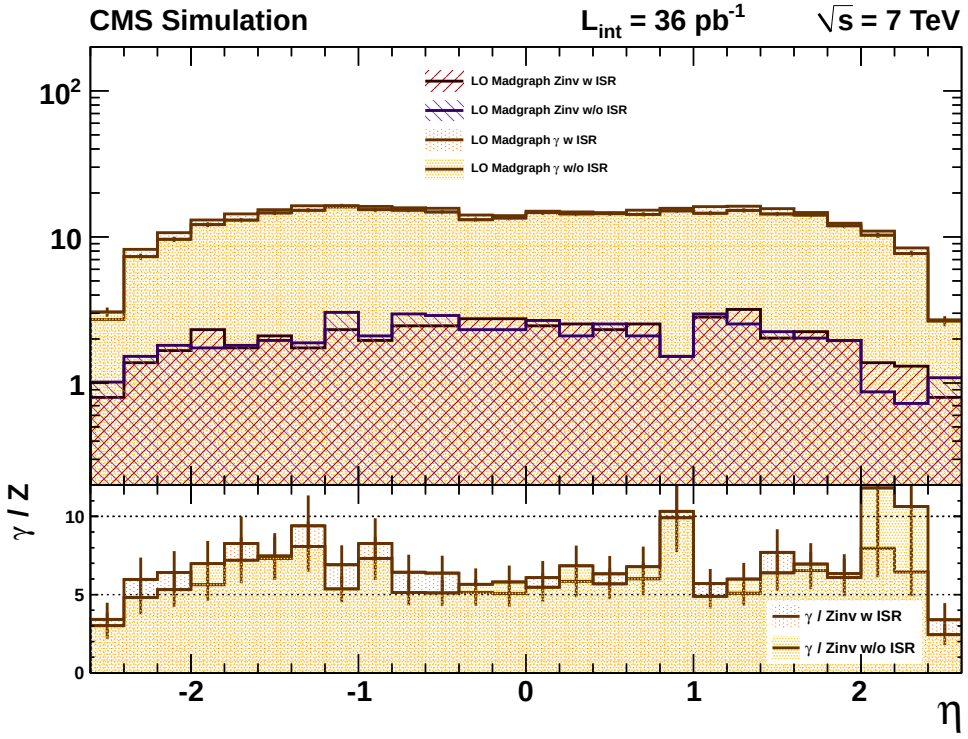

(a) γ/Z ratio for events with three central jets.

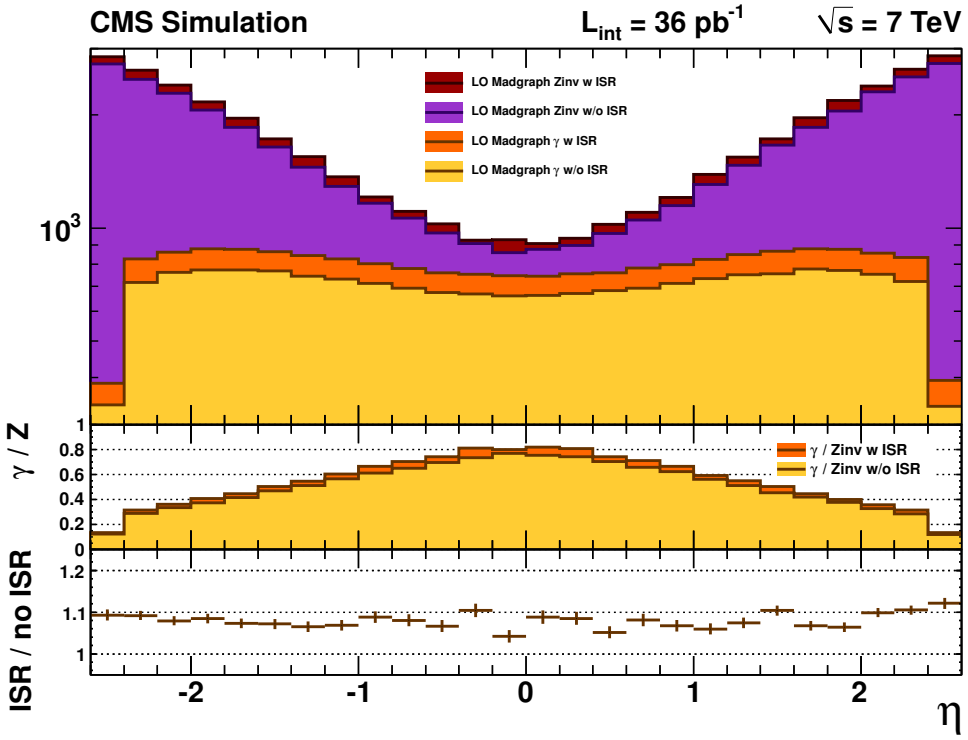

(b) γ/Z ratio for events without jet requirement.

Figure 7.24: The γ/Z ratio for two different ISR scenarios: for events requiring three central jets (a), which is statistically limited; and without jet requirement (b).

For a study of the PDF variations, 45 variations of the CTEQ6.6 PDFs were used. The PDF uncertainty is the envelope of those 45 variations and is obtained through the use of a "Master Equation" [349]:

$$\Delta X^{+}_{\max} = \sqrt{\sum_{i=1}^{N} \left(\max(X_i^{+} - X_0, X_i^{-} - X_0, 0)\right)^2}, \tag{7.14}$$

$$\Delta X^{-}_{\max} = \sqrt{\sum_{i=1}^{N} \left(\max(X_0 - X_i^{+}, X_0 - X_i^{-}, 0)\right)^2}, \tag{7.15}$$

where the X_0 the central value is and $N = 22$. There are 22 "up-variations" and 22 "down-variations" of the PDFs. For the present analysis the influence of the PDFs on the $Z(\nu\nu)/\gamma$ correction factor was investigated, hence the variable X was chosen to be $X = Z(\nu\nu)/\gamma$. Table 7.20 shows the $Z(\nu\nu)/\gamma$ correction factor together with the PDF up-variation ($\Delta X^{+}_{\max}$) and the down-variation ($\Delta X^{-}_{\max}$). No p_{T} cut on the Z boson was applied, while the photon was required to have $p^{\gamma}_{\mathrm{T}} > 100\,\mathrm{GeV}/c$. The last two columns show the up and down variation due to the PDF uncertainties. The PDF variations are of the order of 2.5% and are well within the statistical uncertainty of the Monte-Carlo simulation.

Table 7.20: γ to Z scaling factors in events with $p^{\gamma}_{\mathrm{T}} > 100$ GeV/c for 36.1 pb^{-1} after detector simulation and reconstruction, together with the PDF up-and-down variations. Only statistical uncertainties are shown.

Cut Flow	$\mathrm{Z} \to \nu\bar{\nu}$	γ	$\mathrm{Z} \to \nu\bar{\nu}/\,\gamma$	PDF variations	
Boson + Jets $\geq$ 3:	131.4±3.1	188.0±2.0	0.699±0.018	+0.010	-0.012
Baseline Selection:	16.5±1.1	40.92±0.80	0.402±0.028	+0.010	-0.010
High H_{T} Selection::	4.45±0.57	10.21±0.40	0.436±0.059	+0.015	-0.017
High$\not{H}_{\mathrm{T}}$ Selection:	4.90±0.60	10.25±0.40	0.477±0.062	+0.009	-0.010

7.9.3 Signal contamination

To estimate the backgrounds in the search regions from data, control regions were used. For the $Z(\nu\nu)$ background, the control region is a high-p_{T} photon-plus-jet region without missing transverse energy, while for the hadronic tau background, a high-p_{T} muon-plus-jet region is used. These control regions are chosen such that in the light of the signal being sought, the event count in the control region is dominated by the Standard Model physics processes. However, the new physics we are looking for can manifest itself also in other event signatures. Instead of only jets and missing transverse energy, also leptons and photons can be produced in these interactions, contaminating the control regions we used to estimate the backgrounds in the search region. This is called "signal contamination".

The signal contamination for the $Z(\nu\nu)$ background estimate was investigated for a few points in the broad mSUGRA space, relevant to the calculation of the exlusion limit in the CMSSM. For each point 10 000 events were simulated and the amount of events predicted by the γ-method are tabulated in Table 7.21. To estimate the signal contamination probability, the appropriate cross sections for the different points in the mSUGRA space need to be used. In Table 7.22 the LO cross sections for the mSUGRA points in Table 7.21 are used to calculate the signal contamination. The signal contamination is of the order of 0.02–0.03 events, with one exception

peaking to 0.2–0.3 events in 36 pb^{-1}. This is a negligible amount of signal contamination in the photon-plus-jet control sample, which is not surprising since these mSUGRA models do not predict events containing hard photons. The signal contamination is most probably due to high-energy electrons identified as photons.

Table 7.21: Signal Contamination Event Yield (on event by event basis) for different search regions calculated for some points in the mSUGRA space.

mSUGRA parameters					Processed	MC γ-predicted Events		
$\tan\beta$	A	μ	m_0	$m_{1/2}$	Events	Baseline	High H_T	High $\not{H}_T$
10	0	>0	200	280	10000	3	2	3
10	0	>0	200	290	10000	7	5	6
10	0	>0	500	170	10000	7	6	6
10	0	>0	800	230	10000	5	4	3
3	0	>0	200	280	10000	9	8	7
3	0	>0	200	290	10000	6	4	3
3	0	>0	400	300	10000	11	7	7
3	0	>0	400	310	10000	9	9	5

Table 7.22: Signal Contamination Prediction for different search regions calculated for some mSUGRA scans with their LO cross sections for 36 pb^{-1}.

mSUGRA parameters					X-section	MC γ-predicted Events in 36 pb^{-1}		
$\tan\beta$	A	μ	m_0	$m_{1/2}$	σ [pb]	Baseline	High H_T	High $\not{H}_T$
10	0	>0	200	280	1.952	0.021	0.014	0.021
10	0	>0	200	290	1.611	0.041	0.029	0.035
10	0	>0	500	170	10.38	0.263	0.225	0.225
10	0	>0	800	230	1.572	0.028	0.023	0.017
3	0	>0	200	280	1.973	0.064	0.057	0.050
3	0	>0	200	290	1.633	0.035	0.024	0.018
3	0	>0	400	300	0.885	0.033	0.022	0.022
3	0	>0	400	310	0.736	0.024	0.024	0.013

7.10 Conclusions and outlook

The estimation of $Z(\nu\nu)$ was performed well in time for the jets-plus-missing-momentum SUSY search shown in Moriond [350]. The method using photons proved to deliver a high precision estimate of the irreducible $Z(\nu\nu)$ background.

For future use, the performance and robustness of the analysis could be improved by implementing the purity methods pioneered by the photon cross section papers [164, 208]. This would ensure robustness of the analysis, since one does not depend on (changes in) other analyses. For instance, the measurement of the photon purity on the full 36 pb^{-1} of data recorded in 2010 had a slightly different photon selection than the initial measurement on a 3 pb^{-1} of data.

The background estimate would also benefit from the implementation of a smooth cone photon isolation with a high signal efficiency, while rejecting all fragmentation photons. This, however, will probably not be the first improvement to be implemented. The more important issues to be

tackled would be the integration of particle-flow photons, such that the event description would be entirely consistent. Furthermore huge increases in instantaneous luminosity are expected the next years. During 2011 we observed an increase of the instantaneous luminosity from $2 \cdot 10^{32}\,\mathrm{cm}^{-2}\mathrm{s}^{-1}$ at the end of 2010 to $3.65 \cdot 10^{33}\,\mathrm{cm}^{-2}\mathrm{s}^{-1}$ at the end of 2011 data taking. The prospects for 2012 are that LHC will be running at $5\text{–}7{\cdot}10^{33}\,\mathrm{cm}^{-2}\mathrm{s}^{-1}$, but with 50 ns bunch spacing instead of 25 ns. This means that each (interesting) event will be superimposed on 24–34 minimum bias interactions, with an increasing probability for a second relatively hard interaction. Therefore, the priorities will be the development of triggers with high efficiency on photon objects, that can cope with the high rates, and selection and isolation optimization in these crowded events.

Now all three different Standard Model backgrounds (W/top, QCD, $Z(\nu\nu)$) have been estimated for the jets plus missing transverse momentum search. The results of these three backgrounds are presented in the next chapter, where the results are interpreted in the context of mSUGRA and SMS.

Chapter 8

Results and interpretation

8.1 Results and limits

The number of events observed in data for the jets-plus-$\not\!\!H_T$ search and the event yields predicted by the different background estimation methods, discussed in the previous chapters, are summarized in Table 8.1 for the three different event selections. The first four rows present the background estimations for the different Standard Model backgrounds. The result of the $Z(\nu\nu)$ + jets estimation is taken from Table 7.16 in chapter 7. The sum of the backgrounds is shown in the fifth row and can be compared with the amount of events observed in data in the sixth row. The seventh row shows the 95% Confidence Level (CL) upper limit on the amount of data events possibly hiding in the data.

Table 8.1: The number of predicted background events and data events for the baseline and search selections. The total background and the combined (statistical and systematic) uncertainty is obtained as explained in the text. The last line gives the 95% confidence limit on the number of possible signal events in the data.

Background process	Baseline selection	High-$\not\!\!H_T$ selection	High-H_T selection
$Z(\nu\nu)$ + jets (γ + jets method)	26.3 ± 4.8	7.1 ± 2.2	8.4 ± 2.3
$W/t\bar{t} \to e, \mu$	33.0 ± 8.1	4.8 ± 1.9	10.9 ± 3.4
$W/t\bar{t} \to \tau_h$	22.3 ± 4.6	6.7 ± 2.1	8.5 ± 2.5
QCD multijet (R+S method)	29.7 ± 15.2	0.16 ± 0.10	16.0 ± 7.9
Total background Events	111.3 ± 18.5	18.8 ± 3.5	43.8 ± 9.2
Events observed in data	111	15	40
95% CL upper limit on signal	40.4	9.6	19.6

The total uncertainty on the background prediction is calculated in a Bayesian framework and is a so-called "overall" prior. The probability distributions corresponding to each of the uncertainty sources are convoluted using a Monte-Carlo integration technique to obtain the probability distribution for the overal background estimation. The uncertainties were modelled with either Gaussian, bifurcated Gaussian (for asymmetric systematic uncertainties), Poisson or uniform distributions. The presence of several sources of uncertainties makes the overall combination quite Gaussian in shape. The mean and standard deviation are tabulated in the fifth row of Table 8.1, and are used as the central value and uncertainty in the limit calculations.

This total background estimation is compared to the amount of events found in data in the sixth row. No excess of events in the data has been observed. The contributing systematic uncertainties contain the jet energy scale and resolution, the lepton veto, the cleaning including the veto on large energy loss in masked ECAL cells, the trigger, the intial- and final-state radiation, the parton distribution functions, the luminosity and the statistical uncertainty. This prior is used as an input for the limit calculation within both the CMSSM, discussed in section 8.2, and the Simplified Model Spectra (SMS), detailed in section 8.3.

Although the agreement between the predicted background and the observed event yields in data seems very good, one should keep in mind that the search regions are correlated. If the background is underfluctuating, some signal events can hide in the total event yield. The maximum number of events that could be present in the data at the 95% confidence level is 40.4, 9.6 and 19.6 for the baseline selection, the high-$\not{H}_T$ and the high-H_T selection respectively and is given in the last line of Table 8.1.

8.2 Interpretation in the CMSSM

To interpret the obtained results within the CMSSM framework, one also needs to know the signal acceptance and the signal selection efficiency. These are determined by applying the analysis on a simulated CMSSM sample. The CMSSM is not just one model, but rather a family of models, as discussed in section 1.4. The parameter space is spanned by 5 parameters, all defined at the grand unification scale Λ_{GUT}: m_0, $m_{1/2}$, $\tan\beta$, μ, and A_0. m_0 is the universal scalar mass, $m_{1/2}$ the universal gaugino mass, μ is the sign of the Higgs mixing parameter, $\tan\beta$ the ratio of the vacuum expectation values of the two Higgs fields, and A_0 the universal trilinear coupling.

The signal acceptance and signal efficiency is obtained by applying the selection cuts on the Monte-Carlo simulated samples for the CMSSM model. The mass parameters m_0 and $m_{1/2}$ were varied in steps of 10 GeV, for three different values of $\tan\beta = 3$, 10, and 50, while the other two were kept constant: sgn $\mu > 0$ and $A_0 = 0$. The cross sections were calculated at leading order with IsaJet [351] and corrected using next-to-leading order k-factors, calculated using Prospino [323]. The total signal efficiency, consisting of the geometrical acceptance on the one hand and the selection efficiency on the other hand, ranges between 20-30% for the high-H_T selection and 10-20% for the high-$\not{H}_T$ selection [299]. Figure 8.1 shows the signal efficiency for the CMSSM for the $\not{H}_T$ and the H_T selections.

The limits are calculated with a technique called the modified frequentist procedure CLs [352, 353]. Strictly speaking, it is not a confidence level, but a ratio of confidence levels. CLs is a modified frequentist procedure because it aims to avoid the exclusion of signals that the analysis is not really sensitive to. Sometimes experiments observe less events than predicted for the background, which would lead to negative cross sections. This says more about the fluctuations of the background than about the hypothetical signal the analysis is looking for. This is avoided by normalizing the confidence level of the signal-plus-background hypothesis, CL_{s+b}, to the confidence level in the background only hypothesis, CL_b. CLs is defined as:

$$CLs = \frac{CL_{s+b}}{CL_b}, \tag{8.1}$$

where CL_{s+b} is the confidence level of the signal-plus-background hypothesis, and CL_b the con-

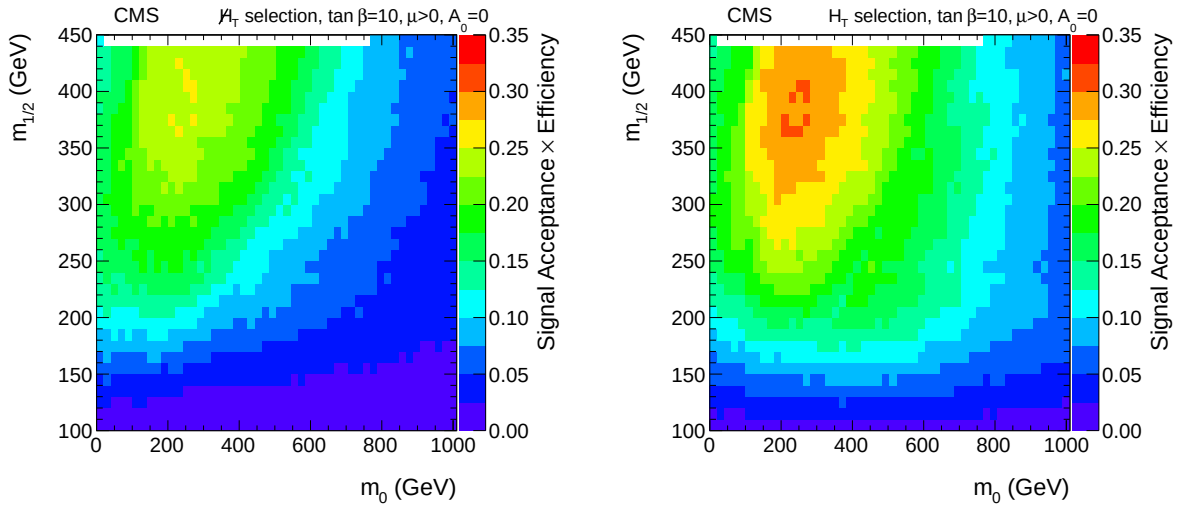

Figure 8.1: Total signal efficiency for the $\not{H}_T$ (left) and H_T (right) selections, as a function of m_0 and $m_{1/2}$ in the CMSSM. The other CMSSM parameters are $\tan\beta = 10$, $\mu > 0$, and $A_0 = 0$.

fidence level of the background only hypothesis. The confidence level of a specific hypothesis H is given by the probability that the test-statistic $t(x)$ is less than or equal to the observed value in data $t(x_{\text{obs}})$:

$$\text{CL}_H = P\left(t(x) \leq t(x_{\text{obs}})|H\right). \tag{8.2}$$

Consider the background-only hypothesis as the null-hypothesis H_0, with alternative H_1 the signal plus background hypothesis. One can prove (Neyman-Pearson lemma) that the optimal critical region is given by the following test statistic:

$$t(x) = \frac{P(x|H_1)}{P(x|H_0)} = \frac{\text{L}_{s+b}}{\text{L}_b}, \tag{8.3}$$

which is called the likelihood ratio, since $P(X|H)$ could be interpreted as the likelihood L_H to observe the data X given the hypothesis H. The test statistic $t(X)$ can then be interpreted as the likelihood ratio. For Poisson distributed background and signal-plus-background processes, the likelihoods can be written as the probability density functions (pdfs), with n the number of observed events, b the expected background events and $(s + b)$ the expected signal-plus-background events:

$$\text{L}_b = \frac{b^n e^{-b}}{n!} \qquad \text{L}_{s+b} = \frac{(s+b)^n e^{-(s+b)}}{n!} \tag{8.4}$$

The test statistics were obtained by generating a large number of pseudo experiments with s and b chosen according to the expected number of signal and background events, taking into account the statistical and systematic uncertainties.

Expected limits are calculated in the background-only hypothesis; observed limits in the signal-plus-background hypothesis. Signal contamination happens when "new physics" is also contributing to the event count in the control regions of the background estimates. These events are then wrongly considered as being due to standard model processes, resulting in overprediction of the standard model backgrounds.

The background estimates from data were used to calculate the expected upper limits on the CMSSM cross sections, under the no-signal hypothesis. The observed upper limits were calcu-

lated with the background estimates corrected for signal contamination. The μ + jets control region, used by the lost-lepton method and the hadronic tau estimate, is affected the most by contamination. The signal contamination was calculated for each simulated CMSSM point and removed from the background estimate. For both selections (high-H_T and high-$\not{H}_T$), the signal contamination was 2-3 events for the lost lepton method and 1-2 events for the hadronic tau decays. The signal contamination in the γ + jets control region was found to be negligible, while the QCD multijet background estimation was not affected at all.

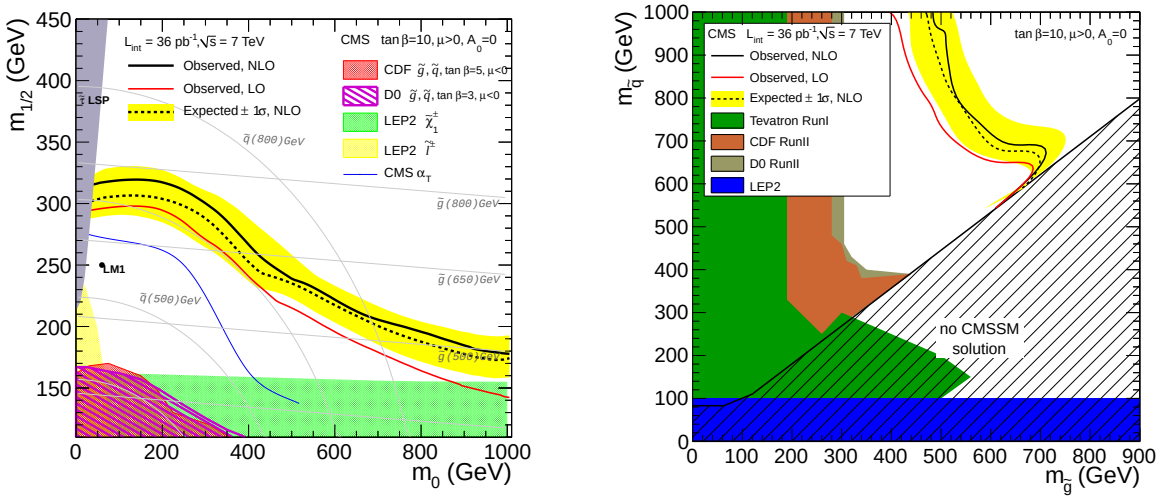

Figure 8.2: The expected and observed 95% CL upper limits in the CMSSM m_0–$m_{1/2}$ (left) and gluino–squark (right) mass planes for LO and NLO cross sections. The $\pm 1\sigma$ band corresponds to the expected limit. The contours are the combination of the H_T and the $\not{H}_T$ selections such that the contours are the envelope with respect to the best sensitivity. The CMSSM parameters are $\tan\beta = 10$, $\mu > 0$, and $A_0 = 0$. The limit from the earlier CMS analysis is shown as a blue line and limits from other experiments as the shaded regions. For the area labeled "$\tilde{\tau}$ LSP" the stau becomes the LSP. The LM1 SUSY benchmark scenario is shown as a point. The excluded area is inbetween the x-axis, the y-axis and the curves.

Figure 8.2 shows the observed and expected CLs 95% confidence level upper limits in the CMSSM m_0-$m_{1/2}$ (left) and the gluino-squark (right) mass planes for $\tan\beta = 10$, $\mu > 0$, and $A_0 = 0$. The 95% confidence level upper limits were first calculated in the m_0-$m_{1/2}$ mass plane, which is at the GUT scale, and then transformed to the gluino-squark mass plane, which is at the Electroweak scale, by solving the renormalization group equations with the aid of the ISAGEN SUSY generator. This generator calculates the sparticle mass spectrum using the CMSSM parameters m_0, $m_{1/2}$, $\tan\beta$, μ, and A_0 used for the scan. Each point in the m_0-$m_{1/2}$ space is then translated to a point in the gluino-squark space, since for a given SUSY model (here mSUGRA soft supersymmetry breaking in the CMSSM) this is a true bijective transformation.

Limits were set for both the high-H_T and the high-$\not{H}_T$ region and the envelope with respect to the best sensitivity is shown in Figure 8.2(left). These contours exclude the area under the curve for the CMSSM model for the fixed parameters $\tan\beta = 10$, $\mu > 0$, and $A_0 = 0$ in the m_0-$m_{1/2}$ mass plane. For $m_0 < 450$ GeV the $\not{H}_T$ selection is more powerful, while for high m_0 the H_T selection is more important.

A previously published search by CMS for supersymmetry in hadronic events [298] addressing

also the dijet topology, using the event shape observable α_{T} [354] is shown for reference. Although the α_{T} analysis covers also the dijet topology, their strategy to aim for the best possible removal of the QCD multijet background, reduces their signal selection efficiency. The analysis is particularly powerful for small jet multiplicities and high missing transverse momenta, but not powerful at all for high jet multiplicities, as could be seen for the rather weak exclusion at high m_0. The present analysis is powerful thanks to the high signal selection efficiency in a large fraction of the phase-space, in spite of the larger background compared to the α_{T} selection. Therefore this analysis was able to improve the limits previously set by the α_{T} analysis [299].

8.3 Interpretation with Simplified Model Spectra

The results obtained in this analysis are also interpreted in a more general manner using the simplified model spectra (SMS) approach [355, 356]. Simplified models are designed to characterize experimental data in terms of a small number of basic parameters such as masses, branching ratios, and cross sections, that are easily experimentally accessible. They exploit the fact that at the LHC the final-state kinematics of new physics are largely dominated by the parton distribution functions and phase-space factors associated with two- and three-body decays, rather than the mass differences and cross sections predicted by detailed models such as CMSSM. Using these simplified models, the experimental results can then be translated into any desired framework [299].

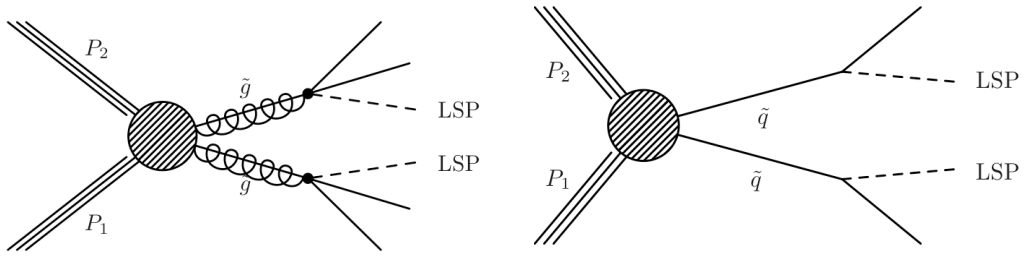

(a) SMS Topology T1: Gluino pair production (b) SMS Topology T2: Squark pair production

Figure 8.3: Diagrams of the studied simplified models. Left: gluino pair production; right: squark pair production.

The two simplified model topologies used to interpret the data are shown in Figure 8.3. Both models start from the strong production of heavy particles in pairs, whose decay chains ultimately result in a stable weakly interacting massive particle, denoted as LSP. The supersymmetric particles most likely to be produced in the strong interaction are the partners of quarks and gluons. In supersymmetry these would be the squarks ($\tilde{q}$) and gluinos ($\tilde{g}$). The Simplified Models are in fact more general than SUSY: also other models of Beyond the Standard Model (BSM) physics can lead to a jets-plus-missing transverse momentum signature. Nonetheless, the SUSY nomenclature is used further to refer to these new heavy particles and the choice of these models is discussed from a SUSY point of view.

For the gluino pair production, shown in Figure 8.3(a), $m_{\tilde{g}} \ll m_{\tilde{q}}$ is assumed. This is a reasonable assumption since, if $m_{\tilde{g}} \gg m_{\tilde{q}}$, the squark pair production would dominate. The observation of the gluino pair production would be almost impossible and it would be certainly impossible to distinguish the gluino pair production from squark pair production. Since the two-body decay $\tilde{g} \to q\tilde{q}$ is kinematically not allowed, the gluino can only decay through an off-shell squark: $\tilde{g} \to (q\tilde{q}^*) \to qq\tilde{\chi}_0$, leading to the topology shown in figure 8.3(a). Note that the gluino decay to a gluon and a neutralino is not allowed since gluinos do not carry weak charge. The decay to a gluon and higgsino is not allowed either, since the coupling strength is proportional to the mass, and the higgsino is massless.

The squark pair production, shown in Figure 8.3(b), is modeled in the assumption of $m_{\tilde{q}} \ll m_{\tilde{g}}$ for the same reason as the gluino pair production above. If the gluinos would have less mass, their production would dominate, making it impossible to distinguish the squark pair topology from the gluino pair topology. Each squark decays to a light quark and an LSP: $\tilde{g} \to q\tilde{\chi}_0$. A third topology, the squark-gluino associated production $pp \to \tilde{q}\tilde{g} \to q\tilde{\chi}_0 qq\tilde{\chi}_0$ is not considered, since it will only dominate if $m_{\tilde{q}} \approx m_{\tilde{g}}$, else it would be less abundant than gluino-gluino or squark-squark production.

The simplified models are simulated with the Pythia generator, CTEQ6L1 parton distribution functions [96], and the parametrized CMS detector simulation. For each topology samples are generated for a range of masses of the particles involved and thus more masses splittings are explored than in the CMSSM, where the ratio of the gluino and the LSP masses is approximately fixed. The measured cross section upper limits are compared to a typical reference next-to-leading order cross section from Prospino. For the calculation of the gluino pair production reference cross section, the squarks were decoupled as well ($m_{\tilde{q}} \gg m_{\tilde{g}}$, i.e. the squark mass was set at a kinematically inaccessible scale). In the case of the squark pair production, this reference cross section corresponds to the squark-antisquark cross section with four light flavours included and decoupled gluinos ($m_{\tilde{g}} \gg m_{\tilde{q}}$, i.e. the gluino mass was set at a kinematically inaccessible scale).

Figures 8.4(a) and 8.4(b) show the signal efficiency of the high-$\not{H}_T$ and the high-H_T regions, respectively, for gluino pair production (topology T1, shown in Figure 8.3(a)) as a function of the gluino mass and the LSP mass. The signal efficiencies for the high-$\not{H}_T$ and high-H_T regions for the squark pair production are shown in Figures 8.4(c) and 8.4(d), respectively, as a function of the squark mass and the LSP mass. Note that only the lower half of the planes are filled, since the models are only valid when the gluino or squark masses are higher than the mass of the LSP. The signal selection efficiency increases for higher gluino and squark masses and is low on the diagonal. On the diagonal, where $m_{\tilde{g}\,\text{or}\,\tilde{q}} \gtrsim m_{\text{LSP}}$, the mass splitting is small and jets are produced with lower transverse momentum. This also results in low momentum for the massive LSP, and hence small $\not{H}_T$, complicating new physics discoveries in this corner of phase-space. The efficiency is highest for squarks or gluinos with masses higher than twice the LSP mass, which leads to hard jets and sizeable missing transverse momentum. The selection efficiency for the gluino pair production is also higher than the selection efficiency for the squark pair production, which is not surprising, since the search is optimized for at least three jets.

The limit calculation in the SMS space is performed using the Bayesian framework, also used for the 95% CL limits on the signal reported in Table 8.1, with, as described above, a nearly Gaussian prior for the background and a flat prior for the signal. Signal contamination was not

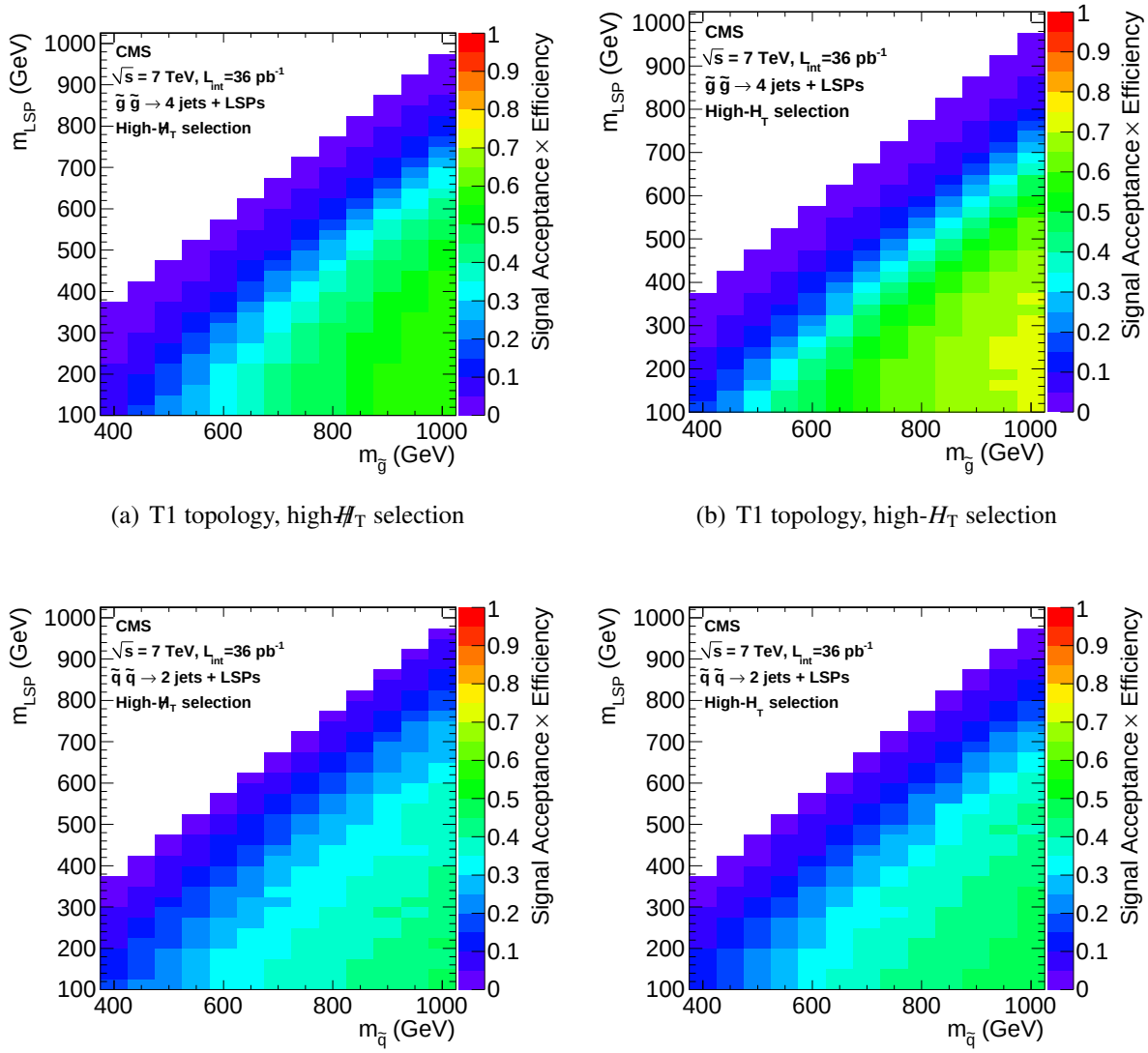

(a) T1 topology, high-$\not{H}_T$ selection

(b) T1 topology, high-H_T selection

(c) T2 topology, high-$\not{H}_T$ selection

(d) T2 topology, high-H_T selection

Figure 8.4: Total high-$\not{H}_T$ (a) and high-H_T (b) selection efficiencies for gluino production as a function of the gluino mass and the LSP mass. Total high-$\not{H}_T$ (c) and high-H_T (d) selection efficiencies for squark production as a function of the squark mass and the LSP mass.

considered since the studied topologies do not produce prompt muons or photons and hence do not contaminate the background estimation control regions.

The third generation is not considered in the signal generation for the squark pair production since the analysis was not designed to be sensitive to stop pair production or sbottom pair production. A search for heavy flavour squarks would need a totally different approach. Stop particles are most likely to decay to their top counterparts if the decay is kinematically allowed. This needs a totally different analysis optimized for $t\bar{t}$ like signatures. If the stop cannot decay to a top, the most probable decay would be to sbottom and a W or a bottom and a chargino $\tilde{\chi}^{\pm}$. Both would lead to events with an enhanced amount of leptons, not efficiently covered by

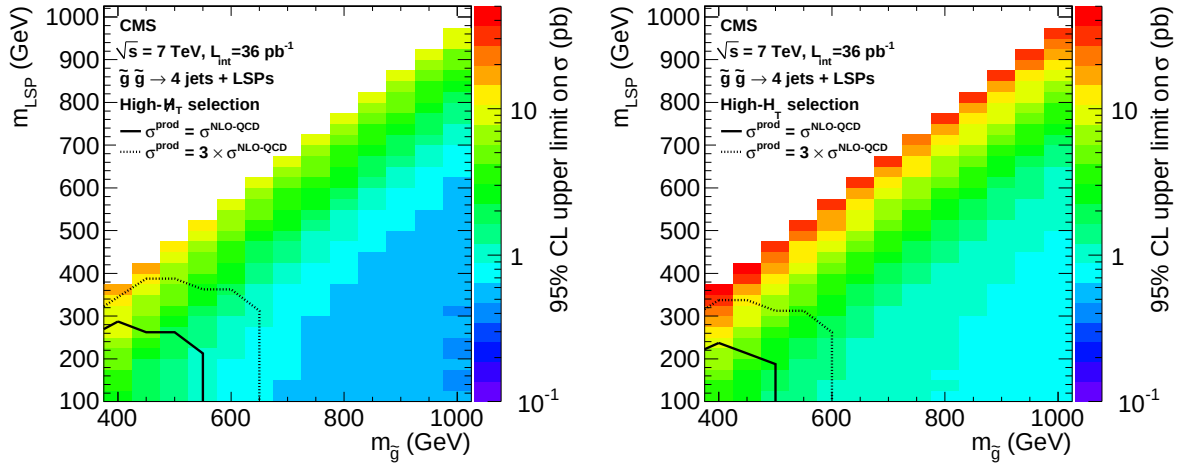

(a) T1 topology, high-$\not\!\!H_T$ selection

(b) T1 topology, high-H_T selection

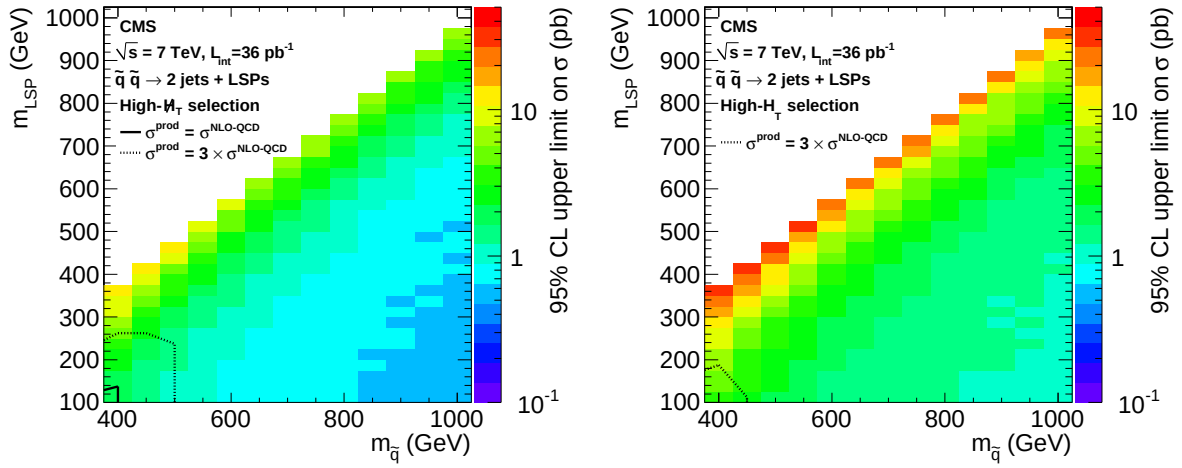

(c) T2 topology, high-$\not\!\!H_T$ selection

(d) T2 topology, high-H_T selection

Figure 8.5: (Top) 95% CL upper limits on the gluino pair-production cross section for the high-$\not\!\!H_T$ selection (top left) and the high-H_T selection (top right), as a function of the gluino mass and the LSP mass. (Bottom) 95% CL upper limits on the squark pair-production cross section for the high-$\not\!\!H_T$ selection (bottom left) and the high-H_T selection (bottom right), as a function of the squark mass and the LSP mass. The contours where the reference cross section and three times this cross section can be excluded are shown.

an all-hadronic (i.e. jets-plus-missing transverse momentum) search. The discovery of these signatures would profit from a search with b-tagging. Further on, covering these topologies would make the estimation of signal contamination more difficult to handle, while nothing is gained in terms of sensitivity.

The 95% Confidence Level (CL) upper limits on the cross section of di-squark production and di-gluino production for both the high-$\not\!\!H_T$ search region and the high-H_T search region are shown in Figure 8.5. The area where the reference cross section for di-squark and di-gluino production,

calculated with PROSPINO, can be excluded is inside the contour. Also the contour excluding three times the reference cross section is shown as a dashed line. The search is found to be more sensitive to the gluino pair production than to the squark pair production. This is a consequence of the three central jets requirement. In order to be sensitive to di-squark production, at least one additional central high-p_{T} ISR jet needs to be radiated by the di-squark system. Therefore the di-squark topology is covered more efficiently by the α_T and Razor dijet searches.

The high-$\not\!\!H_{\mathrm{T}}$ selection is found to be more sensitive than the high-H_{T} selection for both the squark and gluino pair production. Although the "Signal Acceptance × Efficiency" plots for the Simplified Models (Figure 8.4) show that – as expected – the high-H_{T} region has a higher selection efficiency than the high-$\not\!\!H_{\mathrm{T}}$ region, this effect is spoilt by the remaining Standard Model background in this region. The high-$\not\!\!H_{\mathrm{T}}$ region is "depleted" from background events (19 events expected), while more then twice this amount can show up in the high-H_{T} region (44 events expected). These 95% CL upper limits on the cross section can be translated into a limit on any complete model, SUSY or non-SUSY, predicting a jets and missing transverse energy topology.

8.4 Overview of the 2010 results

The results of the jets-plus-$\not\!\!H_{\mathrm{T}}$ search were compared to a previous all-hadronic SUSY analysis in CMS with the α_{T}-variable, and a later analysis with the Razor variables within the context of the CMSSM in Figure 8.6.

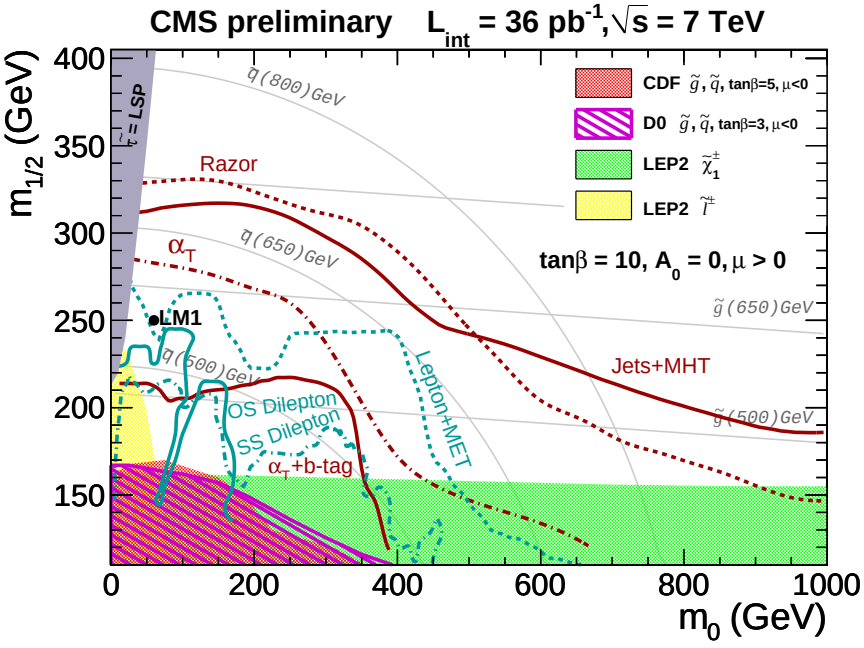

Figure 8.6: Results of the 2010 CMS SUSY analyses, interpreted as exclusion regions (below the curves) in the CMSSM. The all-hadronic analyses are shown as red contours, while the leptonic analyses are shown as cyan contours.

The all-hadronic analyses are shown as red contours, while the leptonic analyses are shown as cyan contours and the exclusion regions are in between the curves and the x- and y-axes. The

CMSSM predicts more hadronic final states, than final states with leptons. Therefore the the all-hadronic analyses are more sensitive and excluding bigger regions of phase-space.

The results of the 2010 all-hadronic analyses have also been interpreted in the simplified model spectra. Figure 8.7 shows the 95% C.L. exclusion limits on the cross section of the T1 (di-gluino production) and T2 (di-squark production) topologies as a function of the LSP mass and the gluino/squark mass. The LSP and gluino/squark masses excluded by the combination of the three all-hadronic searches is shown by the black contour line. The regions confined by the contours and the x- and y-axes are excluded. For this combination, the most sensitive search region of the present analysis, the high-$\not{H}_T$ selection, was combined with the results of the α_T- and Razor-search. One can also see that the models in which the mass difference between the LSP on the one hand, and the gluino/squark on the other hand, is small, is not efficiently covered by the present searches, since rather high cross sections are not excluded. This topology is not easily covered, since a small mass difference does not allow for much visible and invisible momentum in the events, making it (almost) impossible to distinguish these events from the huge QCD background.

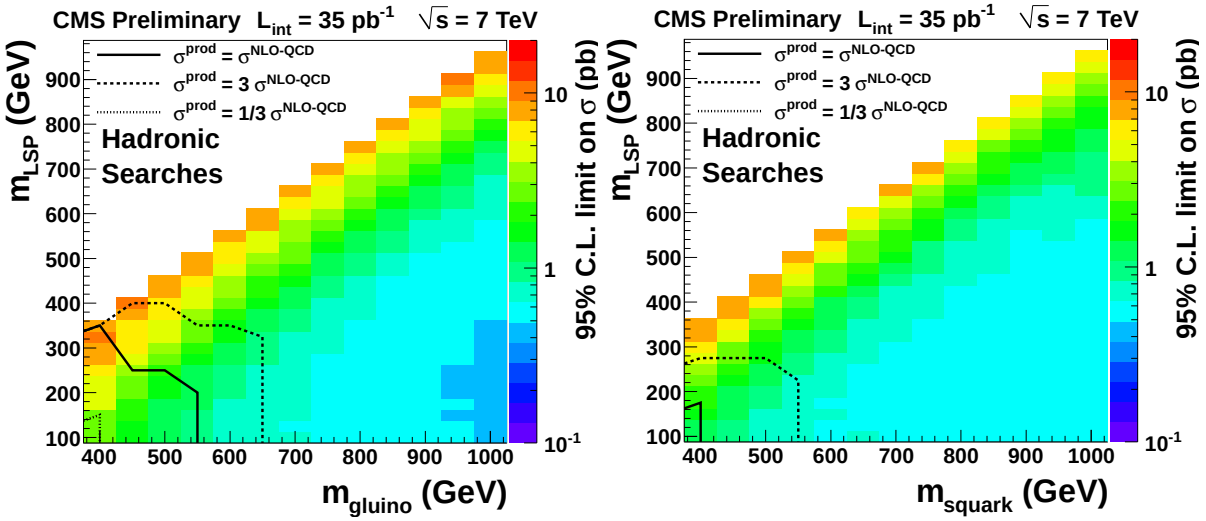

Figure 8.7: 95% C.L. exclusion limits of the combined all-hadronic SUSY searches in CMS on the cross section of the T1 and T2 topologies as a function of the LSP mass and the gluino/squark mass, obtained with 35–36 pb^{-1} of data recorded in 2010.

Part IV

Glossary, Summary and References

Glossary

- **2HDM**: Two Higgs Doublets Model: minimal non-trivial extension of the SM Higgs sector.
- **ALCT**: Anode Local Charged Track: CSC muon segment built using only wire information, used for BX-assignment.
- **ALICE**: A Large Ion Collider Experiment, a dedicated heavy ion experiment at LHC.
- **AMSB**: Anomaly Mediated Supersymmetry Breaking.
- **AN**: Analysis Note: internal document describing a physics analysis.
- **APD**: Avalanche Photo Diode: part of ECAL (EB) readout, converts scintillation light into an electric current.
- **ARC**: Analysis Review Committee: group of physicists in charge of reviewing an analysis.
- **ASIC**: Application Specific Integrated Circuit: programmable chip, used in Level-1 Trigger electronics.
- **ATLAS**: A ToroidaL ApparatuS: a general-purpose LHC experiment.
- **BCM**: Beam Condition Monitor: diamond detector installed close to the beampipe, part of the BRM system.
- **BRM**: Beam Radiation Monitoring: system measuring the beam radiation, used for monitoring the beams.
- **BSC**: Beam Scintillation Counter: scintillators installed on HF, indicating whether an inelastic collision happened inside CMS.
- **BPTX**: Beam Pickup ant Timing for the eXperiments: detectors picking up the radio-frequent signal of proton beams when they pass through it.
- **BSM**: Beyond the Standard Model: physics theories and frameworks (families of theories) that are possible extensions of the Standard Model.
- **BX**: Bunch Crossing: the exact moment when two bunches of a beam cross each other in the center of the detector, possibly giving rise to a proton-proton collision. At design luminosity, bunches will cross every 25 ns.
- **BR**: Branching Ratio: probability for a mother particle to decay to certain daughter particles.
- **CDF**: Collider Detector Facility: general-purpose experiment at Tevatron, Chicago, Illinois.
- **CDM**: Cold Dark Matter: DM that moves slow compared to the speed of light.

- **CERN**: European Organization for Nuclear Research, housed in Geneva. Historically: "Conseil Européen pour la Recherche Nucléare".
- **CLCT**: Cathode Local Charged Track: CSC muon segment built using only strip information.
- **CMS**: Compact Muon Solenoid: a general-purpose LHC experiment.
- **CMSSM**: Constrained Minimal Supersymmetric extension of the Standard Model.
- **CT10**: One of the three groups in the global analysis of hadronic data, providing PDFs. Formerly known as CTEQ.
- **CTEQ**: One of the three groups in the global analysis of hadronic data, providing PDFs. Now CT10.
- **DØ**: Detector at collision point Ø: general-purpose experiment atTevatron, Chicago, Illinois.
- **DAQ**: Data Acquisition: Readout electronics and computing infrastructure responsible for the readout and online selection of events.
- **DESY**: Deutsche Elektronen Synchrotron: German research centre for particle physics.
- **DM**: Dark Matter: a currently undetermined type of matter which accounts for a large part of the mass of the Universe.
- **DPG**: Detector Performance Group: groups CMS physicists working on the same subdetector, In CMS there are 6 DPGs: Trigger (L1 + HLT); ECAL; Forward detectors; HCAL; Muon; and Tracker.
- **ECAL**: Electromagnetic Calorimeter:
  - **EB**: ECAL Barrel;
  - **EE**: ECAL Endcap.
- **FEB**: Front-End Board: readout electronics of the various subdetectors of CMS, mounted directly on the detector (the "Front-End" of the readout chain).
- **FED**: Front-End Driver: part of the DAQ that extracts the data from the front-end electronics on the detector upon a L1A signal.
- **FSR**: Final State Radiation: quarks or gluons radiated by the partons after the hard interaction took place.
- **GMSB**: Gauge Mediated Supersymmetry Breaking.
- **GUT**: Grand Unification Theory: Theory unifying the electromagnetic, weak and strong force.
- **HCAL**: Hadronic Calorimeter:
  - **HB**: HCAL Barrel;
  - **HF**: HCAL Forward;
  - **HE**: HCAL Endcap;
  - **HO**: HCAL Outer.
- **HERA**: Hadron Elektron Ring Anlage: electron-proton collider at DESY, Hamburg.
- **HLT**: High-Level-Trigger: second level of event selection in CMS, relies on a commercial pc farm.

- **HM**: High-Mass benchmark points in the mSUGRA space used by CMS to have abroad coverage of experimental signatures
- **HPD**: Hybrid Photo Diode: part of HCAL (HB, HE, HO) readout, converts scintillation light into an electric current.
- **IP**: Interaction Point, (0,0,0), the origin of the CMS reference frame. Place where two beams are brought into collision.
- **IR**: Interaction Region: underground areas of the LHC that could be used for proton-proton interactions.
- **ISR**: Initial State Radiation: quarks or gluons radiated by the partons before the hard interaction takes place.
- **JER**: Jet Energy Resolutions: the accuracy of the jet energy measurement in CMS.
- **JES**: Jet Energy Scale: calibration of the jet energy measurement in CMS.
- **JSON**: JavaScript Object Notation: easy readable format, used in CMS for bookkeeping the good data (good lumisections) in the different runs of the data taking period.
- **L1**: Level-1 Trigger: first level of event selection in CMS, built with custom electronics.
- **L1A**: Level-1 Accept: signal indicating that an event is selected by the L1 Trigger. The L1A is sent to the CMS Frontend electroncs to start the readout of the detailed event information kept in the various buffers located on the detector.
- **LCT**: Local Charged Track: muon track segment in the CSC system, built from an ALCT and a CLCT.
- **LEP**: Large Electron Positron collider, precessor of the LHC as flagship accelerator at CERN, Geneva.
- **LHC**: Large Hadron Collider, the world most powerful particle accelerator, built at CERN, Geneva.
- **LM**: Low-Mass benchmark points in the mSUGRA space used by CMS to have a broad coverage of experimental signatures.
- **LSP**: Lightest Supersymmetric Particle: SUSY with R-parity predicts the existence of a stable supersymmetric particle.
- **Luminosity section**: a fixed period of time, set to 2^{20} LHC orbits, corresponding to 93 s, during which the trigger thresholds and prescales are not changed.
- **MC**: Monte-Carlo Simulation: simulation of the physics process in CMS. It consists of:
  - Event generation;
  - Simulation of the energy deposits of the stable particles that are tracked through the detector;
  - Simulation of the trigger on these energy deposits;
  - Reconstruction of the event.
- **MET**: Missing Transverse Energy: the magnitude of the transverse momentum $|\vec{\not{E}}_{\mathrm{T}}|$, obtained by summing the p_{T} of all particles in the detector: $\vec{\not{E}}_{\mathrm{T}} := \sum_i \vec{p}_{\mathrm{T}}(i)$. Missing

transverse energy is often denoted $\not{E}_{\mathrm{T}}$ or $E_{\mathrm{T}}^{\mathrm{miss}}$.

- **MSSM**: Minimal Supersymmetric extension of the Standard Model: minimal version of Supersymmetry accomodating the Standard Model.
- **MSTW**: Martin, Stirling, Thorne, Watt: one of the three groups in the global analysis of hadronic data, providing PDFs.
- **mSUGRA**: Minimal Supergravity: minimal version of supergravity, a field theory combining supersymmetry and general relativity.
- **NNPDF**: One of the three groups in the global analysis of hadronic data, providing PDFs.
- **NUHM**: Non-Universal Higgs Mass models: BSM models with different Higgs particles that have different masses at the unification scale.
- **PAG**: Physics Analysis Group: groups CMS physicists working on the same physics. In CMS there are 9 PAGs: B-physics and quarkonia; Electroweak physics; Exotica; Forward physics; Heavy Ion physics; Higgs physics; QCD; SUSY; and Top-quark physics;
- **PAS**: Public Analysis Summary: public document describing the physics analysis. Used for conferences and often the starting point for a paper.
- **POG**: Physics Object Group: groups CMS physicists working on the same physics object, used later on in analysis. In CMS there are 6 POGs: B-tagging and vertexing; Electrons and Photons (EGamma); Jets and Missing Transverse Energy (JetMET); Muons; Particle-Flow and Tau ID; and Tracking.
- **PDF**: Parton Distribution Function: function describing the distribution of the parton momenta inside the proton.
- **PETRA**: Positron Electron Tandem Ring Anlage: elektron positron collider at DESY, Hamburg.
- **PS**: Proton Synchrotron: accelerator part of the LHC injection chain.
- **PF**: Particle-Flow: algorithm reconstructing all stable particles in an event.
- **PMSB**:Planck-scale Mediated Supersymmetry Breaking.
- **PMT**: Photo Multiplier Tube: part of HCAL (HF) readout, converts scintillation light into an electric current.
- **RBX**: Readout BoX: box containing HCAL on-detector electronics.
- **RG**: Renormalization Group: equations used to propagate the coupling constants between different scales.
- **RPC**: Resistive Plate Chamber: fast muon detector used in the CMS experiment.
- **RTFM**:Read The F*!#in'Manual, best advice one can give to a Ph.D. Student.
- **SCX**: Surface Control eXperiment: surface building with control room, online PC farm for HLT, etc.
- **SEU**: Single Event Upset: non-permanent failure of a micro-electronics device (such as a microprocessor or semiconductor memory). SEUs are caused by particles striking the electronics and freeing electric charge by ionization. This results in a change of state (for instance a bit flip $\mathtt{0} \rightarrow \mathtt{1}$). The faulty electronics are resolved by resetting

or reloading the software of the electronics. This is one of the softest radiation effects seen in LHC and CMS electronics, leading to down-time of the detector during data-taking.

- **SGX**: Surface Gas eXperiment: surface building holding all gas services.
- **SLC**: Stanford Linear Collider at Stanford University, California.
- **SM**: Standard Model of particle physics.
- **SMS**: Simplified Model Spectra:
- **S$\bar{\text{p}}$pS**: Super anti-proton proton Synchrotron: first proton anti-proton collider, built at CERN, Geneva.
- **SPS**: Super Proton Synchrotron: accelerator installed in the S$\bar{\text{p}}$pS tunnel, part of the LHC injection chain.
- **SUSY**: Supersymmetry, framework for the extension of the Standard Model, in which every fermion has a bosonic partner and vice versa.
- **SX**: Surface eXperiment: surface assembly hall.
- **TDR**: Technical Design Report: document detailing the technical design of a section of the CMS experiment.
- **TOF**: Time Of Flight: flight time of a particle.
- **TOTEM**: TOTal Elastic and diffractive cross section Measurement: dedicated pp-collision cross section measurement experiment at the LHC.
- **TRK**: Tracker:
  - **TIB**: Tracker Inner Barrel;
  - **TOB**: Tracker Outer Barrel;
  - **TID**: Tracker Inner Disks;
  - **TOD**: Tracker Outer Disks.
- **UA1**: Experiment at S$\bar{\text{p}}$pS located at the Underground Area 1.
- **UA1**: Experiment at S$\bar{\text{p}}$pS located at the Underground Area 2.
- **UE**: Underlying Event: part of the proton proton collision caused by the coloured proton-remnants not involved in the hard interaction.
- **UFO**: Unidentified Falling Objects: dust particles interacting with the proton beams inside the beampipe, leading to beam losses.
- **USC**: Underground Service Cavern: underground cavern for electronics and services.
- **UXC**: Underground eXperiment Cavern: experimental cavern.
- **VPT**: Vacuum Photo Triode: part of ECAL (EE) readout, converts scintillation light into an electric current.

Executive Summary

RPC Upgrade Simulation Studies

The Muon system of the CMS detector was not completed for the initial years of LHC running. Compared to the detector foreseen in the Technical Design Report, the fourth muon station is not fully installed for both the CSC system as the RPC system. For the RPC system the whole fourth layer is missing, while for the CSC system the chambers closest to the beam pipe were already installed. Furthermore, the RPC detectors are only installed up to a pseudorapidity of $|\eta| \leq 1.6$, while the original design included RPCs up to $|\eta| \leq 2.1$.

Due to financial reasons, the high-η chambers and all chambers of the fourth station were "descoped" (i.e. removed from the installation schedule). The RPC-system installed was restricted to the minimum necessary for the first years of low luminosity running of the LHC. Furthermore, it was not certain if the RPC technology would be able to withstand the high rates expected at $1.6 \leq |\eta| \leq 2.1$.

In the past, a modification to the RPC design in CMS was proposed to enhance the trigger efficiency and lower the trigger rate in the endcaps of the RPC system. Installing five layers instead of four would yield more or less the same trigger efficiency by requiring 4-out-of-5 coincidences instead of 3-out-of-4 coincidences, but would provide a better measurement of the transverse momentum and would be less vulnerable to "fake" muons. In this way the trigger rate could be lowered sufficiently. Unfortunately, an independent fifth layer was not feasible in the endcap, but the idea was modified to a double layered second station, where one could reduce the fake rate by asking for a coincidence of hits in both layers. This required to remove the existing second station and install it as the fourth station, while a completely new double layered station would be built.

I started my Ph.D. investigating the working principle of the RPC detector and preparing the experimental hall at the Institute for Nuclear Sciences at the Ghent University, to start the RPC construction. The quality tests used in the past for the CMS RPC production were investigated and the different test stands were built. A gas mixer was designed and built in collaboration with the CERN Gas Group. Although the preparations were proceeding well, the CMS Collaboration decided to wait for more studies confirming the new design. I decided to perform a simulation study to show the improvements of the double second station to the RPC Trigger.

First of all I made sure the simulation software was performing properly and past results obtained in the TDR geometry could be reproduced. I studied in detail the different backgrounds in the muon system for the LHC running at its design energy and luminosity. The fifteen year old FLUKA simulations turned out to have made pretty good predictions, still standing after all these years. For the endcap muon system $\eta \leq 1.6$ a maximum background rate of $10\,\mathrm{Hz/cm^2}$ as upper limit is a reasonable estimate. Since no varying background could be implemented in the

RPC simulation, the study was performed with an overall background of 10 Hz/cm^2.

The RPC trigger simulation showed an increase of the RPC trigger efficiency with 20%, due to the addition of a fourth layer, as such becoming a fully independent trigger system in CMS. This restores the originally designed redundancy of the muon system. When comparing the TDR geometry (with four layers) to the new geometry with a double layered second station, the rate reduction, as obtained in the previous study with five independent stations, could not be obtained. The crucial difference between an independent fifth layer and a doubled second layer is the increased the increased lever arm, which improves the p_{T} assignment. This improved p_{T} measurement results in a much lower fake rate. A slightly lower trigger rate was obtained by requiring a coincident hit in both layers of the new double layered second station. However this reduction was not significant and not worth the additional cost and risk associated with building a new second station and removing and reinstalling the properly working current station. Hence, the CMS Collaboration has opted to complete the design geometry, consisting of the installation of the fourth station of RPC detectors.

As a side project also the robustness of the RPC trigger was investigated by switching off a single layer. This study showed that the second station has no longer the privileged status as the "trigger seed station". If the hit in the second station is missing, another station is chosen by the RPC trigger logic to seed the muon candidate. The most important measurement not to miss is the first station, which is indispensable to measure any bending of the track, indispensable to estimate the transverse momentum of muon candidate.

To study the influence of the RPC trigger on the Global Muon Trigger, the neutron background has to be treated in the same way in the simulation of all muon detectors. The implementation of the neutron background in the simulation of the muon detectors had always been of low priority, although the CSC simulation experts had been continuously working on it. Together with the CSC simulation experts I worked on the implementation of the neutron background simulation in the RPC system and this collaboration turned into a working neutron simulation for both the CSC and the RPC system. This result was crucial to perform Global Muon Trigger studies for the upgrade of the CMS detector. Furthermore, the improvements in GEANT in the past ten years resulted in a trustworthy neutron background simulation that even could reproduce the fifteen year old FLUKA simulations, performed in a far less detailed geometry and which used a very rough sensitivity factor for neutrons to cause hits in the muon detectors.

Datadriven Z($\nu\nu$) Prediction

Supersymmetry is a good candidate to describe phenomena beyond the Standard Model. At hadron colliders, new particles are expected to be produced in pairs (assuming R-parity), mainly by the strong interaction. Generally, these particles can decay to one or more jets (depending on their colour charge) or leptons, plus a Lightest Supersymmetric Particle (LSP) which interacts only very weakly with matter. Final states consist of leptons, visible transverse momentum (H_{T}) due to the jets, plus missing transverse momentum ($\not{H}_{\mathrm{T}}$) from the LSP. In this thesis a search for Supersymmetry in the zero-lepton channel is performed, with the jets plus missing transverse momentum search. In most of the SUSY models the all-hadronic channel is believed to be the most sensitive channel, since the QCD-coupling to squarks and gluinos is much stronger than the electroweak coupling required for the production of heavy flavour quarks and leptons. The jets and missing transverse momentum search is one of the most sensitive searches in

this channel due to its inclusive nature. Unfortunately, Standard Model processes have similar signatures with $\not{H}_T$ introduced by vector bosons decaying to leptons or jet mismeasurements in QCD multijet events. The quest for Supersymmetry observation in events with this final state is challenging due to the large background.

One of the largest backgrounds is the Z + jets background, where the Z-boson decays to two neutrinos. This background is irreducible since its signature consist exactly of jets and missing transverse momentum. I estimated this background from data using a sample of γ + jet events, using the electroweak correspondence between the photon and the Z-boson. Although the photon is massless and the Z-boson is massive, the mass effects are negligible at energies higher than the Z-boson mass. At $p_T^\gamma > 100\,\text{GeV}/c$ photon and Z production are very similar, with only a minor different due to different electroweak couplings. The photon method has big advantages with respect to other methods to estimate the $Z(\nu\nu)$ background. While the $Z(\mu\mu)$ sample is much cleaner than theγ + jet sample, the latter has a factor ≈ 6 more statistics, allowing a much more precise estimation. The $Z(\nu\nu)$ background can also be estimated from a $W(\mu\nu)$ sample, but this method suffers from W contamination from the decay of $t\bar{t}$ events. For the jets plus missing momentum search in the 2010 data, the photon method was adopted to estimate the $Z(\nu\nu)$ background.

The method started with the selection of a clean photon + jets sample. The PF-jet related to the photon was removed from the jet list and all event properties (H_T and$\vec{\not{H}}_T$) were recomputed. The jets plus missing transverse momentum event selection was then applied to this photon + jets sample. A precise photon to Z-boson correction factor was estimated from Monte-Carlo simulation. The systematic uncertainty on the scale (LO Monte-Carlo simulation scaled to a NLO cross section) was determined with the aid of BlackHat theorists. Z + 2 jet events and γ + 2 jet events were simulated at NLO with the BlackHat computing routines and compared to LO simulations. They estimated the scale uncertainty to 4 to 6% for the different search regions. A limiting systematic uncertainty on the photon to Z-boson correction factor came from the Monte-Carlo simulation statistics, being 7% to 13% for the different search regions. The photon purity and photon selection efficiency were taken from the QCD photon cross section measurement, were the photon purity measurement contributed dominantly to the overall systematic uncertainty: 9% to 10% for the different search regions. Furthermore a contribution of 5% of fragmentation photons was subtracted from the photon + jets sample, since no similar channel is available for the production of Z plus jet events is available.

The final prediction lead to a 14% to 17% precise estimation of the $Z(\nu\nu)$ background to the jets plus missing momentum search. Combined with other precise estimations of the QCD and the W/top background lead this to the prediction of 111.3 ± 18.5 events in the baseline selection, while 111 events were observed; 18.8 ± 3.5 events predicted in the high-$\not{H}_T$ selection, 15 observed; and 43.8 ± 9.2 events predicted in the high-H_T selection, 40 observed. These results were then interpreted in both the CMSSM model as in model independent Simplified Model Spectra. This analysis pioneered many new methods for the estimation of Standard Model backgrounds with very high precision. These methods are now in use in several other CMS analysis, not restricted to the search for Supersymmetry.

Nederlandstalige Samenvatting

Gedurende de twintigste eeuw is er enorme vooruitgang gemaakt in het begrijpen van de materie rondom ons. Dit voortschrijdend inzicht werd bewerkstelligd door zowel grote vooruitgang in de experimentele fysica als grote sprongen in de theoretische fysica. Ernest Rutherford kon in 1911 uit experimenten waarbij hij α-deeltjes op een goudfolie schoot het bestaan van de atoomkern aantonen. Niels Bohr kon daarenboven een theoretisch model opstellen dat atomen beschreef als een wolk van elektronen in verschillende energietoestanden die rond een zware atoomkern cirkelen. Tijdens de eerste helft van de twintigste eeuw werd ook de kwantum-mechanica ontwikkeld. In de tweede helft van de twintigste eeuw werden zeer nauwkeurige beschrijvingen voor de elektromagnetische, en de sterke en zwakke kracht ontwikkeld en samengebald tot het zogenaamde Standaard Model.

Het Standaard Model van de deeltjesfysica beschrijft alle fundamentele deeltjes, nl. zes quarks en zes leptonen, en de interacties tussen deze deeltjes, overgedragen door de ijkbosonen γ, W, Z en g. De voorspellingen van het Standaard Model werden in de laatste decennia bevestigd door metingen, verricht aan deeltjesversnellers, met een nauwkeurigheid van één op een miljoen. Dit is een ongekend succes voor een theorie die zo'n breed gedeelte van de fysica beschrijft. Er is echter nog een ontbrekend puzzelstukje. Het Standaard Model is essentieel een theorie van massaloze deeltjes maar verklaart slechts ten dele uit waar de massa van de deeltjes vandaan komt. De Belgen Robert Brout en François Englert, en de Schot Peter Higgs, stelden in 1964 een model voor waarin de deeltjes van het Standaard Model massa krijgen door interactie met het zogenaamde Higgs-veld. Het Higgs-deeltje is het kwantum van dit veld en is tot vandaag nog niet gevonden. De zoektocht naar dit deeltje is een van de belangrijkste bestaansredenen voor de krachtigste deeltjesversneller van vandaag: de Large Hadron Collider (LHC), gebouwd door het Europees Centrum voor Kern- en Deeltjesfysica, CERN, in Genève.

Met de ontdekking van het Higgs deeltje zal het verhaal van het Standaard Model echter nog niet afgelopen zijn. Als het Higgs deeltje blijkt te bestaan (er zijn ook andere, minder plausibele, theorieën voor het genereren van de massa's van de deeltjes van het Standaard Model zonder het Higgs deeltje), is er geen verklaring waarom het de massa zou hebben die experimentele waarnemingen van het Standaard Model vereisen. Dit leidde tot het ontwikkelen van allerlei nieuwe theoriën, waarvan het Standaard Model enkel de laag-energetische variant zou zijn. Een van deze theoriën is Supersymmetrie. Deze theorie voorspelt dat voor elk bestaand deeltje er een nieuw, nog niet ontdekt, partnerdeeltje moet bestaan. Het voorspelt dus een heel nieuw spectrum aan deeltjes, waarvan het deeltje met de laagste massa niet veel meer dan een factor tien zwaarder zou mogen zijn dan het Higgs deeltje. Het onderzoek verricht in deze thesis speelt zich af in de zoektocht naar deze nieuwe supersymmetrische deeltjes aan de LHC.

De LHC is de krachtigste deeltjes versneller ter wereld, in gebruik genomen op 30 maart 2010. In deze versneller worden protonen versneld tot energieën van 7 TeV en daarna tot botsing

gebracht. Rondom de punten waar protonen botsen werden experimenten opgebouwd om alle eigenschappen van de botsingen op te meten. De Belgische universiteiten sloegen de handen in elkaar en besloten samen te werken in één experiment, de Compact Muon Solenoid (CMS). Aan dit experiment werken zo'n 3000 wetenschappers, van 750 instituten, uit niet minder dan 40 landen. CMS is één van de twee polyvalente experimenten gebouwd aan de LHC, heeft een lengte van 25 m, breedte van 15 m, weegt meer dan 12 500 ton en heeft meer dan 70 miljoen uitleeskanalen.

De CMS detector is gebouwd om de proton-proton botsingen uiterst nauwkeurig te reconstueren, en gebruikt daarvoor een spoordetector voor het detecteren van het traject van deeltjes gecreëerd in de botsingen en calorimeters voor het opmeten van de energie van deze deeltjes. Een speciaal deeltje, het muon, wordt maar heel zelden geproduceerd in proton-proton botsingen, en is heel belangrijk voor het opmeten van zeer zeldzame processen in CMS. Omdat de energie van dit deeltje niet goed gemeten wordt in de calorimeters, werden er muondetectoren gebouwd rondom deze calorimeters, die heel precies de snelheid van de muonen meten.

Wanneer de LHC op volle kracht draait, zal er elke 25 nanoseconden een botsing optreden. Dit betekent zo'n slordige 40 miljoen botsingen per seconde. Met de huidige computer- en informatietechnologie is het onmogelijk om alle informatie van deze botsingen op te slaan. Daarom zijn er selectieprocedures geïnstalleerd, die "triggers" worden genoemd. Deze triggers werden opgedeeld in twee niveau's: de Level-1 Trigger, die uit speciaal vervaardigde elektronische circuits bestaat, en de High-Level-Trigger, die gebruik maakt van computers voor het berekenen van geavanceerde selectie algoritmes.

De muon trigger was niet volledig geïnstalleerd voor de eerste run van de LHC in 2010: een gedeelte ontbrak, namelijk de vierde laag Resistive Plate Chambers (RPCs). Drie lagen werden reeds geïnstalleerd, maar voor een vierde laag werden er niet genoeg fondsen gevonden. Verder was het ook niet nodig het volledige systeem te installeren in 2010, omdat de eerste jaren de LHC nog niet op volle kracht zal werken. In een eerdere studie was aangetoond dat een vijfde laag RPCs voor een aanzienlijk betere werking van de muon trigger zou zorgen. Helaas is het niet mogelijk om een effectieve vijfde laag te installeren, maar er werd geopperd dat de verdubbeling van de tweede laag ook voor een verbeterde werking zou zorgen. Om dit te onderzoeken, werd de geometrie van CMS in de simulatie veranderd. Vier verschillende modellen werden getest: de huidige geometrie met drie lagen RPCs, de geometrie van het oorspronkelijke design met vier lagen RPCs en dan twee geometrieën met een dubbele laag RPCs: één geïnstalleerd in de tweede laag, en één met een dubbele laag geïnstalleerd in de vierde laag RPCs. Een miljoen muonen werden gesimuleerd en gevolgd door de verschillende CMS geometriën.

Als de LHC werkt op zijn voorziene kracht komen er ontzettend veel laag-energetische neutronen vrij. Deze zorgen voor grote achtergrondstraling in de muon detectoren, waarvoor midden jaren 1990 studies uitgevoerd waren. Ik vergeleek de resultaten van deze studies met meer recentere resultaten waarin de gevoeligheid van RPCs voor neutronen werd vergeleken met simulaties en vond dat een achtergrondstraling van 10 Hz/cm^2 een goede afschatting was van de "hitrate" van de RPC detectoren. Deze achtergrondstraling werd in de simulatie geïntegreerd, samen met enkele zeer conservatieve (worst-case) aannames voor de achtergrondstraling.

De simulaties toonden dat een vierde laag zeer noodzakelijk is voor de goede werking van de muon trigger gebaseerd op RPC detectoren. De efficiëntie om een muon te detecteren wordt

verhoogd van net iets minder dan 80% naar net iets minder dan 100%, wat het eigenlijke design criterium was. Simulaties van de dubbele tweede laag toonden aan dat deze geometrie iets beter is in het ondubbelzinnig ontdekken van een muon, waardoor de trigger beter werkt. Maar die verbetering is niet zo groot als verwacht voor een volledig onafhankelijk vijfde laag. Door de hoge kost werd, op basis van deze simulaties, besloten om verder te gaan met het bouwen van de ontbrekende vierde laag, zoals voorzien in het originele plan, en af te zien van de bouw van de dubbele tweede laag.

In deze thesis werd ook meegewerkt aan de zoektocht naar supersymmetrische deeltjes. Tussen maart 2010 en november 2010 werd de LHC versneller geopereerd voor steeds grotere intensiteit (lees: meer proton-proton botsingen op kortere tijd). Gedurende deze periode werd de intensiteit van de machine langzaam maar stelselmatig opgedreven tot één vijftigste van zijn design intensiteit. Ondanks deze betrekkelijk lage intensiteit werden toch meer dan 1 miljard botsingen geregistreerd door de CMS detector. Deze botsingen werden onderzocht naar compatibiliteit met de mogelijkheid op het creëren van supersymmetrische deeltjes. Supersymmetrie voorspelt dat supersymmetrische deeltjes in paren geproduceerd worden, en dat er een lichtste supersymmetrisch deeltje ongedetecteerd doorheen de detector verdwijnt. Het verval van deze supersymmetrische deeltjes gaat gepaard met de productie van hoog-energetische jets (geconcentreerde energie in de calorimeters) en missende transversale energie. Dit komt doordat in proton-proton botsingen het initieel transversaal momentum nul is, en dit moet behouden zijn na de botsing. Als er echter deeltjes doorheen de detector vliegen zonder gedetecteerd te worden, klopt het totaal beeld van de botsing niet meer, en dit vertaalt zich in missende transversale energie.

In het Standaard Model zijn er echter enkele processen die een zeer gelijkaardige voetafdruk hebben. Indien het Z-deeltje geproduceerd wordt in proton-proton botsingen, kan dit gepaard gaan met de productie van een aantal jets, men spreekt dan van "Z-plus-jets" evenementen. In 20% van de gevallen, vervalt het Z-deeltje naar twee neutrinos: $Z \rightarrow \nu\nu$ of kortweg $Z(\nu\nu)$. In het geval de productie van het Z deeltje gepaard gaat met jet-productie, ziet dit proces er exact hetzelfde uit als de vervalproducten van een supersymmetrisch deeltje. Het neutrino gaat immers ook ongezien door de detector heen en creëert daardoor eveneens missende transversale energie. Dit proces is één van de grootste achtergronden voor de zoektocht naar supersymmetrische deeltjes. In deze thesis werd een methode ontwikkeld om deze achtergrond af te schatten, vertrekkende van andere processen in het Standaard Model.

In het Standaard Model is de productie van fotonen (γ) erg gerelateerd aan de productie van Z deeltjes. Door evementen met fotonen en jets te selecteren en het foton te verwijderen kan men "Z plus jets"evenementen imiteren. Om deze methode te gebruiken werd heel precies de zuiverheid van de "foton plus jets" evementen bepaald, omdat ook andere processen er uit kunnen zien als "foton plus jets". Verder werd de selectie-efficientie bepaald, samen met een nauwkeurige afschatting van de verschillen tussen Z-deeltjes en fotonen. Door de gevonden "foton plus jets" evenementen te corrigeren voor de zuiverheid en selectie-efficientie en daarna te schalen naar de waarschijnlijkheid om een Z-deeltje te creëeren, kon een zeer nauwkeurige afschatting van de "$Z(\nu\nu)$ plus jets" evenementen gemaakt worden. Deze afschatting werd gecombineerd met zeer nauwkeurige afschattingen van andere achtergronden. In een eerste selectiegebied, waar men verwacht dat Standaard Model processen domineren, werden 40 achtergrond evenementen voorspeld en 40 evenementen opgemeten. In geoptimalizeerde zoekgebieden werd eenzelfde overeenkomst gevonden tussen voorspelde en gemeten waarden. Hierdoor konden we uitsluiten

dat er supersymmetrische deeltjes geproduceerd werden in een aanzienlijk gedeelte van de fysische ruimte waar deze deeltjes verwacht werden.

De methode ontwikkeld in deze thesis, werd eveneens gebruikt in verschillende analyses van de gegevens geregistreerd in 2011 waar $Z(\nu\nu)$ evenementen voor een achtergrond zorgen ten opzichte van nieuwe processen, onderzocht door wetenschappers in CMS. In deze thesis werd de eerste data, geleverd door de LHC én bruikbaar voor fundamenteel onderzoek, geanalyzeerd met een nieuwe techniek. Er werden geen nieuwe (supersymmetrische) deeltjes ontdekt. Dit is slechts het topje van de ijsberg, want in de komende jaren wordt er verwacht dat de LHC nog 10 000 tot 100 000 keer meer protonen zal laten botsen.

In 2011 werd er 100 keer meer data onderzocht en werden er hints gezien dat het Higgs-boson zou bestaan. Om het bestaan van het Higgs-deeltje te bewijzen, moet er echter meer data geanalyzeerd worden, waardoor er waarschijnlijk pas op het einde van 2012 een krachtige uitspraak kan worden gedaan over het al dan niet bestaan van dit deeltje. Het is een ongelooflijk spannende tijd om op dit moment onderzoek te mogen doen naar de fundamenten van de materie. Het werk in deze thesis is beindigd, maar ik kijk nu al ongelooflijk uit naar nieuwe data om te analyzeren en mijn steentje bij te dragen aan upgrades voor de detector, zodat het registreren van data ook in de toekomst verzekerd zal zijn!

References

Notes:

(a) CMS Notes are available at http://cms.cern.ch/iCMS/ unless otherwise noted.

(b) References marked **doi** should be prefixed with http://dx.doi.org/.

---

[1] William Wordsworth, "The Complete Poetical Works". Macmillan and Co., London, 1888. Bartleby.com, 1999. www.bartleby.com/145/.

[2] Bertrand Russel, "A History of Western Philosophy". George Allen & Unwin Ltd, London, 1946. ISBN-9780671201586.

[3] G. Kane, "The Dawn of Physics beyond the Standard Model", *Scientific American* **Sp 15** (2006) 4–11. doi:10.1038/scientificamerican0206-4sp.

[4] F. Halzen and A. D. Martin, "Quarks and Leptons: An Introductory Course In Modern Particle Physics". John Wiley & Sons Inc., New York, USA, 1984. ISBN-9780471887416.

[5] Particle Data Group Collaboration, "Review of particle physics", *J.Phys.G* **G37** (2010) 075021. doi:10.1088/0954-3899/37/7A/075021.

[6] P. W. Higgs, "Broken symmetries, massless particles and gauge fields", *Phys.Lett.* **12** (1964) 132–133. doi:10.1016/0031-9163(64)91136-9.

[7] F. Englert and R. Brout, "Broken Symmetry and the Mass of Gauge Vector Mesons", *Phys.Rev.Lett.* **13** (1964) 321–322. doi:10.1103/PhysRevLett.13.321.

[8] P. W. Higgs, "Broken Symmetries and the Masses of Gauge Bosons", *Phys.Rev.Lett.* **13** (1964) 508–509. doi:10.1103/PhysRevLett.13.508.

[9] G. Guralnik, C. Hagen, and T. Kibble, "Global Conservation Laws and Massless Particles", *Phys.Rev.Lett.* **13** (1964) 585–587. doi:10.1103/PhysRevLett.13.585.

[10] Y. Nambu, "Axial vector current conservation in weak interactions", *Phys.Rev.Lett.* **4** (1960) 380–382. doi:10.1103/PhysRevLett.4.380.

[11] Y. Nambu and G. Jona-Lasinio, "Dynamical Model of Elementary Particles Based on an Analogy with Superconductivity. I.", *Phys.Rev.* **122** (1961) 345–358. doi:10.1103/PhysRev.122.345.

[12] Y. Nambu and G. Jona-Lasinio, "Dynamical Model of Elementary Particles Based on an Analogy with Superconductivity. II.", *Phys.Rev.* **124** (1961) 246–254. doi:10.1103/PhysRev.124.246.

[13] J. Goldstone, "Field Theories with Superconductor Solutions", *Nuovo Cim.* **19** (1961) 154–164. doi:10.1007/BF02812722.

[14] J. Goldstone, A. Salam, and S. Weinberg, "Broken Symmetries", *Phys.Rev.* **127** (1962) 965–970. doi:10.1103/PhysRev.127.965.

[15] A. Djouadi and R. M. Godbole, "Electroweak symmetry breaking at the LHC", arXiv:0901.2030.

[16] A. Djouadi, "The Anatomy of electro-weak symmetry breaking. I: The Higgs boson in the standard model", *Phys.Rept.* **457** (2008) 1–216, arXiv:hep-ph/0503172. doi:10.1016/j.physrep.2007.10.004.

[17] G. 't Hooft and M. Veltman, "Regularization and Renormalization of Gauge Fields", *Nucl.Phys.* **B44** (1972) 189–213. doi:10.1016/0550-3213(72)90279-9.

[18] Gargamelle Neutrino Collaboration, "Search for elastic Muon-Neutrino Electron Scattering", *Phys.Lett.* **B46** (1973) 121–124. doi:10.1016/0370-2693(73)90494-2.

[19] Gargamelle Neutrino Collaboration, "Observation of Neutrino Like Interactions Without Muon Or Electron in the Gargamelle Neutrino Experiment", *Phys.Lett.* **B46** (1973) 138–140. doi:10.1016/0370-2693(73)90499-1.

[20] Gargamelle Neutrino Collaboration, "Observation of Neutrino Like Interactions without Muon or Electron in the Gargamelle Neutrino Experiment", *Nucl.Phys.* **B73** (1974) 1–22. doi:10.1016/0550-3213(74)90038-8.

[21] UA1 Collaboration, "Experimental observation of isolated large transverse energy electrons with associated missing energy at $\sqrt{s} = 540\,\text{GeV}$", *Phys. Lett.* **B122** (1983) 103–116. doi:10.1016/0370-2693(83)91177-2.

[22] UA2 Collaboration, "Observation of single isolated electrons of high transverse momentum in events with missing transverse energy at the CERN anti-p p collider", *Phys. Lett.* **B122** (1983) 476–485. doi:10.1016/0370-2693(83)91605-2.

[23] UA1 Collaboration, "Experimental observation of lepton pairs of invariant mass around $95\,\text{GeV}/c^2$ at the CERN SPS collider", *Phys. Lett.* **B126** (1983) 398–410. doi:10.1016/0370-2693(83)90188-0.

[24] UA2 Collaboration, "Evidence for $Z^0 \to e^+e^-$ at the CERN anti-p p collider", *Phys. Lett.* **B129** (1983) 130–140. doi:10.1016/0370-2693(83)90744-X.

[25] Super-Kamiokande Collaboration, "Evidence for oscillation of atmospheric neutrinos", *Phys. Rev. Lett.* **81** (1998) 1562–1567, arXiv:hep-ex/9807003. doi:10.1103/PhysRevLett.81.1562.

[26] SNO Collaboration, "Direct evidence for neutrino flavor transformation from neutral-current interactions in the Sudbury Neutrino Observatory", *Phys. Rev. Lett.* **89** (2002) 011301, arXiv:nucl-ex/0204008. doi:10.1103/PhysRevLett.89.011301.

[27] LEP Electroweak Working Group (LEP EWWG)). LEP EWWG website: http://lepewwg.web.cern.ch/LEPEWWG/.

[28] A. Sirlin, "Thirty years of precision electroweak physics", *J.Phys.G* **G29** (2003) 213–224, arXiv:hep-ph/0209079. doi:10.1088/0954-3899/29/1/322.

[29] ALEPH Collaboration, DELPHI Collaboration, L3 Collaboration, OPAL Collaboration, SLD Collaboration, LEP Electroweak Working Group, SLD Electroweak Group, SLD Heavy Flavour Group, "Precision electroweak measurements on the *Z* resonance", *Phys.Rept.* **427** (2006) 257–454, arXiv:hep-ex/0509008. doi:10.1016/j.physrep.2005.12.006.

[30] ALEPH Collaboration, DELPHI Collaboration, L3 Collaboration, OPAL Collaboration, LEP Electroweak Working Group, "A Combination of preliminary electroweak measurements and constraints on the standard model", arXiv:hep-ex/0612034.

[31] ALEPH Collaboration, DELPHI Collaboration, L3 Collaboration, OPAL Collaboration, LEP Electroweak Working Group, "Precision Electroweak Measurements and Constraints on the Standard Model", arXiv:0712.0929.

[32] M. Baak et al., "Updated Status of the Global Electroweak Fit and Constraints on New Physics", *submitted to Eur. Phys. J. C* (2011) arXiv:1107.0975.

[33] Zfitter, "A Fortran package for the evaluation of radiative corrections as predicted in the Standard Model of elementary particles". Zfitter website: http://zfitter.com/.

[34] D. Y. Bardin, M. S. Bilenky, A. Chizhov et al., "ZFITTER: An analytical program for fermion pair production in e+ e- annihilation", arXiv:hep-ph/9412201.

[35] D. Y. Bardin and G. Passarino, "The Standard Model in the making: Precision study of the electroweak interactions". Oxford University Press, 1999. The International Series of Monographs on Physics, 104. ISBN-9780198502807.

[36] Gfitter Group, "A Generic Fitter Project for HEP Model Testing". GFitter website: http://gfitter.desy.de/.

[37] H. Flaecher et al., "Revisiting the Global Electroweak Fit of the Standard Model and Beyond with Gfitter", *Eur. Phys. J.* **C60** (2009) 543–583, arXiv:0811.0009. doi:10.1140/epjc/s10052-009-0966-6.

[38] CDF and D0 Collaboration Collaboration, "Updated Combination of CDF and D0 Results for the Mass of the W Boson", arXiv:0908.1374.

[39] TEVNPH (Tevatron New Phenomena and Higgs Working Group), CDF and D0 Collaboration Collaboration, "Combined CDF and D0 Upper Limits on Standard Model Higgs Boson Production with up to 8.6 fb-1 of Data", arXiv:1107.5518.

[40] J. M. Butterworth, B. E. Cox, and J. R. Forshaw, "WW scattering at the CERN LHC", *Phys. Rev.* **D65** (2002) 096014, arXiv:hep-ph/0201098. doi:10.1103/PhysRevD.65.096014.

[41] S. D. Rindani, "Strong gauge boson scattering at the LHC", arXiv:0910.5068.

[42] A. Lahiri and D. Mukhopadhyay, "Unitarity in $WW \to WW$ elastic scattering without a Higgs boson", arXiv:1107.1501.

[43] L. Susskind, "Dynamics of spontaneous symmetry breaking in the Weinberg-Salam theory", *Phys. Rev. D* **20** (Nov, 1979) 2619–2625. doi:10.1103/PhysRevD.20.2619.

[44] X. Tata, "What is supersymmetry and how do we find it?", arXiv:hep-ph/9706307.

[45] R. Barbieri and G. Giudice, "Upper bounds on supersymmetric particle masses", *Nuclear Physics B* **306** (1988), no. 1, 63–76. doi:10.1016/0550-3213(88)90171-X.

[46] G. Bhattacharyya, "Electroweak Symmetry Breaking Beyond the Standard Model", arXiv:1201.1403.

[47] S. P. Martin, "A Supersymmetry primer", arXiv:hep-ph/9709356.

[48] H.-C. Cheng, "Little Higgs, Non-standard Higgs, No Higgs and All That", arXiv:0710.3407.

[49] S. Weinberg, "Implications of Dynamical Symmetry Breaking", *Phys.Rev.* **D13** (1976) 974–996. doi:10.1103/PhysRevD.13.974.

[50] S. Weinberg, "Implications of Dynamical Symmetry Breaking: An Addendum", *Phys.Rev.* **D19** (1979) 1277–1280. doi:10.1103/PhysRevD.19.1277.

[51] E. Gildener, "Gauge Symmetry Hierarchies", *Phys.Rev.* **D14** (1976) 1667. doi:10.1103/PhysRevD.14.1667.

[52] L. Susskind, "Dynamics of Spontaneous Symmetry Breaking in the Weinberg-Salam Theory", *Phys.Rev.* **D20** (1979) 2619–2625. doi:10.1103/PhysRevD.20.2619.

[53] N. Arkani-Hamed, A. G. Cohen, and H. Georgi, "Electroweak symmetry breaking from dimensional deconstruction", *Phys. Lett.* **B513** (2001) 232–240, arXiv:hep-ph/0105239. doi:10.1016/S0370-2693(01)00741-9.

[54] N. Arkani-Hamed, A. G. Cohen, E. Katz et al., "The littlest Higgs", *JHEP* **07** (2002) 034, arXiv:hep-ph/0206021. doi:10.1088/1126-6708/2002/07/034.

[55] N. Arkani-Hamed et al., "The Minimal Moose for a Little Higgs", *JHEP* **08** (2002) 021, arXiv:hep-ph/0206020. doi:10.1088/1126-6708/2002/08/021.

[56] S. Weinberg, "Implications of dynamical symmetry breaking: An addendum", *Phys. Rev. D* **19** (Feb, 1979) 1277–1280. doi:10.1103/PhysRevD.19.1277.

[57] H. Baer and X. Tata, "Weak scale supersymmetry: From superfields to scattering events". Cambridge University Press, 2006. ISBN-9780521857864.

[58] H. Murayama, "Supersymmetry phenomenology", arXiv:hep-ph/0002232.

[59] P. G. O. Freund, "Introduction to Supersymmetry". Cambridge University Press, 1986. Cambridge Monographs On Mathematical Physics. ISBN-9780521356756.

[60] M. Kaku, "Quantum field theory: A Modern introduction". Oxford University Press, New York, USA, 1993.

[61] H. Miyazawa, "Baryon Number Changing Currents", *Prog. Theor. Phys.* **36** (1966) 1266–1276. doi:10.1143/PTP.36.1266.

[62] H. Miyazawa, "Spinor Currents and Symmetries of Baryons and Mesons", *Phys. Rev.* **170** (1968) 1586–1590. doi:10.1103/PhysRev.170.1586.

[63] J. Wess and B. Zumino, "Supergauge Transformations in Four Dimensions", *Nucl. Phys. B* **70** (1974) 39. doi:10.1016/0550-3213(74)90355-1.

[64] E.Witten, "Dynamical Breaking of Supersymmetry", *Nucl. Phys.* **B188** (1981) 513. doi:10.1016/0550-3213(81)90006-7.

[65] S.Dimopoulos and H.Georgi, "Softly Broken Supersymmetry and SU(5)", *Nucl. Phys.* **B 193** (1981) 150. doi:10.1016/0550-3213(81)90522-8.

[66] H. Baer, V. Barger, and A. Mustafayev, "Implications of a 125 GeV Higgs scalar for LHC SUSY and neutralino dark matter searches", arXiv:1112.3017.

[67] CMS Collaboration, "CMS Physics Technical Design Report, Volume II: Physics Performance", *J. Phys. G* **34** (2006) 995–1579. 669 p. CERN-LHCC-2006-021. CMS-TDR-008-2. http://cdsweb.cern.ch/record/942733. doi:10.1088/0954-3899/34/6/S01.

[68] J. R. Ellis, T. Falk, K. A. Olive et al., "Exploration of the MSSM with Non-Universal Higgs Masses", *Nucl. Phys.* **B652** (2003) 259–347, arXiv:hep-ph/0210205. doi:10.1016/S0550-3213(02)01144-6.

[69] H. Baer, A. Mustafayev, S. Profumo et al., "Direct, indirect and collider detection of neutralino dark matter in SUSY models with non-universal Higgs masses", *JHEP* **07** (2005) 065, arXiv:hep-ph/0504001. doi:10.1088/1126-6708/2005/07/065.

[70] UA1 Collaboration, "Events with Large Missing Transverse Energy at the CERN Collider. 3. Mass Limits on Supersymmetric Particles", *Phys. Lett.* **B198** (1987) 261–270. doi:10.1016/0370-2693(87)91509-7.

[71] UA2 Collaboration, "Search for exotic processes at the CERN p anti-p collider", *Phys. Lett.* **B195** (1987) 613. doi:10.1016/0370-2693(87)91583-8.

[72] F. Jegerlehner, "Essentials of the Muon g-2", *Acta Phys.Polon.* **B38** (2007) 3021, arXiv:hep-ph/0703125.

[73] Muon G-2 Collaboration, "Final report of the muon E821 anomalous magnetic moment measurement at BNL", *Phys. Rev.* **D73** (2006) 072003, arXiv:hep-ex/0602035. doi:10.1103/PhysRevD.73.072003.

[74] CMS Collaboration, "Search for the rare decay $B_s^0 \to \mu^+\mu^-$ at the LHC with the CMS and LHCb experiments", *CMS Physics Analysis Summary CMS-PAS-BPH-11-019 (2011).* http://cdsweb.cern.ch/record/1374913.

[75] CDF Collaboration, "Search for $B_s \to \mu^+\mu^-$ and $B_d \to \mu^+\mu^-$ Decays with CDF II", *Phys.Rev.Lett.* **107** (2011) 239903, arXiv:1107.2304. doi:10.1103/PhysRevLett.107.191801.

[76] A. Akeroyd, F. Mahmoudi, and D. Santos, "The decay $B_s \to \mu^+\mu^-$: updated SUSY constraints and prospects", *JHEP* **1112** (2011) 088, arXiv:1108.3018. doi:10.1007/JHEP12(2011)088.

[77] CMS Collaboration Collaboration, "Search for $B_s^0 to \mu^+\mu^-$ and $B^0 to \mu^+\mu^-$ decays", *JHEP* **1204** (2012) 033, arXiv:1203.3976. CMS-BPH-11-020. CERN-PH-EP-2012-086. http://cdsweb.cern.ch/record/1432924. doi:10.1007/JHEP04(2012)033.

[78] CMS Collaboration, "Search for the rare decays B_s and B_0 to dimuons at the LHC with the ATLAS, CMS and LHCb experiments", *CMS Physics Analysis Summary CMS-PAS-BPH-12-009 (2012).* http://cdsweb.cern.ch/record/1456504.

[79] O. Buchmueller, R. Cavanaugh, A. De Roeck et al., "Likelihood Functions for Supersymmetric Observables in Frequentist Analyses of the CMSSM and NUHM1", *Eur.Phys.J.* **C64** (2009) 391–415, arXiv:0907.5568. doi:10.1140/epjc/s10052-009-1159-z.

[80] O. Buchmueller et al., "Predictions for m_t and m_W in Minimal Supersymmetric Models", *Phys. Rev.* **D81** (2010) 035009, arXiv:0912.1036. doi:10.1103/PhysRevD.81.035009.

[81] ALEPH, DELPHI, L3 and OPAL Collaborations, "Joint SUSY Working Group", *LEPSUSYWG/02-06-2.* http://lepsusy.web.cern.ch/lepsusy.

[82] ZEUS Collaboration, "Search for stop production in R-parity-violating supersymmetry at HERA", *Eur. Phys. J.* **C50** (2007) 269–281, arXiv:hep-ex/0611018. doi:10.1140/epjc/s10052-007-0240-8.

[83] H1 Collaboration, "A Search for selectrons and squarks at HERA", *Phys. Lett.* **B380** (1996) 461–470, arXiv:hep-ex/9605002. doi:10.1016/0370-2693(96)00640-5.

[84] CDF Collaboration, "Search for Supersymmetry in p anti-p Collisions at $\sqrt{s} = 1.96\,\text{TeV}$ Using the Trilepton Signature of Chargino-Neutralino Production", *Phys. Rev. Lett.* **101** (2008) 251801, arXiv:0808.2446. doi:10.1103/PhysRevLett.101.251801.

[85] CDF Collaboration, "Inclusive Search for Squark and Gluino Production in p anti-p Collisions at $\sqrt{s} = 1.96\,\text{TeV}$", *Phys. Rev. Lett.* **102** (2009) 121801, arXiv:0811.2512. doi:10.1103/PhysRevLett.102.121801.

[86] D0 Collaboration, "Search for squarks and gluinos in events with jets and missing transverse energy using 2.1 fb^{-1} of p anti-p collision data at $\sqrt{s}$ = 1.96 TeV", *Phys. Lett.* **B660** (2008) 449–457, arXiv:0712.3805. doi:10.1016/j.physletb.2008.01.042.

[87] D0 Collaboration, "Search for associated production of charginos and neutralinos in the trilepton final state using 2.3 fb^{-1} of data", *Phys. Lett.* **B680** (2009) 34–43, arXiv:0901.0646. doi:10.1016/j.physletb.2009.08.011.

[88] Committee on Data for Science and Technology (CODATA). http://www.codata.org/ Set of Physical Constants may be found at the National Institute for Standards and Technology http://physics.nist.gov/constants.

[89] M. Davier, A. Hoecker, B. Malaescu et al., "Reevaluation of the Hadronic Contributions to the Muon g-2 and to alpha(M_Z)", *Eur.Phys.J.* **C71** (2011) 1515, arXiv:1010.4180. doi:10.1140/epjc/s10052-010-1515-z.

[90] S. Bethke, "The 2009 World Average of $\alpha(s)$", *Eur.Phys.J.* **C64** (2009) 689–703, arXiv:0908.1135. doi:10.1140/epjc/s10052-009-1173-1.

[91] D0 Collaboration Collaboration, "Determination of the strong coupling constant from the inclusive jet cross section in ppbar collisions at $\sqrt{s}$ = 1.96 TeV", *Phys.Rev.* **D80** (2009) 111107, arXiv:0911.2710. doi:10.1103/PhysRevD.80.111107.

[92] TOTEM Collaboration, "The TOTEM Experiment at the CERN LHCCollaboration", *Journal of Instrumentation* **3** (2008), no. 08, S08007. doi:10.1088/1748-0221/3/08/S08007.

[93] TOTEM Collaboration, "First measurement of the total proton-proton cross-section at the LHC energy of $\sqrt{s} = 7\,TeV$", *EPL (Europhysics Letters)* **96** (2011), no. 2, 21002. doi:10.1209/0295-5075/96/21002.

[94] B. Povh, C. Scholz, K. Rith et al., "Particles and nuclei: An introduction to the physical concepts". Springer, Berlin, Germany, 1993. ISBN-978-3540201687.

[95] J. M. Campbell, J. Huston, and W. Stirling, "Hard Interactions of Quarks and Gluons: A Primer for LHC Physics", *Rept.Prog.Phys.* **70** (2007) 89, arXiv:hep-ph/0611148. doi:10.1088/0034-4885/70/1/R02.

[96] D. Stump, J. Huston, J. Pumplin et al., "Inclusive jet production, parton distributions, and the search for new physics", *JHEP* **0310** (2003) 046, arXiv:hep-ph/0303013.

[97] P. M. Nadolsky, H.-L. Lai, Q.-H. Cao et al., "Implications of CTEQ global analysis for collider observables", *Phys.Rev.* **D78** (2008) 013004, arXiv:0802.0007. doi:10.1103/PhysRevD.78.013004.

[98] H.-L. Lai, M. Guzzi, J. Huston et al., "New parton distributions for collider physics", *Phys.Rev.* **D82** (2010) 074024, arXiv:1007.2241. doi:10.1103/PhysRevD.82.074024.

[99] A. Martin, W. Stirling, R. Thorne et al., "Parton distributions for the LHC", *Eur.Phys.J.* **C63** (2009) 189–285, arXiv:0901.0002. doi:10.1140/epjc/s10052-009-1072-5.

[100] W.J. Stirling, "Tevatron and LHC parton luminosity comparison plots". http://www.hep.phy.cam.ac.uk/$\sim$wjs/plots/plots.html.

[101] CMS Collaboration Collaboration, "First Measurement of the Underlying Event Activity at the LHC with $\sqrt{s} = 0.9$ TeV", *Eur.Phys.J.* **C70** (2010) 555–572, arXiv:1006.2083. doi:10.1140/epjc/s10052-010-1453-9.

[102] CMS Collaboration Collaboration, "Measurement of the Underlying Event Activity at the LHC with $\sqrt{s} = 7$ TeV and Comparison with $\sqrt{s} = 0.9$ TeV", *JHEP* **1109** (2011) 109, arXiv:1107.0330. doi:10.1007/JHEP09(2011)109.

[103] T. Gleisberg, S. Hoeche, F. Krauss et al., "Event generation with SHERPA 1.1", *JHEP* **0902** (2009) 007, arXiv:0811.4622. doi:10.1088/1126-6708/2009/02/007.

[104] T. Sjostrand, S. Mrenna, and P. Z. Skands, "PYTHIA 6.4 Physics and Manual", *JHEP* **0605** (2006) 026, arXiv:hep-ph/0603175. doi:10.1088/1126-6708/2006/05/026.

[105] G. Corcella, I. Knowles, G. Marchesini et al., "HERWIG 6.5 release note", arXiv:hep-ph/0210213.

[106] M. Bahr, S. Gieseke, M. Gigg et al., "Herwig++ Physics and Manual", *Eur.Phys.J.* **C58** (2008) 639–707, arXiv:0803.0883. doi:10.1140/epjc/s10052-008-0798-9.

[107] J. Alwall, P. Demin, S. de Visscher et al., "MadGraph/MadEvent v4: The New Web Generation", *JHEP* **0709** (2007) 028, arXiv:0706.2334. doi:10.1088/1126-6708/2007/09/028.

[108] M. L. Mangano, M. Moretti, F. Piccinini et al., "ALPGEN, a generator for hard multiparton processes in hadronic collisions", *JHEP* **0307** (2003) 001, arXiv:hep-ph/0206293.

[109] M. L. Mangano, M. Moretti, and R. Pittau, "Multijet matrix elements and shower evolution in hadronic collisions: $Wb\bar{b} + n$ jets as a case study", *Nucl.Phys.* **B632** (2002) 343–362, arXiv:hep-ph/0108069. doi:10.1016/S0550-3213(02)00249-3.

[110] M. L. Mangano, M. Moretti, F. Piccinini et al., "Matching matrix elements and shower evolution for top-quark production in hadronic collisions", *JHEP* **0701** (2007) 013, arXiv:hep-ph/0611129. doi:10.1088/1126-6708/2007/01/013.

[111] S. Catani, F. Krauss, R. Kuhn et al., "QCD matrix elements + parton showers", *JHEP* **0111** (2001) 063, arXiv:hep-ph/0109231.

[112] F. Krauss, "Matrix elements and parton showers in hadronic interactions", *JHEP* **0208** (2002) 015, arXiv:hep-ph/0205283.

[113] C. Quigg, "LHC Physics Potential vs. Energy", arXiv:0908.3660.

[114] L. Evans and P. Bryant, "LHC Machine", *Journal of Instrumentation* **3** (2008), no. 08, S08001. doi:10.1088/1748-0221/3/08/S08001.

[115] O. Brüning and P. Collier, "Building a behemoth", *Nature Insight: The Large Hadron Collider* **448** (2010), no. 7151, 285–289. doi:10.1038/nature06077.

[116] O. S. Brüning, P. Collier, P. Lebrun et al., "LHC Design Report Volume 1: The LHC Main Ring". CERN, Geneva, 2004. CERN-2004-003-V-1. http://cdsweb.cern.ch/record/782076.

[117] O. S. Brüning, P. Collier, P. Lebrun et al., "LHC Design Report Volume 2: The LHC Infrastructure and General Services". CERN, Geneva, 2004. CERN-2004-003-V-2. http://cdsweb.cern.ch/record/815187.

[118] M. Benedikt, P. Collier, V. Mertens et al., "LHC Design Report Volume 3: The LHC Injector Chain". CERN, Geneva, 2004. CERN-2004-003-V-3. http://cdsweb.cern.ch/record/823808.

[119] CERN Document Server, "LHC Project Illustration: Cross section of LHC dipole". http://cdsweb.cern.ch/record/842530.

[120] CERN Document Server, "Damage of the LHC magnets in sector 3-4 of the LHC, provoked by the incident which happened on 19 September 2008". http://cdsweb.cern.ch/record/1185822.

[121] CERN Document Server, "CMS collision events: LHC restart 2009". http://cdsweb.cern.ch/record/1223971.

[122] CERN Document Server, "First 900 GeV Collisions". http://cdsweb.cern.ch/record/1429618.

[123] X. C. Vidal and R. C. Manzano, "Taking a closer look at LHC". Outreach website: www.lhc-closer.es.

[124] International Linear Collider (ILC) Collaboration, "Crabbing in the cavity", 12 July 2007. http://newsline.linearcollider.org/.

[125] CMS Collaboration, "CMS Luminosity – Public Results". CMS Luminosity website.

[126] ATLAS Collaboration, "ATLAS Online Luminosity Fill 1883". http://cdsweb.cern.ch/record/1361360.

[127] ATLAS Collaboration, "ATLAS Luminosity – Public Results". ATLAS Luminosity website.

[128] ATLAS Collaboration, "ATLAS Event Display – Public Results". ATLAS Event Display website.

[129] CMS Collaboration, "Technical Proposal for the Upgrade of the CMS detector through 2020", technical report, CERN, Geneva, Jun, 2011. CERN-LHCC-2011-006. LHCC-P-004. http://cdsweb.cern.ch/record/1355706.

[130] Steve Myers, "LHC present status and prospects for the future". Division of Particles and Fields of the American Physical Society (APS DPF) conference at Providence, Rhode Island, 8–13 August 2011. CERN Indico: 129980.

[131] CMS Collaboration, "The CMS Experiment at the CERN LHCCollaboration", *Journal of Instrumentation* **3** (2008), no. 08, S08004. doi:10.1088/1748-0221/3/08/S08004.

[132] M. Pimiä, M. Della Negra, K. Eggert et al., "Compact Muon Solenoid". CERN, Geneva, 1990. Proceedings of the Large Hadron Collider Workshop Aachen, 4-9 October 1990, p.547. CERN-90-10-V-3. ECFA-90-133-V-3. http://cdsweb.cern.ch/record/215299.

[133] CMS Collaboration, "CMS Expression of Interest". CERN, Geneva, 1992. Proceedings of the General Meeting on LHC Physics and Detectors, Evian-les-Bains, France, 5-8 Mar 1992, pp.165-217. http://cdsweb.cern.ch/record/247455.

[134] CMS Collaboration, "Letter of intent: by the CMS Collaboration for a general purpose detector at LHC". Letter of Intent. CERN, Geneva, 1992. CERN-LHCC-92-003. LHCC-l-1. http://cdsweb.cern.ch/record/290808.

[135] CMS Collaboration, "Technical proposal". LHC Tech. Proposal. CERN, Geneva, 1994. CERN-LHCC-94-38. LHCC-P-1. http://cdsweb.cern.ch/record/290969.

[136] CMS Collaboration, "The CMS magnet project: Technical Design Report". Technical Design Report CMS. CERN, Geneva, 1997. CERN-LHCC-97-010. CMS-TDR-001. http://cdsweb.cern.ch/record/331056.

[137] CMS Collaboration, "The CMS hadron calorimeter project: Technical Design Report". Technical Design Report CMS. CERN, Geneva, 1997. CERN-LHCC-97-031. CMS-TDR-002. http://cdsweb.cern.ch/record/357153.

[138] CMS Collaboration, "The CMS muon project: Technical Design Report". Technical Design Report CMS. CERN, Geneva, 1997. CERN-LHCC-97-032. CMS-TDR-003. http://cdsweb.cern.ch/record/343814.

[139] CMS Collaboration, "The CMS electromagnetic calorimeter project: Technical Design Report". Technical Design Report CMS. CERN, Geneva, 1997. CERN-LHCC-97-033. CMS-TDR-004. http://cdsweb.cern.ch/record/349375.

[140] CMS Collaboration, "The CMS tracker system project: Technical Design Report". Technical Design Report CMS. CERN, Geneva, 1997. CERN-LHCC-98-006. CMS-TDR-005. http://cdsweb.cern.ch/record/368412.

[141] "CMS TriDAS project: Technical Design Report 1: the trigger systems". Technical Design Report CMS. CERN, Geneva, 2000. CERN-LHCC-2000-038. CMS-TDR-006-1. http://cdsweb.cern.ch/record/706847.

[142] "CMS TriDAS project: Technical Design Report 2: Data-acquisition and high-level trigger". Technical Design Report CMS. CERN, Geneva, 2002. CERN-LHCC-2002-026. CMS-TDR-006-add-2. http://cdsweb.cern.ch/record/578006.

[143] CMS Collaboration, "CMS Computing: Technical Design Report". Technical Design Report CMS. CERN, Geneva, 2005. CERN-LHCC-2005-023. CMS-TDR-007. http://cdsweb.cern.ch/record/838359.

[144] CMS Collaboration, "CMS Physics Technical Design Report Volume I: Detector Performance and Software". Technical Design Report CMS. CERN, Geneva, 2006. CERN-LHCC-2006-001. CMS-TDR-008-1. http://cdsweb.cern.ch/record/922757.

[145] B. Bianchi and H. Laporte, "Choice Of Slope For The LEP Tunnel", *CERN-LEP-Note-248*. *http://cdsweb.cern.ch/record/443235*.

[146] CERN Document Server, "Photos of the LHC 2008 Open Day at CERN". http://cdsweb.cern.ch/record/1109982.

[147] D. Green, "The physics of Particle Detectors", *Cambridge Monographs on Particle Physics, Nuclear Physics and Cosmology* **12** (2000) 361. ISBN-9780521662260.

[148] D. Green, "At the leading edge: The ATLAS and CMS LHC experiments". World Scientific, 2010. ISBN-9789814277617.

[149] W. Riegler, "Fundamentals of Particle Detectors and Developments in Detector Technologies for future Experiments", 21-04-2008. Academic Training Lecture Regular Programme: CERN Indico 24765.

[150] W. Riegler, "Signals in Particle Detectors", 05-09-2008. Detector Seminar: CERN Indico 40444.

[151] CMS Collaboration, "Precise Mapping of the Magnetic Field in the CMS Barrel Yoke using Cosmic Rays", *JINST* **5** (2010) T03021, arXiv:0910.5530. CMS-CFT-09-015. http://cdsweb.cern.ch/record/1215500. doi:10.1088/1748-0221/5/03/T03021.

[152] CERN Document Server, "The CMS solenoid descends to 100 Kelvin". http://cdsweb.cern.ch/record/930268.

[153] CMS Collaboration, "Performance of the CMS muon detector with pp collisions at $\sqrt{s} = 7$ TeV at the LHC", *CMS Physics Analysis Summary CMS-PAS-MUO-11-001 (not yet published)*.

[154] W. Blum, L. Rolandi, and W. Riegler, "Particle detection with drift chambers". Berlin, Germany: Springer, 2008. ISBN-9783540766834.

[155] F. Sauli, "Principles of operation of multiwire proportional and drift chambers", p. 92. CERN, Geneva, May, 1977. CERN-77-09. http://cdsweb.cern.ch/record/117989.

[156] W. Shockley, "Currents to Conductors Induced by a Moving Point Charge", *Journal of Applied Physics* **9** (1938) 635. doi:10.1063/1.1710367.

[157] S. Ramo, "Currents Induced by Electron Motion", *Proceedings of the IRE* **9** (1939) 584–585. doi:10.1109/JRPROC.1939.228757.

[158] CERN Document Server, "CMS collision events: di-muons in the B_s meson mass window". http://cdsweb.cern.ch/record/1373706.

[159] CMS Collaboration, "CMS Tracking Performance Results from Early LHC Operation", *Journal of High Energy Physics* **70** (2010), no. 4, 1165–1192, arXiv:1007.1988. CMS-TRK-10-001. CERN-PH-EP-2010-019. http://cdsweb.cern.ch/record/1258204. doi:10.1140/epjc/s10052-010-1491-3.

[160] T. Miao, N. Leioatts, H. Wenzel et al., "Beam Position Determination Using Tracks", *CMS Note CMS-NOTE-2007-021 (2007).* *http://cdsweb.cern.ch/record/1061285*.

[161] W. Waltenberger, R. Früwirth, and P. Vanlaer, "Adaptive Vertex Fitting", *CMS Note CMS-NOTE-2007-008 (2007).* *http://cdsweb.cern.ch/record/1027031*.

[162] CMS Collaboration, "Tracking and Primary Vertex Results in First 7 TeV Collisions", *CMS Physics Analysis Summary CMS-PAS-TRK-10-005 (2010).* *http://cdsweb.cern.ch/record/1279383*.

[163] CMS Collaboration, "Studies of Tracker Material", *CMS Physics Analysis Summary CMS-PAS-TRK-10-003 (2010).* *http://cdsweb.cern.ch/record/1279138*.

[164] CMS Collaboration, "Measurement of the Differential Cross Section for Isolated Prompt Photon Production in pp Collisions at 7 TeV", *Phys. Rev.* **D84** (2011) 052011, arXiv:1108.2044. CMS-QCD-10-037. CERN-PH-EP-2011-128. http://cdsweb.cern.ch/record/1374176. doi:10.1103/PhysRevD.84.052011.

[165] CMS ECAL Collaboration, "CMS Preshower Project website". http://cms-ecal.web.cern.ch/cms-ecal/preshower.

[166] P. Adzic et al., "Energy resolution of the barrel of the CMS electromagnetic calorimeter", *JINST* **2** (2007) P04004. doi:10.1088/1748-0221/2/04/P04004.

[167] CMS Collaboration, "Missing transverse energy performance of the CMS detector", *JINST* **6** (2011) P09001, arXiv:1106.5048. CMS-JME-10-009. CERN-PH-EP-2011-051. http://cdsweb.cern.ch/record/1361632. doi:10.1088/1748-0221/6/09/P09001.

[168] CMS Collaboration, "Measurement of energy flow at large pseudorapidities in pp collisions at $\sqrt{s} = 0.9$ and 7 TeV", *JHEP* **1111** (2011) 148, arXiv:1110.0211. CMS-FWD-10-011. CERN-PH-EP-2011-086. http://cdsweb.cern.ch/record/1350822. doi:10.1007/JHEP11(2011)148.

[169] CMS Collaboration, "Transverse-momentum and pseudorapidity distributions of charged hadrons in pp collisions at $\sqrt{s} = 0.9$ and 2.36 TeV", *Journal of High Energy Physics* **2010** (2010) 41, arXiv:1002.0621. CMS-QCD-09-010. CERN-PH-EP-2010-003. http://cdsweb.cern.ch/record/1237408. doi:10.1007/JHEP02(2010)041.

[170] CMS Collaboration, "Performance of the CMS Level-1 Trigger during commissioning with cosmic ray muons and LHC beams", *Journal of Instrumentation* **5** (2010), no. 03, T03002, arXiv:0911.5422. CMS-CFT-09-013. http://cdsweb.cern.ch/record/1225373. doi:10.1088/1748-0221/5/03/T03002.

[171] S. Cittolin, "CMS DAQ Poster: Data Flow". http://home.fnal.gov/~ichiro/cmsevm.

[172] CMS HLT Collaboration, "HLT config browser". http://j2eeps.cern.ch/cms-project-confdb-hltdev/browser/.

[173] CERN Communication Group, "The Grid (CERN Brochure)", *CERN, Geneva* (2009). CERN-Brochure-2009-008-Eng http://cdsweb.cern.ch/record/1214400.

[174] CMS Collaboration, "Commissioning of the CMS experiment and the cosmic run at four tesla", *Journal of Instrumentation* **5** (2010), no. 03, T03001, arXiv:0911.4845. CMS-CFT-09-008. http://cdsweb.cern.ch/record/1223942. doi:10.1088/1748-0221/5/03/T03001.

[175] ALEPH Collaboration, "Performance of the ALEPH detector at LEP", *Nucl.Instrum.Meth.* **A360** (1995) 481–506. CERN-PPE-94-170 http://cdsweb.cern.ch/record/272484. doi:10.1016/0168-9002(95)00138-7.

[176] CDF Collaboration, "Measurement of $\sigma(p\bar{p} \to Z) \cdot \mathcal{B}(Z \to \tau\tau)$ in $p\bar{p}$ Collisions at $\sqrt{s} = 1.96\,\text{TeV}$", *Phys. Rev. D* **75** (2007) 092004. doi:10.1103/PhysRevD.75.092004.

[177] Galea, C.F., "Measurement of $\sigma(p\bar{p} \to Z) \cdot \text{Br}(Z \to \tau^+\tau^-)$ and search for Higgs bosons decaying to $\tau^+\tau^-$ at $\sqrt{s} = 1.96\,\text{TeV}$", *PhD thesis, NIKHEF (2008)* PDF File.

[178] CMS Collaboration, "Particle-Flow Event Reconstruction in CMS and Performance for Jets, Taus and $E_{\text{T}}^{\text{miss}}$", *CMS Physics Analysis Summary CMS-PAS-PFT-09-001 (2009).* http://cdsweb.cern.ch/record/1194487.

[179] CMS Collaboration, "Commissioning of the Particle-Flow Reconstruction in Minimum-Bias and Jet Events from pp Collisions at 7 TeV", *CMS Physics Analysis Summary CMS-PAS-PFT-10-002 (2010).* http://cdsweb.cern.ch/record/1279341.

[180] Bernet, C., "Status of PF Photons", *CMS HyperNews:* susy-allhadronic/246.

[181] Benedetti, D., "Photon PF integration: status, plans and possible gains for the analysis", 17-05-2011. Talk at the CMS Physics Week: CERN Indico 139197.

[182] Janot, P., "Particle Flow Event Reconstruction from LEP to LHC", 05-02-2011. Talk at EDIT 2011: CERN Indico 96989.

[183] James A.C. Ballin, "Particle Flow at CMS & the ILC", *Ph.D. Thesis, CERN-THESIS-2010-086* (2010). http://cdsweb.cern.ch/record/1272459.

[184] CMS Collaboration, "Track reconstruction in the CMS Tracker", *CMS Physics Analysis Summary CMS-PAS-TRK-09-001 (2009).* *http://cdsweb.cern.ch/record/934067*.

[185] CMS Collaboration, "Identification and Filtering of Uncharacteristic Noise in the CMS Hadron Calorimeter", *JINST 5 (2010)* T03014, arXiv:0911.4881. CMS-CFT-09-019. http://cdsweb.cern.ch/record/1223941. doi:10.1088/1748-0221/5/03/T03014.

[186] CMS Collaboration, "HCAL performance from first collisions data", *CMS Detector Performance Summary CMS-DP-2010-025 (2010).* *http://cdsweb.cern.ch/record/1364222*.

[187] CMS Collaboration, "Electromagnetic calorimeter commissioning and first results with 7 TeV data", *CMS Note CMS-NOTE-2010-012 (2010).* *http://cdsweb.cern.ch/record/1278160*.

[188] CMS Collaboration, "Isolated Photon Reconstruction and Identification at $\sqrt{s} = 7$ TeV", *CMS Physics Analysis Summary CMS-PAS-EGM-10-006 (2010).* *http://cdsweb.cern.ch/record/1324545*.

[189] CMS Collaboration, "Commissioning of the Particle-Flow Event Reconstruction with the first LHC collisions recorded in the CMS detector", *CMS Physics Analysis Summary CMS-PAS-PFT-10-001 (2010).* *http://cdsweb.cern.ch/record/1247373*.

[190] G. P. Salam, "Towards Jetography", *Eur. Phys. J.* **C67** (2010) 637–686, arXiv:0906.1833. doi:10.1140/epjc/s10052-010-1314-6.

[191] CMS Collaboration Collaboration, "Determination of Jet Energy Calibration and Transverse Momentum Resolution in CMS", *JINST* **6** (2011) P11002, arXiv:1107.4277. CMS-JME-10-011. CERN-PH-EP-2011-102. http://cdsweb.cern.ch/record/1369486. doi:10.1088/1748-0221/6/11/P11002.

[192] CMS Collaboration, "The Jet Plus Tracks Algorithm for Calorimeter Jet Energy Corrections in CMS", *CMS Physics Analysis Summary CMS-PAS-JME-09-002 (2009).* *http://cdsweb.cern.ch/record/1190234*.

[193] CMS JETMET POG, "Plans for Jet Energy Corrections at CMS", *CMS Internal Analysis Note CMS-AN-2007-055 (2008) related to Analysis CMS-PAS-JME-07-002*.

[194] R. Harris and K. Kousouris, "MC Truth L2 & L3 Factorized Jet Corrections at CMS", *CMS Analysis Note CMS-AN-2008-003 (2008) related to Analysis CMS-PAS-JME-07-002*.

[195] K. Kousouris. Private Communication, 2011.

[196] R. Ciesielski, H. Held, P. Schieferdecker et al., "Jet Energy Resolutions Derived from QCD Simulation for the Analysis of First $\sqrt{s} = 7$ TeV Collision Data", *CMS Analysis Note CMS-AN-2010-121 (2010) related to Analysis CMS-PAS-JME-10-003*.

[197] Mark Joseph Oreglia, "A study of the reactions $\psi' \to \gamma\gamma\psi$", *Ph.D. Thesis, SLAC (1980). Crystal Ball experiment at SPEAR.* `slac-r-236.pdf`.

[198] CMS Collaboration, "Jet performance in pp Collisions at $\sqrt{s} = 7$ TeV", *CMS Physics Analysis Summary CMS-PAS-JME-10-003 (2010).* `http://cdsweb.cern.ch/record/1279362` (2010).

[199] CMS Collaboration, "Search for new physics at CMS with jets and missing momentum", *CMS Physics Analysis Summary CMS-PAS-SUS-10-005 (2011).* `http://cdsweb.cern.ch/record/1343076`.

[200] CMS Collaboration, "Missing Transverse Energy Performance in Minimum-Bias and Jet Events from Proton-Proton Collisions at $\sqrt{s} = 7$ TeV", *CMS Physics Analysis Summary CMS-PAS-JME-10-004 (2010),* `http://cdsweb.cern.ch/record/1279142`.

[201] CMS ECAL, HCAL and MUON DPG, "Beam Halo Event Identification in CMS Using the CSCs, ECAL and HCAL", *CMS Internal Analysis Note CMS-AN-2010-111 (2010) related to Analyses CMS-PAS-JME-10-004 and CMS-PAS-MUO-10-004*.

[202] CMS Collaboration, "Photon reconstruction and identification at $\sqrt{s} = 7$ TeV", *CMS Physics Analysis Summary CMS-PAS-EGM-10-005 (2010).* `http://cdsweb.cern.ch/record/1279143`.

[203] CMS ECAL DPG, "Review of clustering algorithms and energy corrections in ECAL", *CMS Internal Note CMS-IN-10-008 (2010)*.

[204] Pasquale Musella, "Measurement of the inclusive photon production cross section and study of associated W-photon production in proton-proton collisions at the LHC", *Ph.D. Thesis CMS TS-2011-50 CERN-THESIS-2010-240* (2010). `http://cdsweb.cern.ch/record/1386726`.

[205] CMS Collaboration, "Electromagnetic calorimeter calibration with 7 TeV data", *CMS Physics Analysis Summary CMS-PAS-EGM-10-003 (2010).* `http://cdsweb.cern.ch/record/1279350`.

[206] CMS Collaboration, "Time reconstruction and performance of the CMS electromagnetic calorimeter", *Journal of Instrumentation* **5** (2010), no. 03, T03011. 27p., `arXiv:0911.4044`. CMS-CFT-09-006 `http://cdsweb.cern.ch/record/1223866`. `doi:10.1088/1748-0221/5/03/T03011`.

[207] CMS Collaboration, "Track finding and identification of converted photons", *CMS Note CMS-NOTE-2006-005 (2006).* `http://cdsweb.cern.ch/record/927374`.

[208] CMS Collaboration, "Measurement of the Isolated Prompt Photon Production Cross Section in pp Collisions at sqrt(s) = 7 TeV", *Phys. Rev. Lett.* **106** (2011) 082001, arXiv:1012.0799. CMS-QCD-10-019. CERN-PH-EP-2010-053. http://cdsweb.cern.ch/record/1311554. doi:10.1103/PhysRevLett.106.082001.

[209] Andrew Askew, "The Overcomplete Annotated reco::Photon", 2009. CMS Internal Twiki page: PhotonIDTechnicalBreakout.

[210] T. C. Awes et al., "A simple method of shower localization and identification in laterally segmented calorimeters", *Nucl. Instrum. Meth.* **A311** (1992) 130. doi:10.1016/0168-9002(92)90858-2.

[211] CMSSW Source Code: http://cmslxr.fnal.gov/lxr/source/RecoEgamma/EgammaIsolationAlgos/src/PhotonTkIsolation.cc.

[212] CMSSW Source Code: http://cmslxr.fnal.gov/lxr/source/RecoEgamma/PhotonIdentification/python/isolationCalculator_cfi.py.

[213] CMS ECAL DPG, "Photon Efficiency Measurements using Tag and Probe", *CMS Internal Analysis Note CMS-AN-2010-292 (2010) related to Analysis CMS-PAS-EGM-10-006*.

[214] Tabarelli, T., "Status Report on ECAL spike events", 10-02-2010. Talk at the CMS General Weekly Meeting (GWM 5): CERN Indico 81371.

[215] CMS ECAL DPG, "Data-Driven Estimation of Residual Spike Contamination in Photon Candidates", *CMS Internal Analysis Note CMS-AN-2010-340 (2010) related to Analysis CMS-PAS-EGM-10-006*.

[216] CMS QCD Photons Group, "Measurement of isolated photon production cross section in pp collisions at $\sqrt{s}$ = 7 TeV", *CMS Internal Analysis Note CMS-AN-2010-268 (2010) related to Analysis CMS-PAS-QCD-10-019*.

[217] Janot, P., "ECAL Cleaning and PF integration", 4-11-2010. Talk at the ECAL DPG Meeting: CERN Indico 107816.

[218] S. Argiro, "Rechit flagging and spike cleaning in CMSSW 4.2", 3-03-2011. Talk at the ECAL DPG Meeting: CERN Indico 129589.

[219] CMS Collaboration, "Measurements of Inclusive W and Z Cross Sections in pp Collisions at sqrt(s)=7 TeV", *JHEP* **01** (2011) 080, arXiv:1012.2466. CMS-EWK-10-002. CERN-PH-EP-2010-050. http://cdsweb.cern.ch/record/1313495. doi:10.1007/JHEP01(2011)080.

[220] CMS Collaboration, "Reconstruction of Electrons with the Gaussian-Sum Filter in the CMS Tracker at the LHC", *CMS Note CMS-NOTE-2005-001 (2005).* *http://cdsweb.cern.ch/record/815410*.

[221] CMS Collaboration, "Electron reconstruction and identification at $\sqrt{s}$ = 7 TeV", *CMS Public Analysis Summary CMS-PAS-EGM-10-004 (2010).* http://cdsweb.cern.ch/record/1299116.

[222] CMS Collaboration, "Performance of CMS muon reconstruction in pp collision events at $\sqrt{s}$ = 7 TeV", *Submitted to JINST* (2012). CMS-MUO-10-004. CERN-PH-EP-2012-173. http://cdsweb.cern.ch/record/1456510.

[223] CMS Collaboration, "Performance of CMS Muon Reconstruction in Cosmic-Ray Events", *JINST 5 (2010)* (2010) T03022, arXiv:0911.4994. CMS-CFT-09-014. http://cdsweb.cern.ch/record/1224837. doi:10.1088/1748-0221/5/03/T03022.

[224] CMS Collaboration, "Measurement of Tracking Efficiency", *CMS Physics Analysis Summary CMS-PAS-TRK-10-002 (2010).* http://cdsweb.cern.ch/record/1279139.

[225] CMS Collaboration, "Performance of tau-lepton reconstruction and identification in CMS", *JINST* **7** (2012) P01001, arXiv:1109.6034. CMS-TAU-11-001. CERN-PH-EP-2011-137. http://cdsweb.cern.ch/record/1385560. doi:10.1088/1748-0221/7/01/P01001.

[226] CMS Collaboration, "Measurement of the Inclusive Z Cross Section via Decays to Tau Pairs in pp Collisions at $\sqrt{s}$ = 7 TeV", *JHEP* **1108** (2011) 117, arXiv:1104.1617. CMS-EWK-10-013. CERN-PH-EP-2011-035. http://cdsweb.cern.ch/record/1343465. doi:10.1007/JHEP08(2011)117.

[227] N. Dawe, "Tau reconstruction and identification performance in the ATLAS experiment". Poster at the PLHC 2011 Conference: CERN Indico 141546.

[228] M. Menegotto, G. Bruno, P. Zych et al., "Study on Additional RPC Planes for the Muon Trigger", *CMS Internal Note* (2001). CMS-IN-2001/003.

[229] R. Santonico and R. Cardarelli, "Development of resistive plate counters", *Nucl. Instrum. Meth.* **187** (1981) 377–380. doi:10.1016/0029-554X(81)90363-3.

[230] R. Santonico, R. Cardarelli, A. Di Biagio et al., "Progress in resistive plate counters", *Nucl. Instrum. Meth.* **A263** (1988) 20–25. doi:10.1016/0168-9002(88)91011-X.

[231] F. Ceradini, F. Cesaroni, F. Lacava et al., "A fast tracking level 1 muon trigger for high luminosity colliders using resistive plate chambers", *Proceedings of the Large Hadron Collider Workshop, Aachen, 4-9 October 1990, p.99. CERN-90-10-V-3. ECFA-90-133-V-3.* http://cdsweb.cern.ch/record/215299 (1990).

[232] G. L. Bencze et al., "Study of resistive plate chambers for muon detection at hadron colliders", *Nucl. Instrum. Meth.* **A340** (1994) 466–473. doi:10.1016/0168-9002(94)90127-9.

[233] CMS Collaboration, "Performance study of the CMS barrel resistive plate chambers with cosmic rays", *Journal of Instrumentation* **5** (2010), no. 03, T03017,

arXiv:0911.4045. CMS-CFT-09-010.
http://cdsweb.cern.ch/record/1223867.
doi:10.1088/1748-0221/5/03/T03017.

[234] M. Abbrescia, A. Colaleo, G. Iaselli et al., "New developments on front end electronics for the CMS Resistive Plate Chambers", *Nucl.Instrum.Meth.* **A456** (2000) 143–149. doi:10.1016/S0168-9002(00)00980-3.

[235] A. Fridman and L. A. Kennedy, "Plasma Physics and Engineering". Taylor and Francis, New York, 2004. ISBN-9781560328483.

[236] N. Aleksandrov and E. Bazelyan, "Ionization processes in spark discharge plasmas", *Plasma Sources Science and Technology* **8** (1999), no. 2, 285. doi:10.1088/0963-0252/8/2/309.

[237] R. Cardarelli, A. Di Ciaccio, and R. Santonico, "Performance of a resistive plate chamber operating with pure CF_3Br", *Nucl. Instrum. Meth.* **A333** (1993) 399–403. doi:10.1016/0168-9002(93)91182-M.

[238] LAA Project Collaboration, "The Nonspark mode and high rate operation of resistive parallel plate chambers", *Nucl. Instrum. Meth.* **A337** (1993) 370–381. doi:10.1016/0168-9002(94)91105-3.

[239] I. Crotty, J. Lamas Valverde, G. Laurenti et al., "Further studies of avalanche mode operation of resistive parallel plate chambers", *Nucl. Instrum. Meth.* **A346** (1994) 107–113. doi:10.1016/0168-9002(94)90693-9.

[240] R. Cardarelli, R. Santonico, and V. Makeev, "Avalanche and streamer mode operation of resistive plate chambers", *Nucl. Instrum. Meth.* **A382** (1996) 470–474. doi:10.1016/S0168-9002(96)00811-X.

[241] M. Abbrescia et al., "Resistive plate chambers in avalanche mode: A comparison between model predictions and experimental results", *Nucl. Instrum. Meth.* **A409** (1998) 1–5. doi:10.1016/S0168-9002(97)01225-4.

[242] BaBar Collaboration, "The BaBar instrumented flux return performance: Lessons learned", *Nucl. Instrum. Meth.* **A494** (2002) 455–463. doi:10.1016/S0168-9002(02)01532-2.

[243] BABAR RPC Collaboration, "Experience with the resistive plate chamber in the BaBar experiment", *Prepared for 9th ICATPP Conference on Astroparticle, Particle, Space Physics, Detectors and Medical Physics Applications, Villa Erba, Como, Italy, 17-21 Oct 2005*. ttslac-pub-12204.pdf.

[244] Y. Hoshi, N. Kikuchi, T. Nagamine et al., "Performance of the endcap RPC in the Belle detector under high luminosity operation of the KEKB accelerator", *Nucl. Phys. Proc. Suppl.* **158** (2006) 190–194. doi:10.1016/j.nuclphysbps.2006.07.013.

[245] C. Lu, "RPC experience: Belle, BaBar and BESIII", *ECONF* **C0508141** (2005) ALCPG1001. slac-pub-11744.pdf.

[246] M. Abbrescia et al., "Effect of the linseed oil surface treatment on the performance of resistive plate chambers", *Nucl. Instrum. Meth.* **A394** (1997) 13–20. doi:10.1016/S0168-9002(97)00597-4.

[247] M. Abbrescia, "The dynamic behaviour of Resistive Plate Chambers", *Nucl. Instrum. Meth.* **A533** (2004) 7–10. doi:10.1016/j.nima.2004.06.119.

[248] R. Guida, "The Resistive Plate Chamber detectors at the Large Hadron Collider experiments", 02-10-2009. Detector Seminar: CERN Indico 68937.

[249] M. Abbrescia et al., "Properties of $C_2H_2F_4$ based gas mixture for avalanche mode operation of resistive plate chambers", *Nucl. Instrum. Meth.* **A398** (1997) 173–179. doi:10.1016/S0168-9002(97)00689-X.

[250] F. Loddo, "Front end electronics for RPC detectors of CMS", *Scientifica Acta Universita degli studi di Pavia* **XIII** (1998). Proceedings of the IV International Workshop on Resistive Plate Chambers and Related Detectors, Napoli Oct 15–16 1997, http://siba.unipv.it/fisica/Scientifica Acta scanner originali/XIII/XIII_2.pdf.

[251] Y. Ban et al., "Beam Test of the First Production Forward RPC", *CMS Note* (2004). CMS-NOTE-2004/037.

[252] I. Ahmed et al., "Radiation Environment Simulations for the CMS Detector", *CMS Note* (2008). CMS-NOTE-2008/030.

[253] F. Loddo. Private Communication, 2008.

[254] M. Abbrescia et al., "The simulation of resistive plate chambers in avalanche mode: Charge spectra and efficiency", *Nucl. Instrum. Meth.* **A431** (1999) 413–427. doi:10.1016/S0168-9002(99)00374-5.

[255] W. Riegler, "Induced signals in resistive plate chambers", *Nucl. Instrum. Meth.* **A491** (2002) 258–271. doi:10.1016/S0168-9002(02)01169-5.

[256] G. Carboni et al., "A Model for RPC detectors operating at high rate", *Nucl. Instrum. Meth.* **A498** (2003) 135–142. doi:10.1016/S0168-9002(02)02082-X.

[257] C. Lippmann, R. Stock, and W. Riegler, "Detector Physics of Resistive Plate Chambers", *CERN-THESIS-2003-035* (2003). http://cdsweb.cern.ch/record/1303626.

[258] S. H. Ahn et al., "Aspects of operational conditions of a double gap prototype RPC for the CMS/LHC experiment", *Nucl. Instrum. Meth.* **A465** (2001) 447–454. doi:10.1016/S0168-9002(01)00623-4.

[259] M. Abbrescia et al., "Performance of a Resistive Plate Chamber operated in avalanche mode under ^{137}Cs irradiation", *Nucl. Instrum. Meth.* **A392** (1997) 155–160. doi:10.1016/S0168-9002(97)00240-4.

[260] E. Cerron Zeballos et al., "A New type of resistive plate chamber: The Multigap RPC", *Nucl. Instrum. Meth.* **A374** (1996) 132–136. doi:10.1016/0168-9002(96)00158-1.

[261] A. Akindinov et al., "The multigap resistive plate chamber as a time-of-flight detector", *Nucl. Instrum. Meth.* **A456** (2000) 16–22. doi:10.1016/S0168-9002(00)00954-2.

[262] W. Riegler, C. Lippmann, and R. Veenhof, "Detector physics and simulation of resistive plate chambers", *Nucl. Instrum. Meth.* **A500** (2003) 144–162. doi:10.1016/S0168-9002(03)00337-1.

[263] W. Riegler and C. Lippmann, "The physics of resistive plate chambers", *Nucl. Instrum. Meth.* **A518** (2004) 86–90. doi:10.1016/j.nima.2003.10.031.

[264] C. Lippmann and W. Riegler, "Space charge effects in resistive plate chambers", *Nucl. Instrum. Meth.* **A517** (2004) 54–76. doi:10.1016/j.nima.2003.08.174.

[265] M. Abbrescia et al., "An environmental safe gas mixture for resistive plate chambers operated at low pressure", *Nucl. Instrum. Meth.* **A417** (1998) 16–23. doi:10.1016/S0168-9002(98)00657-3.

[266] P. Camarri, R. Cardarelli, A. Di Ciaccio et al., "Streamer suppression with SF_6 in RPCs operated in avalanche mode", *Nucl. Instrum. Meth.* **A414** (1998) 317–324. doi:10.1016/S0168-9002(98)00576-2.

[267] M. Abbrescia et al., "Resistive plate chambers performances at cosmic rays fluxes", *Nucl. Instrum. Meth.* **A359** (1995) 603–609. doi:10.1016/0168-9002(94)01698-4.

[268] M. Abbrescia et al., "Resistive plate chambers performances at low pressure", *Nucl. Instrum. Meth.* **A394** (1997) 341–348. doi:10.1016/S0168-9002(97)00681-5.

[269] S. H. Ahn et al., "Temperature and humidity dependence of bulk resistivity of bakelite for resistive plate chambers in CMS", *Nucl. Instrum. Meth.* **A451** (2000) 582–587. doi:10.1016/S0168-9002(00)00329-6.

[270] G. Aielli et al., "Electrical conduction properties of phenolic-melaminic laminates", *Nucl. Instrum. Meth.* **A533** (2004) 86–92. doi:10.1016/j.nima.2004.07.006.

[271] CMS Collaboration, "Muon System", *CMS Detector Posters* (2000). cms-docdb: CMS-doc-4227-v1.

[272] G. Bruno, J. Krolikowski, M. I. Kudla et al., "RPC System Geometry Simulated in CMSIM 118-120 and ORCA 4.2", *CMS Internal Note* (2000). CMS-IN-2000/054.

[273] J. Krolikowski, P. Zych, and G. Wrochna, "Acceptance of the Baseline and Modified RPC System Geometry", *CMS Internal Note* (2001). CMS-IN-2001/026.

[274] G. Bruno and M. Konecki, "Simulation of the Baseline RPC Trigger System for CMS: Efficiency and Output Rates in Single Muon Topology", *CMS Internal Note* (2001). CMS-IN-2001/012.

[275] M. Huhtinen, "Radiation Environment Simulations for the CMS Detector", *CMS Technical Note* (1995). CMS-TN-1995/198.

[276] N. A.I.Drozhdin, M.Huhtinen, "Accelerator Related Background in the CMS Detector at LHC", *CMS Technical Note* (1996). CMS-TN-1996/056.

[277] A. I. Drozhdin, M. Huhtinen, and N. V. Mokhov, "Accelerator related background in the CMS detector at LHC", *Nucl. Instrum. Meth.* **A381** (1996) 531–544. doi:10.1016/S0168-9002(96)00807-8.

[278] M. Huhtinen et al., "Conceptual design and performance of the CMS forward shielding", *CMS Internal Note* (2000). CMS-IN-2000/051.

[279] M. Huhtinen et al., "Optimization of the CMS forward calorimeter radiation shielding", *CMS Internal Note* (2000). CMS-IN-2000/055.

[280] M. Huhtinen, "Optimization of the CMS forward shielding", *CMS Internal Note* (2000). CMS-IN-2000/068.

[281] M. Huhtinen, "Shielding of the high-eta edges of the endcap CSC chambers", *CMS Internal Note* (2002). CMS-IN-2002/001.

[282] M. Huhtinen, "Shielding of the HF photomultipliers", *CMS Internal Note* (2002). CMS-IN-2002/007.

[283] A. Fasso, A. Ferrari, J. Ranft et al., "FLUKA: Present status and future developments", *Given at 4th International Conference on Calorimetry in High-energy Physics, La Biodola, Italy, 19-25 September 1993,* http://www.fluka.org (1993).

[284] Cox, Timothy, "Tim Cox Homepage". Neutron background simulation in the Endcap Muon CSCs: http://ptc.web.cern.ch/ptc/down/nbgnd.html.

[285] T. Cox, "Progress on Neutron Background Studies for the Endcap Muon CSCs", 27-03-2001. Talk at the CMS Muon PRS Meeting: HTML Presentation, available at Tim Cox Homepage.

[286] T. Cox, "Review of neutron background studies in the Endcap Muon CSCs", 26-04-2001. Talk at the CMS Muon PRS Meeting: HTML Presentation and PDF Presentation, both available at Tim Cox Homepage.

[287] Grzegorz Wrochna, "Muon Trigger of the CMS Detector for LHC", *CMS Note and Ph.D. Thesis* (1997). CMS-NOTE-1997/096.

[288] M. Abbrescia and et al, "Resistive plate chamber neutron and gamma sensitivity measurement with a ^{252}Cf source", *Nucl. Instrum. Meth.* **A506** (2003), no. 1-2, 101 – 109. doi:10.1016/S0168-9002(03)01378-0.

[289] V. Khotilovich and R. Wilkinson, "Neutron Background Simulation: Infrastructure and Validation", 30-08-2010. Talk at the CMS Full Simulation Meeting: CERN Indico 98920.

[290] Y. Fisyak, K. McFarlane, and G. Mitselmakher, "Neutron and Gamma backgrounds in GEM & CMS Muon Systems", *CMS Technical Note* (1994). CMS-TN-1994/147.

[291] Y. Fisyak, K. McFarlane, and G. Mitselmakher, "Evaluation of the CMS Muon Endcap Shielding", *CMS Technical Note* (1996). CMS-TN-1996/076.

[292] V. Khotilovich, "RPC Simulation Related Issues for the Upgrade", 07-10-2010. Talk at the CMS RPC & RC Meeting: CERN Indico 109165.

[293] V. Khotilovich, R. Wilkinson, and A. Safonov, "Neutron Backgrounds Simulation in CSC", 21-09-2010. Talk at the CMS CSC Neutron Meeting: CERN Indico 107674.

[294] Constantini, Silvia, "Muon Performance Paper: Background Section", 29-03-2011. Talk at the CMS RPC DPG Meeting: CERN Indico 132149.

[295] Hannes Sakulin, "Design and Simulation of the First Level Global Muon Trigger for the CMS Experiment at CERN", *Ph.D. Thesis* (2002). http://cdsweb.cern.ch/record/1324143.

[296] R. Wilkinson, I. Bloch, and N. Neumeister, "Recent ME4/2 simulation work", 26-07-2008. Talk at the CMS CSC ME1/1 Meeting: CERN Indico 38295.

[297] R. Wilkinson and T. Cox, "Neutron Background Simulation", 27-04-2009. Talk at the CMS DPG-PH Muon Meeting: CERN Indico 55712.

[298] CMS Collaboration, "Search for Supersymmetry in pp Collisions at 7 TeV in Events with Jets and Missing Transverse Energy", *Phys. Lett. B* **698** (2011) 196, arXiv:1101.1628. CMS-SUS-10-003. CERN-PH-EP-2010-084. http://cdsweb.cern.ch/record/1320934. doi:10.1016/j.physletb.2011.03.021.

[299] CMS Collaboration, "Search for New Physics with Jets and Missing Transverse Momentum in pp collisions at sqrt(s) = 7 TeV", *JHEP* **1108** (2011) 155, arXiv:1106.4503. CMS-SUS-10-005. CERN-PH-EP-2011-065. http://cdsweb.cern.ch/record/1360985. doi:10.1007/JHEP08(2011)155.

[300] CMS Collaboration, "Inclusive search for squarks and gluinos in pp collisions at sqrt(s) = 7 TeV", *Phys. Rev.* **D85** (2012) 012004, arXiv:1107.1279. CMS-SUS-10-009. CERN-PH-EP-2011-099. http://cdsweb.cern.ch/record/1365689. doi:10.1103/PhysRevD.85.012004.

[301] CMS Collaboration Collaboration, "Search for supersymmetry in pp collisions at sqrt(s)=7 TeV in events with a single lepton, jets, and missing transverse momentum", *JHEP* **1108** (2011) 156, arXiv:1107.1870. CMS-SUS-10-006. CERN-PH-EP-2011-084. http://cdsweb.cern.ch/record/1366381. doi:10.1007/JHEP08(2011)156.

[302] CMS Collaboration Collaboration, "Search for new physics with same-sign isolated dilepton events with jets and missing transverse energy at the LHC", *JHEP* **1106** (2011) 077, arXiv:1104.3168. CMS-SUS-10-004. CERN-PH-EP-2011-033. http://cdsweb.cern.ch/record/1345080. doi:10.1007/JHEP06(2011)077.

[303] CMS Collaboration Collaboration, "Search for Physics Beyond the Standard Model in Opposite-Sign Dilepton Events at $\sqrt{s}$ = 7 TeV", *JHEP* **1106** (2011) 026, arXiv:1103.1348. CMS-SUS-10-007. CERN-PH-EP-2011-016. http://cdsweb.cern.ch/record/1333985. doi:10.1007/JHEP06(2011)026.

[304] CMS Collaboration, "Search for Physics Beyond the Standard Model in Z + MET + Jets events at the LHC", *CMS Physics Analysis Summary CMS-PAS-SUS-10-010 (2011).* http://cdsweb.cern.ch/record/1354224.

[305] CMS Collaboration Collaboration, "Search for Physics Beyond the Standard Model Using Multilepton Signatures in pp Collisions at sqrt(s)=7 TeV", *Phys.Lett.* **B704** (2011) 411–433, arXiv:1106.0933. CMS-SUS-10-008. CERN-PH-EP-2011-046. http://cdsweb.cern.ch/record/1356211. doi:10.1016/j.physletb.2011.09.047.

[306] CMS Collaboration Collaboration, "Search for Supersymmetry in pp Collisions at $\sqrt{s}$ = 7 TeV in Events with Two Photons and Missing Transverse Energy", *Phys.Rev.Lett.* **106** (2011) 211802, arXiv:1103.0953. CMS-SUS-10-002. CERN-PH-EP-2011-007. http://cdsweb.cern.ch/record/1333965. doi:10.1103/PhysRevLett.106.211802.

[307] CMS Collaboration Collaboration, "Search for supersymmetry in events with a lepton, a photon, and large missing transverse energy in pp collisions at sqrt(s) = 7 TeV", *JHEP* **1106** (2011) 093, arXiv:1105.3152. CMS-SUS-11-002. CERN-PH-EP-2011-058. http://cdsweb.cern.ch/record/1349283. doi:10.1007/JHEP06(2011)093.

[308] CMS Collaboration Collaboration, "Search for Supersymmetry in Events with b Jets and Missing Transverse Momentum at the LHC", *JHEP* **1107** (2011) 113, arXiv:1106.3272. CMS-SUS-10-011. CERN-PH-EP-2011-067. http://cdsweb.cern.ch/record/1359615. doi:10.1007/JHEP07(2011)113.

[309] CMS SUSY RA2 group, "Inclusive Search for new physics at CMS with the jets and missing momentum signature", *CMS Internal Analysis Note CMS-AN-2010-417 (2010) related to Analysis CMS-PAS-SUS-10-005.*

[310] CMS SUSY RA2 group, "Inclusive search for SUSY at CMS with the jets plus missing momentum signature", *CMS Internal Analysis Note CMS-AN-2010-260 (2010).*

[311] CMS SUSY RA2 group, "Data-Driven Prediction with the Reabalance+Smear Method of the QCD Background for the RA2 Inclusive Hadronic SUSY Search", *CMS Internal Analysis Note CMS-AN-2010-401 (2010) related to Analysis CMS-PAS-SUS-10-005.*

[312] CMS Collaboration, "Measurement of the Inclusive Jet Cross Section in pp Collisions at sqrt(s) = 7 TeV", *Phys. Rev. Lett.* **107** (2011) 132001, arXiv:1106.0208. CMS-QCD-10-011. CERN-PH-EP-2011-053. http://cdsweb.cern.ch/record/1355680. doi:10.1103/PhysRevLett.107.132001.

[313] CMS QCD PAG, "Measurement of the inclusive jet and b-jet production in pp collisions at $\sqrt{s} = 7$ TeV using Particle Flow", *CMS Internal Analysis Note CMS-AN-2010-128 (2010) related to Analysis CMS-PAS-QCD-10-011 and CMS-PAS-BPH-10-009*.

[314] CMS Physics Validation Team, "Collisions 2010 Recipes". CMS Internal Twiki page: `Collisions2010Recipes`.

[315] CMS Prompt Feedback Group, "CMS Pixel Background and Beambackground 2010". CMS Internal Twiki page: `CmsBkgPixel`, CMS Internal Twiki page: `BeamBackground2010`.

[316] N. Bacchetta, "Beam Background Summary". CMS HyperNews: `prompt-feedback/91`.

[317] CMS SUSY RA2 Group, "Studies on ECAL Dead and Masked Channel Contributions to High MET and MHT", *CMS Internal Analysis Note CMS-AN-2010-354 (2010) related to Analysis CMS-PAS-SUS-10-005*.

[318] CMS SUSY RA2 Group, "Fake high missing momentum events in the RA2 analysis", *CMS Internal Analysis Note CMS-AN-2010-383 (2010) related to Analysis CMS-PAS-SUS-10-005*.

[319] N. Saoulidou, "PF Jet ID and High MHT Tails", 25-11-2010. Talk at the JETMET Jet Algorithms Meeting: CERN Indico 114252.

[320] S. Agostinelli et al., "GEANT4 – A Simulation Toolkit", *Nucl. Instrum. and Meth.* **506** (2003) 250. `doi:10.1016/S0168-9002(03)01368-8`.

[321] N. Kidonakis, "Next-to-next-to-leading Soft-Gluon Corrections for the Top Quark Cross Section and Transverse Momentum Distribution", *Phys. Rev. D* **82** (2010) 114030, `arXiv:1009.4935`. `doi:10.1103/PhysRevD.82.114030`.

[322] K. Melnikov and F. Petriello, "Electroweak Gauge Boson Production at Hadron Colliders through $O(\alpha(s)^2)$", *Phys. Rev.* **D74** (2006) 114017, `arXiv:hep-ph/0609070`. `doi:10.1103/PhysRevD.74.114017`.

[323] W. Beenakker, R. Hopker, and M. Spira, "PROSPINO: A program for the PROduction of Supersymmetric Particles In Next-to-leading Order QCD". 1996. `arXiv:hep-ph/9611232`.

[324] CMS SUSY RA2 group, "W and $\mathrm{t\bar{t}}$ background estimation for all-hadronic searches for new physics", *CMS Internal Analysis Note CMS-AN-2010-203 (2010) related to Analysis CMS-PAS-SUS-10-005*.

[325] CMS SUSY RA2 group, "Data-Driven Prediction of the Hadronically Decaying Tau Background for the RA2 Inclusive Hadronic SUSY Search", *CMS Internal Analysis Note CMS-AN-2010-402 (2010) related to Analysis CMS-PAS-SUS-10-005*.

[326] Sue Ann Koay, "A Search for Dark Matter Production with Jets and Missing Momentum Signature in Proton-Proton Collisions at 7 TeV", *Ph.D. Thesis CMS TS-2011-024 CERN-THESIS-2011-091* (2011). `http://cdsweb.cern.ch/record/1382400`.

[327] CMS SUSY RA2 group, "QCD background prediction by factorization for all-hadronic SUSY searches", *CMS Internal Analysis Note CMS-AN-2010-204 (2010) related to Analysis CMS-PAS-SUS-10-005*.

[328] CMS Collaboration, "Data-Driven Estimation of the Invisible Z Background to the SUSY MET Plus Jets Search", *CMS Physics Analysis Summary CMS-PAS-SUS-08-002 (2008).* http://cdsweb.cern.ch/record/1194471.

[329] J. Incandela et al., "Data-Driven Estimation of the Invisible Z Background to the Early MET plus Jets search", *CMS Internal Analysis Note CMS-AN-08-036 (2008) related to Analysis CMS-PAS-SUS-08-002*.

[330] S. Ask, M. Parker, T. Sandoval et al., "Using gamma+jets Production to Calibrate the Standard Model Z(nunu)+jets Background to New Physics Processes at the LHC", *JHEP* **1110** (2011) 058, arXiv:1107.2803. doi:10.1007/JHEP10(2011)058.

[331] S. Frixione, "Isolated photons in perturbative QCD", *Phys. Lett.* **B429** (1998) 369–374, arXiv:hep-ph/9801442. doi:10.1016/S0370-2693(98)00454-7.

[332] C. F. Berger et al., "Next-to-Leading Order QCD Predictions for W+3-Jet Distributions at Hadron Colliders", *Phys. Rev.* **D80** (2009) 074036, arXiv:0907.1984. (BlackHat Collaboration). doi:10.1103/PhysRevD.80.074036.

[333] C. F. Berger et al., "Next-to-Leading Order QCD Predictions for Z,gamma* + 3-Jet Distributions at the Tevatron", *Phys. Rev.* **D82** (2010) 074002, arXiv:1004.1659. (BlackHat Collaboration). doi:10.1103/PhysRevD.82.074002.

[334] H. Ita et al., "Precise Predictions for Z + 4 Jets at Hadron Colliders", *Phys. Rev.* **D85** (2012) 031501, arXiv:1108.2229. (BlackHat Collaboration). doi:10.1103/PhysRevD.85.031501.

[335] Z. Bern et al., "Driving Missing Data at Next-to-Leading Order", *Phys.Rev.* **D84** (2011) 114002, arXiv:1106.1423. (BlackHat Collaboration). doi:10.1103/PhysRevD.84.114002.

[336] CMS Collaboration, "Measurement of W-gamma and Z-gamma production in pp collisions at sqrt(s) = 7 TeV", *Phys. Lett.* **B701** (2011) 535–555, arXiv:1105.2758. CMS-EWK-10-008. CERN-PH-EP-2011-045. http://cdsweb.cern.ch/record/1350795. doi:10.1016/j.physletb.2011.06.034.

[337] R. Ichou and D. d'Enterria, "Sensitivity of isolated photon production at TeV hadron colliders to the gluon distribution in the proton", *Phys. Rev.* **D82** (2010) 014015, arXiv:1005.4529. doi:10.1103/PhysRevD.82.014015.

[338] CMS QCD Photons Group, "Theoretical Predictions for the Isolated Photon Cross Section in pp collisions at $\sqrt{s} = 7$ TeV and Correction of Non-perturbative Effects", *CMS Internal Analysis Note CMS-AN-10-272 (2010) related to Analysis CMS-PAS-QCD-10-019*.

[339] Z. Bern et al. (BlackHat Collaboration). Private Communication, 2010–2011.

[340] CMS QCD Photons Group, "Measurement of inclusive isolated photons with showershape in the endcap", *CMS Internal Analysis Note CMS-AN-2010-295 (2010) related to Analysis CMS-PAS-EGM-10-006*.

[341] CMS QCD Photons Group, "Measurement of Inclusive Isolated Photon Yields at sqrt(s)=7 TeV with Combined-isolation Template", *CMS Internal Analysis Note CMS-AN-2010-289 (2010) related to Analysis CMS-PAS-EGM-10-006*.

[342] CMS Collaboration, "Measurement of the Differential Isolated Prompt Photon Production Cross Section in pp Collisions at $\sqrt{s} = 7$ TeV", *CMS Physics Analysis Summary CMS-PAS-QCD-10-037*. http://cdsweb.cern.ch/record/1374176.

[343] CMS Collaboration, "Measuring Electron Efficiencies at CMS with Early Data", *CMS Physics Analysis Summary CMS-PAS-EGM-07-001 (2010)*. http://cdsweb.cern.ch/record/1194482.

[344] D. d'Enterria. Private Communication, 2010.

[345] A. Gehrmann-De Ridder and E. W. N. Glover, "Final state photon production at LEP", *Eur. Phys. J.* **C7** (1999) 29–48, arXiv:hep-ph/9806316. doi:10.1007/s100520050382.

[346] CMS SUSY RA3 Group, "A First Search for General Gauge Mediated Supersymmetry", *CMS Internal Analysis Note CMS-AN-2010-271 related to Analysis CMS-PAS-SUS-10-002*.

[347] CMS SUSY RA1 Group, "Search for a missing energy signature from New Physics in di-jet and multi-jet events", *CMS Internal Analysis Note CMS-AN-2010-242 related to Analysis CMS-PAS-SUS-10-003*.

[348] CMS ECAL DPG, "Test of the energy scale of the CMS ECAL with Z*ee* decays", *CMS Internal Analysis Note CMS-AN-2010-363*.

[349] D. Bourilkov, R. C. Group, and M. R. Whalley, "LHAPDF: PDF use from the Tevatron to the LHC", arXiv:hep-ph/0605240.

[350] Colin Bernet for the CMS Collaboration, "Searches for Supersymmetry at CMS using the 2010 Data", arXiv:1105.5911. Proceedings of the Moriond Electroweak 2011 conference.

[351] F. E. Paige et al., "ISAJET 7.69: A Monte Carlo Event Generator for pp, $p\bar{p}$, and e^+e^- Reactions". 2003. arXiv:hep-ph/0312045.

[352] A. L. Read, "Presentation of Search Results: The CL(s) Technique", *J. Phys. G* **28** (2002) 2693. doi:10.1088/0954-3899/28/10/313.

[353] T. Junk, "Confidence Level Computation for Combining Searches with Small Statistics", *Nucl. Instrum. and Meth. A* **434** (1999) 435. doi:10.1016/S0168-9002(99)00498-2.

[354] L. Randall and D. Tucker-Smith, "Dijet Searches for Supersymmetry at the LHC", *Phys. Rev. Lett.* **101** (2008) 221803, arXiv:0806.1049. doi:10.1103/PhysRevLett.101.221803.

[355] LHC New Physics Working Group Collaboration, "Simplified Models for LHC New Physics Searches", arXiv:1105.2838.

[356] J. Alwall, P. Schuster, and N. Toro, "Simplified Models for a First Characterization of New Physics at the LHC", *Phys.Rev.* **D79** (2009) 075020, arXiv:0810.3921. doi:10.1103/PhysRevD.79.075020.